UNIVERSITY OF ADELAIDE LIBRARY

Analysis of Composite Steel and Concrete Flexural Members that exhibit Partial Shear Connection

by

Matthew Burnet

Thesis Submitted for the Degree of

Doctor of Philosophy

Department of Civil and Environmental Engineering

University of Adelaide

Australia

Statement of Originality

I hereby declare that this thesis contains no material which has been accepted for the award of any other degree or diploma in any university and that, to the best of my knowledge and belief, this thesis contains no material previously published or written by any other person, except where due reference is made in the text of the thesis.

I consent to the thesis being made available for photocopying and loan if accepted for the award of the degree.

Signed ..... Dated 16/2/98

Synopsis

This thesis presents an analysis of composite members of steel and concrete which exhibit partial shear connection. Such situations are found in many structural systems which include but are not limited to composite beams, composite slabs, profiled beams, reinforced concrete beams strengthened by external plates and composite walls. Each of these composite structural systems uses a variety of methods to ensure adequate connection between the concrete and steel elements. The breakdown in bond between the concrete and the steel causes a reduction in the strength and stiffness of the composite member. It is the parameters controlling the behaviour of the interface bond that are the focus of this research.

Stud shear connectors, which are the most common form of shear connection in composite beams, have limited ductility and are prone to failure by fracture in beams with low degrees of shear connection. A new mathematical model has been developed which determines the maximum end slip at the ultimate moment, based on the geometric and material properties of the beam. This theoretical end slip can then be compared to the slip capacity of the shear connectors, and the design of the member changed if necessary. The results of the mathematical model compare favourably with published experimental results.

In composite members incorporating light gauge steel sheeting, such as in composite slabs and profiled beams, the shear connection is most commonly provided by mechanical interlock between the concrete and the rib geometry of the sheeting. Embossments are commonly provided on the ribs to enhance the shear connection performance. The performance of the shear connection is usually assessed by a number of full scale slab tests, using a range of parameters which encompass those expected in practice. A small scale test procedure is proposed as an alternative to full scale testing. This allows the shear connection performance of different rib and embossment geometries to the tested with relative ease.

The small scale test procedure accurately represents the forces acting on the sheeting and the concrete away from the supports. This is achieved by removing any external lateral clamping forces acting on the specimen. It was found for most rib geometries incorporating

embossments, including re-entrant dove-tail ribs, that as longitudinal slip progressed there was a tendency for the sheeting to move laterally away from the concrete. This result indicates that any externally applied lateral force during testing of the specimen, will effect the resulting behaviour.

Three series of tests were carried out on small scale specimens in order to investigate general qualitative effects of varying parameters such as the rib geometry, surface condition and thickness of the sheeting. It was found that shear resistance increased for ribs with an increasing re-entrant geometry, and increased with an increase in sheeting thickness. The relationship between shear resistance and sheeting thickness was approximately cubic, indicating that the shear resistance increased with the cube of the sheeting thickness. This increase was due to the greater passive normal forces that develop due to the increase in 'spring action', which in turn result in greater longitudinal shear resistance. There was a marked increase in the shear resistance with the addition of embossments.

A model describing the ultimate moment capacity of profiled beams has been developed. It is based on rigid plastic analysis, and requires an understanding of the load-slip characteristics of the sheeting used. Equations are derived which give the ultimate moment capacity of the profiled beam based on the degree of shear connection at the critical cross-section. The equations are derived for two different forms of construction; welded construction and clipped construction. It is shown that greater development lengths are required to develop full shear connection when clipped construction is used.

The behaviour of profiled beams was investigated through a series of 6 full scale profiled beam tests. The load-deflection response was determined, as well as the variation in slip at different locations along the beam. It was found that close to complete interaction was achieved for the 4 beams which incorporated L-Ribs in the profiled sheeting, whereas the 2 beams which had Dove-Tail ribs exhibited partial interaction. The loss in moment capacity due to the loss in shear connection was only slight. The results from the experimental tests were in close agreement with the values predicted using the theory developed.

A series of tests were carried out to investigate the effect of the side profiled sheeting on the transverse shear strength of profiled beams. A small scale test specimen was designed and used to obtain results on the shear performance of different rib geometries, as well as to determine the influence of various parameters such as sheeting thickness, surface condition and development length. The results of the tests were compared to predicted values using theory developed by other researchers. It was found that with modifications, the theory provided a reasonable estimate for the increase in transverse shear resistance due to the side profiled sheets.

Preface

This thesis is submitted for the degree of Doctor of Philosophy in the University of Adelaide, Adelaide Australia. The work described in the thesis was carried out by the candidate during the years 1992 - 1997 in the Department of Civil and Environmental Engineering under the supervision of Dr. Deric Oehlers.

The Bye-Laws of the University of Adelaide require a statement to be made which indicate which portions of the work are original. The author submits that, unless otherwise referenced in the text, the work presented in this thesis is original.

A number of journal and conference papers were written based on the work presented in this thesis. These are:

1. Burnet, M.J. and Oehlers, D.J., (1994), "Application of Profiled Sheeting as Integral Formwork for the Sides of Reinforced Concrete Beams", Australasian Structural Engineering Conference, Sydney, Australia, pp. 1139-1144.

2. Burnet, M.J. and Oehlers, D.J., (1995), "Design of steel and concrete composite beams with few shear connectors", Building for the 21st Century, Proceedings of the Fifth East Asia-Asia Pacific Conference on Structural Engineering and Construction (Edited by Loo, Y-C). Brisbane, Australia, pp. 481-486.

3. Burnet, M.J. and Oehlers, D.J. (1995), "Partial Shear Connection Design of Composite Beams", Structural Stability and Design, Proceedings of the International Conference on Structural Stability and Design (Edited by Kitipornchai, S., Hancock, G.J. and Bradford, M.A.). Sydney, Australia, pp. 283-287.

4. Oehlers, D.J., Wright, H.D. and Burnet, M.J., (1994), "Flexural Strength of Profiled Beams," Journal of Structural Engineering, ASCE, Vol. 120, No. 2, pp 378-393.

5. Oehlers, D.J. and Burnet, M.J. (1994), "Strengthening and Stiffening Existing Reinforced Concrete Slabs by Bonding Steel Plates to Their Tension Face", Australasian Structural Engineering Conference, Sydney, Australia, pp. 919-924.

6. Oehlers, D.J and Burnet, M.J. (1995), "Reinforced Concrete Beams Constructed using Profiled Sheeting as Permanent and Integral Shuttering", Building for the 21st Century, Proceedings of the Fifth East Asia-Asia Pacific Conference on Structural Engineering and Construction (Edited by Loo, Y-C). Brisbane, Australia, pp. 457-462.

Acknowledgments

There have been numerous people who have played a part in this thesis coming to fruition. The author wishes first of all to thank his supervisor, Dr. Deric Oehlers who guided and directed the work from its initial stages through to completion. His patience and perseverance through what seemed as an eternal process of completing this thesis is greatly appreciated. His helpfulness and approachability were second to none, and were vital to the completion of this thesis.

The experiments in this thesis were funded by a large Australian Research Council Grant made available by the Department of Employment, Education and Training of the Commonwealth of Australia. This grant was provided for collaborative research between Dr. Deric Oehlers at The University of Adelaide, and Professor Mark Bradford at The University of New South Wales. Brian Uy who undertook his PhD studies under the supervision of Professor Mark Bradford as part of the collaborative research is also thanked for his friendship and involvement in the work.

Woodroffe Industries of South Australia kindly contributed to the research project by supplying and fabricating cold formed steel sheet used in many of the experiments undertaken. They are warmly thanked for their participation in the research, and it is hoped that more industry participation may continue in the future.

The experimental program was made possible by the involvement of Bob Kelman, David Hale and Greg Atkins in The Department of Civil and Environmental Engineering at The University of Adelaide. Their help is gratefully acknowledged.

Over the course of the author's candidature there were numerous post graduate students in The Department of Civil and Environmental Engineering who each had special significance. These include Abir Ghosh, Zahrul Islam, Mohamed Elchalakani, Paul Morgan, Ninh Nguyen, Marfique Ahmed, Rudi Seracino, Ranganath Bathur, Hua Sun and John Ndiritu.

The author also wishes to express gratitude for the support offered by his family and friends. Their patience and continued encouragement were a tremendous help. In particular, the author recognises the support of his mother, as well as Duncan McKellar, Grant Donnan, and Natalie Weir.

Furthermore, the author recognises that completion of this thesis would not have been possible without the love and support of his wonderful wife, Laila. A great debt of gratitude is owed, due to her understanding and unfailing support.

Finally, the author wishes to thank the one person through whom all things have been made possible, including completion of this thesis, Jesus Christ.

Contents

Synopsis i

Preface iv

Acknowledgments vi

Contents viii

List of Figures xiii

List of Tables xxiv

Notation xxvi

Chapter 1. Introduction

1.1 Background 1

1.2 Scope and Objectives 2

Chapter 2. Composite Beams

2.1 Introduction 5

2.2 Literature Review 6

2.2.1 General 6

2.2.2 Rigid Plastic Analysis 6

2.2.3 Behaviour of Stud Shear Connectors 11

2.2.4 Fracture of Shear Connectors 16

2.2.5 Uplift Effects 27

2.2.6 Concrete Cracking 28

2.2.7 Tension Stiffening 32
2.2.8 Ductility 33
2.2.9 Plastic Hinge 36
2.2.10 Strain Hardening 41
2.3 Scope of current work 43
2.4 Mathematical Model 44
2.4.1 Introduction 44
2.4.2 First Tier Analysis 45
2.4.3 Second Tier Analysis 55
2.4.4 Worked Example 96
2.5 Comparison with Test Results 101
2.6 Conclusions 103

Chapter 3. Push Tests

3.1 Introduction 105
3.2 Literature Review 106
3.2.1 Introduction 106
3.2.2 Lateral Restraining Force 119
3.3 Current Procedure 124
3.3.1 Introduction 124
3.3.2 Specimen Geometry 124
3.3.3 Preparation Procedure 128
3.3.4 Test Setup 129
3.3.5 Test Procedure 133
3.4 Experimental Results 135
3.4.1 Introduction 135
3.4.2 Test Parameters 136
3.4.3 Preliminary Series 137
3.4.4 Series 1 144
3.4.5 Series 2 158
3.4.6 Series 3 175
3.4.7 Series 4 193
3.5 Summary 211

3.6 Analysis of Results 219
3.6.1 Effect of Rib Opening 219
3.6.2 Effects of Sheeting Thickness 220
3.7 Conclusions 224
3.7.1 Push Test 224
3.7.2 Behaviour of Re-entrant and Open Rib Profiles 225

Chapter 4. Profiled Composite Beams

4.1 Introduction 227
4.2 Literature Review 229
4.2.1 Overview 229
4.2.2 Long Term Deflections 233
4.2.3 Local Buckling 235
4.3 Flexural Strength Analysis 242
4.3.1 Buckling of Profiled Sheeting 243
4.3.2 Welded Construction 245
4.3.3 Clipped Construction 254
4.3.4 Worked Example 264
4.4 Conclusions 266

Chapter 5. Profiled Beam Tests

5.1 Introduction 267
5.2 Test Setup 268
5.3 Profiled Sheeting 269
5.4 Test Results 271
5.4.1 General 271
5.4.2 Push Tests 273
5.4.3 Beam CB1 275
5.4.4 Beam PB1 277
5.4.5 Beam PB2 287
5.4.6 Beam PB3 294
5.4.7 Beam PB4 303
5.4.8 Beam PB5 308

5.4.9 Beam PB6 317
5.5 Summary 321
5.6 Comparison of Results 324
5.6.1 Rigid Plastic Analysis 324
5.6.2 Non-Linear Computer Simulations 327
5.7 Conclusions 332

Chapter 6. Shear Tests

6.1 Introduction 333
6.2 Literature Review 334
6.2.1 General Shear Tests 334
6.2.2 Shear in Profiled Beams 338
6.2.3 Conclusions 347
6.3 Current Test Setup 347
6.4 Test Program 350
6.5 Test Results 354
6.5.1 Series 1 354
6.5.2 Series 2 368
6.5.3 Series 3 377
6.5.4 Summary 384
6.6 Analysis of Results 392
6.7 Conclusions 399

Chapter 7. Computer Analysis of Composite Member with Partial Interaction

7.1 Introduction 401
7.2 Literature Review 402
7.3 Analysis Procedure 403
7.3.1 Introduction 403
7.4 General Considerations 406
7.4.1 Bounds of Tolerance 406
7.4.2 Material Properties 406

7.5 Cross Sectional Analysis 413
7.5.1 Introduction 413
7.5.2 Partial Interaction Analysis 414
7.6 Member Analysis 419
7.6.1 Introduction 419
7.6.2 Simply supported members 420
7.6.3 Ultimate Moment 424
7.6.4 Deflected Shape 426
7.7 Comparison with Experimental Results 428
7.7.1 Composite Beams 428
7.8 Conclusions 433

Chapter 8. Conclusions

8.1 Introduction 435
8.2 Conclusions 436
8.2.1 Composite Beams 436
8.2.2 Interface Bond Push Tests 437
8.2.3 Flexural Strength of Profiled Beams 439
8.2.4 Shear Strength of Profiled Beams 441
8.3 Further Research 442

References

Appendix A. Design of Weld Joints

A .1 Profiled Beam PB1 463
A .2 Profiled Beam PB3 465

List of Figures

Chapter 1

Fig. 1.1 Composite Profiled Beams 2

Chapter 2

Fig. 2.1. Rigid Plastic Analysis - Full Shear Connection 6
Fig. 2.2. Reinforced Concrete Stress Block 7
Fig. 2.3. Rigid Plastic Analysis - Partial Shear Connection 10
Fig. 2.4. Moment Interaction Diagram 11
Fig. 2.5. 19 mm Stud Shear Connectors 12
Fig. 2.6. Idealised Load vs Slip 15
Fig. 2.7. Values of Maximum Slip (Johnson and Molenstra, 1991) 20
Fig. 2.8. Values of Maximum Slip (Aribert, 1992) 23
Fig. 2.9. Values of Maximum Slip (Oehlers and Sved, 1995) 26
Fig. 2.10. Variation of Stiffness with Interaction (Wright and Francis 1990) 30
Fig. 2.11. Equivalent Strain Distributions 33
Fig. 2.12. Ductility Requirements for Simply Supported Beams 35
Fig. 2.13. Plastic Rotations for Reinforced Concrete and Composite Beams 38
Fig. 2.14. Stress Strain Relationship for Steel 42
Fig. 2.15. Composite Beam Stress Distribution 46
Fig. 2.16. Slip Distribution 47
Fig. 2.17. Linear Elastic Analysis 49
Fig. 2.18. Analysis for Fracture of Connectors 51
Fig. 2.19. Cross-Section of Composite Beam 54
Fig. 2.20. Variation in Moment to Cause Fracture with Degree of Shear Connection 55
Fig. 2.21. Effect of Load Distribution on Yield Zone 56
Fig. 2.22. Strain Distribution for Full Shear Connection 57
Fig. 2.23. Location of Concrete Cracking 58
Fig. 2.24. Change in Slip Strain due to Concrete Cracking 61
Fig. 2.25. Analysis for Concrete Cracking 64

Fig. 2.26. Variation in Moment to Cause Fracture 68
Fig. 2.27. Effect of Concrete Cracking on Slip Strain 69
Fig. 2.28. Extent of Yielding 70
Fig. 2.29. Moment Curvature Response for a Steel Beam 72
Fig. 2.30. Plastic Moment with Variable Connector Force. 73
Fig. 2.31. Curvature Variation 75
Fig. 2.32. Yield in Steel Section 76
Fig. 2.33. Variation in Yield Moment 77
Fig. 2.34. Yield Moment with zero connector force. 77
Fig. 2.35. Yield Moment with Variable Connector Force. 78
Fig. 2.36. Influence of Axial Force on Steel Section 84
Fig. 2.37. Variation in β with Degree of Shear Connection 86
Fig. 2.38. Design for Yielding 89
Fig. 2.39. Variation in Moment to Cause Fracture 92
Fig. 2.40. Stress and Strain Distributions in Plastic Hinge 93
Fig. 2.41. Variation in Moment to Cause Fracture 97
Fig. 2.42. Variation in Moment-Curvature 98
Fig. 2.43. Variation in Moment - Slip 99
Fig. 2.44. Variation in Slip for Worked Example 100

Chapter 3

Fig. 3.1. Shear Bond Regression 108
Fig. 3.2. Porter and Ekberg Test Setup 110
Fig. 3.3. Bond Stress vs Embedment Length 110
Fig. 3.4. Daniels Test Setup 112
Fig. 3.5. Typical Shear-Slip Relationships for Daniels 112
Fig. 3.6. Patrick Test Arrangement 114
Fig. 3.7. Push Test Results 114
Fig. 3.8. Test Results for Patrick (1990) 116
Fig. 3.9. Test Results for Patrick (1991) 117
Fig. 3.10. Test Setup for Stark 118
Fig. 3.11. Test Setup for Airumyan 119
Fig. 3.12. Lateral Force Distribution 120
Fig. 3.13. Profile Deformations 121
Fig. 3.14. Internal Force Distribution for Daniels' Test Setup 123
Fig. 3.15. Internal Force Distribution for Patrick's Test Setup 124

Fig. 3.16. Specimen Geometry 125
Fig. 3.17. Specimen Geometry 126
Fig. 3.18. Specimen Ready for Pouring 129
Fig. 3.19. Schematic of Test Setup 131
Fig. 3.20. Restraining Clamps 131
Fig. 3.21. Bases for loading Rig 132
Fig. 3.22. Load Dispersion Plates 132
Fig. 3.23. Load Transfer Plate 133
Fig. 3.24. Test Specimen 133
Fig. 3.25. Use of Side Clamps to Limit Sheeting Distortion. 135
Fig. 3.26. Sheet distortion without side clamps 135
Fig. 3.27. Comform Profile 138
Fig. 3.28. Specimen PTP1 after Testing 139
Fig. 3.29. Shear Stress-Slip Curve for PTP2 140
Fig. 3.30. Shear Stress-Slip Curve for PTP3 140
Fig. 3.31. Cracking Pattern for PTP4 141
Fig. 3.32. Shear Stress-Slip Curve for PTP4 and PTP5 142
Fig. 3.33. Shear Stress-Slip Curve for PTP3 and PTP6 142
Fig. 3.34. Typical Rib Geometry 144
Fig. 3.35. Profiled Sheeting Stress-Strain Curve 146
Fig. 3.36. Typical Load-Slip Curve for Series 1 147
Fig. 3.37. Lap Joint for PT1.1, PT1.2 and PT1.3 148
Fig. 3.38. Shear Stress vs Slip Curve for PT1.1 and PT1.2 149
Fig. 3.39. Shear Stress vs Slip for PT1.3 and PT1.4 150
Fig. 3.40. Shear Stress vs Slip for PT1.5 150
Fig. 3.41. Shear Stress vs Slip for PT1.6 and PT1.8 151
Fig. 3.42. Shear Stress vs Slip for PT1.10 152
Fig. 3.43. Shear Stress vs Slip for PT1.11 and PT1.12 152
Fig. 3.44. Warping of the Loading Beam 153
Fig. 3.45. Cracking of PT1.12 153
Fig. 3.46. Chemical Bond Strength vs Rib Opening for Series 1 156
Fig. 3.47. Residual Stress vs Rib Opening for Series 1 157
Fig. 3.48. Stress at 5 mm Slip vs Rib Opening for Series 1 157
Fig. 3.49. Detail of Embossments 160
Fig. 3.50. Shear Stress vs Slip for PT2.1 160
Fig. 3.51. Sheeting and Concrete After Testing of PT2.1 161
Fig. 3.52. Shear Stress vs Slip for PT2.2 and PT2.3 162

Fig. 3.53. Sheeting Deformation for PT2.2 162
Fig. 3.54. Specimen PT2.2 after Testing 162
Fig. 3.55. Shear Stress vs Slip for PT2.4 and PT2.5 163
Fig. 3.56. Sheeting and Concrete after Testing PT2.4 163
Fig. 3.57. Shear Stress vs Slip for PT2.6 and PT2.7 164
Fig. 3.58. Sheeting and Concrete after Testing PT2.6 164
Fig. 3.59. Shear Stress vs Slip for PT2.8 and PT2.9 165
Fig. 3.60. Sheeting and Concrete after Testing PT2.8 165
Fig. 3.61. Sheeting for Specimen PT2.9 166
Fig. 3.62. Shear Stress vs Slip for PT2.10 and PT1.8 166
Fig. 3.63. Concrete after Testing PT2.10 167
Fig. 3.64. Shear Stress vs Slip for PT2.11 and PT2.12 167
Fig. 3.65. Specimen PT2.11 after Testing 168
Fig. 3.66. Concrete after Testing PT2.11 168
Fig. 3.67. Summary of Embossed Specimens for Series 2 170
Fig. 3.68. Summary of Non-Embossed Specimens for Series 2 170
Fig. 3.69. Chemical Bond Stress vs Rib Opening for Series 2 171
Fig. 3.70. Residual Bond Stress vs Rib Opening for Series 2 172
Fig. 3.71. Stress at 5 mm Slip vs Rib Opening for Series 2 173
Fig. 3.72. Mechanical Bond Stress vs Opening for Series 2 174
Fig. 3.73. Slip at Max Load vs Opening for Series 2 174
Fig. 3.74. Movement of Profiled Sheeting 174
Fig. 3.75. Profile Deformations 175
Fig. 3.76. Shear Stress vs Slip Curve for PT3.1 and PT2.1 178
Fig. 3.77. Specimen PT3.1 after testing 178
Fig. 3.78. Shear Stress vs Slip Curve for PT3.2 and PT3.3 179
Fig. 3.79. Specimen PT3.2 after testing 180
Fig. 3.80. Specimen PT3.3 after testing 180
Fig. 3.81. Shear Stress vs Slip Curve for PT3.4 and PT3.5 181
Fig. 3.82. Specimen PT3.4 after testing 181
Fig. 3.83. Concrete Surface of PT3.5 182
Fig. 3.84. Shear Stress vs Slip Curve for PT3.6 183
Fig. 3.85. Specimen PT3.6 after testing 183
Fig. 3.86. Specimen PT3.7 after testing 184
Fig. 3.87. Shear Stress vs Slip Curve for PT3.8 and PT3.9 185
Fig. 3.88. Concrete Surface for PT3.8 and PT3.9 185
Fig. 3.89. Shear Stress vs Slip Curve for PT3.10 186

Fig. 3.90. Specimen PT3.10 after testing 186
Fig. 3.91. Specimen PT3.10 after testing 186
Fig. 3.92. Shear Stress vs Slip Curve for PT3.11 187
Fig. 3.93. Concrete Surface of PT3.11 and PT3.12 after testing 188
Fig. 3.94. Specimen PT3.12 after testing 188
Fig. 3.95. Chemical Bond Stress vs Rib Opening for Series 3 190
Fig. 3.96. Residual Shear Stress vs Rib Opening for Series 3 190
Fig. 3.97. Mechanical Bond Stress vs Rib Opening for Series 3 191
Fig. 3.98. Stress at 5 mm Slip vs Rib Opening for Series 3 192
Fig. 3.99. Slip at Max Shear Stress vs Rib Opening for Series 3 193
Fig. 3.100. Bondek II Profile 194
Fig. 3.101. Stress-Strain Curves for Profiled Sheeting 196
Fig. 3.102. Series 4 Specimens 196
Fig. 3.103. Shear Stress vs Slip Curve for PT4.1, PT4.2 and PT4.3 197
Fig. 3.104. Concrete Cracking for PT4.1 and PT4.2 198
Fig. 3.105. Concrete Cracking for PT4.3 199
Fig. 3.106. Concrete Scour for PT4.3 199
Fig. 3.107. Shear Stress vs Slip Curve for PT4.4 and PT4.5 200
Fig. 3.108. Concrete Scour for PT4.4 200
Fig. 3.109. Concrete Cracking for PT4.5 201
Fig. 3.110. Shear Stress vs Slip Curve for PT4.6, PT4.7 and PT4.8 201
Fig. 3.111. Concrete Cracking for PT4.6 202
Fig. 3.112. Concrete Cracking for PT4.7 202
Fig. 3.113. Shear Stress vs Slip Curve for PT4.9 and PT4.10 203
Fig. 3.114. Concrete Cracking for PT4.9 204
Fig. 3.115. Lateral Movement of Sheeting for PT4.9 204
Fig. 3.116. Concrete Cracking for PT4.10 205
Fig. 3.117. Shear Stress vs Slip Curve for PT4.11 and PT4.12 205
Fig. 3.118. Push Test PT4.12 206
Fig. 3.119. Mechanical Shear Stress vs Sheeting Thickness 208
Fig. 3.120. Slip at Max Shear Stress vs Sheeting Thickness 209
Fig. 3.121. Embossment Details 210
Fig. 3.122. Shear Stress at 5 mm Slip 210
Fig. 3.123. Chemical Bond Strength vs Rib Opening 214
Fig. 3.124. Simplified Model for Chemical Bond Strength vs Rib Opening 215
Fig. 3.125. Mechanical Bond Strength vs Rib Opening 216
Fig. 3.126. Simplified Model for Mechanical Bond Strength vs Rib Opening 217

Fig. 3.127. Bond Strength at 5 mm Slip vs Rib Opening 218
Fig. 3.128. Effect of Rib Opening 219
Fig. 3.129. Determination of Angle α 220
Fig. 3.130. Chemical Bond Strength vs Sheeting Thickness 221
Fig. 3.131. Mechanical Bond Strength vs Sheeting Thickness 221
Fig. 3.132. Stress at 5 mm Slip vs Sheeting Thickness 222
Fig. 3.133. Deformation at Embossments 222
Fig. 3.134. Log - Log Plot for Mechanical Bond Strength 223
Fig. 3.135. Log - Log Plot for Bond Strength at 5 mm Slip 223

Chapter 4

Fig. 4.1. Profiled Beam and Slab 228
Fig. 4.2. Pan Floor System (McBean, 1990) 230
Fig. 4.3. Externally Reinforced Beam (Daalov and Petrov, 1990) 231
Fig. 4.4. Profiled Composite Slab and Band Beam System (Patrick and Bridge, 1988) 232
Fig. 4.5. Beam Cross Sections (Oehlers, 1993) 233
Fig. 4.6. Flexural Strength of Profiled Beams (Oehlers, 1993) 233
Fig. 4.7. Beam Cross-Sections (Uy and Bradford, 1994) 234
Fig. 4.8. Deflection Time History (Uy and Bradford, 1994) 234
Fig. 4.9. Profiled Beam Cross-Sections 235
Fig. 4.10. Derivation of α 238
Fig. 4.11. Slenderness vs Dimensionless Critical Stress (Uy and Bradford, 1993c) 239
Fig. 4.12. Effective Width Concept for Simply Supported Plates 241
Fig. 4.13. Construction Techniques for Profiled Composite Beams. 243
Fig. 4.14. Cross Section of Profiled Steel Unit 244
Fig. 4.15. Idealisation of Composite Profiled Beam 245
Fig. 4.16. Idealised Shear Stress vs Slip Relationship 247
Fig. 4.17. Strain Distribution in Composite Beam 248
Fig. 4.18. Behaviour of Reinforced Concrete Element 249
Fig. 4.19. Behaviour of Profiled Box Element 251
Fig. 4.20. Clipped Profiled Beam Construction 254
Fig. 4.21. Stress and Strain Distributions in Profiled Sheeting 255
Fig. 4.22. Behaviour of Composite Member 257
Fig. 4.23. Strain Distributions in Clipped Construction 257
Fig. 4.24. Equivalent Stresses in Profiled Units 259
Fig. 4.25. Internal Forces in Clipped Profiled Beam 260

Fig. 4.26. Moment Contribution from Profiled Unit in Tension Region 261
Fig. 4.27. Moment Contribution from Profiled Unit in Compression Region 262

Chapter 5

Fig. 5.1. Test Arrangement for Profiled Beams 269
Fig. 5.2. Profiled Sheeting Stress-Strain Curve 269
Fig. 5.3. Construction of Profiled Beams 271
Fig. 5.4. Push Test Specimen for Beams PB1 and PB2 273
Fig. 5.5. Buckling of Push Test Specimen for Beams PB1 and PB2 274
Fig. 5.6. Push Test Result for Beams PB1 and PB2 275
Fig. 5.7. CB1 ready for testing 275
Fig. 5.8. Load Deflection Plot for CB1 276
Fig. 5.9. Failure of CB1 277
Fig. 5.10. Profiled Sheeting for PB1 277
Fig. 5.11. Construction of PB1 278
Fig. 5.12. Testing strength of welds 278
Fig. 5.13. Load Deflection Curve for Beam PB1 279
Fig. 5.14. Buckling in PB1 280
Fig. 5.15. Arrangement of Slip Measurement for PB1 281
Fig. 5.16. Detail of transducer location 281
Fig. 5.17. Slip Distribution for Beam PB1 282
Fig. 5.18. Theoretical Slip Distribution for Beam PB1 283
Fig. 5.19. Load vs Displacement for Transducers 7, 10 and 11 285
Fig. 5.20. Adjusted Load vs Slip for Transducers 10 and 11 286
Fig. 5.21. Load vs Slip for Transducers 7, 8, 9 and 10 287
Fig. 5.22. Assembly of PB2 288
Fig. 5.23. Load vs Midspan Deflection for Beam PB2 288
Fig. 5.24. Location of Transducers for Beam PB2 290
Fig. 5.25. Load vs Slip for Transducers 9, 11 and 4 290
Fig. 5.26. Adjusted Load vs Slip for Transducers 9, 11 and 4 291
Fig. 5.27. Variation in Slip with Height above Soffit 292
Fig. 5.28. Longitudinal Variation in Slip for Beam PB2 292
Fig. 5.29. Load vs Slip for Beam PB2 294
Fig. 5.30. Profiled Beam PB3 295
Fig. 5.31. Load vs Slip for Profiled Sheeting for PB3 and PB4 296
Fig. 5.32. Premature Buckling of Push Test 296

Fig. 5.33. Load vs Midspan Deflection for Beam PB3 297
Fig. 5.34. Transducer Location for Beam PB3 298
Fig. 5.35. Detail of Top Transducer Attachment 298
Fig. 5.36. Longitudinal Variation in Slip at Bottom Rib for Beam PB3 299
Fig. 5.37. Longitudinal Variation in Slip at Top Rib for Beam PB3 300
Fig. 5.38. Strain Readings for Beam PB3 301
Fig. 5.39. Detail showing Demec Arrangement 301
Fig. 5.40. Moment vs Curvature for Beam PB3 302
Fig. 5.41. Variation in Strain in Concrete and Steel Sections in PB3 303
Fig. 5.42. Load vs Midspan Deflection Curve for Beam PB4 304
Fig. 5.43. Failure of Beam PB4 304
Fig. 5.44. Arrangement of Transducers for PB4 305
Fig. 5.45. Longitudinal Variation in Slip for Beam PB4 306
Fig. 5.46. Variation in Slip at Section C 307
Fig. 5.47. Variation in Concrete and Sheeting Strain for Beam PB4 308
Fig. 5.48. Profiled Beam PB5 and PB6 309
Fig. 5.49. Construction of Beam PB5 309
Fig. 5.50. Load vs Slip for Dove Tail Sheeting 310
Fig. 5.51. Load Deflection Curve for Beam PB5 311
Fig. 5.52. Arrangement of Transducers for Beam PB5 312
Fig. 5.53. Longitudinal Variation in Slip for Beam PB5 312
Fig. 5.54. Transverse Variation in Slip for PB5 314
Fig. 5.55. Concrete and Sheeting Strain Readings for Beam PB5 315
Fig. 5.56. Moment-Curvature Response for Beam PB5 315
Fig. 5.57. Strain Readings from Profiled Sheeting 316
Fig. 5.58. Load vs Slip for Transducer 1 316
Fig. 5.59. Load vs Midspan Deflection for Beam PB6 317
Fig. 5.60. Longitudinal Variation in Slip in Beam PB6 318
Fig. 5.61. Transverse Variation in Slip in Beam PB6 320
Fig. 5.62. Concrete and Sheeting Strain Readings for Beam PB6 320
Fig. 5.63. Moment vs Curvature for Beam PB6 321
Fig. 5.64. Summary of Series 1 322
Fig. 5.65. Summary of Series 2 322
Fig. 5.66. Idealised Load vs Deflection Curve 323
Fig. 5.67. Comparison of PB1 & PB2 with Computer Results 328
Fig. 5.68. Comparison of PB3 & PB4 with Computer Results 329
Fig. 5.69. Comparison of PB5 & PB6 with Computer Results 330

Fig. 5.70. Comparison of End Slip with Computer Results for PB5 and PB6 330
Fig. 5.71. Sheeting Load vs Slip Relationship used in Computer Program 331
Fig. 5.72. Comparison of Slip Distribution with Computer Results for Beams PB5 & PB6 331

Chapter 6

Fig. 6.1. Previous Test Arrangements 335
Fig. 6.2. Typical Test Results of Mattock (Mattock and Hawkins, 1972) 335
Fig. 6.3. Normal Forces induced by Shear Action (Oehlers, 1993) 338
Fig. 6.4. Shear Strength of Profiled Beams (Oehlers, 1993) 339
Fig. 6.5. Sheeting that is Effective in Resisting Vertical Shear 344
Fig. 6.5. Test Beams used by Bradford and Kyakula (1994) 345
Fig. 6.6. Shear Test Results of Bradford and Kyakula (1994) 345
Fig. 6.7. Shear Test Setup 348
Fig. 6.8. Photo of Shear Test Setup 349
Fig. 6.9. Detail of Loading Plate 350
Fig. 6.10. Detail of Shear Test Setup 350
Fig. 6.11. Stress - Strain Curve for Shear Reinforcing 353
Fig. 6.12. Load vs Displacement for S1.1 and S2.2 355
Fig. 6.13. Schematic of Shear Plane for Plain Specimens 356
Fig. 6.14. Photo of Shear Plane for Plain Specimens 356
Fig. 6.15. Trapezoidal Specimen 357
Fig. 6.16. Load vs Displacement for Trapezoidal Specimens 358
Fig. 6.17. Failure of S1.3 359
Fig. 6.18. Outward Deformation of Sheeting for S1.3 359
Fig. 6.19. Failure surface for S1.3 after removal of sheeting 359
Fig. 6.20. Failure Surface of S1.8 360
Fig. 6.21. Dove Tail Specimen 361
Fig. 6.22. Load vs Displacement for Dovetail Ribs 361
Fig. 6.23. Lateral Deformation of Sheeting for S1.4 362
Fig. 6.24. Shear Deformation of Sheeting for S1.4 362
Fig. 6.25. Diagonal Shear Crack for Specimen S1.5 363
Fig. 6.26. Geometry of L-Rib Specimens 364
Fig. 6.27. Load vs Displacement for L-Ribs 364
Fig. 6.28. Cracking pattern of S1.6 365
Fig. 6.29. Detailed View of End Slip for S1.6 366

Fig. 6.30. Shear Deformation 366
Fig. 6.31. Cracking Pattern for S1.7 367
Fig. 6.32. End View of S1.7 367
Fig. 6.33. Load vs Displacement for S2.1 369
Fig. 6.34. Load vs Displacement for S2.2 and S2.3 370
Fig. 6.35. Failed Shape of S2.2 370
Fig. 6.36. Slip for L-Rib Specimens 371
Fig. 6.37. Cracking Pattern of S2.4 372
Fig. 6.38. Geometry of L-Ribs for S2.5 and S2.6 372
Fig. 6.39. Load vs Displacement Response for S2.3, S2.5 and S2.6 373
Fig. 6.40. Cracking for S2.5 374
Fig. 6.41. Failure of S2.5 374
Fig. 6.42. Load vs Displacement for S2.7 375
Fig. 6.43. Geometry of Sheeting for S2.8 376
Fig. 6.44. Load vs Displacement for S2.8 376
Fig. 6.45. Load vs Displacement for S3.1 378
Fig. 6.46. Load vs Displacement for S3.3 and S3.4 379
Fig. 6.47. Specimen S3.3 after Testing 379
Fig. 6.48. Load vs Displacement for S3.5 and S3.6 380
Fig. 6.49. Specimen S3.5 after Testing 381
Fig. 6.50. End View of Specimen S3.5 381
Fig. 6.51. Load vs Displacement for S3.7 and S3.8 382
Fig. 6.52. Specimen S3.7 after Testing 383
Fig. 6.53. Typical Load vs Displacement Curve 384
Fig. 6.54. Influence of Sheeting Rib Geometry on Shear Strength 387
Fig. 6.55. Influence of Sheeting Thickness on Shear Strength 388
Fig. 6.56. Influence of Sheeting between Ribs on Shear Strength 389
Fig. 6.57. Influence of Longitudinal Bond on Transverse Shear Strength for Uncut L-Ribs 390
Fig. 6.58. Influence of Longitudinal Bond on Transverse Shear Strength for Cut L-Ribs 391
Fig. 6.59. Influence of Internal Stirrups 392
Fig. 6.60. Comparison of Theoretical and Experimental Ultimate Shear Stress 396
Fig. 6.61. Comparison of Shear Test Results with Previous Researchers 397
Fig. 6.62. Regression Analysis of Shear Test Results 398

Chapter 7

Fig. 7.1. Program Flow Diagram 404
Fig. 7.2. Composite Cross Sections 405
Fig. 7.3. Generalised Material Properties 407
Fig. 7.4. Concrete Compression Properties 409
Fig. 7.5. Concrete Tensile Properties 411
Fig. 7.6. Steel Stress-Strain Properties 413
Fig. 7.7. Generalised Cross-Section 414
Fig. 7.8. Segmented Member 419
Fig. 7.9. Generalised Load Slip Characteristics for one Connector 420
Fig. 7.10. Variation of Bond Force along Member 421
Fig. 7.11. Deflections of a segmented member 427
Fig. 7.12. Comparison with Davies (1969) 429
Fig. 7.13. Properties of Beams used by Davies (1969) 429
Fig. 7.14. Load - Slip Characteristics for beams by Davies (1969) 429
Fig. 7.15. Comparison with Davies (1969) 430
Fig. 7.16. Comparison with Yam and Chapman (1968) 431
Fig. 7.17. Properties of Beams used by Yam and Chapman (1968) 431
Fig. 7.18. Load -- Slip Characteristics for Connectors used by Yam and Chapman (1968) 432
Fig. 7.19. Slip Distribution for Yam and Chapman (1968) 432

Appendix A

Fig. A.1. Profiled Sheeting for PB1 464
Fig. A.2. Profiled Sheeting for PB3 465

Errata

P34, Para 2, Line 6:
'Section 0' should read 'Section 2.4.3.8'

P41, Para 3, Line 7:
'Section 0' should read 'Section 2.4.3.8'

P47, Para 2, Line 1:
'Section 0' should read 'Section 2.4.3.8'

P230, Para 3, Line 1:
'Low (1993)' should read 'Lowe (1993)'

P233, Figure Caption:
Delete: Fig_Oehlers_Cross_Sections \!

P257, Para 1, Line 6:
'that passes through' should read 'that pass through'

P271, Para 1:
Insert: 'Beams were constructed on the ground for ease of construction. Propped construction would also have been possible'

P273, Para 2, Line 4
'unwedded' should read 'unwelded'

P294, Para 1, Line 4:
'increase in the distance required' should read 'increase in the bond length required'

P317, Para 2, Line 1:
After 'shown in Fig. 5.48.' insert 'Due to construction differences the overall depth of the section was 416 mm instead of the nominal 410 mm, while the width of the section was 195 mm instead of the nominal 200 mm. All other dimensions were the same as for Beam PB5.'

P136, Para 1:
Insert: 'The test procedure provides quantitative results on the load vs slip behaviour of profiled sheeting. However, it was found that the results are dependant on many different factors such as geometry of the ribs, thickness of the sheeting, type and placement of embossments, and surface condition of the sheeting. Due to the many different combinations of the above variables, it was decided to provide qualitative data from the tests, as these would have a wider range of applicability than would quantitative data which was specific to any one combination of variables.'

P340, Table 6.1:
'Yeilding' should read 'Yielding'

P365, Para 3, Line 7:
Delete: 'and imperturbable'

P428, Para 6:
Insert: 'For the beams analysed the cross-section was divided into 80 slices; 50 slices for the concrete element and 30 slices for the steel element. The beam was divided into 51 segments. An odd number of segments was required for the analysis to provide one central segment.'

P445

Insert Reference:
Airumyan, E., Belyaev, V. and Rumyancev, I., (1990), "Efficient Embossment for Corrugated Steel Sheeting." IABSE Symposium on Mixed Structures Including New Materials. Brussels, Belgium, pp. 137-142.

List of Tables

Chapter 2

Table 2.1. Variation of λ with span 30
Table 2.2. Properties of Composite Beam 54
Table 2.3. Worked Example 100
Table 2.4. Comparison with Published Results 101

Chapter 3

Table 3.1. Range of Parameters in Push Tests 137
Table 3.2. Preliminary Series 138
Table 3.3. Summary of Preliminary Series 143
Table 3.4. Series 1 145
Table 3.5. Measured Concrete and Steel Properties 146
Table 3.6. Summary of Series 1 154
Table 3.7. Series 2 159
Table 3.8. Summary of Series 2 169
Table 3.9. Series 3 176
Table 3.10. Summary of Series 3 189
Table 3.11. Series 4 194
Table 3.12. Concrete and Steel Properties for Series 4 194
Table 3.13. Summary of Series 4 207
Table 3.14. Summary of Series 1, 2 and 3 213
Table 3.15. Summary of Chemical Bond Strength 215
Table 3.16. Summary of Mechanical Bond Strength 217
Table 3.17. Summary of Bond Stress at 5 mm Slip 218
Table 3.18. Coefficients for Variation of Bond Strength with Thickness 223

Chapter 4

Table 4.1. Allowable Plasticity Slenderness Limits 237

Chapter 5

Table 5.1. Summary of Profiled Beams 270
Table 5.2. Measured Concrete Properties for Profiled Beams 272
Table 5.3. Measured Steel Properties for Profiled Beams 272
Table 5.4 . Summary of Profiled Beam Tests 323
Table 5.5 . Summary of Profiled Beam Tests 324

Chapter 6

Table 6.1. Shear Strength of Profiled Beams (Oehlers, 1992) 340
Table 6.2. Comparison with Theory and Experiment 346
Table 6.3. Summary of Shear Tests 351
Table 6.4. Measured Concrete Properties 352
Table 6.5. Measured Steel Properties 353
Table 6.6. Summary of Shear Tests 386
Table 6.7. Bond Strength Results for Profiled Sheeting 393
Table 6.8. Comparison between Theory and Experiment 395

Notation

A_c	=	Area of concrete element
A_{cv}	=	Area of concrete forming the shear plane = $b_v d_v$ for a rectangular section.
A_f	=	Area of the flange of the steel beam
A_m	=	Area under the applied moment diagram between the location of maximum moment and the end of the beam
A_{mc}	=	Area under the applied moment curve in the shear span where the concrete is cracked
A_{my}	=	Area under applied moment diagram over which yielding is present
A_{pc}	=	Area under the longitudinal shear force diagram in the shear span where the concrete is cracked
A_p	=	Area under axial force diagram between the location of maximum moment and the end of the beam
A_{pv}	=	Area of profiled sheeting crossing the shear plane
A_{py}	=	Area under longitudinal shear force diagram over which yielding is present
A_{sh}	=	Area under the axial force diagram between the location of maximum moment and the end of the beam
A_{st}	=	Area of steel beam
A_{sv}	=	Area of full anchored longitudinal steel crossing shear plane
A_w	=	Area of the web of the steel beam
D	=	Total depth of the composite beam
D_e	=	Effective depth of profiled beam
E_c	=	Young's modulus of concrete

E_o = Initial stiffness of concrete

E_s = Young's modulus of steel

$(EI)_c$ = Flexural rigidity of the concrete element

$(EI)_s$ = Elastic flexural stiffness of the steel beam

$(EA)_c$ = Axial rigidity of the concrete element

$(EA)_s$ = Axial rigidity of the steel element

F = Lateral restraining force

$F_{b,fsc}$ = Bond strength required to achieve full shear connection

F_{bu} = Bond strength developed in each profiled unit in clipped profiled beam

F_c = Maximum design longitudinal force in concrete slab

F_{ov} = Buckling shear strength

F_{pu} = Yield strength of profiled unit in clipped profiled beam

F_{py} = Yield strength of entire profiled sheeting cross-section in profiled beam

F_s = Maximum design longitudinal force in steel beam

F_{sy} = Yield strength of reinforcing in profiled beam

H_{rib} = Shear flow resistance per rib due to mechanical interlock,

$K_1 - K_7$ = Coefficients for the determination of end slip

I_e = Equivalent moment of inertia of composite section transformed into steel

I_f = Moment of inertia of the fully composite section

I_s = Moment of inertia of the steel section

L = Length of the beam

L' = Length of shear span, for a uniform load, $L' = L/4$.

L_p = Length of push specimen

L_r = Contact perimeter of the rib surface

ΔM = Increase in moment required to achieve full plastic moment of member

M = Total externally applied moment

M_c = Moment in the concrete element

$M_{frac,c}$ = Moment to cause fracture of the shear connectors incorporating cracking of the concrete

$M_{frac,h}$ = Moment to cause fracture of the shear connectors incorporating cracking of the concrete, yielding of the steel and the plastic hinge

$M_{frac,y}$ = Moment to cause fracture of the shear connectors incorporating cracking of the concrete and yielding of the steel

M_{fsc} = Plastic moment for the composite section with full shear connection

M_{fsy} = Yield moment for full shear connection

M_p = Moment in profiled sheeting element

M_{pi} = Moment component in profiled unit about its centroid

M_{psc} = Plastic moment for the composite section with partial shear connection

M_s = Moment in the steel element

M_{sp} = Plastic moment of resistance of the steel beam with zero axial load

M_{sy} = Yield moment of steel section with no axial load

M_u = Ultimate moment of composite beam

M_y = Applied moment to cause yield

M_{zsc} = Ultimate moment of composite beam with zero shear connection

N = Number of shear connectors in the shear span

N_c = Depth to concrete neutral axis from top fibre in profiled beam

N_f = Number of shear connectors required for full shear connection

N_p = Depth to the profiled sheeting neutral axis below top fibre

N_r = Number of ribs in cross-section

P_{cr} = Axial force in the concrete at which cracking occurs

P_d = Design strength of the connectors

P_{fsc} = Axial force transmitted by the shear connectors to achieve full shear connection

P_{sh} = Longitudinal shear force developed in the shear span

P_u = Ultimate strength of stud shear connectors

P_y = Axial force transferred by the connectors at the location of first yield

S = Non-dimensionalised stress = σ/σ_u

S_r = Interface perimeter of a single rib

T = Transition point between flexural failure and failure due to fracture of the shear connectors, based on equilibrium analysis

T' = Transition point between flexural failure and failure due to fracture of the shear connectors, based on interpolation analysis

T_{lin} = Transition point between flexural failure and failure due to fracture of the shear connectors, based on first tier analysis

V_b = Transverse shear resistance of sheeting between ribs in profiled beam

V_e = Maximum experimental vertical shear at failure

V_r = Transverse shear resistance of ribs in profiled sheeting

V_u = Total transverse shear resistance of profiled beam

V_{uc} = Transverse shear strength of reinforced concrete beam without shear stirrups

$V_{uc,s}$ = Transverse shear strength of reinforced concrete beam with shear stirrups

V_{us} = Increase in transverse shear strength of reinforced concrete beam due to shear stirrups

b_c = Width of concrete slab

b_e = Effective of profiled sheeting in compression

b_f = Width of the flange

b_p = Length of the block,

b_r = Width of rib opening

b_s = Width of slab

d_b = Depth to centroid of bond force from top fibre

d_c = Depth of the concrete slab

d_e = Effective slab depth, distance from extreme concrete compression fibre to centroidal axis of the full cross section of steel deck

d_i = Distance from top fibre to centroid of the i^{th} profiled unit

d_o = Distance from the extreme compression fibre of the concrete to the centroid of the outermost layer of tensile reinforcement

d_s = Depth of the steel beam

d_{sh} = Diameter of stud

f_b = Bond strength between profiled sheeting and concrete

$f_{b,m}$ = Maximum mechanical bond strength between profiled sheeting and concrete

$f_{b,0.5}$ = Bond strength between profiled sheeting and concrete at 5 mm slip

f_{bu} = Maximum average bond stress in push test specimen

f_c = Ultimate compressive strength of the concrete

f_{ct} = Tensile strength of the concrete

f_{ov} = Buckling shear stress

f_{py} = Yield stress of profiled sheeting

f_{sy} = Yield stress of steel beam

f_v = Shear reinforcement parameter

h_c = Distance from centroid of the concrete element to concrete-steel interface

h_e = Half the height of the elastic core of a yielded steel beam

h_p = Height of push test specimen

h_r = Height of rib

h_s = Distance from centroid of the steel element to concrete-steel interface

h_s^* = Distance from the centroid to the bottom fibre of the steel beam. For a steel beam with equal flanges, $h_s = h_s^*$

k = Reduced intercept of regression line of full scale slab tests

m = Reduced slope of regression line of full scale slab tests

n = Modular ratio = E_s/E_c

n_c = Depth of concrete compression block in profiled beam

n_r = Number of ribs in profiled beam

n_s = Number of side profiled units in profiled beam

q_{sh} = strength of shear connectors per unit length of beam

s = Slip at the connectors

s_{cr} = Increase in end slip over linear elastic analysis due to concrete cracking

s_{end} = End slip of composite beam

s_h = Increase in end slip due plastic hinge formation

s_o = End slip based on elastic analysis

$s_{o,cr}$ = End slip incorporating effects of concrete cracking

s_{max} = Maximum slip at the interface

s_{sh} = Slip at which the load in the connectors is a maximum

s_y = Yield slip of the connectors, taken as the slip at which the load in the connectors is $0.95P_u$

s_u = Slip at fracture of the connectors, taken as the slip at which the load in the connectors has decreased after the maximum to $0.95P_u$

t_{bm} = Base metal thickness of profiled sheeting

t_e = Effective thickness of profiled sheeting

t_f = Thickness of the flange

t_p = Thickness of profiled sheeting

t_w = Thickness of the web

v_u = Ultimate shear stress

w = Applied uniformly distributed load on beam

w_e = Effective width of profiled beam

x_c = Distance from end of beam to location of first cracking

x_y = Distance from end of beam to location of first yielding

x_{ult} = Distance from end of beam to location of ultimate moment

$\bar{y}$ = Centroid of the profiled steel element, measured from top fibre

y_c = Depth of concrete in compression

y_{ns} = Steel neutral axis location, measured from the concrete top compression fibre,

y_{nc} = the concrete neutral axis location.

y_{pl} = Depth of the plastic neutral axis below the top of the slab

α = Coefficient to describe decrease in flexural rigidity of concrete element due to cracking

β = Coefficient to describe decrease in flexural rigidity of steel element due to yielding

δ_c = Midspan deflection for a fully composite beam

δ_s = Midspan deflection for the steel beam alone, for the same applied load

ε_c = Normalised concrete strain = $\varepsilon/\varepsilon'_c$

ε'_c = Strain at which σ_u occurs

ε_{cr} = Cracking strain of the concrete

ε_{max} = Maximum strain recorded during any previous load step in computational analyses

ε_o = Top fibre concrete compression strain

$\varepsilon_{slip,o}$ = Slip strain based on elastic analysis

$\varepsilon_{slip,c}$ = Slip strain including effects of concrete cracking

$\Delta\varepsilon_{slip,c}$ = Increase in slip strain due to cracking of the concrete

$\Delta\varepsilon_{slip,y}$ = Increase in slip strain due to yielding of the steel

ε_y = Yield strain of the steel

ϕ = Curvature in the beam

ϕ_p = Curvature at which full plastic moment of steel beam is reached

ϕ_y = Curvature in beam to cause yielding

$\Delta\phi_y$ = Increase in curvature due to yielding of the steel

γ = Concrete compression stress block reduction factor

γ_1 = Initial slope of non-dimensionalised concrete stress-strain curve

γ_2 = Ultimate strain of the concrete, as a ratio of the strain at the maximum stress

η = Degree of shear connection

η_c = Degree of shear connection for clipped profiled beam construction

η_T = Degree of shear connection at transition from flexural failure to failure due to fracture of the shear connectors

η_w = Degree of shear connection for welded profiled beam construction

λ = Exponent to determine effective moment of inertia based on the span of the beam.

λ_a = Allowable plasticity slenderness limit

λ_e = Actual plate slenderness = $b/t\sqrt{f_{py}/550}$

μ = Coefficient of friction.

ν = Exponent to describe load-slip behaviour of shear connectors

ρ = Reinforcement ratio of steel deck area to effective concrete area = A_s/bd.

σ_{bu} = Bearing stress in profiled sheeting at base of push specimen

σ_{ol} = Critical stress to cause buckling

σ_u = Compressive strength of concrete

τ_b = Longitudinal rib shear strength

ω = Exponent to describe load-slip behaviour of shear connectors

ψ = Ratio of flexural rigidities of concrete and steel elements = $(EI)_c/(EI)_s$

UNIVERSITY OF ADELAIDE LIBRARY

Chapter 1

Introduction

1.1 Background

Composite steel and concrete construction is now used widely in many different applications. Advantages such as increased strength and stiffness over non-composite forms of construction are well known in the construction industry. Another factor that is widely taken advantage of is the increased speed of construction of composite systems, as compared to other forms of construction. A common design consideration in the use of composite construction concerns the loss of interaction or shear connection that can occur between the concrete and steel elements.

The behaviour of composite beams can be strongly influenced by the strength and stiffness of the connection between the steel and concrete elements of the composite beam. If the connectors do not posses sufficient strength and ductility, then they may fail prematurely due to excessive slip. This problem has received attention in the past, but a simple analytical model that adequately describes the relationship between the parameters that control fracture of the connectors is yet to be determined.

A recent development in the area of composite construction is in the use of composite profiled beams, which are shown schematically in Fig. 1.1 These have many of the advantages of other forms of composite construction, but are only just now receiving attention in the research of their fundamental behaviour. As the body of knowledge is established on their properties and behaviour, and more experience is gained in their construction, then the use of profiled composite beams is likely to increase.

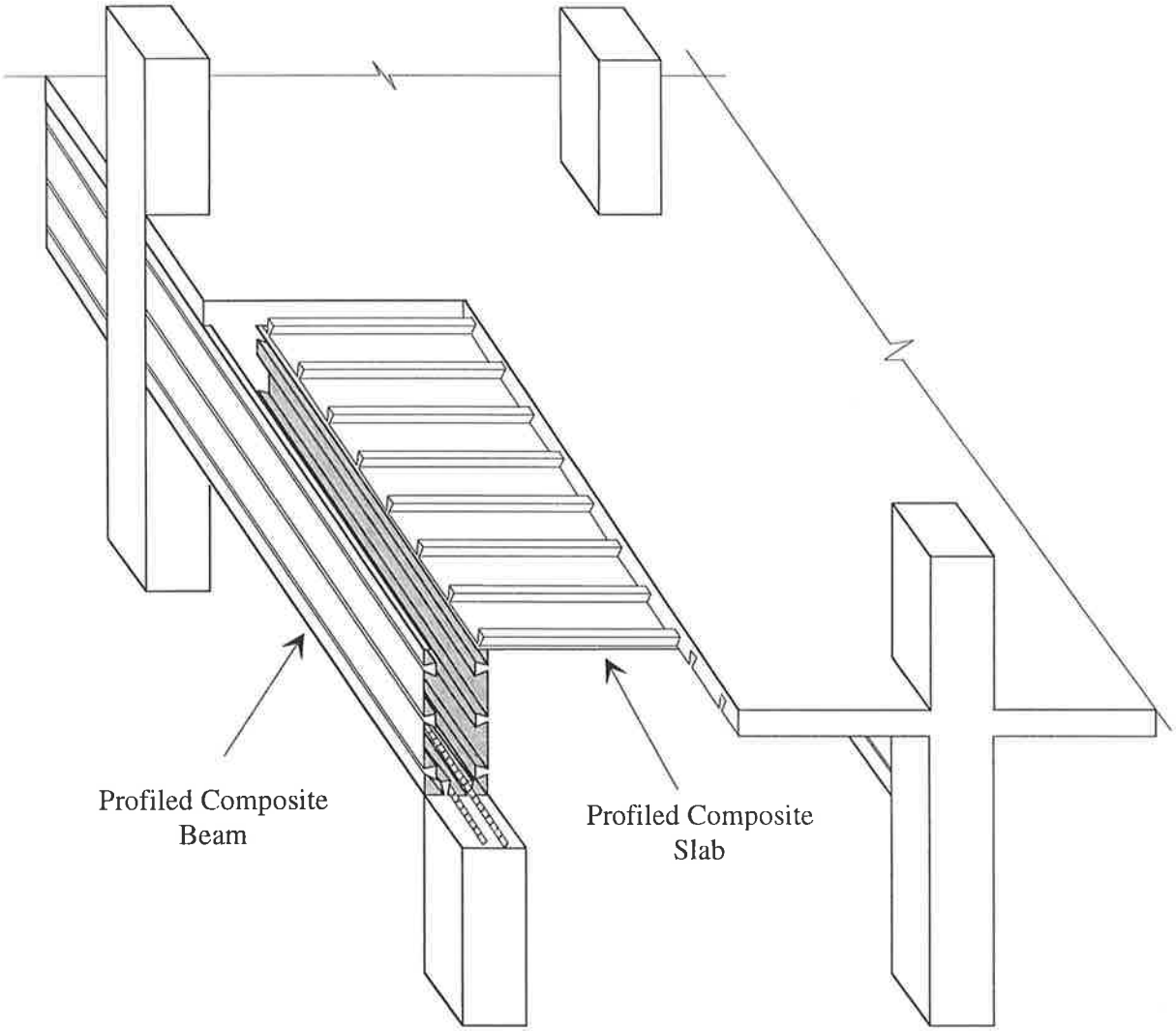


Fig. 1.1 Composite Profiled Beams

1.2 Scope and Objectives

This thesis covers a number of different areas related to composite structures composed of steel and concrete. It began as an investigation into the behaviour of composite profiled beams, and expanded into a more general analysis of composite flexural members.

Chapter 2 details the theoretical analysis of simply supported composite steel and concrete beams. In particular, it describes a method for determining the total end slip that occurs in a composite beam under ultimate moment conditions, and compares this calculated end slip to the allowable slip capacity of the connection. The chapter starts with a review of the current work in the area, covering the design of composite beams with partial shear connection, fracture of the shear connectors, and overall load-slip behaviour of stud shear connectors. It then presents a two tiered form of analysis. The first tier is a simple linear elastic model, while the second tier is a full non-linear analysis.

Chapter 3 describes a new form of push test that was developed to determine the shear connection behaviour of profiled steel sheeting when used compositely with concrete. A discussion of other methods for determining the shear connection behaviour is carried out at the start of the chapter, followed by a step by step explanation of the proposed procedure. The results of a series of push tests are presented, and some general trends describing the behaviour of profiled sheeting are presented.

Chapter 4 describes the theoretical analysis of profiled composite beams. It begins with a presentation of the previous research that has been carried out in the area of profiled beams. It then discusses the design of composite profiled beams, and presents a method to determine their flexural strength. The effect that longitudinal slip between the sheeting and the concrete has on the moment capacity is investigated. This chapter addresses the issue of local buckling of the profiled sheeting, and the effect it has on determining the flexural strength.

Chapter 5 presents the results of a series of flexural tests that were carried out on a number of profiled composite beams. The results are compared to theoretically predicted values, based on the theory of Chapter 4.

Chapter 6 focuses on the transverse shear strength of profiled composite members. Firstly, a review of other work in the area of shear strength determination of reinforced concrete members and profiled composite member is presented. Following this, the results of a series of shear tests that were carried out to determine the effectiveness of profiled sheeting in resisting transverse shear are presented. Finally, the results are compared with the theoretical values calculated from the theory presented earlier. A modification to the existing equations is then proposed based on the findings of the experimental program.

Chapter 7 describes the computer program that was written as part of this research. The program was developed to aid in the understanding of the behaviour of composite members. The chapter starts with a review of other work in the area, and then goes on to describe the program used in this research. The program is divided into two main sections, which are dealt with separately; cross-section analysis, and member analysis. Finally, a comparison is made between predicted results from the computer analysis, and measured results as reported in Chapter 5.

Chapter 2

Composite Beams

2.1 Introduction

The behaviour of composite beams can be strongly influenced by the strength and stiffness of the connection between the steel and concrete elements of the composite beam. If the connectors do not posses sufficient ductility, then they may fail prematurely due to excessive slip. This chapter details the theoretical analysis of simply supported composite beams. In particular, it describes a method for determining the total end slip that occurs in a composite beam, under ultimate moment conditions, and compares this calculated end slip to the allowable slip capacity of the connection. As the problem of premature fracture of shear connectors occurs in beams with low degrees of shear connection, this study will limit itself to the analysis of beams with partial shear connection. Also excluded from the scope this analysis is the serviceability requirements of composite beams with partial shear connection.

The chapter starts with a review of the current work in the area, covering the design of composite beams with partial shear connection, fracture of the shear connectors, and overall load-slip behaviour of stud shear connectors. It then presents a two tiered form of analysis.

The first tier analysis assumes linear elastic material properties with plastic shear connectors, while the second tier is a full non-linear analysis.

2.2 Literature Review

2.2.1 General

This section begins with a brief description of the procedure used to determine the flexural strength of composite beams with partial shear connection, neglecting the effects of fracture of the shear connectors. Research into the limited ductility of the shear connectors is then presented and discussed. This leads onto a review of the design procedures to determine the flexural strength of composite beams that allow for the finite ductility of the shear connectors. A total of four different design approaches which allow for fracture of the shear connectors, are presented and discussed.

2.2.2 Rigid Plastic Analysis

In the design of composite beams, rigid plastic analysis is used in order to determine the ultimate flexural capacity of the beam (Ansourian and Roderick, 1978; Eurocode 4, 1992; Johnson and Molenstra, 1991). In this analysis, it is assumed that the material properties of the concrete and steel can be idealised as rigid-plastic. An example of rigid-plastic analysis is shown in Fig. 2.1. Figure 2.1a shows a typical cross-section of a composite beam, while (b)

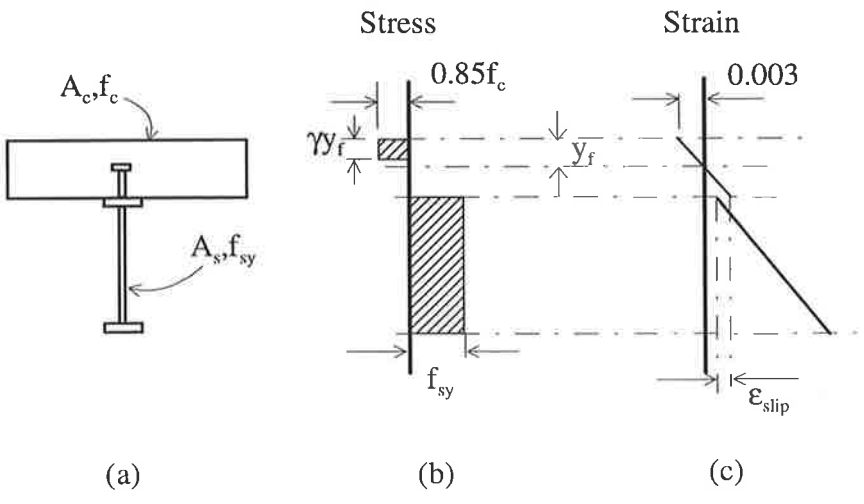


Fig. 2.1. Rigid Plastic Analysis - Full Shear Connection

and (c) show the stress and strain distributions respectively, for full shear connection. It can be seen in Fig. 2.1b that the stress in the steel section is assumed to be constant at the yield stress of the material f_{sy}, and that the concrete compressive stress is also assumed to be constant, while the tensile stress in the concrete is assumed to be zero.

Shown in Fig. 2.2a is a typical cross-section for a reinforced concrete beam, with the strain profile shown in (b), which indicates the location of the neutral axis at a depth of y_c, and the resulting non-linear stress distribution is shown in (c). In the analysis of ordinary reinforced concrete structures, it is common practice in rigid plastic design to assume a constant concrete compressive stress of $0.85f_c$ as in (d), where f_c is the ultimate compressive strength of the concrete (Warner et al., 1989). The depth over which this compressive stress acts is taken as a fraction γ of the depth of concrete which is in compression.

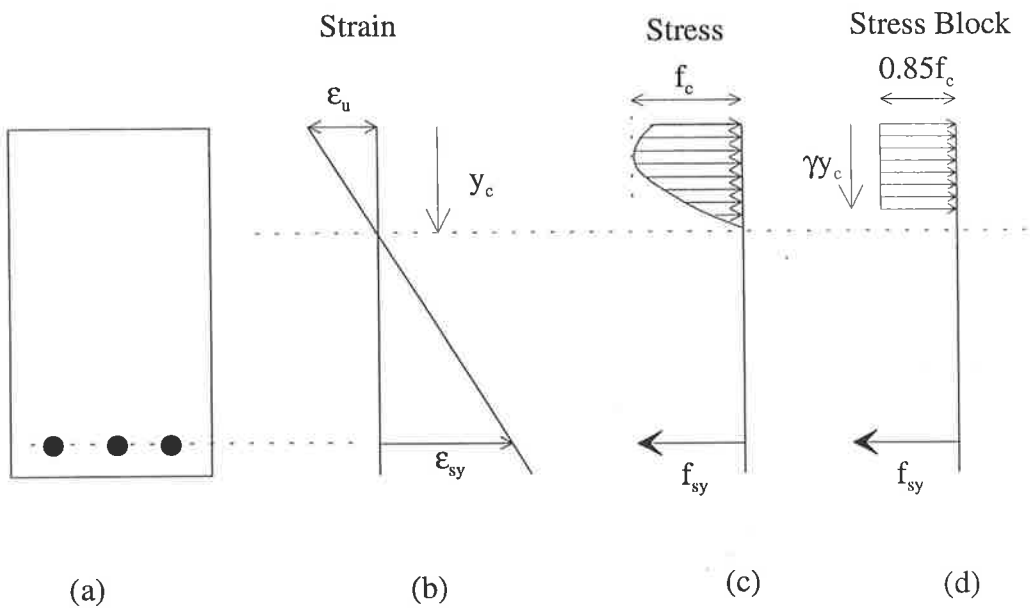


Fig. 2.2. Reinforced Concrete Stress Block

In order for simplified hand calculations of the ultimate moment, the non-linear stress-distribution of Fig. 2.2c is transformed into the equivalent rectangular stress-distribution of (d), with a uniform compressive concrete stress and a reduced area over which it acts. For reinforced concrete design, the depth of the compression block is taken as γy_c, where γ is given by Eq. 2.1 (SAA, 1988a; ACI 318, 1989). The important point to note from this discussion, is that the concrete compressive stress is considered to act over of a portion of the depth of concrete in compression.

$$\gamma = 0.85 - 0.007(f_c - 28) \quad (2.1)$$

where

$$0.65 \leq \gamma \leq 0.85$$

However in the design of composite beams, it is common practice during ultimate flexural strength calculations to assume a uniform compressive stress acts over the entire depth of concrete in compression (Johnson, 1975; Yam, 1981; Oehlers and Bradford, 1995). Thus, the use of a factor such as given by Eq. 2.1 is not necessary. Hence for most flexural strength calculations, the depth of the compression block is the important parameter as opposed to the neutral axis location. This is found from considering axial equilibrium of the concrete compressive force with either the tensile force from the steel beam for full shear connection, or the strength of the shear connection in the shear span for partial shear connection.

In reinforced concrete design, the importance of the location of the neutral axis arises from the need to check that bottom reinforcing has yielded, which can be carried out by assuming a limiting value for the crushing strain of the concrete, ε_u in Fig. 2.2b. For the analysis procedure presented later in this chapter, the neutral axis locations must be calculated in order to determine the slip strain. As the depth of the compression block can be related to the depth of the neutral axis, and vice versa, the use of Eq. 2.1 is used for this analysis. Alternatively, the value of γ can be set to 1 in the procedure presented.

2.2.2.1 Full Shear Connection

When there are sufficient shear connectors in the shear span, such that adding additional connectors will not increase the strength of the member, then the condition is described as full shear connection. The shear span for a simply supported beam is the distance between the section under consideration and the support, and for a continuous beam it is the distance between the section and the point of contraflexure in the beam. The required strength of the shear connectors P_{sh} to achieve the condition of full shear connection depends on the relative axial strengths of the concrete and steel elements in Fig. 2.1a. When the axial strength of the concrete element, $P_c = 0.85 f_c A_c$, is greater than that of the steel element $P_s = A_s f_y$, then the maximum longitudinal shear that can be transferred between the two

elements is limited by the axial strength of the steel section, and hence full shear connection is obtained when $P_{sh} \geq P_c$. When the axial strength of the steel element is greater than that of the concrete element, then the maximum longitudinal shear is limited by the strength of the concrete element.

Figure 2.1c shows the strain distribution for a composite member with full shear connection. In this figure, the strength of the concrete element is greater than that of the steel element, and so the entire steel element is stressed in tension, whereas only part of the concrete element is stressed in compression. It should be noted that there is a step change in the strain profiles of the steel and concrete elements at the interface. This step change is called the slip strain ε_{slip}, and arises due to the flexibility of the connectors. Mechanical shear connectors, such as welded stud shear connectors, which are the most common form of shear connection in composite beams, require a finite slip in order to develop a shear force. Increasing the number of shear connectors is a shear span will increase the stiffness of the connection, and thus decrease the slip strain, but a finite slip strain at the interface will always remain. By integrating the slip strain at all locations along the beam, the slip at the interface can be determined. Thus, for increasing numbers of shear connectors, the strength of the member will not increase, but there will be a decrease in the magnitude of the slip between the two elements.

2.2.2.2 Partial Shear Connection

When the strength of the shear connectors in a shear span is less than the axial strengths of both the concrete and steel elements, then the strength of the shear connection will limit the flexural strength of the member. Figures 2.3b and c show the stress distribution and the strain distribution respectively for a composite beam with partial shear connection. It can be seen in Fig. 2.3c that there now exists two distinct neutral axes, one in the concrete element, and one in the steel element. The steel section is now only partially stressed in tension, and partially stressed in compression, as compared with the full shear connection in Fig. 2.1c where it is fully stressed in tension. The magnitude of the slip strain in Fig. 2.3c has increased compared to that for the full shear connection case in Fig. 2.1c, and integration of this slip strain along the length of the member will result in much larger slips at the interface.

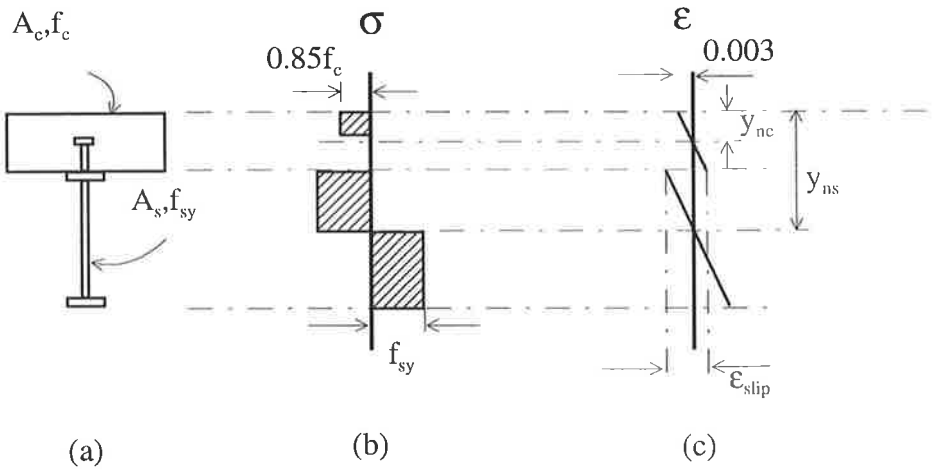


Fig. 2.3. Rigid Plastic Analysis - Partial Shear Connection

2.2.2.3 Degree of Shear Connection

The rigid plastic analysis procedures presented in Sections 2.2.2.1 and 2.2.2.2 may be used to determine the flexural capacity of composite beams with varying degrees of shear connection. The degree of shear connection is defined as:

$$\eta = N/N_f \quad \text{.....(2.2)}$$

where

N = Number of shear connectors in the shear span

N_f = Number of shear connectors required for full shear connection

Figure 2.4 shows the variation in the flexural capacity, M_f, of a composite beam with the degree of shear connection η. It can be seen that for zero shear connection ($\eta = 0$), the strength of the beam is just that of the steel section M_S, and for full shear connection ($\eta = 1$) the strength of the beam is denoted by M_{fsc}. When the degree of shear connection is increased beyond 1.0, then the strength of the beam does not increase above M_{fsc}, as explained in Section 2.2.2.1. The variation of the moment capacity between M_S and M_{fsc} can be found using standard rigid-plastic analysis, as described by Oehlers and Bradford (1995), and is shown in Fig. 2.4 by the curve C-T-B-A. This approach is called the equilibrium method. As an alternative to this method, the variation in moment capacity can be approximated by the straight line C-B, which is called the interpolation method (Johnson, 1975; Yam, 1981; Oehlers and Bradford, 1995).

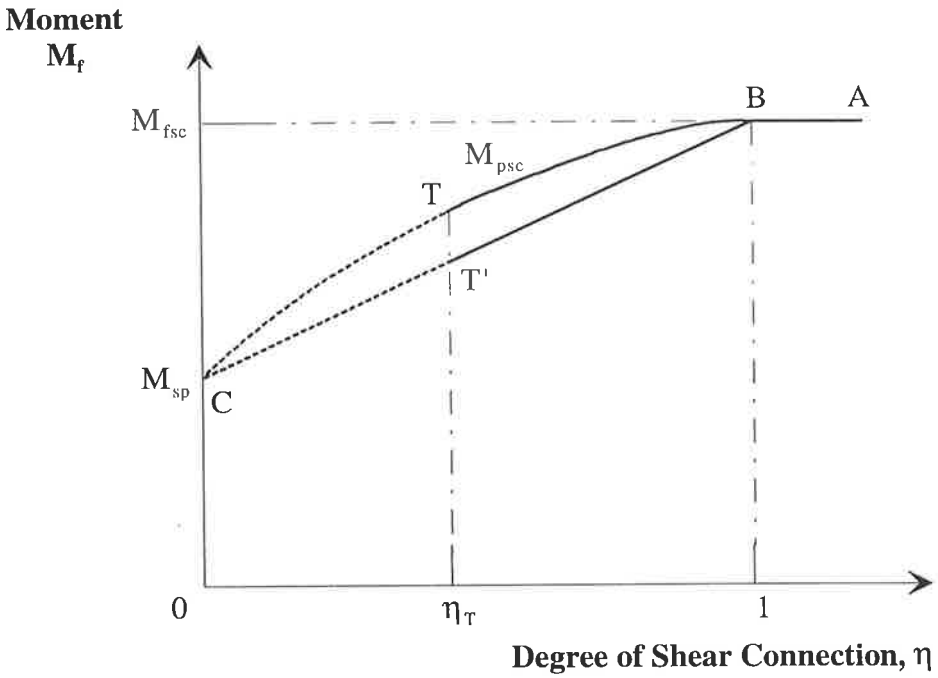


Fig. 2.4. Moment Interaction Diagram

2.2.3 Behaviour of Stud Shear Connectors

As the number of shear connectors in the shear span decreases, the degree of shear connection decreases, and the slip strain at the interface increases. Integration of this increased slip strain in turn leads to an increase in the maximum slip at the interface. Experimental research (Yam and Chapman, 1968; Oehlers and Coughlan, 1986; Johnson and Molenstra, 1991) has shown that welded stud shear connectors have only finite slip capacity, which if exceeded, will lead to fracture of the connectors. Thus, as the degree of shear connection decreases, fracture of the connectors becomes increasingly likely and must be considered in the design process. A review of research on the load-slip characteristics of welded stud shear connectors is presented and discussed, as their behaviour is fundamental to the overall behaviour of the composite beam.

2.2.3.1 Stiffness of Shear Connectors

Typical load-slip characteristics for welded stud shear connectors in solid slabs are shown in Fig. 2.5, where the strength is given as a proportion of the maximum static strength P_u, and the slip is given as a proportion of the diameter of the shank of the stud, d_{sh}. The results shown in Fig. 2.5 are for 19 mm studs in normal density concrete. Tests have shown

(Oehlers and Coughlan, 1986) that the stiffness of the load-slip curve increases with an increase in concrete strength and a decrease in the diameter of the studs. However, when the results are presented non-dimensionally as shown in Fig. 2.5, the stiffness is independent of the diameter of the stud.

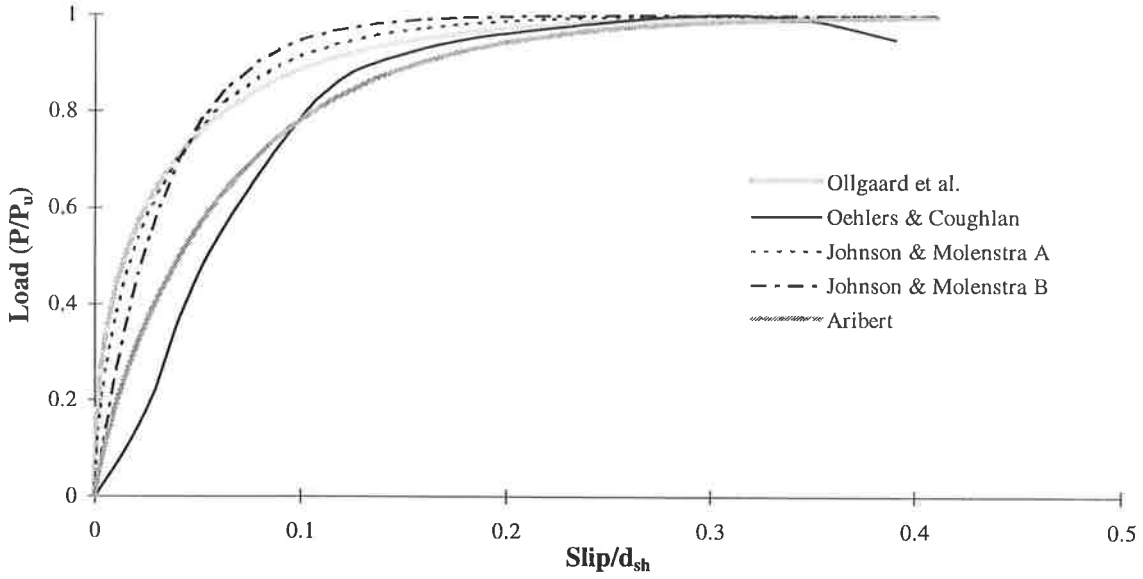


Fig. 2.5. 19 mm Stud Shear Connectors

The curve of Ollgaad et al. (1971), shown in Fig. 2.5, was derived from the results of 6 push-out tests, which were part of a larger series of 48 tests. The curve was considered representative of the test results, which were for 19 mm studs in normal weight concrete, with compressive strengths that varied from 28 MPa to 35 MPa. One third of the specimens were loaded to ultimate load without unloading, while the remaining specimens were loaded to approximately the working load level, which was taken as 45 kN per connector, then unloaded and reloaded to their ultimate load. The curve shown in Fig. 2.5 represents an average of the loaded and unloaded test results, and is given by Eq. 2.3, with $\nu = 0.4$, and $\omega = 0.709$. No analysis was given of the results of the unloaded specimens as the differences were not thought to be significant. However, inspection of the load-slip curves indicate a substantially lower initial stiffness for the initially unloaded specimens, as found by Oehlers and Coughlan (1986).

$$P = P_u\left(1-e^{-\omega s}\right)^{\nu} \qquad \text{.....(2.3)}$$

where

P_u = Design strength of the connectors (kN)

s = Slip at the connectors (mm)

The curve of Oehlers and Coughlan (1986), shown in Fig. 2.5, was determined from a statistical analysis of the results of push tests of stud shear connectors embedded in concrete blocks. The load slip curve by Oehlers and Coughlan is less stiff than those of the other researchers due to the fact that the specimens were not pre-loaded before recording the load-slip curves, and thus included the initial set of the connectors in the concrete. The load-slip curves of those specimens that failed prematurely due to splitting were included prior to splitting and neglected after splitting occurred. Determining the load-slip curves without pre-loading the specimens gives a more accurate representation of the behaviour of stud shear connectors as the connectors are not pre-loaded in practical applications.

The two curves shown by Johnson and Molenstra (1991) in Fig. 2.5 indicate the load-slip curves used in their analyses. Johnson and Molenstra did not perform their own push tests, but stated that their results were representative of the results of other researchers. Reference was made to the results of Menzies (1971), Buttry (1965) and Oehlers and Coughlan (1986), however their results were did not correspond to those of Johnson and Molenstra. The load-slip characteristics for stud-shear connectors shown in Fig. 2.5 were defined using an exponential form, as given by Eq. 2.3. The values of ν and ω were given by Johnson and Molenstra as:

$\nu = 0.558$ and $\omega = 1.0$ for curve A

$\nu = 0.989$ and $\omega = 1.535$ for curve B

It should be noted that in Johnson and Molenstra's analyses, the effect of varying the stiffness of the load-slip curve for the connectors was investigated. It was reported that by halving the initial stiffness of the connectors, the maximum slip at the design ultimate load was increased by less than 5%. Also, when the slip at which the connectors reached 99% of their design strength was doubled, the increase in slip at the design ultimate load was approximately 10%. Thus, it was concluded that the maximum slips derived from their computer analyses were not sensitive to the shape of the load-slip curve.

Also shown in Fig. 2.5 is the load-slip curve used by Aribert (1990, 1993) in the computer simulations which were carried out. This curve follows the same form as the

curves used by Johnson and Molenstra, and given in Eq. 2.3, with the values of $\nu = 0.8$, and $\omega = 0.7$. It was stated in Aribert's paper that the curve used represented the best fit to the mean resistance of push-out tests which were performed in conjunction with full scale beam tests. A range of load-slip curves were investigated, and it was found that the maximum slips were not sensitive to the variation in the curves. However, it was not stated exactly what variation in the load-slip curves was investigated.

It is possible to find values of ν and ω such that the curve given by Eq. 2.3 fits the data derived by Oehlers and Coughlan (1986), and shown in Fig. 2.5. The values are $\nu = 1.86$, and $\omega = 1.1$. These are the values that are used in the computer analysis that is presented in Chapter 7, and will be discussed further in that chapter.

2.2.3.2 Ductility of Shear Connectors

For the purposes of the present research, the region of interest in the curves shown in Fig. 2.5 is that portion where the strength of the connectors is near the maximum value. For the purposes of this thesis, this region will be defined by the range of slip where the strength of the connectors is within 5% of the ultimate strength, as shown in the idealised load-slip curve in Fig. 2.6. This region is bounded by the yield slip s_y, defined in this thesis as when the load in the connectors has reached 95% of their maximum load, and the ultimate slip s_u, which is defined as when the load in the connectors has reduced to 95% of their maximum. The slip at which the maximum load P_u occurs in the shear connectors is denoted by s_{sh}. The use of $0.95P_u$ on the descending branch to locate the ultimate slip, is based on the redistribution between studs that has been observed in tests on beams with solid slabs (Johnson and Molenstra, 1991), before the maximum load is reached. Thus, as the load reduces slightly in those connectors with slips greater than s_{sh}, this is compensated by an increase in the load in other connectors in the shear span which have slips less than s_{sh}. Greater redistribution may be expected in beams with composite slabs, which is why Mottram and Johnson (1990) reported slips from push tests until the load fell below $0.8P_{sh}$ on unloading branch.

The results of the regression analysis of Oehlers and Coughlan (1986) give the slip in the shear connectors for different load levels, based on the concrete strength and the diameter of the stud. From these results and the definition of the yield slip adopted in this thesis, it is

possible to define the yield slip in terms of the stud diameter and the concrete strength, as given by Eq. 2.4.

$$s_y = (0.223 - 0.0012f_c)d_{sh} \quad \text{.....(2.4)}$$

where

s_y = yield slip of the connectors (mm)

d_{sh} = diameter of stud (mm)

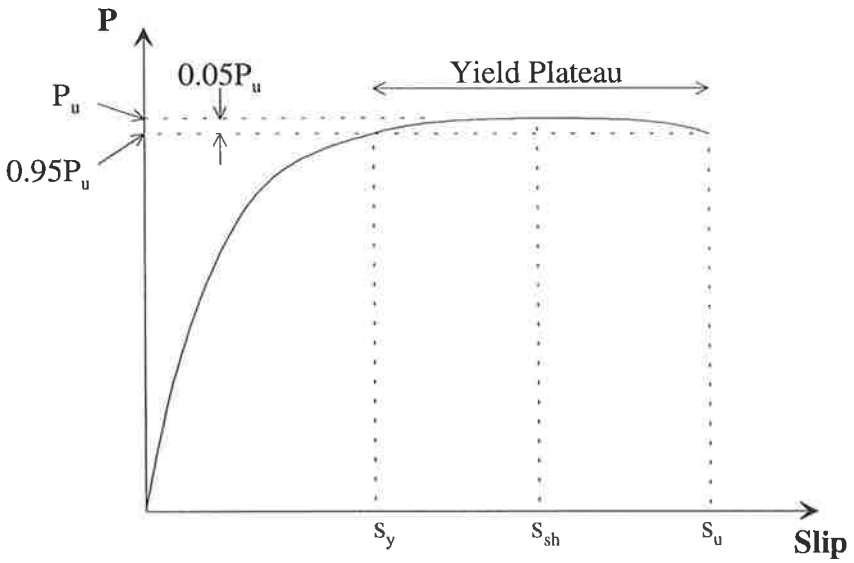


Fig. 2.6. Idealised Load vs Slip behaviour for Stud shear connectors

The ultimate slip capacity of welded stud shear connectors, that do not fail by premature splitting of the concrete, can be considered to occur when the strength of the connectors has reduced to 95% of the maximum strength (Oehlers and Coughlan, 1986; Johnson and Molenstra, 1991). From the results of Oehlers and Coughlan (1986), when the load has reduced to 95% of the maximum the slip in the connectors is given by:

$$s_u = (0.453 - 0.0018f_c)d_{sh} \quad \text{.....(2.5)}$$

where

s_u = Ultimate slip capacity of the connectors (mm)

For 19 mm studs in normal density concrete these formulae give the yield slip as $s_y = 3.4$ mm, and the ultimate slip capacity as $s_u = 7.4$ mm. This shows that the yield plateau

of 19 mm welded stud shear connectors is approximately equal to half the slip capacity. Thus, in the region where the slip along the shear span is greater than half the slip capacity, the connectors can be considered to be fully loaded.

On the other hand, if a more conservative estimate is required for the slip capacity of the shear connectors, then the slip at which the maximum strength of the shear connector is reached, s_{sh} in Fig. 2.6, can be used. This is given by Eq. 2.6 (Oehlers and Coughlan, 1986). Alternatively, if other forms of shear connectors are used, then their load-slip characteristics can be determined from push tests and used in the analysis.

$$s_{sh} = (0.406 - 0.0025f_c)d_{sh} \quad (2.6)$$

where

s_{sh} = Slip at which the maximum load of the connectors is reached (mm)

Aspects which can restrict the ductility of the shear connection in the presence of profiled steel sheeting have been reported (Hawkins and Mitchell, 1984; Patrick and Bridge, 1988), and involve rib punch-through, connector pull-out, and rib shear failures with horizontal splitting of the concrete cover slab. These failure modes are very different from those of connectors failing in shear in solid slabs. However, composite slabs built with the Australian profiled sheetings (described in Chapter 4) resemble solid slabs much more closely (Patrick and Bridge, 1987), than do the wide-ribbed trapezoidal profiles used in the tests which exhibited the punching failure modes. Furthermore, brittle failure modes can be avoided through the following measures: properly detailing transverse reinforcement; restricting the proximity of shear connectors to sheeting ribs; selecting suitable spacing of the shear connectors; and adding reinforcement to the concrete slab at special details.

2.2.4 Fracture of Shear Connectors

Current design rules limit the minimum degree of shear connection and the span of the beam, in order to prevent fracture of the connectors (BS. 5950, 1990; Eurocode 4, 1992; Canadian Standards, 1984). The minimum degree of shear connection η_T, is shown in Fig. 2.4 by the point T for the equilibrium method, and point T' for the interpolation method, and is called the Transition Point. For ductile connectors such as stud shear connectors, the

minimum allowable value of η_T given in the national codes of Britain (BS 5950, 1990), Europe (Eurocode 4, 1992) and Canada (CAN3-S16.1, 1984) ranges from 0.4 to 0.5. The determination of this transition point has been researched only recently (Johnson and Molenstra, 1991; Aribert, 1990, 1993) and each of their approaches will now be discussed further.

2.2.4.1 Johnson and Molenstra

Johnson and Molenstra (1991) carried out non-linear numerical analyses to determine the controlling parameters which govern the maximum slip for composite beams with partial shear connection. The results of their analyses indicated that the maximum slip increased consistently when any of the four groups of variables given by Eq. 2.7 increased.

$$\frac{L}{D}, \frac{M_{fsc} - M_{sp}}{M_{sp}}, \frac{y_{pl}}{d_c + d_s}, \frac{F_c}{F_s} \qquad (2.7)$$

where

L = Length of the beam

D = Total depth of the composite beam

M_{fsc} = Plastic moment for the composite section with full shear connection

M_{sp} = Plastic moment of resistance of the steel beam

y_{pl} = Depth of the plastic neutral axis for full shear connection below the top of the slab

d_c = Depth of the concrete slab

d_s = Depth of the steel beam

F_c = Maximum longitudinal force in concrete slab = $0.85 f_c b_c d_c$

F_s = Maximum longitudinal force in steel beam = $f_{sy} A_{st}$

In their study, fifteen two span beams were analysed, along with 45 single span beams with solid slabs and 28 beams with composite slabs. Multiple linear regressions were carried out on the groups of parameters given by Eq. 2.7, in order to determine an expression for the end slip. The result of their analyses is given by Eq. 2.8, which represented a compromise between simplicity and accuracy. The coefficient of variation of the errors was 4.9% for

$N/N_f = 0.5$, and was 8.0% for $N/N_f = 0.75$, as determined by the difference between the predicted end slip from Eq. 2.8 and that calculated from the non-linear computer analyses.

$$s_u = s_o\left(\frac{L}{D}\right)^{\alpha}\left(\frac{M_{fsc} - M_{sp}}{M_{sp}}\right)^{\beta} \quad \text{.....(2.8)}$$

where

$$s_o = \frac{M_{sp} L d_s}{6(EI)_s} \quad \text{.....(2.9)}$$

s_u = Maximum slip at the interface

$(EI)_S$ = Elastic flexural rigidity of the steel beam

for $N/N_f = 0.5$: $\alpha = -0.13$, $\beta = 1.03$

for $N/N_f = 0.75$: $\alpha = -0.24$, $\beta = 1.70$

The expression for s_o given by Eq. 2.9 is the elastic end slip with zero shear connection, when the steel beam is subjected to the plastic moment M_{sp}. It can be calculated from linear elastic theory, which is covered in Section 2.4.2. The derivation of the expression in Eq. 2.9 assumes that the concrete section does not contribute to the flexural strength or stiffness of the composite member, for the case of zero shear connection.

The method of deriving Eq. 2.8 by use of multiple linear regressions on different sets of parameters provides only limited insight into the behaviour of composite beams. It is worth noting that the coefficient of variation of the errors is low, given the complexity and variability of the nature of end slip determination. However, the choice of controlling parameters appears somewhat arbitrary, and it is possible that another choice of parameter combinations other that those given in Eq. 2.7 may give adequate results, and also lead to a better understanding of the fundamental controlling parameters.

A distinction should be drawn between the fundamental controlling parameters such as the yield strengths of the materials and the dimensions of the beam, and the dependant parameters such as the flexural strength of the beam. Expressions containing combinations of dependant parameters may be rearranged in terms of the fundamental parameters, and may lead to a better insight into the nature of the problem. It is noted that due to the complex

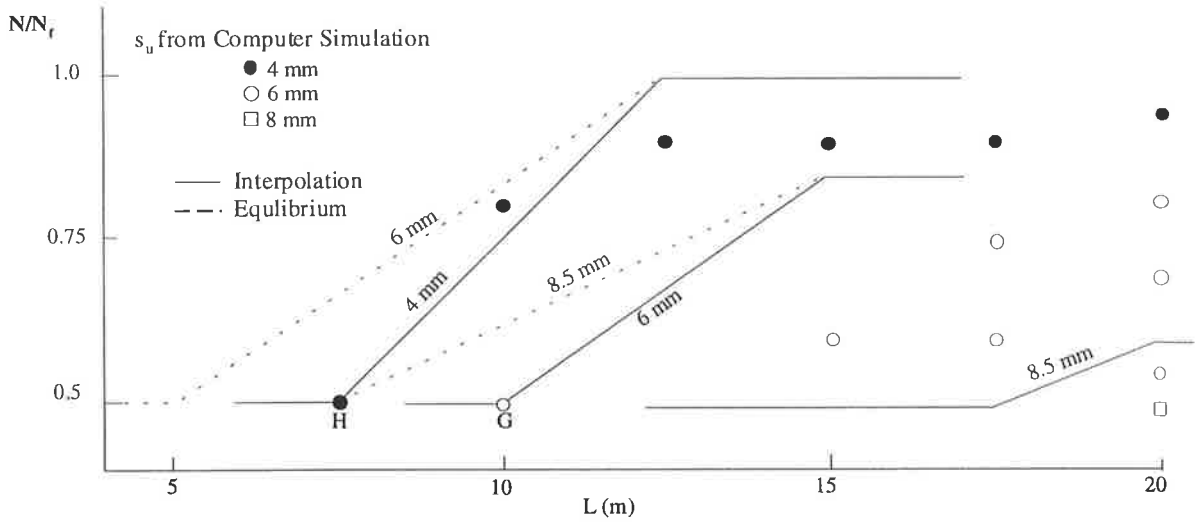
nature of end slip determination, deriving an expression containing simple combinations of the fundamental parameters may not be possible from techniques such as linear regression analysis. What is required is a more fundamental approach based on the properties of the beam and its component materials, which is the subject of this thesis.

The parameters α and β in Eq. 2.8 are only given at $N/N_f = 0.5$ and $N/N_f = 0.75$. It is not clear which values to use for α and β for other values of N/N_f. The negative values of α appear to indicate that as the span to depth ratio increases, the end slip decreases, which is not as expected. However, upon closer inspection it is seen that s_o in Eq. 2.9 contains L, and thus the end slip is proportional to $L^{1+\alpha}D^{-\alpha}$. It should be noted that the Young's Modulus of the concrete E_c, is not included in Eq. 2.8, indicating that caution should be used when applying this equation to beams with light weight concrete.

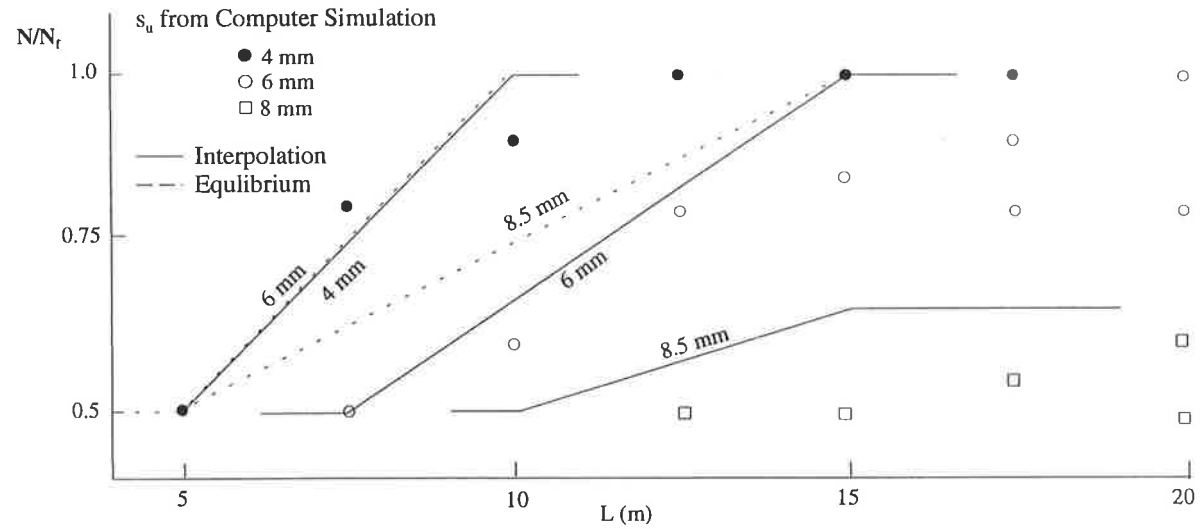
From the results of the computer analyses by Johnson and Molenstra, values of s_u at the design ultimate load were computed for different values of N/N_f and span. These are shown in Fig. 2.7a for beams where the ratio of the areas of the bottom flange to top flange A_b/A_t, is not greater than 1.5, and in Fig. 2.7b for beams where the ratio is between 1.5 and 3. For a given value of N/N_f, slip increases with span, as expected. Similarly, for a given span, the degree of shear connection must increase in order to decrease the slip. The full lines are tentative design rules, one for each value of slip capacity, when the interpolation method is used to design the shear connection. The dashed lines are tentative design rules when the equilibrium method is used.

It should be noted that the values shown above were calculated from numerical studies which included a partial safety factor for concrete of 1.5, for steel of 1.0, and for the shear connectors of 1.25. The partial safety factors were included in both the design of the beams and in the numerical simulations. As most of the beams analysed had the neutral axis for full shear connection in the concrete element, the use of the partial safety factor for concrete resulted an increase in the depth of the compressive stress block, which was still within the depth of the concrete (Johnson and Molenstra, 1990). The effect of the partial safety factor for concrete reduces the lever arm, and thus reduces the plastic moment M_{fsc}, and the last term in brackets in Eq. 2.8 will reduce even further. Thus, the inclusion of the partial safety factor for concrete tends to underestimate the slip, compared to that when the real material

properties are used. As the parameters α and β were determined from the output of the computer simulations, they will be affected by the inclusion of the partial safety factors.



(a) $1.0 \leq A_b/A_t < 1.5$



(b) $1.5 \leq A_b/A_t \leq 3$

Fig. 2.7. Values of Maximum Slip (Johnson and Molenstra, 1991)

The use of the partial safety factor for the shear connectors is ambiguous. Due to the fact that the strength of the shear connectors was decreased in the determination of the design strength M_{psc}, as well as in the computer simulations, the ratio of N/N_f is unaffected by the inclusion of the partial safety factor.

This computer parametric analysis represents simple method of checking the controlling parameters of maximum slip in a composite beam. Figure 2.7 presents a simple design method to determine the minimum degree of shear connection for a composite beam

to prevent fracture of the connectors, and Eq. 2.8 for describing the maximum slip in the beam. However, this analysis does not present a design procedure which is based on a fundamental understanding of the interactions causing slip. The relative effects of numbers of variables are excluded, in order to attain simplicity. This simplicity is required for use in a design office, but does not allow a more thorough analysis without the use of computer modelling.

2.2.4.2 Aribert

Aribert (1990; 1993) also carried out a series of non-linear numerical analyses on composite beams, in order to determine maximum slips for a variety of beam geometries, and various degrees of shear connection. The analytical model consisted of dividing the composite beam into a series of segments, and a number of differential equations were set up for each segment. These differential equations described the moment equilibrium of the cross-section, and the strain compatibility at the steel and concrete interface, as well as equations to describe the behaviour relationship of the cross-section and the connector behaviour. This procedure is similar to that adopted in this thesis, and is described fully in Chapter 7. The solution of the differential equations is carried out using a transfer matrix, and then checking the boundary conditions at the ends of the beam.

The analyses were restricted to composite beams with solid slabs, and welded headed studs as connectors. The load-slip relationship of the connectors that was used in the analysis had a mean ultimate slip s_u equal to 5 mm, and was discussed previously in Section 2.2.3. It was stated that a variety of load-slip curves were used, with slightly different values of s_u, and the results did not change significantly. However, the different values of s_u were not reported.

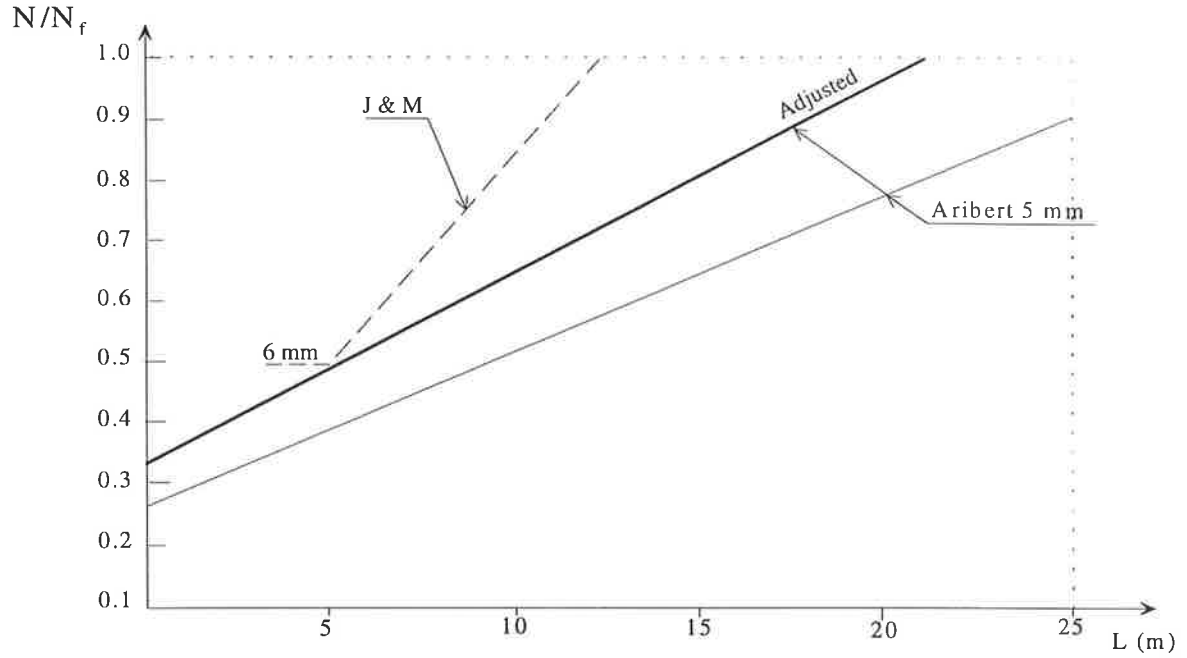
A parametric analysis was carried out on over 300 composite beams, in which the variables included: span, degree of shear connection, ratio of bottom flange to top flange areas, ratio of axial strength of concrete to axial strength of steel, and concrete strength. The transition point, as indicated by point T in Fig. 2.4, was calculated for each of the beams studied, and collated. A regression was carried out on the data to produce a single line for a maximum probability of 5% of over-estimation of the minimum allowed degree of shear connection. The results are shown in Fig. 2.8a for composite beams with steel sections with

equal flanges, and Fig. 2.8b for unequal flange beams. It should be pointed out that these results are derived using the equilibrium method, as point T in Fig. 2.4 was used, and not point T'. A partial safety factor of 1.25 was used for the design of the shear connection in the analyses, whereas the computer analyses did not incorporate partial safety factors. There were no other partial safety factors used in the analyses.

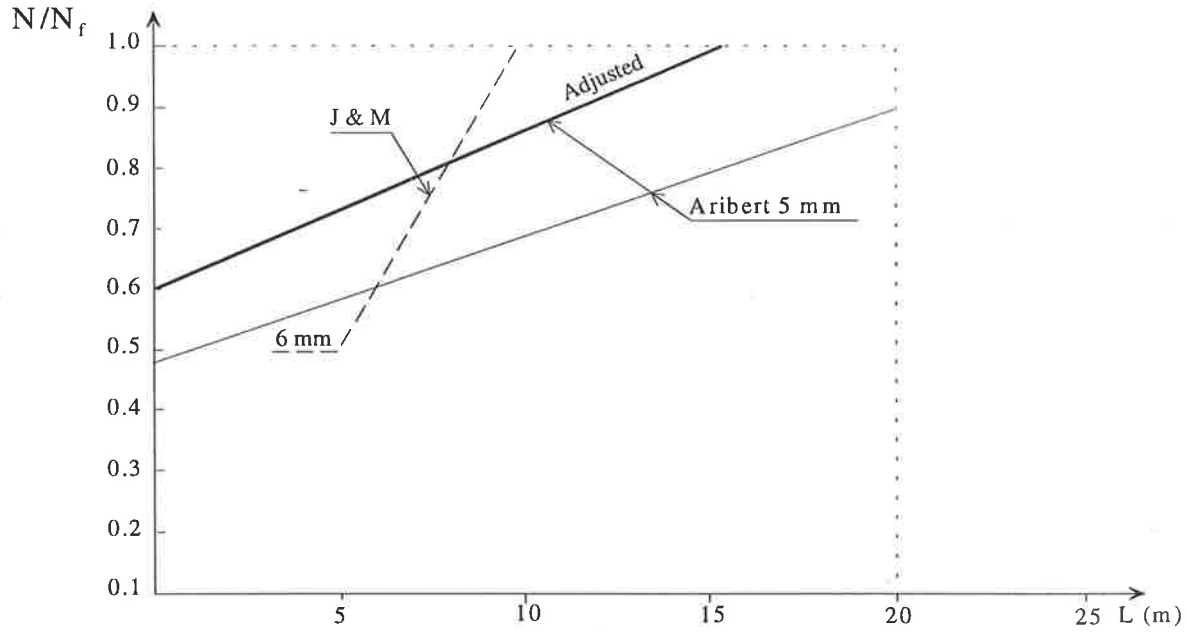
The effect of the inclusion of the partial safety factor in the design of the shear connection, but not in the numerical model, is to change the values of N/N_f by a factor of 1.25. Thus, for a degree of shear connection of say 0.8 in Fig. 2.8, the actual degree of shear connection used in the computer model is 0.8 x 1.25 = 1.0. The adjusted curve is shown in Fig. 2.8.

Also shown in Fig. 2.8 are the values proposed by Johnson and Molenstra (1991), which are indicated by the label J & M. It can be seen that their values are more conservative than those of Aribert for the equal flange beams, as shown in (a), while the values proposed by Aribert are generally more conservative for the unequal flange beams shown in (b). The reason for this discrepancy can largely be explained by the difference in the choice of the line describing the scatter of the data. The lines shown in Fig. 2.7 were described as 'safe approximations to the computed results', without any discussion on how they were related to the data. On the other hand, the design guidelines proposed by Aribert and shown in Fig. 2.8, were determined by regression to produce a single line for a maximum probability of 5% of over-estimation of the minimum allowed degree of shear connection.

The procedure adopted by Aribert for the determination of the allowable degree of shear connection is similar to that proposed by Johnson and Molenstra (1991). As such it is subject to the same limitations as mentioned earlier in Section 2.2.4.1. The results shown in Fig. 2.8 present a simple design method to determine the minimum degree of shear connection for a composite beam to prevent fracture of the connectors. However, this analysis does not present a design procedure which is based on a fundamental understanding of the interactions causing slip. The relative effects of numbers of variables are excluded, in order to attain simplicity.



(a) $A_b/A_t = 1$



(b) $1.5 \leq A_b/A_t \leq 3$

Fig. 2.8. Values of Maximum Slip (Aribert, 1992)

2.2.4.3 Oehlers and Sved

Oehlers and Sved (1995) derived a procedure which uses linear-elastic material properties and rigid-plastic shear connectors, in order to determine the location of the transition point. This analysis is the basis of the first tier method of analysis used in this thesis, and is described fully in Section 2.4.2. Their work is an extension of the procedure

proposed by Newmark et al. (1951), which used a linear elastic analysis with linear shear connectors. The work by Oehlers and Sved allows for yielding of the shear connectors. The use of linear elastic analysis for the determination of maximum slip, under ultimate moment conditions, was considered appropriate due to the fact that the effects of plasticity in the steel and concrete would not greatly alter the overall slip distribution.

The maximum slip that occurs in single span composite beam can be found numerically by integrating the slip strain along the entire length of the beam, and thus is a function of the material properties of the whole length of the beam. It was stated that the regions affected by plasticity in the concrete and steel would be small in comparison the whole length of the beam, and thus could be ignored as a first approximation. Conversely, the connectors would be at yield over much of the length of the beam, except for a small portion near the ultimate moment location.

The results of the analysis for a simply supported beam with a uniform distribution of shear connectors is given by Eq. 2.10. A more generalised analysis is detailed in Section 2.4.2. Equation 2.10 gives the slip at the end of the beam as a function of the geometric and material properties of the beam, the loading, and the degree of shear connection.

$$s_{max} = \frac{M_{max} L}{3} K_1 - \frac{P_{max} L}{4} K_2 \quad \text{.....(2.10)}$$

where

$$K_1 = \frac{h_s + h_c}{(EI)_s + (EI)_c} \quad \text{.....(2.11)}$$

$$K_2 = \frac{(h_s + h_c)^2}{(EI)_s + (EI)_c} + \frac{1}{(EA)_s} + \frac{1}{(EA)_c} \quad \text{.....(2.12)}$$

h_s = Distance from centroid of the steel element to concrete-steel interface

h_c = Distance from centroid of the concrete element to concrete-steel interface

$(EI)_c$ = Flexural rigidity of the concrete element

$(EI)_s$ = Flexural rigidity of the steel element

$(EA)_c$ = Axial rigidity of the concrete element

$(EA)_S$ = Axial rigidity of the steel element

By rearranging Eq. 2.10 in terms of M_{max}, and replacing s_{max} by the slip capacity of the shear connectors, s_u, then the moment capacity at which fracture occurs can be determined, and is given by Eq. 2.13. This equation can be plotted on an interaction diagram such as that shown in Fig. 2.4, and the transition point T can be determined from the intercept of Eq. 2.13 with that for M_{psc} as given in Section 2.2.2.3.

$$M_{frac} = 6(EI)_{sc}\frac{s_u}{DL} + \frac{3F_{psc}}{4}\left(\frac{D}{2} + \frac{2(EI)_{sc}}{D(EA)_{sc}}\right) \quad \text{.....(2.13)}$$

where

$$(EI)_{sc} = (EI)_s + (EI)_c$$

$$(EA)_{sc}^{-1} = (EA)_c^{-1} + (EA)_s^{-1}$$

A comparison with the results from Aribert and Johnson and Molenstra is shown in Fig. 2.9, with the curves labelled as O & S. The curves are shown for limiting slip capacities of 3 and 6 mm. These curves were obtained by deriving the intercept of Eq. 2.13 with M_{psc} in Fig. 2.4 for a given value of s_u and for varying lengths of beam. It should be noted that results were for only one cross-section, with fixed material properties. They do not represent recommended lower bounds to the degree of shear connection as do the curves shown by Johnson and Molenstra, and Aribert. As such, it is not possible to make a direct comparison between the results of Oehlers and Sved and those of the other researchers. The results of Oehlers and Sved shown in Fig. 2.9 would represent a lower bound to the minimum degree of shear connection, as different combinations of beam geometries and material properties would likely require higher degrees of shear connection. It can in fact be seen that the curves of Oehlers and Sved do represent lower bounds in comparison to those of Johnson and Molenstra, and Aribert.

The procedure developed by Oehlers and Sved provides a first order method to determine the minimum degree of shear connection to prevent fracture of the shear connectors. This analysis is based on linear elastic steel and concrete properties, plasticity in the shear connectors, and the cross-sectional properties of the beam. While there seemed to be reasonable correlation with the results of more rigorous non-linear analyses, as shown in

Fig. 2.9, this comparison was carried out for only one beam cross-section, and one set of material properties. It is possible that the first order analysis may give unconservative results for some beam arrangements. It is for this reason that further refinement of the analysis procedure should be carried out.

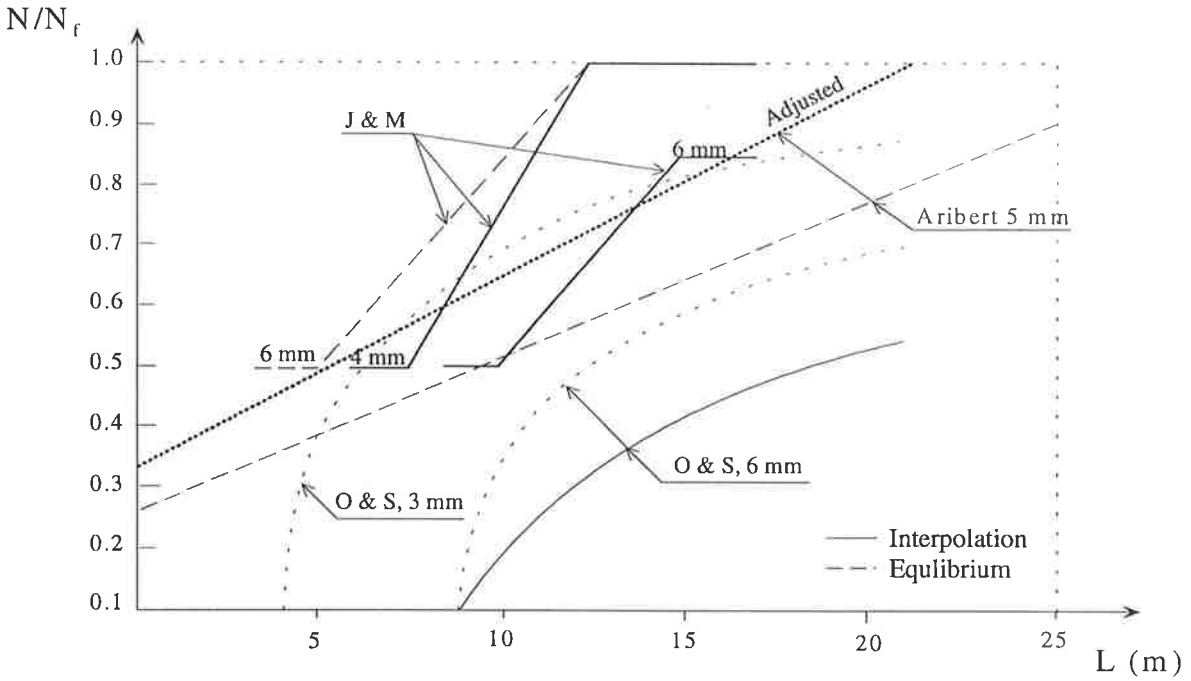


Fig. 2.9. Values of Maximum Slip (Oehlers and Sved, 1995)

2.2.4.4 Conclusions

The analysis procedures of Johnson and Molenstra, and Aribert, resulted in the formulation of minimum degrees of shear connection to prevent fracture of the shear connectors, based on the span of the beam. It was stated (Johnson and Molenstra, 1991) that the results shown in Fig. 2.7 were conservative for most beam geometries, and very conservative for some. This same comment would be true for the curves of Aribert in Fig. 2.8, due to the similarity of their derivation. The procedure lends itself well to a design office, where simplified conservative analyses are required. However, for some beam geometries the procedure will result in degrees of shear connection which are overly conservative.

As an alternative to this simplified approach, the analysis procedure presented by Oehlers and Sved (1995) allows the magnitude of the slip to be calculated based on the material and cross-sectional properties, and the degree of shear connection of each individual

beam. This procedure represents a more rational approach to that of Johnson and Molenstra, and Aribert. However, the procedure is limited by the use of linear elastic concrete and steel properties, and may be unconservative for some beam geometries.

This thesis expands on the approach adopted by Oehlers and Sved (1995), by allowing for yielding of the steel, cracking of the concrete and hinge formation. The fundamental approach of determining the end slip based on the material and cross-sectional properties and the degree of shear connection will be adopted in this thesis.

2.2.5 Uplift Effects

Various researchers have analysed the effects of uplift on the slip distribution of composite beams (Andekola, 1968; Roberts, 1981; Robinson and Naraine, 1988). Results have shown that the variation of the behaviour of the beam due to the inclusion of the uplift effects are minimal. Robinson and Naraine (1988) performed analyses on composite beams that assumed elastic material properties and elastic connection properties, and compared the results to the analyses of Newmark et al. (1951), and found negligible differences between the horizontal shear per unit length distributions for the two analysis procedures.

Aribert and Aziz (1986), and Aribert (1993) used transfer matrix methods and non-linear analyses that are the most comprehensive yet available. They studied widely spaced connectors and loads suspended from the steel beam, and found that uplift had negligible effect on the distribution of slip along the beam. Where loads are applied to the slab, typical values near failure are an uplift of 0.04 mm, and a 3% increase of slip.

Based on the finding of these researchers, the analysis presented in this thesis will neglect the influence of uplift effects on the longitudinal shear distributions and on the slip distributions along the composite beam. This is equivalent to neglecting shear strains in the steel beam and concrete slab. These strains can increase deflections in service by about 10%, but have little influence on behaviour at ultimate load of beams with above average span/depth ratios (Johnson and Molenstra, 1991)

By neglecting the effect of uplift, several other important assumptions may now be made. The most important of these is that the curvatures in the concrete and steel elements are identical. Any difference between the two curvatures must mean a difference in the

vertical deflections of the two elements, which in turn means a difference in the curvatures. This assumption of equal curvatures will be developed further in Section 2.4.2.4.

2.2.6 Concrete Cracking

The problem of end slip determination in a composite member is similar to the problem of estimating short-term deflections of reinforced concrete beams. Both problems require an estimate for the flexural stiffness of the member along the length. A difficulty arises in composite members, however, because the flexural stiffness of the concrete element changes with the curvature in the section, and also with the degree of shear connection for a given curvature. The most common method for determining the short term deflections of reinforced concrete members uses an equivalent flexural stiffness, as determined by Branson's equation (Branson, 1963). The equivalent stiffness that is determined, is assumed to be applicable to the entire length of the member, and deflections are then calculated using standard elastic deflection theory, as given by Warner et al. (1989).

This concept of an equivalent elastic stiffness that is constant along the length of the member is also used by the British design code (BS 5950, 1990), and is recommended by the American design guidelines (AISC, 1985). It is assumed that the stiffness of the composite section varies linearly with the degree of shear connection, and the midspan deflection δ of a composite beam can be calculated by using an equivalent stiffness and simple linear elastic theory. The variation in stiffness with shear connection is expressed indirectly by an expression for the variation in deflection with shear connection, and is given by Eq. 2.14. As the deflection and stiffness are related from linear elastic theory, this equation can be used to describe the variation in stiffness.

$$\delta = \delta_f + 0.3(1-\eta)(\delta_s - \delta_f) \quad \text{.....(2.14)}$$

where

η = Degree of shear connection

δ_f = Midspan deflection for a composite beam with full interaction

δ_s = Midspan deflection for the steel beam alone, for the same applied load

American design guidance (AISC, 1985) uses a non-linear variation of the flexural stiffness of the composite member with the degree of shear connection, as given by Eq. 2.15.

$$I_e = I_s + \eta^{0.5}(I_f - I_s) \quad \text{.....(2.15)}$$

where

I_e = Equivalent moment of intertia of composite section transformed into steel

I_f = Moment of inertia of the composite section with full interaction transformed into steel

I_S = Moment of inertia of the steel section alone.

Wright and Francis (1990) compared the above formulae to test results on 4 composite beams with low degrees of shear connection. The beams were initially set up on roller supports and loaded until the limit of proportionality was reached on the load vs midspan deflection recording. The results are shown in Fig. 2.10, with the stiffness expressed in the form: experimentally derived flexural rigidity of the test beam EI_e minus the elastic flexural rigidity of the steel section alone EI_S, divided by the theoretical flexural rigidity of the full interaction composite beam EI_f minus the flexural rigidity of the steel section alone. Therefore $(EI_e - EI_S)/(EI_f - EI_S) = 1$ for an uncracked beam with full interaction. After these tests were completed, the beams were jacked slightly and the webs of the beams were joined to supporting columns using cleats. The beams were then reloaded, and the stiffnesses recorded. It was found that Eq. 2.15 gave the best correlation to the test results, as shown in Fig. 2.10.

It should be noted, that the beams tested by Wright and Francis were only loaded up to the limit of proportionality. Hence the effects of concrete cracking, steel yielding or non-linearity of the connectors would not have commenced. Thus the values of stiffness represent the initial stiffness of the composite beams, and are upper bounds to the stiffness at higher loads, as the effects of concrete cracking, steel yielding and non-elastic connector slip all decrease the stiffness of the composite beam.

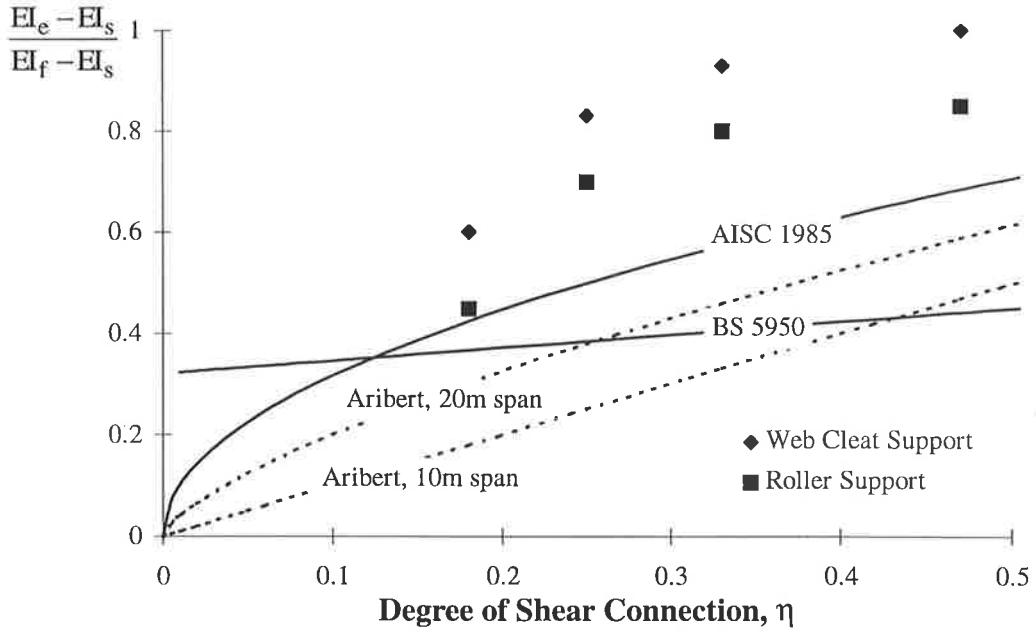


Fig. 2.10. Variation of Stiffness with Interaction (Wright and Francis 1990)

Aribert (1991) proposed a formula for the effective moment of inertia of a composite section which varied with the span of the beam. This formula was derived from the results of numerical analyses performed on composite beams using cold formed angle connectors (Aribert and Aziz, 1985; Aribert, 1989). The effective moment of inertia I_e of the transformed steel section was given by Eq. 2.16, and is shown plotted in Fig. 2.10 for 10 m and 20 m spans.

$$I_e = I_s + \eta^{\lambda}(I_f - I_s) \quad \text{.....(2.16)}$$

where

λ = Exponent based on the span of the beam, as given by Table 2.1.

L (m)	5	10	15	20
λ	1.5	1.0	0.8	0.7

Table 2.1. Variation of λ with span

These values were determined at serviceability load levels, and as such, are applicable to that part of the beam where the moments are within the serviceability load range. It can be seen from Eq. 2.16 that even at the lower serviceability loads for which these results were

determined, that the full moment of inertia of the cross-section is not effective, for degrees of shear connection less that 1.0. The reduction was determined to depend on the degree of shear connection and the span of the beam. A comparison of this equation with the results of Wright and Francis (1990) and the equations adopted in the British design code (BS 5950, 1990) and the American design guidelines (AISC, 1985) is shown in Fig. 2.10. It can be seen that the curves proposed by Aribert fall well below those reported by Wright and Francis, which were for 8 m span beams. The reason for this discrepancy may be due to the different form of connectors that were used. Alternatively, another reason for the difference may be due to the fact that the curves of Aribert were generated by the results of numerical analyses, and not from experimental tests. It was not clear whether the results of the computer analyses were validated against experimental results, and thus may not accurately represent the true behaviour of the composite beams.

Table 2.1 indicates that as the span of the beam decreases the stiffness of the beam decreases for a constant degree of shear connection. The reason for this is not clear, but may be due to the increased influence of concrete cracking for decreasing span of the beam. This is due to the increase in the relative proportion of the cracked section to uncracked section for shorter spans.

The procedures outlined represent simplified approaches to determining the maximum member deflections, and as such have the following drawbacks when compared to more refined analyses. First of all, they all assume a constant flexural stiffness along the length of the beam, which varies only as a function of the degree of shear connection at the position of maximum moment. In actuality, the flexural stiffness of the member will vary along the length, due to the effects of cracking of the concrete and due to the variation of the degree of shear connection along the length of the member. Secondly, the proposed flexural stiffnesses are taken as gross effective values, that incorporates the effects of both slip at the interface, and cracking of the concrete. Finally, these procedures are used to determine the deflections under serviceability loads and as such do not account for the effects of steel yielding.

As has been outlined previously, the effects of concrete cracking and steel yielding will be treated separately in this thesis. However as this analysis is considering the ultimate strength limit state of the beam, the influence of the non-linearity of the concrete element is more pronounced than in these procedures, even when disregarding the effects of the steel

yielding. The model that will be presented in this thesis will look separately at the effects of slip and cracking, so as to better determine the influence of these parameters.

2.2.7 Tension Stiffening

In the determination of serviceability deflections of reinforced concrete members, the tensile behaviour of the concrete can be significant (Branson, 1963; Beeby, 1968; Bazant and Oh, 1984). At load levels below the cracking moment, the concrete behaves as a linear elastic material. However, when the cracking moment is exceeded, the behaviour becomes distinctly non-linear, and is influenced not only by the tensile behaviour of the concrete, but also by the bond transfer between the concrete and the tensile reinforcement. This behaviour has been extensively studied for reinforced concrete beams (Carriera and Chu, 1986; Gupta and Maestrini, 1990; Massicotte et al., 1990). Once the cracking moment of the beam has been exceeded, the concrete between the primary flexural cracks continues to develop significant tensile stresses. These regions of uncracked concrete increase the stiffness of the member, and the effect is know as tension stiffening. More flexural cracks develop as the moment increases, and the effect of tension stiffening decreases until at the ultimate moment the influence is negligible.

There are significant differences between the responses of composite beams and reinforced concrete beams due to the effect of concrete cracking. The effect of concrete cracking on the behaviour of composite beams has not received a great deal of attention to date, with much of the published literature on beam tests not reporting the transverse cracking behaviour of the beam. One of the main differences between a composite beam and a reinforced concrete beam, with regard to the concrete cracking behaviour, is that there is seldom any reinforcement in the tension region of the concrete, for sagging moments. Most reinforcement that is placed in composite beams is either to control shrinkage cracking, which is placed in the top face of the concrete, or is transverse reinforcement to control longitudinal splitting. Both of these types of reinforcement arrangements will have negligible effect on the tensile behaviour of the concrete.

Despite the lack of tension reinforcement in the concrete, results from the composite beam tests have not shown any evidence of a sudden loss of stiffness at the onset of concrete cracking (Robinson, 1969; McGarraugh and Baldwin, 1971; Hawkins and Roderick, 1976; Aribert, 1987). This can be attributed to two main factors. First of all, the shear connectors

remain effective in transferring the longitudinal shear forces after the concrete has cracked. As cracking commences in the most highly loaded regions, there is a gradual transfer of the moment in the concrete element to the moment arising from the connector forces and the moment in the steel element. Secondly, the axial compressive force acting on the concrete section allows it to maintain some moment carrying capacity, even when the tensile capacity of the concrete is ignored. This is shown in Fig. 2.11, which shows the equivalent strain distribution for the concrete section under the combined action of an applied moment and an axial load.

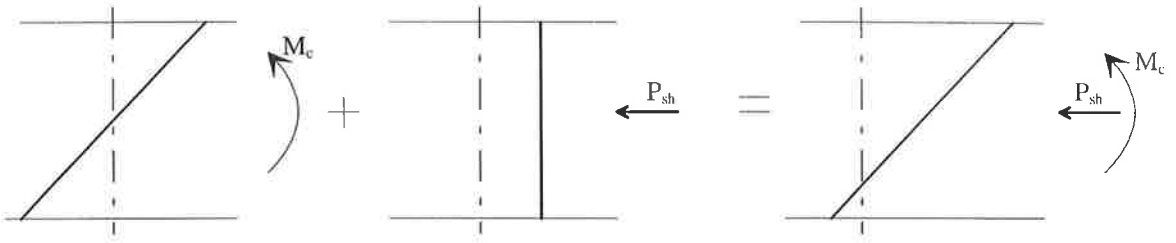


Fig. 2.11. Equivalent Strain Distributions

The analysis presented in this thesis will incorporate the effects of the concrete tensile strength by allowing a gradual reduction in the concrete flexural stiffness from the uncracked value in regions where the concrete tensile strength has not been exceeded, to the fully cracked stiffness in regions of advanced curvature. This will be discussed further in Section 2.4.3.3.

2.2.8 Ductility

Ductility is the ability of a member to deform while maintaining its load-carrying capacity. Ductility is an important concern in the design of continuous members, as it controls the ability to redistribute moments for plastic design; it can account for uncertainty in the applied loading distribution, and gives prior warning of imminent failure. In simply supported beams, the requirement of sufficient ductility arises from the need to ensure adequate deflection of the beam before failure and thereby eliminate any sudden failure, and to ensure sufficient rotation in order to achieve the full plastic moment of the member.

Calculation of the plastic moment capacity of a composite beam, implies large strains and hence large curvatures must be attained. Therefore, the beam must display significant ductility as cross-sections undergo large curvatures, by preventing premature buckling of the

steel section, crushing of the concrete, or failure of the shear connection. Simply supported composite beams designed to achieve the plastic moment capacity must therefore display some degree of ductility.

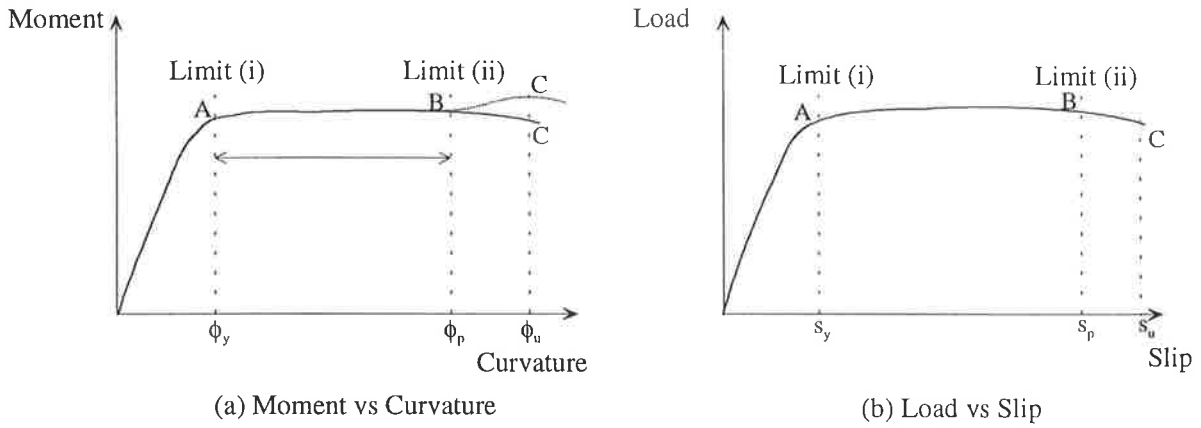
The issue of the slip capacity of the shear connectors is closely linked with the overall ductility requirement of a composite beam. As the required ductility of the beam increases, so does the required rotation capacity. It will be shown in Section 0 that large rotations associated with plastic deformation, lead to large increases in the slip at the concrete-steel interface. Therefore, it becomes necessary to define the required slip capacity of the shear connectors for two different limiting conditions, which are:

(i) To achieve the ultimate moment of the member;
(ii) To provide sufficient rotation capacity of the member to achieve the required degree of ductility.

The amount of rotation capacity that is considered adequate for simply supported beams depends on issues such as: the behaviour of other structural elements associated with the composite beam, including end connections and other adjoining members; the design procedure, whether linear elastic or ultimate strength analysis is used; and the application of safety factors to account for the degree of ductility (Patrick and Bridge, 1987). Various researchers have attempted to define an acceptable level of ductility for simply supported composite beams (Rotter and Ansourian, 1979; 1980; Patrick and Bridge, 1987). These will be discussed here, as it will be seen that the required degree of shear connection depends on the required ductility of the member.

The two conditions of sufficient strength and sufficient ductility are illustrated in Fig. 2.12, which shows a ductile member with a defined yield plateau in the moment-curvature response. Figure 2.12a shows the Moment-Curvature response, while (b) shows the associated Load-Slip curve for the same member. The derivation of (b) will be discussed further in Section 2.4.3. The first condition of sufficient strength is shown as Limit (i). The location of Limit (i) is chosen at the start of the yield plateau, as shown in (a), and is associated with a particular slip at the interface, as shown in (b). The position of the start of the yield plateau will be discussed further in the following section on plastic hinges, and may be defined as that point when the moment has reached say 98% of the ultimate moment of the member. The condition of sufficient ductility, Limit (ii), is based on the required degree of

ductility of the member. It can be seen that the choice of the required ductility limit of the member behaviour as shown in (a), will influence the required slip capacity of the connectors, as shown in (b).



(a) Moment vs Curvature (b) Load vs Slip

Fig. 2.12. Ductility Requirements for Simply Supported Beams

Rotter and Ansourian (1979,1980) proposed a value for the required ductility that is based on limiting the ratio of the curvature at collapse of the beam (assumed to occur when the top fibre strain equals the crushing strain) to the curvature at initiation of strain hardening in the bottom fibre of the steel member ϕ_p, which is typically taken as 10 times the yield strain for mild steel. The ratio of these two curvatures was called the ductility ratio. The curvature at failure ϕ_u, is shown in Fig. 2.12a for a beam which undergoes strain hardening before collapse.

In their original work Rotter and Ansourian concluded that if the value of the ductility ratio was at least 1.2, ie the curvature to cause failure was 20% greater than the curvature to cause strain hardening, then most structural configurations would be adequately ductile. This limit requires that sufficient strain can be developed in the steel section to allow strain hardening to commence before crushing of the concrete occurs. This requirement would then provide a rising 'tail' on the moment-curvature curve, shown by the dashed line in Fig. 2.12a, provided other failure mechanisms were prevented such as lateral torsional buckling. It has been suggested (Patrick and Bridge, 1987) that such requirements are unduly restrictive and not consistent with the design philosophy of other forms of construction. For example, in reinforced concrete design, there is no such requirement that the reinforcing should be able to reach strain hardening before failure (ACI, 1989; SAA, 1988a). However, it should be remembered that reinforced concrete beams do not rely on strain hardening to achieve their rigid plastic moment capacity, whereas composite beams do, and hence the difference in the

requirements. Elsewhere a similar procedure has been adopted to that by Rotter and Ansourian, with the required ductility ratio reduced to a value of 1.0 (SAA, 1980).

Other researchers have proposed ductility requirements that are based on overall member behaviour (Patrick and Bridge, 1987; Warner and Yeo, 1984a; Azman and Warner, 1984), rather than on cross-section behaviour. These are usually based on deflection limits of the member, rather than on limits on the behaviour of the cross-section. Such requirements are more consistent with the design philosophy of providing adequate ductility in continuous members, but usually require major simplifications to the behaviour of the members in the ultimate state, in order to determine the deflections.

Whether member limits are used or cross-section limits are used to determine adequate ductility, there still remains the issue of the interaction between the member ductility and the required slip capacity of the shear connectors, as shown in Fig. 2.12. It is possible that the slip capacity of the shear connectors may be sufficient to achieve the desired strength of the member, shown by Limit (i) in Fig. 2.12b, but is not sufficient to achieve the desired level of ductility, shown by Limit (ii). It would be helpful to the designer to separate these two effects, and design for them as independent limit states. The procedure developed in this chapter allows such an analysis, through the inclusion of a separate term for the slip increment developed in the plastic hinge.

2.2.9 Plastic Hinge

When designing a beam using rigid plastic analysis it is important to ensure that the member is capable of developing the curvatures necessary to attain the full plastic moment of the cross-section. Typically, this requires a check on the b/t ratios of each of the steel elements in compression. However, it is also important to note that large slip strains also develop in the hinge region, which over the length of the hinge, may result in a significant slip increment. An accurate estimation of the hinge length then becomes important, as it leads to a better determination of the slip increment which is developed during the plastic deformation of the member.

There has been much research in the area of plastic hinges in reinforced concrete design (I.C.E., 1962; Sawyer, 1964; Corley, 1966; Park et al, 1982; Bazant, 1984). This work has sought to described the length of the plastic hinge, as well as the rotations that occur in the

hinge region. Research work in the area of plastic hinges in composite beams has focused mainly on negative moment regions above continuous supports (Barnard and Johnson, 1965a; Lay and Galambos, 1967; Climenhaga and Johnson, 1972a, 1972b; Ansourian, 1977; Kemp and Dekker, 1991), while there has also been some research into the rotation capacity and hinge characteristics in positive moment regions (Barnard and Johnson, 1965a, 1965b; Ansourian, 1982). A brief description of the work into plastic hinges in reinforced concrete members will be presented first, followed by an investigation of the research into plastic hinges in composite beams.

2.2.9.1 Reinforced Concrete Beams

Based on experimental investigations on reinforced and prestressed concrete members (Bazant, 1984; Cranston, 1965; Somes, 1966) it has been found that inelastic rotation, involving yielding of the reinforcement and crushing of the concrete, occurs over a finite length region. The finite length over which inelastic rotation is concentrated is known as the hinge length. It is also sometimes called the contamination length or discontinuity length. Both the plastic deformation leading up to the ultimate moment and the softening deformation after the ultimate moment has been reached, are localised over this finite region.

Numerous formulae have been proposed which predict the length of the plastic hinge in reinforced concrete members. These are based on the effective depth d, (the depth to the reinforcement from the top fibre), the amount of tension and compression reinforcement, the strength of the concrete and reinforcing, the length of the member, the length of the shear span, and various other parameters. A comprehensive summary of the different procedures is presented by Foo (1990). In contrast to some of the complex hinge length formulae, other researchers have suggested simple average values for hinge length. Chan (1955) suggested that the hinge length may be taken as 0.4d. Cohn and Petcu (1963) observed that the length of the plastic hinge falls between 0.3d to 0.7d, whereas Park et al. (1982) found that the experimentally measured hinge length had an average value of 0.42D where D is the overall depth of the member.

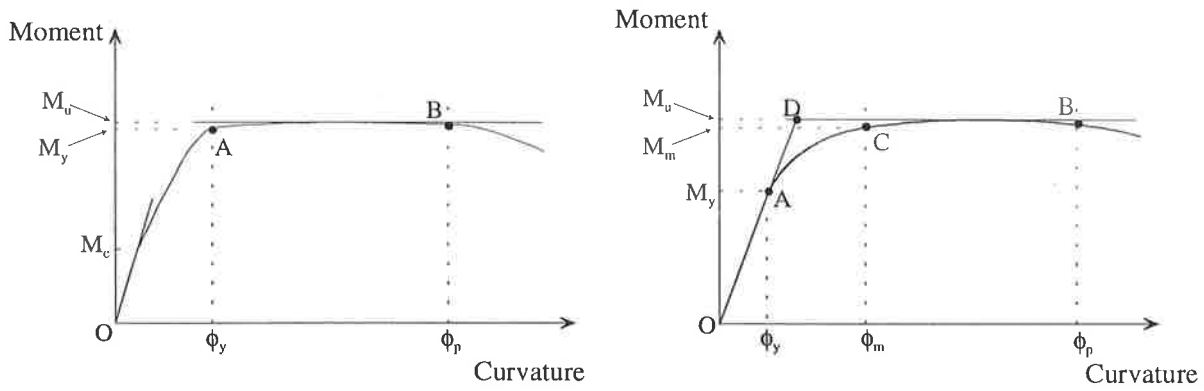
Once the length of the hinge has been ascertained, the curvatures within the hinge region need to be determined in order to calculate the total hinge rotation. This can easily be determined for a reinforced concrete section, as the moment-curvature diagram typically has a distinct yield point, as shown by Point A in Fig. 2.13a. Thus the onset of yielding of the

tension reinforcing can be used to determine the commencement of the plastic plateau. When yielding of the tension reinforcement does not occur, then point A can be defined as that point when the curvature in the cross-section is such that the strain in the top fibre of the concrete has reached the value corresponding to the peak in the concrete stress-strain relationship (Foo, 1990; I.C.E., 1962). Point B represents the point at which strain softening commences, and is found as either when the crushing strain of the concrete is reached (as described in the following paragraph), or when rupture of the steel occurs. The difference between ϕ_p and ϕ_y then represents the increase in curvature that occurs in the plastic hinge.

It is common practice in rigid plastic analysis to assume a limiting criteria of maximum concrete strain ε_u. This strain is commonly taken as 0.003, or can be determined from the Commité Européen du Béton proposal for ε_u (CEB, 1970) as given by Eq. 2.17,

$$\varepsilon_u = 0.0041 - 0.0000206 f_c \quad \text{.....(2.17)}$$

where f_c is in units of N/mm^2 and the term ε_u is unitless.



(a) Reinforced Concrete Beam (b) Composite Beam

Fig. 2.13. Plastic Rotations for Reinforced Concrete and Composite Beams

2.2.9.2 Composite Beams

There has been a lack of research into defining the length of the plastic hinge in the positive moment regions of composite beams. Barnard and Johnson (1965b) reported the results of tests on a series of simply supported beams. They assumed that the length of the plastic hinge extended over the entire constant moment region, which for the two point loading system used in their tests was 914 mm out of a 3658 mm simply supported span. It

was stated (Barnard and Johnson, 1965a) that for one of the tests at the maximum moment condition, 57% of the total rotation occurred within the discontinuity length, while at the final collapse load the proportion was 88%. It was stated that the calculated deflections based on a computer model at the maximum moment were 20 to 50% higher than those observed in the tests, although this was attributed to an overestimation of the curvatures in the inelastic regions. Regardless of the source of the discrepancy for this loading arrangement, this procedure does not provide an adequate definition of the hinge length for other load arrangements.

Other research into plastic deformation of composite beams under positive moment have focused on rotation capacity (Rotter and Ansourian, 1979; Ansourian, 1982) and have not given an adequate definition of the length of the plastic hinge. Due to a lack of supporting research into the length of the plastic hinge for positive bending in composite beams, a value which is representative for steel I-beams or for composite beams under a hogging moment, has been adopted. This value will give a reasonable estimate, as the top flange of the steel beam will be in compression for a composite beam with partial shear connection, as indicated in Fig. 2.3b. However, the presence of the concrete will give a beneficial restraining effect to the top flange, (Uy and Bradford, 1993c; 1994c; Wright, 1990; 1993) and thus influence the actual length of the hinge zone. The hinge length adopted in this thesis may be changed in the future subject to further experimental justification.

The length of the plastic hinge for compact steel I-sections has been defined as the buckled wave length of the compression flange (Lay, 1965; Lukey and Adams, 1969; Kemp and Dekker, 1991). This is taken as the limiting length of the plastic hinge, after which instability due to local buckling of the yielded flange occurs, with subsequent strain softening. In the analysis presented in this chapter, this same criteria is adopted for the length of the plastic hinge for composite beams in positive bending. The equation for the buckled wavelength is given as:

$$L_p = 0.71 \cdot b_f \frac{t_f}{t_w} \left(\frac{A_w}{A_f} \right)^{1/4} \qquad (2.18)$$

where

t_f = Thickness of the flange

t_w = Thickness of the web

b_f = Width of the flange

A_w = Area of the web = $(d_s - 2t_f)t_w$

A_f = Area of the flange = $b_f t_f$

Once the length of the plastic hinge has been determined, the amount of rotation within the hinge region must be calculated. This is found from the product of the hinge length and the increase in curvature in the hinge region. The increase in curvature that occurs in the plastic hinge of a composite beam can not be determined in the same manner as for a reinforced concrete beam. As shown by point A in Fig. 2.13b, the moment at which yielding commences is often not associated with the commencement of the plastic plateau of the moment-curvature relationship. This is due to the significant depth of the steel section in relation to the depth of the member, and the increase in moment that occurs as yielding progresses. Thus, another point must be found which represents the start of the yield plateau.

Rotter and Ansourian (1979) defined a generalised moment-curvature response for composite beams, and found it to depend on the dimensions of the slab, reinforcement in the slab, concrete strength, proportions of the I-section joist, the yield stress of the steel, the length of the yield plateau of the steel, interface slip, and residual stresses in the steel. Their results were determined for beams with full shear connection and the effects of slip were considered negligible. Thus, their formulation of the moment-curvature relationships neglected the effects of slip and slip-strain at the interface. This assumption meant that a single neutral axis was used with a single strain profile throughout the cross-section when calculating the curvatures in the cross-sections. By ignoring the presence of the slip strain, and only considering sections with full shear connection, the curvatures obtained would underestimate those relevant for beams with partial shear connection. The commencement of the yield plateau, as shown by Point C in Fig. 2.13b, was described as occurring when the steel section is completely yielded. Such a situation rarely occurs for a composite beam with partial shear connection, as there will always be a non-yielded region at the location of the steel neutral axis. Thus an alternative representation of the moment-curvature relationship must be determined which can be used for beams with partial shear connection.

Ansourian (1982) defined the rotation capacity of composite beams under positive bending in terms of the ductility parameter as discussed in Section 2.2.6. He then expressed the total plastic rotation of a composite beam before failure, in terms of this ductility

parameter. However, as this procedure incorporated all the effects of non-linearity along the entire length of the beam, it is not useful in this context to define the extent and influence of the plastic hinge.

One possible method to describe the commencement of the yield plateau is to locate a point such as Point C in Fig. 2.13b which represents the condition when a certain proportion of the full plastic moment, such as say 98%, is reached. The difficulty with this procedure is to determine the curvature at which this condition is reached. An alternative method is to take Point D as the start of the yield plateau, where Point D is found from the intersection of the initial elastic stiffness of the beam, with the plastic moment capacity. The drawback with this approach is it defines the behaviour of the beam as either elastic, region O-D, or fully plastic, region D-B, and underestimates the curvature and slip at the commencement of the yield plateau. An alternative approach based on the moment-curvature response of the steel section will be described in Section 2.4.3.6.

The end of the plastic plateau, as shown by Point B in Fig. 2.13b, is found in the same manner as for reinforced concrete beams, and is found either when the crushing strain of the concrete is reached, or when rupture of the steel occurs. Alternative limits to defining Point B are described in the preceding section on ductility. The difference between ϕ_m and ϕ_y then represents the increase in curvature that occurs in the plastic hinge of a composite beam. These values can then be used to determine the total rotation and hence the slip that occurs in the hinge region, as described in Section 0.

2.2.10 Strain Hardening

Shown in Fig. 2.14 are a number of variations of the stress-strain relationship that may be used to represent the behaviour of steel. Figure 2.14a shows an elastic-plastic relationship with no strain hardening, while (b) and (c) include effects of strain hardening. The first strain hardening model in (b) uses a bilinear stress-strain relationship, with a reduced stiffness after yielding, taken as $E_s/100$, where E_s is the Young's Modulus of the steel. The second strain hardening model is shown in (c), and incorporates a plastic yield plateau, with strain hardening occurring after a strain of 10 times the yield strain. The strain hardening modulus is taken as $E_s/6$. The effect of strain hardening on the end slip must be determined in order to adopt the correct form of the steel stress-strain curve. Various researchers have used each of

the three curves shown in Fig. 2.14, each indicating that the effect of incorporating strain hardening is not significant.

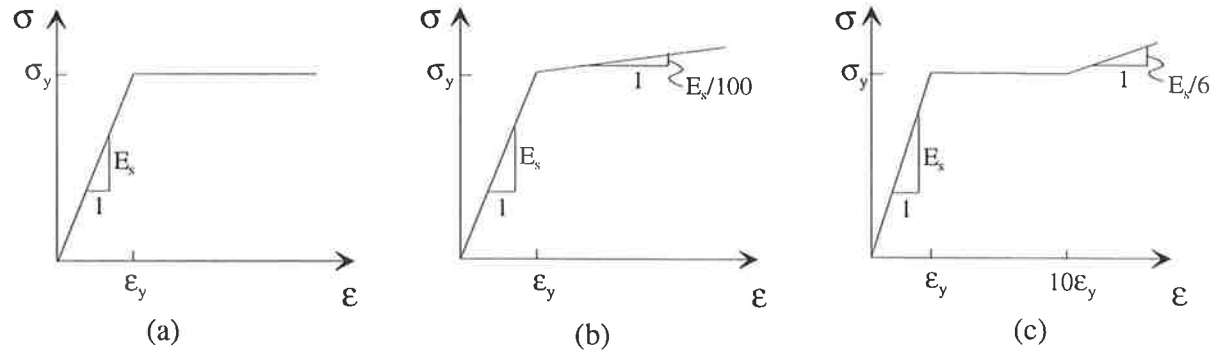


Fig. 2.14. Stress Strain Relationship for Steel

The effect of incorporating strain hardening into the analysis of composite beams is to increase the ultimate moment of the beam. As the beams under consideration in this investigation were considered representative of beams in buildings, the rigid plastic neutral axis of the section under full shear connection is within the depth of the concrete section. Thus for full shear connection, the increase in the force of the steel section due to strain hardening increases the total compressive force in the concrete section for full shear connection.

When the beam has partial shear connection, the compressive force in the concrete section is limited by the strength of the shear connectors, and strain hardening of the steel tends to lower the neutral axis location in the steel section, while the neutral axis in the concrete remains in the same location. This effect by itself would result in an increase in the slip strain, compared to the non-strain hardening case. However, the increase in the strength of the steel section results in a decrease in the curvatures in the cross-section compared to the non-strain hardening case. These two effects tend to offset one another, and the net result is a decrease in the maximum slip when the effects of strain hardening are taken into account.

The increase in slip due to the incorporation of strain hardening depends on the degree of shear connection. The increase in slip strain occurs in the non-linear region, and thus the overall increase in slip also depends on the extent of strain hardening. Yam and Chapman (1968) studied the influence of strain hardening on beams with degrees of shear connection greater than 1.0 using a computer analysis program. For one of the beams analysed the degree of shear connection was 1.25, and the beam was loaded with a point load at the centre.

There was an increase in the ultimate moment capacity of 30% compared to the beam which did not incorporate strain hardening, with a corresponding increase in the total longitudinal shear force of 12%. The failure mode was still flexural, with the maximum slip in the connectors 60% of the slip required to cause fracture. In this case the inclusion of strain hardening did not influence the design of the beam against fracture of the shear connectors.

Aribert (1993), whose analyses were concerned with beams with partial shear connection, stated that strain hardening had practically no effect on the determination of the critical degree of shear connection. Aribert adopted the strain hardening model shown in Fig. 2.14c for some analyses (Aribert and Aziz, 1985), while excluding strain hardening in others (Aribert, 1991). Chrisinel (1990) carried out non-linear computer analyses using the same model as Aribert and Aziz (1985, 1986), using the steel stress-strain curve of Fig. 2.14a.

Johnson and Molenstra (1991) adopted the stress-strain curve of Fig. 2.14b in their non-linear computer analyses, with the slope in the post-yielded region varying between $E_S/70$ and $E_S/210$, however it was not stated what the effects were of varying the slope, nor which stress-strain curve was used in which analysis.

Based on the previous discussion, it can be determined that the incorporation of strain hardening in the computational model does not significantly effect the end slip determination for beams with partial shear connection. Therefore, for the mathematical theory presented in this thesis, the stress-strain behaviour of the steel has been idealised as elastic-plastic, as shown in Fig. 2.14a. Allowance may be made for the effects of strain hardening in the procedure presented here, and will be discussed further in Section 2.4.3.6.4.

2.3 Scope of current work

The work presented in this chapter aims to provide a simplified approach to prevent premature fracture of shear connectors in composite beams that are designed for both strength and ductility. The work contained in this chapter will be limited to the design of simply supported composite beams in buildings and will consider simply supported beams that have any load distribution and any distribution of shear connectors. The work aims to better define the transition point T in Fig. 2.4, in terms of the cross-sectional properties of the beam, the

material properties of the steel and concrete elements, and the load-slip characteristics of the connectors. The scope of this work will be restricted to beams with the following conditions:

- For most composite T-beams used in buildings, ie those with a steel section and a concrete slab as shown in Fig. 2.1a, the area of the concrete A_C is typically much larger than that of the steel section A_S. Hence, the maximum longitudinal compressive strength of the concrete is usually greater than the axial tensile strength in the steel section. This results in the neutral axis of the concrete section being within the depth of the concrete slab for all degrees of shear connection, as shown in Fig. 2.1c and Fig. 2.3c.

- Although the work contained in this chapter relates to any form of shear connection between the concrete and steel elements, specific reference will be made to welded stud shear connectors as these are the most common form of shear connection in composite beams in buildings. The analysis will assume that the connectors can be approximated as having a ductile yield plateau in their load-slip characteristics, as shown in Fig. 2.6 and discussed in Section 2.2.3.

- It will be assumed that the steel sections can be classified as at least plastic or compact, ie that they are able the develop the full yield strength in the compression region. This eliminates the possibility of premature buckling of the steel section before ultimate flexural failure.

2.4 Mathematical Model

2.4.1 Introduction

The first procedure for determining the end slip of a composite beam was derived by Newmark et al (1951). In this analysis, the steel and concrete material properties were considered to be linear elastic, as well as the load-slip characteristics of the shear connectors. This work was expanded by Oehlers and Sved (1995) to include non-linearity in the shear connectors, as discussed in Section 2.2.3. The present work extends the analysis proposed by Oehlers and Sved to allow for the combination of linear and non-linear material properties of the steel and concrete along with non-linearity in the connectors.

A two tiered approach is adopted in the procedure developed here to determine the maximum slip of the composite beam. The first step of the procedure is based on the assumption that the material properties of the steel and concrete are linear elastic, whilst the connectors are fully yielded. The second step allows for the increase in slip through material non-linearity, which is due to steel yielding, concrete cracking and concrete crushing.

2.4.2 First Tier Analysis

2.4.2.1 Generalised Loading

The first order analysis, as developed by Oehlers and Sved (1995), consists of assuming that the concrete and steel material properties are linear elastic, and that the connectors are completely rigid-plastic. These preliminary assumptions can be justified through an understanding of the extent of non-linearity in the material properties, and its influence on overall member behaviour, and will be discussed further here.

2.4.2.2 Material Linearity

Consider a simply supported composite beam with a cross-section as shown in Fig. 2.15a, with a point load acting at section A-A as shown in (b). The maximum moment will occur under the point load, and at the ultimate moment the section will be fully yielded, and will have a stress distribution as shown in Fig. 2.1b for full shear connection or Fig. 2.3b for partial shear connection. At cross-sections along the beam closer to the supports in Fig. 2.15b, the externally applied moment acting on the beam will decrease, and the materials will be linear elastic, as shown in Fig. 2.15b and Fig. 2.17. The extent of yielding in the steel section and non-linearity in the concrete section will depend on the applied moment distribution, the distribution of the shear connectors, and also on the cross-sectional properties of the beam. It will be shown in Section 2.4.3 that the extent of non-linearity in the concrete and steel sections is not always significant and can be ignored in a first tier analysis.

As the maximum slip in a composite member is derived by integrating the slip strain at all locations along the beam, then it follows that the average material properties along the length of the member are important in the determination of maximum slip. Thus, if the

regions of material non-linearity do not extend far over the length of the member, then the average material properties will be dominated by the linear elastic regions.

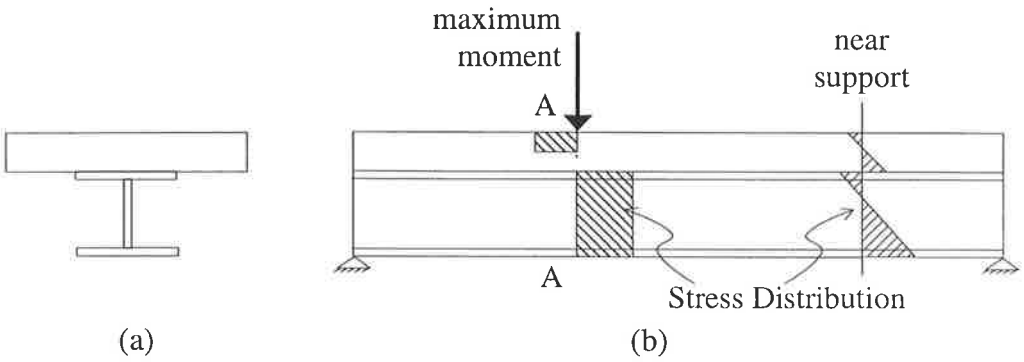


Fig. 2.15. Composite Beam Stress Distribution

2.4.2.3 Connector Non-Linearity

Consider again the beam shown in Fig. 2.15, and repeated in Fig. 2.16a. A typical result for the distribution of slip along the shear span for uniformly distributed connectors, is shown by the solid line in Fig. 2.16b (Robinson, 1969; Hawkins and Roderick, 1976). This indicates that the slip increases from zero at the location of maximum moment to a maximum at the ends of the beam. Although some researchers have reported beam tests that indicated a slight reduction in the slip towards the ends of the spans (McGarraugh and Baldwin, 1971; Aribert, 1987), as shown by the dashed line in (b), this is thought to be due to shrinkage strains in the concrete slab.

It is worth noting that other researchers who recorded significant reductions of the slip near the supports had shear connectors which were outside the shear span (Chapman and Balakrishnan, 1964), or which were placed directly above the supports (Aribert, 1993) and thus not strictly in the shear span. Other cases of highly non-linear slip distributions occurred for beams that had degrees of shear connection in excess of 1.0 (Yam and Chapman, 1968). However, as the likelihood of fracture decreases with increasing degree of shear connection, the situation of the maximum slip not occurring at the end of the shear span rarely if ever effects the flexural strength. Furthermore, the introduction of a non-uniform distribution of shear connectors may also lead to a situation where the maximum slip does not occur at the end of the shear span (Chapman and Balakrishnan, 1964). In conclusion, for most conditions under consideration, the slip at the end of the span will give a good indication of the

maximum slip along the beam, and will be used here as the limiting criteria to prevent fracture of the connectors.

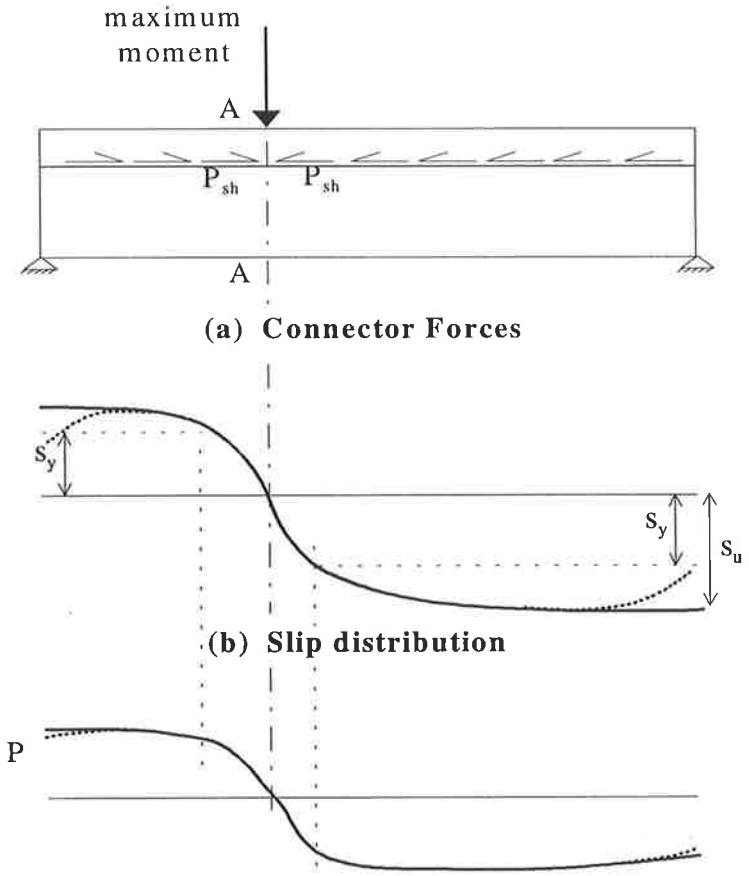


Fig. 2.16. Slip Distribution

It will be shown in Section 0 that at the ultimate load of a composite beam, the slip strain increases rapidly in the regions where yielding has occurred in the member. Furthermore, it will be shown that these yielded regions will be confined to a limited section near the maximum moment of the beam. As the slip strain is represented by the slope of the slip diagram, it follows that the slip will increase rapidly near the yielded regions of the beam, as shown in Fig. 2.16b, and that throughout the rest of the shear span it will change more slowly. This gives rise to the situation where the shear connectors are yielded in regions where the steel and concrete are linear elastic, and the steel and concrete elements are yielded in regions where the connectors are elastic.

When the strength of the connectors in the two shear spans of the composite beam in Fig. 2.16a are equal, then the load in the shear connectors will be directed such that the longitudinal force is the same in both shear spans. In other words, the shear connectors will

be loaded in opposite directions, as shown in Fig. 2.16a. Under these conditions, the slip will be zero at the location of the ultimate moment. Thus, integrating the slip strain from the location of maximum moment, where the slip is known to be zero, to the end of the beam, will give the slip at the end of the beam. In order for the assumption that all the connectors are at their maximum load to be correct, the variation in the slip throughout the shear span must be within the yield region of the load-slip characteristics of the connectors, as was discussed in Section 2.2.3.2.

Both of the variations in slip in Fig. 2.16b indicate that the slip is fairly constant throughout most of the shear span, and that only a small region of the beam, at the location of maximum moment, has a slip significantly under the yield slip which was defined in Section 2.2.3.2. Thus the connectors will be loaded at their maximum value, ie. yielded, throughout most of the shear span, as shown by the distribution of forces in the shear connectors in (c). It can be seen in (c) that there is only a slight reduction in the load in the shear connectors at the ends of the span, when the slip distribution shown by the dashed line in (b) is considered, and only where the slip is less than the yield slip s_y.

2.4.2.4 Mathematical Derivation

Based on the principle of zero separation at the interface, as discussed in Section 2.2.5, it follows that the curvatures are equal in the steel and concrete elements. This is shown in Fig. 2.17, and can be expressed by the following equation for any cross-section along the beam:

$$\phi = \frac{M_c}{(EI)_c} = \frac{M_s}{(EI)_s} \quad \text{.....(2.19)}$$

where

ϕ = Curvature in the beam

M_C = Moment in the concrete element

M_S = Moment in the steel element

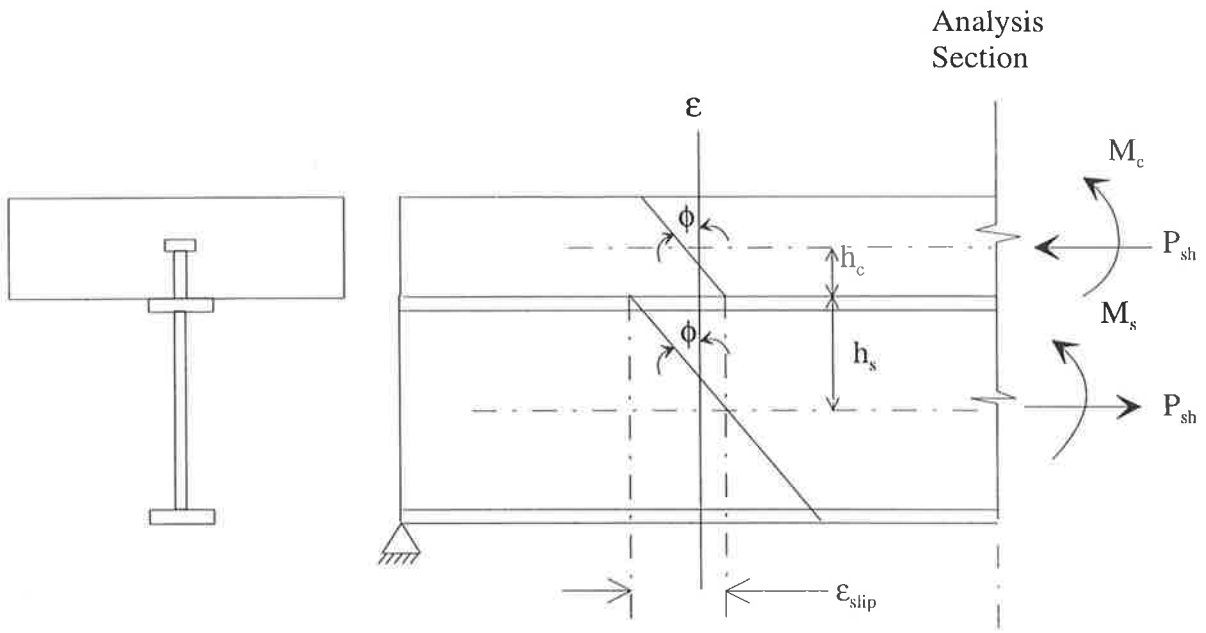


Fig. 2.17. Linear Elastic Analysis

From a consideration of the moment equilibrium of the cross-section shown in Fig. 2.17. the following equation can be defined:

$$M = M_S + M_C + P_{sh}(h_C + h_S) \quad \text{.....(2.20)}$$

where

M	=	Total externally applied moment
P_{sh}	=	Longitudinal shear force developed in the shear span
h_c	=	Distance from centroid of concrete element to the steel-concrete interface
h_s	=	Distance from centroid of the steel element to the steel-concrete interface

Substituting for M_S and M_C from Eq. 2.19 into Eq. 2.20 and rearranging gives:

$$\phi = M\frac{1}{(EI)_s + (EI)_c} - P_{sh}\frac{h_s + h_c}{(EI)_s + (EI)_c} \quad \text{.....(2.21)}$$

It is required to determine the slip strain, ε_{slip} in Fig. 2.17, which is the step change in the strain profiles at the steel-concrete interface. When the connection force P_{sh} acting at the cross-section is zero, the neutral axes of both the steel and the concrete will pass through the centroid of each element, and the slip strain will be:

$$\varepsilon_{slip} = \phi(h_s + h_c) \quad \text{.....(2.22)}$$

As the connection force increases, the compressive force in the concrete increases the compressive strain at the concrete centroid, and shifts the concrete strain profile to the left in Fig. 2.17 and hence reduces the slip strain. Furthermore, the tensile force in the steel element will increase the tensile strain at the steel centroid, which also reduces the slip strain. This change in the strain will be inversely proportional to the axial rigidities of each of the elements, and will be directly reflected by a change in slip strain at the interface. From a consideration of the strain distribution of the cross-section shown in Fig. 2.17, the slip strain for linear elastic steel and concrete properties and yielded connectors $\varepsilon_{slip,o}$, can thus be determined as:

$$\varepsilon_{slip,o} = \phi(h_s + h_c) - P_{sh}\left(\frac{1}{(EA)_s} + \frac{1}{(EA)_c}\right) \quad \text{.....(2.23)}$$

which on substitution of ϕ from Eq. 2.21 gives:

$$\varepsilon_{slip,o} = M\left[\frac{h_s + h_c}{(EI)_s + (EI)_c}\right] - P_{sh}\left[\frac{(h_s + h_c)^2}{(EI)_s + (EI)_c} + \frac{1}{(EA)_s} + \frac{1}{(EA)_c}\right] \quad \text{.....(2.24)}$$

where

$(EA)_S$ = Axial rigidity of the steel element

$(EA)_C$ = Axial rigidity of the concrete element

As the material properties are considered to be linear elastic, the EI and EA terms in Eq. 2.24 will be constant at all locations along the beam. Under such conditions, the terms in the square brackets can be replaced by constants, such that

$$\varepsilon_{slip,o} = \frac{ds}{dx} = MK_1 - P_{sh}K_2 \quad \text{.....(2.25)}$$

where

$$K_1 = \frac{h_s + h_c}{(EI)_s + (EI)_c} \quad \text{.....(2.26)}$$

$$K_2 = \frac{(h_s + h_c)^2}{(EI)_s + (EI)_c} + \frac{1}{(EA)_s} + \frac{1}{(EA)_c} \quad \text{.....(2.27)}$$

Equation 2.25 can now be easily integrated from the location of maximum moment, where the slip is known to be zero as discussed in Section 2.4.2.3, to the end of the beam. This will then give a value of the slip at the end of the beam, s_{max}. Integrating Eq. 2.25 along the shear span gives:

$$s_o = K_1 \int_{span} M dx - K_2 \int_{span} P_{sh} dx \quad \text{.....(2.28)}$$

The integrals $\int M$ and $\int P$ in Eq. 2.28 can be represent pictorially by the areas under the moment and axial force diagrams respectively, between the end of the shear span and the location of maximum moment, as shown in Fig. 2.18b and c.

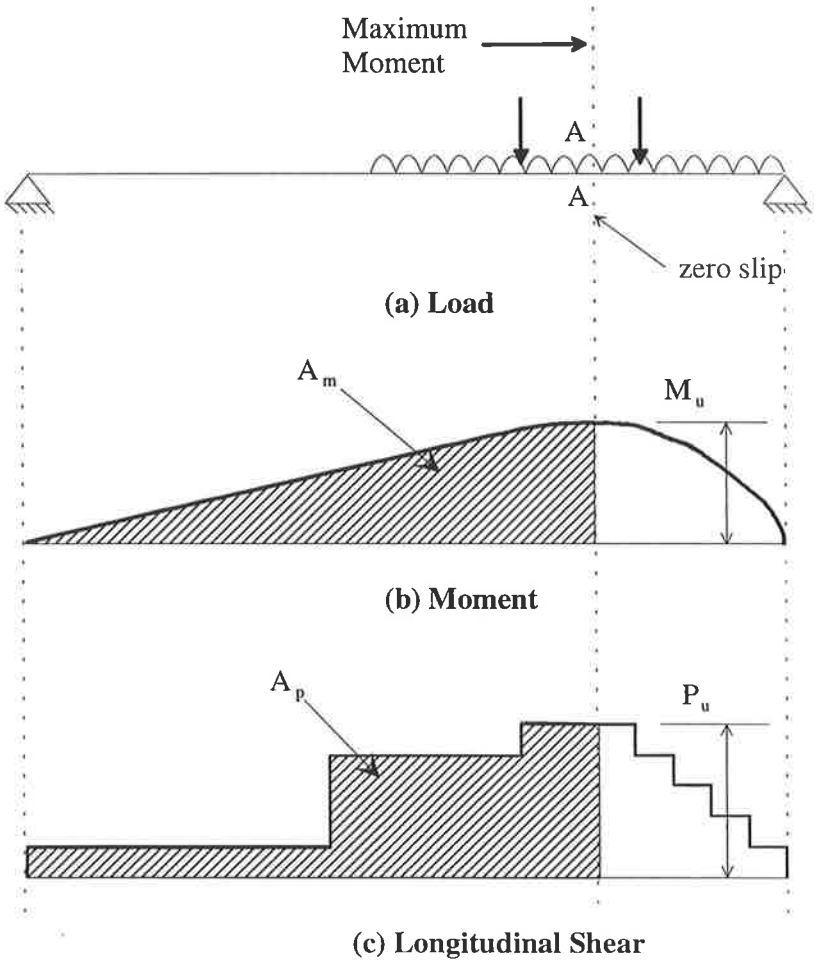


Fig. 2.18. Analysis for Fracture of Connectors

Equation 2.28 can, therefore, be written in the following terms that apply to all loading configurations and shear connector distributions,

$$s_o = A_m K_1 - A_p K_2 \quad \text{.....(2.29)}$$

where

A_m = Area under the applied moment diagram between the location of maximum moment and the end of the beam, as shown in Fig. 2.18b

A_p = Area under the axial force diagram between the location of maximum moment and the end of the beam, as shown in Fig. 2.18c

2.4.2.4.1 Uniformly Distributed Load

Consider the specific case of a simply supported beam of span L with a uniformly distributed applied load, and a uniform distribution of shear connectors of strength q_{sh} per unit length of beam. Then the applied moment diagram will be parabolic, with a maximum value of $M_u = wL^2/8$, and the axial force distribution will be triangular, with a maximum value of $P_u = q_{sh}L/2$. Expressing the axial force transferred by the shear connectors in terms of the degree of shear connection, such that $P_u = \eta P_{fsc}$, then the values of A_m and A_p will be given by Eqs. 2.30 and 2.31 respectively.

$$A_m = M_u L/3 \quad \text{.....(2.30)}$$

$$A_p = \eta P_{fsc} L/4 \quad \text{.....(2.31)}$$

These can be substituted into Eq. 2.29 to give the maximum end slip as:

$$s_o = \frac{M_u L K_1}{3} - \frac{\eta P_{fsc} L K_2}{4} \quad \text{.....(2.32)}$$

2.4.2.4.2 Central Point Load

The same procedure can be applied to a simply supported beam of span L with a centrally applied point load, and a uniform distribution of shear connectors. Under these conditions the maximum slip can be derived as:

$$s_o = \frac{M_u L K_1}{4} - \frac{\eta P_{fsc} L K_2}{4} \quad \text{.....(2.33)}$$

It can be seen from a comparison of Eq. 2.32 with Eq. 2.33 that a uniformly distributed load induces a larger slip than a point load.

2.4.2.5 Ultimate Strength Analysis

It is possible to determine the applied load to cause fracture of the connectors, given the geometry and material properties of the beam, and the slip capacity of the connectors. Considering the case of a uniformly distributed load with a uniform distribution of shear connectors, then Eq. 2.32 can be used to solve for the maximum applied load, as given by:

$$M_{frac} = \frac{S_u + \eta P_{fsc}(L/4)K_2}{(L/3)K_1} \quad \text{.....(2.34)}$$

This is the same as Eq. 2.13, which was developed by Oehlers and Sved (1995). It can be seen that for a given beam, the moment to cause fracture increases linearly with the degree of shear connection, as will be shown by the following worked example.

2.4.2.6 Worked Example

Consider two beams with the properties given in Table 2.2 and shown schematically in Fig. 2.19. Beam 1 is characterised by the neutral axis location in the concrete at the maximum moment for full shear connection, whilst Beam 2 has a neutral axis location in the steel at the maximum moment for full shear connection. It is possible to determine the variation in the flexural strength using the equilibrium approach, and this is shown by the line marked M_{equ} in a for Beam 1 and in (b) for Beam 2. The curves have been non-dimensionalised by dividing by the respective strengths of the beams for full shear connection, M_{fsc}. Also shown in the figures is the variation in the moment to cause fracture of the connectors M_{frac}, as given by Eq. 2.34.

	A_c (mm^2)	A_s (mm^2)	E_s (MPa)	E_c (MPa)	f_{sy} (MPa)	f_c (MPa)	L (m)	h_s (mm)	h_c (mm)
Beam 1	$300x10^3$	7200	$200x10^3$	$30x10^3$	400	35	15	192	75
Beam 2	$100x10^3$	7200	$200x10^3$	$30x10^3$	400	25	15	192	50

Table 2.2. Properties of Composite Beam

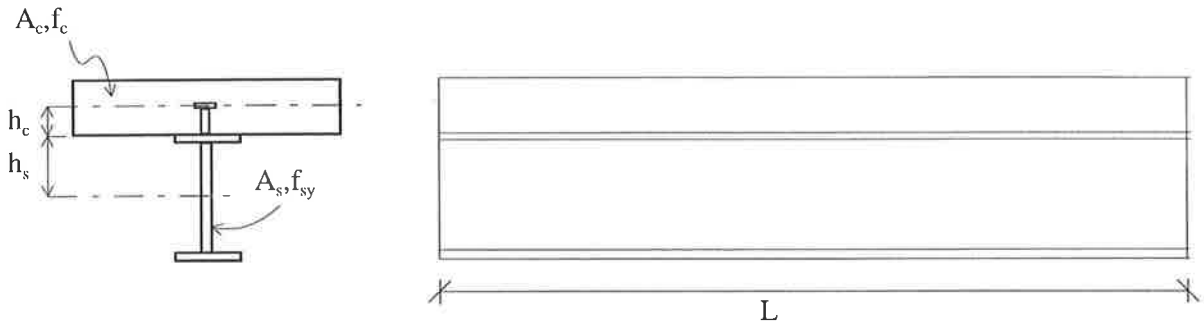
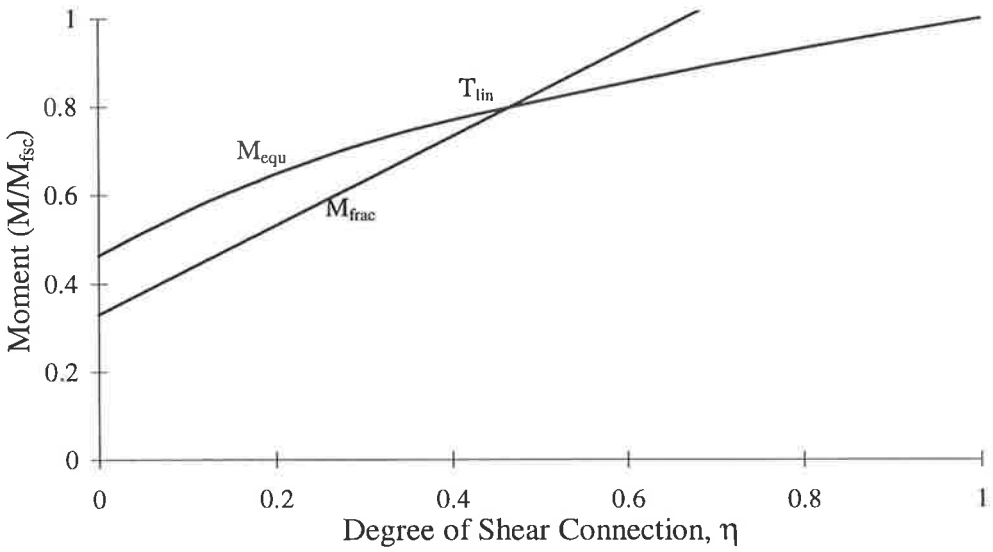
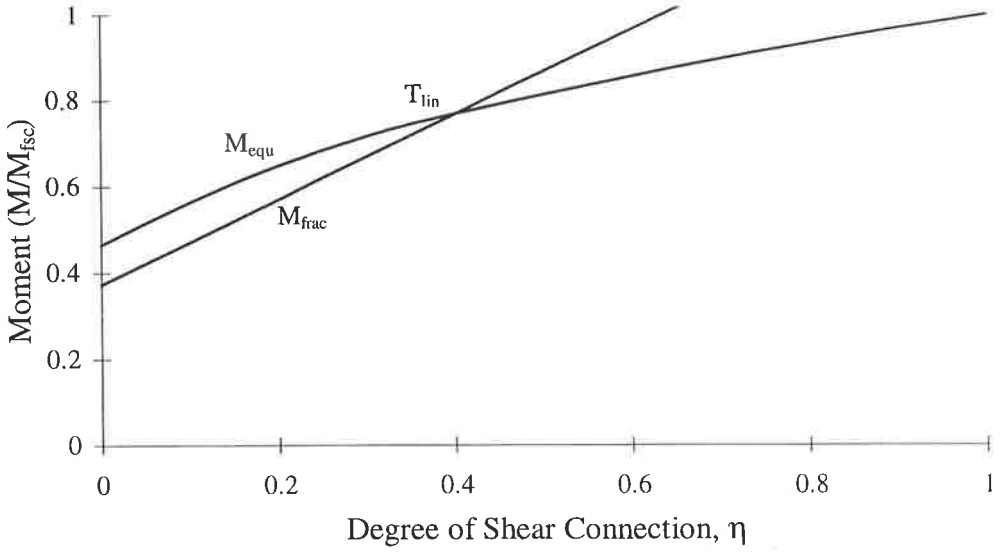


Fig. 2.19. Cross-Section of Composite Beam

It can be seen in Fig. 2.20 that for low degrees of shear connection, the value of M_{frac} is lower than the flexural strength of the beam M_{equ}, thus indicating that fracture of the connectors controls the failure mechanism. As the degree of shear connection increases, the moment to cause fracture of the shear connectors increases, until the two curves meet at the transition point T_{lin}, and the failure mechanism is no longer controlled by fracture of the shear connectors. The subscript *lin* in T_{lin} indicates that linear concrete and steel properties were used to determine the transition point.



(a) Beam 1



(b) Beam 2

Fig. 2.20. Variation in Moment to Cause Fracture with Degree of Shear Connection

2.4.3 Second Tier Analysis

2.4.3.1 Introduction

The analysis developed in this section extends the work by Oehlers and Sved (1995), which was presented in the previous section. In this section allowance will be made for the yielding of the steel, cracking of the concrete, and crushing of the concrete. These effects will be looked at separately, and then combined to provide an analysis procedure which allows for the full non-linearity of the material properties. Firstly, the effect of concrete cracking will be investigated, while assuming that the concrete is linear in compression and the steel is perfectly elastic. Then the effect of steel yielding will be looked at, while using the cracked concrete properties. Then the non-linearity of the concrete in compression will be studied. Finally, all the effects of non-linearity will be combined together.

2.4.3.2 Pattern of Loading

The pattern of loading along the beam has significant effect on the analysis. For a uniformly loaded member, the applied moment distribution is parabolic, and the moment gradient is very small near the location of maximum moment, as shown Fig. 2.21. This then results in the yield region of the member extending a significant distance towards the

supports from the location of maximum moment. For a point loaded member on the other hand, the moment gradient is constant throughout the member and, therefore, at the location of the maximum moment, the moment gradient is much larger than for the UDL case, as shown in Fig. 2.21. Thus the extent of yielding is less for beams which are subject to central point loads, and as a consequence, the case of a uniformly loaded member is the more critical case to analyse.

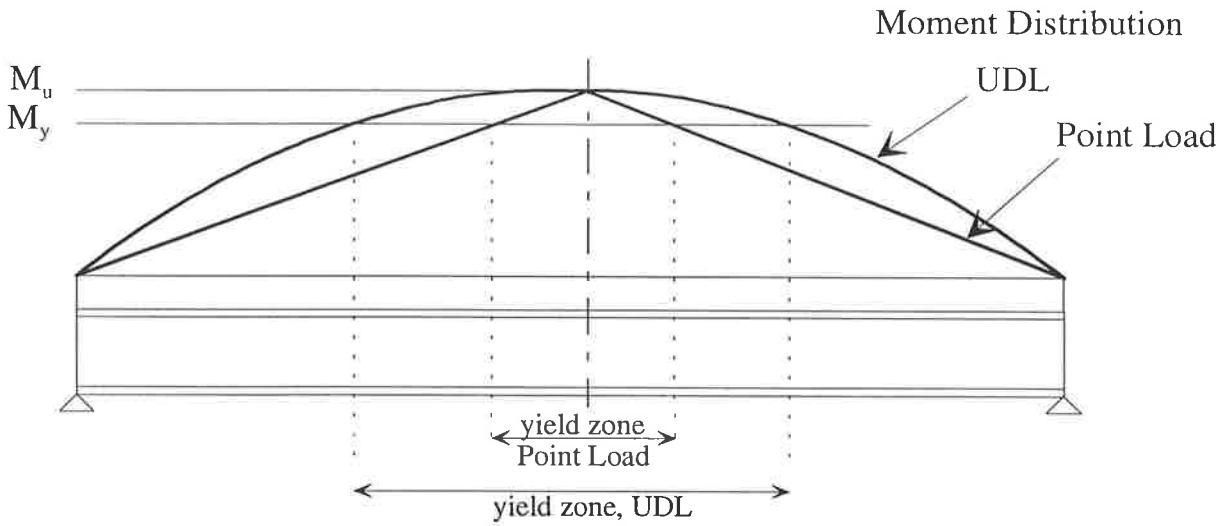


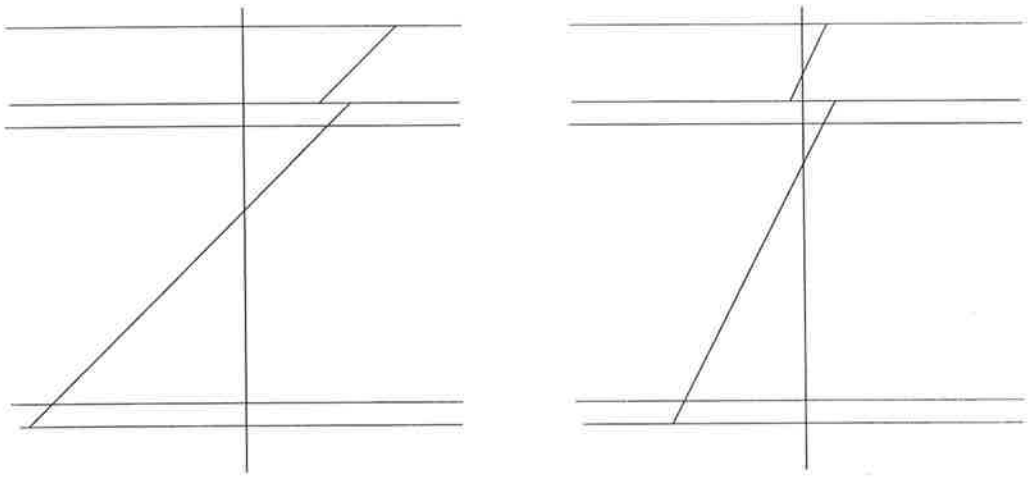
Fig. 2.21. Effect of Load Distribution on Yield Zone

2.4.3.3 Concrete Cracking

As was discussed in Sections 2.2.6 and 2.2.7, the effects of the concrete tensile strength will be incorporated by allowing a gradual reduction in the concrete flexural stiffness. Consider the moment contributions from each component of the composite beam, as given by Eq. 2.20 and shown in Fig. 2.17. As cracking commences in the most highly loaded regions, there is a gradual transfer of the moment in the concrete element M_c to both the moment arising from the connector forces $P_{sh}(h_c + h_s)$ and the moment in the steel element M_s. Furthermore, the axial compressive force acting on the concrete section allows it to maintain some moment carrying capacity, even when the tensile capacity of the concrete is ignored.

For a composite beam in which the neutral axis is in the steel section for full shear connection, then the effect of cracking of the concrete will be greatly reduced at higher degrees of shear connection. This is due to the fact that the concrete cross-section will mostly be in compression, as shown in Fig. 2.11 on Page 33, and thus the tensile properties of the

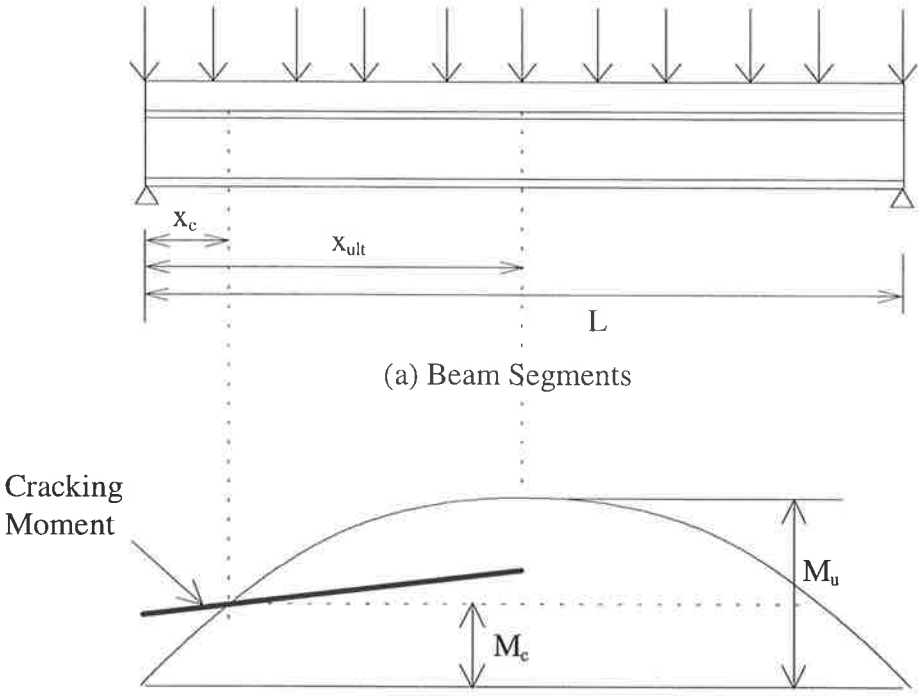
concrete will not influence the behaviour significantly. Despite the fact that for full shear connection the neutral axis may be in the steel section at the critical cross-section, as shown in Fig. 2.22a, the degree of shear connection will decrease towards the supports, and the concrete neutral axis will fall within the concrete element, as shown in Fig. 2.22b. However, as the curvatures are much smaller near the supports, the overall effect of concrete cracking on the behaviour of the member will be small. On the other hand, for a composite beam in which the neutral axis is in the concrete section for full shear connection, then the effect of cracking of the concrete will be significant even at higher degrees of shear connection.



(a) At Critical Location (b) Near Support

Fig. 2.22. Strain Distribution for Full Shear Connection

The procedure adopted here to allow for the tensile behaviour of the concrete consists of dividing the beam into two sections. The first of these is where the tensile strength of the concrete has not been exceeded, and thus this section is still linear elastic. This region is shown in Fig. 2.23a between the support and the location x_c. The derivation of the location of x_c is given in the next section. The next region is between this location, and the position of the maximum moment, as shown by x_{ult} in Fig. 2.23a. In this region an effective value of the flexural stiffness is determined, as described in the next section.



(a) Beam Segments

(b) Cracking Moment

Fig. 2.23. Location of Concrete Cracking

2.4.3.3.1 Extent of Concrete Cracking

The first step in determining the effect of cracking of the concrete is to ascertain the extent of cracking, as shown by the location x_c in Fig. 2.23a. The location at which the concrete cracks can be found by determining the location at which the tensile strength of the concrete is exceeded. The stress at the bottom concrete fibre to cause cracking f_{ct}, is given by:

$$f_{ct} = \frac{M_{cr} h_c}{I_c} - \frac{P_{cr}}{A_c} \quad \text{.....(2.35)}$$

where

P_{cr} = Axial force in the concrete at which cracking occurs

Equation 2.35 can be rearranged and solved for M_{cr}, noting that $f_{ct} = E_c \varepsilon_{cr}$, where ε_{cr} is the cracking strain of the concrete.

$$M_{cr} = \left(E_c \varepsilon_{cr} + \frac{P_{cr}}{A_c} \right) \frac{I_c}{h_c} \quad \text{.....(2.36)}$$

From Eq. 2.19 we get an expression for the moment in the steel section in terms of the moment in the concrete section:

$$M_s = M_c \frac{(EI)_s}{(EI)_c} \quad \text{.....(2.37)}$$

Equations 2.36 and 2.37 can be substituted into Eq. 2.20 to give the total applied moment to cause cracking in the concrete as:

$$M_{cr} = P_{cr} \left(h_c + h_s + \frac{(EI)_s + (EI)_c}{(EA)_c h_c} \right) + \frac{(EI)_s + (EI)_c}{h_c} \varepsilon_{cr} \quad \text{.....(2.38)}$$

A reasonable estimate for the tensile strength of the concrete is $f_{ct} = 0.6\sqrt{f_c}$, where f_{ct} and f_c are in units of N/mm^2, from which the cracking strain can be determined. Equation 2.38 shows that the cracking moment for any given beam, varies linearly with the longitudinal shear force acting at the cross-section. From the known distribution of shear connectors along the length of the beam, the variation in the longitudinal shear force is known. This can be used with Eq. 2.38 to plot the variation in the cracking moment along the beam, as shown by the thick solid line in Fig. 2.23b. When this is plotted on the applied bending moment diagram, the intersection of these lines will give the location x_c where cracking commences. This is shown in Fig. 2.23b for a beam with a uniformly distributed load and a uniform distribution of shear connectors.

The derivation of x_c for a uniformly distributed load with a uniform distribution of shear connectors is given as follows. The variation in the applied moment is given by Eq. 2.39, where x is measured from the support, and M_u is the maximum moment at the centre of the beam. It should be noted that the term P_{cr} in Eq. 2.38 varies along the length of the beam, and for a uniform distribution of shear connectors is given by Eq. 2.40. This can be substituted into Eq. 2.38, and the location of cracking is found from the intersection of Eq. 2.39 with Eq. 2.38. This is found by equating the right hand sides of the two equations, and solving for x_c. The resulting expression for x_c is given in Eq. 2.41.

$$M(x) = M_u \frac{x}{L/2}\left(2 - \frac{x}{L/2}\right) \quad \text{.....(2.39)}$$

$$P = \eta P_{fsc} \frac{x}{L/2} \quad \text{.....(2.40)}$$

$$x_c = \frac{L}{2} - \frac{\eta P_{fsc} L}{4M_u}\left(h_s + h_c + \frac{(EI)_s + (EI)_c}{(EA)_c h_c}\right) + \left(\sqrt{\left[\frac{4M_u}{L} - \frac{2\eta P_{fsc}}{L}\left(h_s + h_c + \frac{(EI)_s + (EI)_c}{(EA)_c h_c}\right)\right]^2 - \frac{16M_u\left((EI)_s + (EI)_c\right)\varepsilon_{cr}}{L^2 h_c}}\right)\frac{L^2}{8M_u} \quad \text{(2.41)}$$

The derivation of x_c for a beam subject to a point load at the centre-span with a uniform distribution of shear connectors is as follows. The variation in the applied bending moment is given by Eq. 2.42.

$$M(x) = M_u \frac{x_c}{L/2} \quad \text{.....(2.42)}$$

The intersection of Eq. 2.42 with Eq. 2.38 gives the location of concrete cracking, and this is given by Eq. 2.43.

$$x_c = \frac{L/2\left((EI)_s + (EI)_c\right)}{h_c\left(M_u - \eta P_{fsc}\left(h_s + h_c + \frac{(EI)_s + (EI)_c}{(EA)_c h_c}\right)\right)}\varepsilon_{cr} \quad \text{.....(2.43)}$$

2.4.3.3.2 Increment of Slip Due to Concrete Cracking

The following procedure can be used to determine the influence of concrete cracking on the slip. The slip strain at any location along the beam, which has a known applied moment M, and longitudinal shear force P_{sh} distribution, is given by Eq. 2.24. Equation 2.24 can be differentiated with respect to $(EI)_c$, to give the change in slip strain due to a change in the concrete flexural stiffness $(EI)_c$, at a section of the composite beam. This is given in Eq. 2.44

$$\frac{\partial}{\partial (EI)_c}\left(\varepsilon_{slip}\right) = -M\frac{h_c + h_s}{\left((EI)_c + (EI)_s\right)^2} + P\frac{\left(h_c + h_s\right)^2}{\left((EI)_c + (EI)_s\right)^2} \quad \text{.....(2.44)}$$

This can be integrated over the range of values of $(EI)_c$ to obtain the total change in the slip strain due to cracking of the concrete at a given section. This is illustrated in Fig. 2.24, which indicates the change in slip strain due to cracking of the concrete. The elastic line represents the variation in slip strain along the length of the beam as given by Eq. 2.24. The increase in slip strain due to concrete cracking as given by Eq. 2.44, is shown by $\Delta\varepsilon_{slip,c}$.

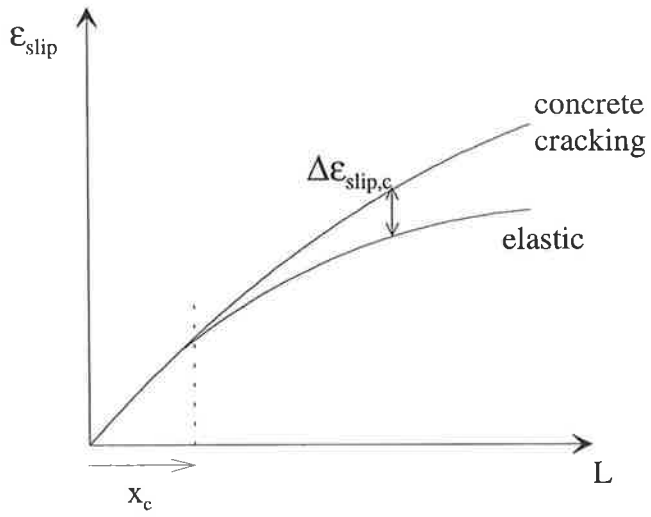


Fig. 2.24. Change in Slip Strain due to Concrete Cracking

Equation 2.44 can be approximated by the following finite difference representation, over the range of $(EI)_c$ values, where the subscript 1 represents the elastic uncracked value of the stiffness, and 2 represents the cracked stiffness at the given section.

$$\Delta\varepsilon_{slip,c} = \left[\frac{d}{d(EI)_c}\left(\varepsilon_{slip}\right)_1 + \frac{d}{d(EI)_c}\left(\varepsilon_{slip}\right)_2\right]\frac{\left((EI)_{c2} - (EI)_{c1}\right)}{2}$$

$$= \left[-M\frac{h_c + h_s}{\left((EI)_{c1} + (EI)_s\right)^2} + P_{sh}\frac{\left(h_c + h_s\right)^2}{\left((EI)_{c1} + (EI)_s\right)^2} - M\frac{h_c + h_s}{\left((EI)_{c2} + (EI)_s\right)^2} + P_{sh}\frac{\left(h_c + h_s\right)^2}{\left((EI)_{c2} + (EI)_s\right)^2}\right]\frac{\left((EI)_{c2} - (EI)_{c1}\right)}{2}$$

$$= M\left(\frac{1}{\left((EI)_{c1}+(EI)_s\right)^2}+\frac{1}{\left((EI)_{c2}+(EI)_s\right)^2}\right)(h_s+h_c)\frac{\left((EI)_{c1}-(EI)_{c2}\right)}{2}$$

$$-P_{sh}\left(\frac{1}{\left((EI)_{c1}+(EI)_s\right)^2}+\frac{1}{\left((EI)_{c2}+(EI)_s\right)^2}\right)(h_s+h_c)^2\frac{\left((EI)_{c1}-(EI)_{c2}\right)}{2}$$

Hence,

$$\Delta\varepsilon_{slip,c} = MK_3 - P_{sh}(h_c+h_s)K_3 \quad \text{.....(2.45)}$$

where

$\Delta\varepsilon_{slip,c}$ = Increase in slip strain due to cracking of the concrete

$$K_3 = \left(\frac{1}{\left((EI)_{c1}+(EI)_s\right)^2}+\frac{1}{\left((EI)_{c2}+(EI)_s\right)^2}\right)(h_s+h_c)\frac{\left((EI)_{c1}-(EI)_{c2}\right)}{2} \quad \text{...(2.46)}$$

For example, at x_c in Fig. 2.24, $(EI)_{c2} = (EI)_{c1}$ = flexural rigidity of the uncracked section. Substituting this into Eq. 2.46 gives $K_3 = 0$, and hence from Eq. 2.45 $\Delta\varepsilon_{slip} = 0$, which is what is expected, as the section has not cracked.

The value of $(EI)_c$ varies from the full elastic value in the uncracked region, within a distance x_c from the support, to a very small value at the location of the ultimate moment. In rigid plastic analysis, the stresses in the cross-section at the maximum moment are as shown in Fig. 2.1b on Page 6 for full shear connection or Fig. 2.3b on Page 10 for partial shear connection, where the concrete is assumed to be only in axial compression and thus has zero flexural stiffness. In reality, the concrete will carry a small moment, however, in comparison to the elastic value of the flexural stiffness, the value at the location of the ultimate moment can be neglected. Thus, at the position of maximum moment Eq 2.46 can be simplified by substituting the elastic value $(EI)_c$ for $(EI)_{c1}$, and neglecting the term $(EI)_{c2}$, as at the maximum moment it will be very small. Hence,

$$K_{3,max} = \frac{1}{2}\left(\frac{1}{\left((EI)_c+(EI)_s\right)^2}+\frac{1}{(EI)_s^2}\right)(h_s+h_c)(EI)_c \quad \text{.....(2.47)}$$

The term K_3 varies along the length of the beam, from zero in the uncracked region up to the location x_c, to the maximum value of $K_{3,max}$ at the position of maximum moment. Adopting a mean value for K_3 gives:

$$\overline{K}_3 = \frac{K_{3,max}}{2} \quad \text{.....(2.48)}$$

Inserting this value into Eq. 2.45, it can now be integrated over the region of the beam where the concrete is cracked, in order to determine the increase in the end slip due to the concrete cracking. This gives:

$$s_{cr} = A_{mc}\overline{K}_3 - A_{pc}(h_c + h_s)\overline{K}_3 \quad \text{.....(2.49)}$$

where

A_{mc} = Area under the applied moment curve in the shear span where the concrete is cracked, as shown in Fig. 2.25a

A_{pc} = Area under the longitudinal shear force diagram in the shear span where the concrete is cracked, as shown in Fig. 2.25b

For a beam with a uniform distribution of shear connectors, and a uniformly distributed load, the values of A_{mc} and A_{pc} are given by:

$$A_{mc} = L_{mc}M_u \quad \text{.....(2.50)}$$

$$A_{pc} = L_{pc}P_u \quad \text{.....(2.51)}$$

where

$$L_{mc} = \frac{L}{3} - x_c^2\left(\frac{1}{L/2} - \frac{x_c}{3(L/2)^2}\right) \quad \text{.....(2.52)}$$

$$L_{pc} = \frac{1}{2}\left(\frac{x_c}{L/2} + 1\right)\left(\frac{L}{2} - x_c\right) \quad \text{.....(2.53)}$$

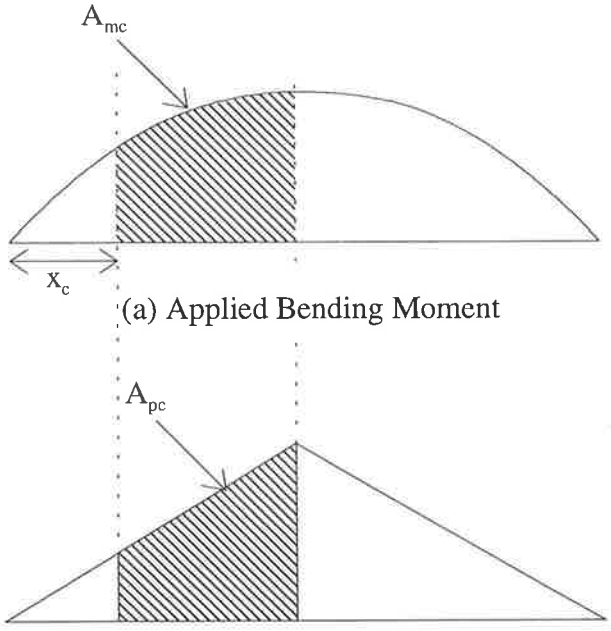


Fig. 2.25. Analysis for Concrete Cracking

Equation 2.49 gives the increment in slip due to cracking of the concrete. Combining this with Eq. 2.29 which gives the end slip with linear elastic concrete and steel properties, gives:

$$s_{end} = s_o + s_{cr}$$

$$= A_m K_1 - A_p K_2 + A_{mc}\overline{K}_3 - A_{pc}(h_s + h_c)\overline{K}_3 \quad \text{.....(2.54)}$$

For the case of a uniformly distributed load with a uniform distribution of shear connectors, it is possible to rearrange Eq. 2.54 to solve for the moment at which fracture of the shear connectors occurs. This is done by substituting L_{mc} and L_{pc} from Eqs. 2.52 and 2.53 into Eqs. 2.50 and 2.51, which are in turn substituted into Eq. 2.54. The result is given by:

$$M_{frac,c} = \frac{S_u + \eta P_{fsc}\left((L/4)K_2 + L_{pc}(h_s + h_c)\overline{K}_3\right)}{(L/3)K_1 + L_{mc}\overline{K}_3} \quad \text{.....(2.55)}$$

The effect of concrete cracking on the endslip is shown in Section 2.4.3.5 by the use of a worked example. The results are compared to the first order analysis which neglects the effects of concrete cracking.

2.4.3.4 Equivalent Average Concrete Stiffness

It is possible to provide an alternative procedure to account for the effects of the concrete cracking on the endslip. This procedure consists of determining an equivalent average concrete stiffness which acts throughout the length of the beam, and results in the same increment in slip as determined using the procedure above. The equivalent average concrete stiffness can be used in the analysis when determining the effects of steel yielding, as described in Section 2.4.3.6.

The slip strain at a cross-section is given by Eq. 2.24 on Page 50 for elastic concrete and steel materials and yielded connectors, and the increment in slip strain due to concrete cracking is given by Eq. 2.45 on Page 62. Thus the total slip strain incorporating the effects of concrete cracking is given by the summation of Eqs. 2.24 and 2.45, and is given by Eq. 2.56.

$$\varepsilon_{slip,c} = \varepsilon_{slip,o} + \Delta\varepsilon_{slip,c}$$

$$= M\left[\frac{h_s + h_c}{(EI)_s + (EI)_c}\right] - P_{sh}\left[\frac{(h_s + h_c)^2}{(EI)_s + (EI)_c} + \frac{1}{(EA)_s} + \frac{1}{(EA)_c}\right] + M\overline{K}_3 - P_{sh}(h_c + h_s)\overline{K}_3 \quad (2.56)$$

It is possible to replace the elastic concrete stiffness $(EI)_c$ in Eq. 2.21 by a reduced stiffness $\alpha(EI)_c$ to allow for cracking, and give the new curvature in the cross-section as given by Eq. 2.57.

$$\phi = M\frac{1}{(EI)_s + \alpha(EI)_c} - P_{sh}\frac{h_s + h_c}{(EI)_s + \alpha(EI)_c} \quad \text{.....(2.57)}$$

When this is substituted into Eq. 2.23, the resulting slip strain incorporating the effects of concrete cracking is given by Eq. 2.58. A value of α must now be determined such that Eq. 2.58 gives the same result as Eq. 2.56. Substituting $\overline{K}_3$ from Eq. 2.48 into Eq. 2.56 and equating with Eq. 2.58 and solving for α gives Eq. 2.59.

$$\varepsilon_{slip,c} = M\left[\frac{h_s + h_c}{(EI)_s + \alpha(EI)_c}\right] - P_{sh}\left[\frac{(h_s + h_c)^2}{(EI)_s + \alpha(EI)_c} + \frac{1}{(EA)_s} + \frac{1}{(EA)_c}\right] \quad \text{.....(2.58)}$$

$$\alpha = \frac{2 + 2\psi - \psi^2}{\psi^3 + 2\psi^2 + 6\psi + 4} \quad \text{.....(2.59)}$$

where

$$\psi = \frac{(EI)_c}{(EI)_s}$$

The value of α given in Eq. 2.59 represents a reduction factor to determine an equivalent reduced concrete stiffness, which when used in Eq. 2.58 will give the same slip strain as when considering the effects of cracking of the concrete separately. Equation 2.58 is valid over that region over which the concrete is cracked. Where the concrete has not cracked, then Eq. 2.24 on Page 50 may be used, with the elastic value of the concrete flexural stiffness $(EI)_c$. However, the error that is introduced by adopting the equivalent cracked concrete stiffness over the full length of the member is not significant, as will be shown in Section 2.4.3.5 by way of a worked example.

With this simple approximation, the end slip due to the effects of concrete cracking can be combined with that assuming linear elastic concrete and steel properties, to give a single term. This is done by substituting $\alpha(EI)_c$ in place of $(EI)_c$ in Eq. 2.24 on Page 50, as shown in Eq. 2.58, and then integrating over the entire length of the shear span. The result is given by Eq. 2.60.

$$s_{o,cr} = A_m K_4 - A_p K_5 \quad \text{.....(2.60)}$$

where

$$K_4 = \frac{h_s + h_c}{(EI)_s + \alpha(EI)_c} \quad \text{.....(2.61)}$$

$$K_5 = \frac{(h_s + h_c)^2}{(EI)_s + \alpha(EI)_c} + \frac{1}{(EA)_s} + \frac{1}{(EA)_c} \quad \text{.....(2.62)}$$

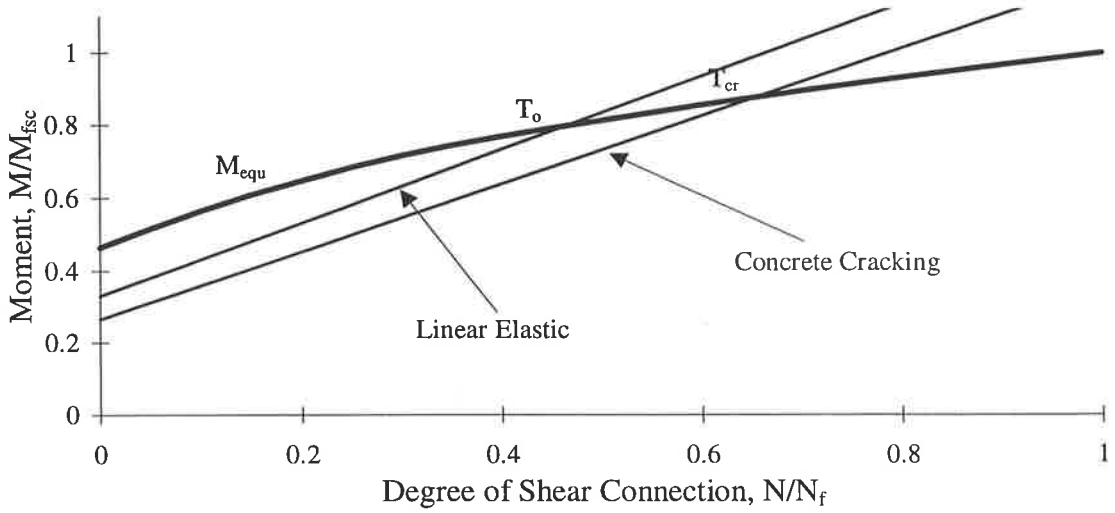
For the case of a uniformly distributed load with a uniform distribution of shear connectors, it is possible to rearrange Eq. 2.60 to solve for the moment at which fracture of the shear connectors occurs. This is done by substituting A_m and A_p from Eqs. 2.30 and 2.31

into Eq. 2.60. The result is given by Eq. 2.63, which can be seen to be a simplification to Eq. 2.55 which does not include the approximation of the average cracked concrete stiffness.

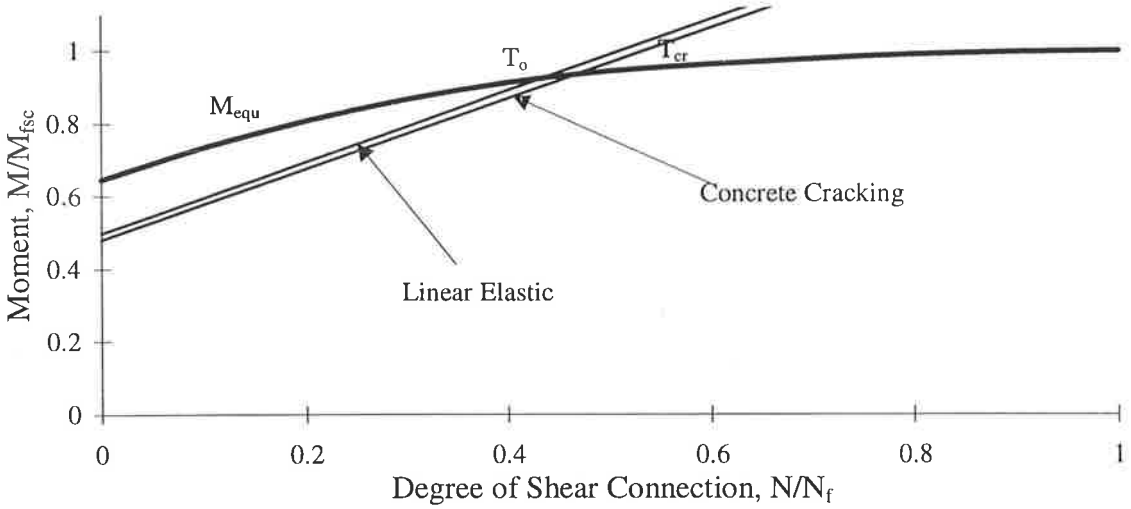
$$M_{frac,c} = \frac{S_u + \eta P_{fsc}(L/4)K_5}{(L/3)K_4} \quad \text{.....(2.63)}$$

2.4.3.5 Worked Example

Consider the two beams that were looked at previously in Section 2.4.2.6, with the properties given in Table 2.2 on Page 54. The variation in the ultimate strength is shown by the line M_{equ} in Fig. 2.26, and the variation in the moment to cause fracture of the shear connectors is also shown. The line labelled Linear Elastic is that from Eq. 2.34 in Section 2.4.2, while the line labelled Concrete Cracking is derived from Eq. 2.63. There is negligible difference between the line plotted from Eq. 2.63 and that from Eq. 2.55. The transition point is given by the intersection of Eq. 2.55 with the line M_{equ} and is labelled T_{cr} to indicate it is calculated incorporating concrete cracking. It can be seen that transition point moves to the right when considering the effects of concrete cracking compared to the first tier solution.



(a) Beam 1



(b) Beam 2

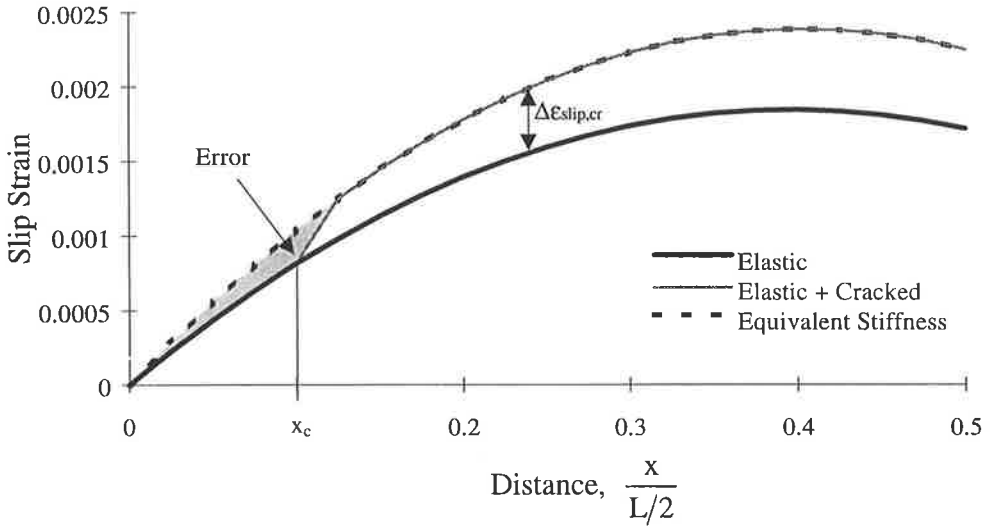
Fig. 2.26. Variation in Moment to Cause Fracture

It can be seen in Fig. 2.26a that for Beam 1 there is a relatively large movement in the position of the transition point due to the incorporation of the effects of concrete cracking. This indicates that for the particular properties given in Table 2.2 that this beam is strongly influenced by concrete cracking. It can be seen in Fig. 2.26b that for Beam 2, which has the neutral axis in the steel element at the maximum moment for full shear connection, that the effects of concrete cracking is not very significant. This is as expected, as a greater portion of the depth of the concrete remains in compression, and thus does not crack.

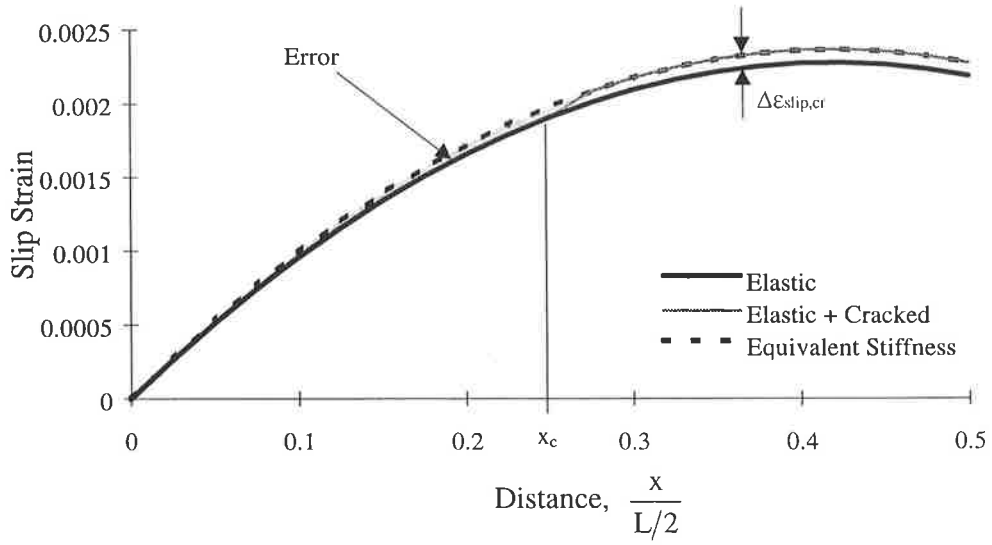
The effect of using the equivalent cracked concrete stiffness $\alpha(EI)_c$ over the entire length of the beam is shown in Fig. 2.27, which shows the different values of slip strain based on the different approaches. The solid dark line, labelled Elastic, gives the slip strain assuming elastic steel and concrete properties, as given by Eq. 2.24, while the line labelled 'Elastic + Cracked' gives the slip strain calculated with linear elastic steel and concrete properties combined with effects of cracking, as given by Eq. 2.56. The difference between the two is due to the effects of concrete cracking, and is labelled $\Delta\varepsilon_{slip,cr}$ and is given by Eq. 2.45. It can be seen that the effects of cracking commence at a location given by x_c, and at distances less than this the elastic slip strain is adopted. Also shown is the slip strain calculated by adopting the equivalent cracked concrete stiffness over the whole length of the beam, as given by Eq. 2.58.

The difference between Eq. 2.56 and Eq. 2.58 is shown shaded in Fig. 2.27 and labelled Error. This indicates the additional slip strain that is incorporated by using the approximation

as apposed to the more rigorous method which involves determining x_c. It can be seen in (a) that when the effects of concrete cracking are significant, ie. $\Delta\varepsilon_{slip,cr}$ is large, then x_c is close to the support, and the error term is small. Alternatively, when x_c is large, the effects of concrete cracking will be small, as indicated by $\Delta\varepsilon_{slip,cr}$ in (b), and the error term will again be small. The integral of error term in (a) results in a difference in end slip of only 0.1 mm, while in (b) the difference in endslip is only 0.05 mm. In any case, the effect is to slightly over-estimate the end slip and hence the result will always be conservative. Thus, as a simple yet accurate approximation, Eq. 2.60 may be used to determine the end slip of a composite beam incorporating the effects of concrete cracking. As a further refinement to this procedure, Eq. 2.54 may be used.



(a) Beam 1



(b) Beam 2

Fig. 2.27. Effect of Concrete Cracking on Slip Strain.

2.4.3.6 Steel Yielding

2.4.3.6.1 Introduction

The effect of steel yielding on the overall behaviour of a composite beam will be approached in two parts. The first will deal with the non-linear behaviour of an ordinary steel beam as it is loaded beyond its elastic limit. This will then lead into an analysis of the behaviour of a steel section in a composite beam. Secondary failures such as instability due to buckling of the steel cross-section will be ignored.

2.4.3.6.2 Steel Beam Behaviour

Consider the steel cross-section shown in Fig. 2.28a. When the maximum stress in the beam is less than the yield stress f_{sy}, the beam behaves elastically with a linear stress distribution such as that shown in (b). Under this condition, the neutral axis passes through the centroid of the cross-section. Let M_y be the moment at which yielding first starts in the outermost fibre. As the moment is increased above the yield moment M_y, the stress at the outer fibres remains constant at the yield stress while the central region remains linear elastic, as shown in Fig. 2.28c. The position of the neutral axis will change, unless the section is doubly symmetric.

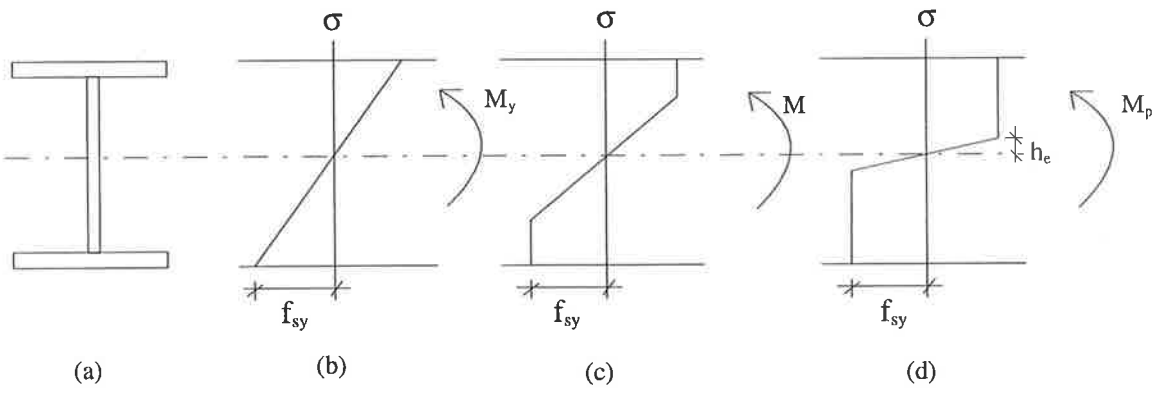


Fig. 2.28. Extent of Yielding

As the bending moment increases, the plastic regions extend further inwards towards the neutral axis until the condition shown in Fig. 2.28d is reached. At this stage the strains in the extreme fibres are approximately 10 times the yield strain ε_y, and the depth of the elastic

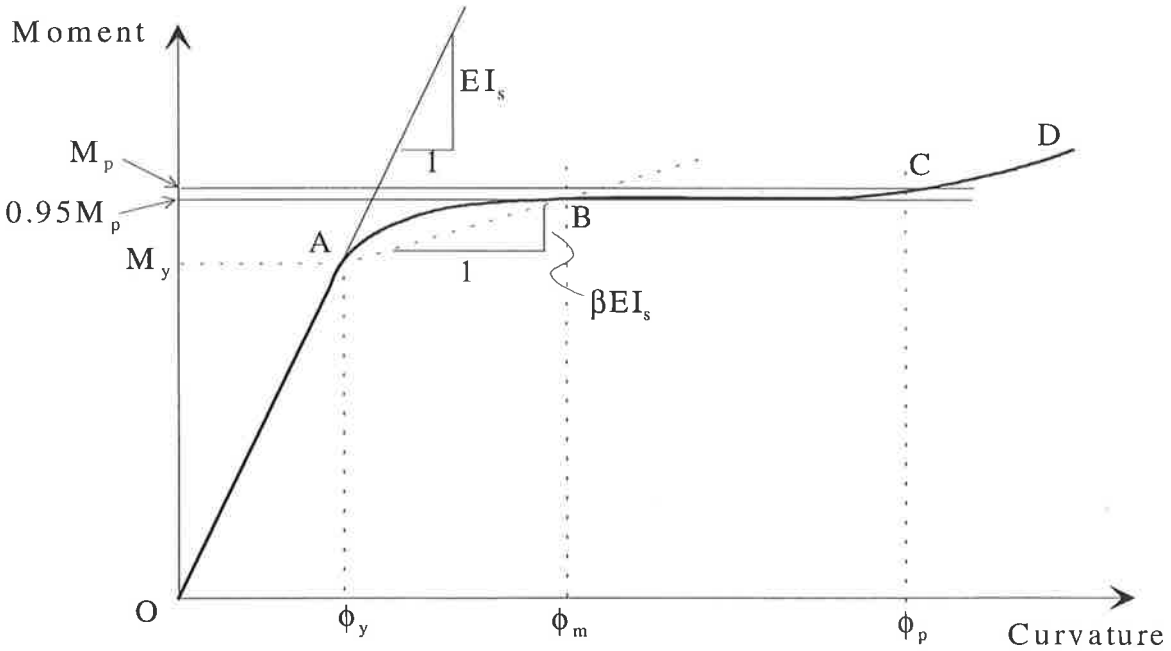
core has reduced to a value of $2h_e$. The moment in the cross-section is taken as the plastic moment of the beam M_p, as the beam has reached its ultimate moment-resisting capacity. Any slight reduction in the moment capacity based on the stress distribution shown in Fig. 2.28d compared to the rigid plastic moment is ignored due to the beneficial effects of strain hardening. Thus the full plastic moment is achieved at the onset of strain hardening in the outermost fibres. The onset of strain hardening is usually taken as when the strain is 10 times the yield strain.

Before the yield moment M_y of the beam is reached, the moment-curvature relationship is perfectly linear with a constant flexural stiffness of $(EI)_s$, as shown by the line O-A in Fig. 2.29. When the applied moment increases beyond M_y, part of the beam will become plastic; the flexural stiffness of the beam will decrease and the moment-curvature relationship then becomes non-linear as shown by the curved path A-B-C in Fig. 2.29a. The slope of the moment-curvature curve tends to zero as the plastic moment is approached. The portion of the curve C-D represents the behaviour of a beam which undergoes strain hardening, which will not be included in the present analysis, as discussed in Section 2.2.10. The point C in Fig. 2.29a is the point at which strain hardening commences in the bottom fibre of the steel beam. This point can also be taken as the point at which the full plastic moment capacity of the steel cross-section is reached, as was discussed previously. The curvature at which this occurs is denoted by ϕ_p, as shown in (a). For curvatures less than this, the fully plastic moment is not reached due to the presence of the elastic portion of the steel near the neutral axis.

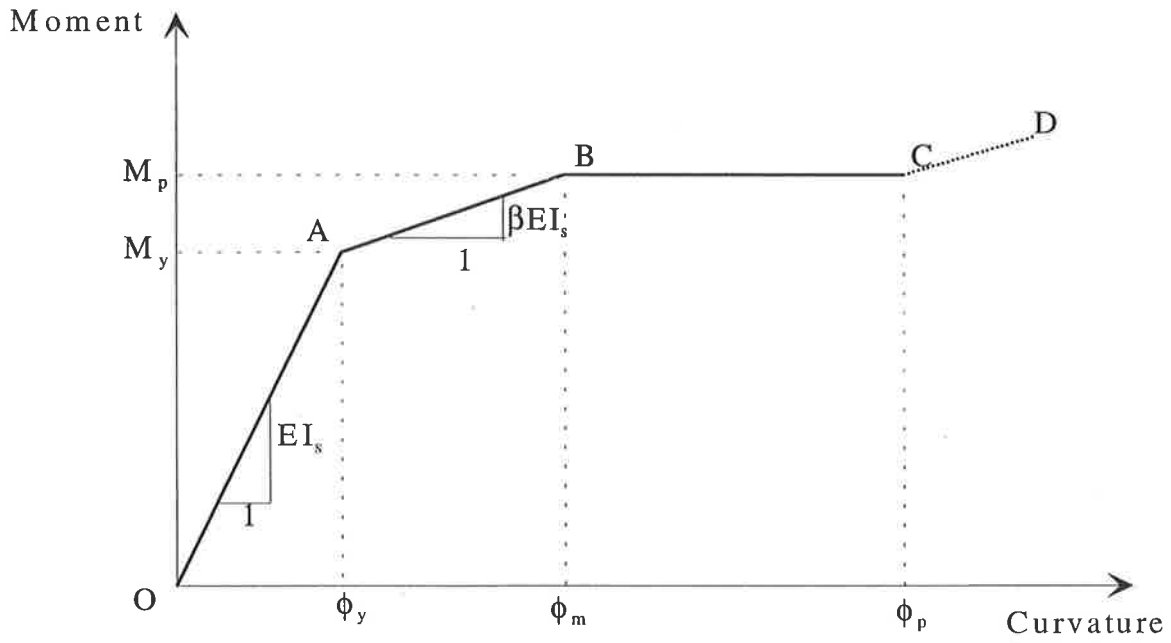
An additional point is identified on the moment-curvature curve of Fig. 2.29a at B, which represents the point at which the beam has achieved close to the full plastic moment of the beam. This can be taken as 95% or 98% of the plastic moment capacity, and the location of this point is discussed further in Section 2.4.3.6.4. With point B identified, the moment curvature curve can be idealised as a tri-linear curve as shown in Fig. 2.29b.

It can be noticed in Fig. 2.29a that there is a change in the slope of the curve when yielding commences at Point A. However, due to the influence of the residual stresses that remain from the roll-forming process, the point at which this occurs is less than the theoretical yield moment. The effect that residual stresses have on moment-curvature responses has been studied by Rotter and Ansourian (1979), and the effect on the vertical

deflection of simply supported composite beams by Ansourian and Roderick (1978). It was found that the residual stresses have no influence at serviceability load levels or at the maximum strength, but increase the curvatures and beam deflections at intermediate load levels. There were slight changes in the maximum moment if the residual stress level was varied dramatically. As a result, residual stresses are not included in the present analysis.



(a) Actual Curve



(b) Idealised Curve

Fig. 2.29. Moment Curvature Response for a Steel Beam

The plastic curvature ϕ_p of Fig. 2.29b at which strain hardening commences in the outer most fibre can be determined from the strain diagram shown in Fig. 2.30b for a section with zero axial load, and (d) for a section with a non-zero axial load. When the axial force in the steel section is zero, the neutral axis position does not vary as the material yields, and the plastic curvature is given by $\phi_p = 10\varepsilon_y / h_s^*$, which is 10 times the yield curvature. When there is an axial tensile force in the steel section, the neutral axis will move upwards, and the plastic curvature will decrease, as shown in (d). The corresponding stress distributions are shown in (c) and (e) respectively.

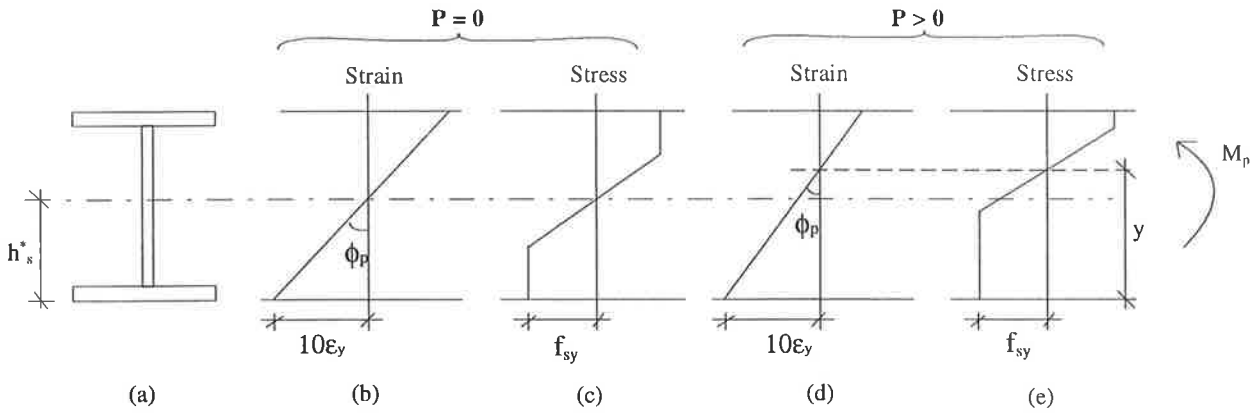


Fig. 2.30. Plastic Moment with Variable Connector Force.

For low degrees of shear connection, the top flange will be completely yielded when strain hardening commences in the bottom fibre. Under these conditions the position of the neutral axis will be given by Eq. 2.64, and the curvature required to attain the plastic moment can be determined by Eq. 2.65.

$$y = h_s^* + \frac{P}{2f_{sy}t_w} \qquad \text{.....(2.64)}$$

$$\phi_p = \frac{10\varepsilon_y}{y} = \frac{10\varepsilon_y}{h_s^* + \dfrac{P}{2f_{sy}t_w}} \qquad \text{.....(2.65)}$$

Equation 2.65 indicates that the plastic curvature decreases as the axial load increases. For higher degrees of shear connection, the top flange will not be fully yielded when strain hardening commences in the bottom fibre, and the height of the neutral axis above the bottom fibre will be less than that given by Eq. 2.64. However, Eq. 2.64 represents a reasonable

approximation to the height of the neutral axis, and using this value of y in Eq. 2.65 will give a conservative estimate for the curvature at which strain hardening commences. Thus point C in Fig. 2.29b is represented by the plastic moment as determined by standard rigid plastic methods (Gere and Timoshenko, 1987), and the plastic curvature as given by Eq. 2.65. With the form of the moment-curvature relationship of the steel element determined, the effect of steel yielding on the behaviour of the member can now be determined.

2.4.3.6.3 Extent of Yielding in Composite Beams

In order to determine the influence of yielding on the overall behaviour of a composite beam, it is first necessary to know the extent of yielding in the steel member. Consider a simply supported composite beam with a uniformly distributed load and at the ultimate moment, as shown in Fig. 2.31a. Near the supports, the applied moment will be low, and the steel stresses will be below the yield stress. The curvature will increase linearly with the increasing applied moment. At some location along the beam, the applied moment will just reach the yield moment M_y of the composite beam, at which yielding commences, as shown in (b). The location of this cross-section at M_y is designated by x_y in (a). At cross-sections closer to the maximum moment, more of the steel section will yield and the curvature will begin to increase more rapidly as shown in (c).

It can be seen in Fig. 2.31b that the longitudinal extent of the zone of yielding in the beam is controlled by the ratio of M_u/M_y of the member, where M_u is the ultimate moment capacity of the member and M_y is the yield moment, which varies along the length of the composite beam as shown by the thick line in (b). The larger this ratio, the larger the longitudinal extent of yielding. In order to find the length of this region, the location x_y where yielding first occurs in the member must be found. It will be shown that the yield moment of a composite beam increases with increasing axial force transferred by the connectors. With zero axial force transferred at the interface, that is zero shear connection, the yield moment is simply that of the steel section alone, assuming that the concrete element is not able to sustain a moment. The yield moment increases with axial force to a maximum at full shear connection.

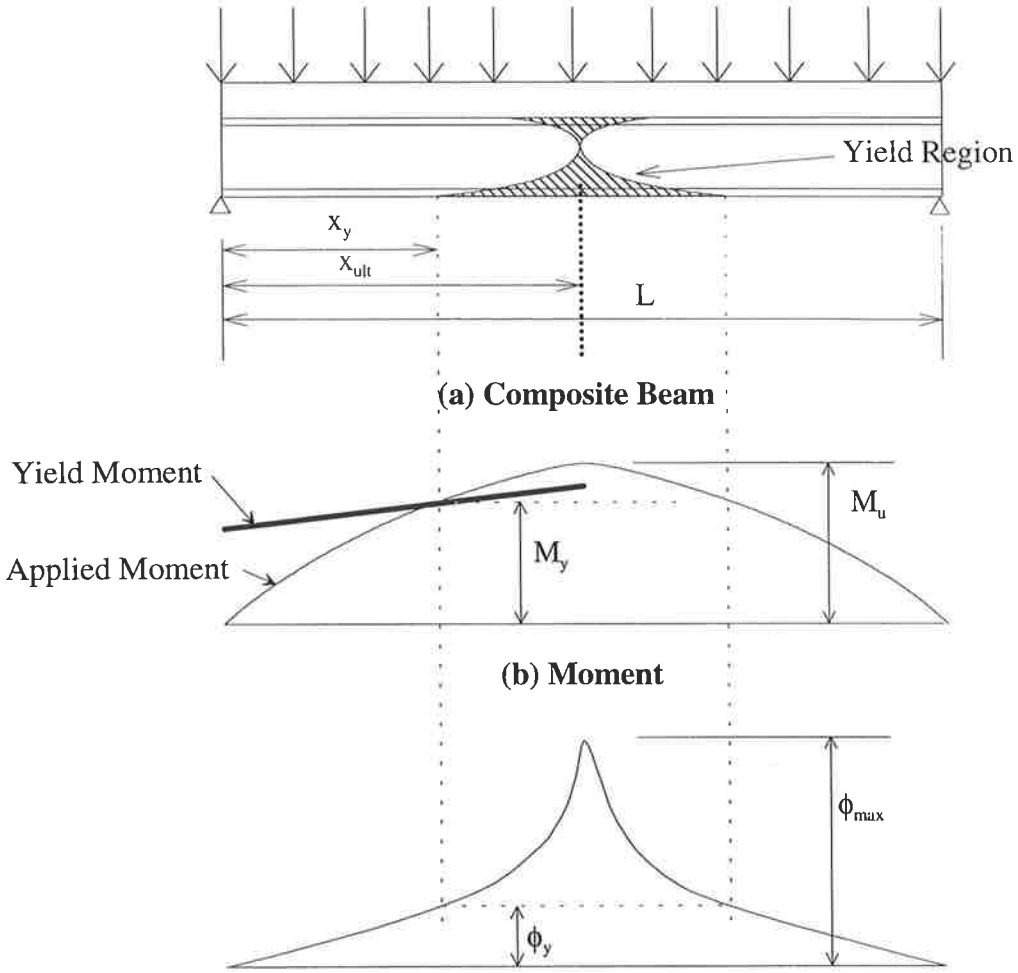


Fig. 2.31. Curvature Variation

In order to determine the extent of yielding, the location at which yielding first commences in the outer most fibre needs to be found. Consider compatibility of the cross-section of the steel element as shown in Fig. 2.32. The curvature to cause yield ϕ_y, can be found as:

$$\phi_y = \frac{\varepsilon_y - P/(EA)_s}{h_s^*} \quad \text{.....(2.66)}$$

where

ε_y = yield strain of the steel.

h_s^* = Distance from the centroid to the bottom fibre of the steel beam. Note that for a steel beam with equal flanges, $h_S = h_s^*$.

Substituting ϕ_y from Eq. 2.66 into Eq. 2.21 on Page 49 and solving for the moment gives:

$$M_y = P_y\left(h_s + h_c - \frac{(EI)_s + (EI)_c}{(EA)_s h_s^*}\right) + \frac{(EI)_s + (EI)_c}{h_s^*}\varepsilon_y \quad \text{.....(2.67)}$$

where

M_y = Applied moment to cause yield

P_y = Axial force transferred by the connectors at the location of first yield.

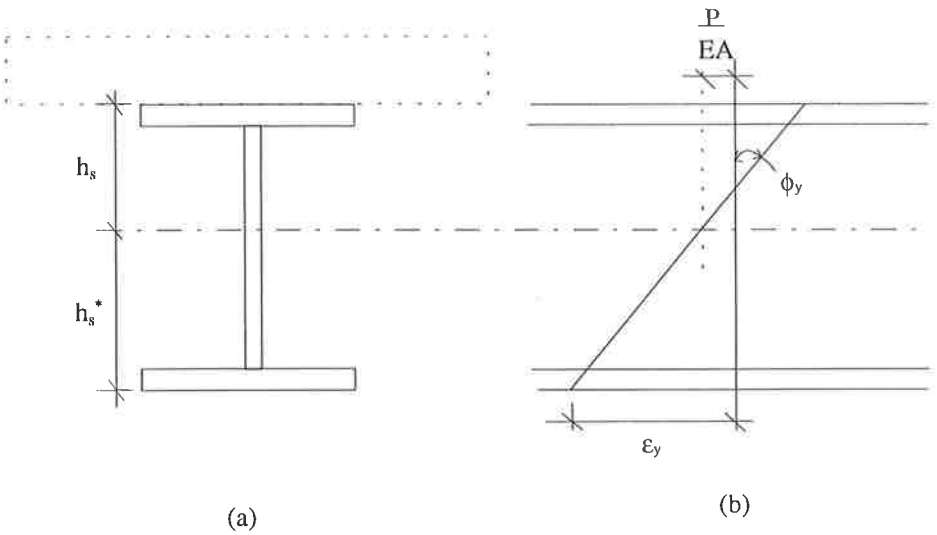


Fig. 2.32. Yield in Steel Section

Equation 2.67 shows that the yield moment varies linearly with the axial force exerted by the shear connectors as shown in Fig. 2.33 by the straight line D-C. This equation assumes that the flexural rigidity of the concrete element $(EI)_c$, remains constant at all degrees of shear connection. However at zero shear connection, the concrete would be fully cracked before the yield moment of the steel section is reached. This can be seen from Fig. 2.34, which shows a composite beam in (a) and the strain distribution for zero axial force in (b). Due to the same curvatures in the concrete and steel elements, from compatibility in (b), the strain at the bottom concrete fibre ε_c is related to the strain in the bottom tension fibre of the steel element ε_y by the ratio of h_c/h_s^*. Even when considering a low yield strength steel, with $\varepsilon_y = 1250\ \mu\varepsilon$, and $h_c/h_s^* = 1/5$, this gives $\varepsilon_c = 250\ \mu\varepsilon$, which is more than double the cracking strain of normal strength concrete. Thus as the concrete is fully cracked,

it is unable to resist any moment, and should not be included in the calculation of the yield moment of a composite beam with zero degree of shear connection.

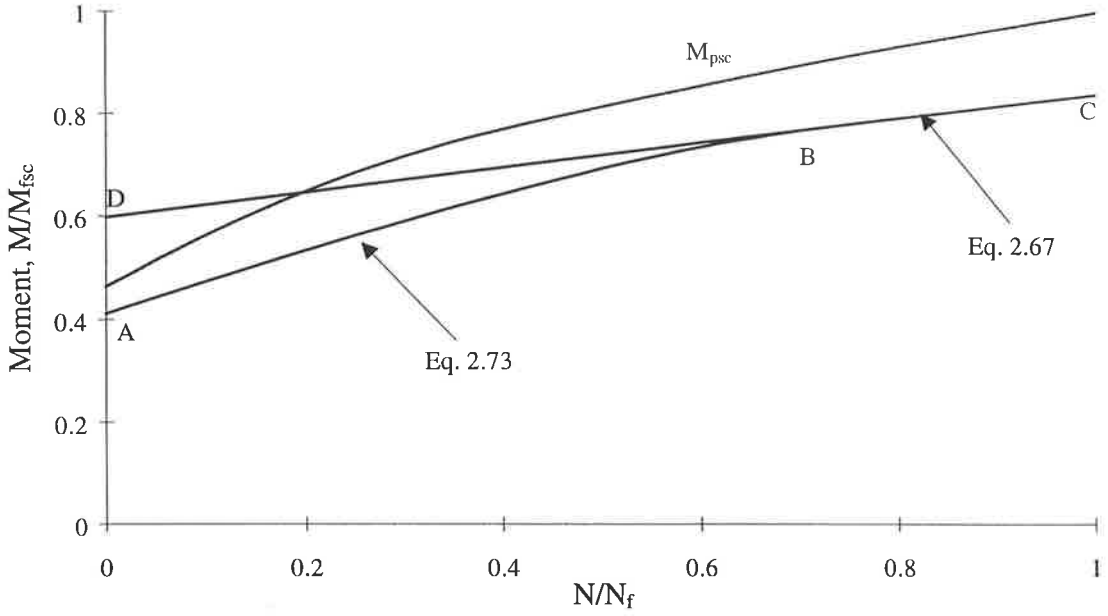


Fig. 2.33. Variation in Yield Moment

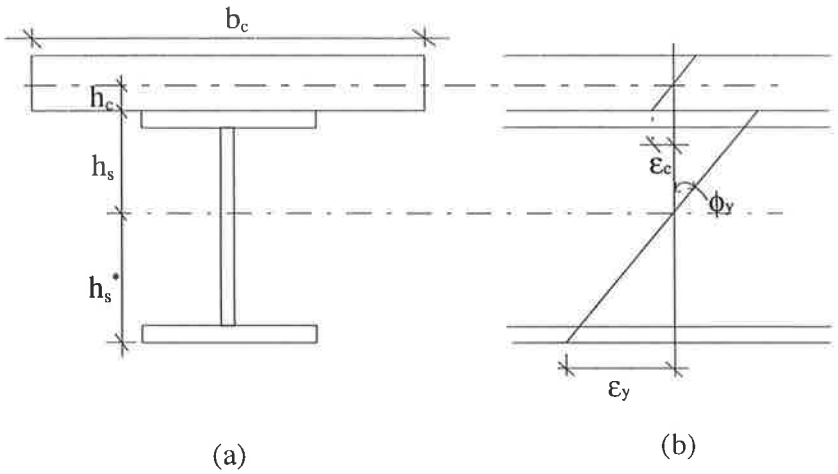


Fig. 2.34. Yield Moment with zero connector force.

Thus the moment to cause yield at zero degree of shear connection is given by the yield moment of the steel section alone, and is thus independent of the concrete element, whereas Eq. 2.67 gives the yield moment in terms of the concrete and steel flexural rigidities. If the dimensions of the beam used in the worked example in Section 2.4.2.6 are used in Eq. 2.67, then the resulting yield moment for $P_y = 0$ is greater than the plastic moment of steel section

alone, which is clearly incorrect. An alternative approach that accounts for the variation of the concrete stiffness is provided below and then the two methods are compared.

The variation of the yield moment with increasing shear connection can be derived explicitly for a cracked concrete section, assuming that the concrete has zero tensile capacity. Shown in Fig. 2.35 is the strain profile of a composite beam, with a total applied moment M_y, and a force P transferred by the connectors. The curvature ϕ_y in the steel section is the same as that in the concrete section, as is given by Eq. 2.66. The neutral axis in the concrete is located at a distance y_c below the top compression fibre, and the compressive strain in the top fibre is given by ε_o. These two values are related by the curvature in the cross-section. It can be assumed that the concrete acts linearly in compression for the purposes of determining the yield moment, thus the depth to the neutral axis can be determined from Eq. 2.68.

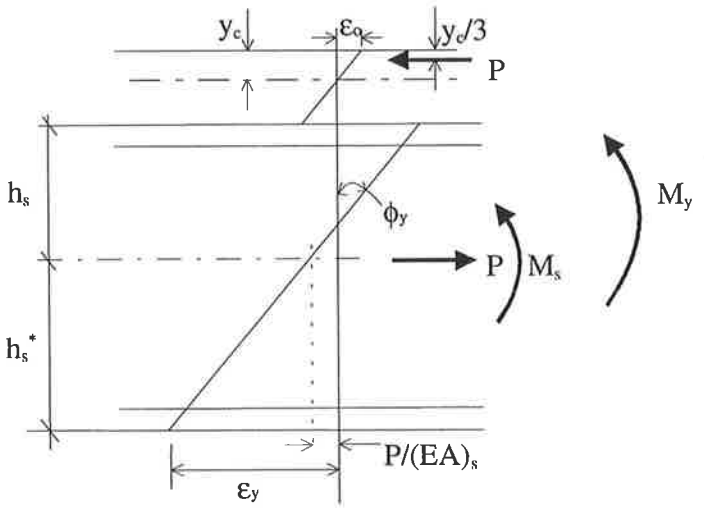


Fig. 2.35. Yield Moment with Variable Connector Force.

$$P = \frac{1}{2}\varepsilon_o E_c b_c y_c \quad \text{.....(2.68)}$$

where b_c = width of the concrete element as shown in Fig. 2.34, and where the top fibre compressive strain is related to the neutral axis location by $\varepsilon_o = \phi_y y_c$, which can be substituted into Eq. 2.68, and then solved for y_c to give:

$$y_c = \sqrt{\frac{2P}{E_c b_c \phi_y}} \quad \text{.....(2.69)}$$

The value of ϕ_y from Eq. 2.66 can be substituted into Eq. 2.69 to give:

$$y_c = \sqrt{\frac{2h_s^* P}{E_c b_c \left(\varepsilon_y - P/(EA)_s\right)}} \quad \text{.....(2.70)}$$

The moment M_S acting in the steel section is given by:

$$M_s = \frac{\left(f_{sy} - P/A_{st}\right) I_s}{h_s^*} \quad \text{.....(2.71)}$$

where

I_S = Moment of inertia of the steel element

When the concrete material behaves linearly in compression, the centroid of the compressive force in the concrete will act at 1/3 of the distance to the neutral axis from the top fibre, as shown in Fig. 2.35. It is now possible to determine the total moment in the cross-section as:

$$M_y = P\left(d_c + h_s - \frac{1}{3}y_c\right) + M_s \quad \text{.....(2.72)}$$

where

d_c = Depth of the concrete element

Substituting in the value for y_c from Eq. 2.70 and M_S from Eq. 2.71 gives:

$$M_y = P\left(d_c + h_s - \frac{1}{3}\sqrt{\frac{2Ph_s^*}{\left(\varepsilon_y - P/(EA)_s\right)E_c b_c}} - \frac{I_s}{A_{st}h_s^*}\right) + \frac{I_s}{h_s^*} f_{sy} \quad \text{.....(2.73)}$$

Equation 2.73 represents the variation in yield moment with the force transferred by the connectors, for a composite beam in which the concrete is linear in compression and has zero tensile strength. This is shown plotted in Fig. 2.33 by the line A-B-C, which indicates the variation in the yield moment with the degree of shear connection. The moment has been non-dimensionalised by dividing by the ultimate moment of the composite beam for full shear connection M_{fsc}. Also shown in the figure is the variation in the flexural strength

M_{psc} for the same composite beam, as determined from the equilibrium method. This varies from the strength at zero shear connection M_{zsc} to the strength at full shear connection M_{fsc}. The third curve shown in the figure is that of Eq. 2.67, indicated by the straight line D-C, which is the variation in the yield moment assuming that the concrete remains linear elastic.

It can be seen in Fig. 2.33 that as the degree of shear connection increases, the curves of Eq. 2.67 and 2.73 converge, and after point B, follow the same path. This point occurs when the neutral axis in the concrete element is equal to the depth of the concrete, and thus the full depth of the concrete is in compression. Thus the concrete element behaves as though it were uncracked, and the whole depth contributes to the overall flexural rigidity of the concrete element. For degrees of shear connection higher than this, the yield moment follows the curve for both materials being linear elastic, ie. the curve described by Eq. 2.67. It was previously stated in Section 2.4.3.3 that near mid-span the flexural rigidity of the concrete element tends towards zero when considering the ultimate moment condition. However, this assumption does not pertain to the present analysis which is concerned with locating the position of first yield, and thus the curvatures are much less than those at the position of the ultimate moment.

Equation 2.38 plots the variation in the cracking moment with increasing axial force along the length of the beam. When the value of the cracking strain ε_{cr} is set to zero, this equation describes the moment at which tensile strains first occur in the concrete. Thus the intersection of Eq. 2.38 with Eq. 2.67 describes the location of the transition point B in Fig. 2.33. Setting these two equations equal with $\varepsilon_{cr} = 0$ and solving for P results in:

$$P = \frac{A_c A_{st} h_c}{n A_{st} h_s^* + A_c h_c} f_{sy} \qquad \text{.....(2.74)}$$

When the neutral axis is in the concrete element at the ultimate moment, then $P_{fsc} = A_{st} f_{sy}$, and Eq. 2.74 can be simplified to:

$$\frac{N}{N_f} = \frac{1}{\frac{n A_{st} h_s^*}{A_c h_c} + 1} \qquad \text{.....(2.75)}$$

where

n = Modular ratio = E_s/E_c

It can be seen in Fig. 2.33 that the straight line interpolation between points A and C will give a conservative estimation of the yield moment for any degree of shear connection. Point A is defined by the yield moment of the steel beam alone M_{sy}. Point C is found by substituting the value of $P_y = P_{fsc} = A_{st}f_{sy}$ into Eq. 2.67. The term f_{sy} can be replaced with $E_s\varepsilon_y$ which gives the yield moment for full shear connection M_{fsy} as:

$$M_{fsy} = (EA)_s \varepsilon_y \left(h_s + h_c - \frac{(EI)_s + (EI)_c}{(EA)_s h_s^*} \right) + \frac{(EI)_s + (EI)_c}{h_s^*} \varepsilon_y$$

This simplifies to:

$$M_{fsy} = P_{fsc}(h_s + h_c) \quad \text{.....(2.76)}$$

The variation in the yield moment is defined as the linear variation between these two points. Adopting $P_{fsc} = A_{st}f_{sy}$, the variation is given by:

$$\begin{aligned} M_y &= M_{sy} + \frac{P}{P_{fsc}} \left(P_{fsc}(h_s + h_c) - \frac{I_s f_{sy}}{h_s} \right) \\ &= M_{sy} + P\left(h_s + h_c - \frac{I_s}{A_{st} h_s} \right) \end{aligned} \quad \text{.....(2.77)}$$

where M_{sy} is the yield moment of the steel section with no axial load,

$$M_{sy} = \frac{I_s f_{sy}}{h_s} \quad \text{.....(2.78)}$$

From the known distribution of shear connectors along the beam, the variation in the longitudinal shear force is known. This can be used with Eq. 2.77 to plot the variation in the yield moment along the beam. When this equation is plotted on the applied bending moment diagram, the intersection of these lines will give the location of first yield, x_y. Figure 2.31 on Page 75 shows a beam with a uniformly distributed load, and with a uniform distribution of

shear connectors. For this case, there will be a linearly varying axial force P, that increases from zero at the supports to a maximum at the location of maximum moment, which gives rise to a linear variation in the yield moment along the member, as shown in (b).

As the degree of shear connection increases, the ultimate moment of the member M_{psc} will increase, as discussed in Section 2.1 and shown in Fig. 2.33. Also shown in Fig. 2.33 as curve A-B-C is the variation in yield moment. It can be seen from a comparison of these two curves that the ultimate moment increases at a greater rate than the yield moment as the degree of shear connection increases. Barnard and Johnson (1965) found the shape factor ratios M_u/M_y ranged from 1.46 - 1.67 for six beams tested with full shear connection. This result can be found to be generally true for most composite beams. This compares to a shape factor of approximately 1.15 for steel I-sections, which indicates the large increase in the shape factor with increasing shear connection. Thus for a member with uniformly distributed connectors, as the degree of shear connection increases, the ratio of M_u/M_y will increase and the location of first yielding x_y will move closer towards the supports, thus increasing the total region of yielding.

For a beam with a uniformly distributed load and a uniform distribution of shear connectors, the derivation of the value of x_y is as follows. The variation in the applied moment is given by Eq. 2.39 on Page 60, whilst the variation the yield moment is given by Eq. 2.77. The variation in axial force along the length of the beam will be the same as that given in Eq. 2.40, which can be substituted into Eq. 2.77. Setting the result equal to Eq. 2.39 and solving for x_y gives:

$$x_y = \frac{L}{2} - \frac{\eta P_{fsc} L}{4M_u}\left(h_s + h_c - \frac{I_s}{A_s h_s}\right) + \left(\sqrt{\left[\frac{4M_u}{L} - \frac{2\eta P_{fsc}}{L}\left(h_s + h_c - \frac{I_s}{A_s h_s}\right)\right]^2 - \frac{16 M_u M_{sy}}{L^2}}\right)\frac{L^2}{8M_u}$$

which can be further simplified to:

$$x_y = \frac{L}{2}\left(\left[1 - \frac{\eta P_{fsc}}{2M_u}\left(h_s + h_c - \frac{I_s}{A_s h_s}\right)\right] + \sqrt{\left[1 - \frac{\eta P_{fsc}}{2M_u}\left(h_s + h_c - \frac{I_s}{A_s h_s}\right)\right]^2 - \frac{M_{sy}}{M_u}}\right) \quad (2.79)$$

The derivation of x_y for a beam subject to a point load at the centre-span with a uniform distribution of shear connectors is as follows. The variation in the applied bending moment is given by Eq. 2.42 on Page 60, and the intersection of Eq. 2.42 with Eq. 2.77 gives the location of first yielding, which is given by Eq. 2.80.

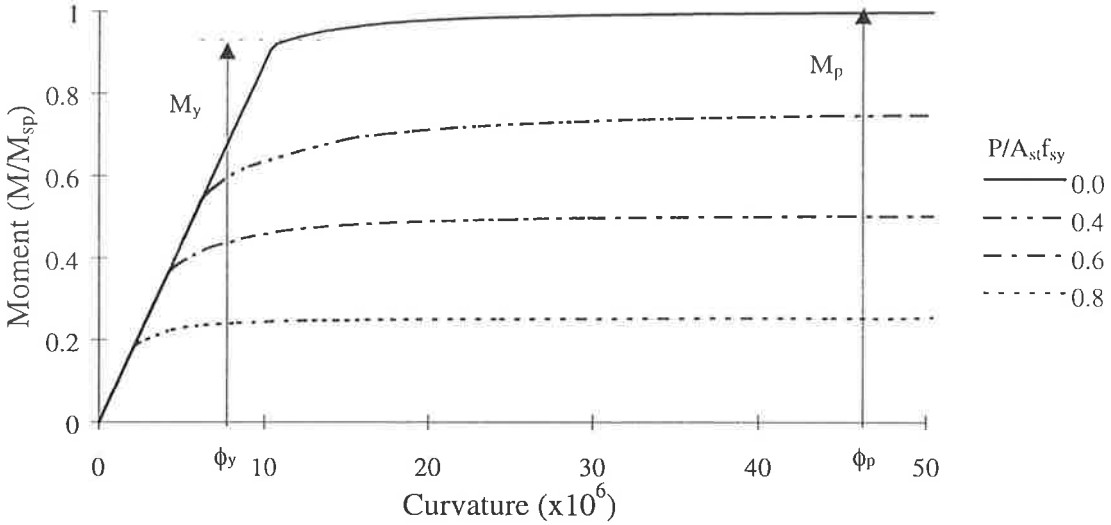
$$x_y = \frac{M_{sy}\, L/2}{M_u - \eta P_{fsc}\left(h_s + h_c - \frac{I_s}{A_s h_s}\right)} \qquad \text{.....(2.80)}$$

2.4.3.6.4 Increment of Slip in Yielded Region

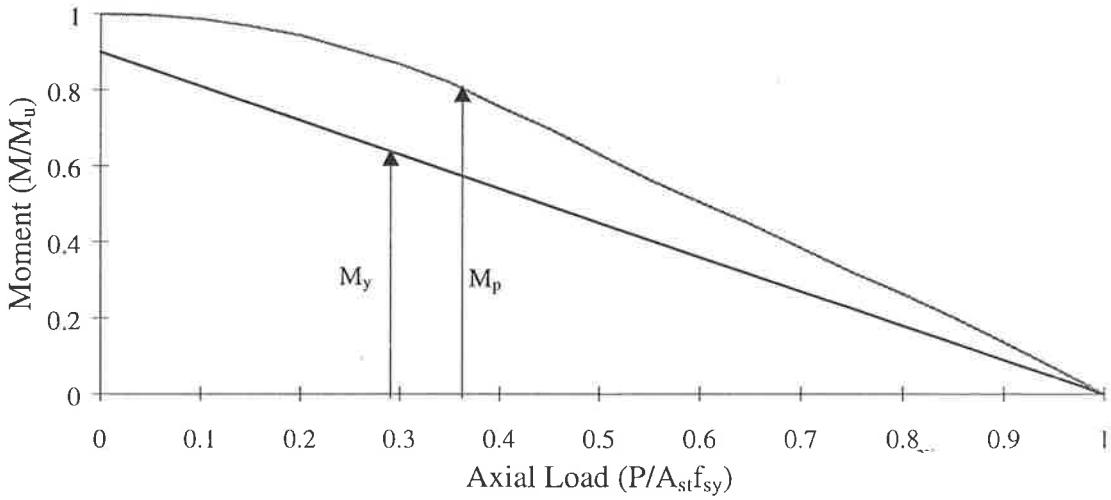
The extent of the zone of yielding was determined in the previous section. The next step in the analysis is to determine the increase in slip due to yielding. The increment in slip that is determined is the increase in slip due to the yielding of the steel over the slip from the analysis incorporating the effects of concrete cracking, as given by Eq. 2.60 on Page 66. In the determination of Eq. 2.24 on Page 50 and Eq. 2.58 on Page 65 it was assumed that the steel element behaved linearly elastically. Thus, the moment developed in the steel section of the composite beam was directly proportional to the curvature in the section as shown by the line O-A in Fig. 2.29a on Page 72. However, as was discussed in Section 2.4.3.2, the flexural stiffness of a steel I-section decreases after the initial onset of yielding, as shown by the curve A-B-C.

Figure 2.29a on Page 72 shows the moment-curvature relationship when there is zero axial load in the steel member of the composite beam, and Fig. 2.36a shows the relationship with various degrees of axial load. The interaction between the axial load P and the moment is shown in Fig. 2.36a, where the axial load is non-dimensionalised by dividing by the yield load of the steel section $A_{st}f_{sy}$, and the moment is non-dimensionalised by dividing by the plastic moment M_{sp} of the steel section with no axial load. The values for the yield moment M_y and the plastic moment M_p are shown in Fig. 2.36a for the case of zero axial load, ie. $P/A_{st}f_{sy} = 0.0$. It can be seen that the yield moment and the plastic moment decrease for increasing axial load. Figure 2.36b shows the variation in the yield moment and plastic moment of a steel I-beam with increasing axial load. This shows that the yield moment of the steel section decreases linearly with increasing axial force, as given by Eq. 2.81, whereas the plastic moment of the steel section decreases non-linearly.

$$M_y = M_{sy} - P\frac{I_s}{A_s h_s^*} \quad \text{.....(2.81)}$$



(a) Moment Curvature for an I-section with increasing axial load



(b) Moment-Axial Force Interaction Curve

Fig. 2.36. Influence of Axial Force on Steel Section

It can be seen in Fig. 2.36b that the value of M_p - M_y changes with the level of the axial load in the member. It can also be seen in (a) that the plastic curvature ϕ_p and the yield curvature ϕ_y also vary for increasing axial load. The yield curvature ϕ_y is related to the yield moment M_y by the steel flexural stiffness, EI_s. The variation in the plastic curvature ϕ_p was given by Eq. 2.65 on Page 73, and was found to decrease for an increase in the axial load. However, the curvature at which the full plastic moment is achieved will give an overestimate of the curvature at point B in Fig. 2.29b. A relationship can be found for ϕ_m, which

represents the curvature at which a certain percentage of the plastic moment of the steel section has been reached. This can be set to say 95% or 98% of the full plastic moment. The effect of the choice of the controlling limit on the value of β will be discussed further.

The stress distribution within a steel I-beam under increasing moment is shown in Fig. 2.28 on page 70, with the stress distribution when the plastic moment is almost reached shown in (d). The increase in moment can be calculated when the stress distribution changes from that shown in (d) to when the section is fully plastic. When the depth of the elastic core is given by $2h_e$, the increase in moment ΔM required to reduce the elastic core to zero can be found as:

$$\Delta M = \frac{1}{3} f_{sy} t_w h_e^2 \quad \text{.....(2.82)}$$

If the increase in the moment is set to 0.05 or 0.02 times M_p, then Eq. 2.82 can be solved for h_e. Once a value of h_e is known, the curvature in the section can be determined from the strain profile, and is given by:

$$\phi_m = \frac{\varepsilon_y}{h_e} = \varepsilon_y \sqrt{\frac{f_{sy} t_w}{3\Delta M}} \quad \text{.....(2.83)}$$

Thus the term ϕ_m varies inversely with ΔM. In other words, if point B in Fig. 2.29b is taken as when 95% of M_p is reached, then $\Delta M = 0.05M_p$, and ϕ_m can be calculated from Eq. 2.83. Alternatively, if point B is assumed to occur when 98% of M_p is reached, then $\Delta M = 0.02M_p$, and ϕ_m will increase.

The parameter β in Fig. 2.29 on Page 72 represents the stiffness reduction factor for the steel beam after the onset of yielding in the lower flange, and can be determined from inspection of Fig. 2.29b, and is given by Eq. 2.84. It can be seen from Fig. 2.36b that the value of $M_p - M_y$ will vary with the degree of shear connection. Furthermore, the value of $\phi_m - \phi_y$ will also vary with the degree of shear connection. A typical variation of β with the degree of shear connection is shown in Fig. 2.37.

$$\beta = \frac{1}{(EI)_s} \frac{M_p - M_y}{\phi_m - \phi_y} \quad \text{.....(2.84)}$$

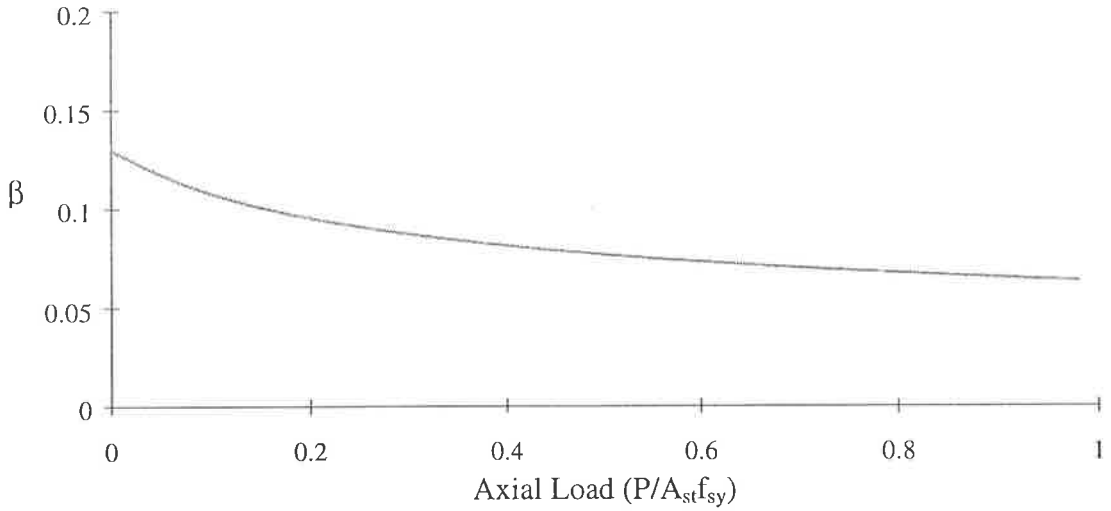


Fig. 2.37. Variation in β with Degree of Shear Connection

As the procedure to determine the end slip is based on integrating along the length of the member, it is appropriate to use an average value for the post-yielding stiffness of the steel member. In other words, a value of β must be determined which is representative of the reduced stiffness of the steel beam over the region of the beam in which there is yielding. Furthermore, even for beams which have a high degree of shear connection, this degree of shear connection will not exist at all points along the shear span. Thus, despite the slight reduction in β with increasing axial load shown in Fig. 2.37, an average value may be adopted with little error.

Adopting a value of β that is determined for a section with zero axial load gives good correlation with experimental results, as discussed in Section 2.5. Adopting a lesser value of β has the effect of increasing the curvature ϕ_m at which the steel beam is considered to have reached its plastic moment, as shown in Fig. 2.29 on Page 72, while at the same time the length of the plastic plateau B-C will be reduced. Thus, when considering the composite beam as a whole, reducing the value of β will result in an increase in the curvatures and hence slip at the ultimate moment, as shown by Point A in Fig. 2.12 on Page 35, with a corresponding decrease in the curvatures and hence slip during plastic deformation, as shown by the plateau A-B.

The value of β can be determined from Eq. 2.84 by substituting Eq. 2.81 for M_y, Eq. 2.83 for ϕ_m, setting $P = 0$, setting $M_p = M_{sp}$ the plastic moment of the steel section with no axial load, and noting that $\phi_y = M_{sy}/(EI)_s$. This gives,

$$\beta = \frac{M_{sp} - M_{sy}}{(EI)_s \varepsilon_y \sqrt{\frac{f_{sy} t_w}{0.15 M_{sp}}} - M_{sy}} \quad \text{.....(2.85)}$$

Adopting the bilinear relationship O-A-B in Fig. 2.29b for the behaviour of the steel section, the equation describing the moment-curvature relationship of the beam in the yield zone between ϕ_y and ϕ_m is given by:

$$M_s = (1-\beta)M_y + \beta(EI)_s \phi \qquad \text{for} \qquad \phi_y \le \phi < \phi_m \quad \text{.....(2.86)}$$

where M_s is the moment component in the steel section.

Before the influence of yielding in the steel can be properly accounted for, an estimate needs to be made for the stiffness of the concrete element in this region. It is not appropriate to use the elastic stiffness of the concrete element, as the curvatures and strains associated with yielding of the steel are sufficient to cause cracking in the concrete. As was described in Section 2.4.3.3, an average value for the stiffness of the concrete element is adopted, which will be denoted by $\alpha(EI)_c$. Thus the moment in the concrete element M_c is related to the curvature ϕ in the cross-section by $M_c = \phi\alpha(EI)_c$. Substituting this value of M_c, with M_s from Eq. 2.86 into Eq. 2.20 and solving for the curvature gives

$$\phi = \frac{M - P(h_s + h_c) - (1-\beta)M_y}{\beta(EI)_s + \alpha(EI)_c} \quad \text{.....(2.87)}$$

Equation 2.87 gives the new curvature in the cross-section with the reduced stiffness of the steel element due to yielding, and the reduced stiffness of the concrete due to cracking. The increase in curvature due to yielding of the steel section can now be determined from the difference of Eq. 2.87 and Eq. 2.57 on Page 65 which gives the curvature incorporating the effects of concrete cracking. This is given by Eq. 2.88.

$$\Delta\phi_y = \frac{M - P(h_s + h_c) - M_y(1-\beta)}{\beta(EI)_s + \alpha(EI)_c} - \frac{M - P(h_s + h_c)}{(EI)_s + \alpha(EI)_c}$$

$$= K_6\left(M - P(h_s + h_c) - M_y K_7\right) \quad \text{.....(2.88)}$$

where

$$K_6 = \frac{(1-\beta)(EI)_s}{\left(\beta(EI)_s + \alpha(EI)_c\right)\left((EI)_s + \alpha(EI)_c\right)} \quad \text{.....(2.89)}$$

$$K_7 = 1 + \frac{\alpha(EI)_c}{(EI)_s} \quad \text{.....(2.90)}$$

Equation 2.81 can be substituted for the yield moment M_y in Eq. 2.88, which on simplification gives Eq. 2.91.

$$\Delta\phi_y = K_6\left(M - P\left(h_s + h_c - \frac{I_s}{h_s^* A_s}K_7\right) - M_{sy}K_7\right) \quad \text{.....(2.91)}$$

Equation 2.91 can be inserted into Eq. 2.23 on Page 50 to give the increase in slip strain due to yielding of the steel. The result is given by Eq. 2.92.

$$\Delta\varepsilon_{slip,y} = \Delta\phi_y(h_s + h_c) \quad \text{.....(2.92)}$$

Equation 2.92 can now be integrated over the segment of the beam which has yielded, in order to determine the increase in slip. Assuming the limits of integration are x_y to x_{ult}, as shown in Fig. 2.31a, then the slip increment due to yielding s_y, is given by:

$$s_y = \int_{x_y}^{x_{ult}} \Delta\varepsilon_{slip,y} = K_6(h_c + h_c)\left(\int_{x_y}^{x_{ult}} M dx - \left(h_s + h_c - \frac{I_s}{h_s^* A_s}K_7\right)\cdot\int_{x_y}^{x_{ult}} P dx - M_{sy}K_7 \cdot \int_{x_y}^{x_{ult}} dx\right)$$

$$= K_6\left(A_{my} - \left(h_s + h_c - \frac{I_s}{h_s^* A_s}K_7\right)A_{py} - M_{sy}K_7\left(x_{ult} - x_y\right)\right) \quad \text{.....(2.93)}$$

where

$$K_6 = (h_s + h_c)\frac{(1-\beta)(EI)_s}{(\beta(EI)_s + \alpha(EI)_c)((EI)_s + \alpha(EI)_c)}$$

A_{my} = Area under applied moment diagram over which yielding is present, as shown in Fig. 2.38b

A_{py} = Area under longitudinal shear force diagram over which yielding is present, as shown in Fig. 2.38c.

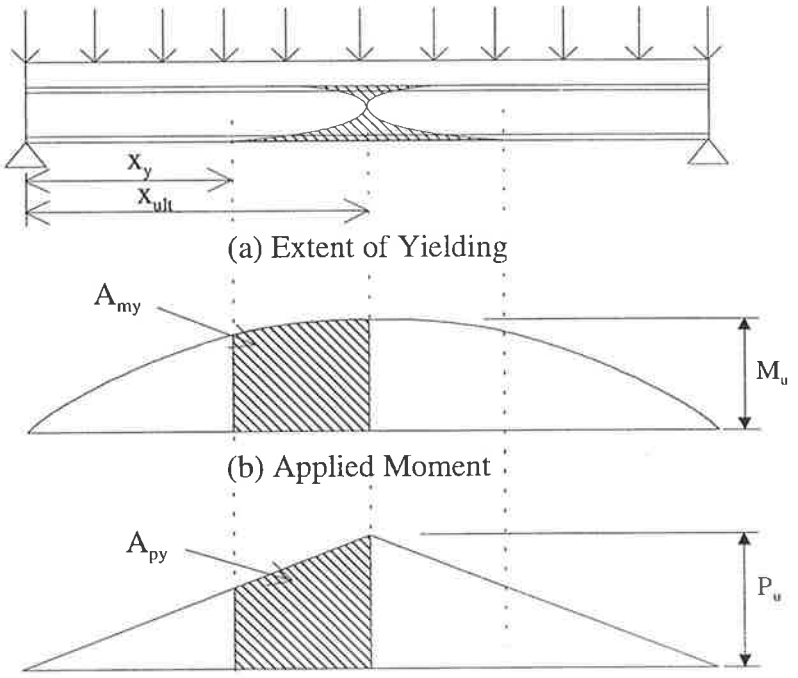


Fig. 2.38. Design for Yielding

Figure 2.38a shows the extent of yielding in a composite beam with a uniform distribution of shear connectors, and subject to a uniformly distributed load. The resulting bending moment diagram is shown in (b), and the variation in longitudinal shear is shown in (c). For a beam with the above conditions, the values of A_{my} and A_{py} are given by:

$$A_{my} = L_{my} M_u \quad \text{.....(2.94)}$$

$$A_{py} = L_{py} P_u \quad \text{.....(2.95)}$$

where

$$L_{my} = \frac{L}{3} - x_y^2\left(\frac{1}{L/2} - \frac{x_y}{3(L/2)^2}\right) \quad \text{.....(2.96)}$$

$$L_{py} = \frac{1}{2}\left(\frac{x_y}{L/2} + 1\right)\left(\frac{L}{2} - x_y\right) \quad \text{.....(2.97)}$$

Equation 2.93 gives the increment in slip due to yielding of the steel. Combining this with Eq. 2.60 on Page 66 which gives the end slip based on linear elastic concrete and steel properties combined with that due to cracking, gives:

$$\begin{aligned} s_{end} &= s_{o,cr} + s_y \\ &= A_m K_4 - A_p K_5 + K_6\left(A_{my} - \left(h_s + h_c - \frac{I_s}{h_s^* A_s} K_7\right)A_{py} - M_{sy} K_7 \left(x_{ult} - x_y\right)\right) \end{aligned} \quad \text{.(2.98)}$$

For the case of a uniformly distributed load with a uniform distribution of shear connectors, it is possible to rearrange Eq. 2.98 to solve for the maximum moment. This is done by substituting L_{my} and L_{py} from Eqs. 2.96 and 2.97 into Eqs. 2.94 and 2.95. The resulting values of A_{my} and A_{py} are in turn substituted into Eq. 2.98. The result is then given by Eq. 2.99.

$$M_{frac,y} = \frac{S_u + \eta P_{fsc}\left(L/4 K_5 + L_{py}\left(h_s + h_c - \frac{I_s}{h_s^* A_s} K_7\right)K_6\right) + M_{sy}\left(L/2 - x_y\right)K_6 K_7}{L/3 K_4 + L_{my} K_6} \quad \text{...(2.99)}$$

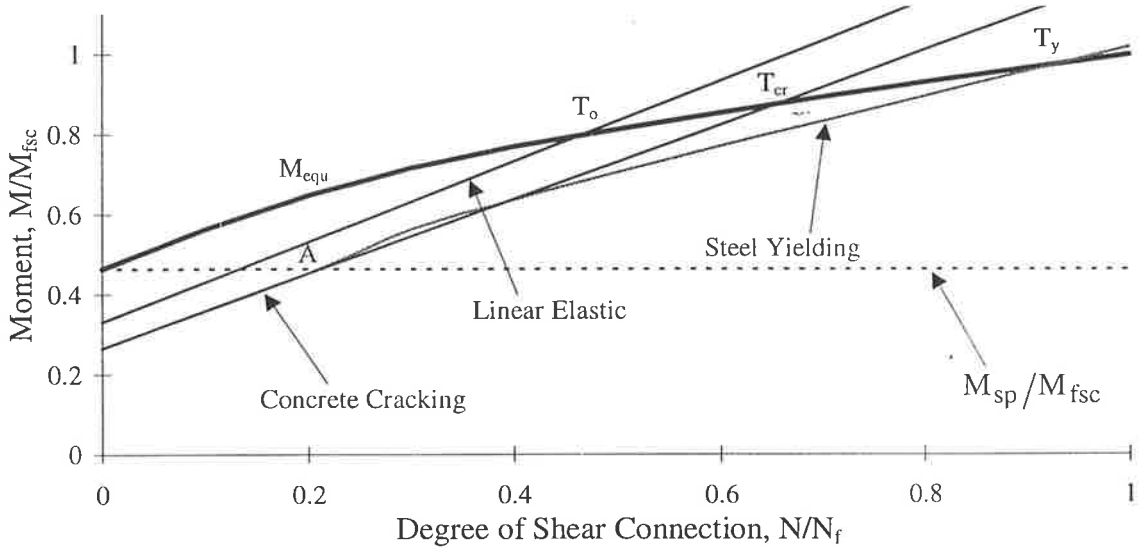
The right hand side of Eq. 2.99 contains the terms L_{my}, L_{py} and x_y which are given by Eqs. 2.96, 2.97 and 2.79 respectively. The first two of the these terms are functions of x_y which is itself a function of M_u, which is the left hand side of Eq. 2.99. It is not possible to solve for M_u explicitly in Eq. 2.99, and it must be solved for iteratively. This is carried out by first estimating x_y from Eq. 2.79 which is then substituted into Eqs. 2.96 and 2.97 to give L_{my} and L_{py} respectively. These are then substituted into Eqs. 2.94 and 2.95 to give A_{my} and A_{py} which are in turn substituted into Eq. 2.99. The resulting value of $M_{frac,y}$ is then

substituted for M_u in Eq. 2.79 to give an improved estimate for x_y. This procedure converges quickly after a few iterations to give the final values for x_y and $M_{frac,y}$.

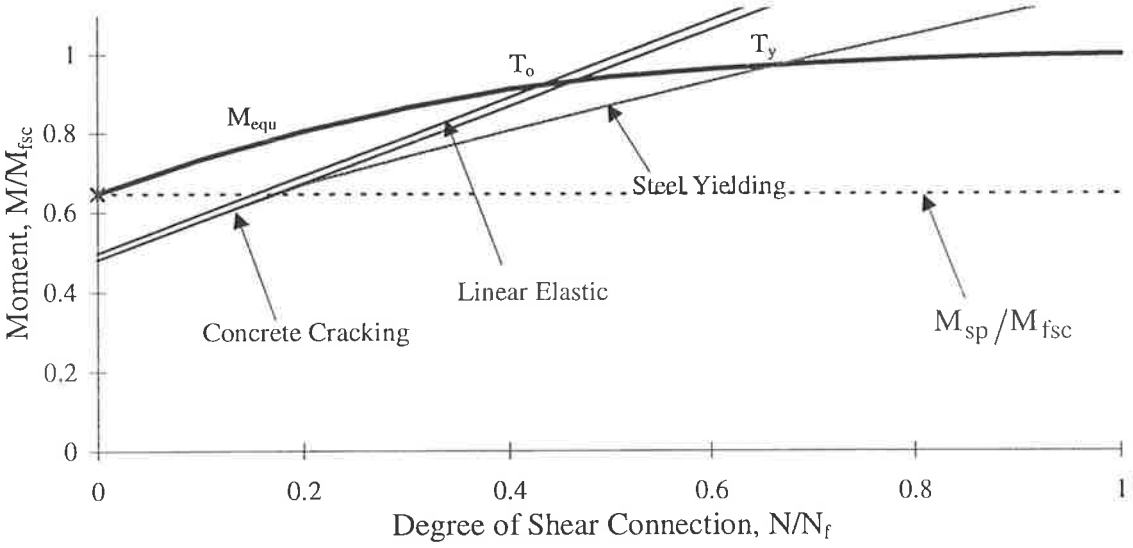
The effect of steel yielding on the endslip is shown in Section 2.4.3.7 by the use of a worked example. The results are compared to the first order analysis, and to the analysis including the effects of concrete cracking.

2.4.3.7 Worked Example

Consider the two beams that were looked at previously in Section 2.4.2.6, with the properties given in Table 2.2. The variation in the ultimate strength is shown by the line M_{equ} in Fig. 2.39, and the variation in the moment to cause fracture of the shear connectors is also shown. The line labelled Linear Elastic is that from Eq. 2.34 in Section 2.4.2; the line labelled Concrete Cracking is derived from either Eq. 2.55 or Eq. 2.63 in Section 2.4.3.3; and the line labelled Steel Yielding is that from Eq. 2.99 in the previous section. The transition point which describes the change in the failure mode from fracture of the shear connectors to flexural failure is shown for each of the three analyses. It can be seen that the incorporation of yielding in the steel in the analysis increases the minimum degree of shear connection required to prevent fracture of the shear connectors, which is as expected.



(a) Beam 1



(b) Beam 2

Fig. 2.39. Variation in Moment to Cause Fracture

At low degrees of shear connection the shear connectors will fracture before yielding of the steel has commenced. This is indicated by the line for Steel Yielding converging to the line for Concrete Cracking in Fig. 2.39a. These two lines converge at the point where the maximum moment in the composite cross-section is equal to the plastic moment of the steel section alone, as shown by Point A. The line incorporating steel yielding initially rises slightly above the line incorporating concrete cracking in Fig. 2.39a. This is due to the slight underestimation of the yield moment, as given by Eq. 2.77, which in turn overestimates the length of the yield region, and leads to a slight overestimate in the effects of steel yielding.

2.4.3.8 Plastic Hinge

When designing a beam using rigid plastic analysis it is important to ensure that the member is capable of developing the curvatures necessary to attain the full plastic moment of the cross-section. Typically, this requires a check on the b/t ratios of each of the steel elements in compression. However, it is also important to note that large slip strains also develop in the hinge region, which over the length of the hinge, may result in a significant slip increment. Section 2.2.9 described the procedure used to determine the hinge length, and proposed the formula given by Eq. 2.18 on Page 39.

The slip strain at the location of the hinge can be found by considering the strain diagram used in the rigid plastic analysis, as shown in Fig. 2.40. Knowing the maximum

strain in the top concrete compression fibre, ε_u, and the locations of the neutral axes in the steel and concrete elements, the slip strain at the plastic hinge is given by

$$\varepsilon_{slip,h} = \varepsilon_u \frac{y_{ns} - y_{nc}}{y_{nc}} \quad \text{.....(2.100)}$$

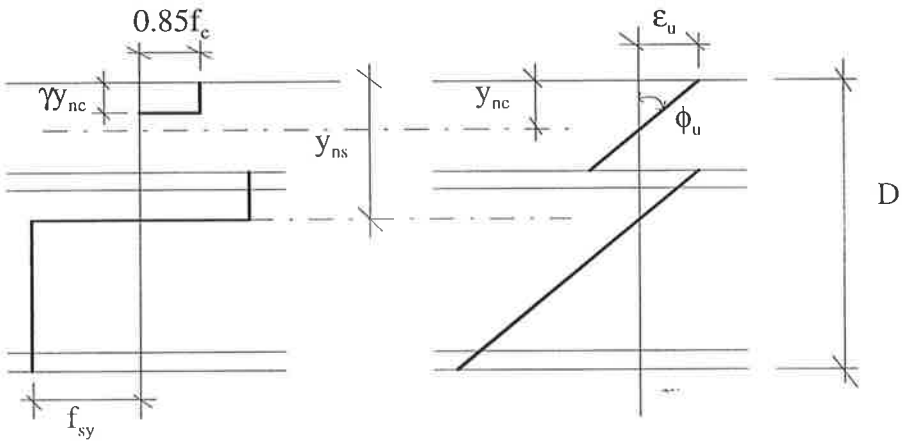
where

y_{ns} = the steel neutral axis location, measured from the concrete top compression fibre,

y_{nc} = the concrete neutral axis location.

The accompanying curvature in the cross-section is shown in Fig. 2.40 as ϕ_u, and is given by:

$$\phi_u = \frac{\varepsilon_u}{y_{nc}} \quad \text{.....(2.101)}$$



(a) Stress (b) Strain

Fig. 2.40. Stress and Strain Distributions in Plastic Hinge

The value of ε_u used in the above formulation is the crushing strain of the concrete, as given by Eq. 2.17 on Page 38, and assumes that the ultimate failure of the composite beam is by crushing of the concrete. However, for very low degrees of shear connection, crushing of the concrete may not be the mechanism to cause final failure of the beam (neglecting other secondary forms of failure such as fracture of the shear connectors). As the degree of shear connection decreases, the neutral axis in the concrete element moves upwards. Thus, to achieve a maximum strain of ε_u in the top fibre, the curvatures in the steel and concrete

elements must increase, with a corresponding increase in the strains. It is possible that the maximum tensile strain in the bottom fibre of the steel beam is reached before crushing of the concrete occurs. The maximum tensile strain of steel is typically taken as $20\varepsilon_y$, where ε_y is the yield strain of the steel. The point at which the maximum strain in the steel becomes the limiting criteria can be found from inspection of Fig. 2.40 as:

$$\frac{y_{nc}}{D-y_{ns}} < \frac{\varepsilon_o}{20\varepsilon_y} \quad \text{.....(2.102)}$$

where the values of y_{nc} and y_{ns} are found from the plastic analysis of the beam. Thus, when Eq. 2.102 is satisfied, the slip strain is given by:

$$\varepsilon_{slip,h} = 20\varepsilon_y \frac{y_{ns}-y_{nc}}{D-y_{ns}} \quad \text{.....(2.103)}$$

The accompanying curvature in the cross-section is given by:

$$\phi_u = \frac{20\varepsilon_y}{D-y_{ns}} \quad \text{.....(2.104)}$$

In addition to checking the maximum tensile strain in the steel bottom fibre as a limiting criterion, the maximum compressive strain in the steel top fibre could also be checked, to ensure that premature buckling does not occur. However, as this thesis is primarily concerned with compact sections, this criterion will not be incorporated.

The slip strain in the hinge is calculated by either Eq. 2.100 or Eq. 2.103, based on whether Eq. 2.102 is satisfied. Once the appropriate value of the slip strain has been determined, the slip increment developed in the plastic hinge in the shear span can now be calculated by multiplying this slip strain by half the hinge length L_p given by Eq. 2.18 on Page 39, such that:

$$s_h = \varepsilon_{slip,h} \frac{L_p}{2} \quad \text{.....(2.105)}$$

The increment in slip given by Eq. 2.105 represents the increase in slip that occurs after the cross-section has attained its maximum design strength. It is the increase in slip that is

required in order for the beam to exhibit large plastic rotation without premature fracture of the shear connectors. This is represented in Fig. 2.12b by the plastic plateau B-C of the load deflection curve. If a smaller degree of ductility is deemed necessary, then the full plastic plateau of Fig. 2.12 need not be used, and a reduced value of the plastic hinge slip s_h in Eq. 2.105 may be used.

Equation 2.105 gives the increment in slip due to plastic rotation of the member. Combining this with Eq. 2.98 which gives the end slip based on linear elastic concrete and steel properties combined with that due to cracking of the concrete and yielding of the steel, gives the total endslip due to full non-linearity of the beam. This is given as:

$$s_{end} = s_{o,cr} + s_y + s_h$$

$$= A_m K_4 - A_p K_5 + K_6\left(A_{my} - \left(h_s + h_c - \frac{I_s}{h_s A_s} K_7\right)A_{py} - M_{sy} K_7 \left(x_{ult} - x_y\right)\right) + \varepsilon_{slip,h} \frac{L_p}{2} \quad ...(2.106)$$

For the case of a uniformly distributed load with a uniform distribution of shear connectors, it is possible to rearrange Eq. 2.106 to solve for the maximum moment. In order to do this, the last term in Eq. 2.106 must first be evaluated, based on the degree of shear connection. This is done by first determining the values of y_{ns} and y_{nc} from the rigid plastic analysis, and then evaluating the term given by Eq. 2.102. Based on the result of this analysis, either Eq. 2.100 or Eq. 2.103 is used to calculate the slip in the plastic hinge s_h. The term x_y is first evaluated by Eq. 2.79 which can then be substituted into Eqs. 2.96 and 2.97 to give L_{my} and L_{py} respectively. These can then be substituted into Eqs. 2.94 and 2.95 to give A_{my} and A_{py} which are in turn substituted into Eq. 2.106. The result is then given by Eq. 2.107. This can then be substituted back into Eq. 2.79 to give a better estimate of x_y, which in turn will result in a better estimate for $M_{frac,h}$. After a small number of iterations the result will be seen to converge to a stable value for $M_{frac,h}$.

$$M_{frac,h} = \frac{S_u - s_h + \eta P_{fsc}\left(L/4 K_5 + L_{py}\left(h_s + h_c - \frac{I_s}{h_s A_s} K_7\right)K_6\right) + M_{sy}\left(L/2 - x_y\right)K_6 K_7}{L/3 K_4 + L_{my} K_6} \quad ..(2.107)$$

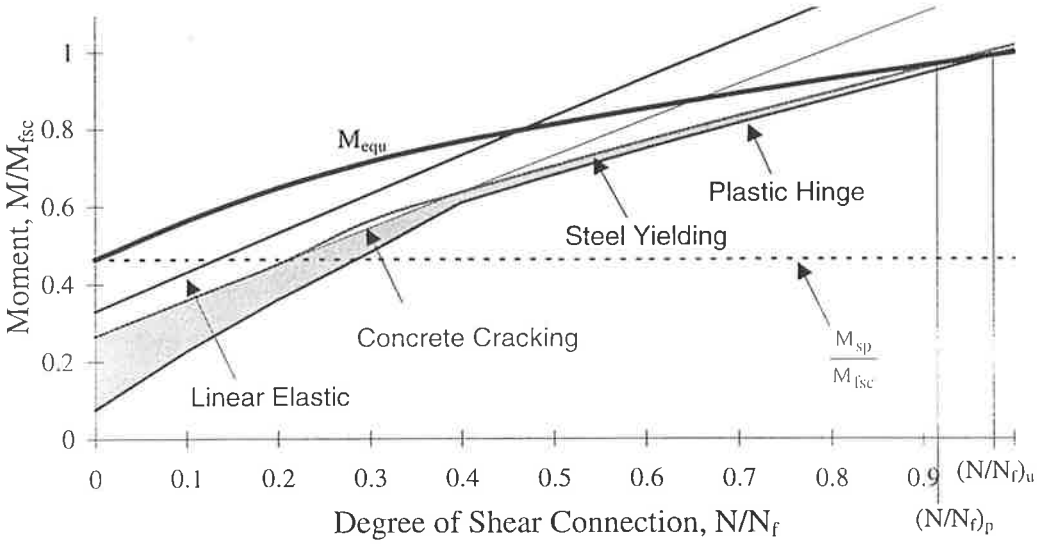
The effect of the plastic hinge on the endslip is shown in Section 2.4.4 by the use of a worked example. The results are compared to the first order analysis, and to the analysis including the effects of concrete cracking and steel yielding.

2.4.4 Worked Example

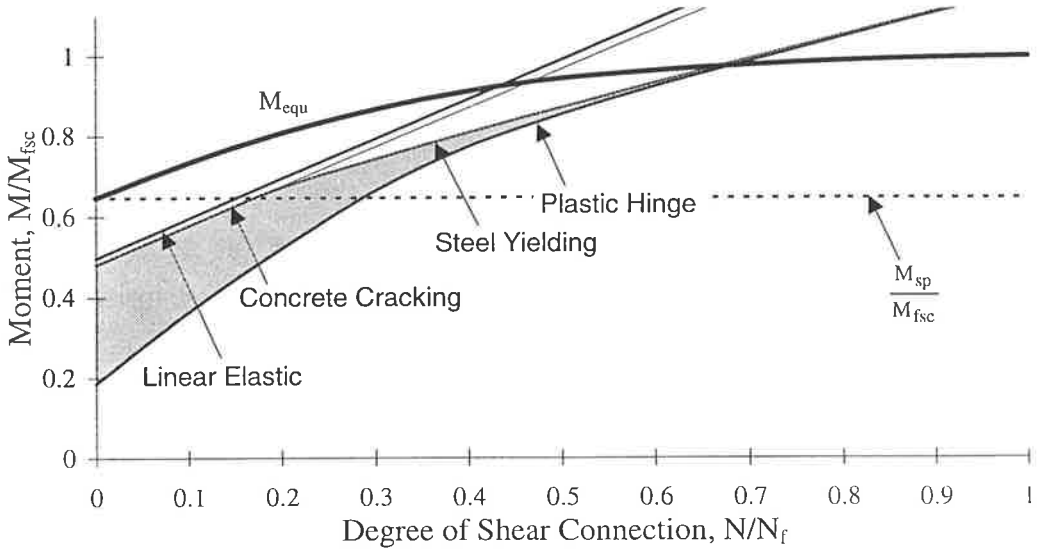
Consider the two beams that have been looked at previously, with the properties given in Table 2.2. The variation in the ultimate strength is shown by the line M_{equ} in Fig. 2.41, and the variation in the moment to cause fracture of the shear connectors is also shown. The line labelled Linear Elastic is that from Eq. 2.34 in Section 2.4.2; the line labelled Concrete Cracking is derived from either Eq. 2.55 or Eq. 2.63 in Section 2.4.3.3; the line labelled Steel Yielding is that from Eq. 2.99 in Section 2.4.3.6.4; and the line labelled Plastic Hinge is that from Eq. 2.107 in the previous section. The shaded areas represent the range in moment that can be applied such that the maximum strength of the section is reached before fracture of the connectors occurs, but maximum ductility of the sections is not achieved.

Consider Beam 1 in Fig. 2.41a as an example. It can be seen that if a degree of shear connection indicated by $(N/N_f)_p$ is adopted, then the full plastic moment of the section can be achieved before fracture of the connectors occurs. On the other hand, if maximum ductility of the member is required, then a degree of shear connection $(N/N_f)_u$ is required. It can be seen in (b) that the effect of the plastic hinge reduces rapidly with an increase in shear connection for Beam 2. This can be explained by the decrease in member ductility that occurs with the increase in shear connection as described below. Furthermore, the region of interest is above the line labelled M_{sp}/M_{fsc}, as this represents the lower bound to the strength of the composite beam. Above this line it can be seen that for the two beams analysed here that the effects of plasticity in the hinge region do not significantly alter the fracture strength.

At higher degrees of shear connection, the member is able to undergo smaller plastic deformation before crushing of the concrete occurs. Hence, there is a smaller increment in slip that accompanies the decreased level of rotation capacity. Such behaviour is typical in reinforced concrete beams, where an increase in the tension reinforcement results in an increase in the ultimate moment of the member, with an accompanying decrease in ductility. The increase in the degree of shear connection in a composite beam has an analogous effect to increasing the strength of the tension reinforcement in a reinforced concrete beam.



(a) Beam 1



(b) Beam 2

Fig. 2.41. Variation in Moment to Cause Fracture

The variation in the moment curvature response with increasing degree of shear connection is shown in Fig. 2.42 for Beam 1. Point A represents the start of the yield plateau for a beam with 25% shear connection. It is found from the plastic moment, which is determined by simple rigid-plastic analysis, and the curvature at which the ultimate moment is reached. The curvature at the commencement of yield plateau can be found from Eq. 2.87 on Page 87, by substituting the ultimate moment M_{fsc} for M, and Eq. 2.81 on Page 84 can be substituted for the yield moment M_y, which gives:

$$\phi_m = \frac{M_{fsc} - \eta P_{fsc}\left(h_s + h_c - \dfrac{(1-\beta)I_s}{A_s h_s^*}\right) - (1-\beta)M_{sy}}{\beta(EI)_s + \alpha(EI)_c} \quad \text{.....(2.108)}$$

Point B in Fig. 2.42 represents the ultimate curvature in the section that occurs when either crushing of the concrete or fracture of the bottom flange occurs. This is found from the smaller of either Eq. 2.101 or Eq. 2.104. The reduction in ductility with increasing degree of shear connection can be seen by the reduction in the plastic plateau for each of the curves. Also shown in Fig. 2.42 are the results from a non-linear computer program which was used to analyse the same beam. The computer results are indicated by the broken lines, while the results of the analyses presented here are indicated by the solid lines. A full description of the program is given in Chapter 7. The high degree of correlation can be seen between the computer simulation and the results of the simplified procedure presented here.

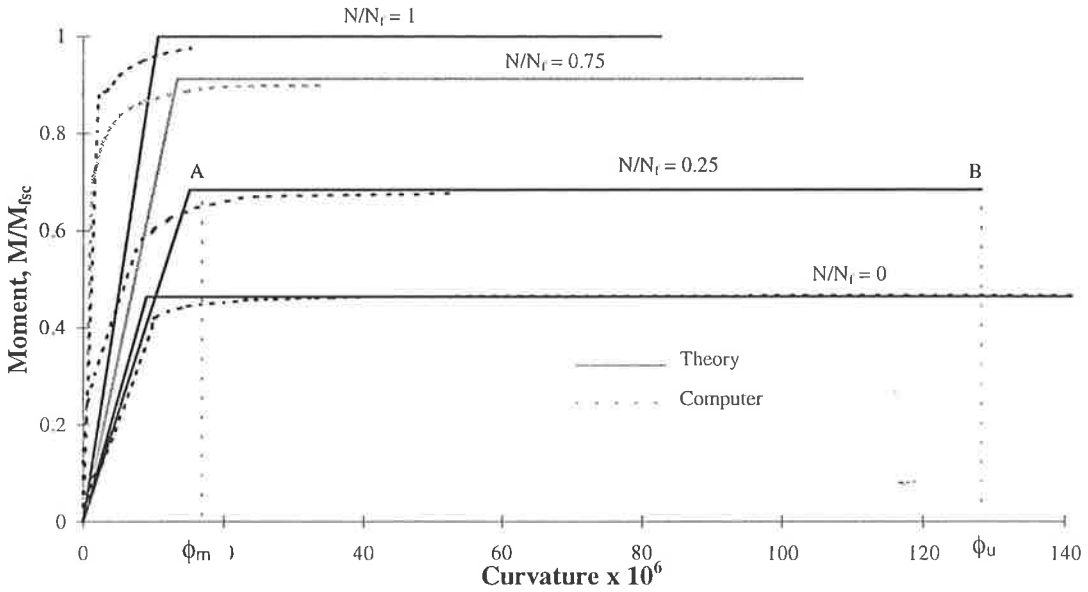


Fig. 2.42. Variation in Moment-Curvature

Figure 2.43 shows the variation in end slip with applied moment for Beam 1. The points A and B correspond to onset of yielding and the ultimate load respectively, for a beam with 25% shear connection. Point A is given by the plastic moment, which is determined by simple rigid-plastic analysis, and the slip at which the ultimate moment is reached. The slip at the commencement of plastic plateau can be found from Eq. 2.98 on Page 90, while the slip at the end of the plastic plateau is given by Eq. 2.106. It can be seen that there is decreasing demand for ductility in the shear connection with increasing shear connection.

The dashed lines indicate the output from the non-linear computer program, and show good correlation with the theoretical results for low degrees of shear connection. At higher degrees of shear connection the theoretical results tend to predict a shorter plastic plateau, with a larger slip at the commencement of the plateau than that determined from the computer program. This effect is due to the choice of the value for β, as discussed in Section 2.4.3.6.

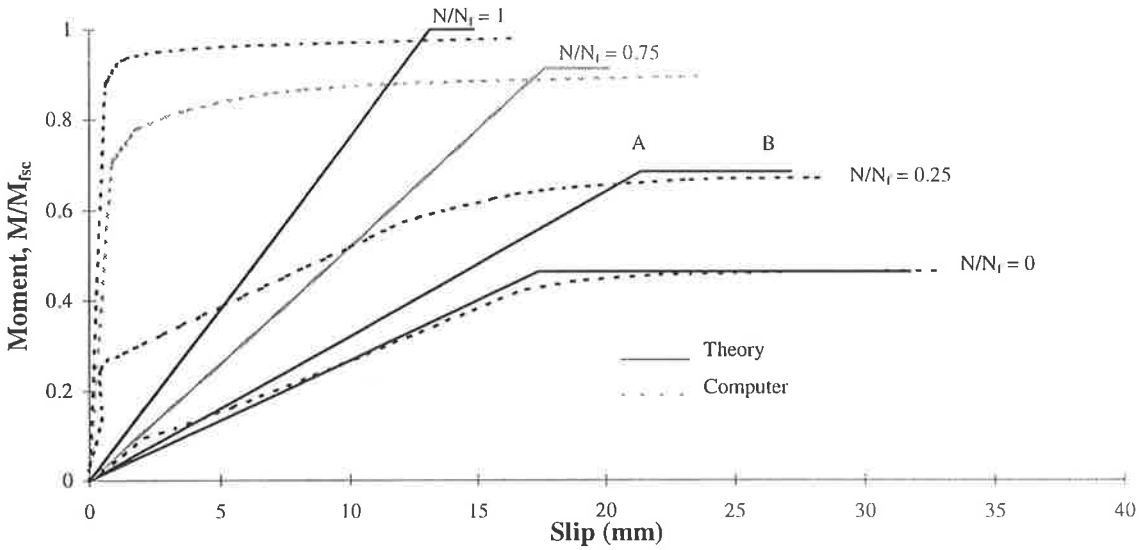
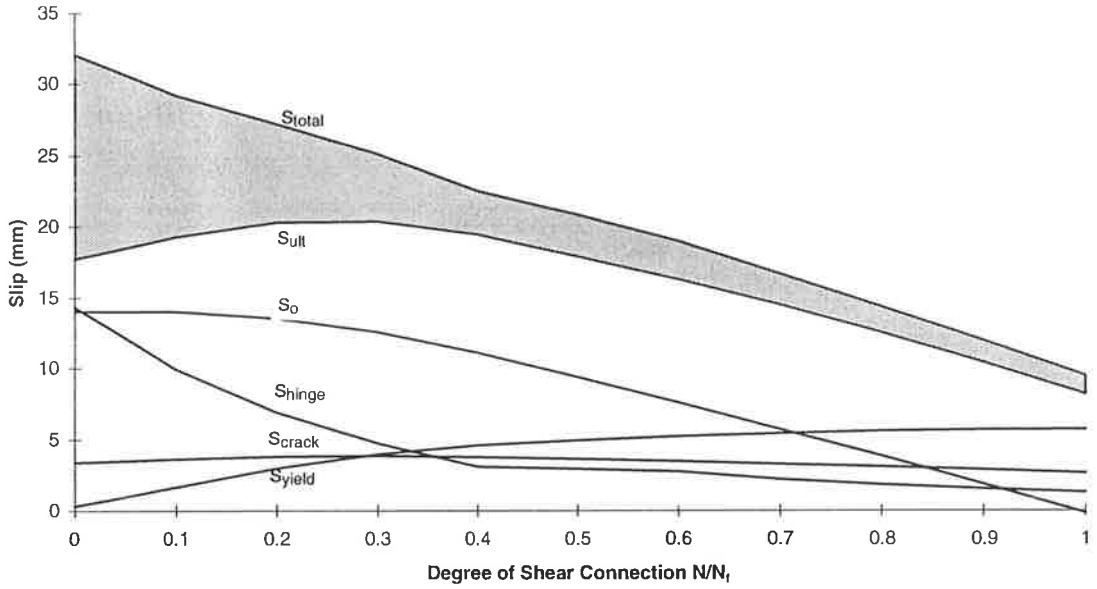


Fig. 2.43. Variation in Moment - Slip

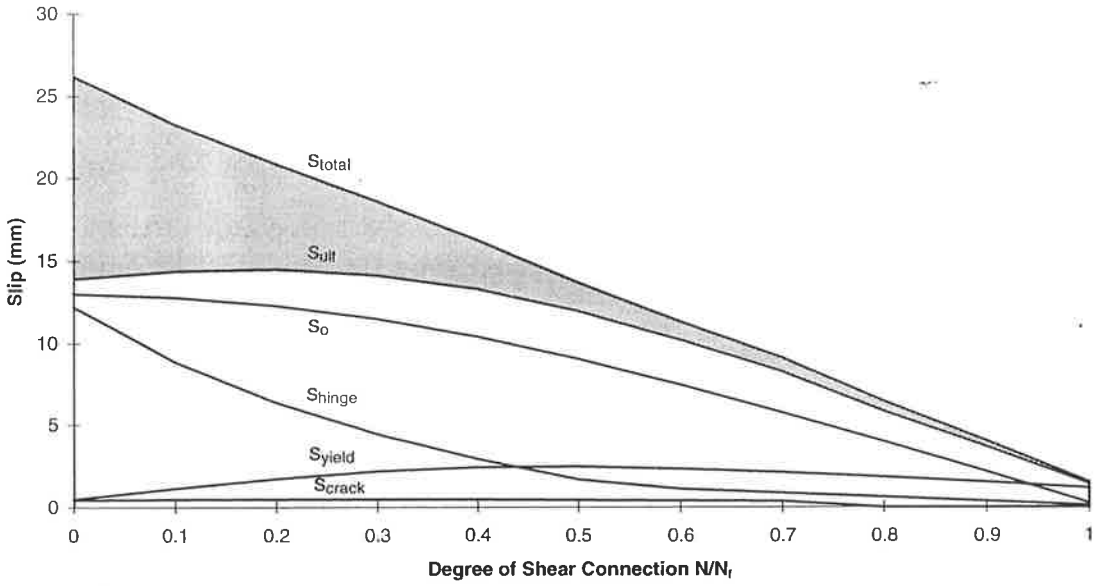
The variation in slip with increasing degree of shear connection for each of the beams is shown in Table 2.3. This table is summarised in Fig. 2.44, which indicates the variation in the different components of the slip for increasing degree of shear connection. The results for Beam 1 are shown in (a), while those for Beam 2 are shown in (b). The line labelled s_{ult} represents the slip at which the ultimate moment of the beam has just been reached, but significant plastic deformation of the member has not occurred. The line labelled s_{total} represents the total end slip, as the sum of the slip calculated with elastic steel and concrete material properties s_o, plus the increment due to cracking of the concrete s_{cr}, yielding of the steel s_y, and the increment due to plastic deformation of the member s_h. The shaded region between the two lines s_{total} and s_{ult} represents the increment in slip that is required to give the member full ductility with no increase in the applied moment.

N/N_f	Beam 1					Beam 2				
	s_o	s_{cr}	s_y	s_h	s_{tot}	s_o	s_{cr}	s_y	s_h	s_{tot}
0	14.0	3.4	0.3	14.3	32.1	13.0	0.4	0.5	12.2	26.2
0.25	13.1	3.8	3.5	5.7	26.2	11.9	0.5	2.0	5.4	19.7
0.5	9.4	3.6	4.9	2.9	20.9	9.1	0.4	2.5	1.7	13.7
0.75	4.8	3.2	5.5	2.5	16.0	4.9	0.3	2.0	0.7	8.0
1	-0.2	2.6	5.7	2.1	10.3	0.3	0.0	1.1	0.1	1.5

Table 2.3. Worked Example



(a) Beam 1



(b) Beam 2

Fig. 2.44. Variation in Slip for Worked Example

UNIVERSITY OF ADELAIDE LIBRARY

It can be seen from Fig. 2.44b that the curve shown by s_o, which is based on linear elastic concrete and steel properties, is a reasonable approximation to the slip calculated based on full non-linearity of the steel and concrete. This indicates that material non-linearity does not markedly effect the calculation of the end slip. However, it can be seen in (a) that this does not hold true for Beam 1, which shows a significant increase in the end slip when the effects of concrete cracking and steel yielding are taken into consideration.

2.5 Comparison with Test Results

A number of published test results were used to check the validity of the results of Eq. 2.107. The results of the comparisons are summarised in Table 2.4. Some points of note arise from inspection of Table 2.4 and are discussed further in this section. The theoretical slips are shown in columns 3 - 8 for each of the beams analysed, while the experimental values are given in column 9. Column 6 gives the theoretical slip required to achieve the full plastic moment, while column 8 gives the theoretical slip required to achieve full member ductility after attaining the plastic moment. The experimental values given in column 9 were those recorded at the peak of the load vs slip curve, or at the conclusion of the test if the test was stopped before any decrease in load was recorded. The connectors did not fail in any of the tests except those by McGarraugh and Baldwin (1971). Column 10 gives the percent difference between the theoretical values in column 8 and the experimental values in column 9.

Researcher	N/N_f	Slip							
		Theory						Test	% Error
		s_o	s_{cr}	s_y	$s_o + s_{cr} + s_y$	s_h	s_{tot}		
(1)	(2)	(3)	(4)	(5)	(6)	(7)	(8)	(9)	(10)
Davies (1969)	0.75	0.7	0.3	0.2	1.2	0.9	2.1	0.4	490%
Chapman & Balakrishnan (1964)	1.45	0.4	0.7	0.4	1.5	1.8	3.3	0.3	998%
Robinson (1969)	0.30	2.2	2.1	0.6	4.9	3.2	8.1	9.8	-17%
Hawkins & Roderick, A1 (1976)	0.66	1.4	0.7	0.9	3.0	1.5	4.4	4.2	5%
McGarraugh and Baldwin, B2 (1971)	0.38	2.9	0.0	1.5	4.4	1.6	6.1	2.5	142%
McGarraugh and Baldwin, B4 (1971)	0.72	1.2	0.0	1.7	2.9	1.3	4.2	4.1	2%

Table 2.4. Comparison with Published Results

The test by Davies (1969) was on a half scale model, with a stud diameter of d_{sh} = 9.5 mm. Load slip characteristics for the studs were quoted with the maximum load occurring at slips of $200x10^{-4}$ in, which is 0.51 mm, or approximately $0.05d_{sh}$. The strength of the concrete was determined to be 51 N/mm^2. These results are much stiffer than results from other push tests, as discussed in Section 2.2.3, which describe the slip at maximum load in terms of the concrete strength. From Eq. 2.6 the slip at the maximum load of the connectors is $0.28d_{sh}$, which is a factor of more than 5 times less stiff than those results of Davies. This large discrepancy in the behaviour of the shear connectors may be the reason for the large overestimation in the slip.

As shown in Table 2.4, the test by Chapman and Balakrishnan (1964) was on a beam with nearly 50% more shear connectors than required for full shear connection. Furthermore, it was stated that bond at the interface between the concrete and the steel flange was not prevented by greasing. Thus, there would likely have been additional transfer of shear force due to frictional forces between the steel flange and the concrete. This is evidenced from the load-slip curves of the tests, which indicated that slip did not occur until 80% of the ultimate load had been reached. Furthermore, the theory predicts the end slip based on the assumption that the shear connectors are fully yielded, which will not be the case when there are more shear connectors than required for full shear connection. Thus, the theoretical values greatly exceed those reported from the tests.

The results of Robinson (1969) compare well with the theoretical values. The slight increase in the experimental results may be due to the large constant moment region that was created by the two point loading arrangement; 3.35 m out of a 6.4 m span. The load-deflection and the load -slip curves that were reported indicated a significant plastic plateau, which would have been influenced by the large length of the constant moment region. Despite this, the agreement between the theory and the measured values is acceptable.

The results from Hawkins and Roderick (1976) compare well with the theoretical values. The theory slightly overestimates the endslip, but the difference is negligible.

The comparison between two beams tested by McGarraugh and Baldwin (1971) indicates close agreement for beam B4, while beam B2 shows a significant overestimation of the endslip. The slip distribution throughout the length of the members were reported, and

indicated a large reduction in the slip at the end of the shear span for beam B2, whilst beam B4 indicated only a minor reduction. The maximum slip for beam B2 occurred at approximately midway along the shear span. The maximum recorded slip for this beam was 4.3 mm, which is only 30% less than the predicted slip. This difference is more acceptable than the 142% difference based on a comparison of the end slips. The reason for the reduction in slip toward the end of the shear span in only one of the beams is not clear, but may be due to large shrinkage strains that develop in the concrete during curing (Aribert, 1987). This effect is more pronounced for lightweight concrete, which was used for the beams tested by McGarraugh and Baldwin.

2.6 Conclusions

This chapter has presented a two tier analysis procedure to determine the total endslip in a composite beam with partial shear connection. The first tier assumes linear concrete and steel material properties and yielded shear connectors, whilst the second tier allows for full non-linear behaviour of the steel, concrete and shear connectors. The first tier may be used as a simple procedure to give an approximate understanding of the controlling parameters that contribute to endslip. However, as this procedure always underestimates the endslip, it is unconservative, and thus should be used with caution. The second tier analysis incorporates separate effects to account for non-linearity in the concrete and the steel, as well as a term which includes the slip increment due to plastic deformation of the member.

Overall, Table 2.4 indicates reasonable agreement between the theoretically predicted maximum slips and those measured from experimental testing. It appears that the theory does not adequately predict end slips for beams with greater than full shear connection. However, as such beams are unlikely to fail by premature fracture of the shear connectors, this result does not effect the validity of the theory presented. Furthermore, when the maximum slip does not occur at the end of the shear span, the theory still shows adequate correlation to the maximum slips within the shear span.

The theory presented here draws a distinction between the slip capacity of the shear connectors that is required to reach the ultimate moment of the member, and that which is required to ensure full plastic deformation of the member. It is possible to distinguish between the two different limit states of sufficient strength, and sufficient ductility.

Chapter 3

Push Tests

3.1 Introduction

This chapter deals with push tests, and their use in the understanding of the interfacial bond stresses that develop between concrete and an embedded or adjacent steel element. Specifically, this chapter will deal with those push tests which are used to determine the bond stresses between concrete and profiled steel sheeting which encases one or more of the external surfaces of the concrete.

The literature review will discuss and compare the various test procedures used by other researchers to determine the bond characteristics. Then the test procedure that was developed for this research project will be discussed. The results of a testing program will be presented, followed by a discussion of the results. Finally, the conclusion will discuss the implications of the findings.

3.2 Literature Review

3.2.1 Introduction

The use of profiled steel sheeting in the construction of composite slabs has become increasingly popular for high rise construction. The steel sheeting is used as formwork during the construction phase, and then as positive moment reinforcement once the concrete has set. At the current time, the strength of composite slabs is assessed through full scale testing, in which basic parameters are varied in the tests, such as span/depth ratio, thickness of the sheeting, and shear span (ASCE, 1992; British, 1982; European, 1990). This empirical approach is known as the 'shear-bond method' and will be discussed briefly in Section 3.2.1.1. This approach has many drawbacks, including the difficulty in developing new forms of profiled sheeting, due to the large number of full scale tests that would be required. Also, it has long been realised that a more fundamental understanding of the behaviour of composite slabs is required.

The following sections in this chapter will discuss the various methods that have been proposed to determine the behaviour of profiled sheeting in composite slabs. These tests represent alternative procedures to full scale testing, and were developed in order to better understand the fundamental behaviour of the profiled sheeting. However, as will be discussed, some of the testing procedures that have been proposed do not adequately represent the condition of the profiled sheeting in the composite slab. This important fact must be considered fully if the results of the tests are to be used with confidence in lieu of full scale tests. Thus, each of the alternative testing procedures that have be adopted by other researchers will be presented and discussed in turn. Finally, a new testing procedure will be proposed in Section 3.3.

There are several terms which are used in the discussion of push test results and different researchers have applied similar terms to describe different phenomenon. In order to avoid confusion with the different terms, the following definitions will apply throughout the remainder of this chapter.

Chemical Bond

Bond resulting from chemical adherence of the cement paste to the steel sheeting. Such bond results in a resistance to applied shear with no slip at the interface. Once this bond is broken, ie. slip is initiated, it reduces to zero and does not reform.

Frictional Bond

Bond resulting directly from the application of active normal forces, which act perpendicular to the steel-concrete interface. This bond resistance is directly proportional to the normal force, so that if the normal force is zero then the frictional force is zero.

Mechanical Bond

Bond resulting from the physical interlocking of the concrete and the steel sheeting. These forces are developed by passive normal forces that arise in response to a mechanism that causes separation. This bond essentially is the resistance to shearing forces that remains in the absence of any chemical bonding, or any applied normal force. It arises from the interference between the sheeting and the concrete at both the small scale of minute surface irregularities, as well as at the large scale of embossments in the profiled sheeting.

3.2.1.1 Shear Bond Method

The Shear Bond Method has been widely adopted to determine the strength of profiled sheeting in composite slabs. (ASCE, 1992; British, 1982; European, 1990). The procedure involves performing a number of full scale slab tests in order to determine a relationship between the applied shear and the geometry of the slab. A regression line is determined from the results of the tests, and the strength for any slab geometry with any sheeting thickness is then determined from the regression line. The equation for the strength of the slab is:

$$\frac{V_e}{b_s d_e \sqrt{f_c'}} = m\frac{\rho d}{L \sqrt{f_c'}} + k \qquad (3.1)$$

where

V_e = Maximum experimental vertical shear at failure

b_s = width of slab

d_e = Effective slab depth, distance from extreme concrete compression fibre to centroidal axis of the full cross section of steel deck.

f_c = Compressive strength of concrete

ρ = Reinforcement ratio of steel deck area to effective concrete area = A_S/bd.

L' = Length of shear span, for a uniform load, L' = L/4.

L = Length of the slab

m = Reduced slope of regression line, as shown in Fig. 3.1

k = Reduced intercept of regression line, as shown in Fig. 3.1

Equation 3.1 determines the shear strength of a composite slab in terms of the dimensions of the slab, the reinforcement ratio and the parameters m and k. The terms m and k are derived from the slope and intercept of the linear regression of the experimental results. The results from the full scale tests are plotted in the form of $V_e/\left(bd\sqrt{f_c}\right)$ against $\rho d/\left(L'\sqrt{f_c}\right)$ as shown in Fig. 3.1, and a linear regression performed on the data. The slope m_1 and the intercept k_1 of the regression line are reduced to ensure that the line approaches a lower bound for the experimental values, as shown by the dashed line. The magnitude of the reduction is either 15% or 10%, depending on the number of tests used to determine m_1 and k_1.

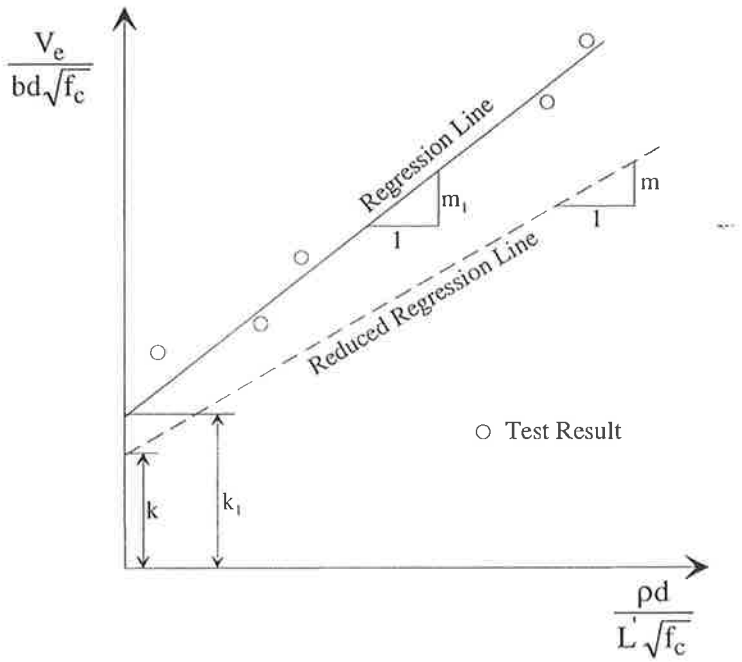


Fig. 3.1. Shear Bond Regression

The above procedure must be performed for each new sheeting geometry, with as many as 54 full scale slab tests required for each new profile, covering the full range of the design parameters such as span, shear span, sheeting gauge thickness, overall slab depth and concrete compressive strength. The values of m and k determined from Fig. 3.1 are then determined for each new sheeting geometry.

There are numerous drawbacks with the shear bond approach to determining the strength of profiled sheeting in composite slabs. Firstly, the effect of other variables such as sheeting thickness or loading arrangement are only treated implicitly in the above procedure. As such, the results can exhibit considerable scatter when expressed as shown in Fig. 3.1 (Patrick, 1990). Also, the procedure is not based on an understanding of the fundamental behaviour of the composite system, and as such does not allow designers to correctly recognise the influence of different variables.

The method of deriving Eq. 3.1 by use of linear regression on different sets of parameters provides only limited insight into the behaviour of composite slabs. What is required is a more fundamental approach based on the properties of the shear connection and the geometry of the slab. In order for this to be possible, the shear connection behaviour of the profiled sheeting must first be quantified. Different methods to determine this behaviour have been proposed by several researchers. These will be each be discussed in turn in the following sections.

3.2.1.2 Porter

Porter (1968) and Porter and Ekberg (1978) were the first researchers to carry out push tests on profiled sheeting. Their test setup is shown in Fig. 3.2. The specimens were produced by casting two blocks of concrete between two sheets as shown. The tests were carried out by placing a hydraulic jack between the concrete blocks and then forcing the blocks apart.

Results from the tests showed that the bond stress varied as a function of the embedment length L', as shown in Fig. 3.3 (Porter and Ekberg, 1978). This figure shows the variation in the bond stress with the length L' of the specimen. The bond-stress u, was based on the total bond area, that is the surface area of the sheeting in contact with the concrete. In

contrast, the relationship u' was based on an effective bond area of the embossed plate elements, however, it was not stated how the effective bonding area was determined. It can be seen that the effective bond stress is approximately 4 times larger than the average bond stress, thus indicating that only ¼ of the total bonding area was used to calculate the effective bond stress.

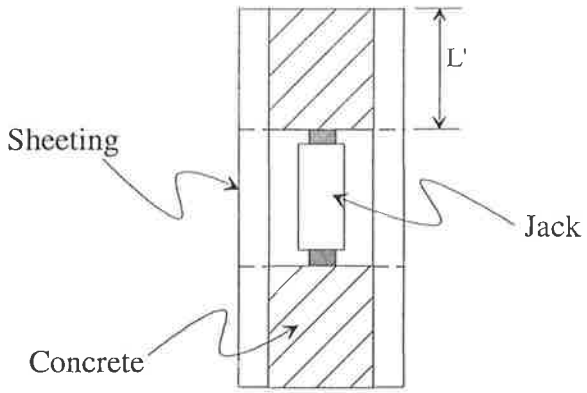


Fig. 3.2. Porter and Ekberg Test Setup

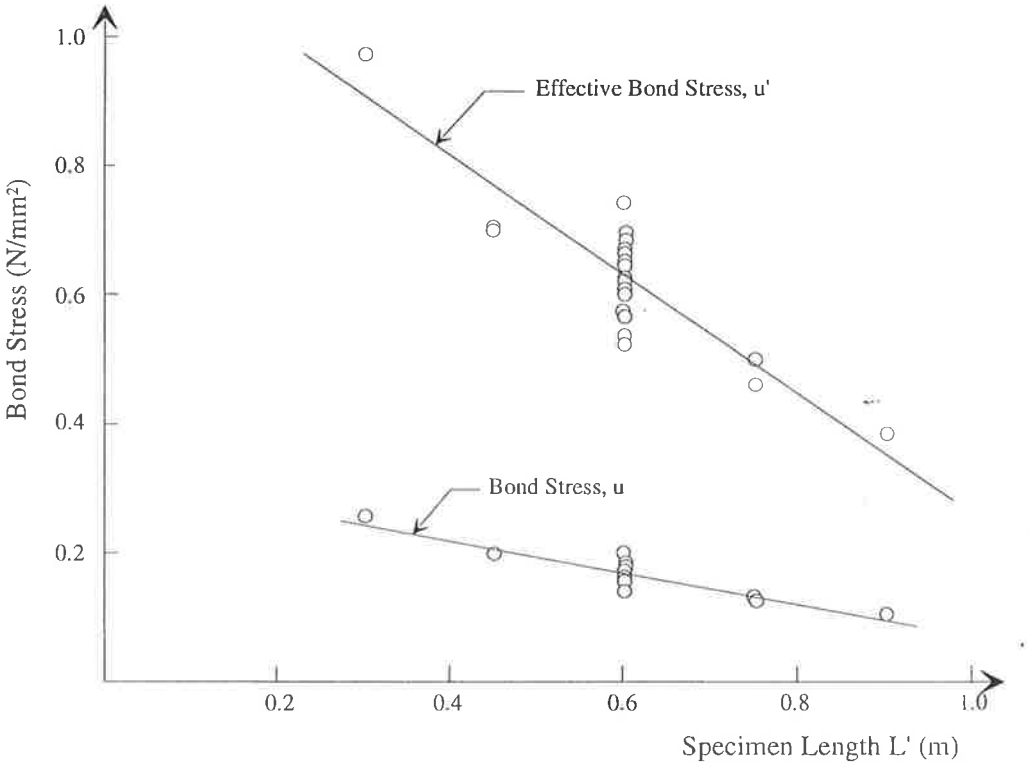


Fig. 3.3. Bond Stress vs Embedment Length

The graphs in Fig. 3.3 show an apparent increase in the bond strength with shorter specimens. This result contradicts that found by Daniels (1988) who determined that there

was no appreciable change in the bond stress with an increase in the specimen length. The reason for the variation in bond stress shown in Fig. 3.3 is not clear, but may have been due to the assumption of uniform stress distribution over interface. The complete bond stress vs slip curves were not reported in the published data, and it was not specified if the bond stress referred to in Fig. 3.3 represented the bond stress at the failure of the chemical bond, or occurred after the initiation of interface slip. This distinction may account for the apparent variation in the bond stress with specimen length. This is due to the fact that the distribution of stresses at the concrete - steel interface is non-uniform when the chemical bond is unbroken (Daniels, 1988; ACI 408, 1966), with the peak stresses occurring near the loaded edge. Failure of the chemical bond occurs when the peak stress reaches the chemical bond strength. Thus, assuming a uniform stress distribution will result in an apparent increase in the average bond stress for shorter specimens.

It was concluded by Porter and Ekberg that the results from the testing did not offer a practical solution to the determination of the bond strength for all deck types. This was attributed to difficulty in correlating the results of the push tests to the bond strength in composite slabs. Consequently this approach was abandoned and full scale testing was adopted as the preferred method to evaluate composite slabs.

3.2.1.3 Daniels

Daniels also developed a push test to define the properties of profiled sheeting (Daniels, 1988). The test arrangement is shown schematically in Fig. 3.4. The specimen is formed by cutting two sections from the sheeting which are one rib spacing in width. These sheets are bolted to either side of a steel attachment plate, and then concrete blocks are poured against the sheeting. The width of the block varies with the sheeting geometry in order to maintain 80 mm of concrete cover over the ribs.

A lateral force F was applied to the concrete blocks before the longitudinal force P was applied to the sheeting. The lateral restraint was applied in either displacement control or force control. In the case of displacement control, the lateral restraint was applied by tightening a clamp around the specimen to a known initial load. When the lateral restraint was applied in force control, springs were used which kept a constant applied force during the test. After the application of the lateral forces, a tensile force P was applied to the sheeting in

the direction of the rib with the resulting compressive force applied to the concrete block as shown in Fig. 3.4. The resulting force-displacement behaviour was then determined. Typical results that were recorded are shown in Fig. 3.5a for a ductile response and Fig. 3.5b for a brittle response. The ductile response was typical of a profiled sheeting with embossments, while the non-ductile response was typical of a profiled sheeting without embossments.

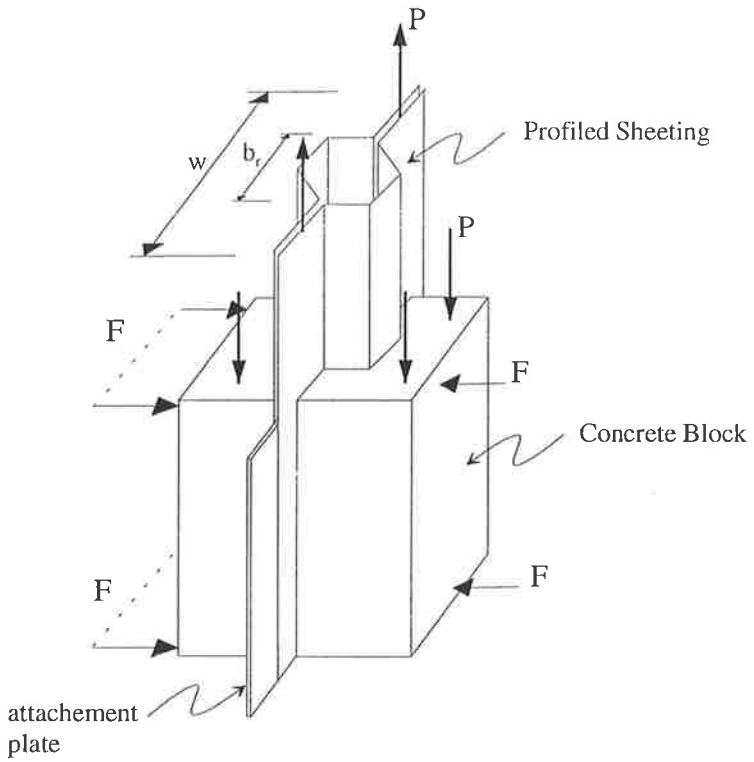
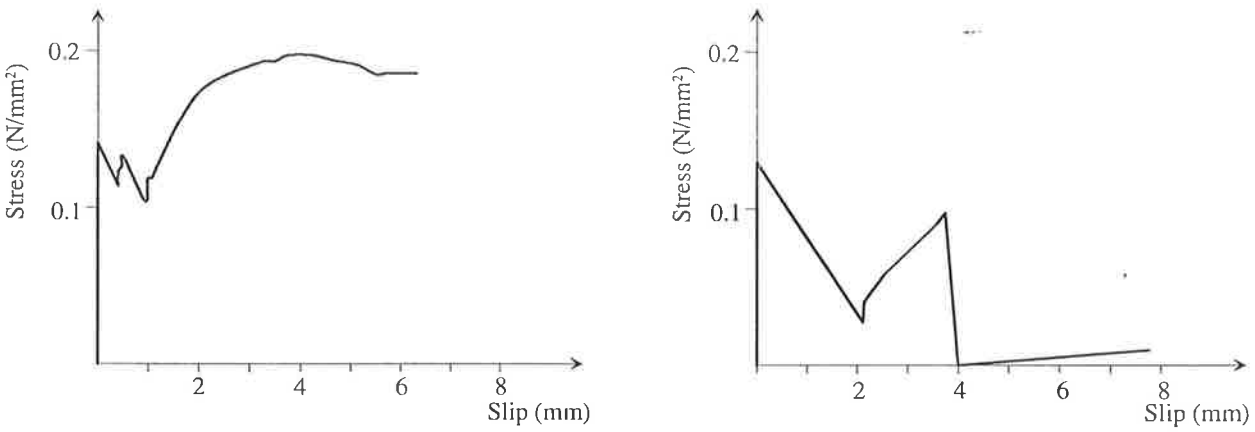


Fig. 3.4. Daniels Test Setup



(a) Ductile Response **(b) Brittle Response**

Fig. 3.5. Typical Shear-Slip Relationships for Daniels

The calculation of the shear stress was determined from the applied load P by dividing by the total surface area of the sheeting in contact with the concrete. The advantage of this approach is that comparisons between sheeting types can be made more easily. However, a disadvantage with this approach is that no account is taken of the different mechanisms that transfer shear and the different areas over which they act. Chemical bond stress is distributed over the entire surface area, whereas mechanical bond stress is concentrated at the locations of the embossments. Using a single area does not take account of this fact, and results in a smaller value of mechanical bond stress. Furthermore, the results will be effected by the overall width w of the test specimen, as shown in Fig. 3.4, and not on the width of the rib b_r. Thus the shape of the test specimen will effect the results without any change to the shape of the profile.

A comparison between the maximum shear stresses shown in Fig. 3.5 and bond stresses derived by Porter in Fig. 3.3 indicates that similar order of magnitudes were obtained. A more thorough comparison is not possible as the exact geometry of the profiled sheeting was not reported by Porter.

The application of the external lateral loads, indicated by F in Fig. 3.4, has important implications in determining the ideal form of the push test. As other researchers have also adopted procedures in which lateral restraining forces are applied to the sheeting, this matter will be discussed at length in Section 3.2.2, after presenting other testing procedures. Briefly, the main considerations deal with whether the application of the lateral load resembles the actual behaviour in a composite slab, and in what way the external force affects the results from the test.

Daniels carried out a number of tests with different values of applied lateral loads, and found that there was no relationship between the magnitude of the lateral loads and the horizontal load at which the chemical bond failed. However, there was a slight increase in the horizontal loads after failure of the chemical bond as the lateral load was increased. The increase in the horizontal resistance of the sheeting with increasing lateral loads is due to the increase in both the frictional resistance component, and the increased mechanical resistance as described in Section 3.2.2. Consequently the results will be influenced by the application of the lateral loads, and will tend to give overestimates of the shear resistance of the profiled sheeting.

3.2.1.4 Patrick

Patrick proposed a push test termed the 'Slip Block Test' (Patrick, 1990; 1994; Patrick and Poh, 1990). The arrangement used is shown in Fig. 3.6. A segment of the sheeting to be tested is cut out and then fastened to a stiff base plate by spot welding through the sheeting, and then concrete is cast on top of the sheeting. A vertical load F, is applied to the block and held constant, while a horizontal force P is applied the block in the direction of the rib. The vertical force is applied in load control, while the horizontal force is applied in displacement control.

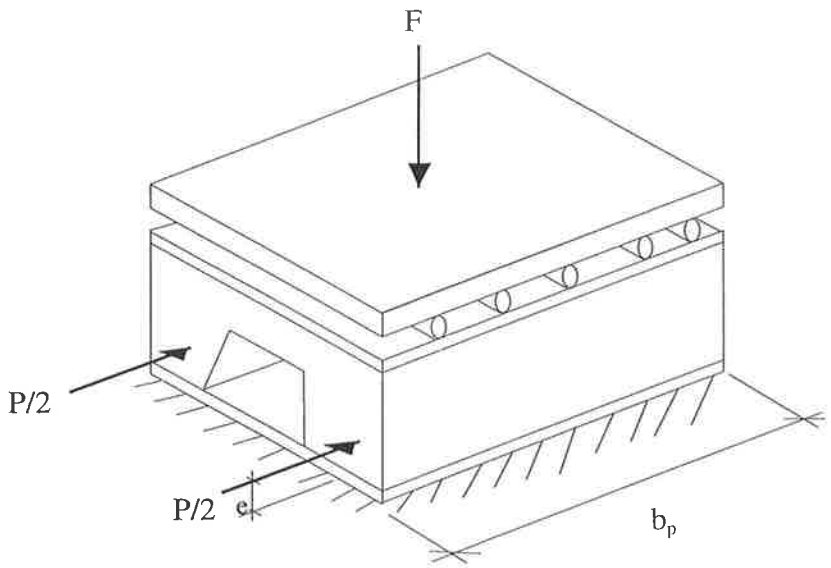
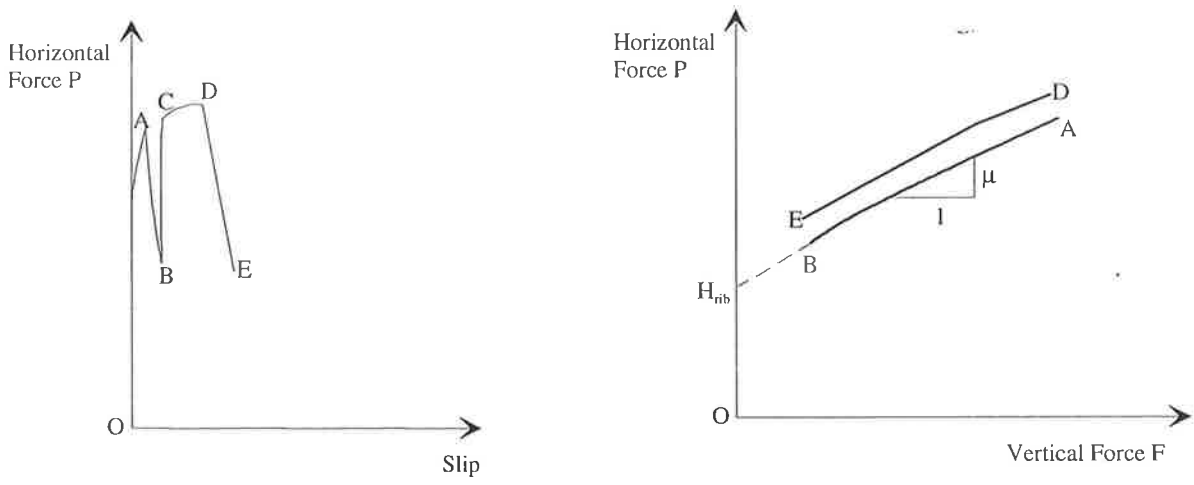


Fig. 3.6. Patrick Test Arrangement



(a) P - Slip Curve **(b) P - F Curve**

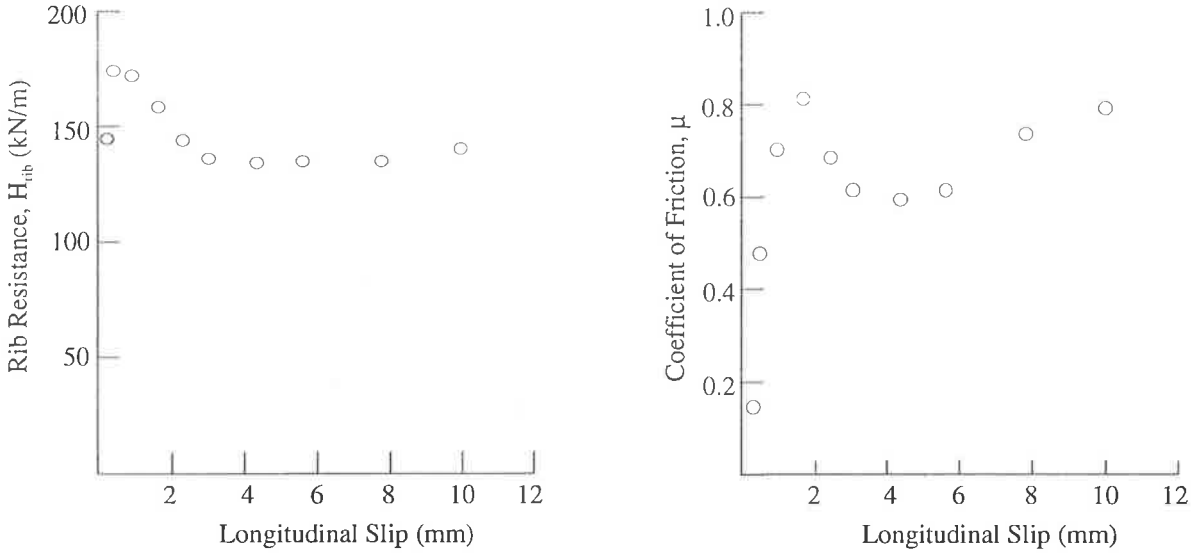
Fig. 3.7. Push Test Results

While the vertical force is held constant, the horizontal force is gradually increased until slip is first recorded. This is indicated in Fig. 3.7a by the curve O-A, where point A represents the point at which the application of the horizontal force is held constant. Then the vertical load is reduced, which causes the block to slip with a resulting reduction in the horizontal force (the horizontal force is in position control). The relationship between the slip and the horizontal force is shown in (a) by the line A-B, and the variation in the horizontal force with decreasing vertical force is shown in (b) by the line A-B. As the vertical load is reduced, eventually a point will be reached at which the block begins to tip over. This is due to the eccentricity, e in Fig. 3.6, between the applied load and the reaction at the base plate. Once this point has been reached, Point B in Fig. 3.7, the vertical load is increased to its original value, Point C in (a), which halts movement of the block. The horizontal force is increased so as to induce further slip in the specimen, as shown by Point D. This cycle is repeated at different values of slip.

In order to determine the bond strength of the sheeting with no vertical clamping force, the line A-B shown in Fig. 3.7b is extrapolated back to the vertical axis at the point labelled H_{rib}. The intercept with the vertical axis gives the value of the resistance due to mechanical interlock alone. The slope of the resulting line gives the coefficient of friction μ, between the concrete and the sheeting. Each of the lines plotted in Fig. 3.7b, such as A-B, are determined at different values of slip, as given by the average of the slips at points A and B in (a). The slope and the intercept of the curves in (b) were determined for different values of slip and then plotted as shown in Fig. 3.8. The resistance of the sheeting to horizontal shear was then summarised by the formula given by Eq. 3.2.

It is possible to convert the values of rib resistance given in Fig. 3.8a into shear stress, so as to compare with the results of Daniels and Porter. The value of b used in the tests was 300 mm, while the width of the specimen was 200 mm. The resulting maximum mechanical shear stress from Fig. 3.8a is calculated as 0.85 N/mm^2. Other tests were reported (Patrick, 1990) which had a resulting maximum mechanical shear stress of 0.25 N/mm^2. This compares favourably with the values obtained by Daniels and Porter. Close comparison is not possible as identical sheeting profiles were not tested, however general comparisons between the overall shapes of the mechanical bond stress vs slip curves can be made. The increase in bond stress with increasing slip in Fig. 3.8a was also noted by Daniels for embossed sheeting, as shown in Fig. 3.5. This increase is due to the embossments bearing

against the concrete, and eventually pushing the sheeting away from the concrete. This behaviour is discussed further in Section 3.2.2.



(a) Mechanical Bond Stress **(b) Coefficient of Friction**

Fig. 3.8. Test Results for Patrick (1990)

$$H_r = b_p H_{rib} + \mu F \quad \text{.....(3.2)}$$

where

b_p = Length of the block,

H_{rib} = Shear flow resistance per rib due to mechanical interlock,

F = Vertical applied load,

μ = Coefficient of friction.

This test setup is essentially similar to that proposed by Daniels, with the simplification of only using one side of sheeting with a single concrete block. As such, it suffers from the same drawbacks which are: the sheeting is trapped by the base plate and restricts the free deformation of the profile away from the concrete; and the application of the external lateral loads results in varying pressure between the sheeting and the concrete. These effects are discussed fully in Section 3.2.2

An important distinction between the two testing procedures is that Patrick estimates the shear resistance with zero applied lateral load, whereas Daniels determines the shear

resistance with a non-zero applied lateral load. Inasmuch as Patrick attempts to account for the effects of the lateral load, his procedure represents an improvement over that of Daniels. However, as the mechanical bond strength is estimated from the results with a vertical load by extrapolating back to the vertical axis. This extrapolation process can result in inaccuracies due to the uncertain behaviour of the specimen at low applied vertical loads. This is indicated in Fig. 3.9 which shows the results of a test on Bondek II profile with light weight concrete (Patrick, 1991). It can be seen that there is considerable non-linearity in the results, and that as the vertical load decreases, there is a considerable decrease in the horizontal resistance. By ignoring this trend and taking an average through the recorded data points, results in an overestimation of the mechanical bond strength.

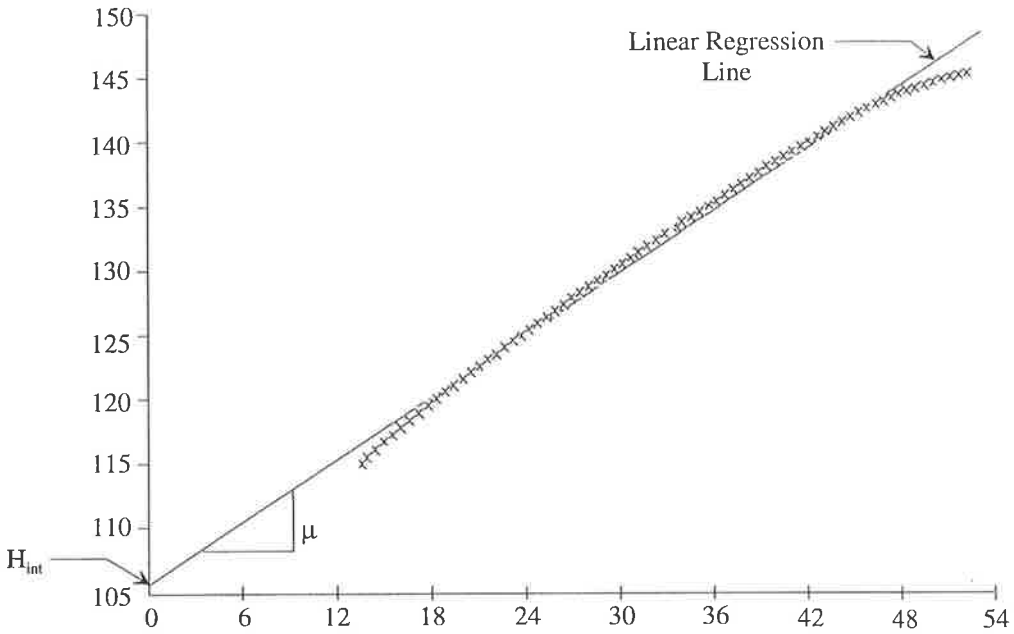


Fig. 3.9. Test Results for Patrick (1991)

3.2.1.5 Stark

Stark initially performed full-scale slab tests to determine the shear connection performance of an embossed trapezoidal sheeting (Stark, 1978). Confirmatory push-out tests were performed to check the results with simple plastic theory. The specimens consisted of concrete sandwiched between pieces of sheeting which were externally clamped against the concrete, as shown in Fig. 3.10. Any effect of the unknown clamping force was neglected in the calculation. It was stated that the results were in reasonable agreement with the plastic theory for the bond behaviour, although the load-slip characteristics were not reported.

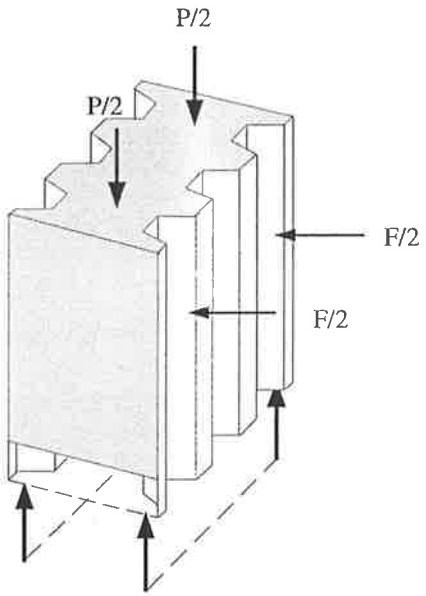


Fig. 3.10. Test Setup for Stark

The application of the external lateral loads would have altered the performance of the profiled sheeting in the push tests, as discussed in Section 3.2.2. Furthermore, the magnitude of the lateral loads remained unknown throughout the test. This is in contrast to the testing procedure of Daniels in Section 3.2.1.3 and Patrick in Section 3.2.1.4, in which the lateral loads were carefully monitored. As was shown by both Daniels and Patrick, the application of the lateral loads affects the results of the push tests, and thus must be carefully considered in the design of push tests, and also in the interpretation of the results. Neither of these steps were taken by Stark, thus making the procedure unreliable in the determination of the shear connection performance of profiled sheeting.

3.2.1.6 Airumyan et al.

Airumyan et al. used the push test shown schematically in Fig. 3.11 to investigate the effect of various embossment geometries on the bond behaviour (Airumyan et al., 1990). The sheeting was anchored at one end, and then a load P applied to the concrete block to cause it to slip relative to the steel. The load-slip curves were only reported up to a maximum of 0.3 mm.

It can be seen from Fig. 3.11 that there was no mechanism to keep the sheeting in contact with the concrete. Thus, as soon as the chemical bond was broken there would be a tendency for the sheeting to pull away from the concrete, and thus reduce the load P to zero.

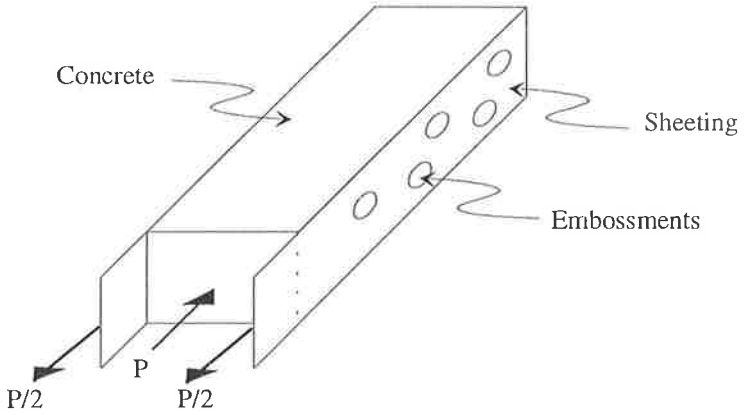


Fig. 3.11. Test Setup for Airumyan

In practice, profiled sheeting has ribs which help maintain contact between the sheeting and the concrete. Adopting a test specimen in which the sheeting does not contain any ribs, or any other mechanism to maintain interaction, will mean the results will not resemble the true shear connection behaviour of profiled sheeting in a composite slab. Furthermore, the aim of these tests was not to determine bond-slip relationships for the various embossments, but rather to qualitatively assess their effects, they thus do not merit further discussion.

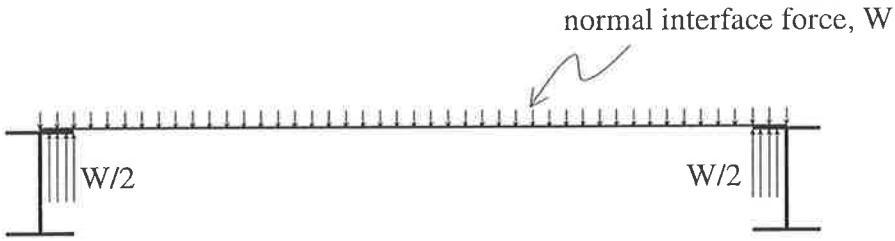
3.2.2 Lateral Restraining Force

The effect of the laterally applied load such F in Fig. 3.4 and Fig. 3.6, will influence the shear connection behaviour in several ways. Before this interaction is discussed, it is worth looking at whether these loads accurately model the behaviour of the sheeting in a composite slab, and thus whether they are justified in such a test.

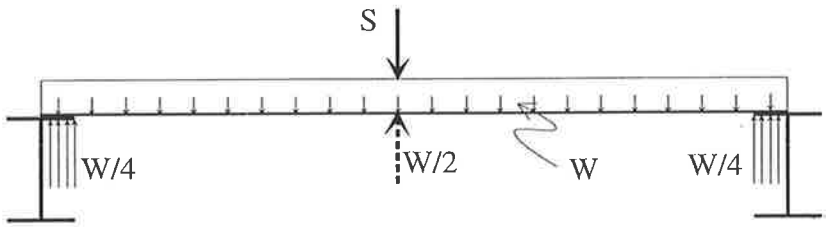
Daniels explained the application of the lateral force by saying that in a composite slab there is a normal force acting between the profile sheeting and the concrete that is equal to the weight of the concrete slab. It is granted that when the slab is poured, the complete weight of the slab is taken by the profile sheeting provided there is no shoring. This is shown in Fig. 3.12a which indicates the lateral forces acting on the sheeting. Assuming that the weight of the concrete slab is carried directly by the profile, then this load must be transferred by the profile through to the supports.

In the situation where the slab is shored during pouring, a significant portion of the dead load is taken by the shoring. When the shoring is removed, the composite slab as a

whole is then subjected to an equivalent point load S equal to the reaction previously taken by the shoring, as shown in Fig. 3.12b. Now, to assume that there is a constant normal force at the interface equal to the full weight of the slab implies that the profile sheeting continues to support the full weight of the concrete, even when the shoring is removed. This cannot be the case, as the profile sheeting only has a limited transverse shear capacity. As the span of the slab increases, the maximum possible normal pressure that the concrete slab can exert on the profile must decrease, as the flexural and shear capacity of the profile is constant. Hence, for long spans the net resultant normal force over the whole length of the member will be very small, but will be concentrated at the supports, as shown in Fig. 3.12b. Another consideration is that even when the concrete is fully cracked it still has significant transverse shear capacity. Thus the weight of the slab will continue to be supported by both the concrete slab and the profile.



(a) No Shoring

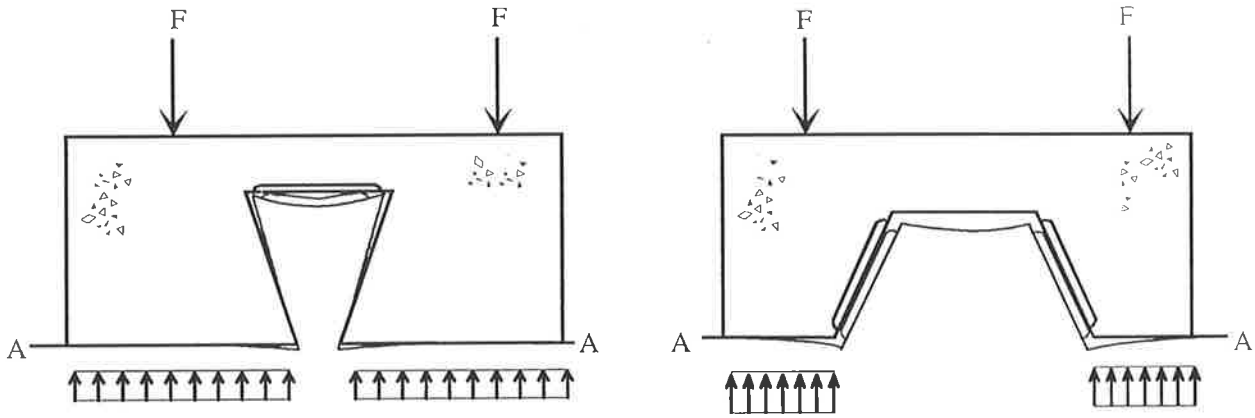


(b) With Shoring

Fig. 3.12. Lateral Force Distribution

A further consideration is that the longitudinal shear forces in the dove-tail section, as shown in Fig. 3.13a, are resisted by the concrete riding over the protrusions and indentations. The surfaces can only slide relative to each other by the profile moving down relative to the concrete. This movement is resisted by the spring action of the dove-tail rib of the profile as the spring is confined within the dove-tail void. This resistance to the movement induces normal forces at the interface that can be described as passive forces as they do not rely directly on externally applied loads. The same relative action in the trapezoidal rib in

Fig. 3.13b will tend to cause separation as the shape of the void does not confine the rib, although some passive forces may be induced by the shape of the embossments.



(a) Dove-Tail (b) Trapaziodal

Fig. 3.13. Profile Deformations

Patrick (1990, 1994) argues that at the supports a direct normal force equal to the reaction restrains the sheeting against the concrete. This is correct, however, as the region at the end supports is very small, application of a uniform lateral force in a push test does not represent the behaviour of composite slabs in propped construction because the interface force is concentrated at the support. Furthermore, not all the weight of the slab is transferred through the profile to the supports as the profiled sheet usually only covers a small portion of the support (most codes of practice recommend minimum requirements as little as 50 mm, ASCE, 1992; British, 1982; European, 1990). Thus, for the in-span regions, the longitudinal shear can only be transferred through the passive normal forces, which are developed as discussed above. This being the case, push tests which incorporate active lateral forces will overestimate the bond strength and lead to an unsafe design.

There are several effects that the lateral loads have on the behaviour of push specimens. Firstly, the application of the lateral loads such as F in Fig. 3.4 and Fig. 3.6 will tend to trap the sheet in the region between the ribs at level A-A in Fig. 3.13. This is shown as a uniform pressure at level A-A in Fig. 3.13. Due to the relative rigidities of the rib of the profiled sheeting and the concrete slab, most of the transverse load that is applied to the specimen will be transmitted directly through the concrete as shown in Fig. 3.13a and Fig. 3.13b. Hence the sheet between the ribs will transfer most of the longitudinal shear which is in contrast to

composite slab behaviour where the pressure at level A-A is close to zero, and hence this region transfers very little shear.

Furthermore, as slip progresses and the embossments ride over the concrete, the trapped region at level A-A in the push specimens will effectively restrain the sheet in the rib region, which does not occur in a composite slab. For profiles with a re-entrant rib geometry, the action of the rib moving away from the concrete is largely contained within the void formed by the rib, as shown in Fig. 3.13a. Thus the externally applied normal force, and the sheet trapped at level A-A will have little influence. However, for open rib geometries, as shown in Fig. 3.13b, as the embossments ride over the concrete the separation of the profile will be restrained by the external normal force. This action in the push tests does not occur in a composite slab and it is felt that it will overestimate the bond strength. This restraining effect obviously favours the open rib profiles, and will be more effective with increased thickness or stiffness of the profile, and with increased embossment height. This is due to the fact that as the thickness of the sheeting increases or as the embossment height increases, there is an increased spring action as the sheeting separates from the concrete due to the embossments riding over the concrete. When this spring action is resisted externally by the application of the lateral loads, there will be larger increase in the shear resistance of the sheeting. Thus, push tests which incorporate lateral restraining forces will not give a conservative estimate of the bond strength because of the restraining effect, and this restraining effect will be greater for open rib profiles.

The second major consideration with regard to the application of the lateral loads is that it creates a non-uniform lateral pressure at the interface. This can be illustrated if one considers the free body of half the test specimen of Fig. 3.4, as shown in Fig. 3.14b. The resultant bond force P, which acts at the steel-concrete interface, is at an eccentricity e to the support reaction, and of equal magnitude to the support reaction as shown in Fig. 3.14b. In order to maintain rotational equilibrium there must be moment component in the transverse loads equal to Pe, which will, therefore, increase in proportion to P. In the case of Daniels' test setup in Fig. 3.3 the external transverse loads F, are applied by springs and hence remain constant during the loading. Therefore the normal interface pressure along A-A will vary as shown in Fig. 3.14b in order to maintain rotational equilibrium, that is resist the moment Pe. Therefore, the transverse loads are not uniformly distributed over the length of the concrete block when P is applied. The transverse pressure as shown along A-A will be uniform only

when P = 0, as shown in (a), and become non-uniform when P is applied as in (b). For the case when the transverse loads are applied in displacement control as also occurred in Daniels' test setup, they will not remain constant, but instead will vary throughout the test, as will the internal pressure distribution at the steel-concrete interface. Hence the bond forces that are measured experimentally from these tests are also a property of the geometry of the specimen and not just a material property as required from such a test specimen.

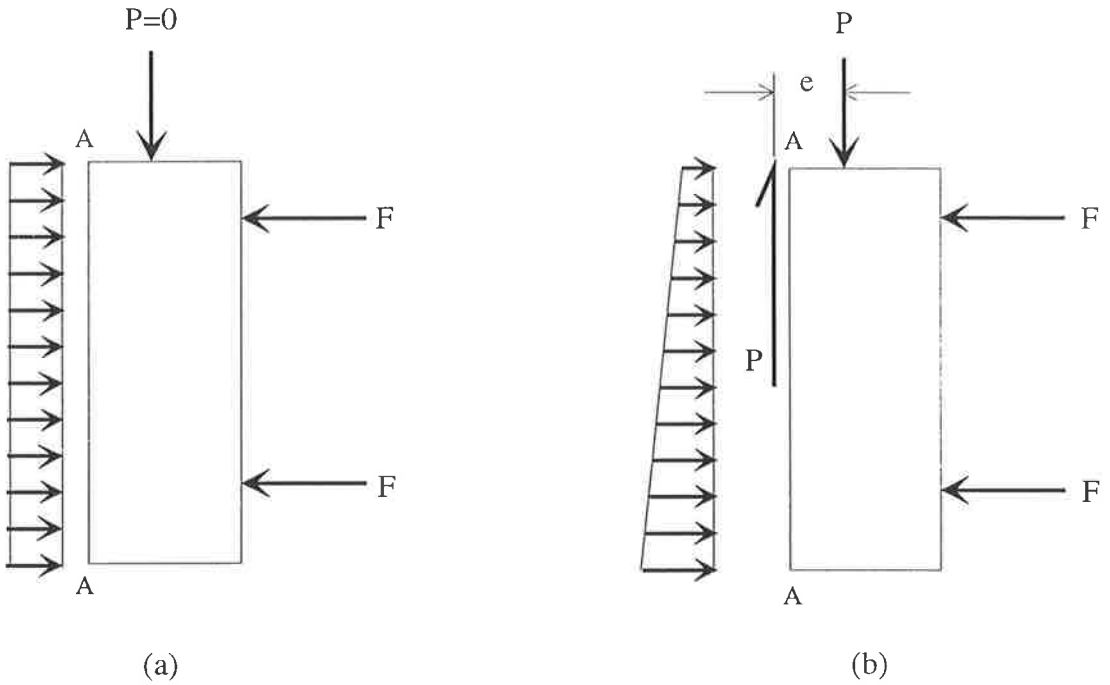


Fig. 3.14. Internal Force Distribution for Daniels' Test Setup

When considering the test setup of Patrick from Fig. 3.6, the free body as shown in Fig. 3.15 can be obtained. The varying interface pressure acting on surface A-A can be replaced by its resultant F, which will act at some eccentricity e_2 to the applied lateral load. The resulting moment Fe_2 will be in equilibrium with the moment due to the axial load, Pe_1. Hence, the value of e_2 can be determined as $e_2 = Pe_1/F$. Thus if e_2 lies outside the middle third of the cross-section then there will be uplift of the specimen, as occurred in practice when F was reduced. Hence, this illustrates that this technique cannot be used to determine the interface bond strength directly, as the application of a lateral force F will always be necessary.

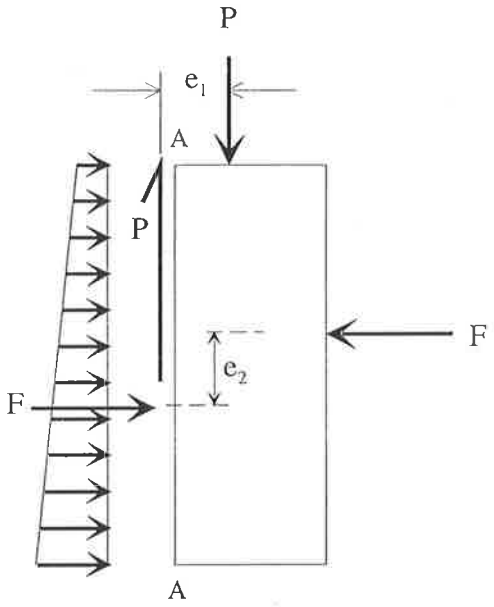


Fig. 3.15. Internal Force Distribution for Patrick's Test Setup

3.3 Current Procedure

3.3.1 Introduction

This section describes an experimental procedure developed by the author to determine the bond characteristics of profiled sheeting. The procedure described here was adopted after careful consideration of the relevant parameters and the drawbacks of the tests proposed by other researchers as detailed in Section 3.2.

A description of the test specimen is given in Section 3.3.2, followed by a step-by-step procedure outlining the manufacture of the specimen in Section 3.3.3. The setup of the specimen ready for testing is then described in Section 3.3.4, followed by a description of the test procedure in Section 3.3.5.

3.3.2 Specimen Geometry

The push test that has been developed during this study is shown in Fig. 3.16. Each specimen consists of two identical sections of sheeting which have a concrete block cast between them, so that in plan view they are symmetrically placed about the block, as shown

in (a). The effective bonding area between the concrete and the profiled sheeting is determined by the height h, and the length L, of the concrete block. Two factors are taken into account in determining these dimensions. Firstly, the interface area should be sufficient to include a reasonable number of embossments, in order to reduce the scatter due to the variability between individual embossments. Secondly, the maximum load developed in the sheeting must not cause buckling in the sheeting at the supports. The arrangement of the test setup is described in Section 3.3.4, which details the load application for the specimen.

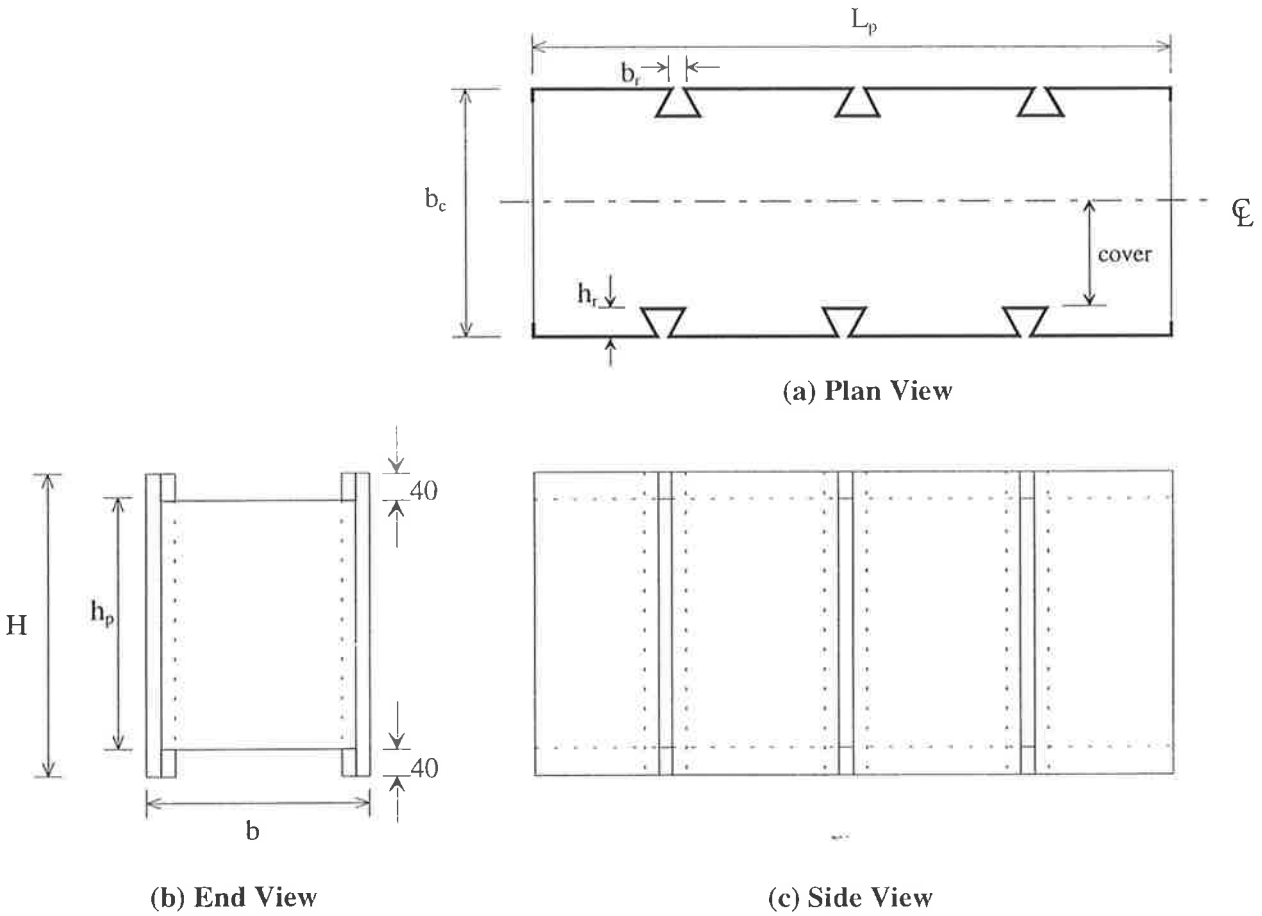


Fig. 3.16. Specimen Geometry

For a given type of sheeting, the height h, will dictate the level of stress developed at the base of the specimen. This can be understood by inspection of Fig. 3.17, which considers the maximum applied load P_u which will be applied to specimen. The value of P_u is given by Eq. 3.3, from which it is possible to determine the stress at the base of the specimen.

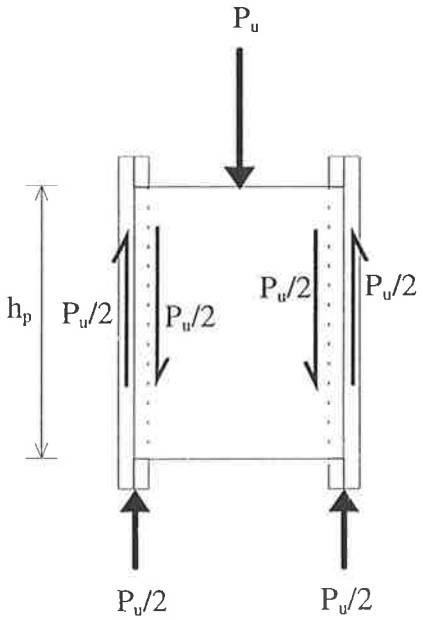


Fig. 3.17. Specimen Geometry

$$P_u = 2f_{bu}h_pL_p \quad \text{.....(3.3)}$$

where

f_{bu} = Maximum average bond stress

h_p = Height of push specimen

L_p = Length of push specimen

Assuming that the height of the rib h_r in Fig. 3.16 is small in comparison to the length of the member, then the area of sheeting bearing on the support can be approximated as $2t_pL$, where t_p is the thickness of the profile. Thus the bearing stress at the base of the profile is given by:

$$\sigma_{bu} = \frac{f_{bu}h_p}{t_p} \quad \text{.....(3.4)}$$

This indicates that the bearing stress for any given profile is based on the height h_p of the specimen. The critical factor in the design of the specimen is that the compressive stress does not cause buckling to occur at any time throughout the test. The bucking strength of the sheeting will depend on the thickness of the sheeting, the effective length between supported edges of the sheeting, and the type of restrain at the sheeting edges. After studying the likely

combinations of maximum bond strength for different profile geometries and sheeting thicknesses, the height of the bonding area chosen for the specimen was 200 mm.

The length L_p of the sheeting was chosen to include more than one rib, and thus increase the bonding area. Most sheeting widths used in practice vary from between 300 mm and 600 mm, and so a specimen length of 700 mm was chosen, to allow at least one complete width of sheeting to be used on each side. As will be discussed in Section 3.3.5 and as shown in Fig. 3.25, small restraints are placed at the ends of the specimen to limit sheeting distortion during testing. As was discussed in Section 3.2.2, it is important that there are no lateral restraining forces that will constrain the sheeting and thus alter its shear resistance. The greater the distance between the ribs and the restraints at the ends of the specimen, then the smaller the effect of the restraints on the behaviour of the sheeting. Thus choosing a specimen length of 700 mm allows sufficient distance between the ribs and the ends of the specimen. Furthermore, some sheeting geometries are asymmetric, with a different lapping rib as shown in Fig. 3.27. This length of specimen allows the entire sheeting to be tested and the overall performance determined. Other test procedures as described in the previous sections (Patrick, 1990), require the individual ribs to be tested, and then some average calculated from the tests to determine the overall performance.

The width b_c, of the block shown in Fig. 3.16a and (b) was based on two criteria. Firstly, premature splitting of the concrete between opposite ribs should be avoided. This splitting failure is similar to the longitudinal splitting observed in some slab tests with re-entrant rib geometries (Patrick, 1994). Secondly, there must be enough clearance between the sheets to apply the load to the concrete block. The width chosen for the specimen was 250 mm, as most sheeting in use have a maximum rib height of 55 mm, giving a total clearance between opposite ribs of 140 mm, or 70 mm cover for each rib to the centre line of the specimen, as shown in Fig. 3.16a.

It can be seen in Fig. 3.16b that the sheeting overhangs the concrete block by 40 mm at the top and bottom of the specimen. The 40 mm overhang at the bottom of the specimen is used to allow clearance for the concrete to slip along the sheeting, as well as provide sufficient gap so that the restraint provided by the base plate does not affect the deformation of the rib at the steel-concrete interface. The arrangement of the base plates is discussed in Section 3.3.4. Maximum slips which are typically observed at the failure of composite

members using profiled sheeting are usually of the order of 5 mm (Prasannan and Luttrell, 1984; Crisinel et al, 1986) with some sheeting geometries achieving slips of up to 10 mm (Patrick 1994; Veljkovic, 1993). The arrangement adopted in this testing procedure gives sufficient room between the bottom of the concrete and the restraint at the support to accommodate slips of up to 20 mm before termination of the test.

3.3.3 Preparation Procedure

A number of preliminary tests were performed in order to determine the optimum specimen arrangement. The following procedure represents the conclusions drawn from the experience gained during the preliminary testing.

1. The first step is to cut the sheeting to be tested to a length of 280 mm. This allows 200 mm of bonded length between the concrete and the steel, and 40 mm of overhang at the top and bottom of the specimen, as shown in Fig. 3.16.

2. The sheeting was cleaned of all oil or grease using acetone. This was carried out so as to produce a uniform surface condition for all sheeting types.

3. The rib geometry and average embossment heights were noted for each specimen.

4. The formwork was assembled, with dimensions 700 long, 250 wide, and 240 high for each specimen. The 240 mm height allows for a concrete block of 200 mm with a 40 mm gap at the bottom of the specimen. This gap is achieved by placing 40 mm of polystyrene foam in the base of the formwork. The sheeting is inserted into the foam by heating it up before placing it in the formwork. This leaves 40 mm of the sheeting above the formwork, which is left to aid in finishing off the specimen after the concrete has been cast. The top surface of the foam was coated in a debonding agent to aid in its subsequent removal.

5. Lifting lugs were placed on the sides of the specimens. A specimen ready for pouring is shown in Fig. 3.18. Note that there is no reinforcement used in the specimen.

6. The specimens were poured, along with test cylinders which were used to determine the strength of the concrete. Both were vibrated during pouring. After pouring, the specimens were left in the formwork and covered with hessian and plastic, and kept moist for two days. After this time they were stripped, and left to cure in the air until testing. Testing was typically 6 weeks after casting.

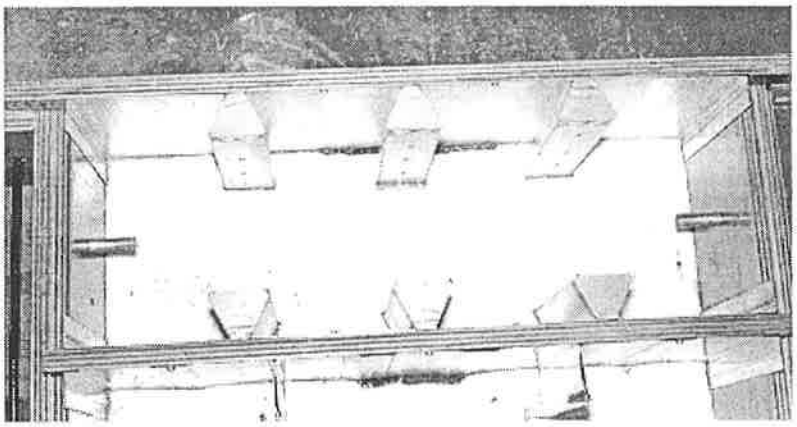


Fig. 3.18. Specimen Ready for Pouring

3.3.4 Test Setup

When the specimens had cured sufficiently, they were prepared for testing using the procedure outlined below. The steps are illustrated in the following figures.

1. Before moving the specimens, clamps are placed on the outer edges to help minimise any disturbances to the sheeting during the test setup. These clamps can be seen in Fig. 3.20. The specimens are then lifted up by the lifting lugs and then rotated, so that the foam on the underside can be removed.

2. The specimen is then placed onto the base of the loading rig. The bases on which the specimen is placed are shallow troughs approximately 10 mm in height and are shown schematically in Fig. 3.19 and also in the photograph in Fig. 3.21. These bases are filled with a fast setting silica paste immediately before the specimen is placed in them. The silica paste is used to constrain the sheeting, so as to provide a fixed support at the base, and thus reduce the likelihood of the sheeting buckling during loading. The paste is removed from inside the ribs, so as to allow the ribs to deform inwards due to the action of the embossments.

3. The bases are placed on rollers, as shown schematically in Fig. 3.19, so that the sheeting is free to deform away from the concrete as the concrete rides over the embossments. This outward movement of the sheeting is discussed in the results of the testing. The bases are initially locked in position as the specimen is placed in the wet paste, but are released during the loading of the specimen.

4. Specimens which had a re-entrant rib geometry, such as an L-Rib or dovetail rib, had 20 mm thick dispersion plates pasted on the top of the specimen to distribute the load around the ribs. These plates are shown schematically in Fig. 3.19 and in the photograph of Fig. 3.22. These plates were used to evenly distribute the load onto the specimen, and to prevent cracking of the concrete around the ribs, due to the high bond stresses which can develop in this area.

5. The top loading beam is pasted in position on the top of the specimen. A thin layer of paste is used to ensure an even bedding surface against the concrete specimen. The loading beam was a stiffened 100 UB, which was used to provide a uniform dispersion of the load from the loading jack to the concrete block. This is shown schematically in Fig. 3.19 and in the photograph of Fig. 3.23.

6. A smaller loading plate was placed in the centre of the loading beam, as a packer between the beam and the loading jack. This plate was carefully centred, and had a layer of paste applied under it so as to ensure an even distribution of load onto the specimen. This is shown in Fig. 3.23. This arrangement was used in place of a spherical seat because of the variability of the shear resistance of the sheeting. If the shear resistance of one of the ribs is different to the others, then this arrangement will maintain an even slip over the specimen, whereas a spherical seat would allow the specimen to rotate, and thus create an uneven slip at each of the ribs.

7. Angles were placed on the top surface of the concrete block to measure the slip. Two transducers were glued on the each side of the specimen in the location shown in Fig. 3.24. These were positioned so as to detect any rotation of the specimen about the long or the short axis, and produce an average value of the slip in the specimen. Fig. 3.24 shows a specimen that is ready for testing.

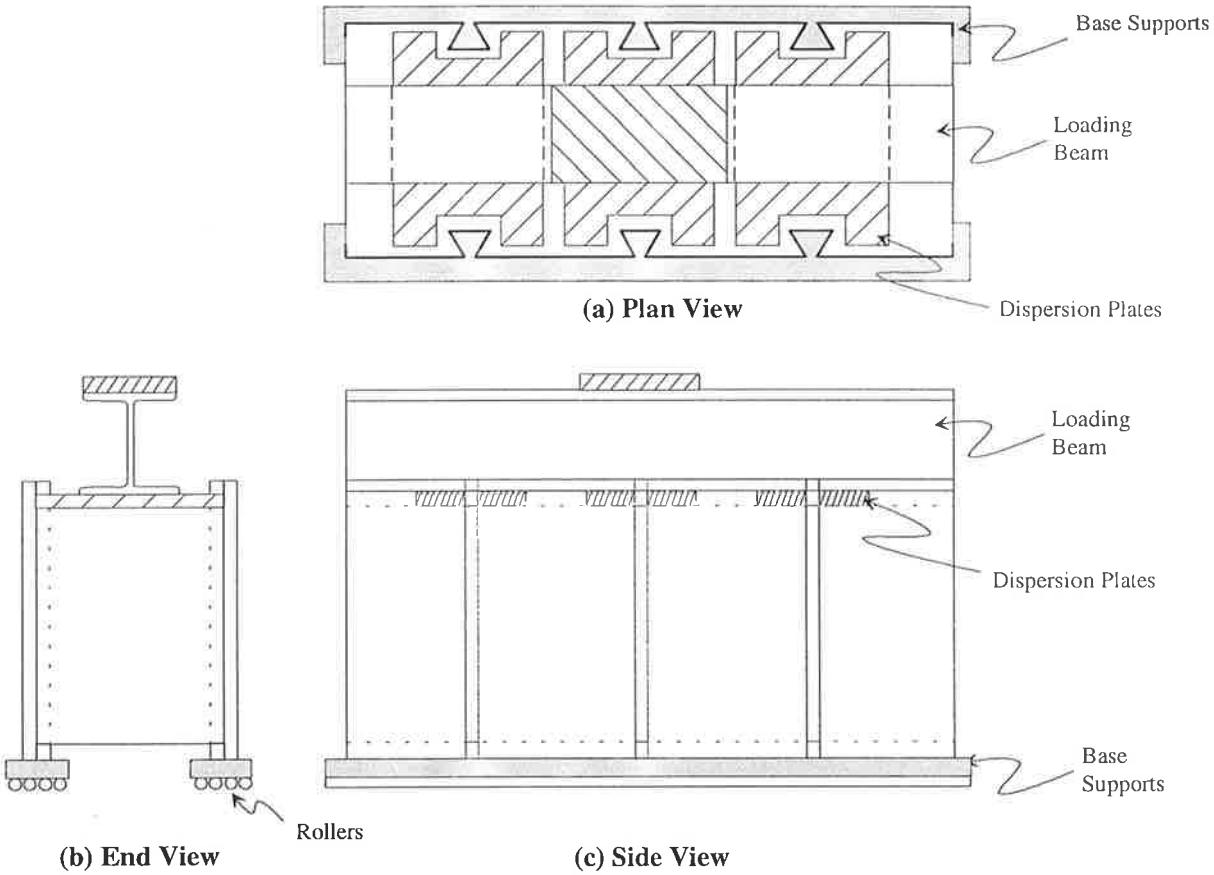


Fig. 3.19. Schematic of Test Setup

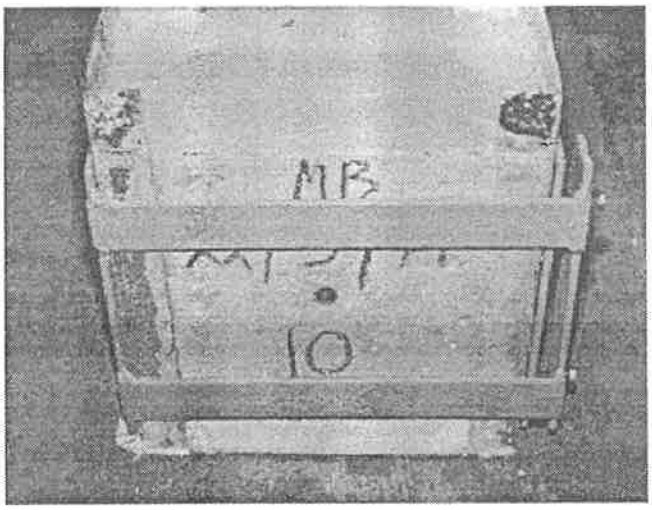


Fig. 3.20. Restraining Clamps

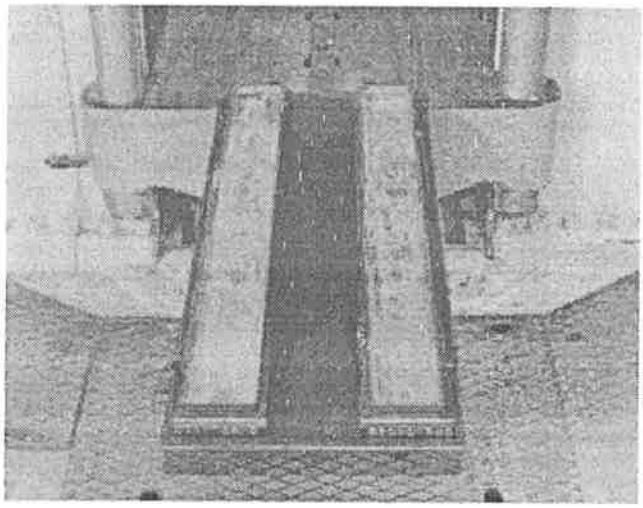
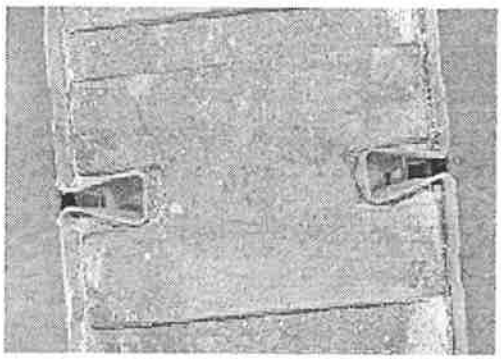
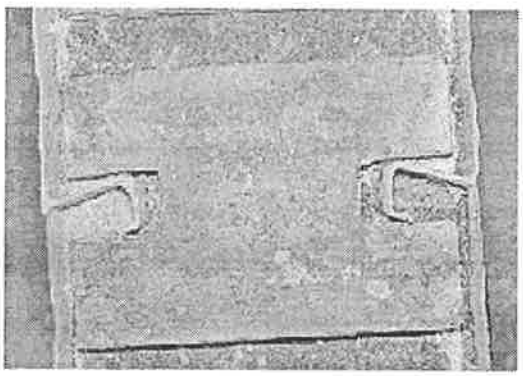


Fig. 3.21. Bases for loading Rig



(a) Dovetail Rib



(b) L-Rib

Fig. 3.22. Load Dispersion Plates

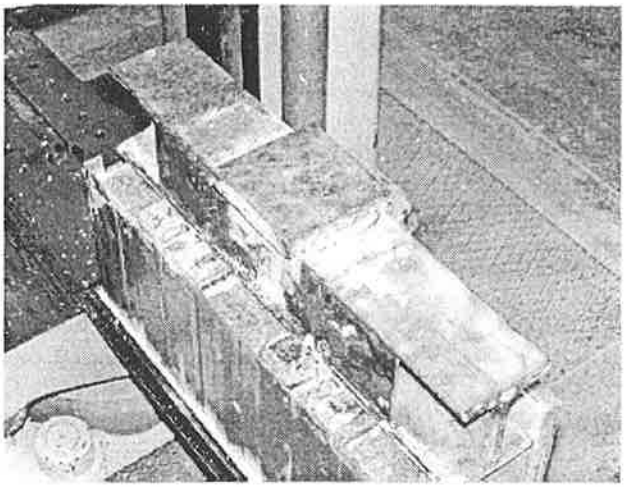


Fig. 3.23. Load Transfer Plate

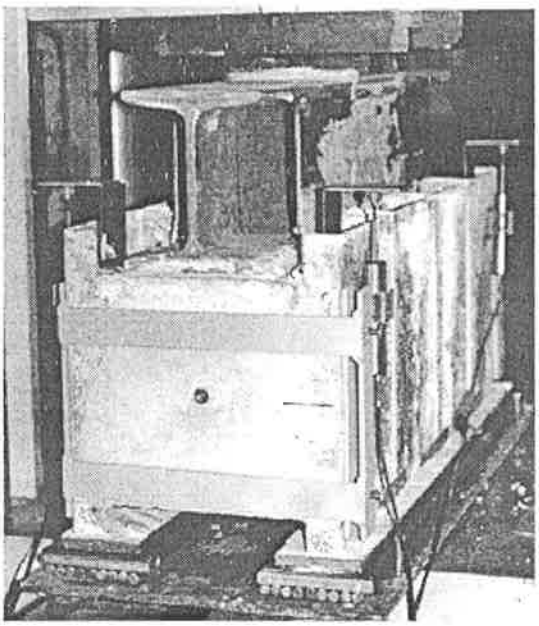


Fig. 3.24. Test Specimen

3.3.5 Test Procedure

The test procedure consisted of two stages. The first part consisted of loading the specimen until the chemical bond was broken and a slip is first recorded. After this initial slip had occurred, the specimen was completely unloaded and the second part of the test involved loading the specimen as the slip progresses.

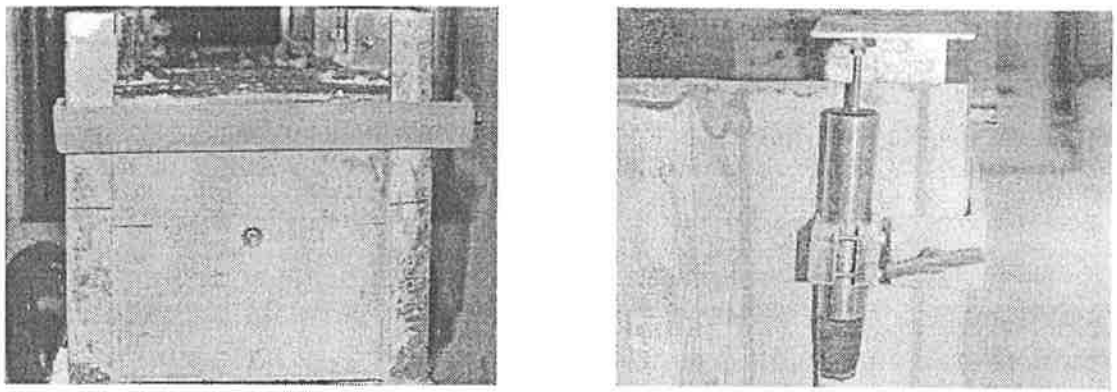
1. The side clamps that were initially placed on the specimens during the test setup, as shown in Fig. 3.20, were kept in place during the initial stage of the loading. The

clamps were tightened only finger tight, so only a small pressure was applied. As there were no embossments at the location of the side clamps there was no tendency for the clamping force to increase during the test. The base plates on the rollers were fixed in position and were not free to move until the chemical bond had been broken. These two measures were taken to prevent the specimen from rotating during the initial stages of the test. This was more critical for the first stage of the loading, due to the large variability and the brittle nature of the chemical bond. The test setup was able to accommodate some non-uniformity in the shear strength of the two sides without significant rotation of the specimen, but if the chemical bond failed completely on one side before the other had failed, then an unacceptable amount of rotation occurred when the above measures were not taken.

2. The applied load was increased at the rate of 30 kN/min, which is an increase in the shear stress of approximately 0.075 MPa/min, depending on the rib geometry and the bonding area. The applied load and slip were continuously logged during the test. The loading rate was kept constant until the chemical bond had completely broken, as indicated by the four transducers recording a slip.

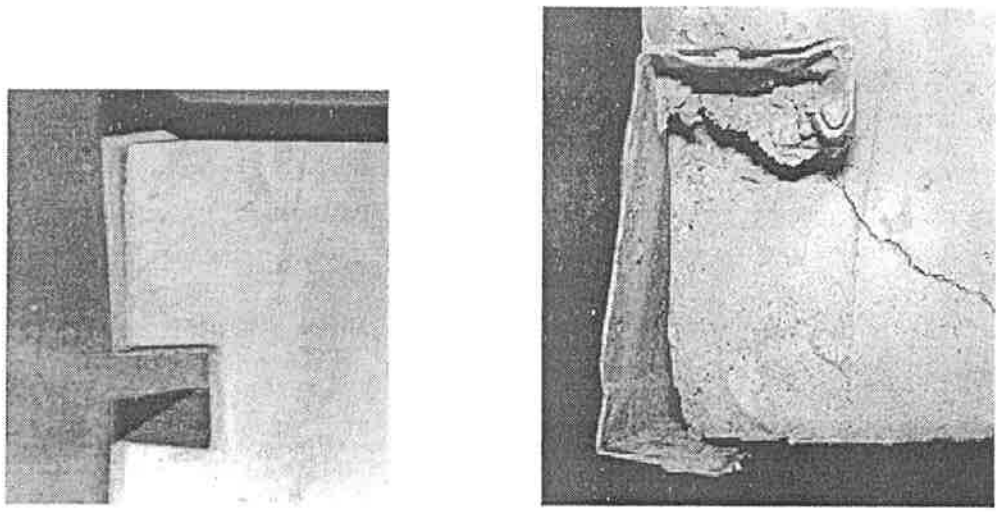
3. After the chemical bond had been completely broken, the load was reduced to zero and the bottom plates were released so that they would be free to move during the remainder of the test. The side clamps were removed, and two smaller clamps were placed on the sides at the top of the specimen. These clamps are illustrated in Fig. 3.25. The clamps were placed so as to reduce the distortion of the sheeting at the ends of the specimen, and hence minimise any change in the degree of restraint offered at the rib boundaries. The free distortion of the sheeting without these clamps is illustrated in Fig. 3.26. The clamps were designed to reduce the end effects of the sheeting distortion, without inhibiting the movement of the sheeting due the effects of the concrete riding over the embossments.

4. After failure of the chemical bond, the load was applied to the specimen to produce a rate of slip of 1 mm/min. The load and the displacement were continuously logged as the slip progressed. The test was terminated when either the specimen was unable to maintain any load, or the limit of slip had been reached when the concrete block came into contact with the bottom plates.



(a) End View (b) Side View

Fig. 3.25. Use of Side Clamps to Limit Sheeting Distortion.



(a) Open Rib (b) L-Rib

Fig. 3.26. Sheet distortion without side clamps.

3.4 Experimental Results

3.4.1 Introduction

This section presents the results of the experimental testing program undertaken as part of this thesis. The testing procedure has already been outlined in Section 3.3. In general, the aim of the testing program was to investigate the qualitative effects of varying different parameters relating to the profiled sheeting. It was not the aim of this investigation to produce quantitative measures, but rather to determine general trends in the shear characteristics of profiled sheeting. The results of the tests are presented as shear stress vs

slip graphs. The shear stress is determined from the applied load by dividing by the contact area between the concrete and the rib portion of the sheeting. The contact area is determined from the perimeter of the rib surface L_r in Fig. 3.27, the number of embedded ribs, and the height of the concrete specimen h in Fig. 3.16.

Most of the tests produced slips of over 20 mm before the test was terminated. However, the shear-stress / slip curves reported in this section usually only proceed as far as 10 mm, as the main area of interest is for slips up to 10 mm. This is because the maximum slips recorded from tests incorporating profiled sheeting are less than 10 mm (Prasannan and Luttrell, 1984; Crisinel et al, 1986; Veljkovic, 1993; Patrick 1994). Often the same trend of the stress-slip curve continues on after 10 mm slip with no discontinuity being recorded. When there is some region of note after 10 mm slip, it is reported for that particular test.

3.4.2 Test Parameters

In total there were five series of tests carried out in this investigation. The series are given in Table 3.1 with the parameters that were varied in each series and the range of values of the different parameters. The preliminary series was conducted to determine the optimal arrangement for the test setup and is described in Section 3.4.3. The effect of the surface condition on the results was also investigated in this series. Series 1 was conducted to investigate the influence of the rib opening b_r in Fig. 3.16a, and is described in Section 3.4.4. Series 2 was conducted to determine qualitative effects of embossments on different profiles and is discussed in Section 3.4.5. Series 3 was conducted to investigate the effects of sheeting thickness and is described in Section 3.4.6. The final series was conducted on proprietary sheeting of varying thickness, and was carried out to investigate the performance of Australian sheeting, and to provide a comparison with results of Patrick (1990). This series is described in Section 3.4.7.

Series	Parameters Varied	Possible Values
Preliminary	Specimen Height h_p Surface Condition	100, 200, 300 mm Greased / Non-Greased
Series 1	Rib Opening b_r	15 - 180 mm
Series 2	Rib Opening b_r Embossments	15 - 180 mm Embossed / Non-embossed
Series 3	Sheeting Thickness, t_p Surface Condition	0.6 - 2.0 mm Greased / Non-Greased
Series 4	Sheeting Thickness, t_p Embossments	0.79 - 1.0 mm Embossed / Non-embossed

Table 3.1. Range of Parameters in Push Tests

3.4.3 Preliminary Series

This series was used to determine the optimal arrangement for the test specimen, as well as for the test setup and the test procedure. As a result, the test setup and procedure which was outline in Sections 3.3.4 and 3.3.5 was not adopted for all the tests in this series. All specimens in this series had a length L_p, shown in Fig. 3.16a, of 500 mm instead of the 700 mm adopted for the subsequent series. The reason for this is described in the following section. The width b_c of the specimen was 200 mm. A short description of each specimen and the test setup is contained in this section.

The slip measurements taken for the first three specimens of this series were obtained by measuring the relative displacement between the top and bottom loading plates. As a result, the measurements also included the settlement that occurs between the supports and the specimen, and between the loading plates and the specimen. This settlement is indicated by the deflection that occurs before the chemical bond has been broken. After the results of the first three tests were analysed, it was concluded that attaching the transducer to the sheeting and measuring the slip at the interface directly would eliminate this problem.

All specimens were constructed using a proprietary profile sheeting which is used in Australia. The sheeting used was manufactured by Woodroffe Industries, and was 1.0 mm gauge embossed Comform sheeting. The geometry of the sheeting is shown in Fig. 3.27. The main parameters that were varied were the height h_p of the specimen, and the surface condition of the sheeting prior to pouring the specimens. Three different heights were used

for the specimens in this series, where the height h_p is as shown in Fig. 3.16a. The reason different heights of specimens were used was to determine if the resultant bond characteristics were dependant on the bond area, as indicated by Porter and Ekberg (1978).

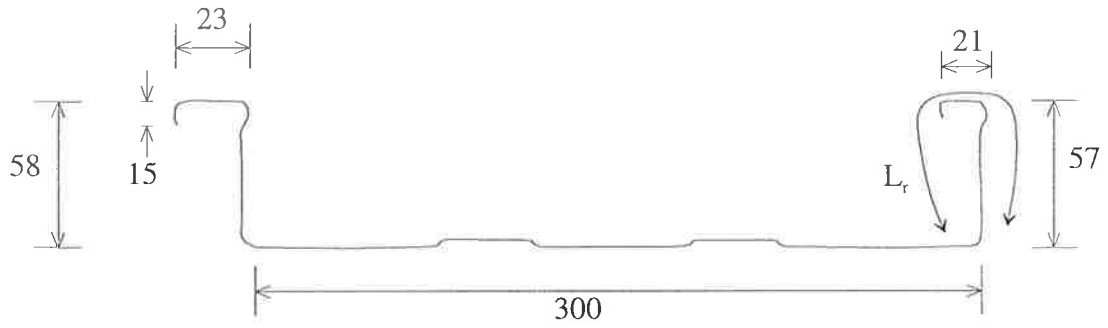


Fig. 3.27. Comform Profile

The surface condition of the sheeting prior to pouring the specimen was prepared in either one of two ways. It was either thoroughly wiped clean with acetone, or it was coated with a debonding agent. The coating of the surface with a debonding agent was carried out to attempt to eliminate the chemical bond between the sheeting and the concrete. This was done because most codes of practice do not allow the chemical bond to be relied upon to resist the longitudinal shear (ASCE, 1992; British, 1982; European, 1990). The uncoated specimens were used to determine the effect of the use of the debonding agent. A summary of the specimens used in the preliminary series is given in Table 3.2.

The following sections contain a description of each push test, as well as the results of the shear-stress / slip curves. A summary of the results is contained in Table 3.3 on Page 143

Test No.	Height, h (mm)	Surface Condition
PTP.1	200	Non-Greased
PTP.2	200	Greased
PTP.3	100	Non-Greased
PTP.4	300	Greased
PTP.5	300	Non-Greased
PTP.6	100	Greased

Table 3.2. Preliminary Series

3.4.3.1 Push Test PTP1

This specimen did not have the loading plates discussed in Step 4 of Section 3.3.4 and shown in Fig. 3.19, which are used to distribute the load around the ribs, and as a result there was extensive cracking of the specimen surrounding the ribs. This is shown in Fig. 3.28, where the location of the loading plate is indicated by the remaining bedding paste. It was this cracking that led to the adoption of the dispersion plates discussed in Step 4 of Section 3.3.4 and shown in Fig. 3.22. There were difficulties with the instrumentation for this test and as a result no load-slip curve was recorded for this specimen.

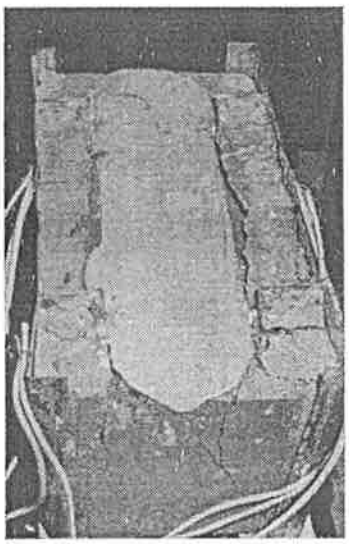


Fig. 3.28. Specimen PTP1 after Testing

3.4.3.2 Push Test PTP2

This specimen was the same as PTP1, except that the profiled sheeting had been coated with a debonding agent before the concrete was cast. The same loading arrangement was used as for the previous test, and the cracking pattern that developed was similar to that shown in Fig. 3.28. The resulting shear stress-slip curve is shown in Fig. 3.29. Point A in Fig. 3.29 represents the load at which the chemical bond broke down. The failure of the chemical bond was evidenced by the cracking sound that was heard at this load, followed by the reduction in the load carrying capacity. As shown in Fig. 3.29, there was a deflection of more than 2 mm before Point A is reached. This deflection represents the settlement of the supports, as discussed in Section 3.4.3. A high degree of ductility can be seen after the peak

load had been reached, as shown by the region B-C in Fig. 3.29 which indicates large levels of slip with no reduction in the shear stress.

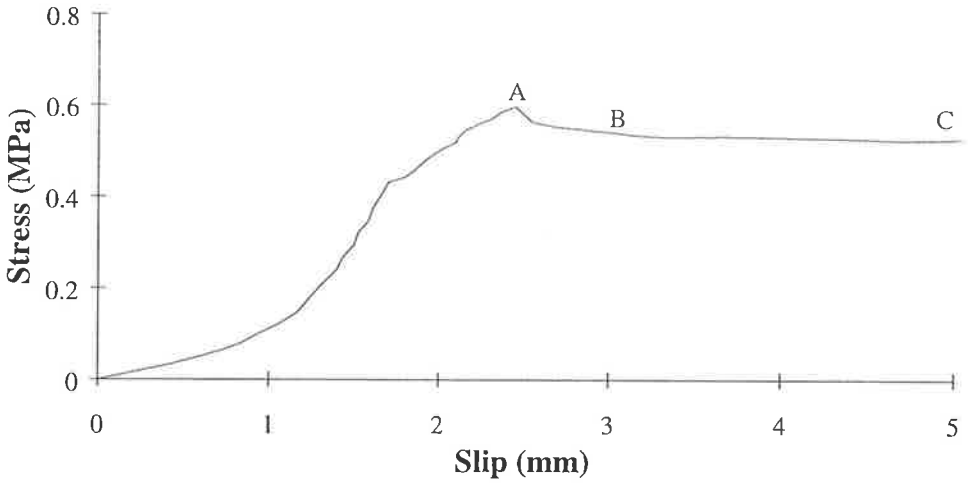


Fig. 3.29. Shear Stress-Slip Curve for PTP2

3.4.3.3 Push Test PTP3

The resulting shear-stress / slip curve is shown in Fig. 3.38. The profiled sheeting in this specimen was not coated with the debonding agent, and it can be seen that the maximum stress is higher than for specimen PTP2 shown in Fig. 3.29, in which the profiled sheeting was coated. Furthermore, that there is a noticeable decrease in the load carrying capacity after the maximum load had been reached, which was not apparent for specimen PTP2. The significant slip before the maximum load was reached was again due to settlement of the supports, as discussed in Section 3.4.3.

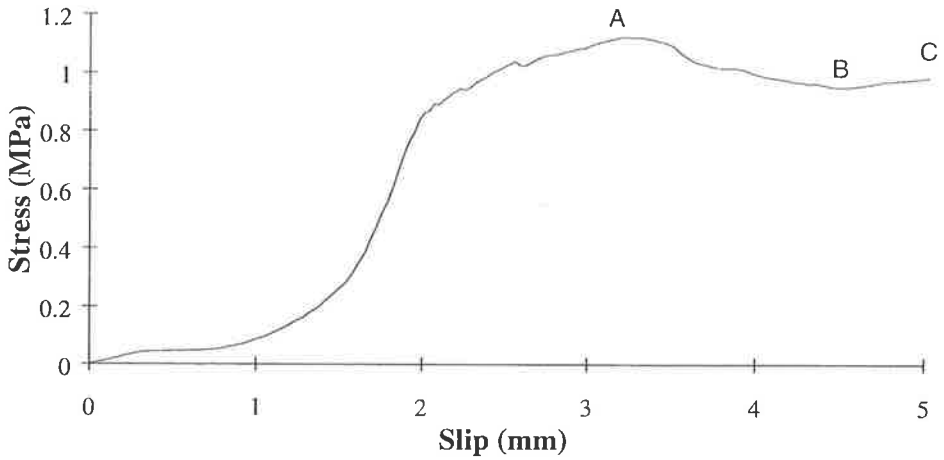


Fig. 3.30. Shear Stress-Slip Curve for PTP3

3.4.3.4 Push Test PTP4 and PTP5

These two specimens were identical except that the sheeting of PTP.4 had been coated with a debonding agent before the concrete was cast, while that of PTP.5 was left uncoated. For these and subsequent specimens, the dispersion plates shown in Fig. 3.22 were used and the cracking shown in Fig. 3.28 was eliminated. However, another cracking pattern was observed and this is shown in Fig. 3.31. This cracking pattern can be attributed to the splitting forces which develop at the rib due to the concrete riding over the embossments in the webs of the ribs. This cracking pattern was observed in all subsequent tests in this series, and as a result the length of the specimen L in Fig. 3.16 was increased from 500 mm to 700 mm. This was done so as to increase the concrete cover to the ribs, and thus reduce the likelihood of cracking.

The resulting shear-stress / slip curves are shown in Fig. 3.32 for specimens PTP4 and PTP5. It can be seen that there is a significant difference between the coated and the uncoated specimens. Specimen PTP4, which was coated with the debonding agent, exhibited almost perfect rigid-plastic behaviour; no interface slip until the maximum shear stress of nearly 0.6 MPa had been reached, after which slip progressed with virtually no change in the shear stress. Specimen PTP5, which was uncoated, exhibited a peak load, after which there was a reduction in the load carrying capacity. Furthermore, the uncoated specimen had a peak shear stress which was more than 1.5 times the equivalent coated specimen. It appears from Fig. 3.32 that the coated and uncoated specimen tend towards a similar shear resistance at large slips. However, as the maximum slips usually produced in structures using profiled sheeting are less than 5 mm, this is not of interest.

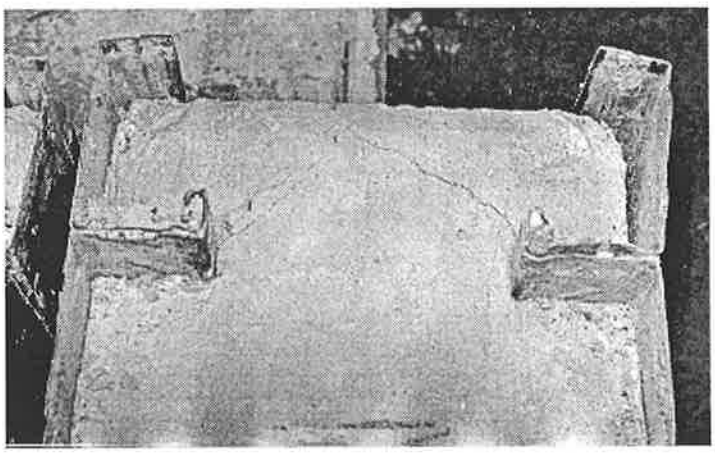


Fig. 3.31. Cracking Pattern for PTP4

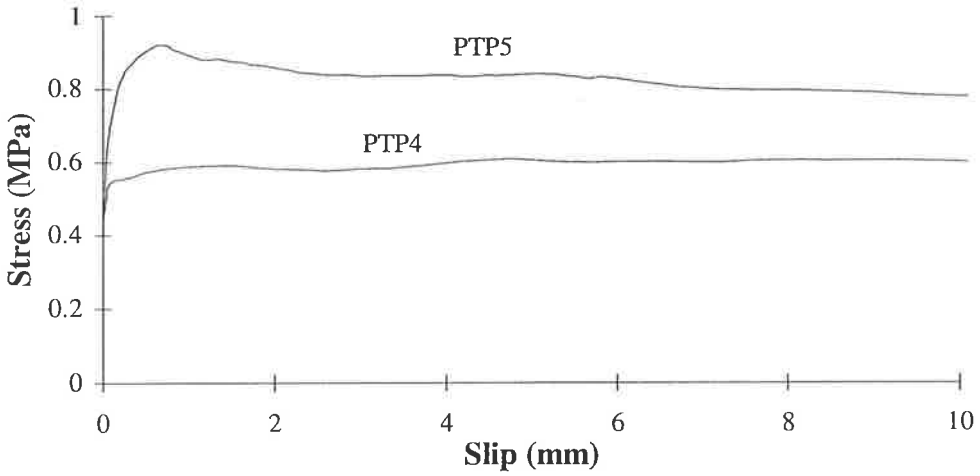


Fig. 3.32. Shear Stress-Slip Curve for PTP4 and PTP5

3.4.3.5 Push Test PTP6

This specimen was identical to PTP3 except that the debonding agent had been applied to the sheeting. It can be seen in Fig. 3.33 that there is a marked change in the behaviour of the specimen with the application of the debonding agent. It must be noted that the rise in shear stress with no slip for PTP6, which was not recorded for PTP3, was due to change in placement of the displacement transducers, as mentioned earlier. The maximum stress of PTP6 is less than half that of the comparable coated specimen. Furthermore, for specimen PTP6 after the maximum load had been reached, there was only a very slight reduction in the load carrying capacity, whereas for the coated specimen there was a significant reduction.

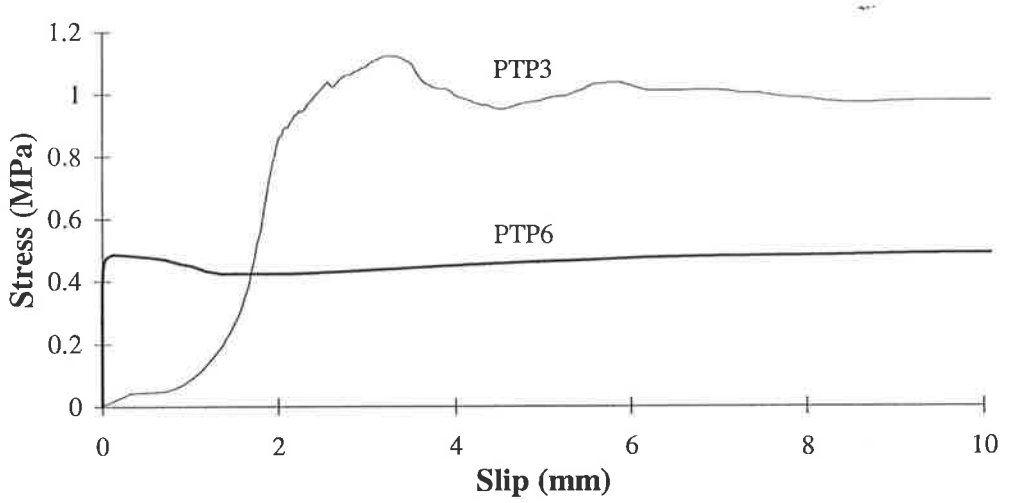


Fig. 3.33. Shear Stress-Slip Curve for PTP3 and PTP6

3.4.3.6 Summary of Preliminary Series

A summary of the results for the preliminary series is presented in Table 3.3. No values were recorded for PTP.1 due to an error with the recording instrumentation. No values were recorded in Table 3.3 for the chemical bond stress for PTP4 or PTP6. This was due to the fact that the sheeting for these specimens was coated with a debonding agent, and there was no discernible point at which the chemical bond failed. Despite the fact that specimen PTP2 was also coated with the debonding agent, this specimen exhibited a reduction is the load carrying capacity after failure of the chemical bond. No value was entered for the residual bond stress of PTP5 as there was no rapid reduction of the shear stress after failure of the chemical bond, but rather a gradual reduction with increasing slip. Hence, the resulting shear-stress / slip curve for this specimen is best described by the maximum bond stress, and the stress at 5.0 mm slip.

Test No.	Height, h (mm)	Surface Condition	Chemical Bond Stress (MPa) (Point A)	Residual Bond Stress (MPa) (Point B)	Stress at 5.0 mm Slip (MPa) (Point C)
PTP.1	200	Non-Greased	*	*	*
PTP.2	200	Greased	0.60	0.53	0.55
PTP.3	100	Non-Greased	1.12	1.0	1.0
PTP.4	300	Greased	-	0.60	0.60
PTP.5	300	Non-Greased	0.92	-	0.84
PTP.6	100	Greased	-	0.49	0.46

Table 3.3. Summary of Preliminary Series

It appears from these tests that the debonding agent has a more marked effect than merely breaking down the chemical bond between the concrete and the profiled sheeting. The response of the specimens seemed to indicate that the debonding agent also acted as a lubricant at the concrete-profiled interface. As a result of these preliminary tests, it was concluded that the use of a debonding agent would not accurately model the surface condition present in real structures.

3.4.4 Series 1

The geometry of the profiled sheeting used for each of the specimens is shown in Table 3.4. There were no embossments on any of the profiles used, except for specimens PT1.11 and PT1.12. The main parameter that was varied in this series was the opening of the rib b_r, shown schematically in Fig. 3.34. The height of the ribs h_r was kept constant at 45 mm, and the width of the rib flange was constant at $b_f = 60$ mm. Specimens PT1.11 and PT1.12 were constructed from Woodroffe Comform as shown in Table 3.4, and do not represent part of this series. They were poured and tested with this series due to other considerations, and will be discussed separately at the end of this section. A short description of each test is given in this section, along with the shear stress-slip curves for each specimen. A summary of results is given in Table 3.6.

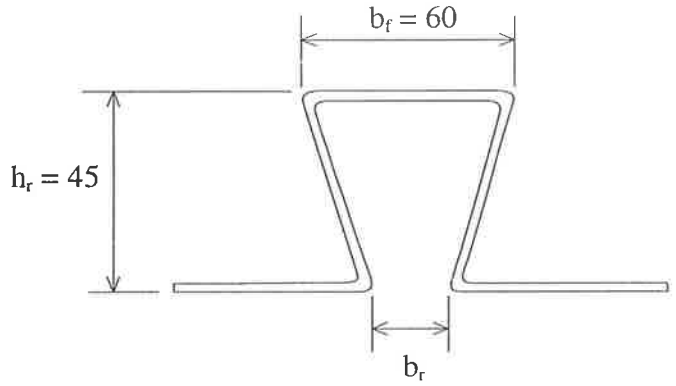


Fig. 3.34. Typical Rib Geometry

All the specimens were constructed from non-embossed sheeting. The sheeting used for all specimens (except PT1.11 and PT1.12) was grade G2 galvanised sheeting, with a Total Coated Thickness of 1.00 mm, and a Base Metal Thickness of 0.98 mm. The individual units were cut to length using a guillotine, and then folded to the required shape using a brake press. A typical stress-strain curve is shown in Fig. 3.35. The results for the values of the yield stress and ultimate stress are given in Table 3.5 for the three series of tests.

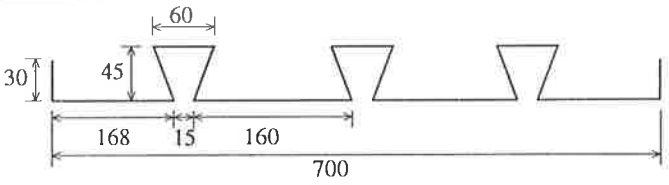
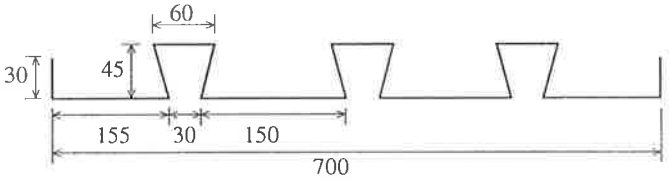
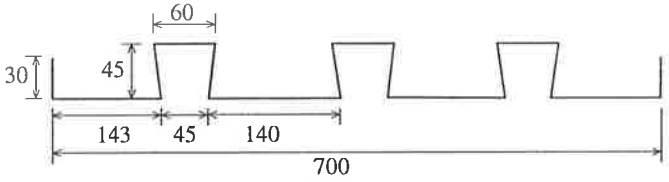
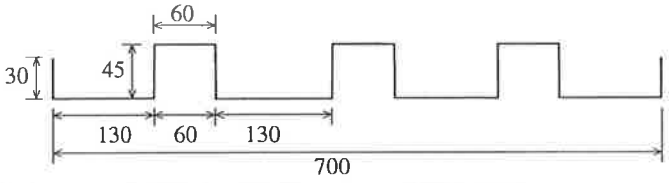
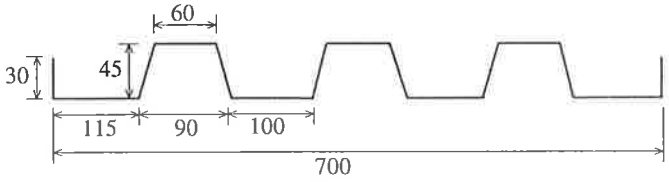
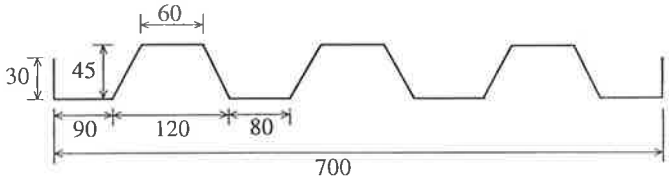
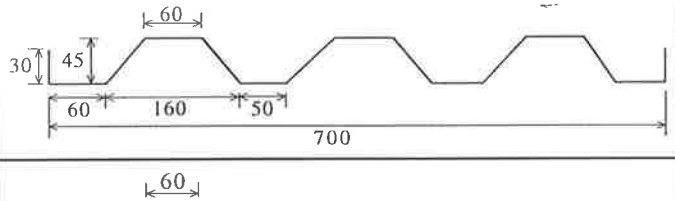
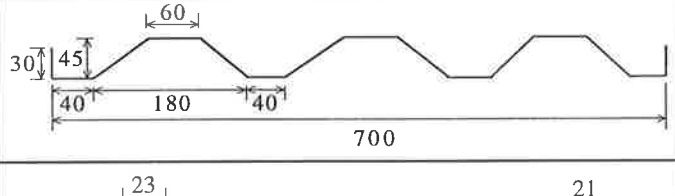
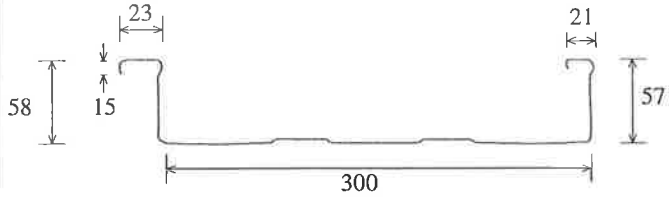
Test No.	Cross Section	Rib Perimeter (mm)
PT1.1 & PT1.2		161
PT1.3 & PT1.4		155
PT1.5		151
PT1.6		150
PT1.7		155
PT1.8		168
PT1.9		194
PT1.10		210
PT1.11 & PT1.12		190

Table 3.4. Series 1

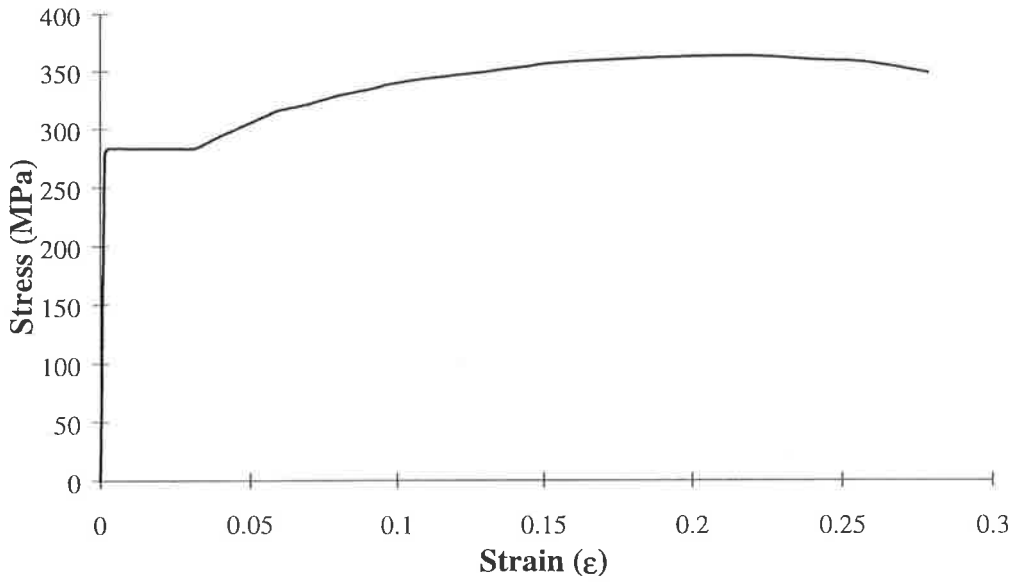


Fig. 3.35. Profiled Sheeting Stress-Strain Curve

Also measured for each series at the time of testing the specimens were the concrete properties which are given in Table 3.5. A minimum of 3 cylinders were tested, and the results shown in the table represent the average of the test results. The compression tests were performed on 100 mm diameter cylinders, using the procedure outlined in the Australian Code (AS 1012.9, 1986). The tensile capacity of the concrete was determined using the Brazilian test, which were performed on 150 mm diameter cylinders. The testing procedure was as outlined the Australian Code (AS 1012.10, 1985). The Young's Modulus of the concrete was determined at the time of testing the specimens, using the procedure outlined in the Australian Code (AS 1012.17, 1976). The concrete test cylinders were tested at the same time that the push tests were carried out.

	Concrete Properties			Steel Reinforcing		Profiled Sheeting	
	f_c* (MPa)	E_c† (MPa)	f_{ct}‡ (MPa)	σ_y§ (MPa)	σ_u** (MPa)	σ_y (MPa)	σ_u (MPa)
Series 1	53	32 600	4.6	442	537	288	365
Series 2	47.0	33 700	3.7	435	535	280	363
Series 3	39.0	33 600	3.2	438	530	284	368

* Compressive Stress ‡ Tensile Strength ** Ultimate Stress
† Young's Modulus § Yield Stress

Table 3.5. Measured Concrete and Steel Properties

The load-slip response of these profiles can be separated into the three main regions shown in Fig. 3.36. First is the initial rise in load with no measured slip, shown by region O-A. This represents the load carried by the chemical bond between the sheeting and the concrete. After the chemical bond has broken, there is a sudden increase in the slip with an associated decrease in the applied load as shown by the region A-B. The shear resistance at point B, after the chemical bond has completely broken down, is termed the *residual strength.* The third region of the curve B-C shows the variation in shear resistance as the slip progresses.

All of the specimens tested with a re-entrant rib geometry had a rising branch B-C, whereas the remaining open rib specimens had a flat or descending branch. This rise in shear resistance with increasing slip may be explained by two different causes. It may be due to either the experimental setup, or to the fundamental behaviour of the sheeting itself. If the rising branch were due to the experimental setup, then the most likely mechanism would be from the increased restraint from the support of the sheeting. This restraint was minimised by placing the supports on rollers which allow movement of the sheeting relative to the concrete. It is more likely that the rising branch is due to increasing roughness of the profile-concrete interface as the slip progresses. The lack of the rising branch for the open rib geometries is due to the ability of the sheeting to move freely away from the concrete.

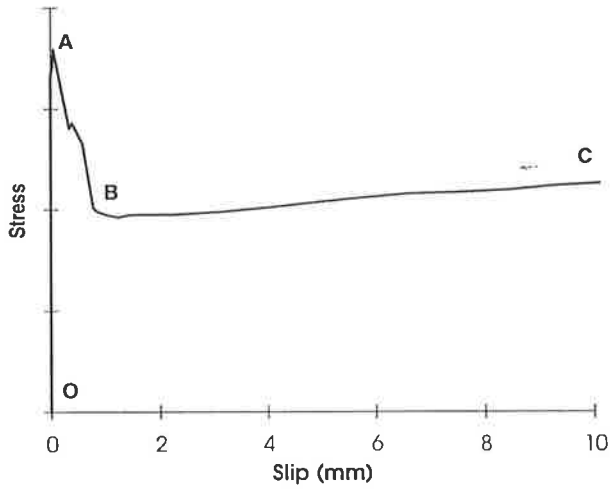


Fig. 3.36. Typical Load-Slip Curve for Series 1

When determining the shear stress from the applied load, the contributing contact surface area must be known. When determining the stress at which the chemical bond breaks, the total bonded area should be used. Whereas after the chemical bond has broken, it

is more appropriate to use the rib surface area, as most resistance to shear is provided by the ribs. This procedure produces a discontinuity in the shear-stress / slip curve when the chemical bond has broken, due to the change in contributing area. To overcome this, throughout the remainder of this chapter, the calculation of the shear-stress / slip curves will be based on the rib contact area. However, when tabulating a summary of the results in Table 3.6, a column of the chemical bond stress based on the entire contact area is also included.

The procedure of placing rollers under the supports as discussed in Section 3.3.4 was not adopted for the first three tests of this series. The effect of this change on the results is not thought to be large, because the re-entrant rib geometry will prevent the sheeting from moving away from the concrete. This restraint is not offered by open rib geometries and thus the rollers are necessary for these tests. The procedure of using a flat plate between the loading jack and the distribution beam was not adopted for the first 5 specimens of this series, and as a result, a number of the specimens suffered from significant rotation during testing.

3.4.4.1 Push Tests PT1.1 and PT1.2

The geometry of these identical specimens are shown in Table 3.4. During the manufacture of these specimens, it was not possible to construct the sheeting from one continuous length. As a result, the sheeting was constructed by lapping 4 separate units together and spot welding at the rib locations. The lap joint is shown in Fig. 3.37, and the spot welds can be seen in Fig. 3.18. The resulting shear-stress / slip curves are shown in Fig. 3.38.

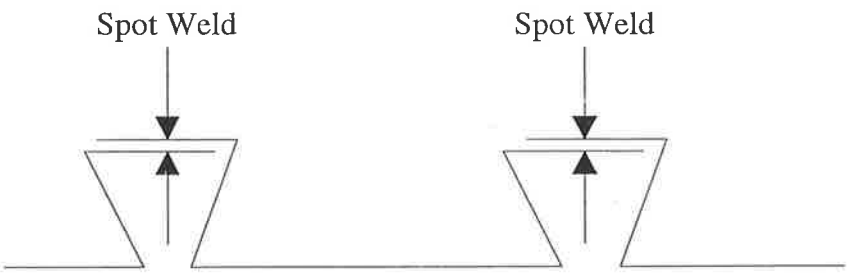


Fig. 3.37. Lap Joint for PT1.1, PT1.2 and PT1.3

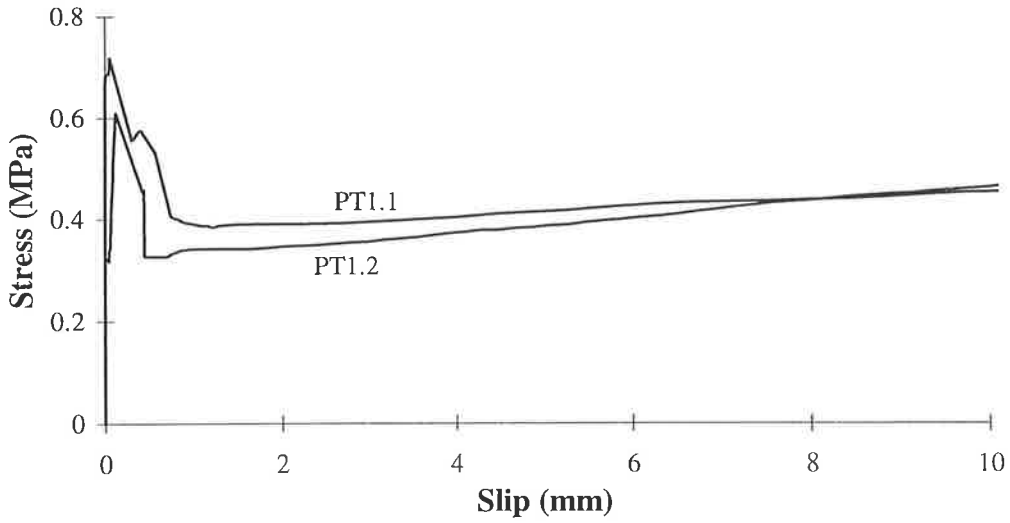


Fig. 3.38. Shear Stress vs Slip Curve for PT1.1 and PT1.2

3.4.4.2 Push Test PT1.3 and PT1.4

Specimen PT1.3 was constructed in the same manner as PT1.1 and PT1.2 with a lap joint in the profiled sheeting at the rib. Specimen PT1.4 had the same geometry as PT1.3, except that the sheeting was manufactured from single piece and thus did not have the lap joint at the rib. The sheeting for all subsequent specimens were constructed from single elements of sheeting, and it was decided to do a comparison between profiles of the same geometry, with and without the lap joint.

The resulting shear stress-slip curve is shown in Fig. 3.39. Both specimens exhibit a similar reduction in shear capacity after the chemical bond is broken, as was noted for PT1.1 and PT1.2. The maximum shear stress for PT1.3 was 0.57 MPa, compared to 0.45 MPa for PT1.4. This variation in the chemical bond is to be expected. The rise in shear capacity of PT1.4 after the failure of the chemical bond was due to a large rotation of the specimen that occurred during loading. This was due to the use of a spherical seat that was placed between the loading jack and the dispersion beam. As a consequence of this rotation, it is not possible to make a valid comparison between these tests to determine if the lap joint in rib makes any difference to the behaviour of the sheeting.

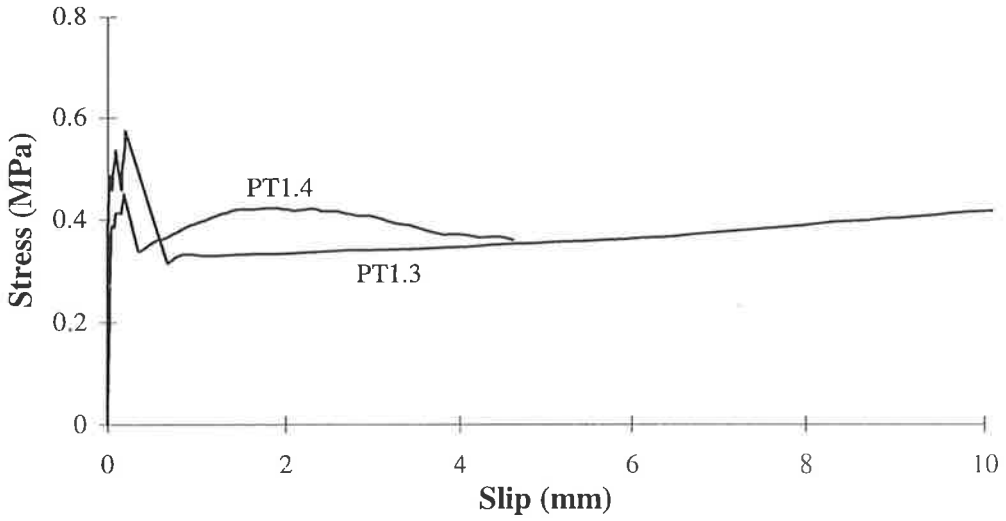


Fig. 3.39. Shear Stress vs Slip for PT1.3 and PT1.4

3.4.4.3 Push Test PT1.5

The shear stress-slip curve for this specimen is shown in Fig. 3.40. This specimen also rotated significantly during the test, with one side measuring over 2.5 mm more slip than the other. This resulted from the breakdown in the chemical bond and the initiation of slip on one side of the specimen, before the chemical bond had fully broken on the other.

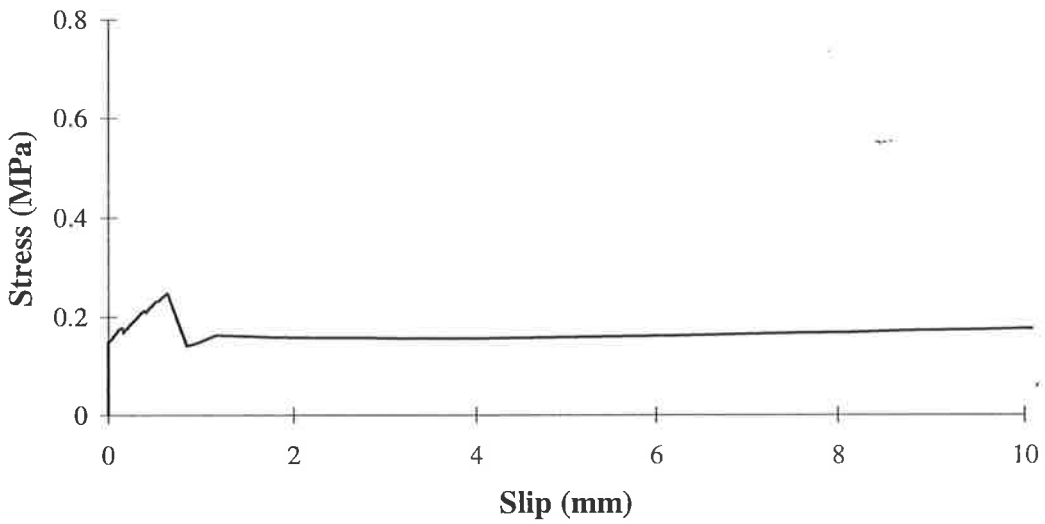


Fig. 3.40. Shear Stress vs Slip for PT1.5

3.4.4.4 Push Test PT1.6, PT1.7, and PT1.8

Push Test PT1.6 also rotated during the test, and was the last specimen to be tested with a spherical seat under the loading jack. After the chemical bond had broken down on one side, and the specimen began to rotate, the test was halted and the spherical seat removed. It was replaced by the rigid loading plate discussed earlier, and the test recommenced. Fig. 3.41 shows the stress / slip curve after reloading.

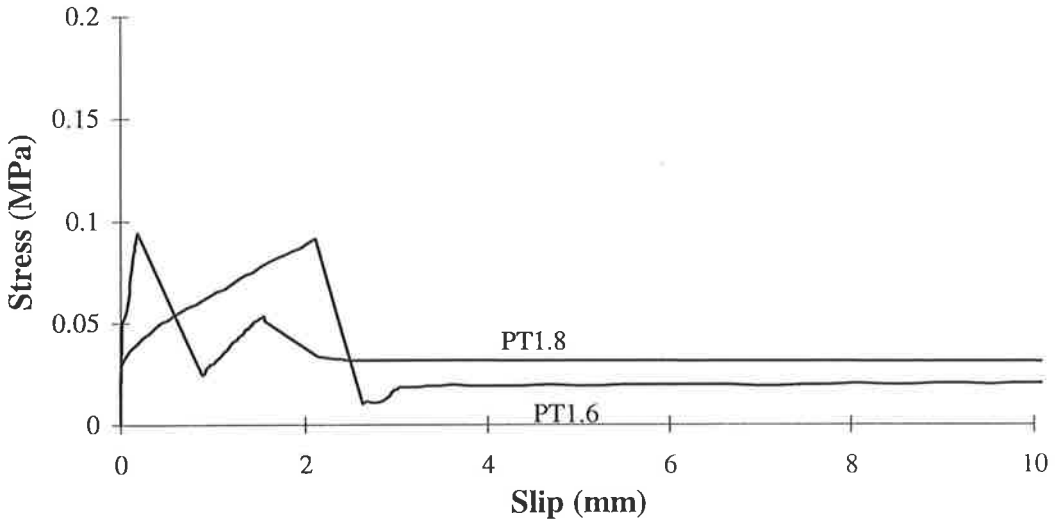


Fig. 3.41. Shear Stress vs Slip for PT1.6 and PT1.8

Push Test PT1.7 was damaged during the preparation, and was not tested.

Push Test PT1.8 showed a similar response to PT1.6 as shown in Fig. 3.41, however there was no rotation of the specimen, due to the use of the rigid loading plate. The residual bond stress was slightly higher, despite the more open rib geometry. This may have been due to the more even distribution of the shear between the two sides of the specimen.

3.4.4.5 Push Test PT1.9 and PT1.10

Push Test PT1.9 failed before being tested, due to the sheeting peeling away from the concrete. This occurred because of the natural shape of the sheeting, which tended to 'curl' when placed inside the formwork during construction of the specimen.

Push Test PT1.10 recorded a maximum deflection of 0.32 mm before failure, as shown in Fig. 3.42.

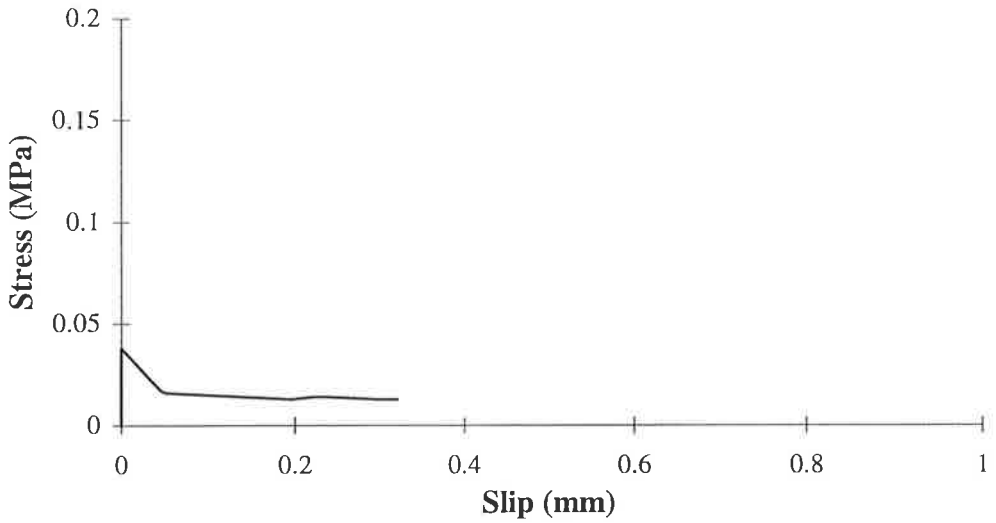


Fig. 3.42. Shear Stress vs Slip for PT1.10

3.4.4.6 Push Test PT1.11 and PT1.12

The shear stress-slip curves are shown in Fig. 3.43. It can be seen that the form of the two curves are similar, except that the result from PT1.11 is lower than PT1.12. This can be explained due to the rotation that occurred during the testing of PT1.11. Despite the use of the flat loading plate, there was significant rotation of the specimen, which was due to

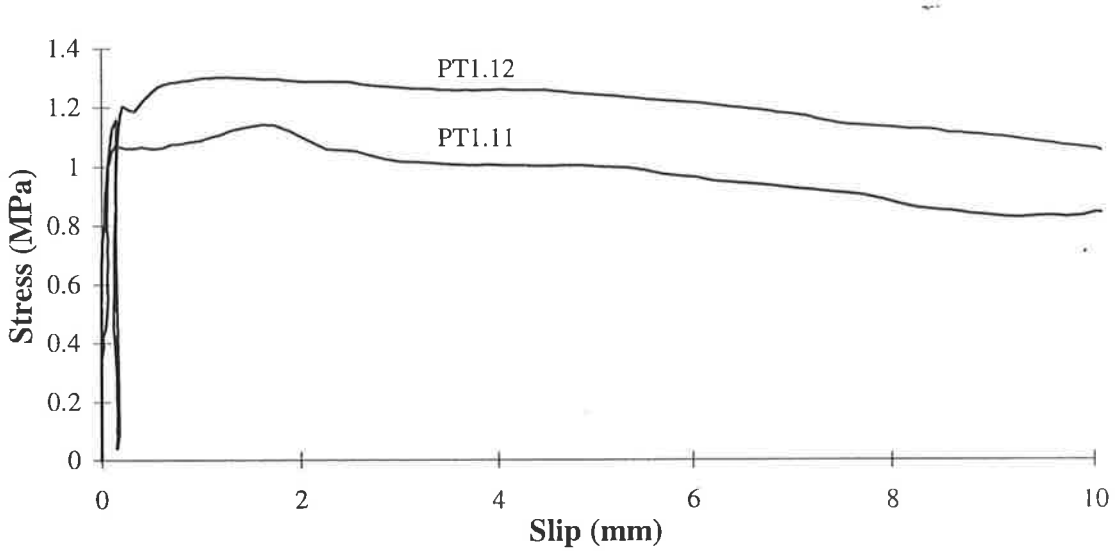


Fig. 3.43. Shear Stress vs Slip for PT1.11 and PT1.12

warping of the loading beam, as shown in Fig. 3.44. This occurred due to the low stiffness of the beam about its weak axis, and the high bond stresses that were present in this specimen. This problem was overcome for subsequent specimens by stiffening the loading beam.

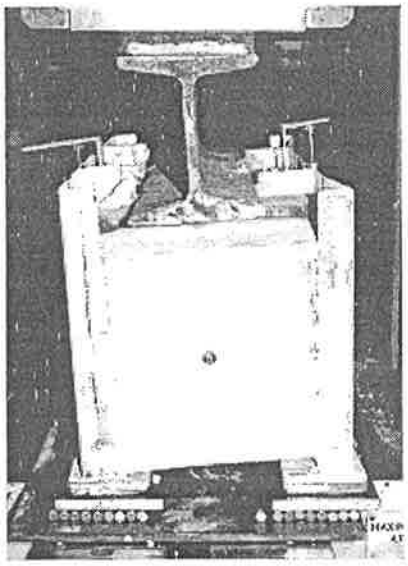


Fig. 3.44. Warping of the Loading Beam

There is no sudden reduction in strength at the failure of the chemical bond, and the shear resistance continued to increase as the slip progressed. However, after the maximum load had been reached, there was a gradual decrease in the shear resistance of the specimens. There was some cracking evident in PT1.12, which is shown in Fig. 3.45. These cracks were observed on the underside of the specimen after the completion of the test, and were not visible from the top of the specimen. The transverse crack between the two ribs is typical of the longitudinal crack that can form along the rib in a composite slab test. The two diagonal

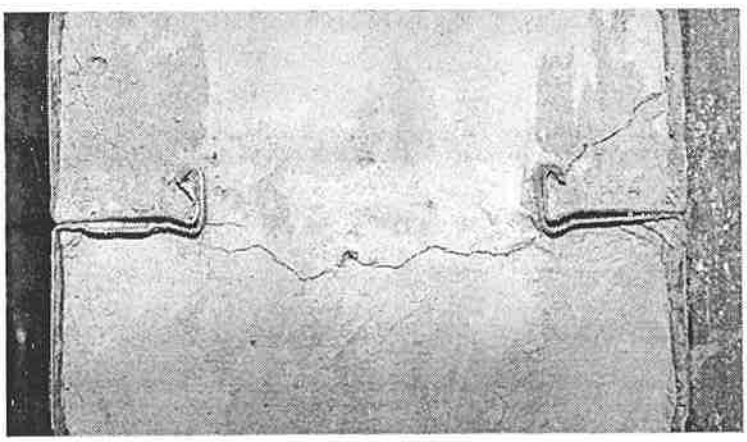


Fig. 3.45. Cracking of PT1.12

cracks from the rib corners occurred as a result of the splitting forces developed at the rib. It has not been reported in the literature whether such cracking is typical for these rib geometries.

3.4.4.7 Summary of Series 1

Table 3.6 shows a summary of results from Series 1. The different profiles have been sorted according to the geometry of the ribs, where the rib opening is shown schematically in Fig. 3.34. The rib opening in Table 3.6 has been non-dimensionalised by dividing by the width of the rib flange b_f. Hence, a value of b_r/b_f less than one represents a re-entrant rib, while a value of b_r/b_f greater than one represents an open or trapezoidal rib geometry.

Test No.	Non-Dimensional Rib Opening (b_r/b_f)	Chemical Bond Stress (MPa) (Total Contact Area)	Chemical Bond Stress (MPa) (Rib Contact Area)	Residual Stress (MPa)	Stress at 5.0 mm Slip (MPa)
PT1.1	0.25	0.29	0.719	0.389	0.415
PT1.2	0.25	0.246	0.609	0.326	0.389
PT1.3	0.5	0.233	0.575	0.312	0.355
PT1.4	0.5	0.183	0.451	0.338	0.360
PT1.5	0.75	0.121	0.248	0.155	0.160
PT1.6	1.0	0.085	0.091	0.019	0.019
PT1.7	1.5	*	*	*	*
PT1.8	2.0	0.074	0.094	0.027	0.00
PT1.9	2.67	*	*	*	*
PT1.10	3.0	0.028	0.38	0.00	0.00

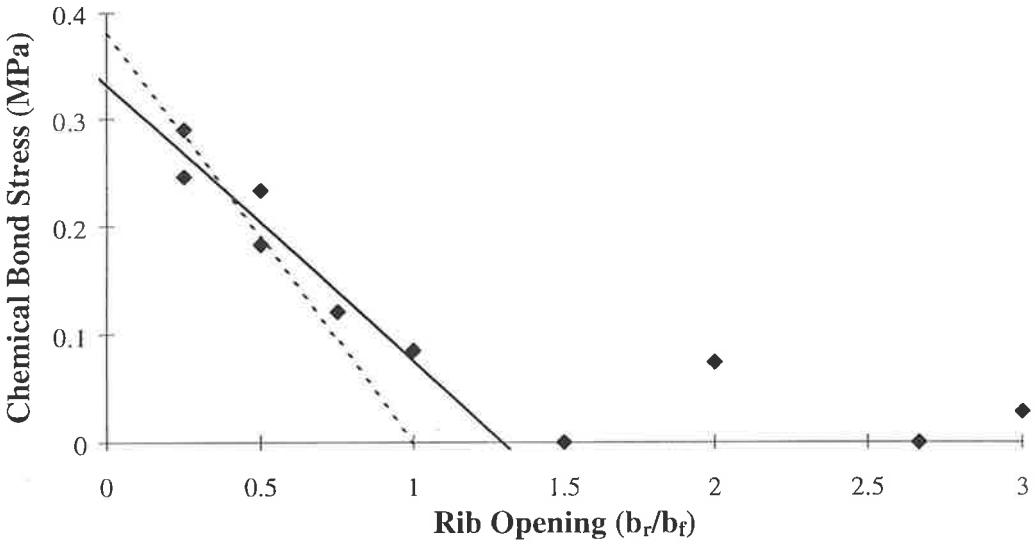
Table 3.6. Summary of Series 1

Two values of the chemical bond strength have been calculated, and are shown in the third and fourth columns. The first value is derived from the load at which the chemical bond failed, such as shown by Point A in Fig. 3.36, by dividing by the entire contact area between the sheeting and the concrete, while the second value is obtained by dividing by the rib contact area. The residual stress after failure of the chemical bond, such as shown by Point B in Fig. 3.36, is shown in the fifth column, while the stress after 5 mm slip is shown in the last column. The last two columns have been calculated based on the rib contact area.

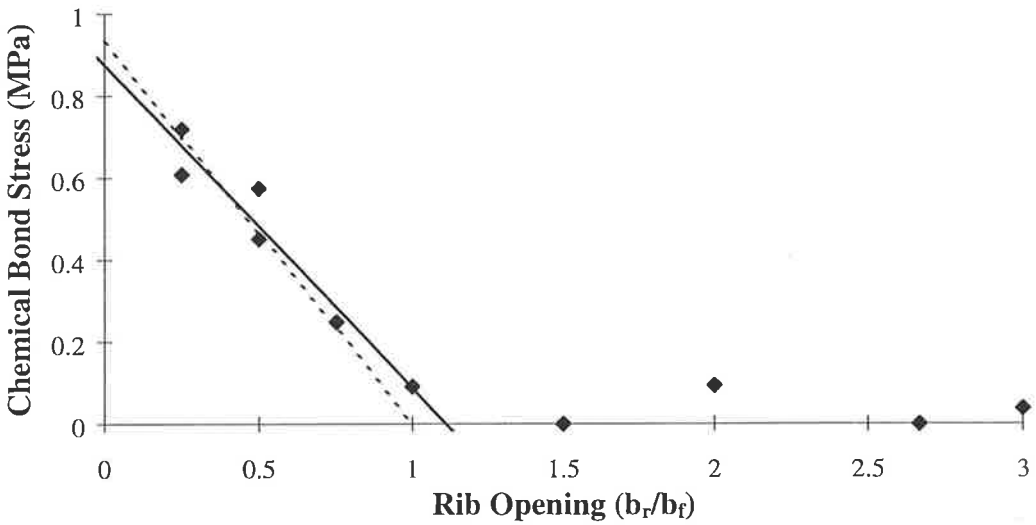
The stress at 5 mm slip was recorded to give some indication of the ductility of the profiled sheeting. When this value is larger than the residual stress, then the profile exhibits an increase in shear resistance with slip, whereas a smaller value indicates a decease in the shear resistance. The choice of 5 mm was somewhat arbitrary, but represented a reasonable estimate for the maximum slips in composite members with profiled sheeting. Other stress values at different levels of slip could be tabulated, however these values can also be obtained from the shear-stress / slip curves.

The variation in the chemical bond strength is shown in Fig. 3.46 plotted against the non-dimensional rib opening. Figure 3.46a shows the chemical bond stress calculated using the entire contact surface area, while (b) shows the chemical bond stress calculated using the rib contact area. The overall forms of the two curves are similar, with the main difference being the magnitudes of the values. It can be seen from both these figures that the chemical bond stress appears to vary with the rib geometry. It is expected, however, that the chemical bond stress would be independent of the rib geometry. Due to the brittle nature of the chemical bond, after failure has commenced at one location of the interface, the breakdown of the bond propagates rapidly across the entire interface. Thus, failure of the chemical bond is more of a peeling action, which accounts for the gradual reduction in the chemical bond strength with increasing rib opening.

It can be seen in Fig. 3.46 that there is a general trend towards zero strength at a rib opening of $b_r/b_f = 1$, and than for $b_r/b_f > 1$ the bond strength is zero. Shown in Fig. 3.46 are two linear regression lines, both of which are fitted through the data which have rib openings with $b_r/b_f \leq 1$. The solid lines represent the regression line which has been determined using the method of least residual sum of squares (Weisberg, 1985). It can be seen in the above two figures that this regression line intercepts the abscissa close to $b_r/b_f = 1$. The broken line is an adjusted regression line through the data points with the abscissa value forced to pass through $b_r/b_f = 1$. The coefficients of determination R^2 for the unadjusted and adjusted regression lines are 0.91 and 0.63 for Fig. 3.46a, and 0.94 and 0.90 for Fig. 3.46b respectively. There is a reduction in the coefficient of determination of the adjusted regression lines compared to the unadjusted lines, as expected. However, the high value of $R^2 = 0.90$ for the adjusted regression line in Fig. 3.46b indicates that fitting the regression line through $b_r/b_f = 1$ is a reasonable approximation to the behaviour.



(a) Chemical Bond based on Entire Contact Area



(b) Chemical Bond based on Rib Contact Area

Fig. 3.46. Chemical Bond Strength vs Rib Opening for Series 1

The significance of fitting the regression line through $b_r/b_f = 1$ is based on the geometry of the rib. At values of $b_r/b_f < 1$ the rib geometry is re-entrant, and the sheeting is restrained from lateral movement by the shape of the rib. For values of $b_r/b_f > 1$ the rib geometry is open, and the sheeting is not restrained from lateral movement away from the concrete. Thus, $b_r/b_f = 1$ represents the transition between re-entrant and open rib geometries, and this point also corresponds to a change the behaviour of the sheeting, as shown in Fig. 3.46. This point will be discussed further in Section 3.6

Figure 3.47 indicates the variation in the residual bond strength with rib opening, while Fig. 3.48 indicates the variation in stress at 5 mm slip. As the strength of the non-embossed profiles increased with increasing slip, the maximum mechanical strength recorded over the 5 mm slip occurred at 5 mm. Thus, the graph indicating the maximum mechanical strength is the same as that shown in Fig. 3.48, and has not been repeated in the text.

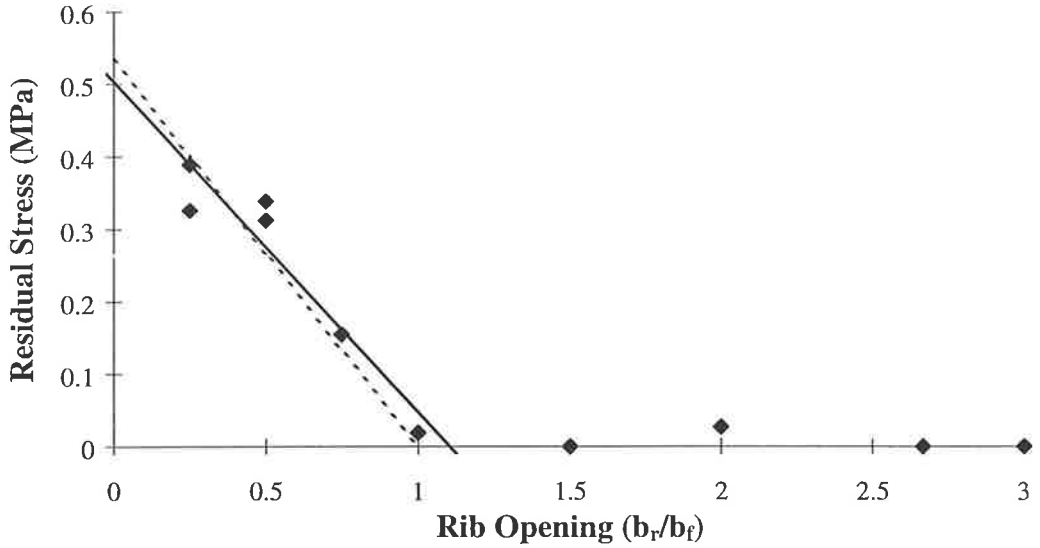


Fig. 3.47. Residual Stress vs Rib Opening for Series 1

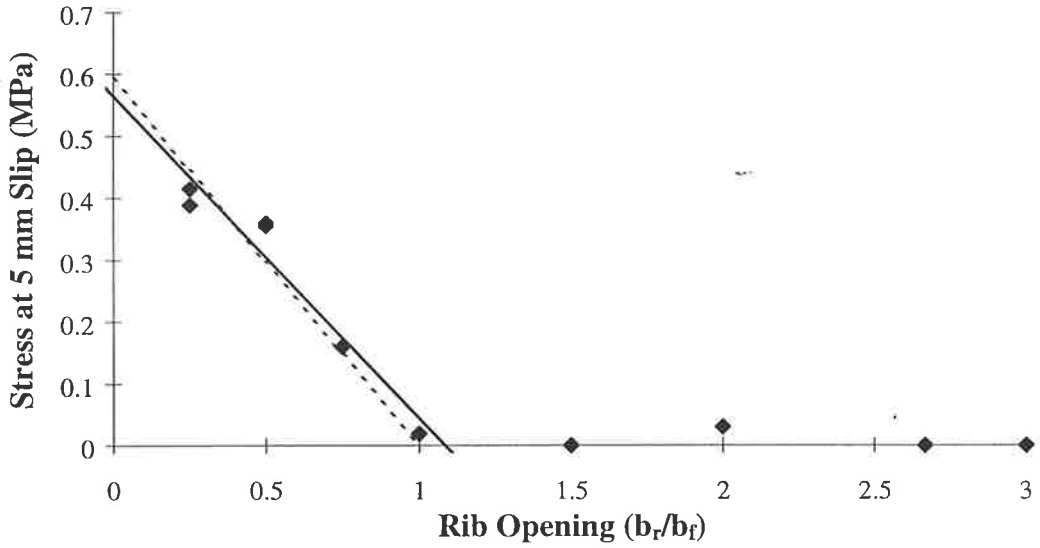


Fig. 3.48. Stress at 5 mm Slip vs Rib Opening for Series 1

The rapid reduction in strength can be seen in both these figures, with both regression lines reducing to zero at a rib opening of $b_r/b_f = 1.1$. The coefficients of determination are 0.90 and 0.93 for the residual bond strength and the stress at 5 mm slip, respectively. The coefficients of determination for the adjusted regression lines that pass through $b_r/b_f = 1$ are 0.86 and 0.90 for the residual bond strength and the stress at 5 mm slip, respectively. The change in the coefficients of determination is only slight for the adjusted regression lines, indicating that the lines still describe the data adequately. These figures indicate the inability of the non-embossed profiles to develop shear resistance when the rib geometry is not re-entrant. This finding will be discussed further in Section 3.5.

3.4.5 Series 2

A summary of the specimens used in Series 2 is shown in Table 3.7. The main parameter that was investigated in this series was the effect of embossments on the behaviour of the profiled sheeting. The overall arrangement of the embossments is shown in Fig. 3.49. For all of the specimens, the distance of the embossments from the outside and inside edges of the ribs remained constant at 20 mm. The average overall height of the embossments was 3.8 mm. A short description of each test is given in this section, along with the shear stress-slip curves for each specimen. A summary of results is given in Table 3.8 in Section 3.4.5.8.

A series of concrete test cylinders were prepared from the same concrete as the push specimens at the time of casting. These were tested at the same time as the push specimens and the results are given in Table 3.5. The sheeting used was the same as that used in Series 1. All the specimens were constructed from grade G2 galvanised sheeting, with a Total Coated Thickness of 1.00 mm, and a Base Metal Thickness of 0.98 mm. The individual units were cut to length using a guillotine, the embossments were pressed into the sheeting, and then the sheeting was folded to the required shape using a brake press. A typical stress-strain curve is shown in Fig. 3.35. The results for the values of the yield stress and ultimate stress are given in Table 3.5.

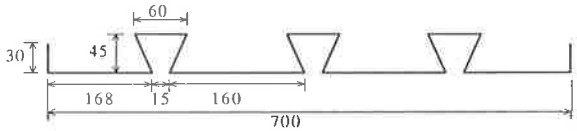
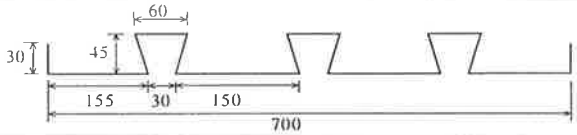
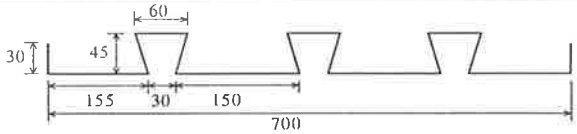
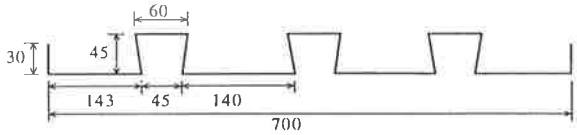
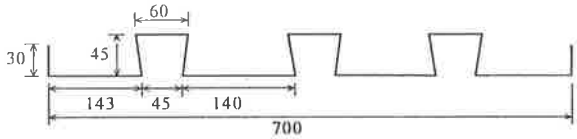
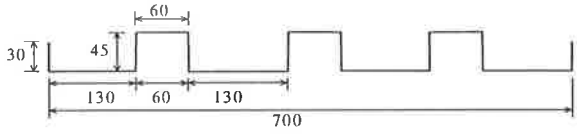
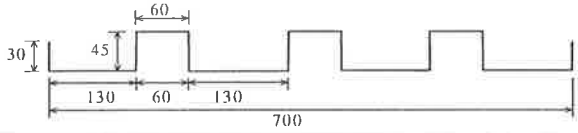
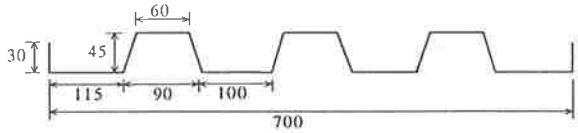
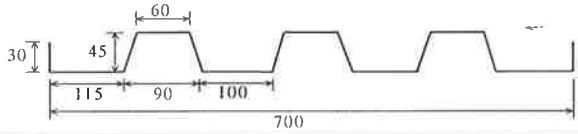
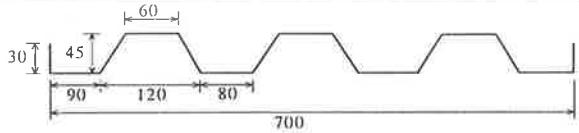
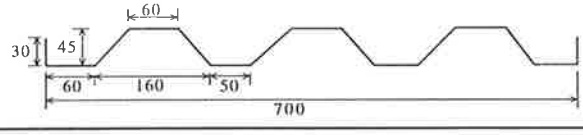
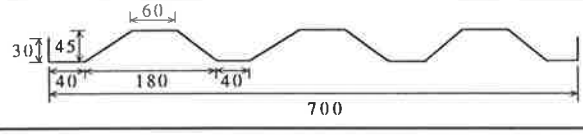
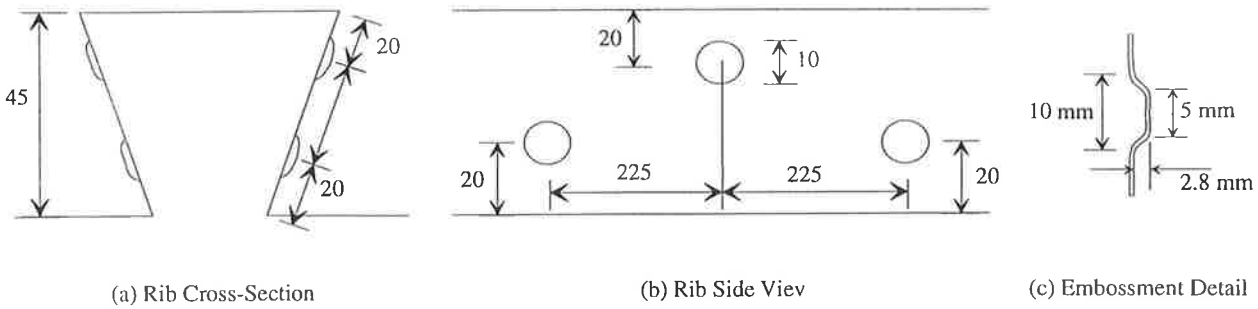
Specimen	Geometry	Embossments
PT2.1		Yes
PT2.2		Yes
PT2.3		No
PT2.4		Yes
PT2.5		No
PT2.6		Yes
PT2.7		No
PT2.8		Yes
PT2.9		No
PT2.10		Yes
PT2.11		Yes
PT2.12		Yes

Table 3.7. Series 2



(a) Rib Cross-Section (b) Rib Side View (c) Embossment Detail

Fig. 3.49. Detail of Embossments

3.4.5.1 Push Test PT2.1

The shear-stress / slip curve for this specimen is shown in Fig. 3.50. It is plotted with the result from PT1.1 which had the same geometry but did not have embossments on the sheeting. From this figure, it can be seen that the embossed and non-embossed sheets have significantly different behaviour after failure of the chemical bond. The chemical bond strength and the residual bond strength after failure of the chemical bond are similar for both specimens. After PT2.1 was reloaded, there was an increasing shear resistance with increasing slip, which was due to the concrete riding over the embossments. After a slip of 2.48 mm, the load began to decrease because the embossments had risen out of the depression in the concrete.

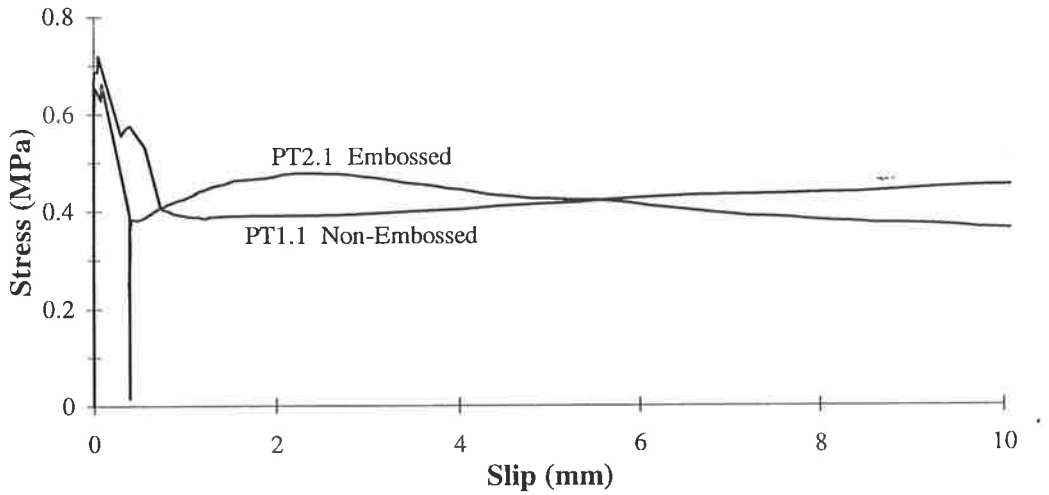
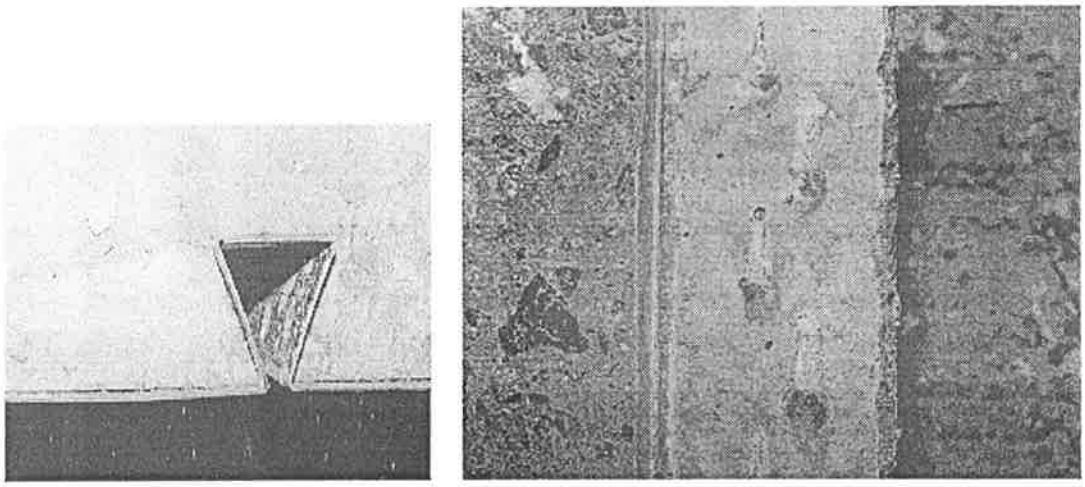


Fig. 3.50. Shear Stress vs Slip for PT2.1

The deformation that occurred in the sheeting due to the interaction between the concrete and the embossments is shown in Fig. 3.51a. It can be seen that the webs of the rib are forced inwards, whilst the flange of the rib remains undeformed. The sheeting between the ribs, or the *pan*, also bows outwards from the concrete, due to the deformation that occurs

in the rib. The scour in the concrete due to the movement of the embossments is shown in Fig. 3.51b.



(a) Rib Deformation (b) Concrete Scour

Fig. 3.51. Sheeting and Concrete After Testing of PT2.1

3.4.5.2 Push Test PT2.2 and PT2.3

These two specimens are identical except that PT2.2 was embossed, whereas PT2.3 was not embossed. The shear-stress / slip curves for PT2.2 and PT2.3 are shown in Fig. 3.52. The behaviour of these specimens is similar to that noted previously. For these two specimens the slip after the failure of the chemical bond is similar, whereas for all the other specimens, the slip is greater for the non-embossed specimen. There is no evident reason for this difference with these specimens. There is a rise in the mechanical shear resistance of PT2.2 to a maximum which occurs at a slip of 2.49 mm, after which there is a gradual decrease. The deformation in the ribs is shown in Fig. 3.53, where it can be seen that the sheeting is forced away from the concrete, due to the action of the concrete riding over the embossments. This movement is visible at the rib as well as in the sheeting pan between the ribs. There was plastic deformation of the rib which is shown in Fig. 3.54 by the residual deformation in the sheeting after removal of the concrete. The sheeting for specimen PT2.3 was reused from the first series. The shear stress-slip curve exhibits a gradual increase in the shear resistance with increasing slip, as for other non-embossed profiles.

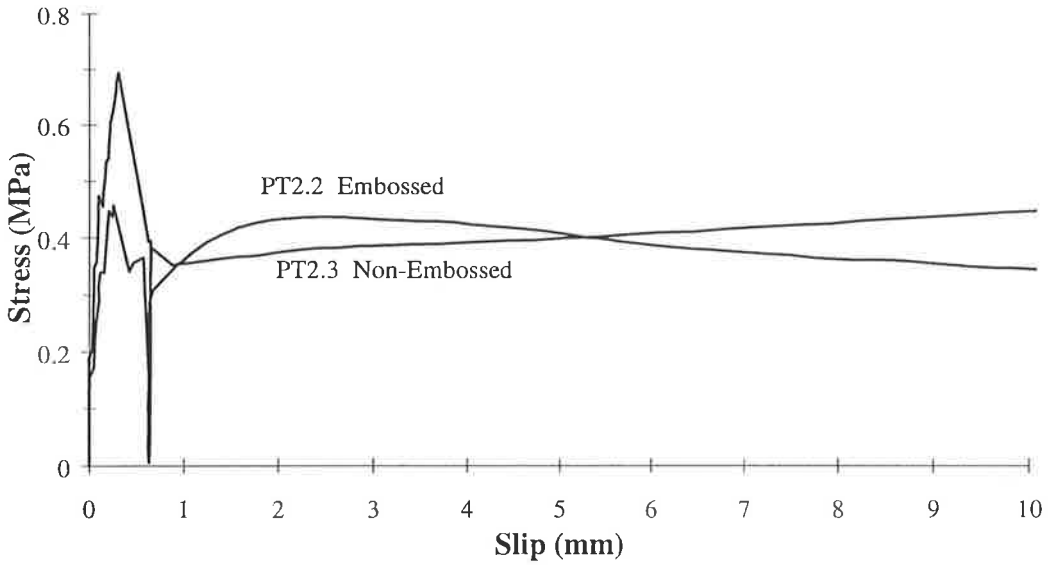


Fig. 3.52. Shear Stress vs Slip for PT2.2 and PT2.3

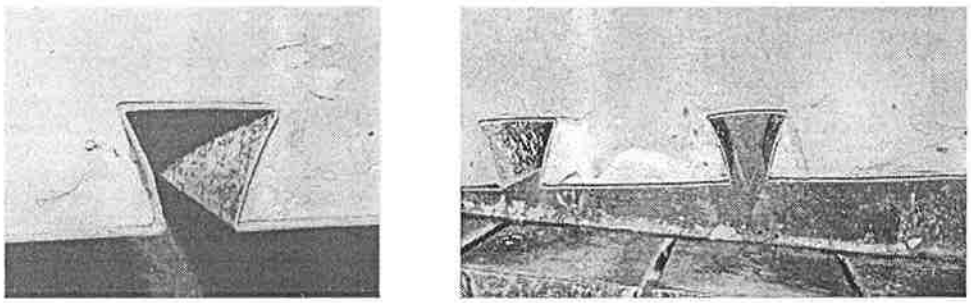
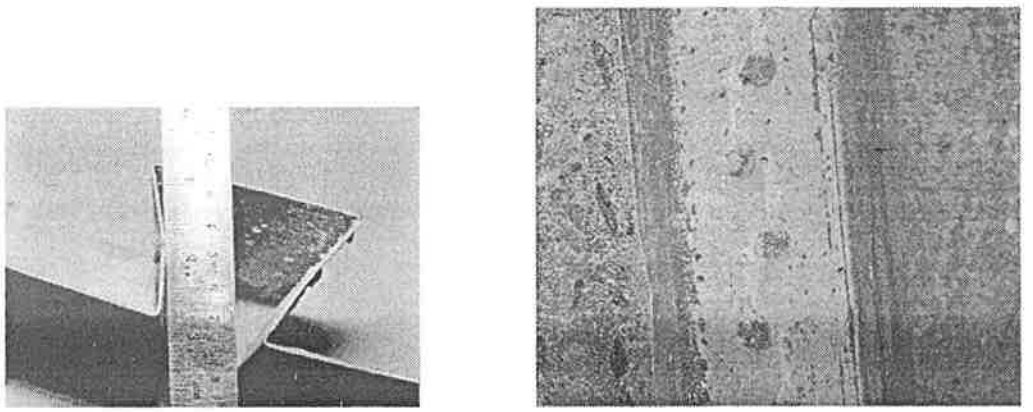


Fig. 3.53. Sheeting Deformation for PT2.2



(a) Rib Deformation (b) Concrete Scour

Fig. 3.54. Specimen PT2.2 after Testing

3.4.5.3 Push Test PT2.4 and PT2.5

The shear stress-slip curves for these specimens is shown in Fig. 3.55. The same general trends can be seen as were noticed for the previous tests. The deformed shape of the sheeting at the conclusion of the test for PT2.4 is shown in Fig. 3.56a, and the concrete surface is shown in Fig. 3.56b. The slip after failure of the chemical bond for specimen PT2.5 is much larger than for PT2.4. This may be attributable to the gradual breakdown in the chemical bond, rather than a sudden complete failure. This is evidenced by the series of spikes in the stress-slip curve.

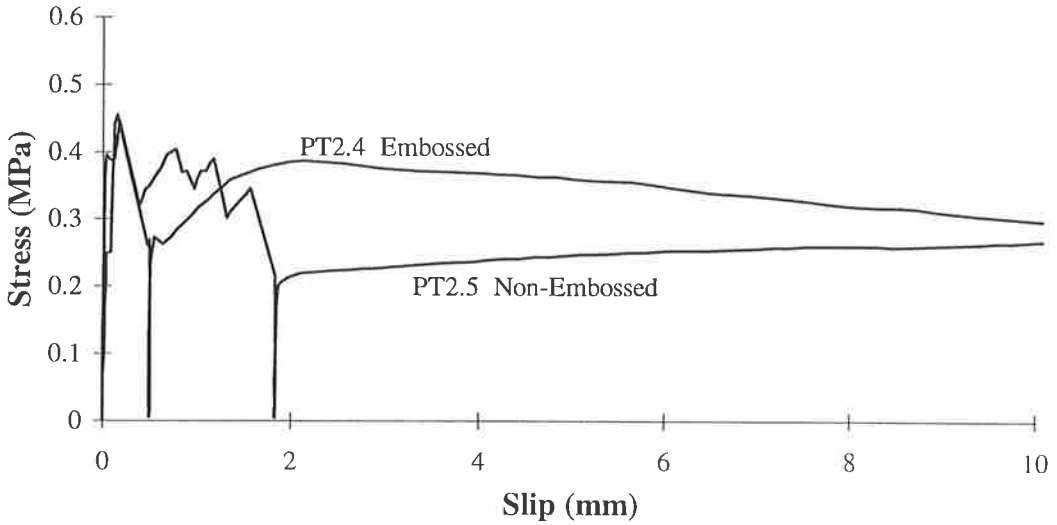
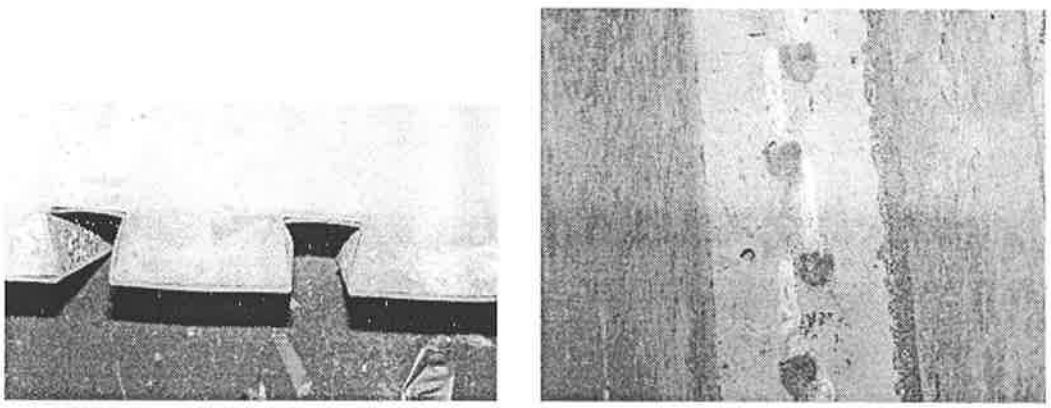


Fig. 3.55. Shear Stress vs Slip for PT2.4 and PT2.5



(a) Rib Deformation (b) Concrete Scour

Fig. 3.56. Sheeting and Concrete after Testing PT2.4

3.4.5.4 Push Test PT2.6 and PT2.7

The shear stress-slip curves for the two specimens are shown in Fig. 3.57. This shows the large increase in the shear strength that occurs with the presence of the embossments, over the same geometry profile without embossments. This increase is much larger than for any of the previous profiles, which have a re-entrant rib geometry. These two specimens have a 'square' rib, and represent the transition between re-entrant ribs and open ribs. The final deformed shape of the sheeting for PT2.6 is shown in Fig. 3.58a, and the concrete surface is shown in Fig. 3.58b.

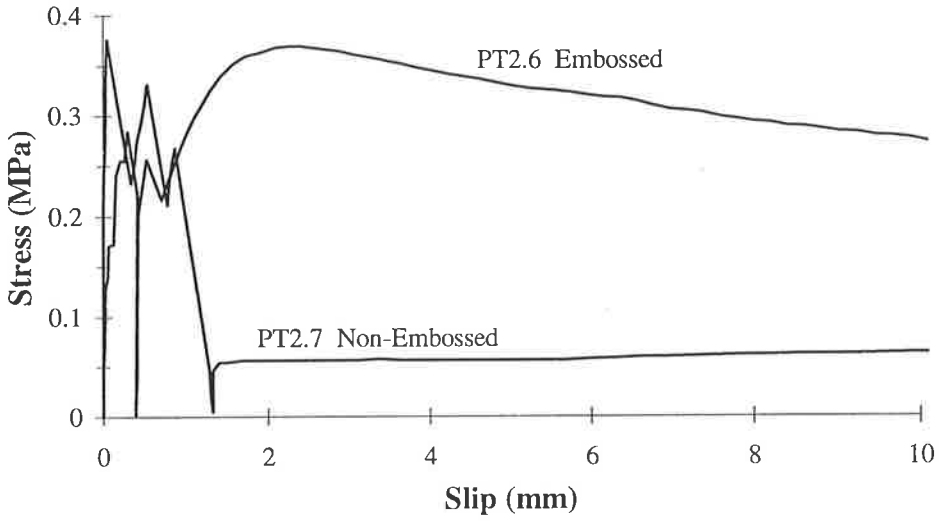
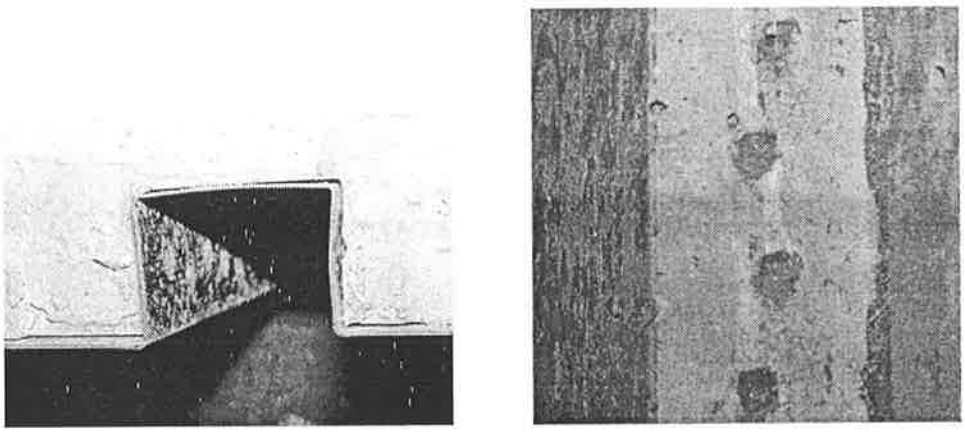


Fig. 3.57. Shear Stress vs Slip for PT2.6 and PT2.7



(a) Rib Deformation (b) Concrete Scour

Fig. 3.58. Sheeting and Concrete after Testing PT2.6

3.4.5.5 Push Test PT2.8 and PT2.9

The resulting shear stress-slip curves for the two specimens are shown in Fig. 3.59. It can be seen that the non-embossed specimen has negligible strength in comparison to the embossed specimen. Fig. 3.60 shows the sheeting and the concrete surface at the completion of PT2.8. The large lateral movement of the sheeting away from the concrete can be seen in Fig. 3.60a. After the failure of the chemical bond in PT2.9, the mechanical shear resistance was almost zero. The test was terminated after a slip of 4 mm. Fig. 3.61 shows the sheeting for PT2.9 at the completion of the test. It can be seen that the sheeting has moved away from the concrete in a similar manner to the embossed sheeting shown in Fig. 3.60a.

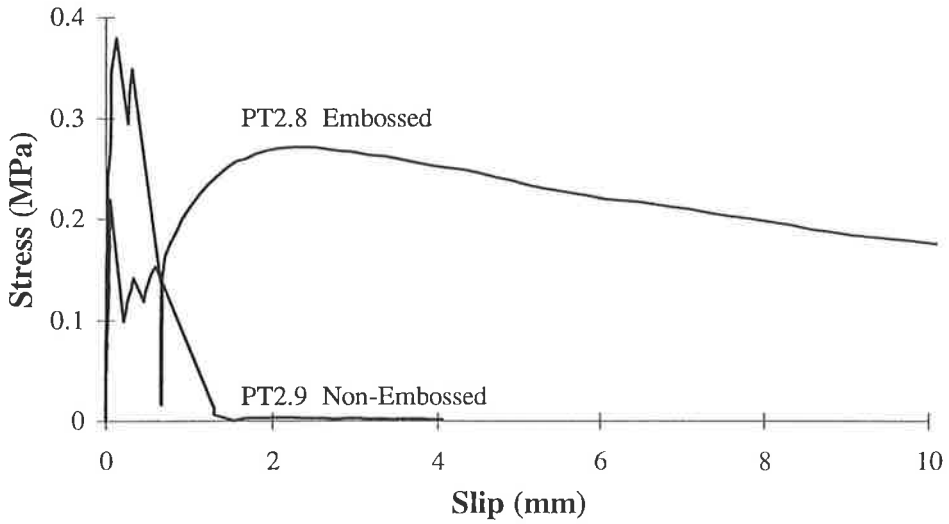
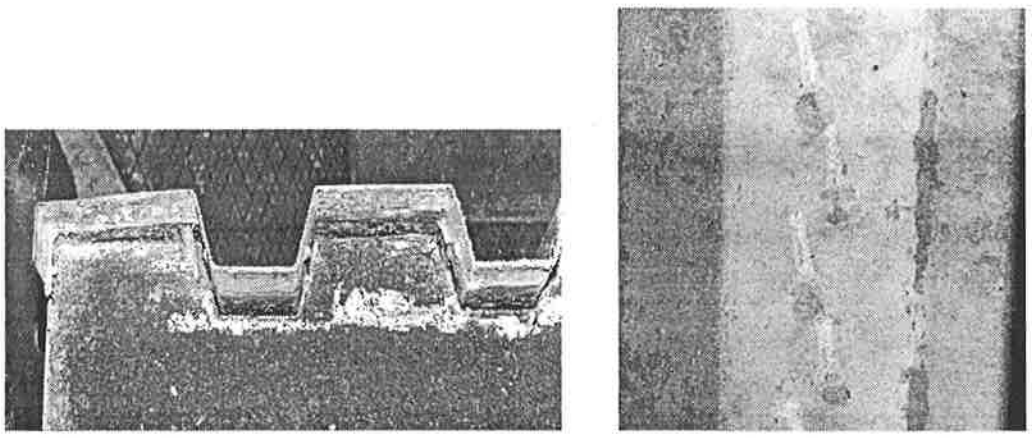


Fig. 3.59. Shear Stress vs Slip for PT2.8 and PT2.9



(a) Rib Deformation **(b) Concrete Scour**

Fig. 3.60. Sheeting and Concrete after Testing PT2.8

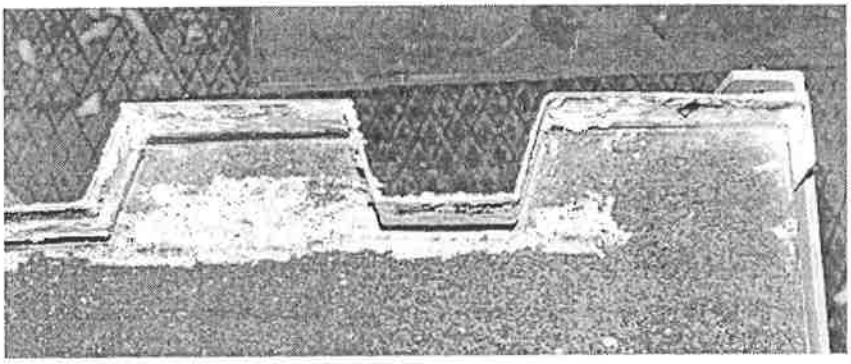


Fig. 3.61. Sheeting for Specimen PT2.9

3.4.5.6 Push Test PT2.10

The shear stress-slip curve is shown in Fig. 3.62, with the curve from PT1.8, which had the same geometry but without embossments. Again, the increase with the use of the embossments is clearly seen. The sheeting for PT2.10 moved laterally away from the concrete during the test in a similar manner as shown previously in Fig. 3.60a. The concrete surface after the test is shown in Fig. 3.63, and indicates that the amount of scour is much less than for the previous tests. This is because of the more open rib geometry, and the lateral forces developed at the embossment can not be resisted by any 'keying' action of the rib, thus forcing the sheeting outward.

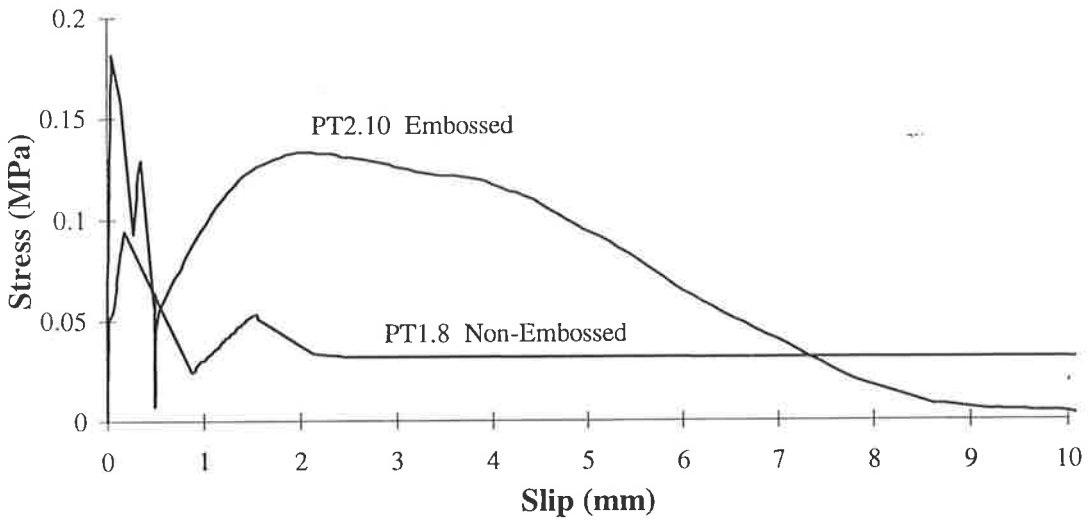


Fig. 3.62. Shear Stress vs Slip for PT2.10 and PT1.8



Fig. 3.63. Concrete after Testing PT2.10

3.4.5.7 Push Test PT2.11 and PT2.12

The shear stress-slip curves for the two specimens are shown in Fig. 3.64. Specimen PT2.11 failed at a slip of 7.4 mm, due to excessive lateral movement of the sheeting. A change was made in the setup procedure for PT2.12, in which the rollers were removed from the supports before testing. The increase in the mechanical shear resistance can be seen in Fig. 3.64, despite the more open rib geometry. This increase in shear resistance goes against the trend of decreasing shear resistance with increasing rib opening, and can be directly attributable to the change in support conditions. This result indicates that push tests which introduce additional lateral restraint to the sheeting will overestimate the bond strength.

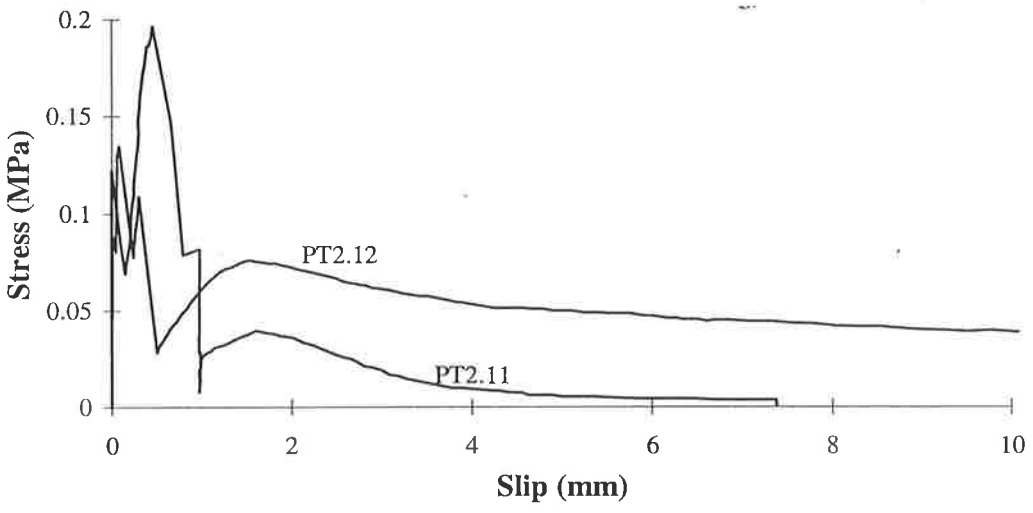


Fig. 3.64. Shear Stress vs Slip for PT2.11 and PT2.12

The concrete surface after removal of the sheeting is shown in Fig. 3.66 for the two specimens. It can be seen that the scour in PT2.12 is greater than in PT2.11, but that the amount of scour in PT2.12 decreases higher up the specimen. This variation in scour is due to the restraint that occurred at the bottom of the specimen, but was not present at the top.

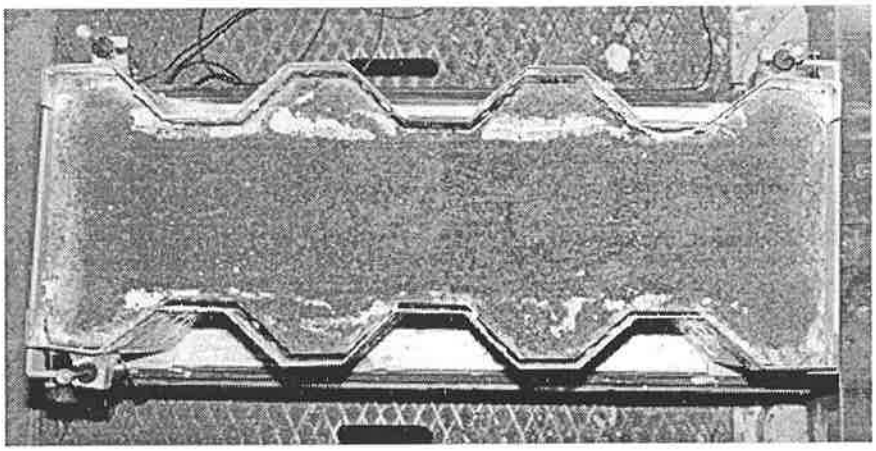
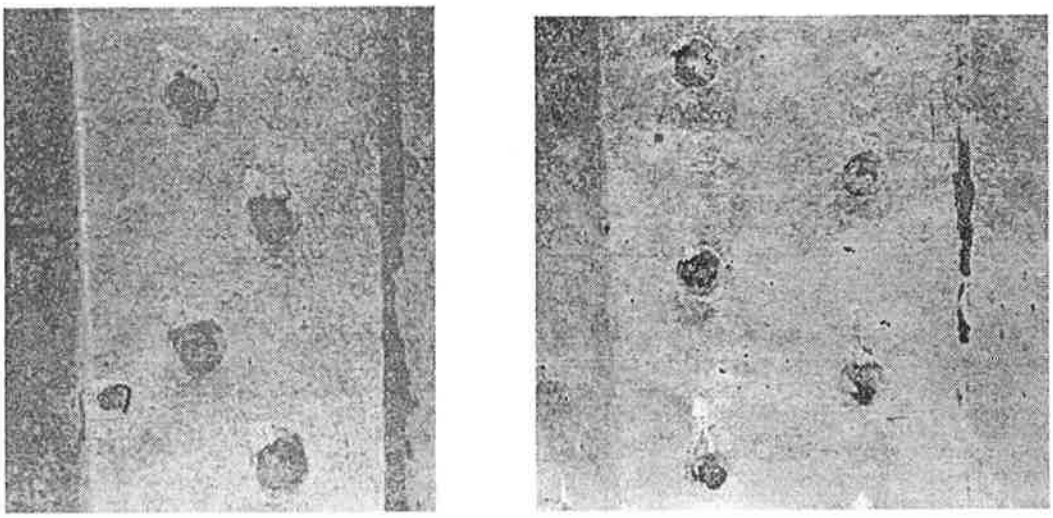


Fig. 3.65. Specimen PT2.11 after Testing



(a) PT2.11 (b) PT2.12

Fig. 3.66. Concrete after Testing PT2.11

3.4.5.8 Summary of Series 2

A summary of the results for Series 2 is presented in Table 3.8. The different properties that were measured for each of the tests were: the chemical bond strength (based on the total contact area between the sheeting and the concrete); the residual bond strength after failure of

the chemical bond; the maximum mechanical bond strength; the slip at which this maximum occurred, and the mechanical bond stress at a slip of 5.0 mm. The maximum mechanical bond strength and the slip at which it occurred were recorded only for the embossed specimens, as the results are not relevant for the non-embossed specimens, due to the continual rise in shear resistance throughout the test. The results have been plotted against the rib opening, which has been non-dimensionalised by dividing by the width of the rib flange b_f in Fig. 3.34.

Specimen	Rib Opening (b_r/b_f)	Chemical Bond Stress (MPa) (Total Contact Area)	Residual Bond Stress (MPa)	Max Mechanical Bond Stress (MPa)	Slip at Max Load (mm)	Bond Stress at 5 mm Slip (MPa)
PT2.1	0.25	0.192	0.384	0.477	2.48	0.425
PT2.2	0.5	0.187	0.306	0.438	2.49	0.409
PT2.3	0.5	0.284	0.376	-	-	0.401
PT2.4	0.75	0.190	0.260	0.387	2.15	0.362
PT2.5	0.75	0.187	0.204	-	-	0.246
PT2.6	1.0	0.161	0.167	0.369	2.39	0.331
PT2.7	1.0	0.164	0.056	-	-	0.057
PT2.8	1.5	0.185	0.161	0.272	2.41	0.237
PT2.9	1.5	0.107	0.003	-	-	0.000
PT2.10	2.0	0.102	0.050	0.134	2.12	0.098
PT2.11	2.67	0.134	0.019	0.039	1.60	0.005
PT2.12	3.0	0.100	0.028	0.076	1.56	0.050

Table 3.8. Summary of Series 2

The shear-stress / slip curves for the embossed and non-embossed specimens are shown in Fig. 3.67 and Fig. 3.68 respectively. These figures show the variation in shear strength with increasing rib opening. The trend towards lower shear resistance is evident from these figures. It can also be seen in Fig. 3.67 that the form of the stress-slip curves are similar, but the magnitudes of the shear strength decreases with increasing rib opening. Figure 3.68 indicates the change in behaviour of the non-embossed profiles with increasing rib opening. It can be seen that for those profiles with a strongly re-entrant shape that the shear stress increases significantly with increasing slip, while for those profiles with an open rib geometry, the increase in shear stress is negligible.

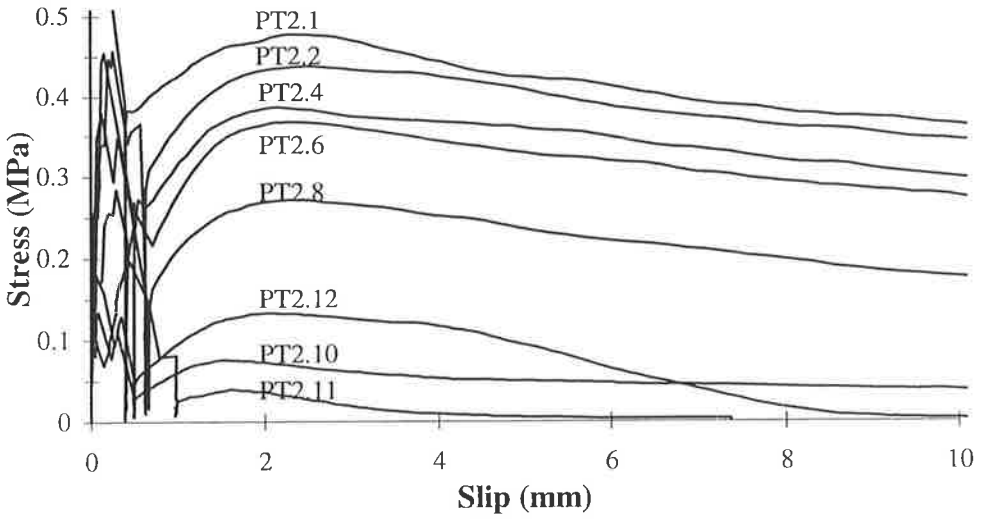


Fig. 3.67. Summary of Embossed Specimens for Series 2

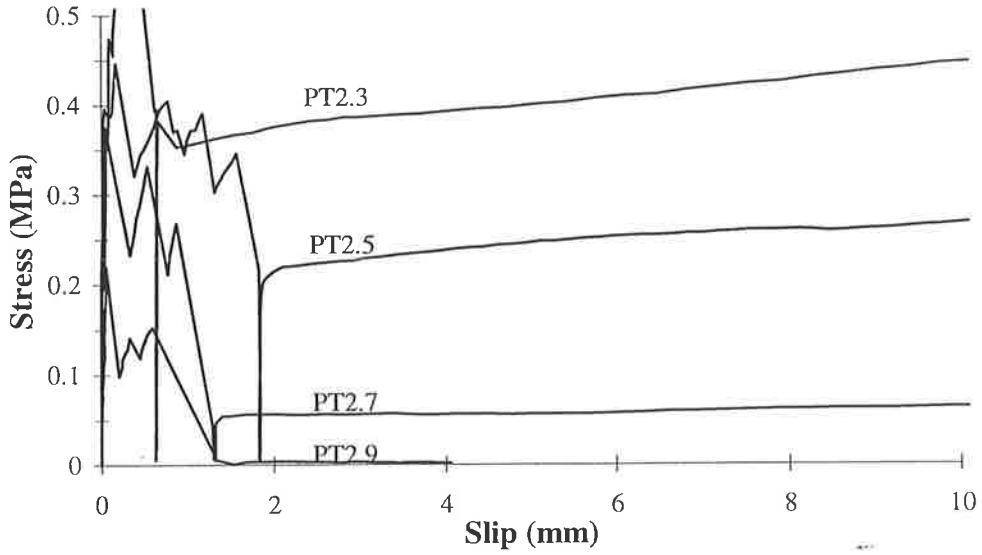


Fig. 3.68. Summary of Non-Embossed Specimens for Series 2

The non-embossed specimens exhibit a similar behaviour to that noted in Series 1, with a gradual increase in shear resistance, after failure of the chemical bond, with increasing slip. This behaviour is not exhibited by the embossed sheets due to the interaction between the embossments and the concrete. As the embossments ride over the concrete, they force the sheeting away from the concrete, and thus do not allow for the increased roughness which occurred in the non-embossed specimens.

The variation in the chemical bond strength with rib opening is shown in Fig. 3.69. This figure indicates a reduction in the chemical bond strength as rib opening increases. This was also noted in Series 1, as discussed in Section 3.4.4.7. This result is due to the brittle nature of the chemical bond, which after failure has commenced at one location of the interface, the breakdown of the bond propagates rapidly across the entire interface. Thus, failure of the chemical bond is more of a peeling action, which accounts for the reduction in the chemical bond strength with increasing rib opening.

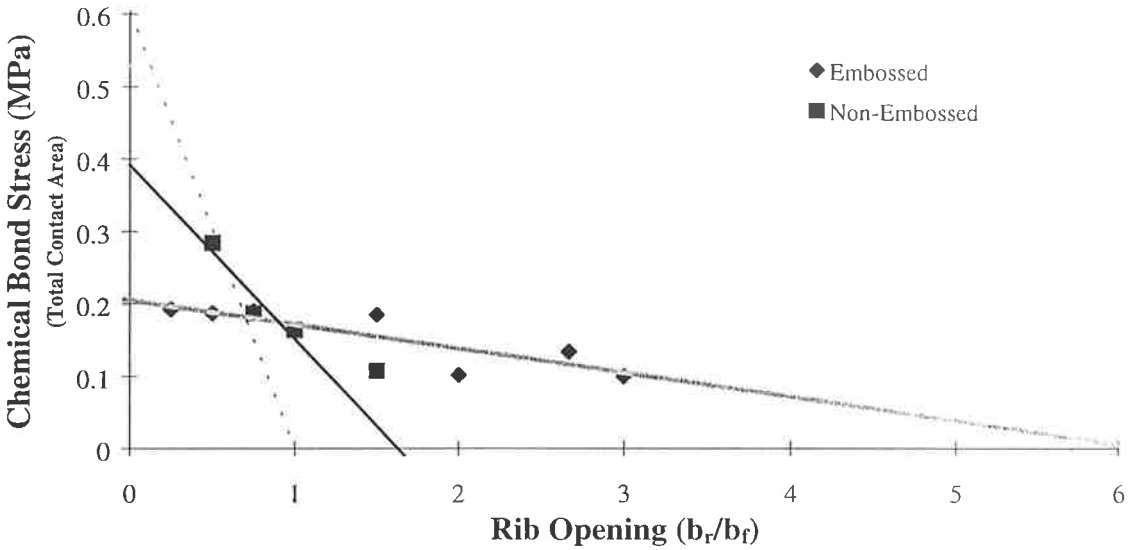


Fig. 3.69. Chemical Bond Stress vs Rib Opening for Series 2

Also shown in Fig. 3.69 are several regression lines. The thick shaded line is the regression line for the embossed profiles, the thin solid line is the regression line for the non-embossed profiles, and the broken line is the adjusted regression line for the non-embossed profiles and passing through $b_r/b_f = 1$. The difference in behaviour between the embossed and non-embossed profiles is evident. This difference would not be expected if the chemical bond strength alone was able to be tested, and indicates the influence of a peeling action. For profiles with a more open rib geometry, the presence of the embossments tends to inhibit the progress of the chemical bond failure, and thus leads to a higher chemical bond strength. The coefficients of determination of the unadjusted and adjusted regression lines through the non-embossed profiles are 0.89 and -2.50 respectively. The negative value for the coefficient of determination for the adjusted regression line indicates a poor correlation with the test data. The regression line for the embossed sheeting has a coefficient of determination of 0.74, and intercepts the abscissa at a value of $b_r/b_f = 6.1$.

The variation in residual bond stress after failure of the chemical bond is shown in Fig. 3.70. This indicates a decrease in the residual bond stress for both the embossed and the non-embossed profiles. However, the embossed profiles maintain a small residual stress for large rib openings, whereas the non-embossed profiles tend to zero residual bond strength for profiles with $b_r/b_f > 1$. The regression lines are again shown, and clearly indicate the different trends of the embossed and non-embossed profiles. The residual bond strength tends to zero at a value of $b_r/b_f = 1.1$ for the non-embossed sheeting, and 2.8 for the embossed sheeting. The intercept of the regression lines with the ordinate axis are 0.69 and 0.36 for the non-embossed and the embossed profiles respectively.

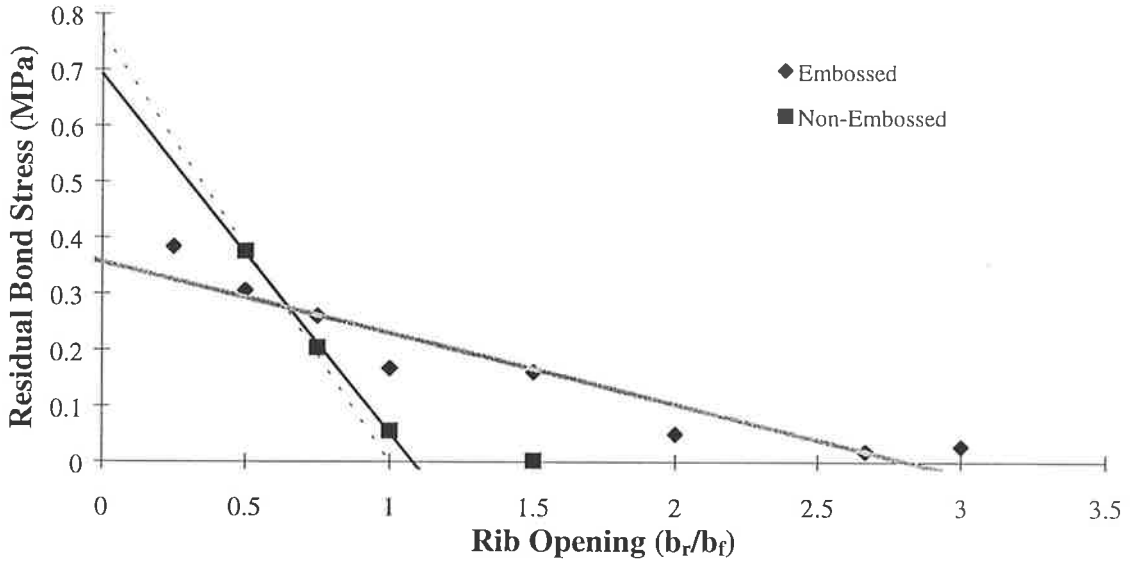


Fig. 3.70. Residual Bond Stress vs Rib Opening for Series 2

The variation in the bond stress at a slip of 5 mm is shown in Fig. 3.71. It can be seen that embossments have a much larger effect as the rib opening increases, and virtually no effect at small rib openings. The regression lines are shown for the embossed and non-embossed profiles, as well as the adjusted regression line for the non-embossed profiles that passes through $b_r/b_f = 1$. The stress at 5 mm slip tends to zero at a value of $b_r/b_f = 1.1$ for the non-embossed profiles and 2.9 for the embossed profiles. The intercept of the regression lines with the ordinate axis are 0.75 and 0.48 for the non-embossed and the embossed profiles respectively.

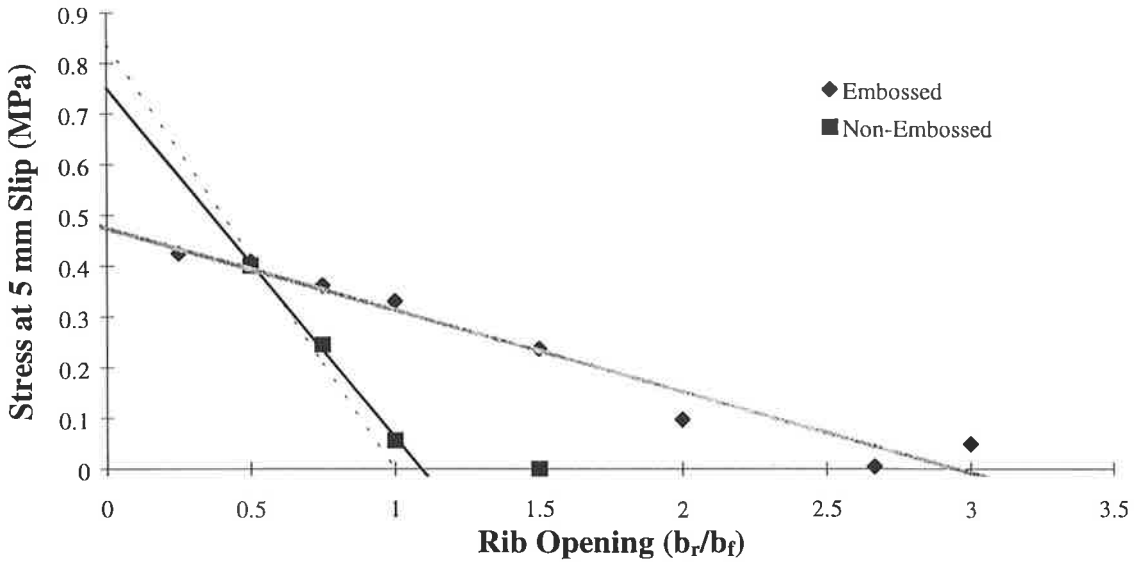


Fig. 3.71. Stress at 5 mm Slip vs Rib Opening for Series 2

The variation in maximum mechanical bond strength with rib opening is shown in Fig. 3.72. This shows the variation in mechanical shear strength to vary almost linearly with rib opening. The maximum mechanical strength tends to zero at a value of $b_r/b_f = 1.1$ for the non-embossed profiles and 3.1 for the embossed profiles. The intercept of the regression lines with the ordinate axis are 0.75 and 0.51 for the non-embossed and the embossed profiles respectively.

The variation in slip at which the maximum load was recorded is shown in Fig. 3.73. This indicates that the slip at the maximum load remains relatively constant at approximately 2.3 mm for rib openings up to $b_r/b_f = 1.5$, after which there is a slight reduction. The diameter of the embossments is 10 mm, as shown in Fig. 3.49c, and the distance from the commencement of the embossment to the highest part is approximately 2.5 mm. Thus the slip at which the maximum mechanical resistance occurs corresponds to the distance taken for the embossment to displace sufficiently to be clear from the depression in the concrete, as shown in Fig. 3.74.

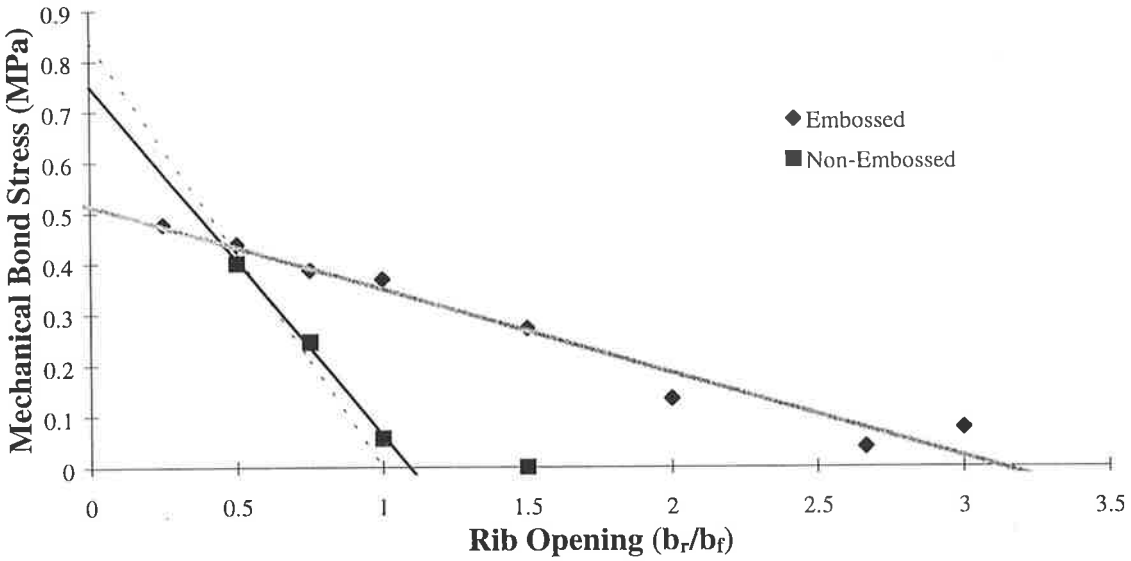


Fig. 3.72. Mechanical Bond Stress vs Opening for Series 2

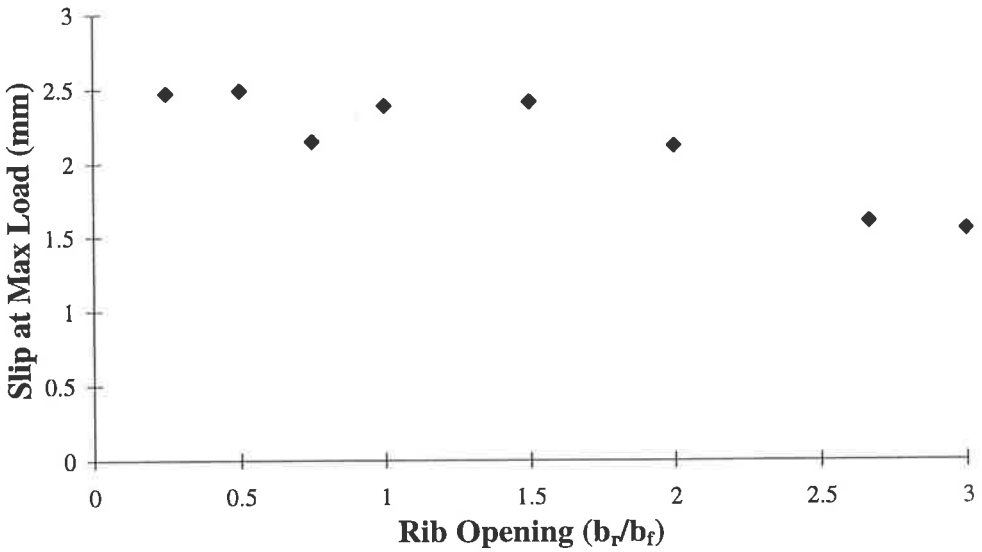


Fig. 3.73. Slip at Max Load vs Opening for Series 2

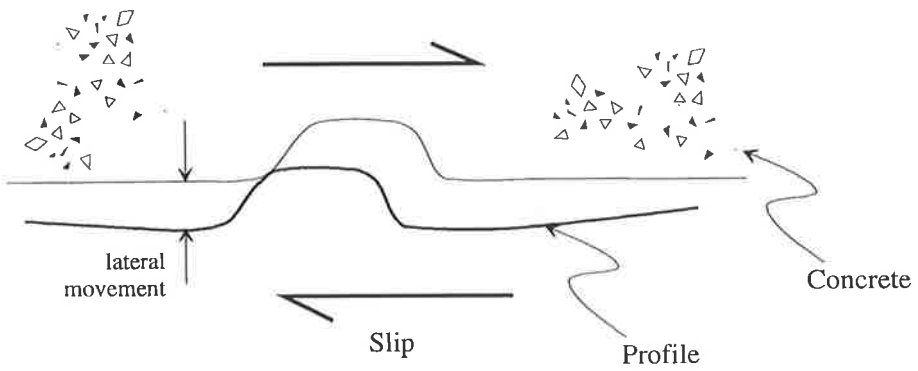


Fig. 3.74. Movement of Profiled Sheeting

An important point of note from all of the embossed tests, is that there is always some deformation in the sheeting which is external to the ribs. This deformation forces the sheeting away from the concrete. Even for the re-entrant rib geometries, the deformation in the ribs causes a corresponding deformation in the adjoining steel elements. This is shown in Fig. 3.75, where external deformation is shown at point B. This result has important implications in the design of the push test, and indicates that the application of an external lateral load will restrict the free deformation of the sheeting external to the ribs, and thus increase the shear strength of the sheeting.

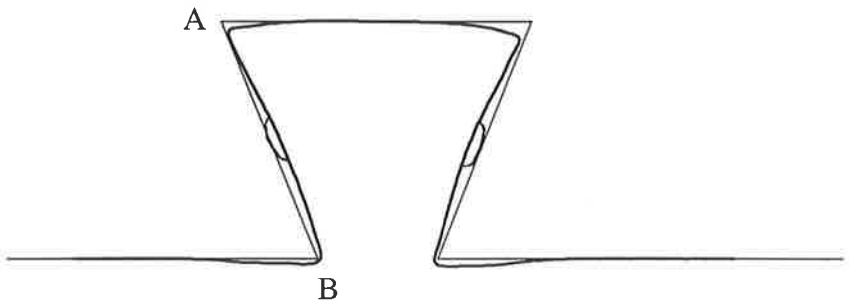


Fig. 3.75. Profile Deformations

3.4.6 Series 3

This series was carried out in order to investigate the effect of sheeting thickness of the shear resistance of profiled sheeting. A range of sheeting thicknesses were used from 0.6 mm to 2.0 mm. These values were thought to represent lower and upper limits to the possible thickness of sheeting used in composite members. The surface condition of the sheeting was varied for some of the specimens by coating with a debonding agent. All specimens were made with embossed sheeting, with the layout of the embossments shown in Fig. 3.49. Embossments were incorporated in each of the specimens as it was expected that the effect of varying the sheeting thickness would be greatest when embossments were present. This is due to the increased spring action that develops as the sheeting is forced away from the concrete during slip, as shown in Fig. 3.75. A summary of the sheeting used for this series is shown in Table 3.9. A short description of each test is given in this section, along with the shear-stress / slip curves for each specimen. A summary of results is given in Table 3.10 in Section 3.4.6.8.

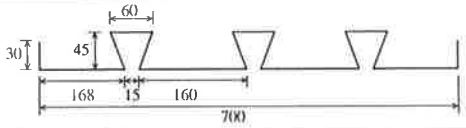
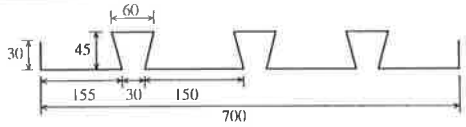
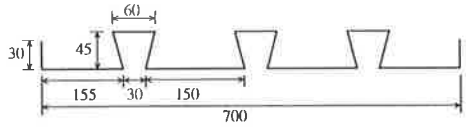
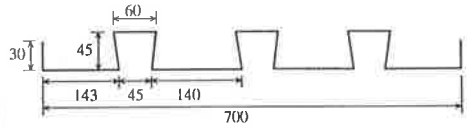
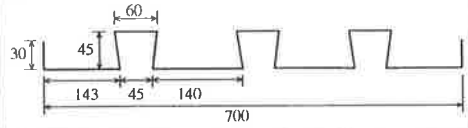
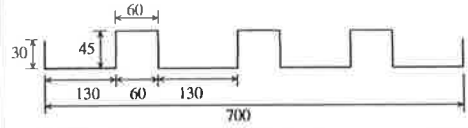
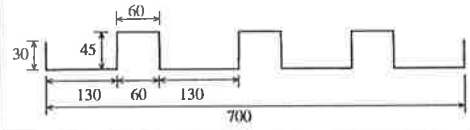
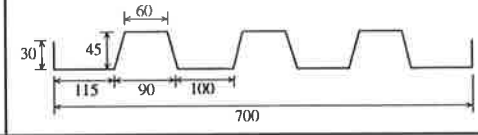
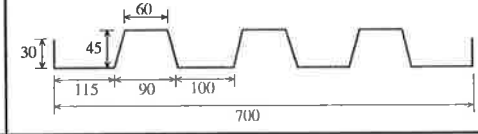
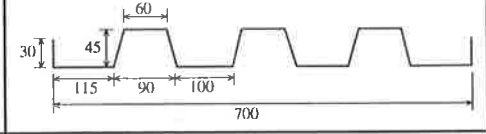
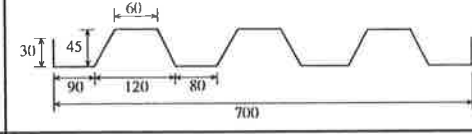
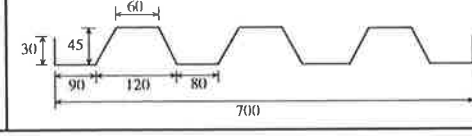
Specimen	Profile Cross-Section	Thickness (mm)	Surface Condition
PT3.1		0.6	Non-Greased
PT3.2		0.6	Non-Greased
PT3.3		0.6	Greased
PT3.4		0.6	Non-Greased
PT3.5		0.6	Greased
PT3.6		0.6	Non-Greased
PT3.7		2.0	Non-Greased
PT3.8		0.6	Non-Greased
PT3.9		0.6	Greased
PT3.10		2.0	Non-Greased
PT3.11		0.6	Non-Greased
PT3.12		2.0	Non-Greased

Table 3.9. Series 3

There were some slight variations in the geometry of the ribs from the nominal dimensions given in Table 3.9. These variations were due to the method of constructing the profiles in the brake press, and were greater for the 0.6 mm sheeting than for the 1.0 mm or 2.0 mm sheeting. The measured dimensions were within ±1.0 mm of the nominal dimensions, but the variations produced more scatter for the 0.6 mm sheeting than for either the 1.0 mm or 2.0 mm specimens. This variation is discussed further in Section 3.5.

A series of concrete test cylinders were prepared from the same concrete as the push specimens at the time of casting. These were tested at the same time as the push specimens and the results are given in Table 3.5 on page 146. The sheeting used was constructed from grade G2 galvanised sheeting, and was the same material as that used in Series 1. The individual units were cut to length using a guillotine, the embossments were pressed into the sheeting, and then the sheeting was folded to the required shape using a brake press. A typical stress-strain curve is shown in Fig. 3.35 on page 146. The results for the values of the yield stress and ultimate stress are given in Table 3.5.

3.4.6.1 Push Test PT3.1

The shear-stress / slip curve for this specimen is shown in Fig. 3.76 and is plotted with the result from PT2.1 as a comparison. This specimen was constructed in the same manner as PT2.1, except that the sheeting was 0.6 mm thick. The rise in mechanical shear resistance with increasing slip, after failure of the chemical bond, is not as pronounced as for the thicker specimen. The final deformed shape of the sheeting is shown in Fig. 3.77a. The scour of the concrete due to the embossments was constant throughout the height of the specimen, and is shown in Fig. 3.77b. This constant scour indicates that all the embossments were effective in resisting shear.

The difference in the behaviour of the two specimens can be directly attributed to the difference in the thickness of the sheeting. The thicker sheeting is able to develop a greater resistance to the outward forces which develop as the embossments bear against the concrete, as shown in Fig. 3.75. The increase in thickness of the sheeting creates a greater spring action, and thus results in a higher shear resistance.

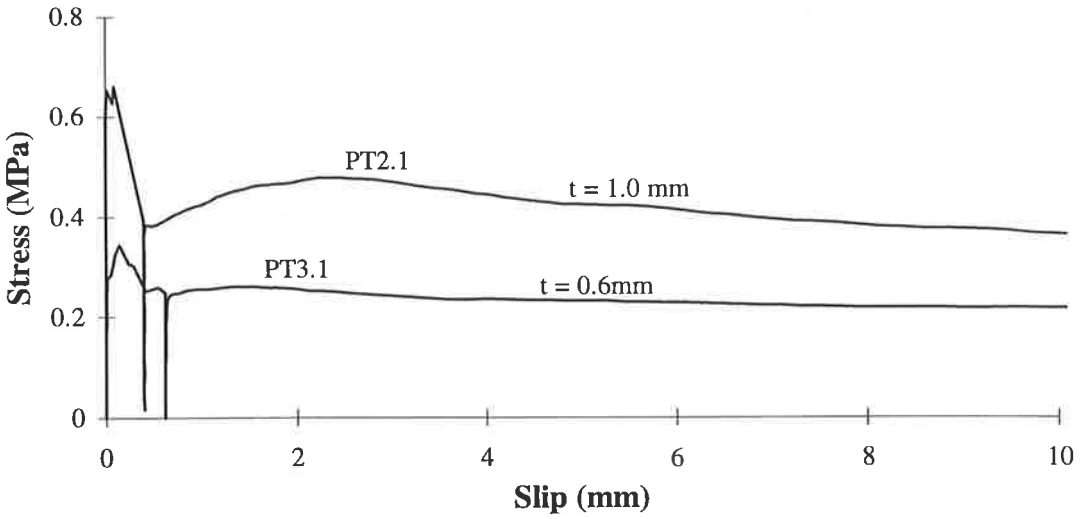
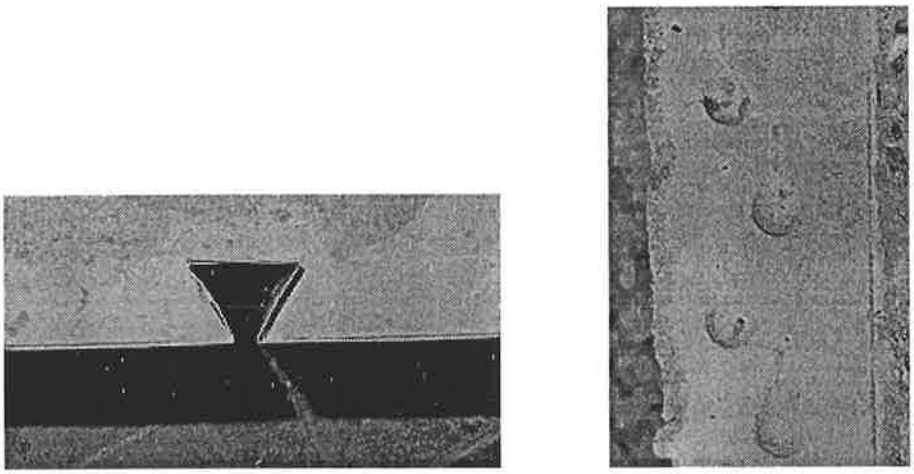


Fig. 3.76. Shear Stress vs Slip Curve for PT3.1 and PT2.1



(a) Rib Deformation (b) Concrete Scour

Fig. 3.77. Specimen PT3.1 after testing

3.4.6.2 Push Test PT3.2 and PT3.3

The shear stress slip curves for PT3.2 and PT3.3 are shown in Fig. 3.78. These two specimens had a similar geometry, except that the sheeting for PT3.3 was coated with a debonding agent before pouring. The difference in the response between the greased and the non-greased specimen is evident from this figure. The maximum mechanical shear stress is reduced, and the slip at which the maximum occurs is much larger for the greased specimen. The sudden decrease in strength at the failure of the chemical bond in the non-greased specimen does not occurs for the greased specimen, indicating that the chemical bond has

been successfully eliminated by the debonding agent. However, as indicated by the reduced shear capacity after failure of the chemical bond, the passive frictional effect is also considerably reduced. This effect was not anticipated, and indicates that the debonding agent also acted as a lubricant, and tended to reduce the internal frictional resistance that develops due to the spring action of the profile.

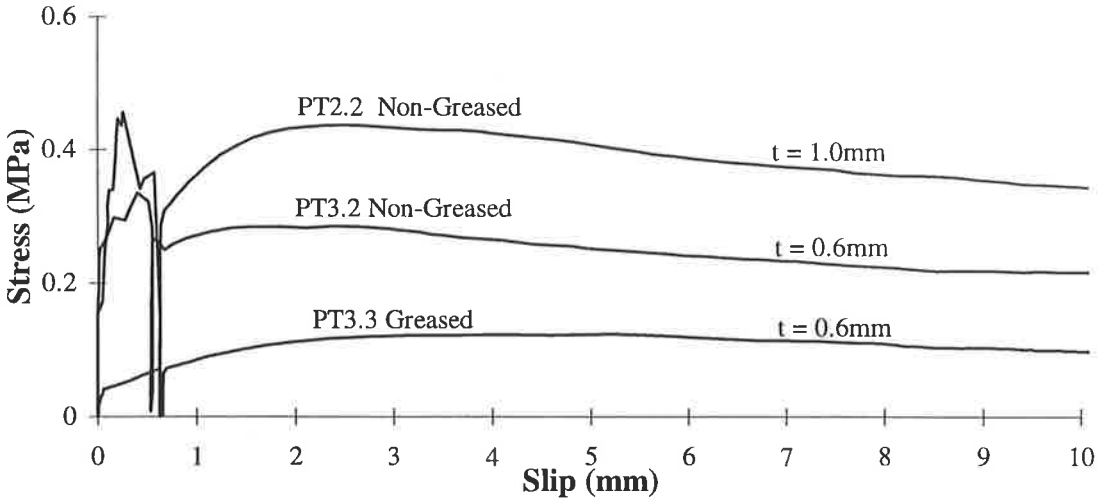
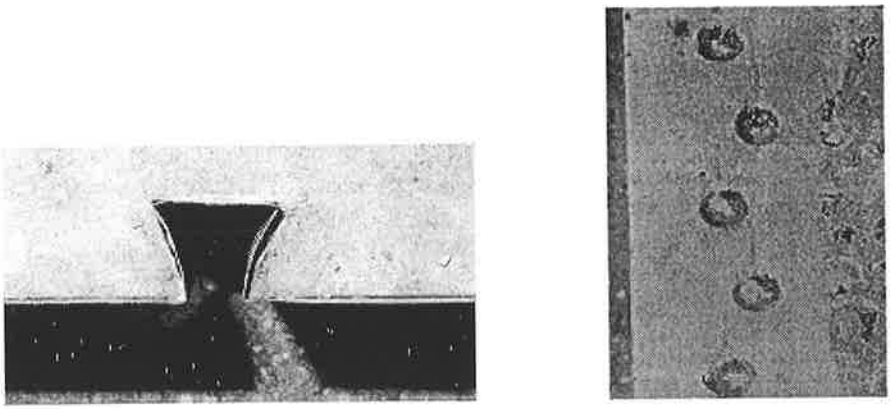


Fig. 3.78. Shear Stress vs Slip Curve for PT3.2 and PT3.3

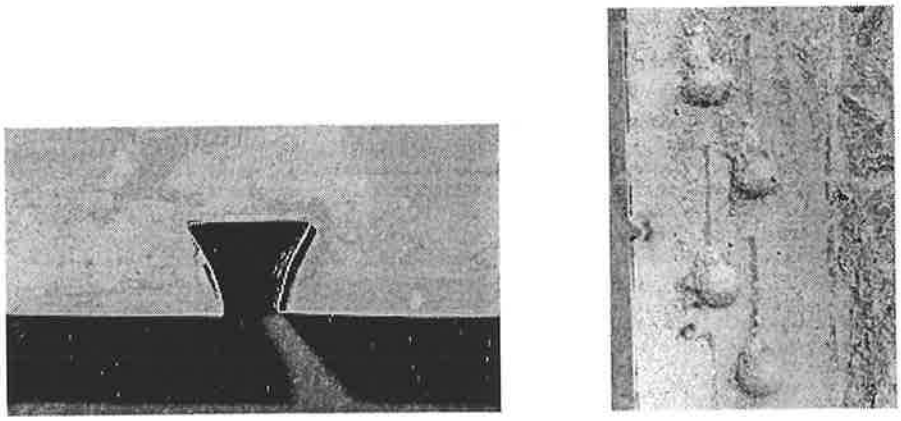
Also shown in Fig. 3.78 is the shear-stress / slip curve for PT2.2, which had the same geometry as both PT3.2 and PT3.3, and also included embossments, but was constructed from 1.0 mm sheeting. The increase in the shear resistance can be seen when comparing the similar non-greased specimens of different thickness. A similar increase was noted for the previous specimens.

The bottom surface of the sheeting for PT3.2 did not sit evenly in the base supports when the specimen was prepared for testing, and as a result the sheeting was not bearing against the supports along its full length. This unevenness was accommodated by the bedding paste, except at the ribs where the paste was removed. The gap which occurred at some of the ribs, between the sheeting and the support, was approximately 2 mm and did not vary throughout the test. The gap appeared to have no effect on the result. The final deformed shape of the specimen and the concrete surface are shown in Fig. 3.79. The scour marks are vertical, indicating that there was no lateral movement of the sheeting.



(a) Rib Deformation (b) Concrete Scour

Fig. 3.79. Specimen PT3.2 after testing



(a) Rib Deformation (b) Concrete Scour

Fig. 3.80. Specimen PT3.3 after testing

The final deformed shape of the sheeting and the concrete surface of specimen PT3.3 are shown in Fig. 3.80. From a comparison between Fig. 3.80b and Fig. 3.79b, it can be seen that the concrete surface of PT3.3 is less smooth and less regular than that for PT3.2, and the concrete surrounding the embossments is less dense. This difference is due to the debonding agent and led to the decrease in mechanical shear strength of the specimen.

3.4.6.3 Push Test PT3.4 and PT3.5

These two specimens were identical except that the sheeting of PT3.5 was treated with the debonding agent, whereas PT3.4 was untreated. The shear-stress / slip curves for these two specimens are shown in Fig. 3.81. The same trend as was observed for PT3.2 and PT3.3 can be seen here also. The maximum mechanical shear stress is less and the slip at maximum load is larger for the greased specimen. This again can be directly attributed to the action of the debonding agent in reducing the passive frictional component of the shear resistance.

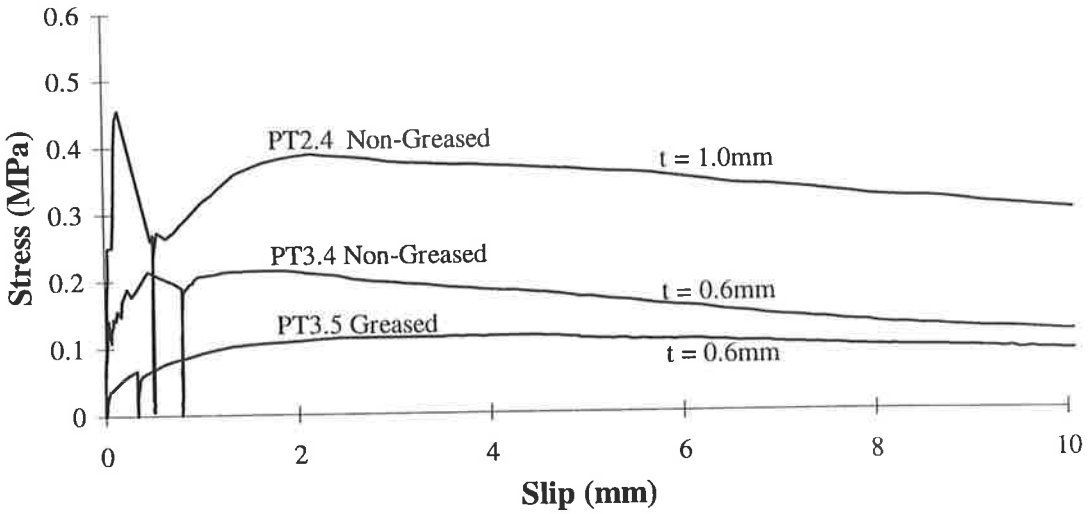
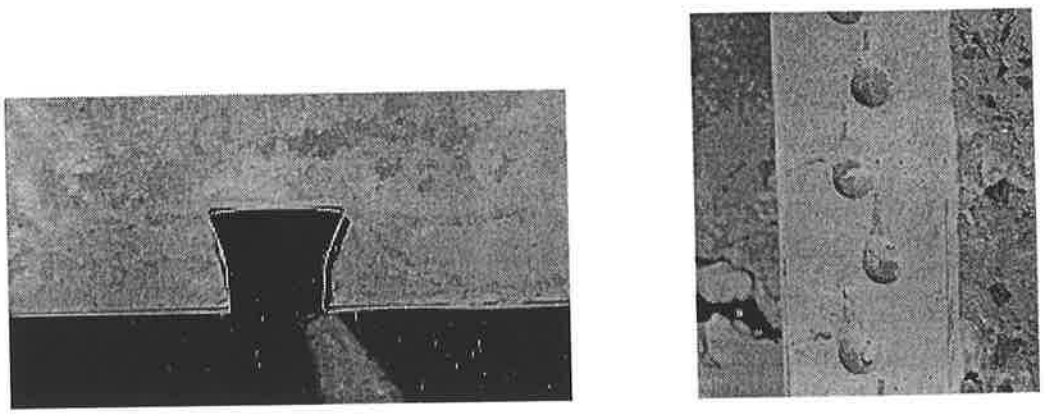


Fig. 3.81. Shear Stress vs Slip Curve for PT3.4 and PT3.5

Also shown in Fig. 3.81 is the shear-stress / slip curve for specimen PT2.4 which had similar geometry, but was constructed with 1.0 mm sheeting. The increase in the shear resistance can be seen when comparing the similar non-greased specimens of different thickness. A similar increase was noted for the previous specimens.

Push Test PT3.4 was not treated with the debonding agent and showed the characteristic decrease in shear strength when the chemical bond failed. As the test progressed, there was some slight outward movement of the rollers under the supports. However, on inspection of the sheeting, there appeared to be little separation of the sheeting from the concrete, as shown in Fig. 3.82a. Figure 3.82b shows the concrete surface at the conclusion of the test, and shows the vertical nature of the scour which indicates that there was no lateral movement of the sheeting.



(a) Rib Deformation (b) Concrete Scour

Fig. 3.82. Specimen PT3.4 after testing

Push Test PT3.5 had a rib opening b_r, which was less than the nominal value of 45 mm, as given in Table 3.9. The average value of the rib opening was 42 mm. Despite this variation in the rib opening, the maximum mechanical shear resistance was 47% of the



Fig. 3.83. Concrete Surface of PT3.5

strength of non-greased specimen, compared to a 43% difference between PT3.2 and PT3.3. A summary of the test results is given in Table 3.10. The final deformed shape of the profile was the same as for PT3.4, which is shown in Fig. 3.82a. The appearance of the concrete surface is similar to the previous greased specimen PT3.3 and is shown in Fig. 3.83. The uneven nature of the concrete surface can be seen, as well as the much reduced scouring compared to Fig. 3.82b. These effects can be attributed to the use of the debonding agent.

3.4.6.4 Push Test PT3.6 and PT3.7

These two specimens had identical geometry, except that PT3.6 was constructed from 0.6 mm sheeting, while PT3.7 was constructed from 2.0 mm sheeting. The resulting shear-stress / slip curves are shown in Fig. 3.84. Push Test PT3.7 had the smallest rib opening that was possible to be manufactured with the 2.0 mm sheeting. During the testing of PT3.7 the chemical bond broke suddenly and at all locations simultaneously. However, the decrease in shear resistance after failure of the chemical bond was only slight, while the peak mechanical shear resistance was nearly 4 times the chemical bond strength. A summary of the results of Series 3 is given in Table 3.10.

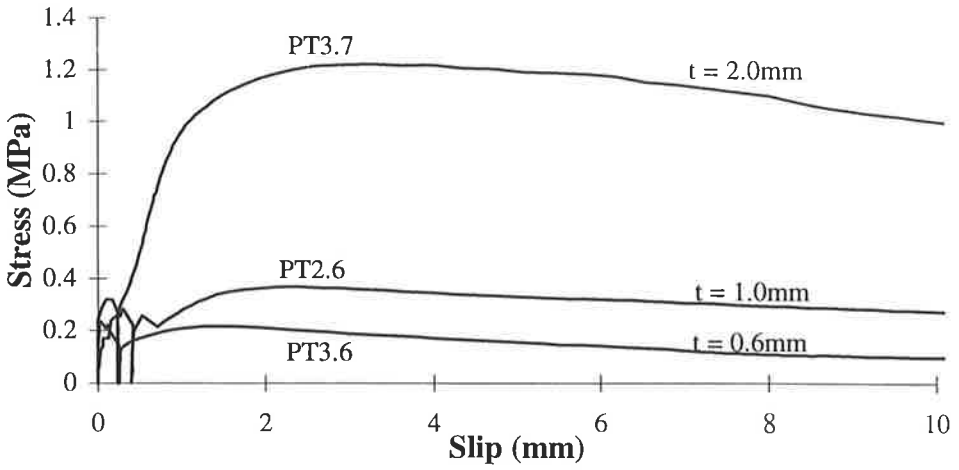
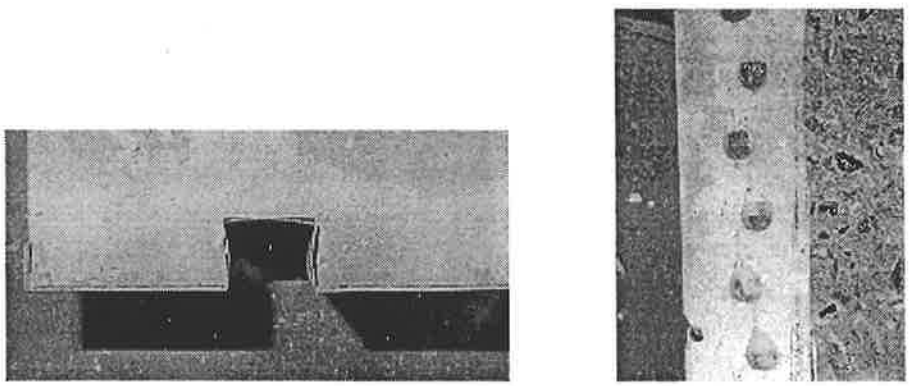


Fig. 3.84. Shear Stress vs Slip Curve for PT3.6

Also shown in Fig. 3.84 is the result from PT2.6 which had the same geometry as PT3.6 and PT3.7 except that the sheeting thickness was 1.0 mm. The same overall behaviour can be observed between the three curves, except for the large increase in mechanical shear resistance that occurs for increasing sheeting thickness. It can be seen that the increase in the mechanical shear resistance is much larger between the 2.0 mm and the 1.0 mm sheeting than between the 1.0 mm and the 0.6 mm sheeting. This result will be investigated further in Section 3.4.6.8. The deformed shape of the sheeting of specimen PT3.6 is shown in Fig. 3.85a, and the concrete surface is shown in Fig. 3.85b. There was some slight outward movement of the sheeting, which can be seen in Fig. 3.85a.

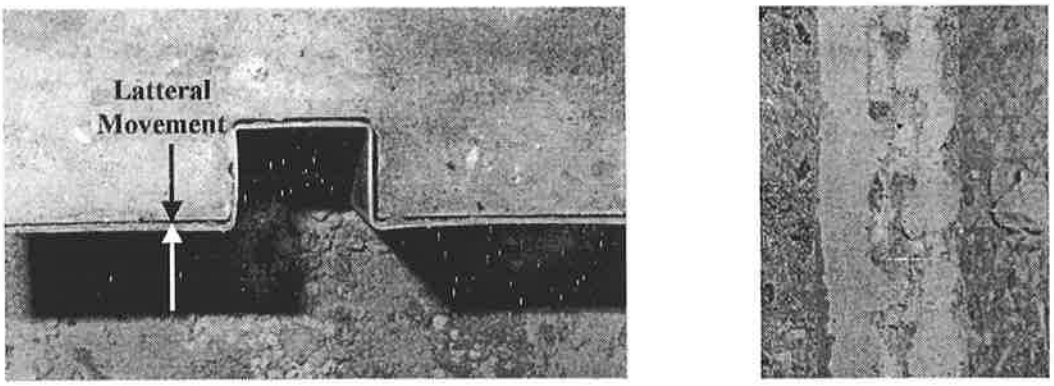


(a) Rib Deformation (b) Concrete Scour

Fig. 3.85. Specimen PT3.6 after testing

The deformed shape of the sheeting of specimen PT3.7 is shown in Fig. 3.86a, which indicates a slight lateral movement of the sheeting away from the concrete. Fig. 3.86b shows the concrete surface after the test, and indicates the deep scouring caused by the

embossments. This scour is deeper than for any of the previous tests on 0.6 mm or 1.0 mm thick sheeting.



(a) Rib Deformation (b) Concrete Scour

Fig. 3.86. Specimen PT3.7 after testing

3.4.6.5 Push Test PT3.8 and PT3.9

The geometry of these two specimens were identical; both had a rib opening of $b_r/b_f = 1.5$, and both were constructed from 0.6 mm sheeting. The sheeting of specimen PT3.9 was coated with the debonding agent, while PT3.8 was left uncoated. The shear-stress / slip curves for the two specimens are shown in Fig. 3.87. The change in behaviour between the coated and uncoated specimens is similar to that noted previously. There was negligible chemical bond for PT3.9, and slip commenced at very low loads. Both specimens were not unloaded until near the maximum load, as shown by Point A in Fig. 3.87, after which time the support rollers were released and free to move. It can be seen that there is a slight change in the behaviour upon reloading with the different support conditions. The original load at Point A was not reached and the slip recommenced at a lower load, as shown by Point B. This difference is not substantial, but does indicated that the rollers reduce the lateral forces on the sheeting, and hence reduce the shear resistance of the profile.

There was some lateral movement of the sheeting relative to the concrete noted during the test. The concrete surface of PT3.8 is shown in Fig. 3.88a, which also shows the lateral movement from the non-vertical scour marks. The surface of the concrete of PT3.9 is shown in Fig. 3.88b, from which it can be seen that the degree of scour is much less than for PT3.8. This can be attributed to the influence of the debonding agent which allows the profile to move against the concrete with less friction, thus causing less scour.

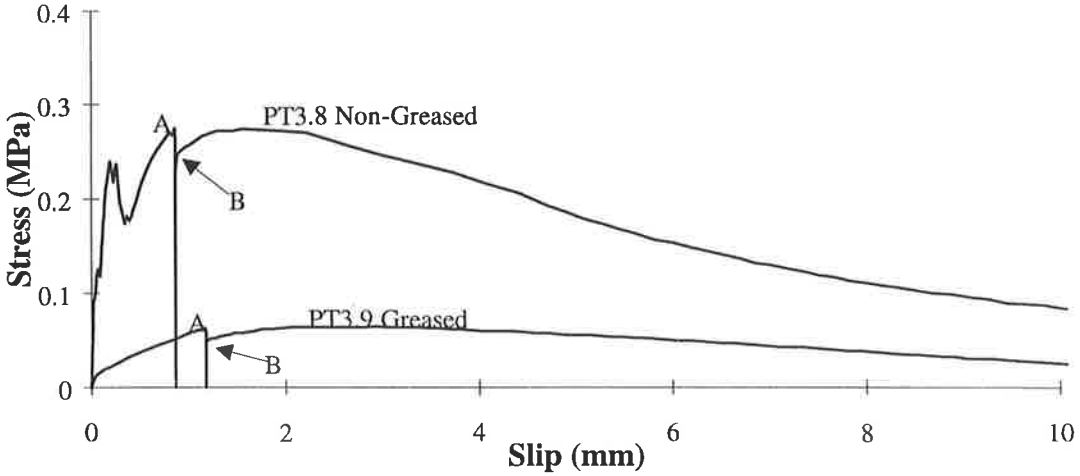
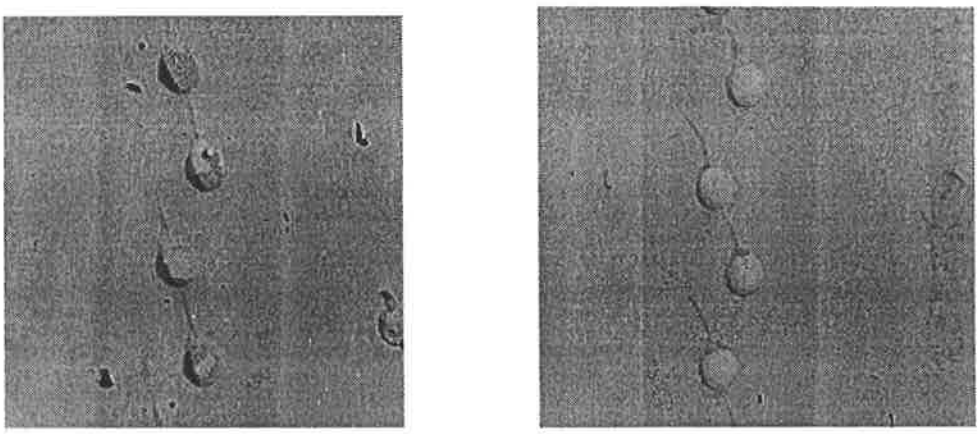


Fig. 3.87. Shear Stress vs Slip Curve for PT3.8 and PT3.9



(a) PT3.8 (b) PT3.9

Fig. 3.88. Concrete Surface for PT3.8 and PT3.9

3.4.6.6 Push Test PT3.10

The shear-stress / slip curve for PT3.10 is shown in Fig. 3.89. Also shown are the results for PT3.8 and PT2.8, which both have similar geometries, but with different sheeting thickness. The large increase in shear resistance of PT3.10 in comparison to the other profiles is evident, as was also shown in Fig. 3.84. Furthermore, the increase in the maximum mechanical shear resistance for an increase from 0.6 mm to 1.0 mm thickness is negligible. A summary of the results of Series 3 is given in Section 3.4.6.8, while a discussion of the effects of the sheeting thickness is given in Section 3.6.2.

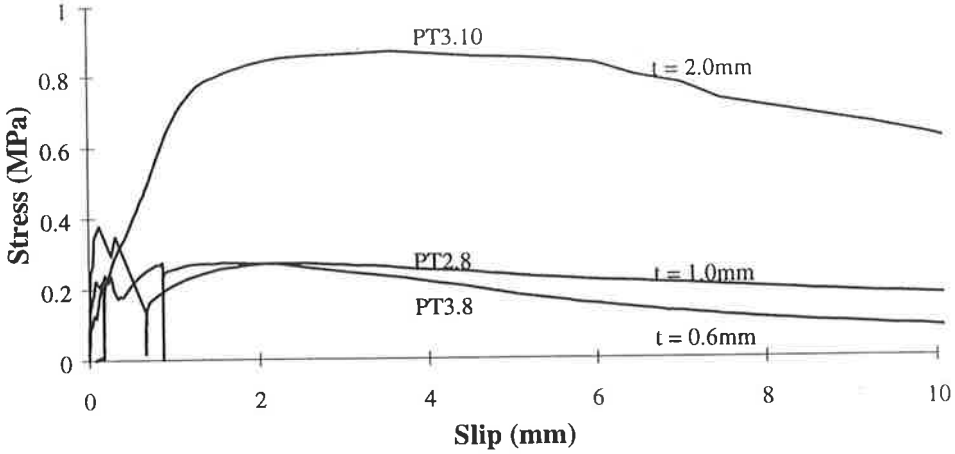


Fig. 3.89. Shear Stress vs Slip Curve for PT3.10

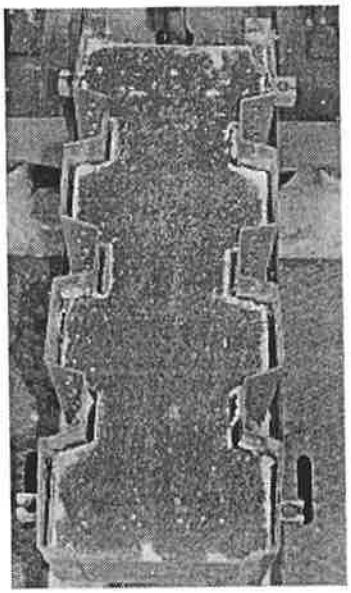
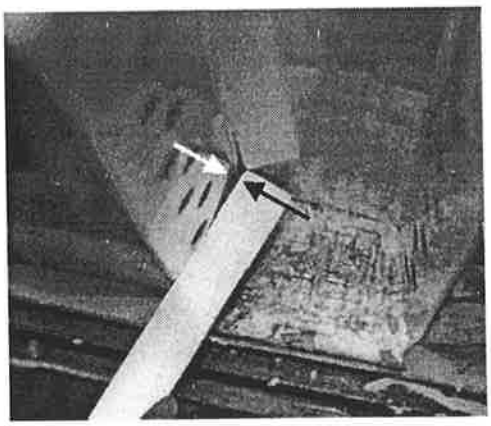
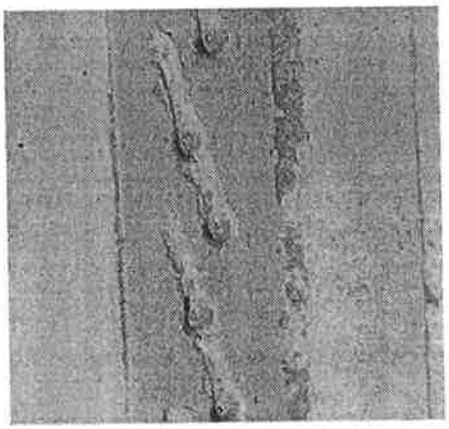


Fig. 3.90. Specimen PT3.10 after testing



(a) Rib Deformation



(b) Concrete Scour

Fig. 3.91. Specimen PT3.10 after testing

During the testing of PT3.10 a small piece of concrete broke off at the location of a bracket for one of the transducers, which caused an error with its readings. This transducer was not used in the determination of the stress-slip curve. The specimen is shown in Fig. 3.90 at the conclusion of the test, indicating the lateral movement of the sheeting. There was considerable distortion in the rib due to the effect of the embossments riding over the concrete, as shown in Fig. 3.91a. This figure shows a ruler being placed against the inside web of a rib to indicate the deformation of the rib, as shown by the arrows. The concrete surface is shown in Fig. 3.91b, which indicates the deep scour caused by the embossments. The scour is not completely vertical, indicating some lateral movement of the sheeting.

3.4.6.7 Push Test PT3.11 and PT3.12

These two specimens had similar rib geometry, except that PT3.12 was constructed with 2.0 mm sheeting, whereas PT3.11 was constructed with 0.6 mm sheeting. The shear-stress / slip curves for these two specimens are shown in Fig. 3.92. During the testing of PT3.12 a small piece of concrete lifted up in the location where one of the brackets was attached for the transducer to measure deflection. This resulted in some inaccuracy for the reading from this transducer, and the result was not used. Also plotted in Fig. 3.92 is the result from PT2.10 which had the same geometry but was constructed using 1.0 mm thick sheeting. The variation in mechanical shear resistance with increasing thickness is similar to that noted previously. Specimen PT3.12 exhibited a substantial increase in mechanical shear resistance after the chemical bond had been broken.

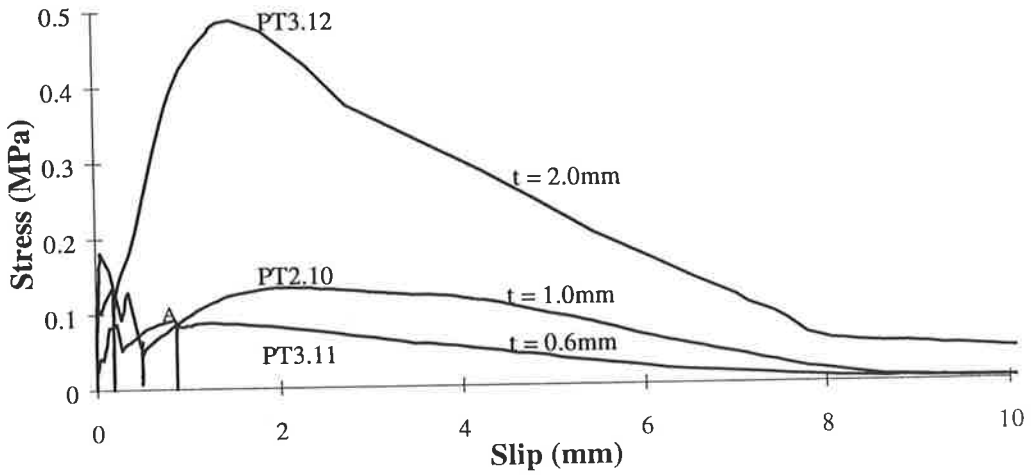
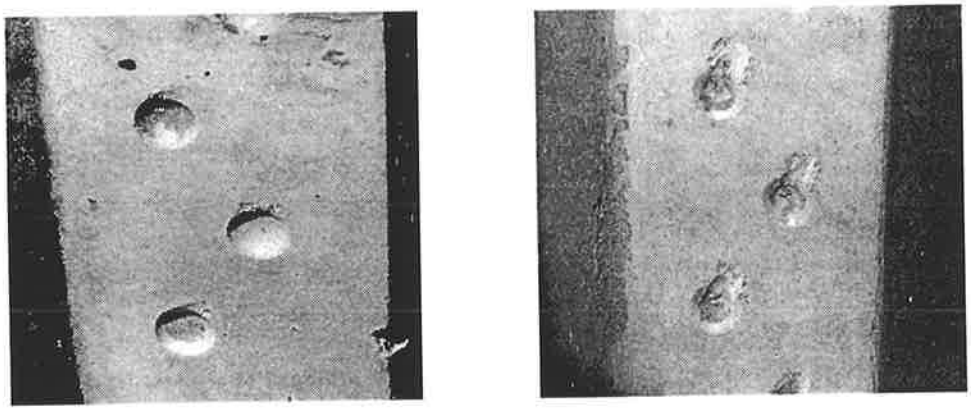


Fig. 3.92. Shear Stress vs Slip Curve for PT3.11

Specimen PT3.11 was unloaded near its maximum load and the roller supports released, as indicated by the drop in load at Point A in Fig. 3.92. There was a slight decrease in the shear capacity of the specimen upon reloading with rollers under the supports. This behaviour was also noted for PT3.8 and PT3.9 in Fig. 3.87.

The concrete surface of PT3.11 after the test is shown in Fig. 3.93a, and it can be seen that the degree of scour is very slight. This is due to the open rib geometry, and the ease of lateral movement of the sheeting away from the concrete surface. The scour at the concrete surface of PT3.12 can be seen in Fig. 3.93b, which shows that the scour was not exactly vertical. This is due to the lateral movement of the sheeting relative to the concrete. This scour is significantly more than from PT3.11, which was the same geometry, except that the sheeting thickness was 0.6 mm. The lateral movement of the sheeting of PT3.12 is shown in Fig. 3.94.



(a) PT3.11 (b) PT3.12

Fig. 3.93. Concrete Surface of PT3.11 and PT3.12 after testing

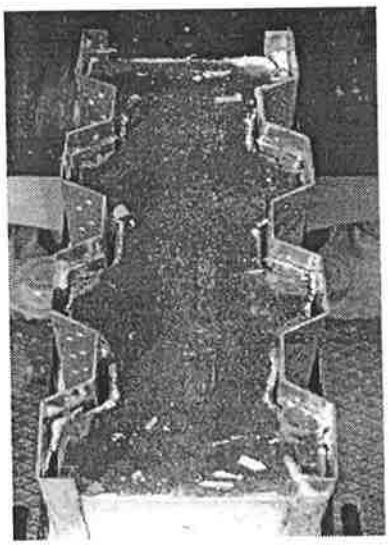


Fig. 3.94. Specimen PT3.12 after testing

3.4.6.8 Summary of Series 3

A summary of the results for Series 3 is presented in Table 3.10. The different properties that were measured for each of the tests were: the chemical bond strength (based on the total contact area between the sheeting and the concrete); the residual bond strength after failure of the chemical bond; the maximum mechanical bond strength; the slip at which this maximum occurred, and the mechanical bond stress at a slip of 5.0 mm. The results have been plotted against the rib opening, which has been non-dimensionalised by dividing by the width of the rib flange b_f in Fig. 3.34.

Specimen	Max Chemical Bond Stress (MPa) (Total Contact Area)	Residual Stress (MPa)	Max Mechanical Stress (MPa)	Slip at max Stress (mm)	Stress at 5.0 mm Slip (MPa)
PT3.1	0.1.39	0.204	0.26	1.52	0.231
PT3.2	0.137	0.266	0.285	2.38	0.25
PT3.3	0.017	0.042	0.123	4.07	0.122
PT3.4	0.090	0.194	0.214	1.50	0.171
PT3.5	0.019	0.045	0.114	4.50	0.11
PT3.6	0.103	0.143	0.218	1.56	0.157
PT3.7	0.140	0.277	1.222	3.27	1.193
PT3.8	0.134	0.174	0.274	1.57	0.179
PT3.9	0.008	0.016	0.065	2.93	0.056
PT3.10	0.109	0.205	0.868	3.56	0.85
PT3.11	0.051	0.084	0.088	1.26	0.039
PT3.12	0.058	0.103	0.488	1.66	0.215

Table 3.10. Summary of Series 3

The variation in chemical bond stress with rib opening for Series 3 is shown in Fig. 3.95. It can be seen that the debonding agent is effective in reducing the chemical bond for all rib openings. Also, there is a similar trend of decreasing chemical bond stress with increasing rib opening as was noted for the previous series. This indicates that there is a slight peeling action which is more pronounced for more open rib geometries. The regression lines are also shown for the greased and ungreased specimens, which indicates the more rapid reduction in chemical bond strength with rib opening for the greased specimens. There is considerable scatter in the results of the non-greased specimens, with a coefficient of

determination of $R^2 = 0.52$. The intercept of the regression line on the abscissa is $b_r/b_f = 3.6$ and 2.3 for the non-greased and greased specimens respectively.

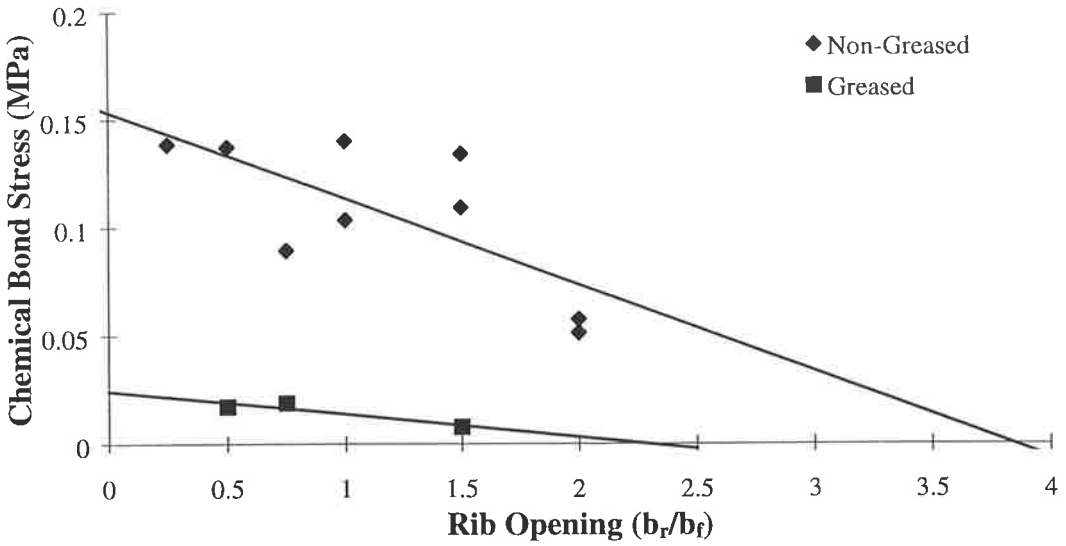


Fig. 3.95. Chemical Bond Stress vs Rib Opening for Series 3

The variation in residual shear stress after failure of the chemical bond is given in Fig. 3.96. A decreasing trend with increasing rib opening is evident for both sheeting thicknesses, however there appears to be more scatter with the 0.6 mm sheeting. The residual shear stress is much lower for the greased specimens as expected, but is not entirely

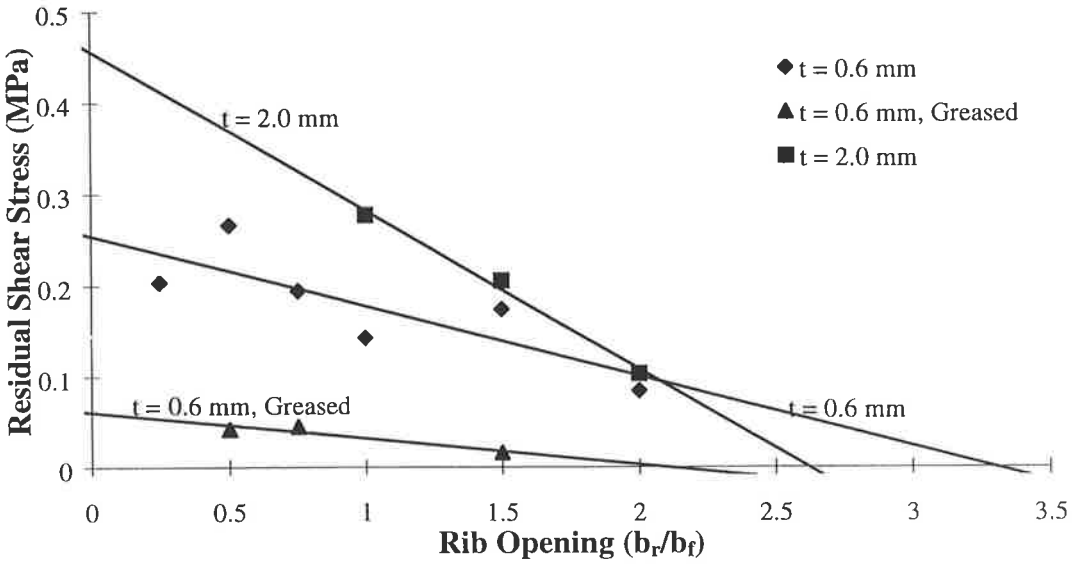


Fig. 3.96. Residual Shear Stress vs Rib Opening for Series 3

eliminated. It also decreases with increasing rib opening. The regression lines are shown for each of the sheeting thicknesses, and indicate the more rapid reduction in residual shear strength with rib opening for the 2.0 mm sheeting, compared to the 0.6 mm sheeting. The residual shear stress tends to zero at a rib opening of $b_r/b_f = 2.6$ for the 2.0 mm sheeting, 3.3 for the ungreased 0.6 mm sheeting and 2.1 for the greased 0.6 mm sheeting. The intercepts on the ordinate axis are 0.46, 0.25 and 0.06 for the same regression lines.

The variation in mechanical shear stress with increasing rib opening is shown in Fig. 3.97. The large increase in mechanical shear resistance of the 2.0 mm sheeting over the other thicknesses can be seen. Also it can be seen that the debonding agent has resulted in lower mechanical shear stress values than the equivalent profile without the debonding agent. This result was not anticipated, as it was hoped the debonding agent would remove the chemical bond without affecting the mechanical shear strength of the profile. However, the debonding agent tended to lubricate the interface, and reduce the passive frictional component of the mechanical shear resistance. The debonding agent also appeared to affect the concrete at the interface, which also would have contributed to the altered mechanical shear stress.

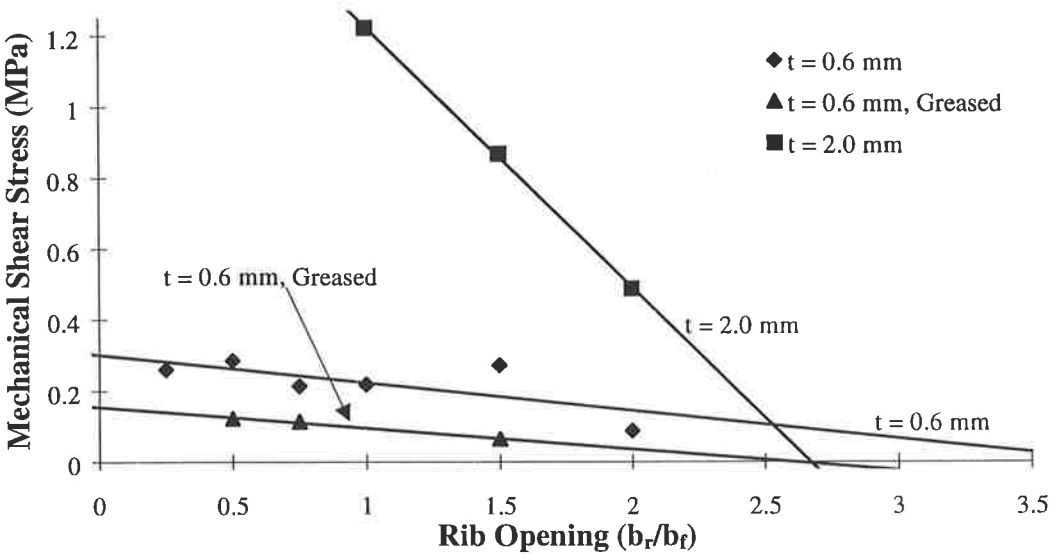


Fig. 3.97. Mechanical Bond Stress vs Rib Opening for Series 3

Also shown in Fig. 3.97 are the linear regression lines for the different sheeting thicknesses. As was noted in Fig. 3.96 the regression lines indicate the more rapid reduction in strength with rib opening for the 2.0 mm sheeting, compared to the 0.6 mm sheeting. The

mechanical bond stress tends to zero at a rib opening of $b_r/b_f = 2.7$ for the 2.0 mm sheeting, 3.9 for the ungreased 0.6 mm sheeting and 2.6 for the greased 0.6 mm sheeting. The intercepts on the ordinate axis are 1.96, 0.30 and 0.16 for the same regression lines.

The variation in the shear stress at 5 mm slip is shown in Fig. 3.98. This indicates the large increase in shear stress for the 2.0 mm profiles over the 0.6 mm profiles. The 2.0 mm profiles show a clear trend of decreasing shear resistance with increasing rib opening, and tend towards zero at $b_r/b_f = 2.3$. The ungreased 0.6 mm profiles exhibit a similar decreasing trend, and tend towards zero at $b_r/b_f = 2.6$, while the greased 0.6 mm profiles tend towards zero at $b_r/b_f = 2.3$. It can be seen that the specimens treated with the debonding agent have lower shear strength at 5 mm than the uncoated specimens. The intercepts of the regression lines on the ordinate axis are 2.22, 0.29 and 0.16 for the 2.0 mm, 0.6 mm and greased 0.6 mm profiles respectively.

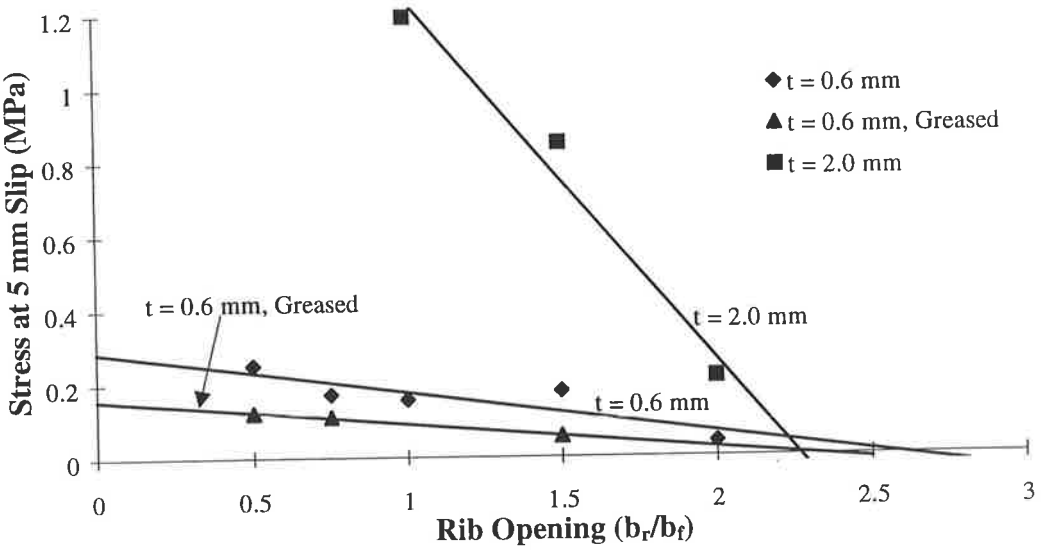


Fig. 3.98. Stress at 5 mm Slip vs Rib Opening for Series 3

The variation in the slip when the maximum mechanical shear stress occurred is shown in Fig. 3.99. It can be seen that the specimens which were coated with the debonding agent had significantly higher slips at the maximum mechanical shear stress. This can be attributed to the lubricating action of the debonding agent, which resulted in a lower but much more extended peak in the shear-stress / slip curve. The 2.0 mm sheeting tended to have higher slips at the maximum shear stress than the 0.6 mm sheeting. This can be explained by the

high degree of scour at the embossments for the 2.0 mm sheeting, which resulted from the strong spring action of the profile. Thus, a greater amount of slip was required before the embossments had pushed free from the depression in the concrete. This effect was greater for the less open rib profiles due to the greater spring action.

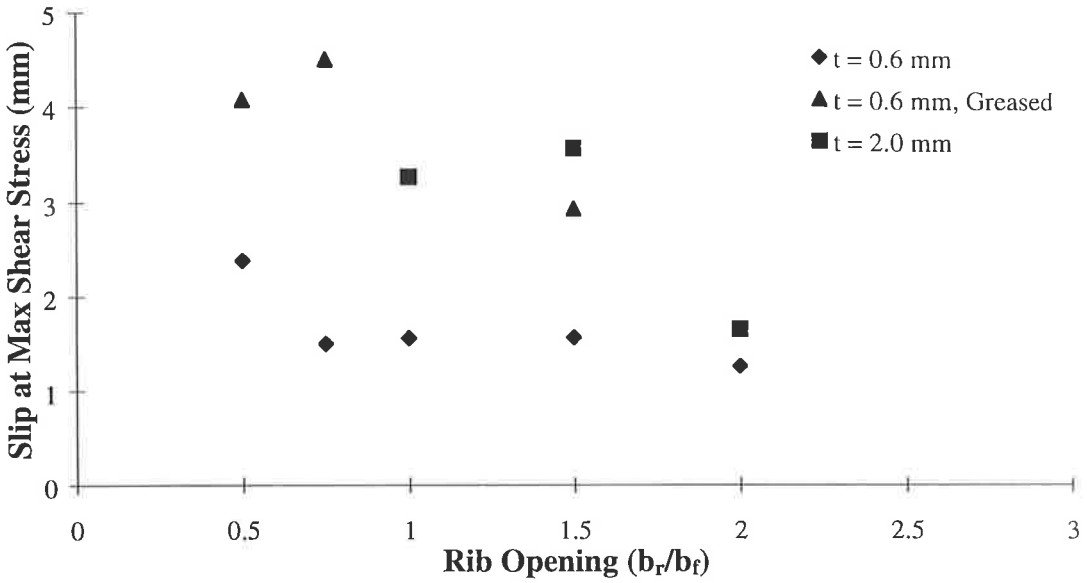


Fig. 3.99. Slip at Max Shear Stress vs Rib Opening for Series 3

3.4.7 Series 4

Series 4 was conducted on proprietary sheeting of varying thickness, and was carried out to investigate the performance of Australian sheeting, and to provide a comparison with results of Patrick (1990). Also, the effect of varying the thickness of the sheeting was investigated, along with the effects of the embossments. The two types of sheeting used were Comform and Bondek II. The Comform sheeting is produced in South Australia by Woodroffe Industries, and is shown previously in Fig. 3.27 on Page 138. The Bondek II sheeting is manufactured by Lysaght Building Industries, and is shown in Fig. 3.100. The effects of the embossments was studied only on the Comform sheeting as it was not possible to obtain samples on the Bondek II sheeting without embossments. A total of 12 specimens were tested, 8 of which were constructed from Comform sheeting, and 4 from the Bondek II sheeting. A summary of the specimens tested in the series is given in Table 3.11.

Specimen	Thickness	Sheeting Type	Embossments
PT4.1	1.0	Comform	Yes
PT4.2	1.0	Comform	Yes
PT4.3	1.0	Comform	Yes
PT4.4	0.79	Comform	Yes
PT4.5	0.79	Comform	Yes
PT4.6	0.79	Comform	No
PT4.7	0.79	Comform	No
PT4.8	0.79	Comform	No
PT4.9	1.0	Bondek II	Yes
PT4.10	1.0	Bondek II	Yes
PT4.11	0.79	Bondek II	Yes
PT4.12	0.79	Bondek II	Yes

Table 3.11. Series 4

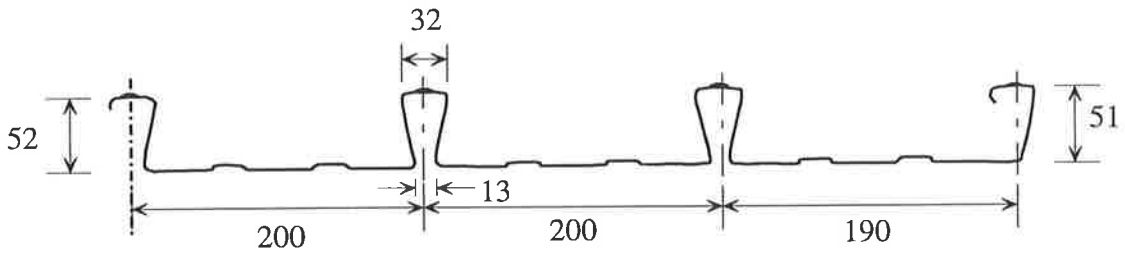


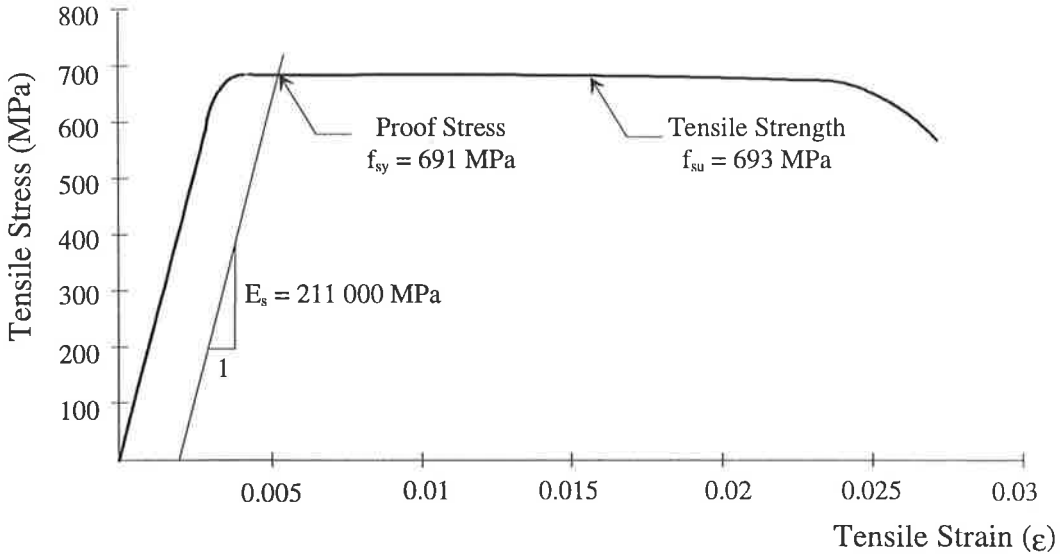
Fig. 3.100. Bondek II Profile A series of concrete test cylinders were prepared from the same concrete as the push specimens at the time of casting. These were tested at the same time as the push specimens and the results are given in Table 3.12. This series was constructed from the same concrete batch as Series 3, and the values of the concrete strength are the same as for that series.

Concrete Properties			Profiled Sheeting Properties					
			Bondek II t_{bm} = 0.75 mm		Bondek II t_{bm} = 1.0 mm		Comform	
f_c (MPa)	E_c (MPa)	f_{ct} (MPa)	σ_y (MPa)	σ_u (MPa)	σ_y (MPa)	σ_u (MPa)	σ_y (MPa)	σ_u (MPa)
39.0	33 600	3.2	691	693	615	620	570	572

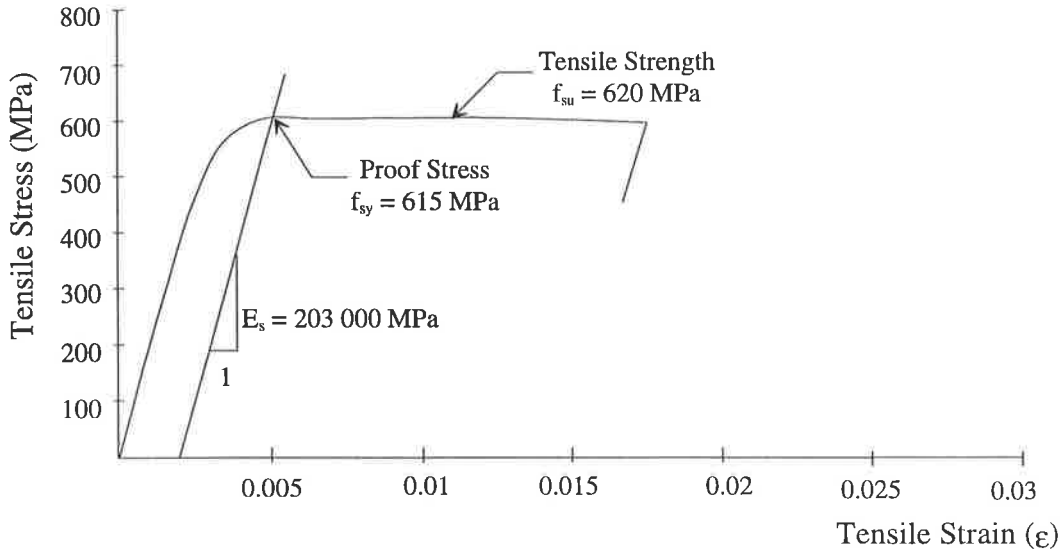
Table 3.12. Concrete and Steel Properties for Series 4

Two tensile stress-strain curves for the Bondek II sheeting with nominal values of t_{bm} = 0.75 mm and t_{bm} = 1.0 mm are given in Fig. 3.101a and Fig. 3.101b respectively. The

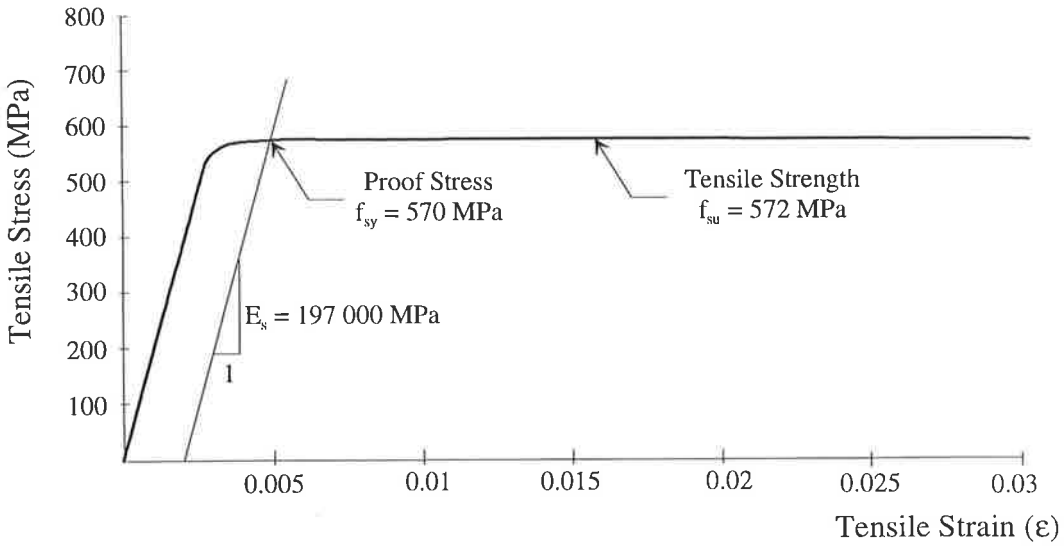
coupons were taken from the flat pan regions of the profile away from any corners or bends, and were oriented in the direction of rolling. The results for the values of the yield stress and ultimate stress are given in Table 3.12. The stress-strain curves did not vary for the different gauge thicknesses of the Comform sheeting. A typical result is shown in Fig. 3.101c and the results are given in Table 3.12.



(a) Bondek II, t_{bm} = 0.75 mm



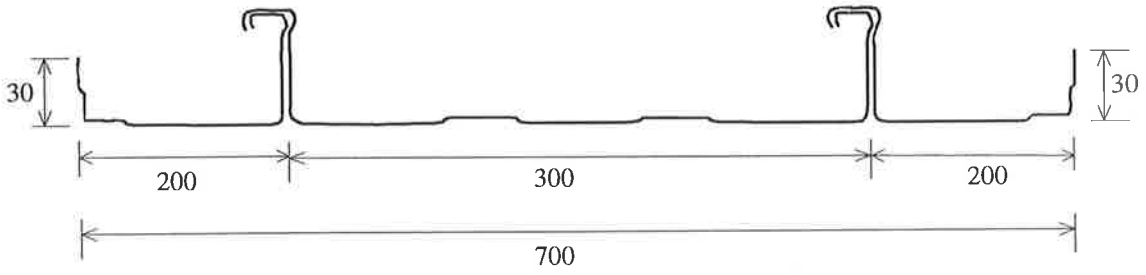
(b) Bondek II, t_{bm} = 1.0 mm



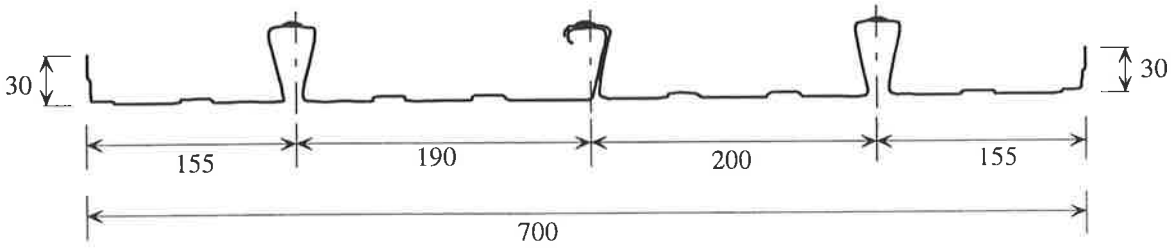
(c) Comform

Fig. 3.101. Stress-Strain Curves for Profiled Sheeting

The Comform specimens were constructed with one whole unit as the centre sheet and two partial edge sheets, as shown in Fig. 3.102a. This arrangement allowed a full width of sheeting to be used with two complete ribs for each side of the specimen. The Bondek II specimens were constructed by assembling two half segments, as shown in Fig. 3.102b. This arrangement allowed a full width of the Bondek II profile to be tested, with one lap rib in the centre, for each side of the specimen.



(a) Comform



(b) Bondek II

Fig. 3.102. Series 4 Specimens

3.4.7.1 Push Test PT4.1, PT4.2 and PT4.3

These three identical specimens were constructed from 1.0 mm thick embossed Comform sheeting, shown in Fig. 3.102a. The resulting shear stress-slip curves are shown in Fig. 3.103. It can be seen from this figure that there is considerable variation between the results, bearing in mind that the three specimens were constructed from the same length of sheeting, poured from the same batch of concrete, and cured under the same conditions.

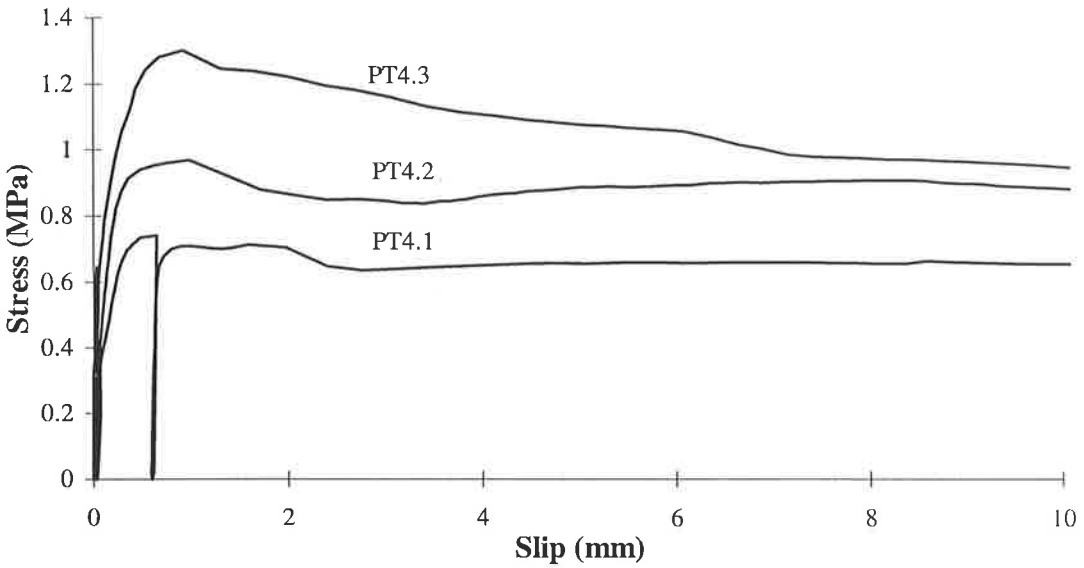


Fig. 3.103. Shear Stress vs Slip Curve for PT4.1, PT4.2 and PT4.3

All the Comform tests were characterised by the same overall behaviour. This can be described as follows:

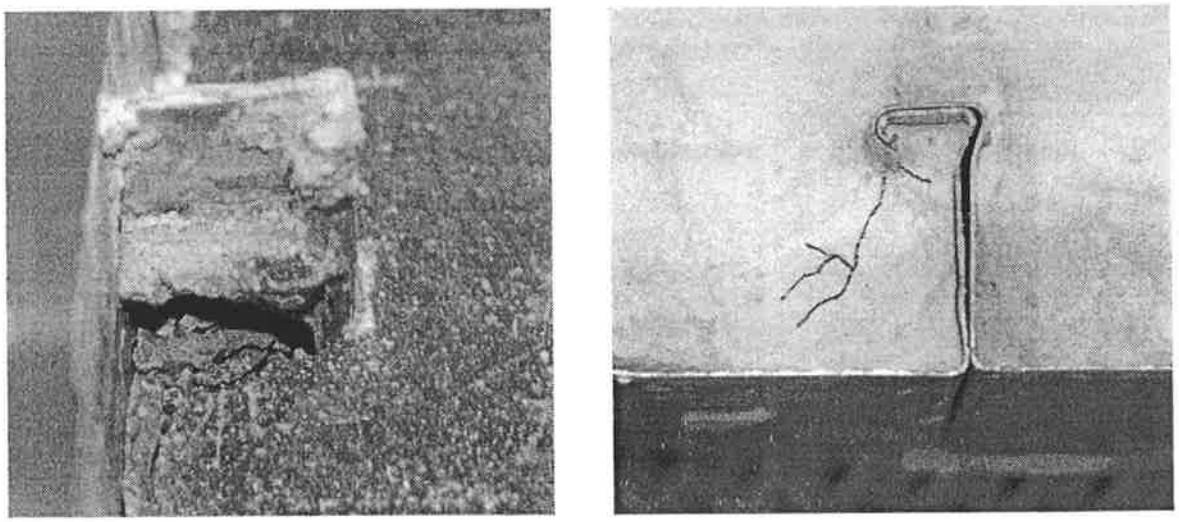
- In the initial stages of the loading, there is an increase in the shear force with no recorded slip;
- At the failure of the chemical bond, ie. when slip is first recorded, there is no sudden reduction in strength;
- There was a continued increase in the shear resistance as the slip progressed;
- After the maximum load had been reached, there was a gradual decrease in the shear resistance of the specimens.

Push Test PT4.1 did not slip evenly at all locations throughout the specimen. When the last transducer commenced recording slip, the maximum slip recorded on the opposite side of the specimen was 0.9 mm. This difference remained approximately constant throughout the

remainder of the test. There was no visible cracking of the specimen throughout the test, except for some minor cracking which occurred on the top surface of the specimen adjacent to the ribs. This cracking was common for all the Comform specimens and is shown in Fig. 3.104a. The depth of cracking was typically only 15 mm.

Push Test PT4.2 exhibited slightly more cracking than observed for PT4.1. There was minor cracking evident on the underside of the specimen at one of the ribs at the conclusion of the test. This is shown in Fig. 3.104b.

Push Test PT4.3 exhibited more cracking that both PT4.1 and PT4.2. There were cracks which extended from two of the ribs, as shown in Fig. 3.105. There was cracking of the concrete which occurred at the location of the transducers, and as a result the reading of slip from that transducer was in error. These readings were not used in the determination of the average slip. The concrete surface after the sheeting has been removed is shown in Fig. 3.106. It can be seen that the degree of scour is very slight, despite the high shear load attained by this specimen. This can be attributed to the high contact area of the embossments, and thus more even distribution of shear over the contact surface, as compared to the specimens with the discrete circular embossments of the previous series.



(a) PT4.1 (b) PT4.2

Fig. 3.104. Concrete Cracking for PT4.1 and PT4.2

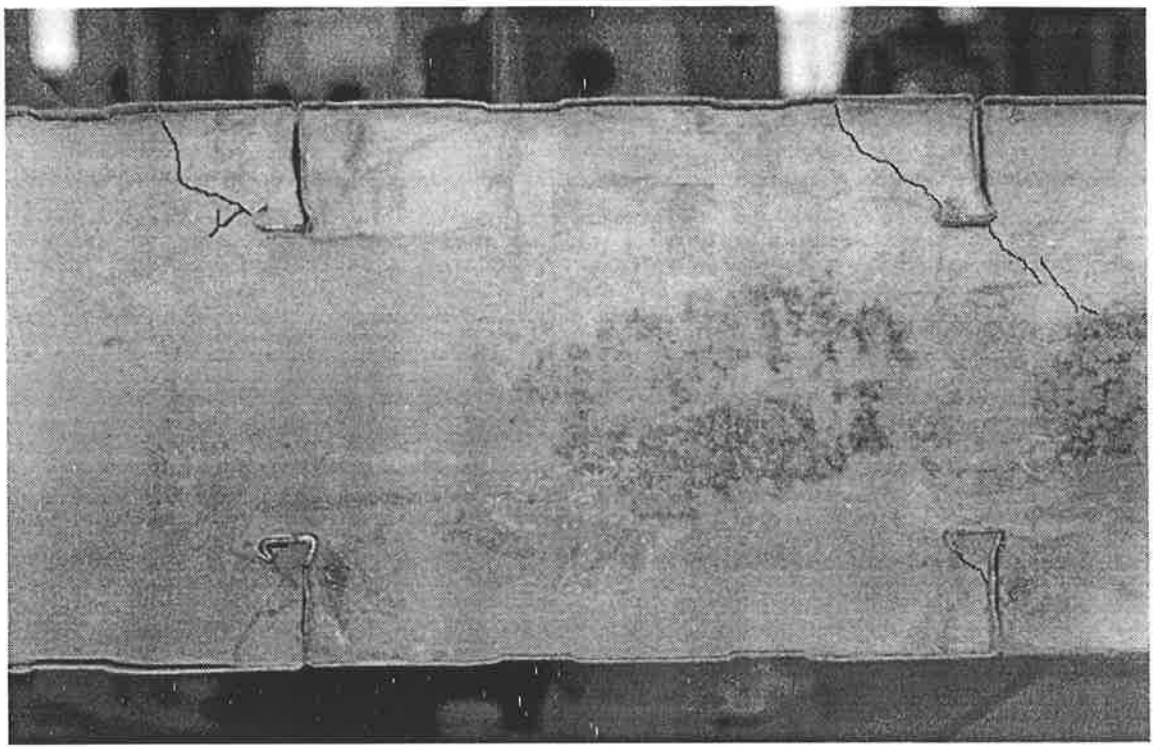


Fig. 3.105. Concrete Cracking for PT4.3

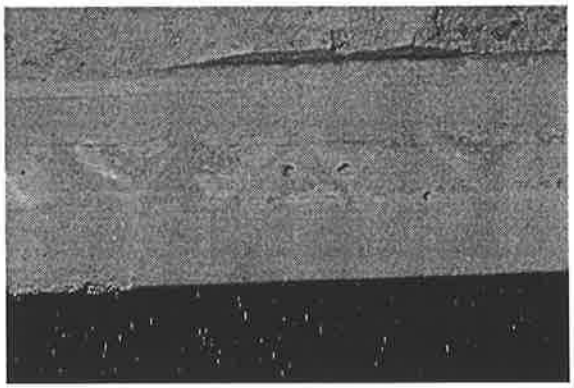


Fig. 3.106. Concrete Scour for PT4.3

3.4.7.2 Push Test PT4.4 and PT4.5

These two identical specimens were constructed from embossed Comform sheeting, with a sheeting thickness of 0.79 mm. The shear-stress / slip curves for these two specimens are shown in Fig. 3.107. The results of these two specimens correspond closely to each other.

Push Test PT4.4 exhibited a slight variation in the width b_c, shown in Fig. 3.16 on Page 125. This variation resulted in the bottom of the specimen being 5 mm wider than the top. This variation may have contributed to the rise in shear strength after the first maximum,

which was not noted for any of the other Comform specimens. There was slight cracking on the top of the specimen, which was the same as the previous specimens, and is shown in Fig. 3.104a. The concrete surface is shown in Fig. 3.108, after the sheeting has been removed. The degree of scour is slight, as was the case for the 1.0 mm sheeting specimen shown in Fig. 3.106.

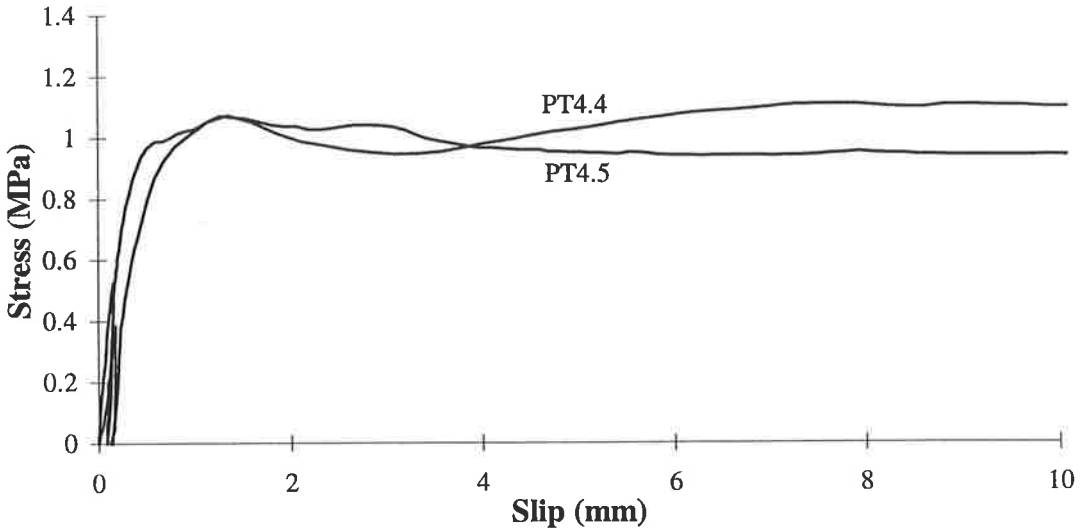


Fig. 3.107. Shear Stress vs Slip Curve for PT4.4 and PT4.5

Push Test PT4.5 had slightly more cracking than was noted for PT4.4. The pattern of cracking was similar to that for PT4.3 and is shown in Fig. 3.109. This cracking was only observed on the underside of the specimen.



Fig. 3.108. Concrete Scour for PT4.4

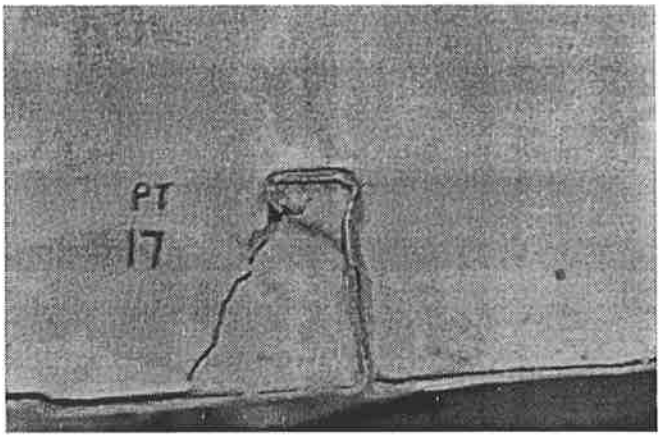


Fig. 3.109. Concrete Cracking for PT4.5

3.4.7.3 Push Test PT4.6, PT4.7 and PT4.8

These identical specimens were each constructed using 0.79 mm non-embossed Comform sheeting. It should be noted that Woodroffe industries does not sell Comform sheeting without embossments, and that these tests were performed to evaluate the influence of the embossments on the behaviour of the sheeting.

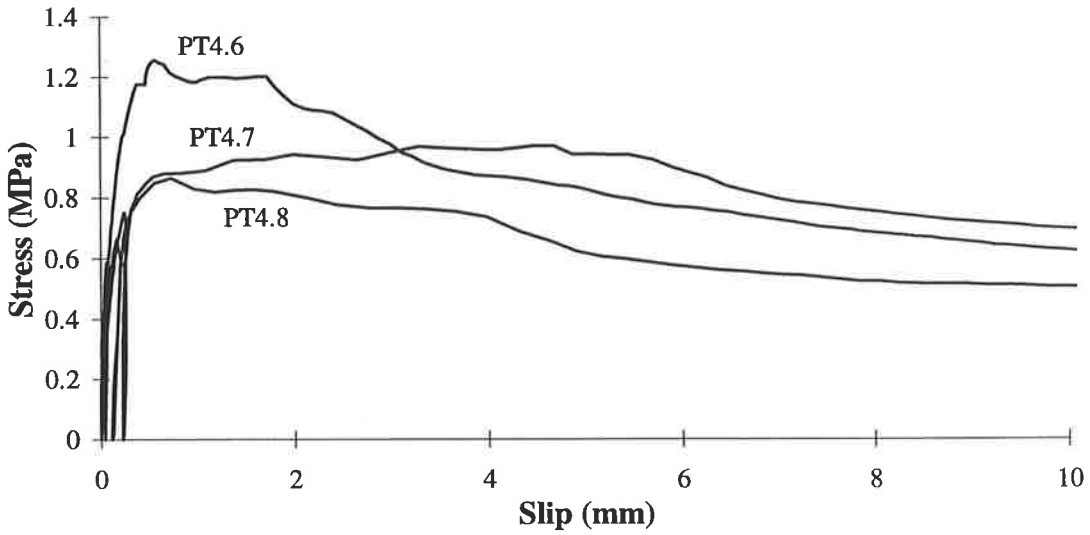


Fig. 3.110. Shear Stress vs Slip Curve for PT4.6, PT4.7 and PT4.8

Push Test PT4.6 exhibited buckling at the base of the profiled sheeting on one side of the specimen. It appeared that the buckling was due to improper placement of the silica paste at the support to the sheeting. The first signs of buckling were evident when the shear stress

reached approximately 1.1 MPa. The buckling increased in magnitude as the applied load increased. There was no bucking evident on the other side of the specimen. There was significant cracking of the specimen, which occurred as a result of the buckling, and the uneven slip of the specimen. The cracking of the concrete, and the buckling of the sheeting are shown in Fig. 3.111. It is likely that the large increase in shear capacity of PT4.6 over the other two similar specimens is related to the buckling at the supports.

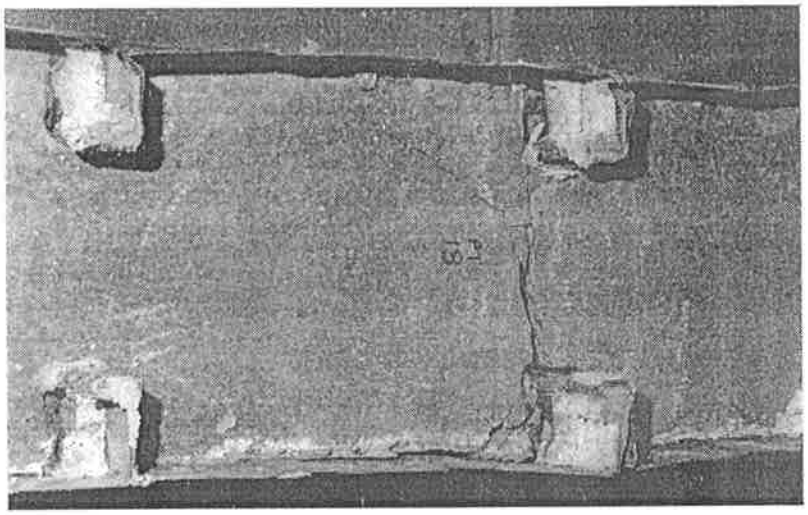


Fig. 3.111. Concrete Cracking for PT4.6

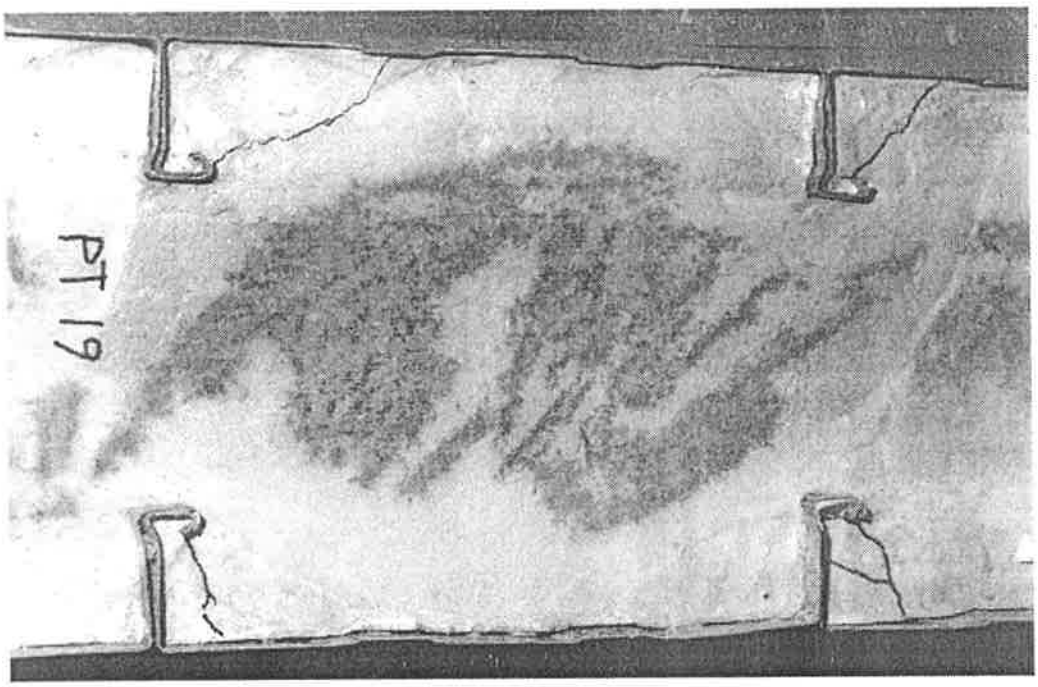


Fig. 3.112. Concrete Cracking for PT4.7

Push Test PT4.7 showed a much larger slip at the maximum load than was observed for any of the other tests. This may have been due in part to the rotation that occurred in the

specimen. Despite the use of the restraints there was still some rotation of the specimen. One side of the specimen tended to slip more than the other, with the maximum difference being approximately 4 mm. The cracking pattern for PT4.7 is shown in Fig. 3.112. This cracking pattern is similar to previous tests.

Push Test PT4.8 did not exhibit any unusual behaviour during the test.

3.4.7.4 Push Test PT4.9 and PT4.10

These two identical specimens were constructed from 1.0 mm thick Bondek II sheeting. The shear-stress / slip curves for these specimens are shown in Fig. 3.113.

Push Test PT4.9 exhibited significant cracking of the concrete, as shown in Fig. 3.114. The top view is shown in (a), while (b) shows the bottom view of the specimen. This cracking occurred in nearly all of the Comform specimens. The transverse crack across the specimen shown in Fig. 3.114b has been observed in full scale slab tests as a longitudinal crack along the rib location. The outward movement of the sheeting from the concrete can be seen in Fig. 3.115. This lateral movement of the sheeting was evident from the underside of the specimen, but not at the top. This indicates that there was a tendency for the sheeting to pull away from the concrete at the supports of the specimen, but not at the top.

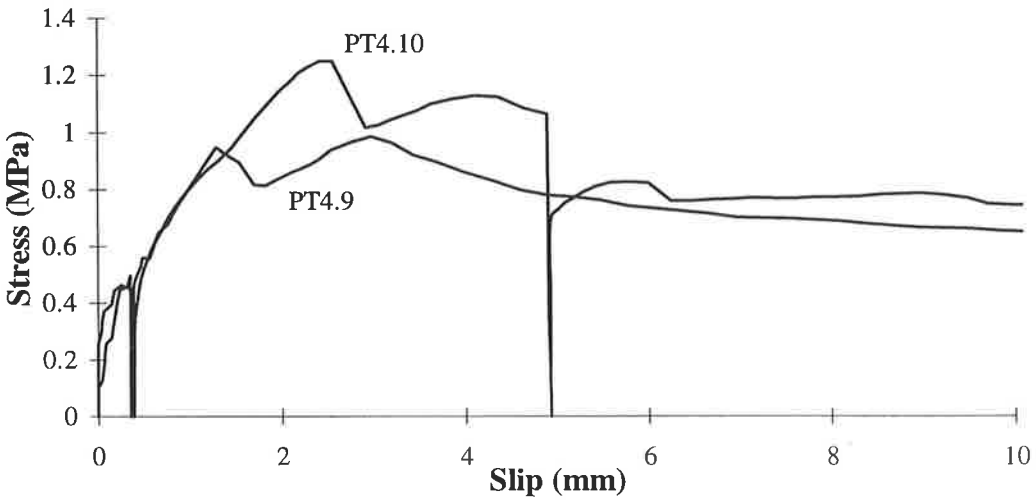
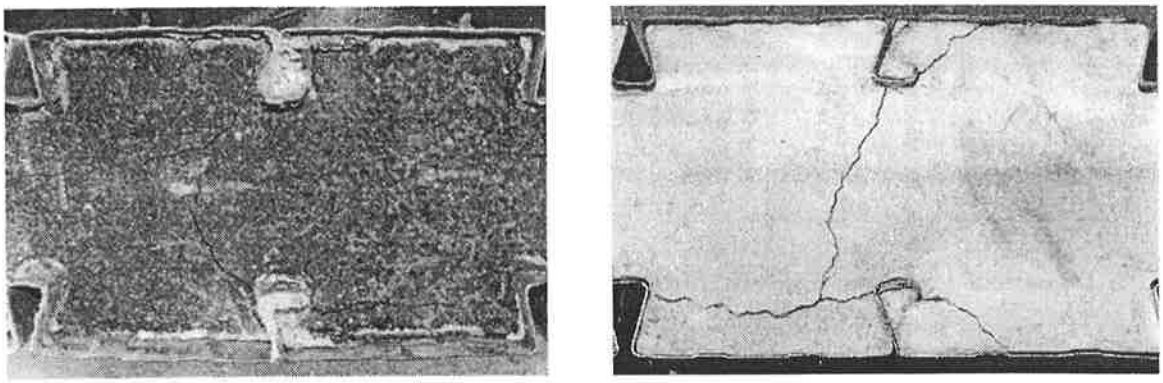


Fig. 3.113. Shear Stress vs Slip Curve for PT4.9 and PT4.10



(a) Top View (b) Bottom View

Fig. 3.114. Concrete Cracking for PT4.9

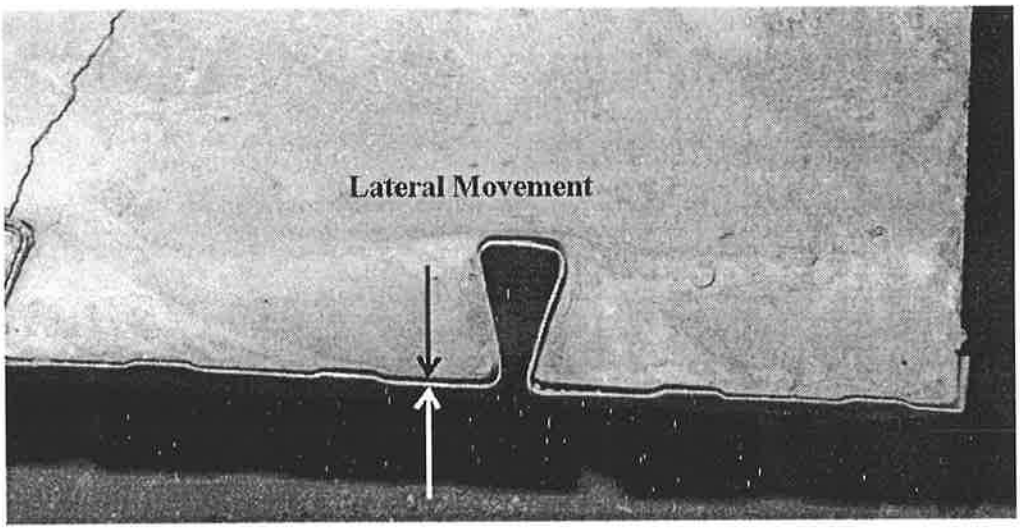


Fig. 3.115. Lateral Movement of Sheeting for PT4.9

Push Test PT4.10 behaved in a similar manner to PT4.9, except that the maximum load was 27% higher. The cracking pattern observed on the underside of the specimen is shown in Fig. 3.116. This cracking was not evident from the top of the specimen, indicating that there may be a variation in the stress distribution throughout the height of the specimen.

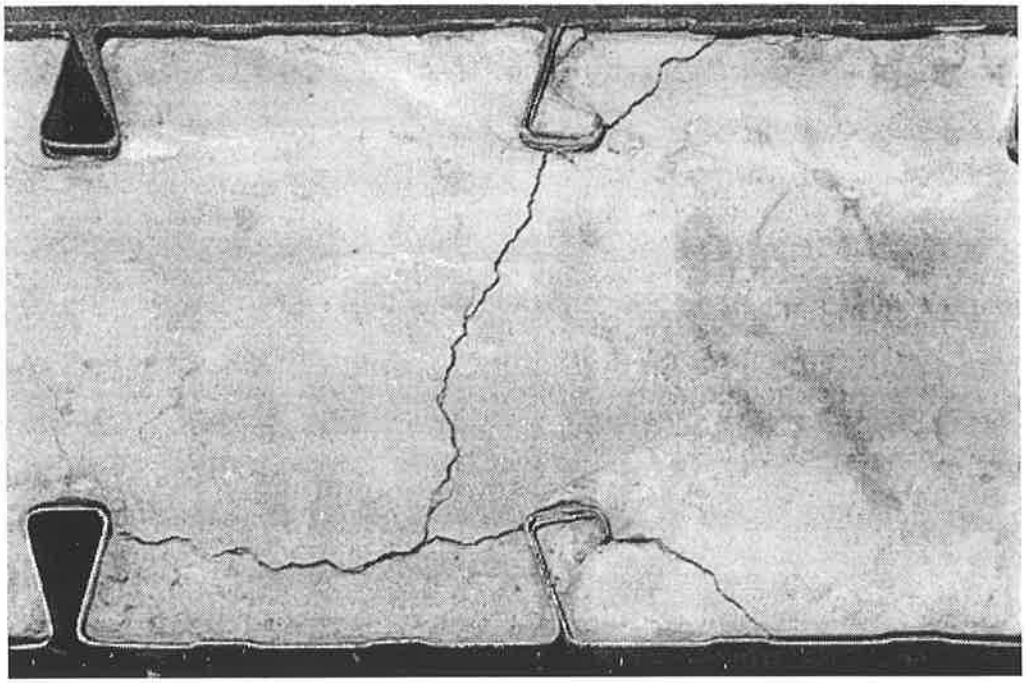


Fig. 3.116. Concrete Cracking for PT4.10

3.4.7.5 Push Test PT4.11 and PT4.12

These two specimens were constructed from 0.79 mm thick Bondek II sheeting. The shear-stress / slip curves are shown in Fig. 3.117.

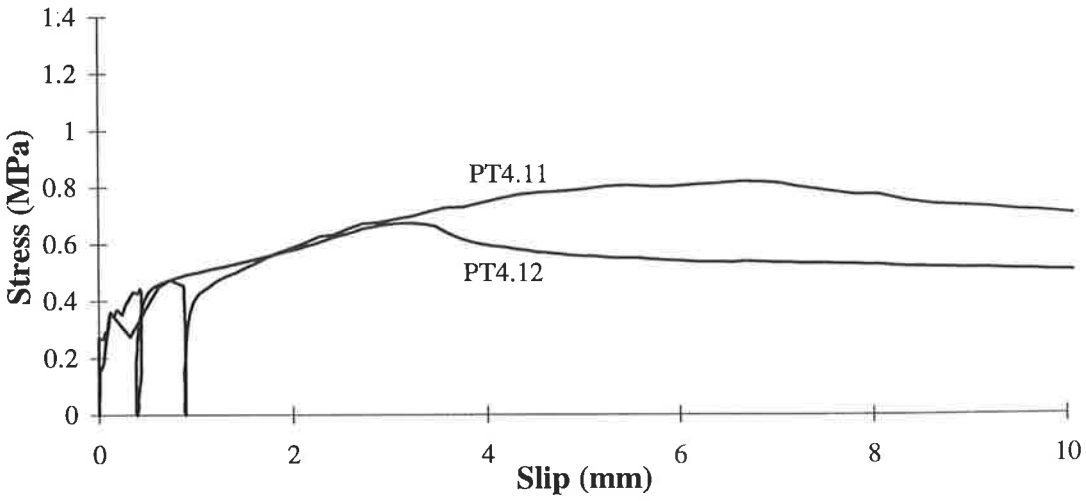
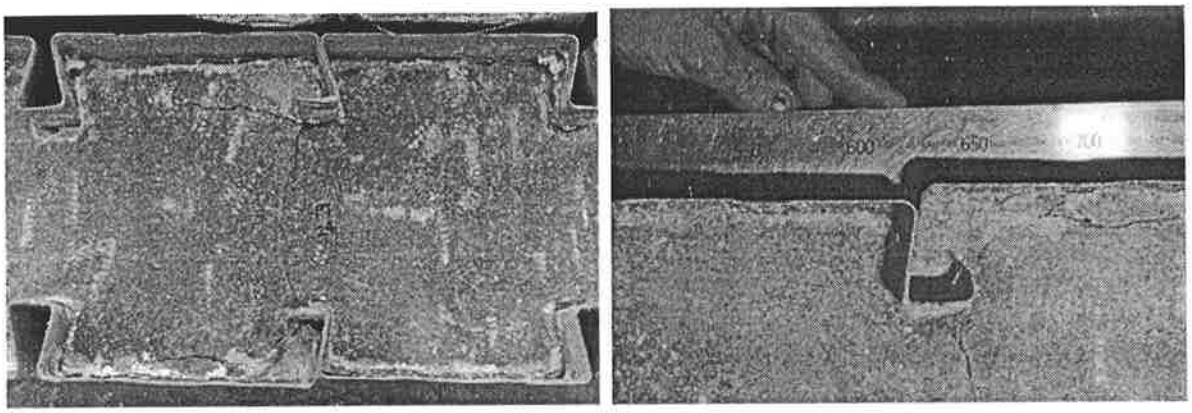


Fig. 3.117. Shear Stress vs Slip Curve for PT4.11 and PT4.12

Push Test PT4.11 exhibited significant buckling when the applied shear stress reached 0.64 MPa. This buckling occurred on only one side of the specimen. This buckling commenced at the support of the specimen, and was due to inadequate preparation of the silica paste around the rib location. It is expected that the form of the stress-slip curve is influenced by the occurrence of the buckling. This is evidenced by the fact that the slip at which the maximum shear resistance occurs is more than double that for PT4.12, and more than 3 times that for any other test in this series.

Push Test PT4.12 exhibited similar cracking to the previous Bondek II specimens, as shown in Fig. 3.118a. There was significant variation in the rib geometry of the sheeting, as supplied by Lysaght. This variation is shown in Fig. 3.118b. The influence of this variation in rib geometry is uncertain, but it may help to account for the difference in behaviour of otherwise identical specimens.



(a) Concrete Cracking (b) Variation in Rib Geometry

Fig. 3.118. Push Test PT4.12

3.4.7.6 Summary of Series 4

A summary of the results for Series 4 is presented in Table 3.13. The different properties that were measured for each of the tests were: the maximum shear strength based on the rib contact area; the maximum shear strength per metre width of sheeting; the slip at which this maximum occurred, and the mechanical bond stress at a slip of 5.0 mm. The shear strength based on the rib contact area was determined by dividing the applied load by the total contact area of all the ribs in the specimen. For the Bondek II specimens, this value represents an average shear stress over the different ribs. The shear strength was also

determined per meter width of sheeting in order to make a more direct comparison between the two profiles. This was obtained by dividing the shear strength per rib contact area by the number of ribs per metre width of sheeting.

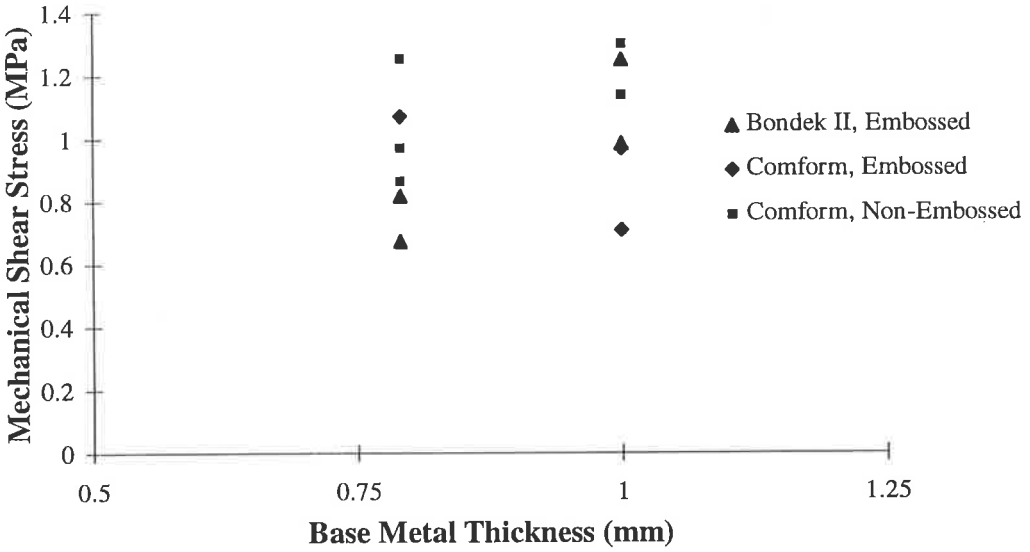
Specimen	Sheeting Type	Embossments	Max Shear Strength (MPa) (Rib Contact Area)	Max Shear Strength (MPa) (Per meter width)	Slip at Max Shear (mm)	Load at 5.0 mm Slip (MPa)
PT4.1	Comform	Yes	0.710	0.426	0.99	0.655
PT4.2	Comform	Yes	0.970	0.582	0.97	0.887
PT4.3	Comform	Yes	1.302	0.782	0.91	1.077
PT4.4	Comform	Yes	1.072	0.643	1.35	1.027
PT4.5	Comform	Yes	1.071	0.643	1.26	0.952
PT4.6	Comform	No	1.256	0.754	0.56	0.824
PT4.7	Comform	No	0.972	0.583	1.26	0.943
PT4.8	Comform	No	0.866	0.520	0.73	0.620
PT4.9	Bondek II	Yes	0.985	0.773	2.99	0.780
PT4.10	Bondek II	Yes	1.251	0.981	2.43	0.728
PT4.11	Bondek II	Yes	0.819	0.642	6.65	0.794
PT4.12	Bondek II	Yes	0.675	0.529	3.25	0.558

Table 3.13. Summary of Series 4

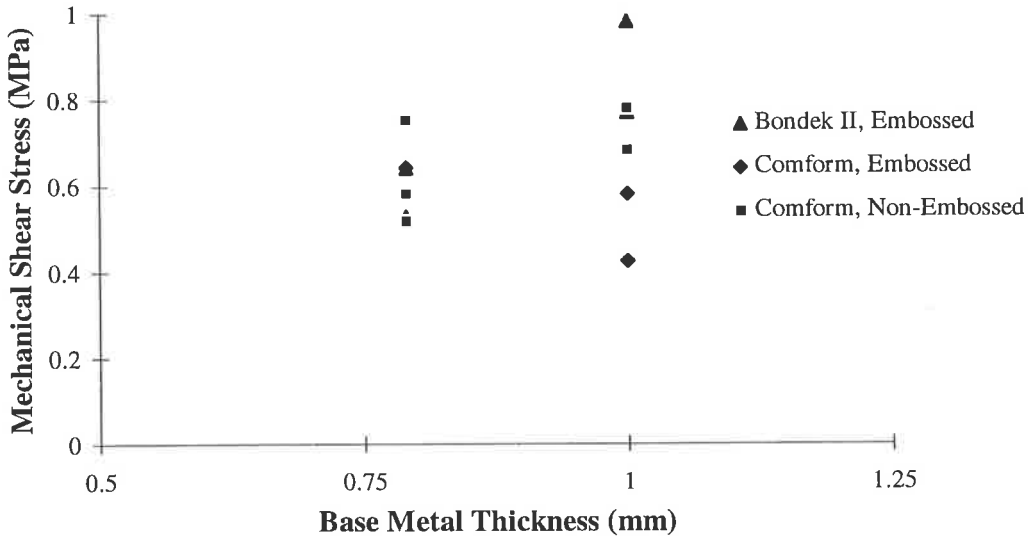
The variation in mechanical bond strength based on the rib contact area is shown in Fig. 3.119a, while the mechanical bond strength per metre width is given in Fig. 3.119b. The Bondek II sheeting shows a clear increase in bond strength with increasing sheeting thickness. An increase in shear resistance with increasing sheeting thickness can also be seen for the non-embossed Comform sheeting. However, the results for the embossed Comform sheeting exhibit significant scatter, and the same clear trend is not apparent. The trends in the mechanical bond strength are similar when expressed per metre width of sheeting, although the strength of the Bondek II sheeting increases relative to the Comform sheeting due to the greater number of ribs per metre width.

The values of maximum shear strength of the non-embossed Comform specimens are comparable to those of the embossed specimens. This result indicates that the presence of the embossments in the Comform profile does not significantly increase the shear strength of the sheeting. This can be explained by the location of the of the embossments in the rib, and the overall geometry of the rib. The embossments are situated in webs of the ribs which are completely encased in concrete, as shown in Fig. 3.102. The diagonal cracking which

originates at the ribs, as shown in Fig. 3.104, Fig. 3.105 and Fig. 3.109 for the embossed sheeting and Fig. 3.111 and Fig. 3.112 for the non-embossed sheeting, indicates that large splitting forces are developed at the ribs. The cracks were observed for the embossed and the non-embossed sheeting, indicating that the forces are developed by the shape of the rib itself, and not just by the embossments. This can be explained by the fact that even the non-embossed sheeting will have minor variations in the geometry of the rib, due to the tolerances of the rolling process. As the sheeting is forced to slip relative to the concrete, these imperfections tend to resist the slip, and develop splitting forces.



(a) Based on Rib Contact Area



(b) Per Metre Width of Sheeting

Fig. 3.119. Mechanical Shear Stress vs Sheeting Thickness

The variation in slip at which the maximum shear strength occurred is shown in Fig. 3.120. This figure indicates that there is no clear trend between the slip at the maximum shear stress and the sheeting thickness. The scatter in the Bondek II results can be attributed to difficulties in the experimental setup, as the high result of 6.7 mm slip was attributed to the bucking that occurred in Specimen PT4.11. The slip at the maximum shear strength for both the embossed and the non-embossed Comform specimens is below those for the Bondek II specimens. This may be attributed to the difference in the geometry of the embossments in the two profiles. The embossments of the Bondek II profile are shown in Fig. 3.121a, while those of the Comform profile are shown in Fig. 3.121b. The embossments of the Bondek II profile have a more pronounced rise, whereas the Comform embossments are more rounded. This difference results in the Bondek II profile obtaining its maximum shear resistance at a larger slip.

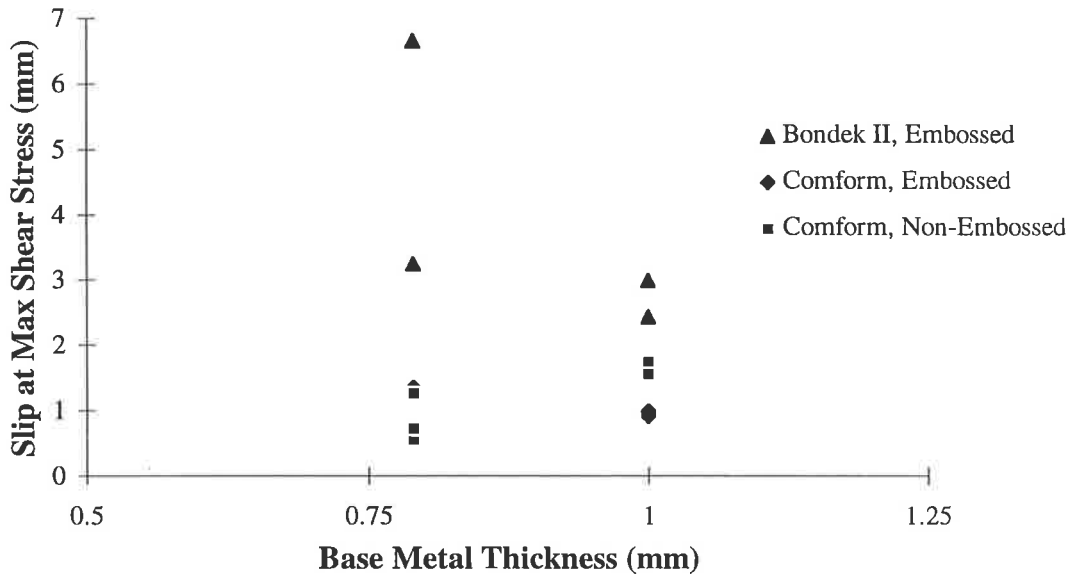
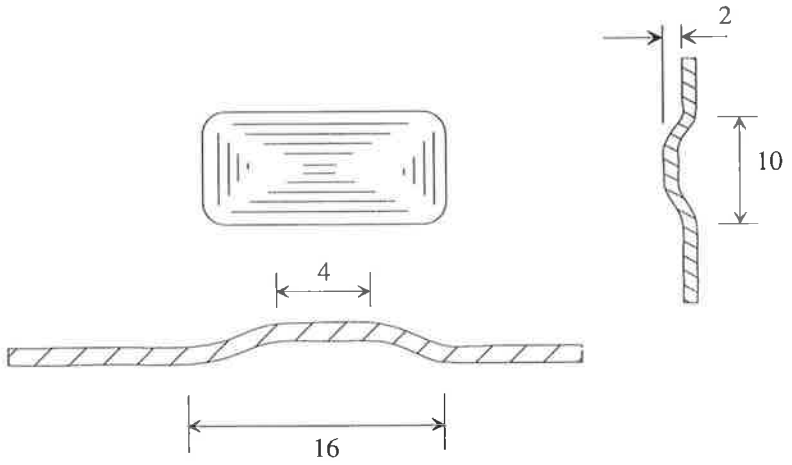
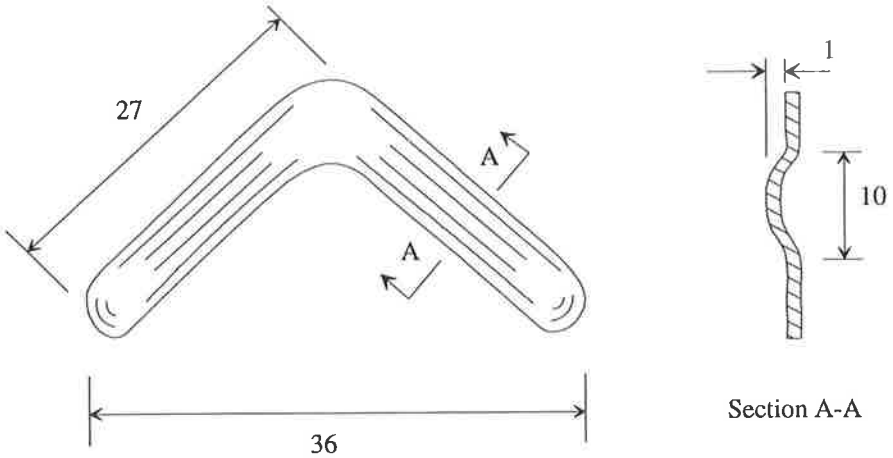


Fig. 3.120. Slip at Max Shear Stress vs Sheeting Thickness

The variation in the shear stress after 5 mm slip is shown in Fig. 3.122. There is a slight increasing trend with increasing sheeting thickness that can be seen for each of the profiles. The embossed Comform profile had a higher shear stress at 5 mm slip than the Bondek II profile for all but one of the tests, as also did the non-embossed Comform.



(a) Bondek II



(b) Comform

Fig. 3.121. Embossment Details

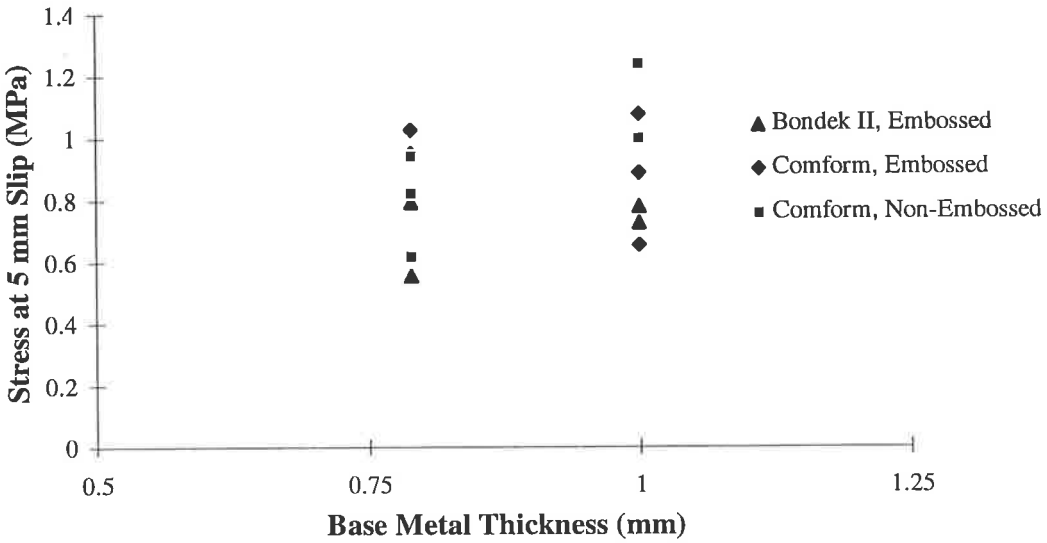


Fig. 3.122. Shear Stress at 5 mm Slip

3.5 Summary

A summary of the results of all the tests in Series 1, 2 and 3 is given in Table 3.14. This table contains the results of the tests on those profiles with a variable rib opening. The results of the preliminary series are not contained in the table as the overall geometry of the specimens was different to the subsequent series, and other aspects of the test setup were changed for each specimen which makes comparison with the other tests difficult. Furthermore, the shape of the profile rib used in the preliminary series was not the same as that for Series 1, 2 and 3. The different parameters that were varied and measured during the testing program are recorded in the table. The variation of the chemical bond stress, the maximum mechanical bond stress and the mechanical bond stress at 5 mm slip is shown plotted against the non-dimensional rib opening.

The maximum mechanical bond stress for the non-embossed specimens was taken as the bond stress at a slip of 5.0 mm. It was necessary to define the maximum bond stress at a certain level of slip as there was a continuous increase in the shear resistance of the non-embossed specimens with increasing slip. The limit of 5 mm was taken as a representative value of the expected maximum slip in a composite member with profiled sheeting. The variation in bond strength with slip for the non-embossed specimens is approximately linear after failure of the chemical bond, and if a limit other than 5 mm is desired, then the maximum bond strength may be changed linearly.

Specimen	Rib Opening (b_r/b_f)	Thickness (mm)	Uncoated	Emboss-ments	Chemical Bond Stress (MPa) (Total Contact Area)	Residual Bond Stress (MPa)	Max Mechanical Bond Stress (MPa)	Slip at Max Load (mm)	Mechanical Bond Stress at 5 mm Slip (MPa)
PT1.1	0.25	1.0	Yes	No	0.29	0.389	0.415	5.0	0.415
PT1.2	0.25	1.0	Yes	No	0.246	0.326	0.389	5.0	0.389
PT2.1	0.25	1.0	Yes	Yes	0.192	0.384	0.477	2.48	0.425
PT3.1	0.25	0.6	Yes	Yes	0.139	0.204	0.26	1.52	0.231
PT1.3	0.5	1.0	Yes	No	0.233	0.312	0.355	5.0	0.355
PT1.4	0.5	1.0	Yes	No	0.183	0.338	0.360	5.0	0.360
PT3.2	0.5	0.6	Yes	Yes	0.137	0.266	0.285	2.38	0.250
PT3.3	0.5	0.6	No	Yes	0.017	0.042	0.123	4.07	0.122
PT2.2	0.5	1.0	Yes	Yes	0.187	0.306	0.438	2.49	0.409
PT2.3	0.5	1.0	Yes	No	0.284	0.376	0.401	5.0	0.401
PT1.5	0.75	1.0	Yes	No	0.121	0.155	0.160	5.0	0.160
PT3.4	0.75	0.6	Yes	Yes	0.090	0.194	0.214	1.50	0.171
PT3.5	0.75	0.6	No	Yes	0.019	0.045	0.114	4.50	0.110
PT2.4	0.75	1.0	Yes	Yes	0.190	0.260	0.387	2.15	0.362
PT2.5	0.75	1.0	Yes	No	0.187	0.204	0.246	5.0	0.246
PT3.6	1.0	0.6	Yes	Yes	0.103	0.143	0.218	1.56	0.157
PT2.6	1.0	1.0	Yes	Yes	0.161	0.167	0.369	2.39	0.331
PT1.6	1.0	1.0	Yes	No	0.085	0.019	0.019	5.0	0.019
PT3.7	1.0	2.0	Yes	Yes	0.140	0.277	1.222	3.27	1.193

Specimen	Rib Opening (b_r/b_f)	Thickness (mm)	Uncoated	Emboss-ments	Chemical Bond Stress (MPa) (Total Contact Area)	Residual Bond Stress (MPa)	Max Mechanical Bond Stress (MPa)	Slip at Max Load (mm)	Mechanical Bond Stress at 5 mm Slip (MPa)
PT2.7	1.0	1.0	Yes	No	0.164	0.056	0.057	5.0	0.057
PT3.8	1.5	0.6	Yes	Yes	0.134	0.174	0.274	1.57	0.179
PT3.9	1.5	0.6	No	Yes	0.008	0.016	0.065	2.93	0.056
PT1.7	1.5	1.0	Yes	No	*	*	*	*	*
PT2.8	1.5	1.0	Yes	Yes	0.185	0.161	0.272	2.41	0.237
PT2.9	1.5	1.0	Yes	No	0.107	0.003	0.00	-	0.00
PT3.10	1.5	2.0	Yes	Yes	0.109	0.205	0.868	3.56	0.850
PT1.8	2.0	1.0	Yes	No	0.074	0.027	0.030	5.0	0.030
PT3.11	2.0	0.6	Yes	Yes	0.051	0.084	0.088	1.26	0.039
PT2.10	2.0	1.0	Yes	Yes	0.102	0.050	0.134	2.12	0.098
PT3.12	2.0	2.0	Yes	Yes	0.058	0.103	0.488	1.66	0.215
PT1.9	2.67	1.0	Yes	No	*	*	*	*	*
PT2.11	2.67	1.0	Yes	Yes	0.134	0.019	0.039	1.60	0.005
PT1.10	3.0	1.0	Yes	No	0.028	0.00	0.00	-	0.00
PT2.12	3.0	1.0	Yes	Yes	0.100	0.028	0.076	1.56	0.050

Table 3.14. Summary of Series 1, 2 and 3

A summary of the variation in the chemical bond strength with rib opening is shown in Fig. 3.123. The individual data points are not shown, but instead the linear regression lines are shown. Each of the data have been shown previously in Figs. 3.46, 3.69 and 3.95. A clear trend towards decreasing chemical bond strength with increasing rib opening can be seen in Fig. 3.123. The chemical bond strength of the 1.0 mm profiles was higher than that for the 0.6 mm profiles, whereas the results of the 2.0 mm profiles showed a decrease in the chemical bond strength when compared to the 1.0 mm profiles. This trend is shown more clearly in Fig. 3.130 and will be discussed further in Section 3.6.2. The embossed profiles tended to record a lower chemical bond stress than the non-embossed profiles for re-entrant rib geometries, ie $b_r/b_f < 1$, but a higher chemical bond for open rib geometries.

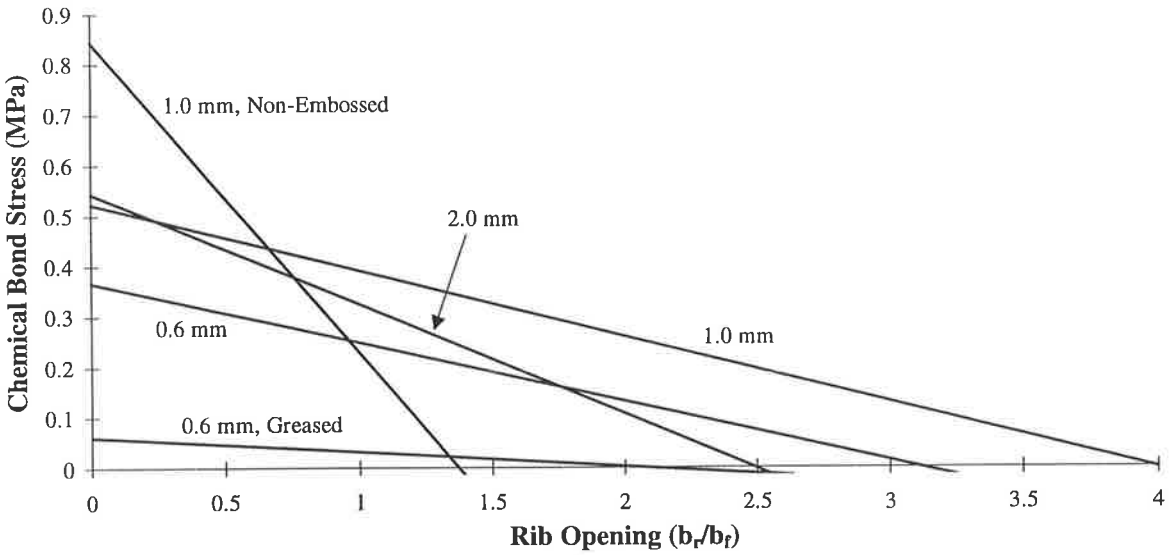


Fig. 3.123. Chemical Bond Strength vs Rib Opening

The results of the chemical bond strength have been summarised in Table 3.15, which gives the intersection of the regression line with the abscissa and ordinate axes, as well as the coefficient of determination. Also given in the table are the properties of the adjusted regression lines, which intersect the abscissa at $b_r/b_f = 2.7$ for the embossed profiles and $b_r/b_f = 1.0$ for the non-embossed profiles. The choice of $b_r/b_f = 2.7$ is based on the rib opening at which the sheeting is free to move laterally away from the concrete surface. This value is discussed further in Section 3.6.1.

Profile	Regression Line			Adjusted Regression Line		
	Abscissa	Ordinate	R^2	Abscissa	Ordinate	R^2
0.6 mm	3.1	0.37	0.68	2.7	0.39	0.64
0.6 mm, Greased	2.1	0.06	0.89	2.7	0.05	0.80
1.0 Non-Embossed	1.4	0.84	0.70	1.0	1.01	0.26
1.0 mm	4.0	0.52	0.92	2.7	0.58	0.29
2.0 mm	2.5	0.54	0.996	2.7	0.50	0.97

Table 3.15. Summary of Chemical Bond Strength

It can be seen in Table 3.15 that the chemical bond tends to zero (abscissa intercept) at values of b_r/b_f that range from 2.1 to 4.0 for the embossed profiles. There is only a slight decrease in the coefficient of determination when the regression line is made to pass through 2.7 on the abscissa, which indicates that this is a good approximation to the behaviour. The only exception is for the 1.0 mm sheeting, which shows a large drop in the coefficient of determination. This may be explained by the high chemical bond stress exhibited by the two specimens with the largest rib opening. If these results are not included, then the coefficient of determination for the adjusted line increases to 0.68, which is only slightly less than that for the unadjusted regression line. The variation in chemical bond strength as predicted by the adjusted regression lines is shown in Fig. 3.124

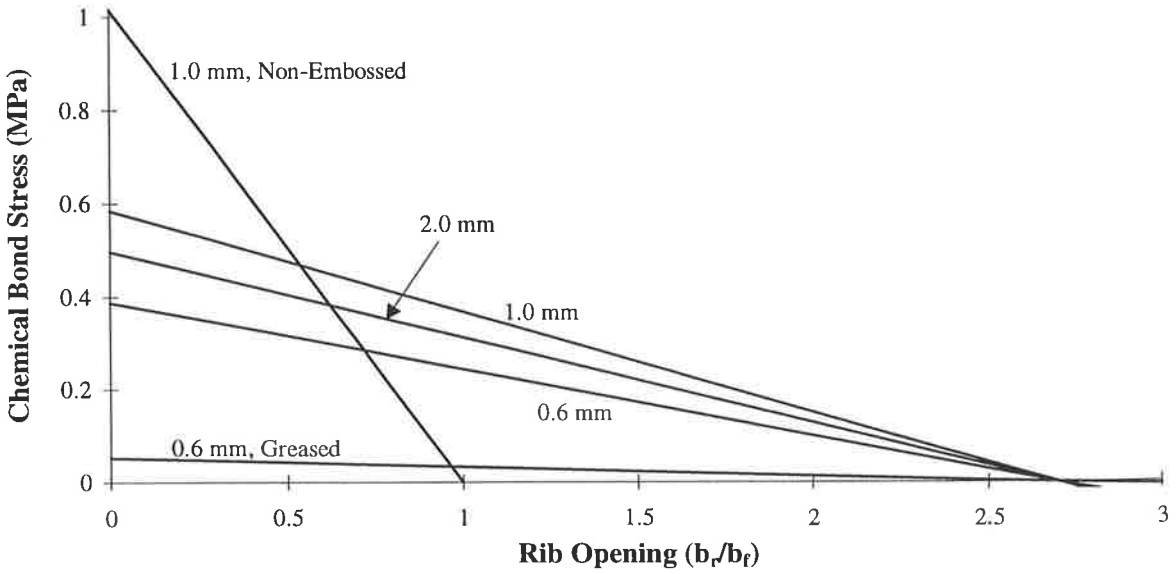


Fig. 3.124. Simplified Model for Chemical Bond Strength vs Rib Opening

A summary of the variation in the mechanical shear stress with rib opening is shown in Fig. 3.125. Each of the results have been shown previously in Figs. 3.72 and 3.97. It can be seen in Fig. 3.125 that the embossments increase the shear resistance of the profile compared to the non-embossed profiles, with the effect being more pronounced for ribs with a larger opening. There is a clear increase in the value of the rib opening at which mechanical bond strength becomes zero, with the addition of the embossments on the profiles. The regression line through the non-embossed profiles intercepts the abscissa at $b_r/b_f = 1.1$, whilst the regression lines for the embossed profiles intercept the abscissa between 2.6 and 3.9, as shown in Fig. 3.125. The results are summarised in Table 3.16. The 2.0 mm sheeting shows a marked increase in the shear resistance over the 1.0 mm sheeting and this effect is discussed further in Section 3.6.2.

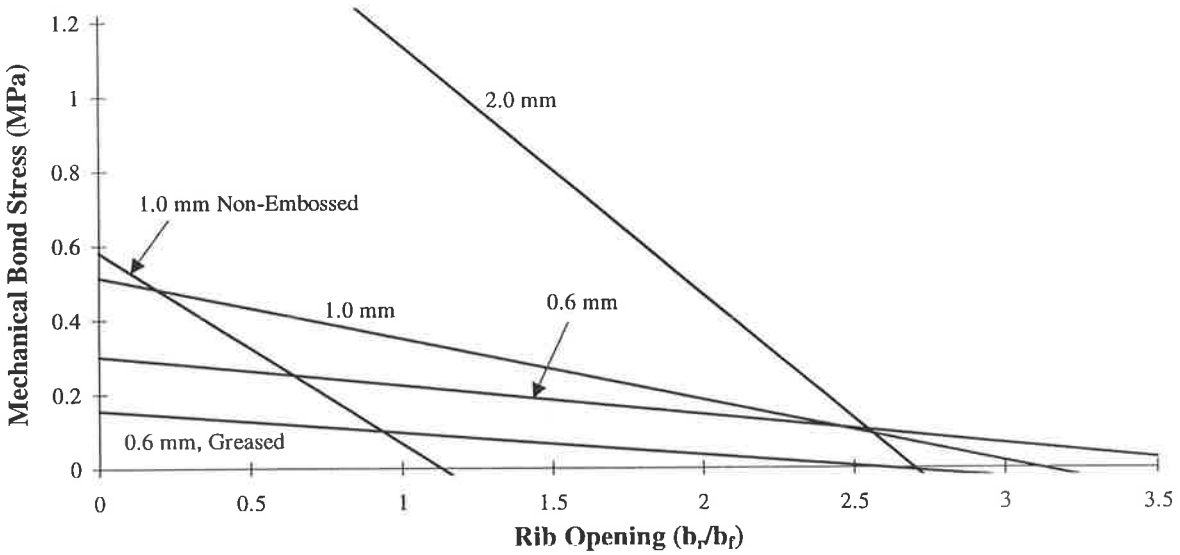


Fig. 3.125. Mechanical Bond Strength vs Rib Opening

The results of the regression analyses are shown in Table 3.16. It can be seen that the coefficients of determination are high for all profiles except the 0.6 mm sheeting. The high values of R^2 indicate a strong linear relationship between mechanical bond strength and rib opening. The lower value for the 0.6 mm sheeting may be attributed to higher variability in the profile geometry that occurred for the thinner sheeting, as discussed in Section 3.4.5. The high values of the coefficients of determination for the adjusted regression lines indicate the validity of setting the trend line through the abscissa values of 1.0 and 2.7 for the non-embossed and embossed profiles respectively. This simplified approximation to the results is shown in Fig. 3.126.

Profile	Regression Line			Adjusted Regression Line		
	Abscissa	Ordinate	R^2	Abscissa	Ordinate	R^2
0.6 mm	3.9	0.3	0.5	2.7	0.34	0.29
0.6 mm, Greased	2.6	0.16	0.99	2.7	0.15	0.99
1.0 Non-Embossed	1.1	0.58	0.89	1.0	0.63	0.83
1.0 mm	3.1	0.51	0.96	2.7	0.54	0.89
2.0 mm	2.7	1.8	0.996	2.7	1.8	0.96

Table 3.16. Summary of Mechanical Bond Strength

It can be seen in Fig. 3.126 that the mechanical bond strength decreases with a decrease in the thickness of the sheeting, and with the application of the debonding agent. The mechanical bond strength of the non-embossed sheeting is generally lower than the strength of the embossed sheeting of the same thickness.

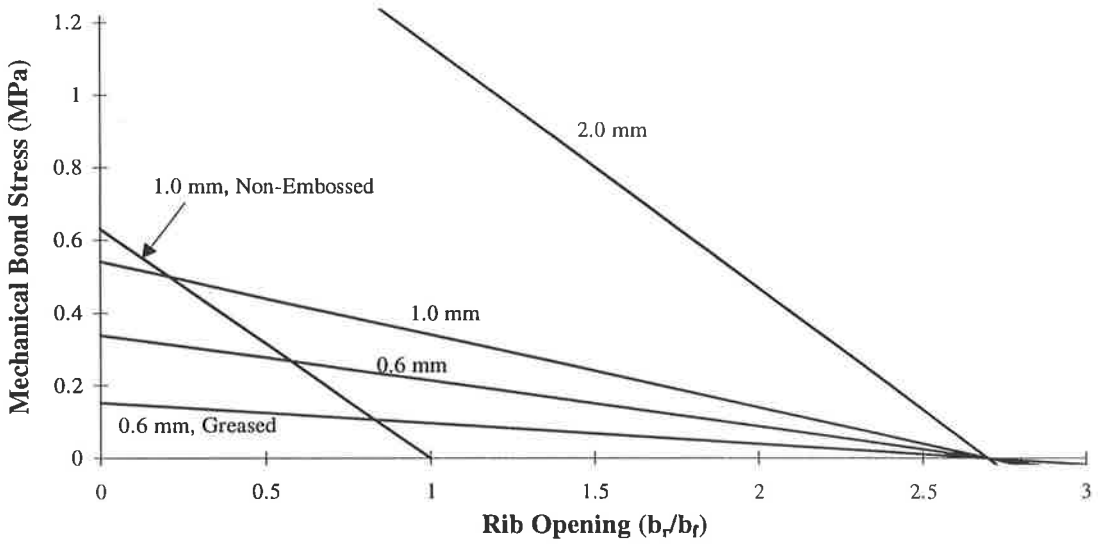


Fig. 3.126. Simplified Model for Mechanical Bond Strength vs Rib Opening

A summary of the variation in the bond stress after 5 mm slip is shown in Fig. 3.127. Each of the data are shown in Figs. 3.48, 3.71 and 3.98. Figure 3.127 indicates a similar trend to that for the mechanical bond strength shown in Fig. 3.125. The regression line through the data for the non-embossed profiles intersects the abscissa at $b_r/b_f = 1.1$, while the regression lines for the greased 0.6 mm profile and the 2.0 mm profile both intercept the abscissa at 2.3, and the non-greased 0.6 mm profile and the 1.0 mm profile intercept the abscissa at 2.7 and 2.9 respectively, as shown in Fig. 3.127. These results are summarised in

Table 3.17. These results are slightly below those which were derived from Fig. 3.125, which may be explained by the fact that at 5 mm slip, the peak in the shear strength has occurred, and the embossment is no longer in the concrete depression.

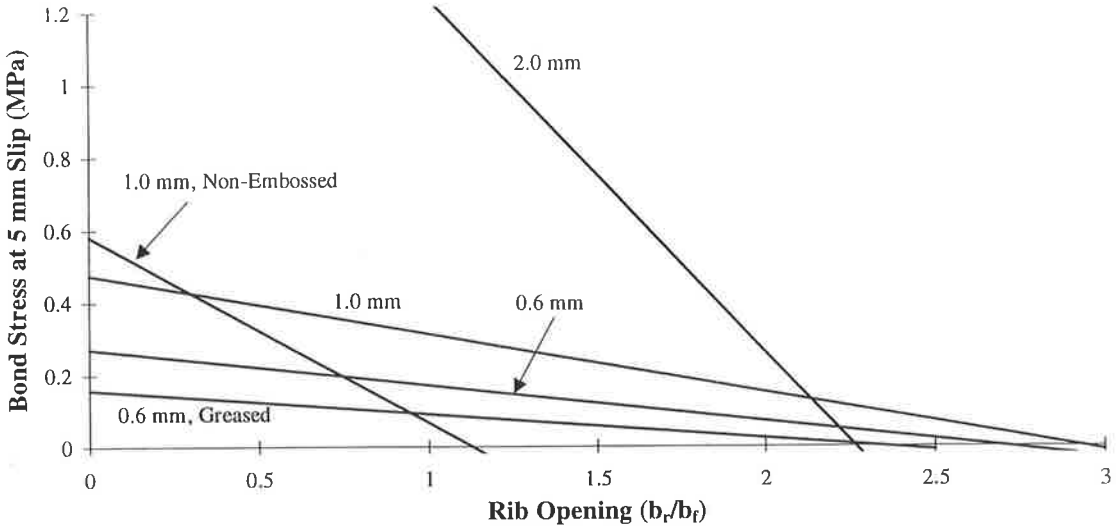


Fig. 3.127. Bond Strength at 5 mm Slip vs Rib Opening

It can be seen in Table 3.17 that the coefficients of determination are all high, except for the 0.6 mm sheeting. The high values of R^2 indicate the highly linear relationship between the bond strength at 5 mm slip and the rib opening. This is the same as the finding for the maximum mechanical strength as given in Table 3.16. The slightly lower R^2 for the 0.6 mm profiles can again be explained by the higher variation in the geometry of the thinner sheeting.

Profile	Regression Line			Adjusted Regression Line		
	Abscissa	Ordinate	R^2	Abscissa	Ordinate	R^2
0.6 mm	2.7	0.27	0.77	2.7	0.27	0.77
0.6 mm, Greased	2.3	0.16	0.995	2.7	0.15	0.96
1.0 Non-Embossed	1.1	0.58	0.89	1.0	0.63	0.83
1.0 mm	2.9	0.48	0.97	2.7	0.49	0.93
2.0 mm	2.3	2.2	0.97	2.7	1.8	0.86

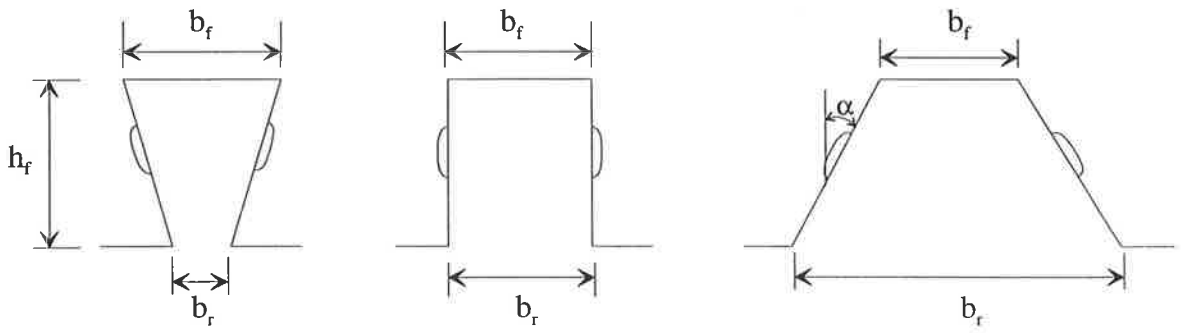
Table 3.17. Summary of Bond Stress at 5 mm Slip

The trend in the results of a decreasing bond strength with increasing rib opening is shown clearly in Figures 3.123, 3.125 and 3.127. This will be explained in the following section, along with the increase in strength with increasing sheeting thickness.

3.6 Analysis of Results

3.6.1 Effect of Rib Opening

From the results presented in this chapter it is clear that there is a decrease in the strength of the shear connection with an increase in the rib opening. The limiting rib opening at which the bond strength tends to zero can be determined from the geometry of the rib and the embossments. Shown in Fig. 3.128 are a series of ribs with increasing rib opening. For the re-entrant rib shown in (a) the lateral forces that are developed at the embossment are resisted by the overall shape of the rib. On the other hand, open rib geometries such as shown in (b) and (c) rely on the embossments to provide keying into the concrete and resist lateral separation. When the tangent to the embossment is vertical, as shown by the angle α in (c), then the sheeting can move freely away from the concrete, and the bond strength will drop to zero.



(a) $b_r/b_f < 1$ (b) $b_r/b_f = 1$ (c) $b_r/b_f > 1$

Fig. 3.128. Effect of Rib Opening

Considering the geometry of the embossments shown in Fig. 3.49c, the angle α can be determined as 48°, as shown in Fig. 3.129. From this value, and knowing that $h_r = 45$ mm and $b_f = 60$ mm, we get $b_r = 161$ mm, or $b_r/b_f = 2.7$. The limiting value of $b_r/b_f = 1.0$ for the non-embossed specimens is as expected, if a value of $\alpha = 0.0$ is used.

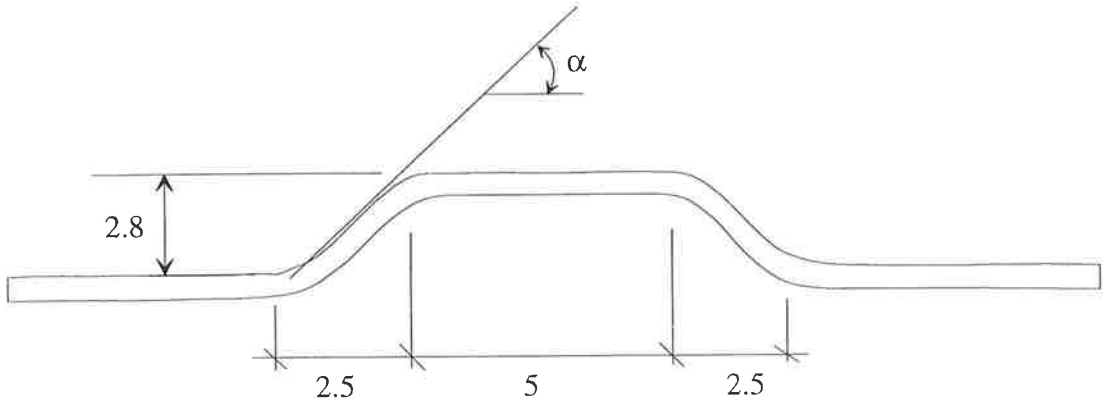


Fig. 3.129. Determination of Angle α

In the same manner that the regression line for the non-embossed sheeting was forced to intersect the abscissa at $b_r/b_f = 1$, the regression line for the embossed sheeting can be forced to pass through $b_r/b_f = 2.7$. The coefficient of determination can then be determined to check the appropriateness of this approximation.

3.6.2 Effects of Sheeting Thickness

The effect of the sheeting thickness on the chemical bond strength is shown in Fig. 3.130. From this figure it can be seen that there is no clear trend between the chemical bond strength and the sheeting thickness. It is expected that the chemical bond is a function of concrete properties and the surface condition of the sheeting, and is thus independent of the thickness of the sheeting. However, it was shown in Section 3.5 that the chemical bond appeared to vary with the rib opening. This result was due more to the peeling action of the failure mechanism than to the true chemical bond. Figure 3.130 indicates that the peeling action is not influenced by the sheeting thickness.

The effect of the sheeting thickness on the maximum mechanical bond strength can be seen in Fig. 3.131, whilst the effect on the mechanical bond strength at a slip of 5 mm can be seen in Fig. 3.132. It can be seen that there is a non-linear increase in the shear resistance of the sheeting as the thickness increases. This increase is due to the increase in the spring action that occurs for thicker sheeting. Referring to the deformation shown previously in Fig. 3.74 on page 174 and repeated in Fig. 3.133 it can be seen that as the concrete rides over the embossments there is a force F that develops at the embossment. This force has a horizontal component F_h and a vertical component F_V. The spring stiffness is proportional to the

flexural rigidity of the sheeting, thus the force F_V is proportional to t_p^3, which in turn means the horizontal component F_h is also proportional to t_p^3. The relationship between the bond strength f_b and the sheeting thickness t_p will be expressed in the form of Eq. 3.5.

$$f_b = a.t_p^n \quad \text{.....(3.5)}$$

where a and n will be determined from an analysis of the data.

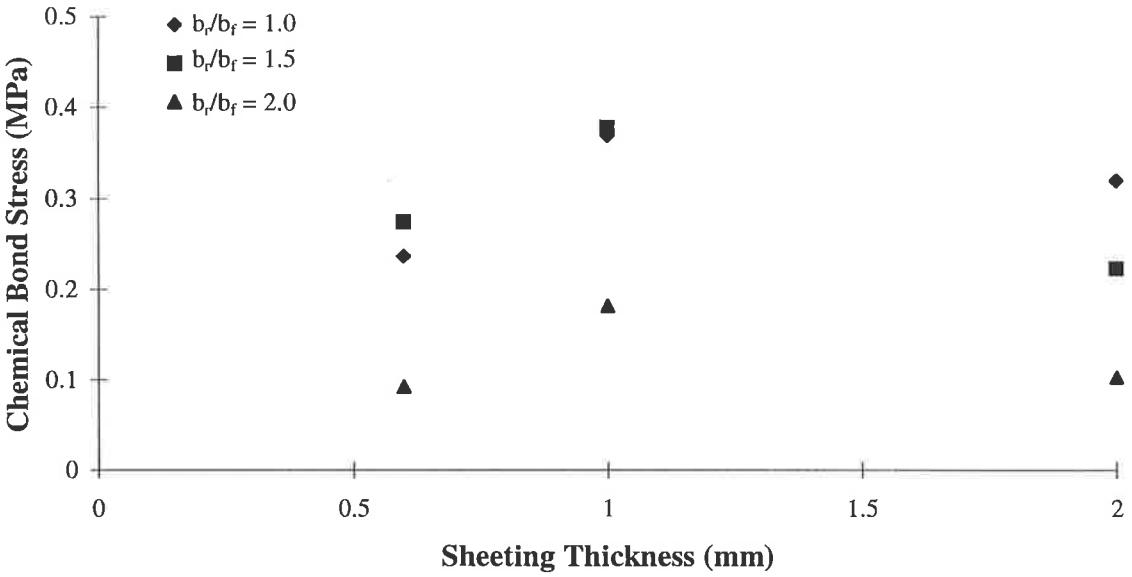


Fig. 3.130. Chemical Bond Strength vs Sheeting Thickness

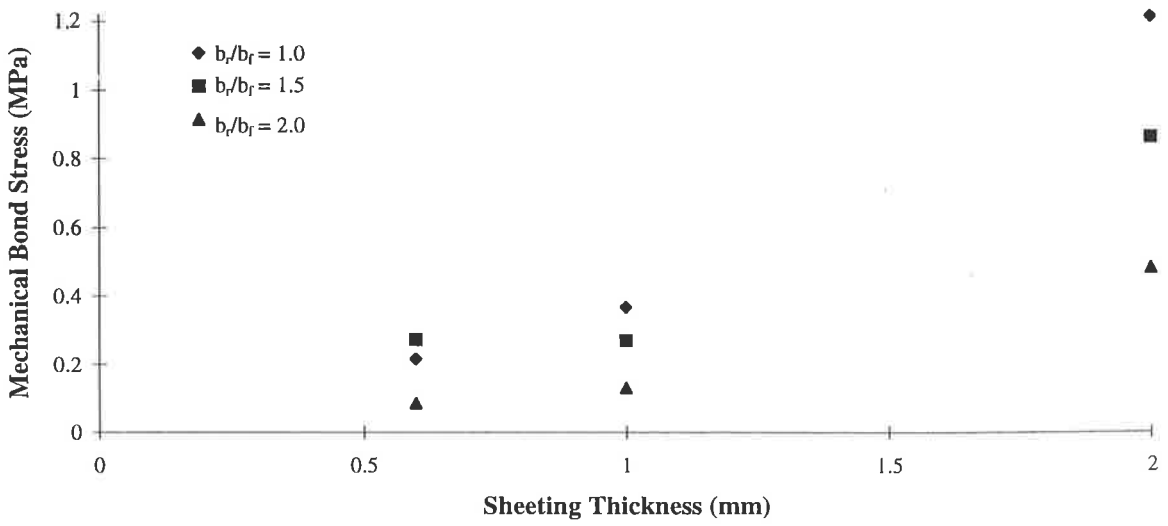


Fig. 3.131. Mechanical Bond Strength vs Sheeting Thickness

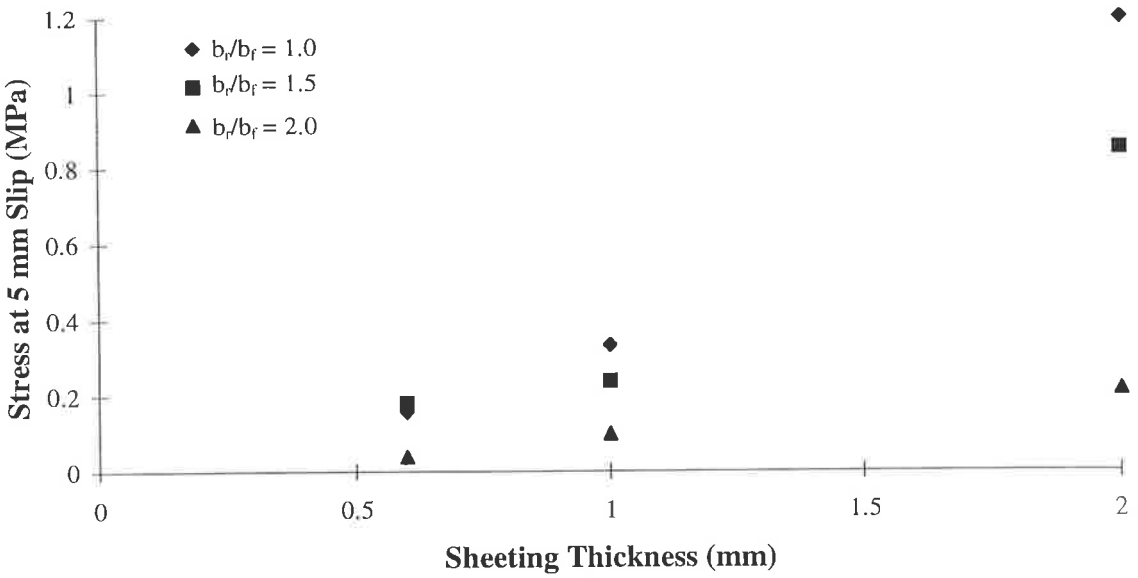


Fig. 3.132. Stress at 5 mm Slip vs Sheeting Thickness

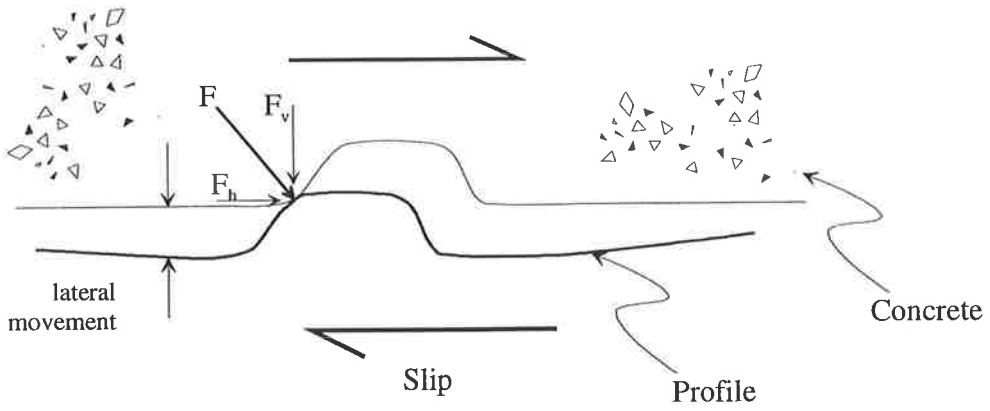


Fig. 3.133. Deformation at Embossments

In order to determine the relationship between bond force and thickness, the results have been plotted in log - log plots, as shown in Fig. 3.134 and Fig. 3.135. The slope of the linear regression line through the data points gives the exponent n in Eq. 3.5, and the intercept gives the coefficient a. In Fig. 3.134 the slopes of the regression lines vary from 1.0 for the profiles with a rib opening of $b_r/b_f = 1.5$, to 1.5 for the profiles with a rib opening of 1.0 and 2.0. In Fig. 3.135 the slopes of the regression lines vary between 1.3 and 1.7. A summary of the regression analysis is given in Table 3.18, which gives the values of the coefficient a and the exponent n for each of the rib openings. Also given in the table in the last row are the values for the coefficient and exponent as determined by the regression

through all of the data. It can be seen that these values represent an average of the values determined for the separate rib openings.

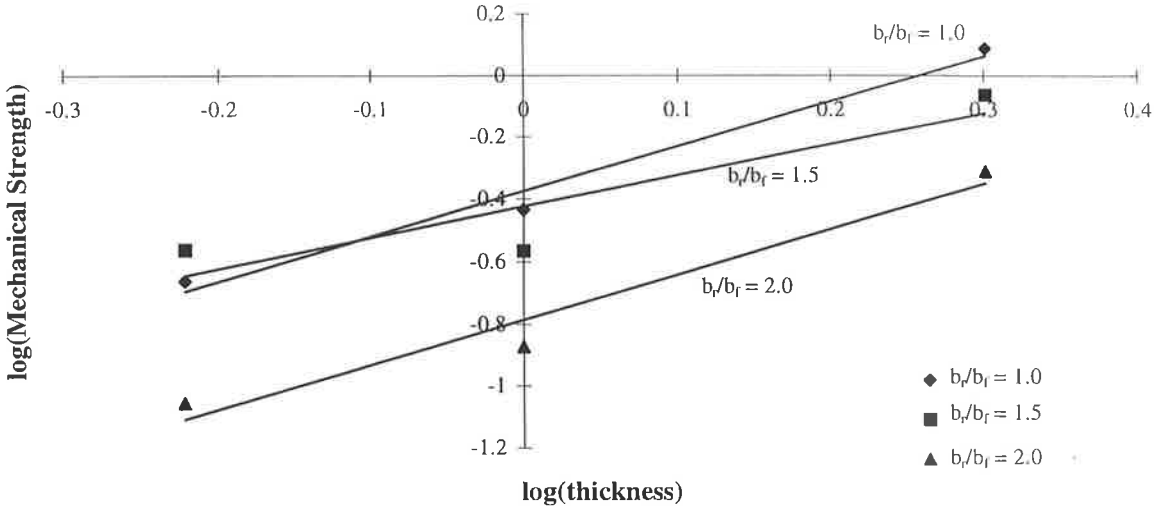


Fig. 3.134. Log - Log Plot for Mechanical Bond Strength

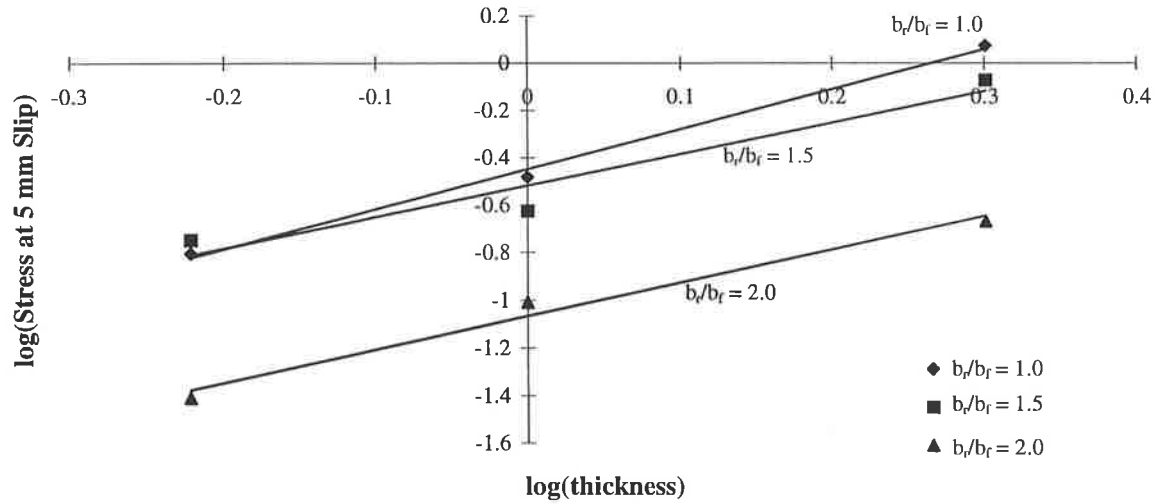


Fig. 3.135. Log - Log Plot for Bond Strength at 5 mm Slip

b_r/b_f	Mechanical Bond Strength		Bond Strength at 5 mm Slip	
	a	n	a	n
1.0	0.42	1.5	0.36	1.7
1.5	0.38	1.0	0.31	1.3
2.0	0.16	1.5	0.09	1.4
All	0.30	1.3	0.21	1.5

Table 3.18. Coefficients for Variation of Bond Strength with Thickness

From Table 3.18 it can be seen that the average variation in the mechanical bond strength with sheeting thickness is given by:

$$f_{b,m} = 0.3t_p^{1.3} \quad \text{.....(3.6)}$$

while the average variation in mechanical bond strength at 5 mm slip is given by:

$$f_{b,0.5} = 0.2t_p^{1.5} \quad \text{.....(3.7)}$$

The value of the exponent is less than 3, which indicates that the mechanism resisting transverse shear is influenced not only by the spring action of the sheeting. Due to the flexibility of the restraints at the sheeting edges, the resistance is less than that predicted from the flexural rigidity of the sheeting. The edges of the sheeting are not constrained from lateral movement, as indicated in Fig. 3.75 on page 175 at points A and B. Thus the force which is exerted by the sheeting on the concrete will be reduced from that which would occur if the sheeting edges were constrained, and hence the exponents in Eqs. 3.6 and 3.7 are less than 3.

3.7 Conclusions

Several conclusions can be made as a result tests carried out in this investigation. These can be grouped into two areas. The first relates to the optimal design of the push test, while the second relates to the behaviour of re-entrant and open rib profiles.

3.7.1 Push Test

These conclusions arose out of the results of the preliminary series of push tests, as well as from an analysis of the results and behaviour of the subsequent specimens. They relate specifically to the design and setup of push tests for the determination of the interface bond properties between profiled sheeting and concrete.

- The accurate measurement of interface bond requires careful consideration of a number of factors. The most important of these is the application of an external lateral restraining force on the sheeting. It has been shown that for profiled sheeting

incorporating embossments, longitudinal slip between the sheeting and the concrete is accompanied by lateral movement of the sheeting away from the concrete surface. This lateral movement is also present for profiles with a re-entrant rib geometry, although the magnitude is less than that observed in open rib profiles. Thus, any external lateral force will restrict the free deformation of the sheeting, and thus alter the shear bond characteristics of the profile.

- The decrease in chemical bond strength with increasing rib opening suggests that peeling action tends to reduce the effectives of the chemical bond for more open rib geometries. It is expected that the chemical bond should remain constant for any rib geometry, and that it should be a function of the concrete properties and the surface condition of the sheeting. The apparent variation in the chemical bond strength as measured from these tests indicates that this test procedure should not be used in the determination of the chemical bond strength of profiled sheeting.
- The application of the debonding agent was effective in reducing the chemical bond significantly, but did not completely remove it. However, the debonding agent also tended to lubricate the surface, and hence changed the subsequent behaviour of the shear-stress / slip relationship. The maximum mechanical bond was reduced, and the slip at which it occurred was increased. Thus, it is recommended that the use of a debonding agent not be used in the preparation of the push test specimens.

3.7.2 Behaviour of Re-entrant and Open Rib Profiles

These conclusions are based on the results of the 36 specimens tested as part of this research project. These conclusions represent a qualitative assessment of the results, and identify general trends that occurred.

- The shear strength of profiled sheeting is related to the rib opening: profiles with a larger rib opening have a decreased shear resistance. This decrease in shear resistance with increasing rib opening occurred for all thicknesses of sheeting, for profiles with and without embossments, and also for sheeting with and without the debonding agent.
- There is a maximum rib opening which if exceeded will result in the complete loss shear capacity after failure of the chemical bond. For profiles without embossments

this limit is approximately $b_r/b_f = 1$, which corresponds to a square rib. For the embossment geometry adopted in this study, the limit is approximately $b_r/b_f = 2.7$. This limit is a function of the embossment geometry and would vary for different embossments.

- The limit in the rib opening is related to the ability of the sheeting to resist the lateral forces which develop during longitudinal slip and tend to force the sheeting away from the concrete. For non-embossed profiles, this limit is reached when the rib opening is equal to the width of the rib flange, and the sheeting is free to move laterally away from the concrete. For profiles with embossments in the webs of the ribs, the limiting rib opening is increased due to the keying action of the embossments. The limiting rib opening is increased by increasing the height of the embossments.

- Embossments improved the mechanical shear resistance of the sheeting. There was little improvement as $b_r/b_f \rightarrow 0$, however the increase in shear resistance was more noticeable for the open rib geometries. The non-embossed profiles with large rib openings failed completely after failure of the chemical bond, whereas the embossed profiles exhibited continued shear resistance after failure of the chemical bond.

- The shear strength of the profile is increased by increasing the thickness of the sheeting. The relationship between the shear strength of the profile f_b and the thickness t_p is of the form $f_b = a.t_p^n$, where n is between 1.3 and 1.5.

Chapter 4

Profiled Composite Beams

4.1 Introduction

The use of profiled steel sheeting as permanent formwork in the construction of reinforced concrete slabs has increased in popularity over the last several decades in commercial construction, and increasingly in domestic construction. Composite profiled beam construction represents a logical extension of the use of profiled sheets in the construction of reinforced concrete structures. It consists of using profiled steel sheets to form the shape of reinforced concrete beams instead of traditional timber formwork. A typical arrangement of a composite profiled beam and slab is shown in Fig. 4.1.

After the concrete has been poured, the ribs in the profiled sheeting provide a positive key into the concrete which allow the profiled sheeting to act compositely with the encased reinforced concrete section, increasing its strength and stiffness (Oehlers, 1993).

This form of construction realises many of the benefits that have made composite slabs a viable alternative to standard slab construction, with several additional benefits. These include (Oehlers, 1993; Uy and Bradford, 1993a; Bradford and Kyakula, 1994):

- The profiled box section becomes a permanent and integral component of the beam, eliminating the need for formwork stripping;
- The side profiled sheeting is equally effective in positive and negative moment regions;
- It increases the shear and flexural strength of the encased beam;
- The profiled sheeting acts integrally with the concrete, and reduces the amount of conventional reinforcement required, with subsequent savings in supply and fixing;
- Encasement of concrete on three sides reduces moisture loss, and hence reduces shrinkage of the concrete. This in turn reduces the long term deflections due to creep and shrinkage, and allows an increase in the span/depth ratios;
- Being manufactured off site and under factory conditions will save in total construction time and delays;
- The light weight of the box section makes transport form the factory easy and cost effective, and
- It provides a clean, attractive streamlined finish that can be left exposed if desired.

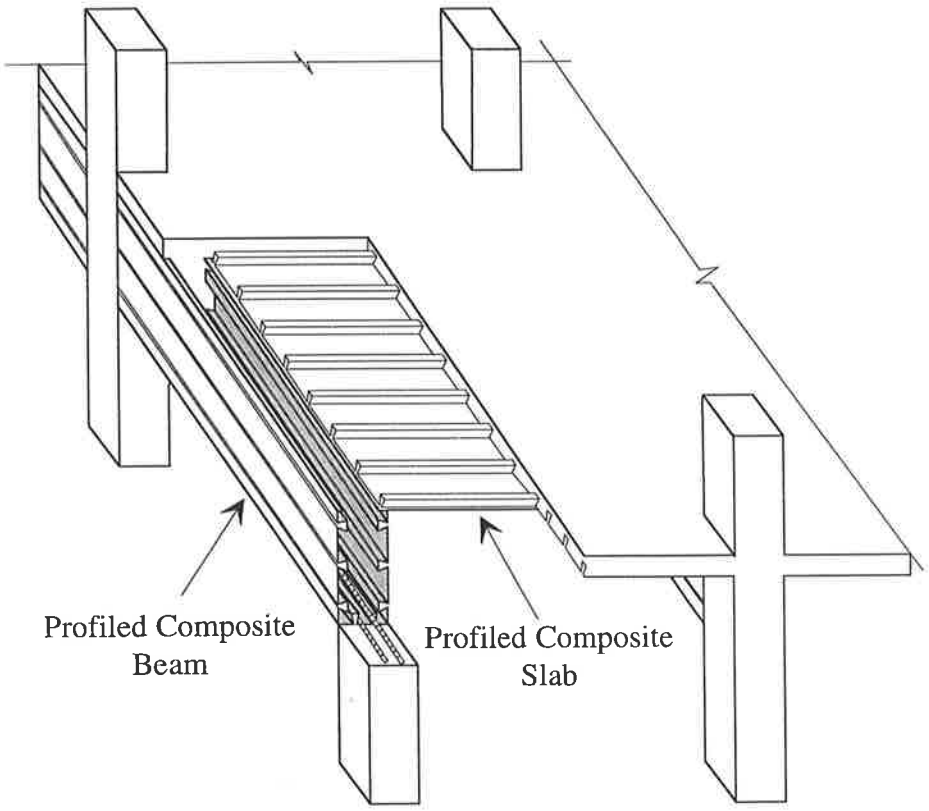


Fig. 4.1. Profiled Beam and Slab

There are some possible drawbacks with this form of construction, some of which are:

- Difficulties in making site alterations to the formwork;
- Off site labour requirements to manufacture the beams;
- Fire proofing may need to be applied to the member if the whole cross-section is used to resist the fire loads;
- Buckling of the profiled sheeting in the compression region can limit construction loads,
- The distance between the ribs needs to be less than for standard composite slab construction, and so current sheet profiles are not appropriate.

This chapter presents the previous research that has been carried out in the area of profiled beams. It then discusses the design of composite profiled beams, and presents a method to determine their flexural strength. It also addresses the issue of local buckling of the profiled sheeting, and the effect it has on determining the flexural strength.

4.2 Literature Review

4.2.1 Overview

The use of profiled sheeting in the construction of composite slabs has been widely adopted, however the use of steel sheeting as permanent formwork in the construction of reinforced concrete beams is relatively new. As a result there has been limited research in this area, and there is little published information. Much of the research that has been carried out to date has been limited to full scale testing of particular configurations, often with no theoretical analyses contained in the published literature.

This literature review will contain a brief description of most of the published data in the area of reinforced concrete beams incorporating steel sheeting as permanent formwork. Some of the references are contained for completeness, and as a background to the current state of knowledge in the area.

The use of steel shuttering as permanent formwork for beam and slab systems has been adopted on various construction sites primarily in order to provide reduced cycle times and shallower beam and slab depths. One such example has been reported in the literature by McBean (1990). The system was known as a pan floor system and used structural steel plate as the formwork for the primary beams, and Z purlins as the formwork for the secondary beams, as shown in Fig. 4.2.

The pan floor system, while providing the benefits for construction, is still not optimal as the universal beam and steel plates in the primary beams and the Z purlins used in the secondary beams were not treated as acting compositely with the enclosed concrete. If longitudinal shear connection was provided, shallower depths could have been achieved.

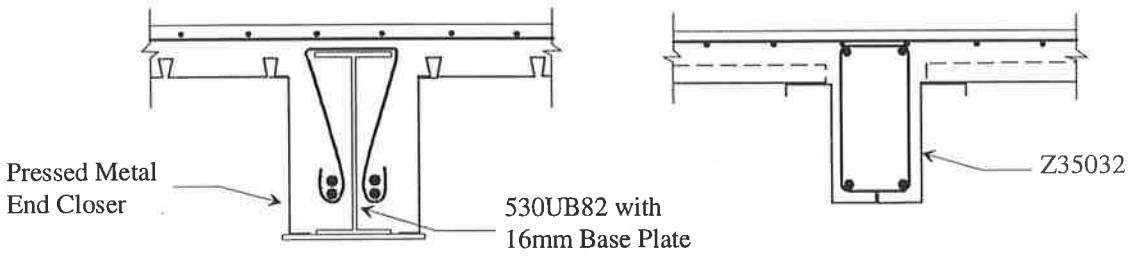


Fig. 4.2. Pan Floor System (McBean, 1990)

Lowe and Choong (1990) and Low (1993) studied a system known as externally reinforced concrete. This system consists of rectangular hollow steel sections which are filled with concrete. This system does not provide longitudinal shear connection, and does not provide restraint to eliminate local buckling of the steel sections. The main benefit of this system is its use as permanent formwork during construction, as well as the increased ductility under reverse loading conditions. However, due to the lack of longitudinal shear connection between the external steel tubing and the enclosed concrete, there is no composite action, and thus the increase in strength due to external reinforcing is not maximised.

Lowe (1991) also suggested that transverse reinforcement is required to support the external tubing against buckling due to the large hydrostatic pressure heads from wet concrete loading during construction. This is a factor which must be considered in a permanent formwork system for a beam, particularly for large depth and long span beams. In such situations the hydrostatic pressure from the wet concrete is significant, and gives rise to large in-plane and out-of-plane stresses acting on the external steel sheeting. These forces can be

carried either through internal bracing as proposed by Lowe (1991) or by external propping (Burnet and Oehlers, 1995; Uy, 1995).

Daalov and Petrov (1990) studied the load-deflection behaviour of beams with cold-formed sheeting used as permanent formwork and external reinforcing, as shown in Fig. 4.3. Their study represented prototype testing for a particular building project, rather than a parametric study of the effect of longitudinal shear connection, and the conclusions drawn were specific to the arrangement of the reinforcement and the shear connection. Experimental results showed an increase in the load carrying capacity of the section of approximately 40% by the addition of L-shaped shear connectors. The shear connectors consisted of cold-formed steel ribs 20 x 20 x 3 mm, welded to the inside soffit at 50 mm intervals, as shown in Fig. 4.3. The strength of the individual shear connectors was not determined, and no estimate of the degree of shear connection was made, thus it is not possible to determine the effectiveness of the shear connectors. The presence of buckling in the sheeting was not reported, although based on the geometry of the section it is likely to have occurred.

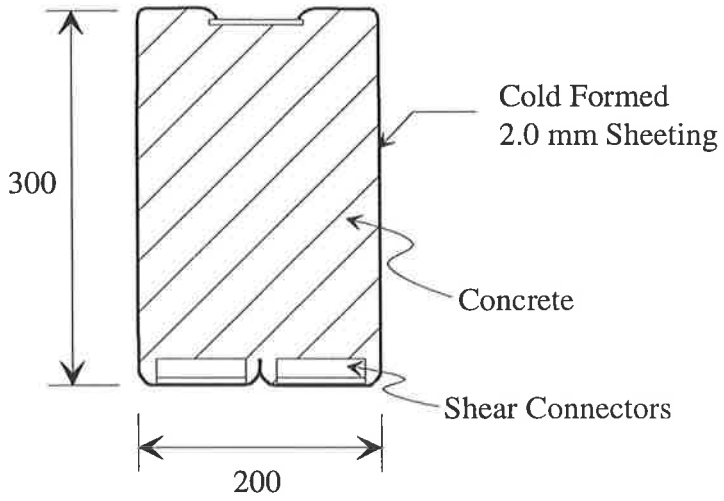


Fig. 4.3. Externally Reinforced Beam (Daalov and Petrov, 1990)

The earliest known use of profiled sheeting in the construction of concrete beams in Australia was in 1987 (Patrick and Bridge, 1988). The profiled sheeting was used as permanent formwork and tensile reinforcement for one way slabs and band beams in a concrete framed building. A cross-section through a band beam is shown in Fig. 4.4. In this arrangement the sheeting was used as soffit reinforcement and formed metal sheeting was used for the sides of the beams.

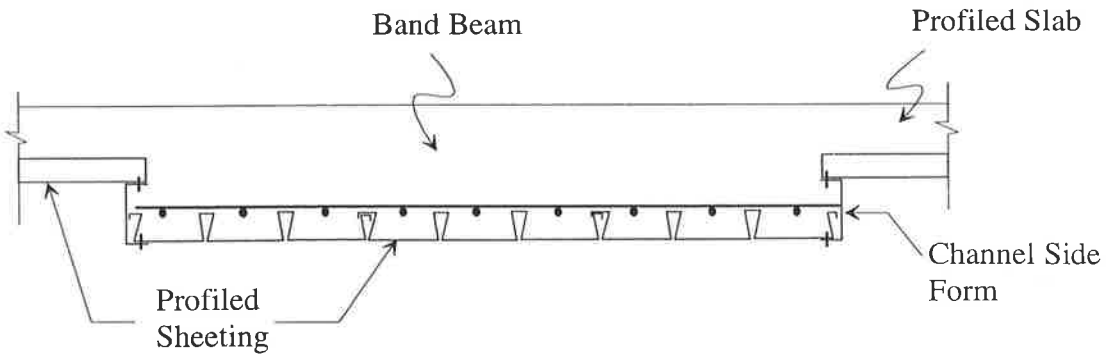


Fig. 4.4. Profiled Composite Slab and Band Beam System (Patrick and Bridge, 1988)

A design procedure was produced (Patrick et al, 1989) which used a code based methodology for the design of composite band beams using proprietary sheeting and end anchors. It was stated that the procedures were only applicable to that one form of sheeting when used in conjunction with the proprietary end anchors. Using the guidelines, the soffit sheeting could be considered to be fully effective in the positive moment regions, however, the edge forms were neglected in all calculations of strength and serviceability. The design procedure was based on the results of full scale testing of profiled band beams, and no attempt was made to develop a rational design procedure allowing for the effects of partial interaction, or the use of other forms of profiled sheeting. Furthermore, the design recommendations were limited to beams within the range of parameters tested, ie. the sheeting thickness must be between 0.70 mm and 0.80 mm thick, the beam length must be between 5.0 m and 10.0 m, the proprietary end anchors must be used and the sheeting must be the same as that tested. As such, the design procedure lacks a rational foundation and gives no insight into the controlling parameters in the design of profiled beams.

The profiled composite beam concept, where the profiled sheets were used compositely for the sides of a concrete beam, as well as the soffit, was first developed by Oehlers (1993). A series of beams were tested in flexure and shear, in order to assess the contribution of the profiled sheeting to the strength and ductility. The beam cross sections are shown in Fig. 4.5, and the resulting load-deflection curves for flexure are shown in Fig. 4.6. The results of the shear tests on the beams are contained in Chapter 6. Results from these tests showed that the side profiled sheeting increases the flexural strength of the encased reinforced concrete beam by approximately 20%, and the shear strength by approximately 110%. It can be seen that the resulting failures are ductile in nature. This is in contrast to the result of adding more tension reinforcement, which reduces ductility.

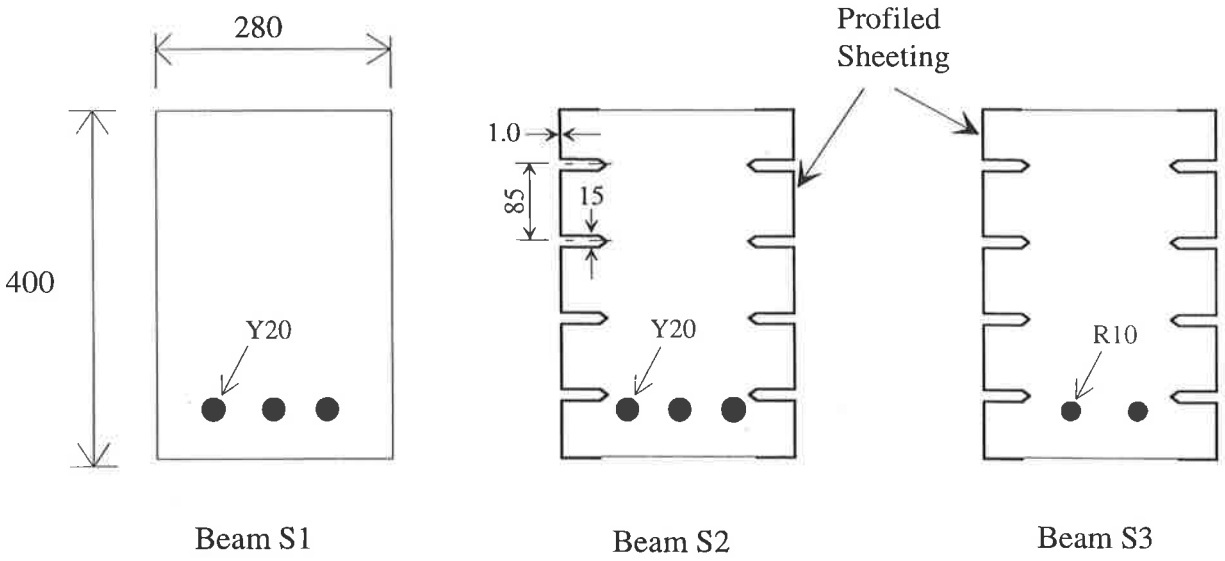


Fig. 4.5. Beam Cross Sections (Oehlers, 1993) Fig_Oehlers_Cross_Sections \!

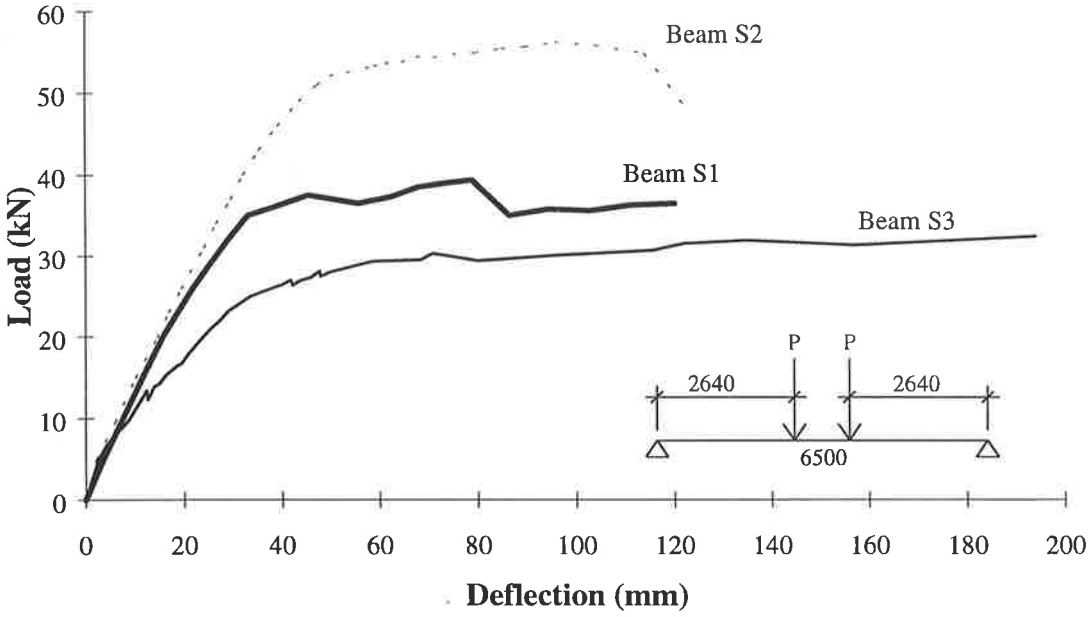


Fig. 4.6. Flexural Strength of Profiled Beams (Oehlers, 1993)

4.2.2 Long Term Deflections

Uy and Bradford (1993a, 1994a) undertook a series of service load tests on profiled composite beams in order to determine the creep and shrinkage effects. The results showed that the time dependant deformations of the profiled composite beams were significantly less than those of the reinforced concrete beams of the same flexural strength. This was due to

the reduction in the creep and shrinkage effects of the concrete, which resulted from the reduced moisture loss from the concrete. The cross-section of the beams used in the tests are shown in Fig. 4.7, and the resulting deflection time histories are shown in Fig. 4.8. The reinforced concrete beams were used as control specimens, and were designed with the same ultimate strength as the profiled beams. Beams R1 and P1 were subjected to self weight only, whereas beams R2 and P2 were subject to a sustained uniformly distributed load of 7.5 kN/m. The test results compared well with theoretical analyses which accounted for the change in free surface area of the profiled beam and the reduced creep and shrinkage coefficients.

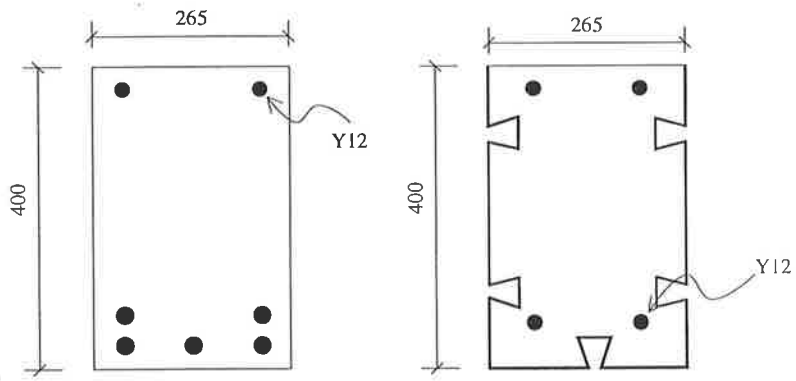


Fig. 4.7. Beam Cross-Sections (Uy and Bradford, 1994)

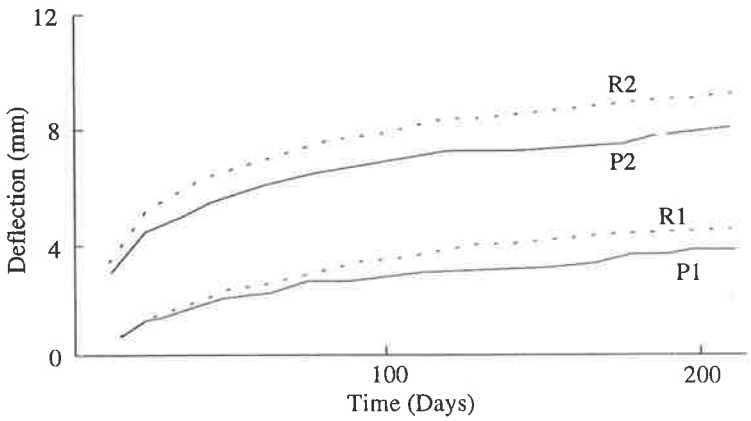


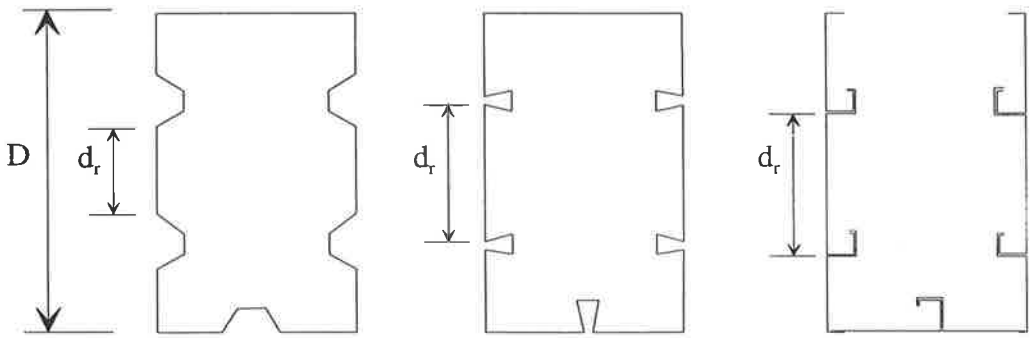
Fig. 4.8. Deflection Time History (Uy and Bradford, 1994)

The results given in Fig. 4.8 indicate the beneficial effect of profiled sheeting in reducing the time-dependant deflections of reinforced concrete beams. Alternatively, for a particular span and limiting deflection, the depth of the beam may be reduced.

Bradford and Kyakula (1994) investigated the influence of the profiled sheeting on the transverse shear strength of profiled composite beams. A series of three beams were tested and the results compared with the Australian standard for concrete structures. The results showed that the simplified theoretical analysis was in good agreement with the shear strengths measured in the tests. A further discussion of the shear strength of composite profiled beams is covered in Chapter 6

4.2.3 Local Buckling

Uy (1995) and Uy and Bradford (1993b, 1995) studied the stability of profiled composite beams during the construction phase. The elastic semi-analytical finite strip method was used to study the local buckling of the unbraced trough sections manufactured from three types of rib geometries, namely Trapezoidal, Dovetail and L-Rib, as shown in Fig. 4.9. The variation of the elastic local buckling coefficient with trough geometry was established and design curves were produced. It was found that the trapezoidal ribs are the most effective rib type for delaying the advent of local buckling. This was followed by the dovetail ribs and then the L-ribs. The difference between the buckling coefficients can be



(a) Trapezoidal Rib (b) Dove Tail Rib (c) L-Rib

Fig. 4.9. Profiled Beam Cross-Sections

explained from inspection of Fig. 4.9, which indicates that for a constant depth of beam D, and constant number of ribs, that the distance between the ribs d_r will be a minimum for the trapezoidal ribs, and a maximum for the L-Rib. Furthermore, the direction changes of the sheeting at the rib are smaller in the trapezoidal ribs than the dove-tail ribs and the L-ribs, which also enhanced the buckling resistance. Despite trapezoidal ribs having a higher

buckling resistance, other considerations such as the development of longitudinal bond favour re-entrant rib geometries such as dovetail and L-ribs. This will be discussed further in Chapter 5.

Oehlers et al. (1994), Uy (1995), Uy and Bradford (1993a, 1993c, 1994b, 1995) and Wright (1990, 1993) investigated the local buckling effects of the sheeting when used compositely with concrete. It was found that the concrete offered beneficial restraint to the sheeting and increased its buckling capacity. Thus, traditional methods of determining the buckling capacity of the profiled sheeting were inaccurate and overconservative.

There are two reasons why the buckling coefficients normally applied to thin walled sections give conservative results when applied to profiled composite beams. Firstly in composite construction, the formation of the buckle is restricted to occur outwards from the concrete, whereas for typical buckling problems, the sheeting is free to buckle in both directions about its equilibrium position (Wright, 1993; Uy and Bradford, 1993c; Oehlers et al., 1994). Secondly, the fold lines between the plate elements do not act as hinges, as is assumed in traditional buckling analysis, but are restrained to act as fully fixed supports. The waveform of the buckle alters from a sine to a cosine form both longitudinally and laterally and the wavelength decreases. These effects act together to increase the bucking strength of the sheeting.

Wright (1990, 1993) and Oehlers et al. (1994) used energy methods to determine relevant buckling coefficients for composite profiled beams. The method is applicable to mild structural steel which exhibits a strain hardening range, with a uniform compression acting across the plate width. Residual stresses were not included in the analysis. This work presented buckling coefficients for the elastic and inelastic range of steel in contact with a rigid medium. These values of the buckling coefficients can be used in the standard buckling equation for plate elements in compression, which is given in Eq. 4.1 (Timoshenko and Gere, 1982).

$$\left(\frac{b}{t}\right)^2 = \frac{k\pi^2 E_s}{12 f_{py}\left(1-\nu^2\right)} \qquad \text{.....(4.1)}$$

where

k = Buckling Coefficient

b = Width of sheeting between supports

t = Sheeting Thickness

E_S = Young's modulus for the profiled sheeting

f_{py} = Yield stress for the profiled sheeting

ν = Poison's ratio

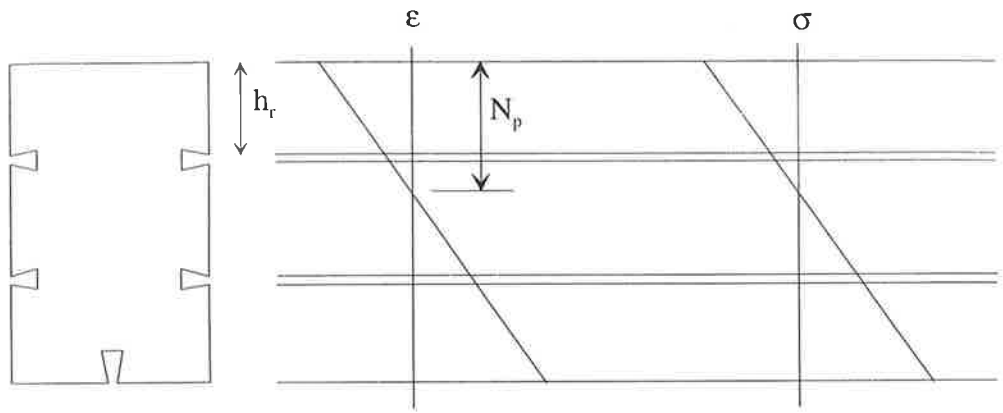
It was found from these analysis that the values of k for an internal plate which was fully supported on both sides was 10.67, and for an edge plate that was full supported on three sides with the other side free was 3.88. These values can be expressed as non-dimensional slenderness ratios, expressed in the form $b/t\sqrt{f_{py}/550}$. For steel with a Young's modulus of 200 000 N/mm^2 and $\nu = 0.29$, this gives $b/t\sqrt{f_{py}/550} = 60.1$ and 36.1 respectively. The results are shown in column 2 of Table 4.1. These compare with the values for a plate element not restrained by concrete of 36.3 and 11.8, for the two cases of an internal plate and an edge plate respectively, as given in column 1. The parameter α is described in the following paragraph.

Boundary Condition	**Unrestrained Sheeting** (1)	**Wright, Elastic Analyis** (2)	**Uy, Elastic Analysis** (3)		**Uy, Inelastic Analysis** (4)	
	α=1	α=1	α=1	α=0	α=1	α=0
Internal Member	36.3	60.1	64.5	83	20	35
External Member	11.8	36.1	25	28	10	17

Table 4.1. Allowable Plasticity Slenderness Limits

The parameter α is a measure of the variation in the stress throughout the depth of the element, as shown in Fig. 4.10. This figure shows a beam cross-section in (a) with a rib spacing of h_r, and the strain profile in the sheeting is shown in (b) where N_p is the depth of the neutral axis below the top. The resulting stress-profile is shown in (c), from which it can be seen that there is considerable variation of the stress throughout the depth of each element of the profiled sheeting. A measure of the variation in stress is given by the expression for α which is given by Eq. 4.2. When the depth to the profile neutral axis is large in comparison to the distance between the ribs then α tends to 1, and the stress is approximately uniform, whereas for large spacing of ribs and a small depth to the profile neutral axis, α tends to zero.

$$\alpha = 1 - \frac{h_r}{N_p} \quad \text{.....(4.2)}$$



(a) Cross-Section (b) Strain Profile (c) Stress Profile

Fig. 4.10. Derivation of α

It should be noted that the procedure adopted by Wright (1990, 1993) and Oehlers et al. (1994) assumes that the compressive stress is constant over the width of the element. That is, they have assumed that $\alpha = 1$. This is true for members in pure compression, but is not the case when the member is subject to bending, as is the case in a composite profiled beam. When the distance between the ribs is small, then the variation in stress over the depth of the compression element will be small and the stress can be approximated as uniform. However, when the distance between the ribs is a significant proportion of the depth of the beam, then the assumption of uniform stress becomes unduly conservative.

Uy (1995) and Uy and Bradford (1993c, 1994b) used a semi-analytical finite strip method to analyse the buckling of a steel plate in contact with a rigid medium. Initially, the study considered elastic behaviour of cold formed steel and assumed the stress-strain relationship was infinitely linear. A non-uniform compressive stress across the depth of the element was allowed for in the procedure. To obtain the minimum buckling stress of a plate assembly, the buckling half wavelength was varied and the local buckling stress was determined. A plot of the local buckling stress against the half-wavelength was then made and the critical stress was then found from the minimum of the curve. This procedure was repeated for different degrees of stress variation α. A summary of the results is given in column 3 of Table 4.1. This table gives the non-dimensionalised slenderness ratio $b/t\sqrt{f_{py}/550}$ necessary to achieve the yield stress before buckling occurs, assuming that the

sheeting remains linear elastic after the yield strain is exceeded. This analysis has limitations, and is used as a first approximation only for the slenderness ratios of partially constrained sheeting.

Subsequent to these analyses, the inelastic buckling behaviour was investigated and a non-linear stress-strain relationship was used (Uy, 1995; Uy and Bradford, 1994b; 1994c). Residual stresses were not included in these analyses as they were considered to have no effect on the bucking behaviour. The results for an element fully supported on all sides is shown in Fig. 4.11, and a summary for the different boundary conditions is given in column 4 in Table 4.1. Figure 4.11 shows the variation in the critical stress to cause buckling σ_{ol}, against the non-dimensional slenderness of the element in compression $b/t\sqrt{f_{py}/550}$. The critical stress is shown non-dimensionalised by dividing by the yield stress of the profile f_{py}. Shown in this figure are the curves for a range of values of α. The derivation of these curves is highly dependant on the choice of the stress-strain curve used for the profile sheeting, however, only one stress-strain curve was used in the analyses. Figure 4.11 can be compiled

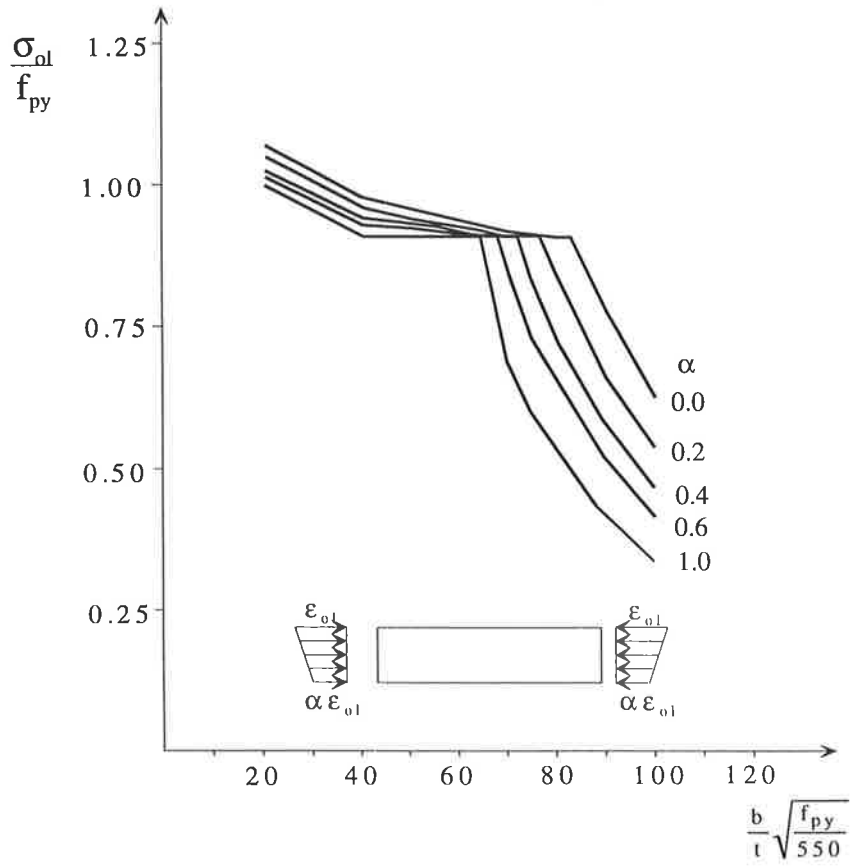


Fig. 4.11. Slenderness vs Dimensionless Critical Stress (Uy and Bradford, 1993c)

for different boundary conditions, from which column 4 in Table 4.1 can be produced, which gives the variation in the non-dimensionalised plate slenderness limits necessary to achieve full yield across the whole of the plate before buckling occurs. Linear interpolation for intermediate values of α may be used when determining the slenderness limits from Table 4.1.

The elastic buckling slenderness limits in columns 2 and 3 of Table 4.1 are in reasonable agreement for the two procedures presented by Wright and Uy. These values represent the limiting slenderness required for buckling to occur just as the yield stress is reached in the profile. However, for the calculation of the ultimate flexural capacity of profiled composite beams, rigid plastic analysis procedures will be used which assume the materials can exhibit significant deformation whilst maintaining the yield stress. Thus the inelastic slenderness limits in Table 4.1, as determined by the inelastic analysis of Uy, are more appropriate for use in the limit states design of profiled composite beams.

As was stated earlier, the values given in Table 4.1 are highly dependant on the form of the stress-strain curve used for the profiled sheeting, however only one stress-strain curve was used. It is recommended, therefore, that further analyses be carried out to check the variation of the slenderness limits for different stress-strain curves. In the absence of other data, the values given in Table 4.1 will be used for the remainder of this thesis.

4.2.3.1 Effective Width

As a plate element is loaded axially to the point of buckling, a non-uniform stress distribution develops across the section. The most highly stressed portions are those regions closest to the unloaded supported edges, as shown in Fig. 4.12a. One way to account for the non-uniform stress distribution is to assume that the maximum edge stress acts over a certain portion of the plate width b_e in Fig. 4.12b, and the remaining plate is ineffective in resisting the applied load. The stressed portion of the plate is called the effective width b_e and is shown in Fig. 4.12b. In this manner, the compression element of actual width b is replaced by one of effective width b_e. Adopting a similar procedure to that outlined by Trahair and Bradford (1988) and used in AS 1538 (SAA, 1988b) and AISI (1987), the effective width of a profiled unit is given by Eq. 4.3. The term λ represents the ratio of the actual plate slenderness ratio to the allowable slenderness limit given in Table 4.1.

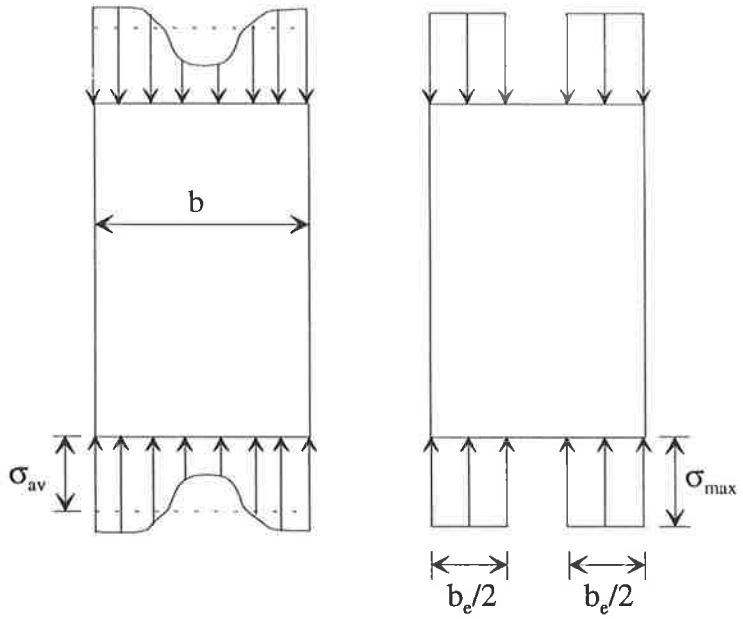
$$b_e = b\lambda(1-0.22\lambda) \quad \text{.....(4.3)}$$

where

λ = λ_a/λ_e

λ_e = Actual plate slenderness $\frac{b}{t}\sqrt{\frac{f_{py}}{550}}$

λ_a = Allowable plasticity slenderness limit given in column 4 of Table 4.1



(a) Actual Stress Distribution (b) Effective Width Concept

Fig. 4.12. Effective Width Concept for Simply Supported Plates

The values of λ_a given in column 4 of Table 4.1 have been obtained from an inelastic finite strip analysis of profiled composite beams performed by Uy and Bradford (1994b). The analysis ignores the beneficial effect of the post-buckling reserve of strength in the profiled steel and, hence, represents a conservative lower bound to the plasticity limits. The strain gradient α, allows for the effect of non-uniform compression, and linear interpolation may be used for intermediate values of α.

4.3 Flexural Strength Analysis

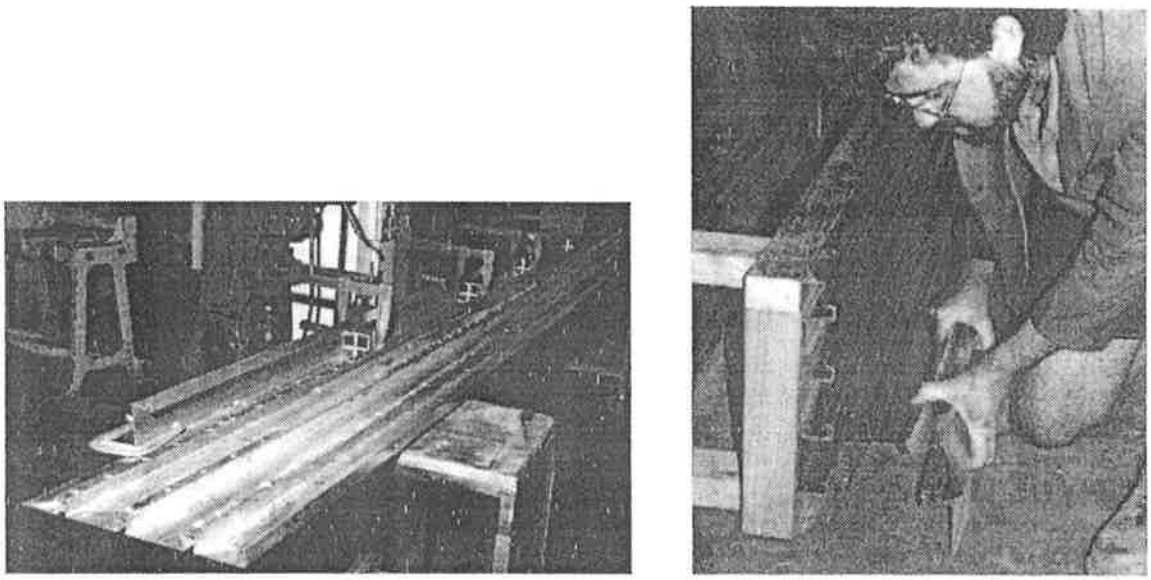
The flexural strength analysis of composite profiled beams is presented here; the analysis is based on the assumptions of rigid plastic behaviour. Rigid plastic design is used with acceptable accuracy in the design of steel beams, reinforced concrete beams, and composite steel and concrete beams. A comparison between the theoretical flexural strength of composite profiled beams based on rigid plastic design, and the results from a number of full scale tests is given in the next chapter. It was found that the results compared favourably, and that rigid plastic design of composite profiled beams represents an accurate means of determining the ultimate flexural strength.

This thesis presents two fundamental methods of constructing profiled composite beams. These two methods will each have different methods of analysis, each of which are presented here. The two methods of construction are:

1. Welded Construction
2. Clipped Construction

Welded construction is when the sheeting is formed into a rigid U-shaped section which encloses the concrete on three sides, such that there is no discontinuity in the sheeting around the perimeter that would permit longitudinal slip. This may be achieved by using a single sheet to form the shape of the beam, as used by Kyakula (1992) and Uy and Bradford (1994). Alternatively, the shape of the beam may be built up from individual units which are subsequently welded together into a braced box section before being erected on site. The units being welded together are shown in Fig. 4.13a. This method of construction will be discussed first in Section 4.3.2.

Clipped construction is when the units are assembled on site by 'clipping' individual units together, and the interlocking is achieved only by the shape of the ribs. Thus the individual units are free to slip longitudinally, relative to one another. The erection of a beam using clipped construction is shown in Fig. 4.13b. This method of construction will be discussed in Section 4.3.3.



(a) Welded Beams (b) Clipped Beams

Fig. 4.13. Construction Techniques for Profiled Composite Beams.

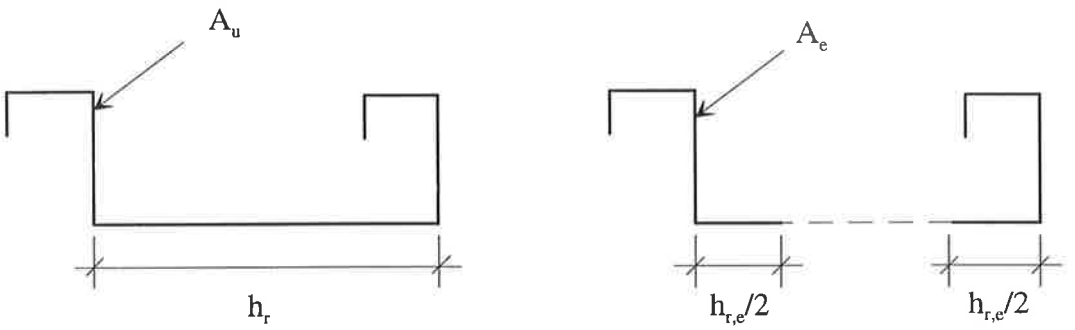
In order for rigid-plastic analysis to be used to determine the flexural strength of a profiled composite beam, buckling of the profiled sheet prior to full plasticity being reached must be allowed for. A procedure which allows for buckling of the profiled sheeting to be incorporated into the rigid-plastic analysis is given in the following section.

4.3.1 Buckling of Profiled Sheeting

In order for the full yield strength of the profiled sheeting in compression to be used in design, buckling of the profiled sheet should not occur until after full plasticity has been reached. This will occur when the unsupported width of the profiled sheeting is within the plasticity limits for the material, as given in column 4 of Table 4.1. However, typical b/t ratios of the profiled sheeting used in a profiled composite beam are usually such that some buckling will occur in the compression region before full plasticity of the sheeting has been achieved. Thus, a procedure is needed to account for the effect of local buckling in the sheeting.

By adopting an effective width for the profiled units in the compression region of a composite profiled beam, a reduced effective area of the profiled units may be obtained. This procedure is outlined in Section 4.2.3.1 and is shown in Fig. 4.14, where the original profiled unit is given in (a) and the equivalent unit with the reduced effective width is given in (b). These units are similar to the units used in the profiled beam shown in Fig. 4.9c. The ribs of

the profiled units are embedded in the concrete, and thus will not buckle, however, the pan between the ribs h_r is susceptible to buckling due to the large unsupported length and high b/t ratio. The effective width $h_{r,e}$ is derived from Eq. 4.3 where h_r is substituted for b. The original cross-sectional area of the profiled unit, A_u in Fig. 4.14a, will be reduced to an effective cross-sectional area A_e in Fig. 4.14b, due to the reduced effective width of the profile pan.



(a) Complete Profile Unit (b) Reduced Effective Width

Fig. 4.14. Cross Section of Profiled Steel Unit

It is possible to determine a reduction ratio β which relates the reduced effective area A_e of the profiled units to their original cross-sectional area A_u. The reduction ratio may be defined as

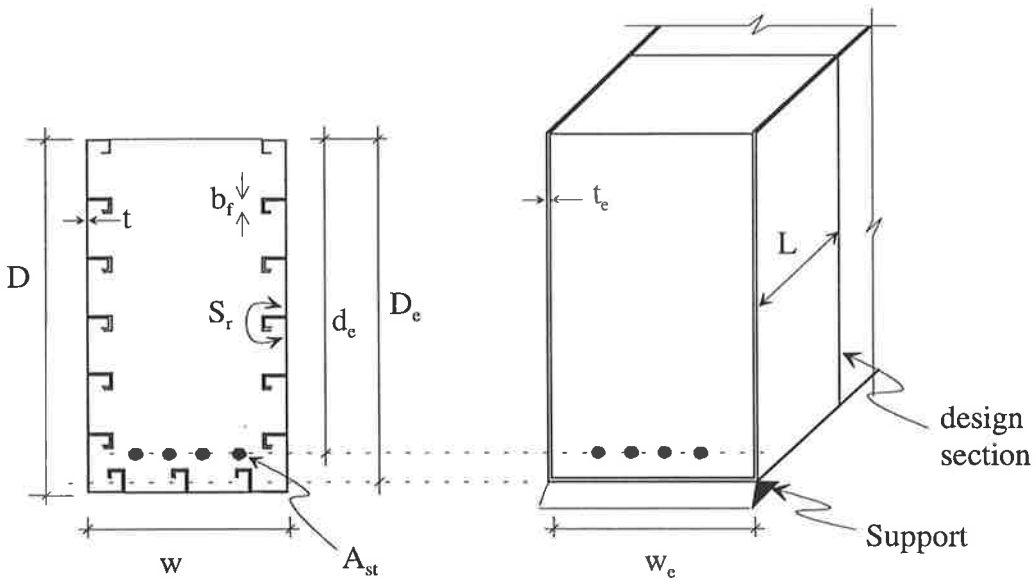
$$\beta = \frac{A_e}{A_u} \quad \text{.....(4.4)}$$

The compressive yield stress f_{py} used in the rigid plastic analysis is then be multiplied by this reduction ratio to give a reduced effective compressive yield stress f_{ye}, to account for the reduced effectiveness of the profiled units, as given in Eq. 4.5. This procedure then allows the total area of profiled sheeting to be used in the analysis, and greatly simplifies the design process. This will be detailed in the following section.

$$f_{ye} = \beta f_{py} \quad \text{.....(4.5)}$$

4.3.2 Welded Construction

A cross section of a profiled beam is shown in Fig. 4.15a, where the external sheeting has been assembled by welding individual profiled units such as those shown in Fig. 4.14a. When the individual ribs are rigidly connected to each other, this cross-section can be simplified to the shape shown in Fig. 4.15b for analysis purposes. This effective cross-section can also be used for systems constructed from a single profiled sheet. The effective width of the profiled beam w_e can be taken as the width of a rectangular block that encloses the same area of concrete as the profiled beam. When the void enclosed by the horizontal ribs is small, such as when L-Ribs are used, then the effective width can be taken as the overall width of the beam.



(a) Actual Cross-Section (b) Idealised Cross-Section

Fig. 4.15. Idealisation of Composite Profiled Beam

The effective depth of the profiled beam D_e can be taken as the distance from the top compression fibre to the centroid of the soffit decking. The centroid of the tension reinforcement of area A_{st} will be assumed to act at a distance d_e from the top fibre. The profiled sheeting is considered to be evenly distributed around the perimeter of the equivalent concrete cross-section, such that the total area of sheeting remains constant. The equivalent thickness is then given by Eq. 4.6.

$$t_e = \frac{A_p}{2D_e + w_e} \quad \text{.....(4.6)}$$

where

A_p = Total cross-sectional area of profiled sheeting

D_e = Effective depth of cross-section

w_e = Effective width of cross-section

The flexural strength of composite profiled beams is dependant on the strength of the shear connection between the sheeting and the concrete. This is analogous to the dependence in a standard composite beam where the strength of the shear connection also influences the flexural strength of the beam.

The development of longitudinal shear between profiled sheeting and concrete has been dealt with in Chapter 4. It was observed that in general, there was a variation in the shear resistance of the sheeting as slip progressed at the interface. However, those ribs with an L-Rib geometry tended to produce a more uniform shear resistance with increasing slip. For the purposes of this analysis, the development of bond between the sheeting and the concrete is modelled as being perfectly rigid-plastic, and is shown diagrammatically in Fig. 4.16 by the thick line. That is, as the applied shear stress increases, there is no slip at the interface until the applied shear stress reaches a limiting value of the bond shear strength, τ_b. The connection can then no longer sustain an increase in the applied shear and slip commences. As slip progresses, the shear stress remains constant at τ_b. The value of τ_b which is used in the analysis depends on the geometry of the profile being used. When the profile exhibits significant variation in the shear resistance with slip, as shown by the thin line in Fig. 4.16, then an estimate of τ_b must be made. As a conservative estimate the residual stress after the peak in the curve may be taken as the strength of the shear connection.

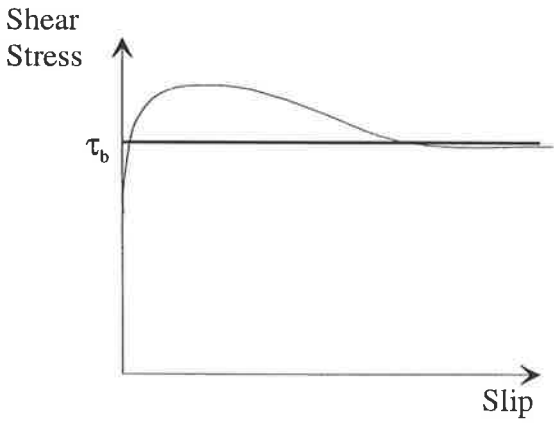


Fig. 4.16. Idealised Shear Stress vs Slip Relationship

For this analysis, it is assumed that the location of maximum moment in the beam has been determined and is at a distance L from the nearest support, as shown in Fig. 4.15. The maximum bond force that can be developed between the support and the critical cross-section, at a distance L from the support, is given by Eq. 4.7.

$$F_b = \tau_b S_r n_r L \quad \text{.....(4.7)}$$

where

τ_b = The rib shear strength

S_r = The interface perimeter of a single rib, as shown in Fig. 4.15

n_r = Number of ribs in the cross-section.

4.3.2.1 Partial Shear Connection

Consider the section of the composite profiled beam shown in Fig. 4.17a. The design point is at a distance L from the end of the beam as shown in Fig. 4.17b. When a moment is first applied to the beam the same strain distribution ε_{fsc} exists through the reinforced concrete section as well as through the profiled section, as shown in (c). The subscript fsc in (c) refers to full shear connection, and psc in (d) refers to partial shear connection. The composite beam with the strain profile in (c) is said to exhibit full interaction as there is no slip across the steel-concrete interface, and the slip strain is zero. The bond force across the interface prevents slip occurring and hence ensures that the position of the neutral axis N, in the reinforced concrete element is coincident with the neutral axis of the profiled box element. As the curvature ϕ is increased, the moment increases, thereby causing an increase

in the interface bond force. If the maximum moment capacity is reached without the interface bond force exceeding the interface bond strength, then the composite section is said to have full shear connection as well as to exhibit full interaction. In this form of construction, full shear connection is synonymous with full interaction.

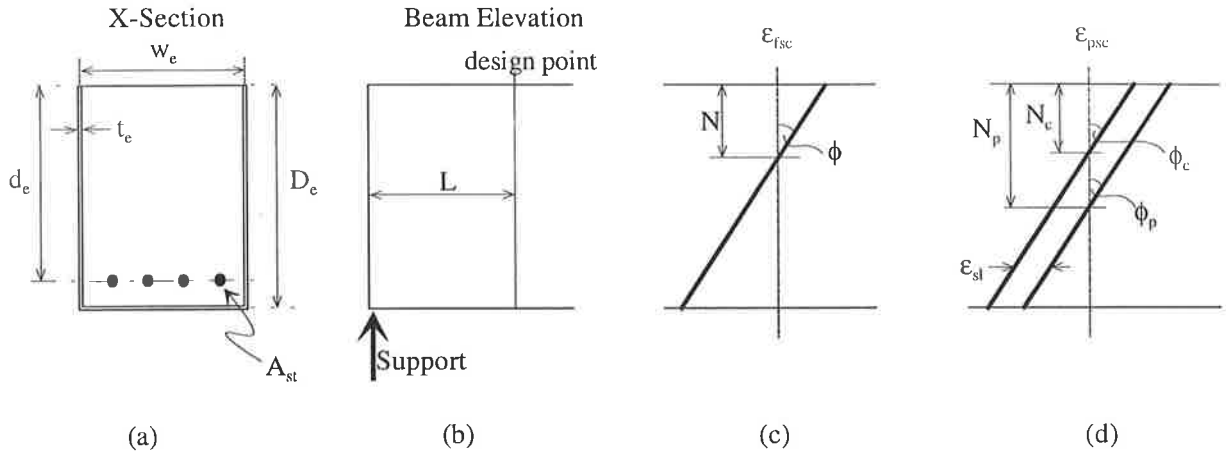


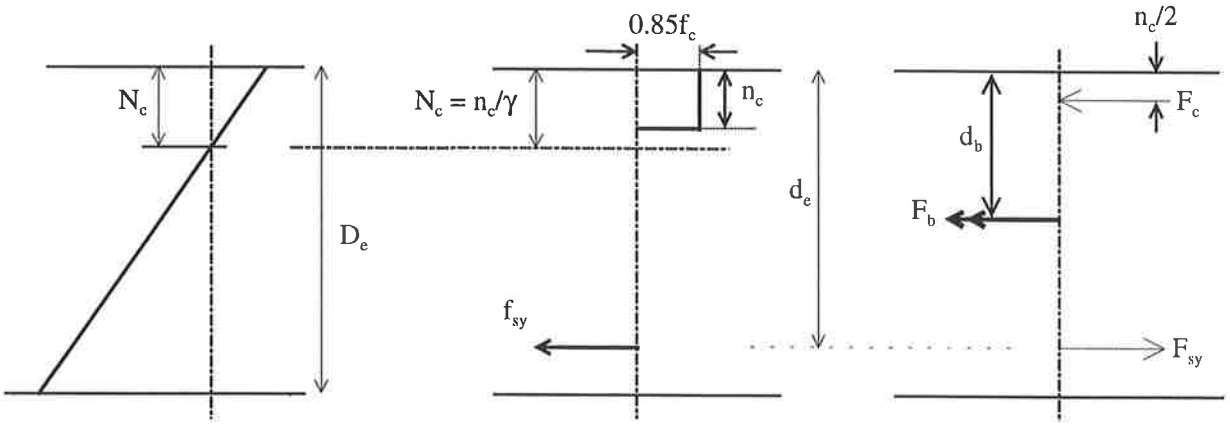
Fig. 4.17. Strain Distribution in Composite Beam

Should the interface bond force exceed the interface bond strength as the moment is increased, then slip occurs across the interface and the composite section is said to exhibit partial interaction. There is now a step change between the strain profiles through the reinforced concrete section, that now has a neutral axis at a depth N_c, and through the profiled box section that now has a neutral axis at a depth N_p. This step change is shown in Fig. 4.17d as ε_{sl}.

The ribs in the profiled sheeting that are embedded into the concrete ensure that the curvature within the concrete section ϕ_c is the same as the curvature within the profiled section ϕ_p. This fact is important, as the slip strain ε_{sl} is, therefore, constant throughout the depth of the section. This then leads to a uniform slip throughout the depth of the beam, and thus uniform development of bond stress throughout the depth. As the bond strength is less than the bond force required at ultimate moment for full interaction, then slip occurs at the interface. Thus the composite section is said to exhibit partial shear connection. In this form of construction, partial shear connection is synonymous with partial interaction.

The flexural strength of a composite profiled beam with partial shear connection can be determined by considering the distribution of forces within each element of the composite

section; ie the reinforced concrete element and the profiled box element. The strain ε, stress σ, and force F distributions within the reinforced concrete element at the ultimate moment are shown in Fig. 4.18. In Fig. 4.18a, the neutral axis is shown to occur at a distance N_c from the top compression fibre. The stress distribution is shown in Fig. 4.18b, where n_c is the depth of the rectangular concrete compressive stress block. The force distribution associated with this stress distribution is shown in Fig. 4.18c, where F_c is the total compressive force in the concrete, F_{sy} is the tensile force from the longitudinal reinforcing in the concrete section, and F_b is the axial force transferred between the profiled box element and the concrete element.



(a) Strain Distribution (b) Stress Distribution (c) Force Distribution

Fig. 4.18. Behaviour of Reinforced Concrete Element

From a consideration of the axial equilibrium of the forces in the section in Fig. 4.18c gives:

$$F_c - F_{sy} = F_b \quad \text{.....(4.8)}$$

where the compressive force in the concrete F_c is given by:

$$F_c = 0.85\gamma f_c w_e N_c \quad \text{.....(4.9)}$$

where

f_c = Concrete compressive stress

The term γ in Eq. 4.9 represents the stress block reduction factor, and is commonly given by Eq. 4.10 (Warner et al., 1989; SAA, 1990). However, Ahmed (1996) investigated the effect of varying the value of γ on the bond force and on the ultimate moment. His results indicated that using Eq. 4.10 tended to underestimate γ, and lead to an unconservative estimate in the value of the bond force, while there was very little effect on the ultimate moment calculations. Ahmed suggested adopting a value of $\gamma = 1$, the effect of which will be looked at in Section 4.3.4 in a worked example.

$$\gamma = 0.85 - 0.007(f_c - 28) \quad \text{.....(4.10)}$$

Substituting F_c from Eq. 4.9 into Eq. 4.8 and solving for the depth of the concrete neutral axis N_c, gives:

$$N_c = \frac{F_{sy} + F_b}{0.85\gamma f_c w_e} \quad \text{.....(4.11)}$$

where

F_{sy} = $A_{st} f_{sy}$
A_{st} = Area of tension reinforcing
f_{sy} = Yield stress of tension reinforcing

Taking moments of the forces shown in Fig. 4.18c about the top fibre gives:

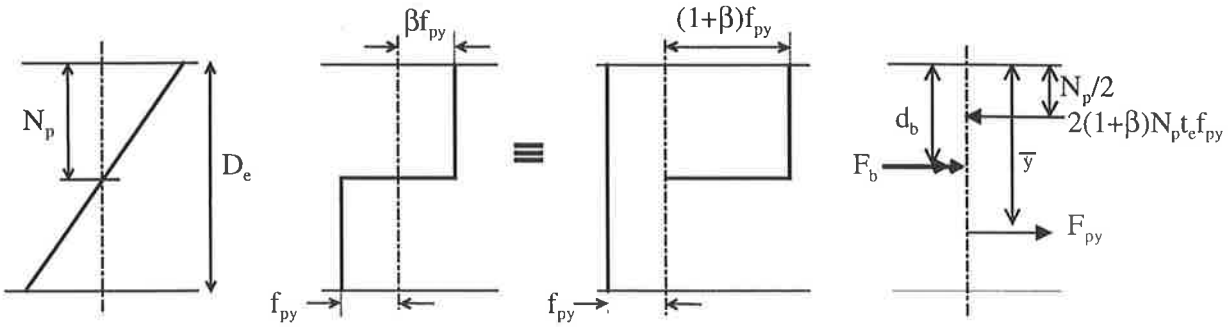
$$M_c = F_{sy} d_e - F_c n_c/2 - F_b d_b \quad \text{.....(4.12)}$$

Substituting F_c from Eq. 4.9, noting that $n_c = \gamma N_c$ and simplifying gives:

$$M_c = F_{sy} d_e - \frac{1}{2} 0.85\gamma^2 f_c w_e N_c^2 - F_b d_b \quad \text{.....(4.13)}$$

A similar analysis can be carried out for the profiled box section shown in Fig. 4.19. The strain profile is shown in Fig. 4.19a, with the neutral axis location at a depth N_p. The corresponding stress profile is shown in Fig. 4.19b, which is exactly equivalent to the stress profile shown in Fig. 4.19c. It can be seen that the compressive stress has been modified to account for possible buckling of the profile, using the value of β from Eq. 4.4. The resultant

forces acting on the cross section are shown in Fig. 4.19d, where the force F_b represents the total bond force exerted on the profile box section. From interface equilibrium, this bond force must be equal in magnitude, opposite in sign and act at the same position to the bond force shown acting on the concrete section in Fig. 4.18.



(a) Strain Profile (b) Stress Profile (c) Equivalent Stress (d) Force Profile

Fig. 4.19. Behaviour of Profiled Box Element

The equilibrium of the forces in Fig. 4.19d can be expressed as:

$$2(1+\beta)N_p t_e f_{py} - F_{py} = F_b \quad \text{.....(4.14)}$$

where F_{py} is the yield strength of the total profiled steel area, and is given by:

$$F_{py} = (2D_e + w_e)t_e f_{py} \quad \text{.....(4.15)}$$

where

f_{py} = profiled steel yield stress

The term $\bar{y}$ in Fig. 4.19d is the centroid of the profiled steel element and is given by Eq. 4.16.

$$\bar{y} = \frac{D_e^2 + w_e D_e}{2D_e + w_e} \quad \text{.....(4.16)}$$

From Eq. 4.14 the depth of the neutral axis can be determined and is given by:

$$N_p = \frac{F_{py} - F_b}{2(1+\beta)t_e f_{py}} \quad \text{.....(4.17)}$$

Taking moments of the forces shown in Fig. 4.19d about the top fibre gives:

$$M_p = F_{py}\bar{y} - 2(1+\beta)N_p t_e f_{py} N_p/2 + F_b d_b \quad \text{.....(4.18)}$$

Substituting F_{py} from Eq. 4.15 and $\bar{y}$ from Eq. 4.16 and simplifying gives:

$$M_p = t_e f_{py}\left(D_e^2 + w_e D_e - (1-\beta)N_p^2\right) + F_b d_b \quad \text{.....(4.19)}$$

The moment capacity of the composite profiled beam section with partial shear connection M_{psc}, can be determined by summing the moment contribution from the concrete element M_c in Eq. 4.13, and the moment contribution from the profiled steel element M_p in Eq. 4.19. The contribution of the bond force to the moment capacity is zero because it acts in opposite directions and at the same location in the two sections. Thus the moment capacity is given by:

$$M_{psc} = t_e f_{py}\left(D_e^2 + w_e D_e - (1+\beta)N_p^2\right) + F_{sy} d_e - \frac{1}{2}0.85\gamma^2 f_c w_e N_c^2 \quad \text{.....(4.20)}$$

4.3.2.2 Full Shear Connection

For the special case of full shear connection, the slip strain ε_{sl} in Fig. 4.17d is zero, hence $N_c = N_p$. Therefore, the bond strength required to achieve full shear connection, $F_{b,fsc}$, can be determined by equating the right hand sides of Eqs 4.11 and 4.17:

$$F_{b,fsc} = \frac{0.85\gamma f_c w_e F_{py} - 2(1+\beta)t_e f_{py} F_{sy}}{0.85\gamma f_c w_e + 2(1+\beta)t_e f_{py}} \quad \text{.....(4.21)}$$

Once the bond force for full shear connection is defined, it is now possible to define the degree of shear connection, as the ratio of the strength of the shear connection to the strength required for full shear connection, and is given by Eq. 4.22. Note the use of the subscript w,

to indicate that this is the degree of shear connection for a welded construction. A different equation will be derived later for clipped construction.

$$\eta_w = F_b / F_{b,fsc} \quad \text{.....(4.22)}$$

When the strength of the shear connection is known, the distance from a point of contraflexure to the point where full shear connection is achieved can be calculated. This is given by Eq. 4.23. At cross-sections which are less than this distance for the end of the beam or a point of contraflexure, there will be partial shear connection, whereas for those sections which are at a distance greater than that given by Eq. 4.23 there will be full shear connection.

$$L_{fsc} = \frac{F_{b,fsc}}{\tau_b n_r S_r} \quad \text{.....(4.23)}$$

where

n_r = Number of ribs in the cross-section

The flexural capacity for full shear connection can be derived by substituting $F_{b,fsc}$ from Eq. 4.21 for F_b in either Eq. 4.11 or Eq. 4.17, which then gives the location of the neutral axis in the composite section for full interaction. This is given in Eq. 4.24. This is in turn substituted into Eq. 4.20, which gives the following equation for the flexural capacity for full shear connection:

$$d_n = \frac{F_{py} + F_{sy}}{0.85\gamma f_c w_e + 2(1+\beta)t_e f_{py}} \quad \text{.....(4.24)}$$

$$M_{fsc} = t_e f_{py}\left(D_e^2 + w_e D_e - (1+\beta)d_n^2\right) + F_{sy} d_e - \frac{1}{2}0.85\gamma^2 f_c w_e d_n^2 \quad \text{.....(4.25)}$$

4.3.2.3 Zero Shear Connection

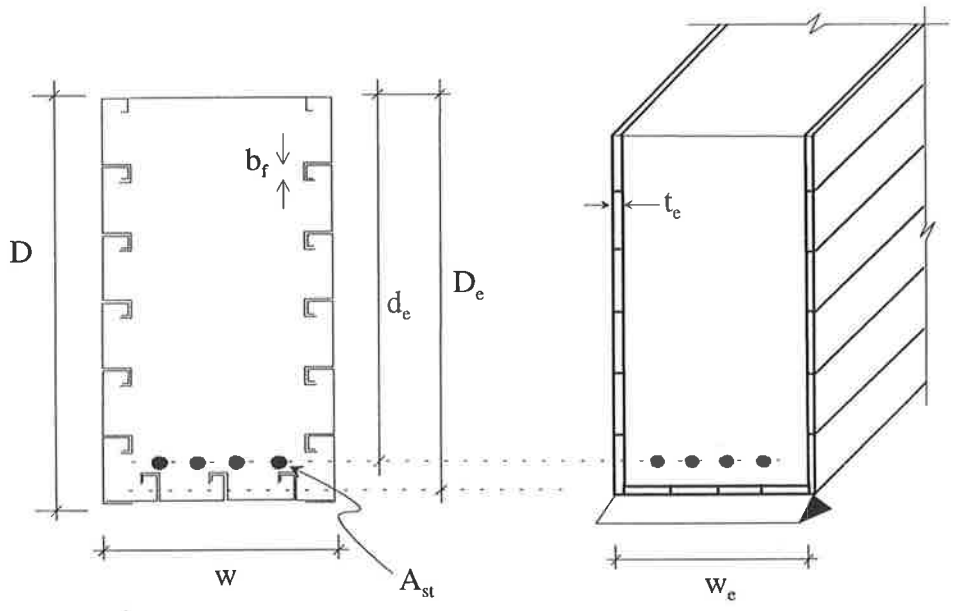
For the special case of zero shear connection, $F_b = 0$, which can be substituted into Eqs 4.11 and 4.17. The resulting values of N_c and N_p can be substituted into Eq. 4.20 to determine the flexural capacity with no shear connection. This is simply the sum of the flexural capacities of the individual components. The resulting equation is given by:

$$M_{zsc} = t_e f_{py}\left(D_e^2 + w_e D_e - \frac{(2D_e + w_e)^2}{4(1+\beta)}\right) + F_{sy} d_e - \frac{1}{2}\frac{F_{sy}^2}{0.85 f_c w_e} \quad \text{.....(4.26)}$$

It can be seen that full and zero shear connection are special cases of partial shear connection.

4.3.3 Clipped Construction

The first case where the sheeting is rigidly welded is shown in Fig. 4.15, where the profiled steel is considered as a single U-section surrounding three sides of the enclosed concrete beam. Shown in Fig. 4.20 is the idealisation used when the sheeting is not rigidly welded, and thus slip may occur between the individual units. This occurs when the units are 'clipped' together, as shown in Fig. 4.13b. 4.3.3



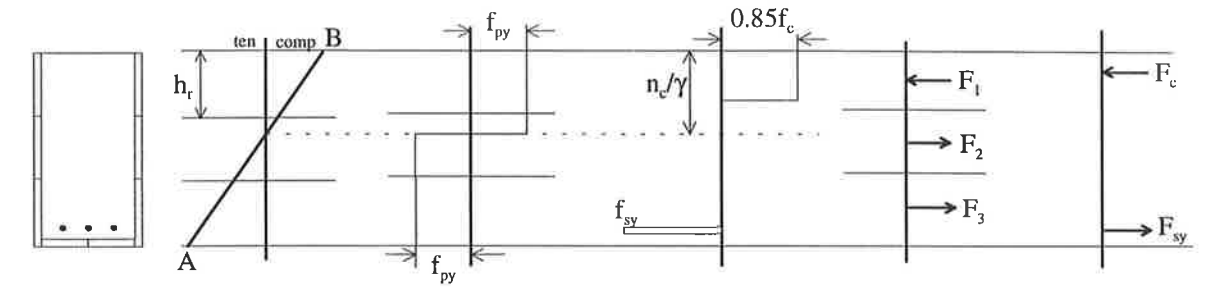
(a) Actual Cross-Section (b) Idealised Cross-Section

Fig. 4.20. Clipped Profiled Beam Construction

The procedure used to determine the flexural strength for the clipped construction is based on similar principles of rigid plastic analysis as used for the welded construction case. However, it will be shown that this method of construction results in significantly higher bond stresses at the concrete-sheeting interface. The remainder of this discussion will focus on the ultimate flexural strength of a profiled beam constructed from individual units which are free to slip relative to each other.

4.3.3.1 Full Shear Connection

Consider the cross-section shown in Fig. 4.21a which shows an idealised composite profiled beam that has been constructed with three profiled units on each side, and two along the soffit. Under conditions of full shear connection and full interaction, the strain in the concrete will be the same as the strain in the steel, as shown by the line A-B in (b). This gives rise to the stress distribution in the profiled sheeting shown in (c) and the stress distribution in the concrete element as shown in (d). The resulting internal forces in the profiled section are shown in (e) and in the concrete section are shown in (f).



(a) Cross-Section (b) Strain Profile (c) Profiled Sheeting Stress (d) Concrete Stress (e) Profiled Sheeting Forces (f) Concrete Forces

Fig. 4.21. Stress and Strain Distributions in Profiled Sheeting

For full shear connection, each unit will be fully yielded in either compression or tension, except for the unit through which the neutral axis passes, as shown in Fig. 4.21c. Thus the force in each profiled unit, as shown in (e), can be derived from the yield load in the profiled units, and is given by Eq. 4.27 for those units not effected by buckling, and by Eq. 4.28 for those units which are effected by buckling.

$$F_{pu} = h_r t_e f_{py} \quad \text{.....(4.27)}$$

$$F_{pu} = h_r t_e \beta f_{py} \quad \text{.....(4.28)}$$

Under conditions of full shear connection, the force in each of the profiled units is given by either Eq. 4.27 or 4.28. Thus the shear force that must be transferred at the interface between the concrete and each individual unit for full shear connection F_{pu}, is equal to the yield load of the unit. The bond force developed in each unit F_{bu}, is given by Eq. 4.29, which must be less than the yield load of the profiled unit, F_{pu}.

$$F_{bu} = \tau_b S_r L \leq F_{pu} \quad \text{.....(4.29)}$$

where

F_{bu} = bond force developed in a single unit, over a distance L from the support

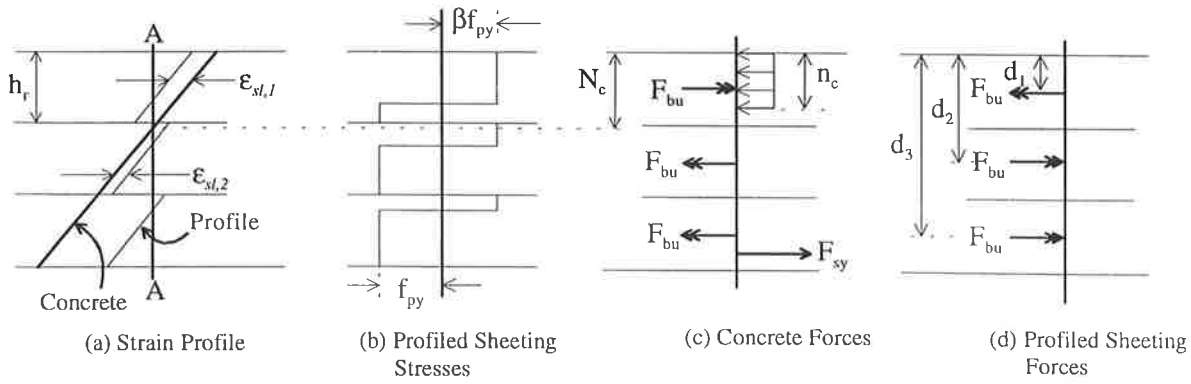
L = distance from design point to point of contraflexure in the composite beam

Thus the distance required to develop sufficient bond force for full shear connection can be determined by substituting F_{pu} from Eq. 4.27 or 4.28 for F_{bu} in Eq. 4.29 and solving for L.

Under conditions of full shear connection and full interaction, the analysis for the clipped construction of the composite profiled beam is exactly the same as for the welded construction. This is due to the fact that no slip at the interface between the sheeting and the concrete enforces a condition of no slip between the individual profiled units. The location of the neutral axis can thus be found in a similar manner to that for the welded construction, and is given by Eq. 4.24, and the moment capacity of the section is given by Eq. 4.25. Furthermore, the influence of the profiled unit which has the neutral axis pass through it does not need to be considered separately for full shear connection, as its contribution is accounted for in the derivation of Eq. 4.25.

4.3.3.2 Partial Shear Connection

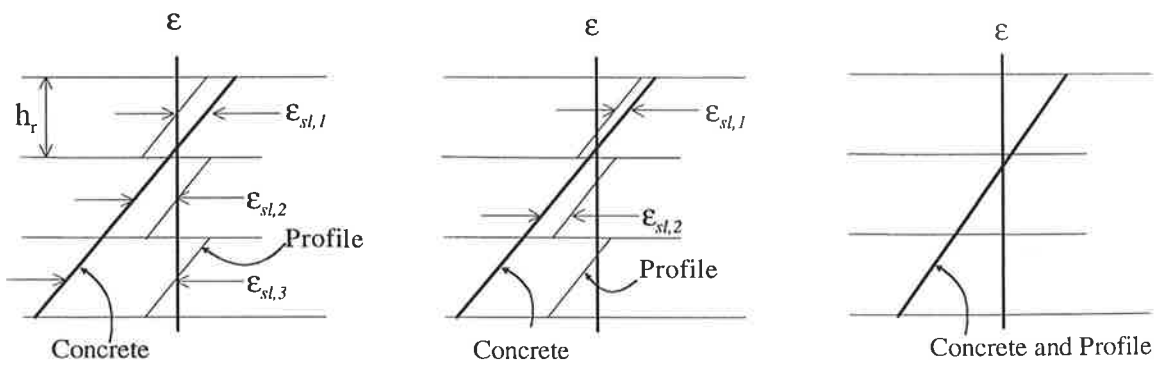
If the bond force required for full interaction cannot be achieved at the required cross-section, then the section exhibits partial interaction, and Eq. 4.29 can be used to determine the bond transferred at the interface of each unit. Once the degree of shear connection decreases from full shear connection, there now exists distinct strain distributions between each of the profiled units, with different neutral axes in each. The strain distributions in the profiled units are shown in Fig. 4.22a by the thin solid lines, where it can be seen that the loss of interaction causes the strain profiles to move toward the reference axis A-A. Under the assumption of rigid-plastic behaviour, the resulting stress distribution in the profiled units is shown in (b), which indicate that each unit will have a portion stressed in tension, and a portion stressed in compression. This situation will only occur under large curvatures, but it gives an upper bound to the ultimate moment capacity, as do all rigid plastic analyses.



(a) Strain Profile (b) Profiled Sheeting Stresses (c) Concrete Forces (d) Profiled Sheeting Forces

Fig. 4.22. Behaviour of Composite Member

The direction of the bond force between the concrete and the sheeting will be determined by the strain in the concrete at the location of the profiled unit. This can be explained with the aid of Fig. 4.23 which indicates the strain distributions in the concrete element and profiled units for zero, partial and full shear connection. For the case of zero shear connection as shown in Fig. 4.23a, the concrete element and each of the profiled units will have a neutral axis that passes through each of their respective centroids. It can be seen in (a) that the direction of the slip strain changes sign for profiled units above the concrete neutral axis compared to those below. When there is partial shear connection, as shown in (b), the magnitude of the slip strain between each of the profiled units and the concrete element decreases, while the sign remains the same. Thus, when there is a compressive strain in the concrete, the bond between the sheeting and concrete will tend to induce a compressive strain in the external sheeting. In the tensile region the bond between the sheeting and the concrete will tend to induce a tensile strain in the external sheeting. In order to determine the direction of the bond force for each unit, it is necessary to first find the location of the neutral axis in the concrete section, and thus know which units are in compression, and which are in tension.



(a) Zero Shear Connection (b) Partial Shear Connection (c) Full Shear Connection

Fig. 4.23. Strain Distributions in Clipped Construction

An important distinction between the analyses for clipped and welded construction, is that in clipped construction the direction of the bond stress exerted between the concrete and the profiled sheeting reverses across the neutral axis, whereas in welded construction, the bond stress will act in the same direction throughout the depth of the member. This variation in bond stress is shown by the difference in the sign of the slip strain ε_{sl} across the neutral axis, as seen in Fig. 4.22a for the clipped construction.

The location of the neutral axis in the concrete section can be determined from a consideration of the forces acting on the reinforced concrete element. Figure 4.22c shows the resulting force distribution in the concrete element. The forces F_{bu} shown on the left side of Fig. 4.22c are the bond forces exerted by each of the profiled sheeting units on the concrete. They are equal and opposite to the forces in Fig. 4.22d which shows the forces exerted by the concrete on the profiled sheeting. When the cross-sections of each of the profiled units are identical then τ_b and S_r in Eq. 4.29 will be constant for each unit and thus F_{bu} will also be constant, as shown in Fig. 4.22c. The forces from the soffit sheeting are not shown in (c) or (d) for clarity, but are included in the calculation of the neutral axis location and the ultimate moment.

The degree of shear connection for clipped construction can be defined as the ratio of the bond transferred by one unit F_{bu}, to the yield load of a unit F_{pu}. When the individual profiled units are identical then F_{bu} and F_{pu} will be the same for each unit, thus resulting in the same degree of shear connection for each of the profiled units. The degree of shear connection is given in Eq. 4.30, where the subscript c refers to clipped construction. This is slightly different from the definition of the degree of shear connection for the welded construction, which is given in Eq. 4.22. The distinction becomes apparent when calculating the degree of shear connection for two beams which are identical in all aspects except the method of construction. This will illustrated with a worked example in Section 4.3.4. The need to reformulate the degree of shear connection in terms of the individual units arises from their ability to slip relative to each other, and thus act independently.

$$\eta_c = F_{bu} / F_{pu} \quad \text{.....(4.30)}$$

Once the efficiency of the shear connection is determined, the forces transferred from the profiled sheeting to the concrete can be determined. The stresses in the profiled units for

a beam with partial shear connection shown in Fig. 4.22b are repeated in Fig. 4.24a. When considering axial equilibrium, an alternative representation to the stress distribution is shown in (b), where the yield stress is reduced by the degree of shear connection. By reducing the effective yield stress of the material, the combination of the compressive and tensile stresses acting in each of the profiled units can be replaced by a single resultant stress which is tensile below the concrete neutral axis, and compressive above it. The equivalent stress distribution shown in (b) is only applicable when considering axial equilibrium, as the stress distribution does not produce an equivalent moment to that from (a). However, this step is only used to determine the axial loads in the sheeting and the concrete, and the determination of the moment is carried out later on. On the other hand, it will be shown that the internal moment contribution from each of the units is small, and reduces as the number of side units increases. The stress distribution shown in (b) is equivalent to that shown in (c), where a uniform tensile stress acts throughout the depth of each profiled unit and the compressive stress is increased accordingly. This is similar to the equivalent stress distribution adopted in the welded construction as shown in Fig. 4.19.

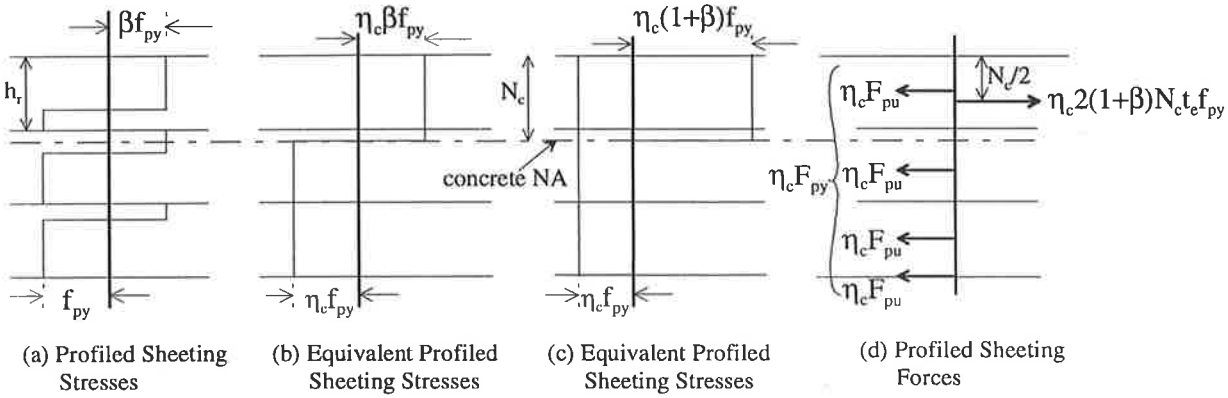
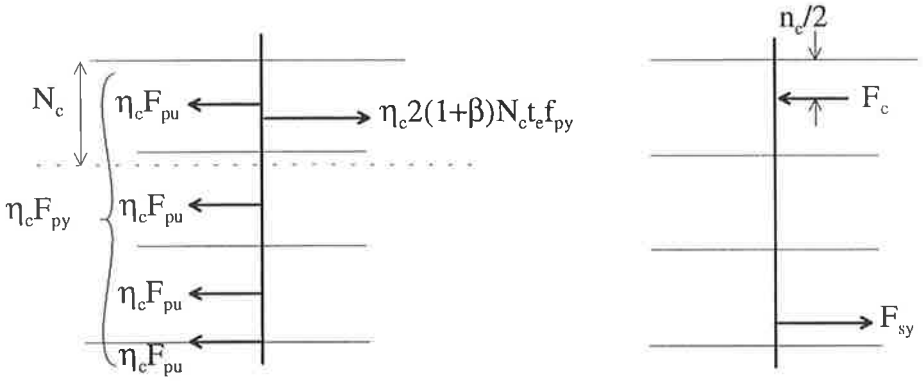


Fig. 4.24. Equivalent Stresses in Profiled Units

Figure 4.24d shows the internal resultant axial forces in the profiled sheeting, based on the equivalent internal stress distribution of (c). The resultant tensile force in each of the units is given by the degree of shear connection times the yield load of each unit, while the equivalent compressive force in the sheeting is given by the equivalent compressive stress $\eta_c(1+\beta)f_{py}$ times the area of the profiled sheeting in compression $2N_c t_e$.

The axial forces acting in the profiled sheeting, shown in Fig. 4.24d, are equal and opposite to the axial forces exerted by the sheeting on the concrete. The axial forces in the profiled sheeting are shown repeated in Fig. 4.25a, with the internal forces in the concrete

element shown in (b). The two force systems shown in (a) and (b) must be in equilibrium with each other, as there are no externally applied axial loads to the member. Expressing equilibrium of these forces gives Eq. 4.31.



(a) Profiled Sheeting Forces

(b) Concrete Forces

Fig. 4.25. Internal Forces in Clipped Profiled Beam

$$0.85\gamma f_c w_e N_c - F_{sy} = \eta_c F_{py} - \eta_c 2(1+\beta)t_e f_{py} N_c \quad \text{.....(4.31)}$$

where

F_{py} = nF_{pu} = $(2D_e + w_e)t_e f_{py}$

n = the number of individual units.

Equation 4.31 can be rearranged to solve for the concrete neutral axis location, and is given by Eq. 4.32. It can be seen that this equation is similar to Eq. 4.24, except for the introduction of the degree of shear connection.

$$N_c = \frac{\eta_c F_{py} + F_{sy}}{0.85\gamma f_c w_e + \eta_c 2(1+\beta)t_e f_{py}} \quad \text{.....(4.32)}$$

In the determination of the moment contribution from the profiled sheeting M_p, there are two components to consider. The first component will be due to the axial forces in the profiled units, which are present due to the transfer of the bond force. The second component will be due to the moment developed within each unit, which is due to the flexural stresses due to bending. These two components can be determined from a consideration of the stress distribution in the profiled units as shown in Fig. 4.26. Figure 4.26a shows the stress

distribution in the profiled sheeting from Fig. 4.24a, while Fig. 4.26b shows a magnification of the stress distribution in the bottom profiled unit, although the following discussion is valid for any unit. The stress distribution shown in (c) is equivalent to that shown in (b), which can be represented by the force distribution shown in (d). This shows an axial force acting through the centroid of the unit, and a force acting at some distance from the centroid. This can be represented by the force and moment combination shown in (e).

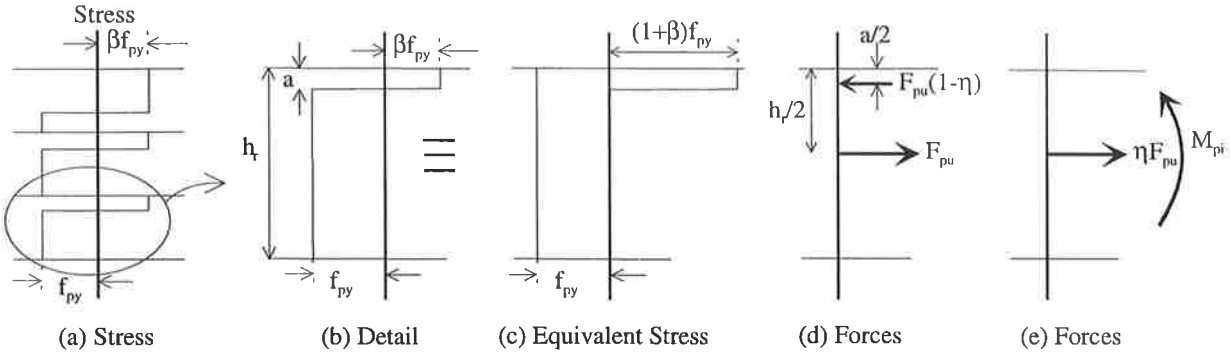


Fig. 4.26. Moment Contribution from Profiled Unit in Tension Region

The moment component in the profiled unit about its centroid M_{pi} can be calculated from the force distribution shown in Fig. 4.26d. The distance 'a' can be found such that the resultant axial force shown in (b) is equal to ηF_{pu}, which gives:

$$(h_r - a)t_e f_{py} - \beta a t_e f_{py} = \eta h_r t_e f_{py} \quad \text{.....(4.33)}$$

Solving this for 'a' gives:

$$a = b\frac{1-\eta}{1+\beta} \quad \text{.....(4.34)}$$

The moment M_{pi} in Fig. 4.26d can be found as:

$$M_{pi} = F_{pu}(1-\eta)\frac{h_r - a}{2}$$

Substituting 'a' from Eq. 4.34 gives:

$$M_{pi} = F_{py}\frac{h_r}{2}\frac{(1-\eta)(\beta+\eta)}{1+\beta} \quad \text{.....(4.35)}$$

Equation 4.35 represents the moment component of a single profiled unit about its centroid. This moment acts in combination with the axial force ηF_{pu} also acting through the centroid. This combination of axial force and moment will act in each side profiled unit which is below the concrete neutral axis. For those units above the concrete neutral axis, a similar series of steps can be carried out as shown in Fig. 4.27. Figure 4.27a shows the stress distribution in the profiled sheeting from Fig. 4.24a, while Fig. 4.27b shows a magnification of the stress distribution in the top profiled unit. The stress distribution shown in (c) is equivalent to that shown in (b), which can be represented by the force distribution shown in (d). These forces can be represented by the force and moment combination shown in (e), which it can be seen is the same as that shown in Fig. 4.26e, except that the direction of the axial force ηF_{pu} is reversed. Thus, the moment contribution M_{pi} given in Eq. 4.35 acts in all side profiled units which are above and below the concrete neutral axis. If this moment is small, then the idealisation of Fig. 4.24d is an adequate representation.

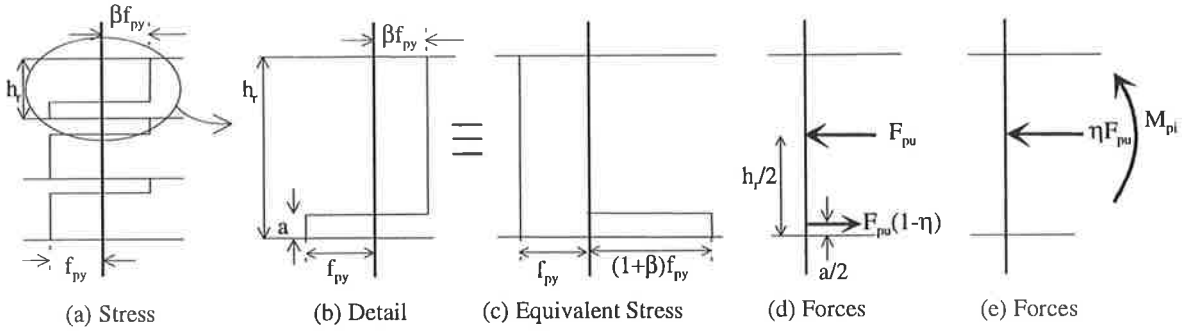


Fig. 4.27. Moment Contribution from Profiled Unit in Compression Region

The profiled unit which has the concrete neutral axis pass through it is neglected in the calculation of the overall moment in the cross section. This simplifies the calculations, as it is tedious to determine the compressive and tensile force contributions from the one unit, and it results in only a small error due to the small moment contribution of the forces near the neutral axis. It should be noted, however, that the net axial force in all units is considered to determine the location of the neutral axis in the concrete in Eq. 4.32. The profiled units which are in the soffit of the beam are oriented such that moment about their own axis will be negligible, and can be ignored.

The total moment contribution from all the profiled units M_p about the top fibre can now be found by adding the contributions from each of the units. Each profiled unit has an axial force component ηF_{pu} acting at its centroid, while each of the side profiled units has an additional moment M_{pi} acting at its centroid. In order to take account of the change in direction of ηF_{pu} above and below and the concrete neutral axis, another term is introduced, $\eta F_{pu,i}$. This has the same magnitude as ηF_{pu} but has a negative sign for those profiled units above the concrete neutral axis, and a positive sign for those below. Taking moments about the top fibre gives:

$$M_p = \sum_{i=1}^{n} \eta F_{pu,i} d_i + n_s M_{pi} \quad \text{.....(4.36)}$$

where

d_i = Distance from top fibre to centroid location of the i^{th} unit

$F_{pu,i}$ = Yield load of each profiled unit; negative for units above the concrete neutral axis, positive for those below.

M_{pi} = Internal moment in the profiled units about their centroid

n = total number of profiled units

n_s = number of side profiled units

Typically, the internal moment capacity of the profiled units is small, and the second term on the right hand side of Eq. 4.36 can be ignored with little error. The total moment in the cross section can now be found as the sum of the moments in the reinforced concrete element, and the moment contribution from the external sheeting, and is given by Eq. 4.37.

$$M_{psc} = M_p + F_{sy} d_e - 0.85\gamma^2 f_c w_e N_c^2/2 \quad \text{.....(4.37)}$$

For full shear connection, $\eta = 1$ and from Eq. 4.35 M_{pi} is zero, and from Eq. 4.36 the moment contribution of the profiled sheeting comes from the pure axial force in each unit.

4.3.3.3 Zero Shear Connection

For zero shear connection, the net axial force in each of the units must be zero, and the moment contribution of the profiled sheeting comes from the internal moment developed in each of the units. Substituting $\eta = 0$ into Eq. 4.35 gives:

$$M_{pi} = F_{py} \frac{h_r}{2} \frac{\beta}{1+\beta} \quad \text{.....(4.38)}$$

This can then be substituted into Eq. 4.36, which is in turn substituted into Eq. 4.37 to give the total moment capacity. The internal moment in each of the units M_{pi} given by Eq. 4.38 was derived assuming an equivalent profiled unit of uniform thickness t_e, as given by Eq. 4.6. As an alternative, the true profiled unit geometry may be used, and the plastic moment capacity determined. This additional refinement is not warranted for most profiled unit geometries, and the value of M_{pi} from Eq. 4.38 will give a reasonable estimate of the plastic moment capacity of a single rib. This will be illustrated in the following worked example.

4.3.4 Worked Example

A composite profiled beam, such as the one shown in Fig. 4.15, is to be made with the following geometric and material properties: $t = 1.00$ mm, $w = w_e = 250$ mm, $D = 480$ mm, $D_e = 467$ mm, $d_e = 435$ mm, $A_{st} = 930$ mm^2, $f_c = 30$ MPa, $f_{py} = 550$ MPa, $f_{sy} = 450$ MPa, $E_s = 205\,000$ MPa.

The cross-section of an individual profiled unit is shown in Fig. 4.14 with $b = 80$ mm, and $A_u = 198$ mm^2. The number of ribs in the cross-section is $n_r = 15$. The rib shear strength is $\tau_b = 0.8$ MPa, and the rib interface perimeter is $S_r = 140$ mm. The total area of profiled steel is $A_p = 2910$ mm^2, and from Eq. 4.6 $t_e = 2.46$ mm. To determine the effective width of the profile in compression, an initial estimate must be made for α, which describes the variation in stress throughout the depth of a profiled unit. Adopting an initial value of $\alpha = 0.4$ gives $\lambda_a = 26$ from the inelastic analysis column of Table 4.1 for an internal member, and from Eq. 4.3 $b_e = 24$ mm. This gives $A_e = 142$ mm^2 and from Eq. 4.4, $\beta = 0.72$.

Welded Construction

For this example the bond strength required for full shear connection is found from Eq. 4.21 to be $F_{b,fsc} = 659$ kN when γ is given by Eq. 4.10, and 748 kN when $\gamma = 1$ is used. This represents a 14% increase in the estimate of the bond force, depending on the value of γ used. The length required to develop this strength can be found from Eq. 4.7 to be $L = 610$ mm or $L = 693$ mm. The flexural strength for full shear connection is found by substituting $F_{b,fsc}$ for F_b in Eq. 4.11 and Eq. 4.17, and for no shear connection by setting $F_b = 0$ in Eq. 4.11 and Eq. 4.17. The resulting value of d_n is 202 mm for full shear connection, and 343.8 mm and 78.6 mm for N_c and N_p respectively for zero shear connection. These can then be substituted into Eq. 4.20, and the respective values for the flexural strength for the two cases are 449 kNm and 346 kNm. Thus it can be seen that a complete break down in bond reduces the strength by 23%. Adopting a value of $\gamma = 1$ in Eq. 4.20 gives the moment for full shear connection as 450 kNm, which is virtually unchanged from 449 kNm, which was derived from using Eq. 4.10 to determine γ. For distances from the support less than 610 mm, the bond force that can be developed is found from Eq. 4.7, which is then used to determine the moment capacity.

The neutral axis in the profiled steel element varies from 344 mm for zero shear connection to 202 mm for full shear connection. Thus, actual values for α can be calculated from Eq. 4.2, and are 0.23 and 0.40 for the two cases. Adopting a value of $\alpha = 0.23$ reduces the flexural strength by 1%, which is negligible. It is worth noting that the flexural strength of the reinforced concrete beam without the profiled sheeting is 168 kNm, which is only 37% of the fully composite strength.

Clipped Construction

The bond force required to fully yield one unit is given by Eq. 4.27 as $F_{pu} = 108$ kN, and from Eq. 4.29 this gives the required development length as $L = 1500$ mm. This is approximately 2.5 times greater than the distance required for full interaction for the welded construction. Hence, in much of the beam there is partial shear connection. The flexural strength for full shear connection is the same as for the welded construction, 449 kNm. For zero shear connection, the moment contribution for each of the side profiled units is only 2.2 kNm, and the total contribution of all the side profiled units is 26.4 kNm. From Eq. 4.37 the total moment in the cross-section is 195 kNm. Thus, for zero shear connection,

the profiled sheeting contributes 14% of the total moment, whereas for welded construction, the profiled sheeting contributes 50% of the total moment.

4.4 Conclusions

A procedure has been presented which allows the flexural strength of composite profiled beams to be calculated. This procedure is based on simple rigid-plastic theory, and depends on the material properties as well as the degree of shear connection at the location of interest. It has been shown that the thin profiled sheeting is prone to buckling, but that the decrease in effective area of the profiled sheeting can be allowed for in the design. Furthermore, the reduction in the effective area due to buckling may be small.

Two forms of profiled beam construction were presented: Welded Construction and Clipped Construction. Two different analysis techniques were derived to calculate the flexural capacity of the two construction methods. It was shown that larger bond forces are developed in clipped construction than in welded construction, but that under conditions of full shear connection, the flexural strengths of the two construction methods are the same.

It was shown that for profiled beam analysis, full shear connection is only achieved by full interaction. However, the reduction in moment capacity due to partial shear connection may not be very large. The reduction in moment capacity with decreasing shear connection is greater for clipped construction than for welded construction.

Chapter 5

Profiled Beam Tests

5.1 Introduction

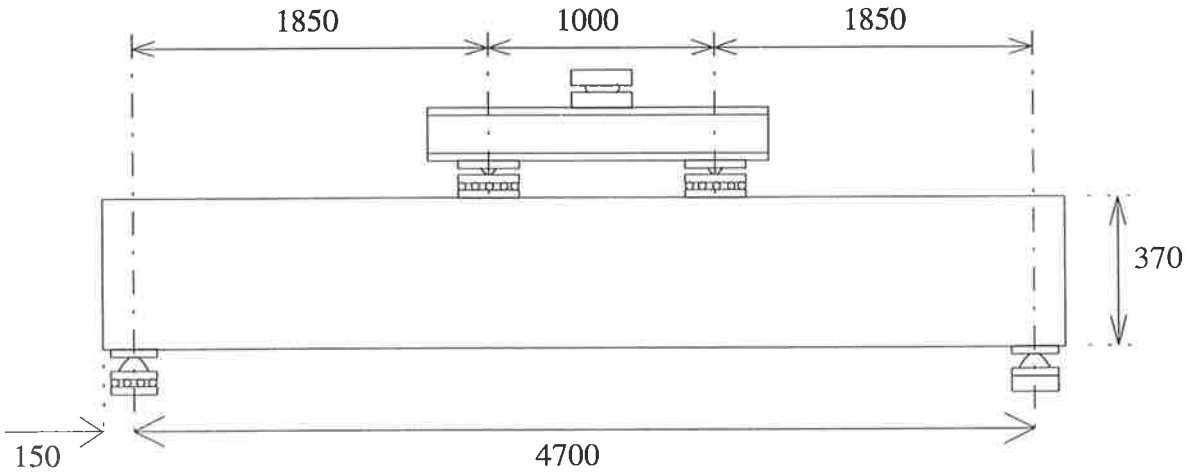
This chapter presents the results of a series of tests that were carried out on full scale profiled beams. The aim of these tests was to investigate the behaviour of composite profiled beams and to determine the validity of the theories that have been developed as part of this research. It is also expected that the results of these tests would provide benchmark results for further research in the area of composite profiled beam construction. There was a total of 7 beams tested as part of this research project. This chapter describes each of the beams and details the results of each of the tests. A summary of the results is given in Section 5.5, which includes the tabulated load vs midspan deflection for each of the tests. Section 5.6 compares the experimental results with the Rigid Plastic analysis of Chapter 4 and the computer simulations using the theory from Chapter 7.

Seven beams were constructed and tested in two series. The first series consisted of a control beam, CB1, and two profiled beams, PB1 and PB2. The results from the two profiled beams of this series indicated that there was negligible slip between the sheeting and the concrete. As one of the aims of the testing program was to check the adequacy of the partial interaction

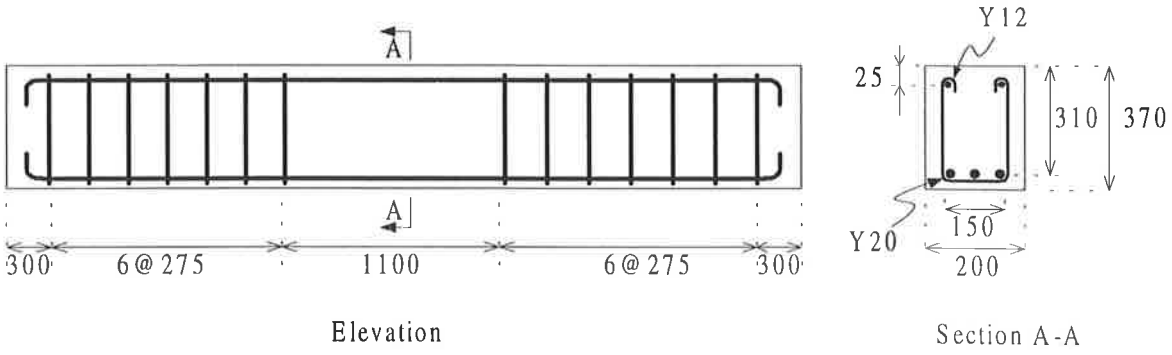
theory, the second series of beams were designed to provide a lower degree of shear connection. It was expected that this would be accomplished by reducing the size of the ribs, and increasing their spacing. A brief summary of each of the beams tested is given in Table 5.1 on Page 270, while the full details of the geometrical arrangement of the profiled sheeting for each of the profiled beams will be discussed in the following sections.

5.2 Test Setup

The overall arrangement of the beam tests is shown in Fig. 5.1a. All the beams were tested under two point loading, with shear spans of 1.85 m, and a constant moment region of 1.0 m. The total length of the beams was 5.0 m, with a distance between supports of 4.7 m, as shown in Fig. 5.1a. The load was applied through a spherical seat onto a steel I-section. This was placed on roller supports, with a 100 mm wide by 10 mm thick packing plate underneath to distribute the load onto the concrete. One support underneath the beam was on rollers, to allow for any longitudinal movement, whilst the other support was fixed. Both supports allowed free rotation of the beam to occur in the longitudinal direction by use of a semi-circular loading edge. The support reaction was distributed over a 200 x 200 mm area, using a 10 mm thick steel packing plate. The arrangement of the reinforcement was the same for all the beams in order to assess the effects of varying the profiled sheeting dimensions. The arrangement of the reinforcing is shown in Fig. 5.1b.



(a) Loading Arrangement



(b) Reinforcement Arrangement

Fig. 5.1. Test Arrangement for Profiled Beams

5.3 Profiled Sheeting

The profiled sheeting used for all the beam tests was grade G2 galvanised sheeting, with a Total Coated Thickness of 1.00 mm, and a Base Metal Thickness of 0.98 mm. The individual units were cut to length using a guillotine, and then folded to the required shape using a brake press. No embossments were pressed into the sheeting. A typical stress-strain curve is shown in Fig. 5.2, which indicates the yield plateau, and the significant strain-hardening region of the curve. Average results for the values of the yield stress and ultimate stress are given in Table 5.3 for the two series of beams.

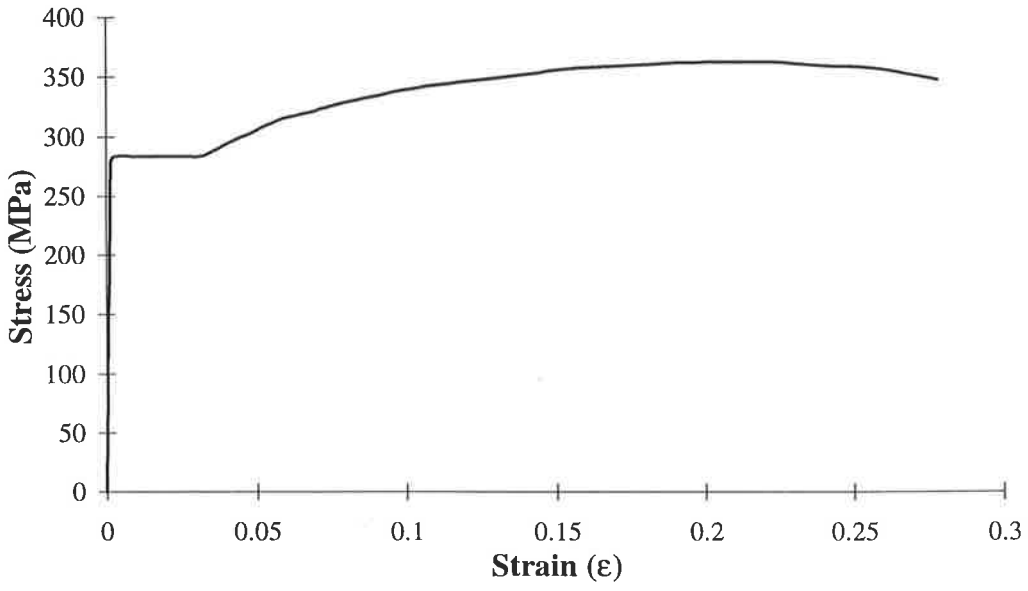


Fig. 5.2. Profiled Sheeting Stress-Strain Curve

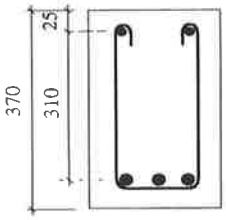
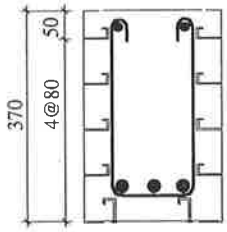
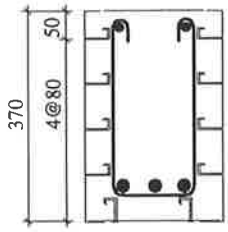
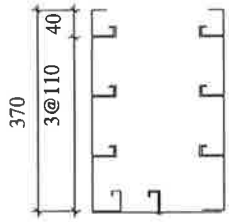
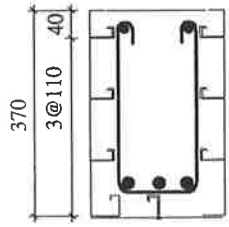
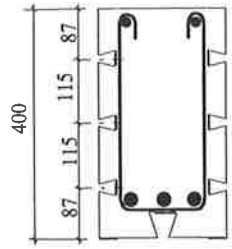
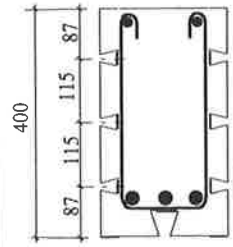
Beam	Cross-Section	Rib Type	Rib Spacing, b_r	Rib Height, h_r	Welded
CB1		None	-	-	-
PB1		L-Rib	80	40	Yes
PB2		L-Rib	80	40	No
PB3		L-Rib	110	30	Yes
PB4		L-Rib	110	30	No
PB5		Dove Tail	115	25	Yes
PB6		Dove Tail	115	25	Yes

Table 5.1. Summary of Profiled Beams

5.4 Test Results

5.4.1 General

All the beams were constructed on the ground, with the profiled sheeting fully supported along its entire length. An example of the construction of the specimens is shown in Fig. 5.3. In this figure the placement of the reinforcement can also be seen.

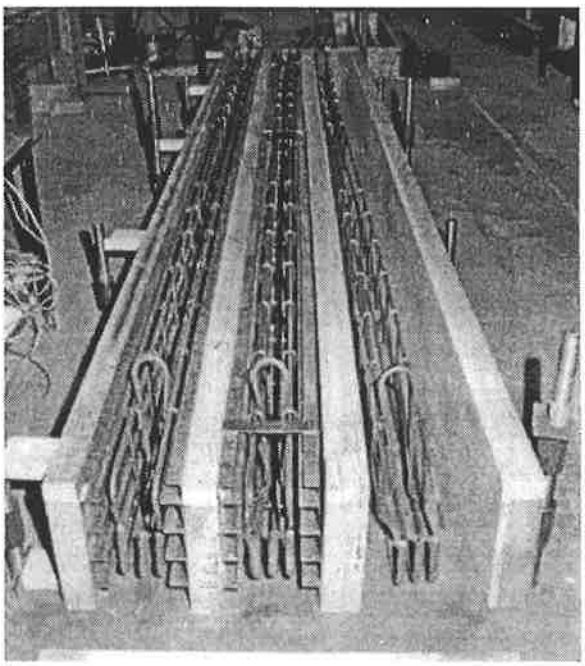


Fig. 5.3. Construction of Profiled Beams

For each of the series, the concrete mix was ordinary Portland cement with a maximum aggregate size of 10 mm, a target strength of 32 N/mm^2 and a slump of 80 mm. After pouring the beams, they were covered with hessian and plastic, and kept moist for two weeks. Companion test cylinders were taken from the mix and tested at the time of testing the beams.

The properties of the concrete were determined from the test cylinders, and are shown in Table 5.2. The tests for Series 1 were carried out 73 days after pouring, while those of Series 2 were carried out 39 days after pouring. The compression tests were performed on 100 mm diameter cylinders, using the procedure outlined in the Australian Code (AS 1012, Part 9, 1986). The tensile capacity of the concrete was determined using the Brazilian test, which were performed on 150 mm diameter cylinders. The testing procedure was as outlined in the Australian Code (AS 1012, Part 10, 1985). The Young's Modulus of the concrete was

determined at the time of testing the beams, using the procedure outlined in the Australian Code (AS 1012, Part 17, 1976). The results from the tests on the steel reinforcing and the profiled sheeting used for the beams are shown in Table 5.3.

Cylinder No.	f_c* (MPa)	E_c† (MPa)	f_{ct}‡ (MPa)
	Series 1		
1	52.0	30 700	4.6
2	53.9	33 100	4.1
3	54.0	34 100	5.1
Ave	53.3	32 600	4.6
	Series 2		
1	48.4	32 500	4.0
2	45.3	32 100	3.3
3	47.2	36 600	3.7
Ave	47.0	33 700	3.7

* Compressive Stress ‡ Tensile Strength † Young's Modulus

Table 5.2. Measured Concrete Properties for Profiled Beams

	Steel Reinforcing		Profiled Sheeting	
	σ_y§ (MPa)	σ_u** (MPa)	σ_y (MPa)	σ_u (MPa)
Series 1	428	530	288	365
Series 2	435	535	282	357

§ Yield Stress ** Ultimate Stress

Table 5.3. Measured Steel Properties for Profiled Beams

For all the beams tested, the load was applied using an hydraulic actuator, which was operated in position control. This was to allow the descending branch of the loading curve to be followed. The load was applied in a gradual controlled manner between readings, and held constant when readings of deflection, strain and slip were taken. All the beams were unloaded before the maximum load was reached, in order to investigate the elastic recovery of the profiled sheeting.

All profiled beams had the sheeting removed from the soffit for 300 mm from each end. This was so the sheeting would not be constrained between the support and the concrete, and thus contribute an unknown amount to the longitudinal slip resistance of the profiled sheeting.

5.4.2 Push Tests

Each of the profiled beams had companion push tests which were cast from the same batch of concrete used in the beams and were cured under the same conditions. The push specimens were then tested at the same time the beams were tested. These tests were performed to determine the bond characteristics between the profiled sheeting and the concrete. The arrangement of the test setup for the push tests is described in Chapter 3.

Beams PB1 and PB2 had identical rib geometries, as discussed in Section 5.4.4, with the only difference between them being the spot welding between the ribs. It was assumed that there would be negligible difference in the bond behaviour between the welded and the unwedded sheeting, as the spot welds did not significantly alter the surface geometry of the sheeting. The overall arrangement of the sheeting used in the push tests is shown in Fig. 5.4. The sheeting used in the push tests was not welded together. The sheeting used to construct the push test specimens was the same material as used for the beam construction. The surface of the sheeting was left untreated before placement of the concrete, to simulate the condition of the sheeting in the beam.

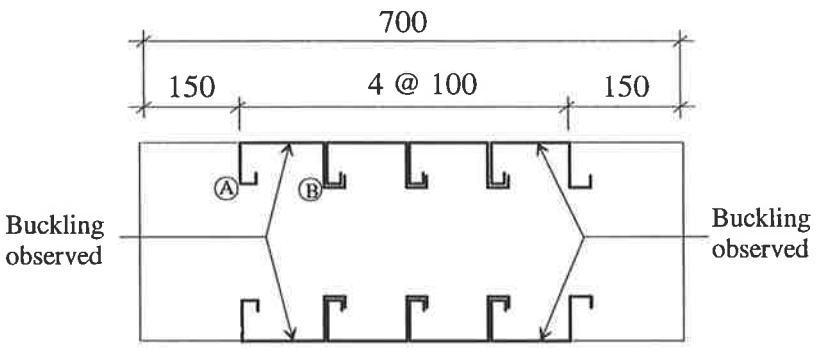


Fig. 5.4. Push Test Specimen for Beams PB1 and PB2

A total of three push tests were carried out with the geometry shown in Fig. 5.4. The first two tests exhibited significant buckling of the sheeting in the region shown in Fig. 5.4 and Fig. 5.5. This was due to the high bond stresses that developed at the outer ribs, as indicated by Ⓐ in Fig. 5.4. The high bond stress developed due to the fact that a single thickness of sheeting was rigidly restrained by the concrete on both surfaces. However, for the ribs indicated by Ⓑ the small gap between the sheets allowed some movement of the sheeting away from the concrete, and thus gave a lower bond stress.

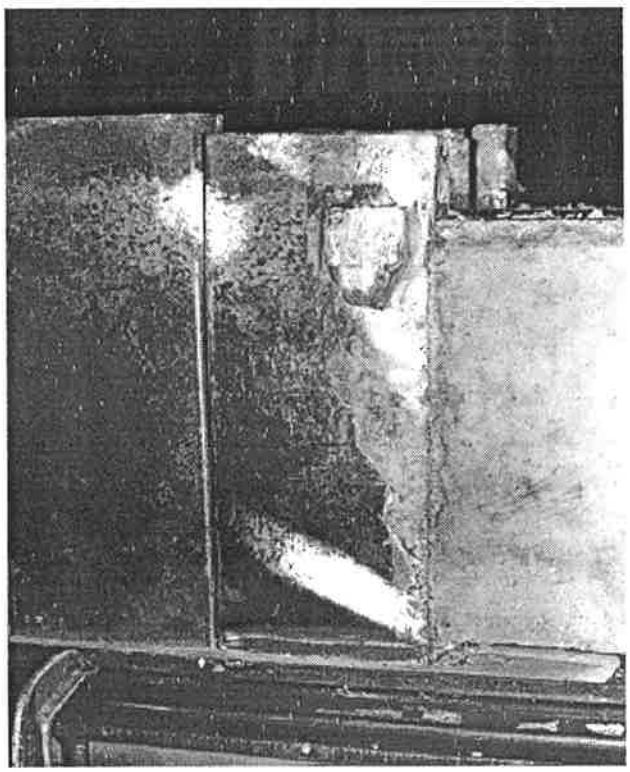


Fig. 5.5. Buckling of Push Test Specimen for Beams PB1 and PB2

The third specimen was altered by testing only the inner ribs on each side, indicated by the type Ⓑ ribs in Fig. 5.4. As there were no type Ⓐ ribs in the profiled beams, this push test represented a more appropriate specimen arrangement. The resulting shear-stress / slip curve is shown in Fig. 5.6. It can be seen that the sheeting is able to develop its full bond strength with no slip at the interface. For the purposes of this research, it is proposed that the chemical bond between the sheeting and the concrete be neglected in the determination of the bond strength. This is consistent with the design practice elsewhere (ASCE, 1992; British, 1982; Commission, 1990; Patrick, 1990). Thus, after the chemical bond had been completely broken, the specimen was unloaded and then reloaded again, as was discussed in Chapter 4. The failure of the chemical bond was signified by the initiation of slip at all locations on the specimen, and is shown by Point A in Fig. 5.6. It can be seen, that after the failure of the chemical bond, the unloading and reloading curves, shown by B-C, are identical and nearly vertical. Thus, the sheeting still develops its full bond capacity with negligible slip. Upon closer inspection, it is found that there is a slip of 0.025 mm from the point of unloading C to the maximum stress of 0.87 MPa, Point B. For the design of the beams, a bond stress of 0.8 MPa was used, as this represented the stable value to which the bond stress tended towards.

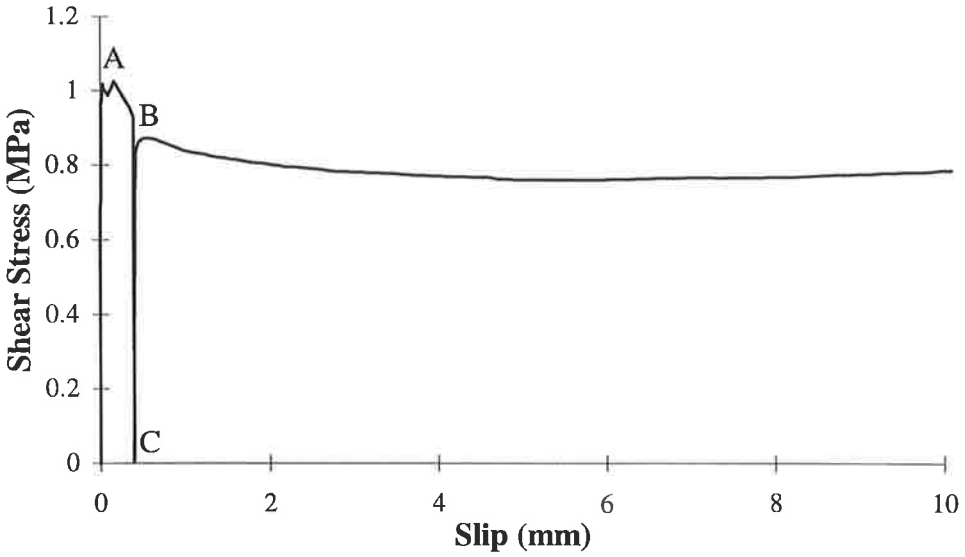


Fig. 5.6. Push Test Result for Beams PB1 and PB2

5.4.3 Beam CB1

As was discussed previously, this beam was a control test with no profiled sheeting present. The test arrangement and dimensions are as shown in Fig. 5.1a and (b). The beam ready for testing is shown in Fig. 5.7. The resulting load vs midspan deflection plot from the test is shown in Fig. 5.8.

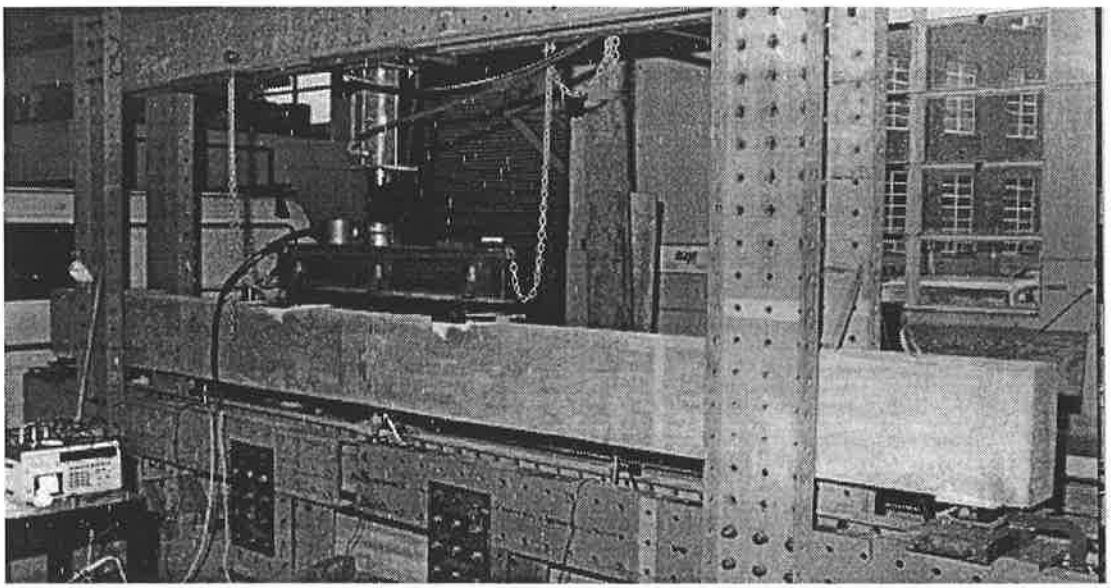


Fig. 5.7. CB1 ready for testing

Figure 5.8 shows the characteristic decrease in stiffness at the onset of concrete cracking at Point A. From the curve, it can be seen that cracking commences at an applied load of approximately 30 kN, as indicated by the change in stiffness at Point A. This corresponds to an applied moment of 27 kNm, which is slightly higher than the calculated

cracking moment of 20 kNm. The unloading and re-loading curves are nearly co-linear, with very little offset at the location where unloading commenced. This is a typical response for a reinforced concrete beam.

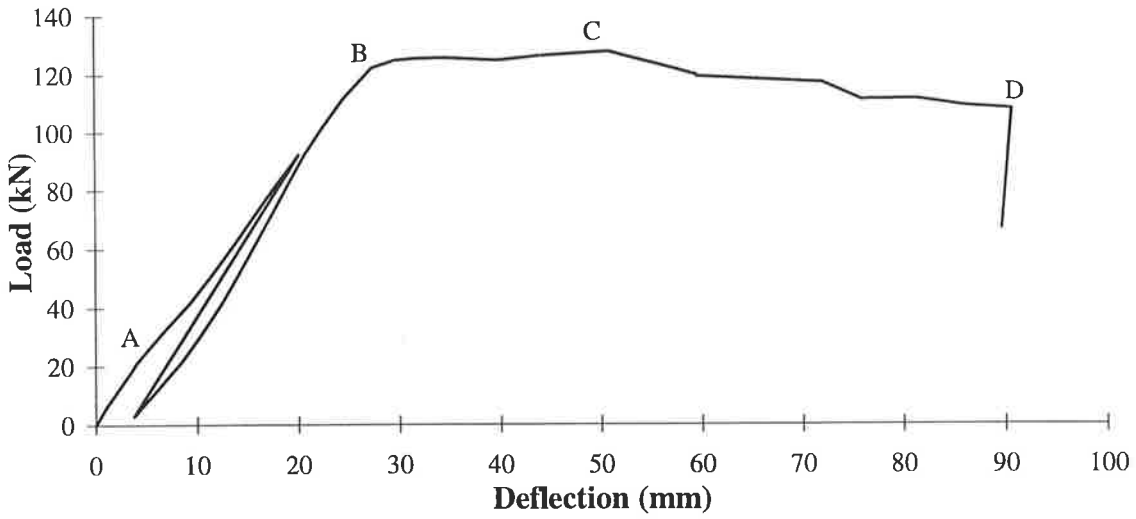


Fig. 5.8. Load Deflection Plot for CB1

It can be seen that this beam exhibits significant ductility, as shown by the length of the plastic plateau, B-C-D. The maximum applied load was 128 kN at a deflection of 51 mm, shown by Point C in Fig. 5.8. There is a gradual decrease in the load carrying capacity of the beam after Point C, until Point D is reached at a load of 108 kN and a deflection of 91 mm, after which there is a large decrease. The sudden decrease in load at Point D was due to buckling of the compression steel. The gradual decrease in the moment resistance between C and D is due to the crushing of the concrete, which was seen to commence at the time the maximum load was reached. The final failure of the beam was due to buckling of the compression reinforcement, which occurred after the concrete cover had crushed, and was no longer able to restrain the reinforcement from buckling. The failed beam is shown in Fig. 5.9. The results of the Load vs Midspan Deflection curves are summarised in Table 5.4.

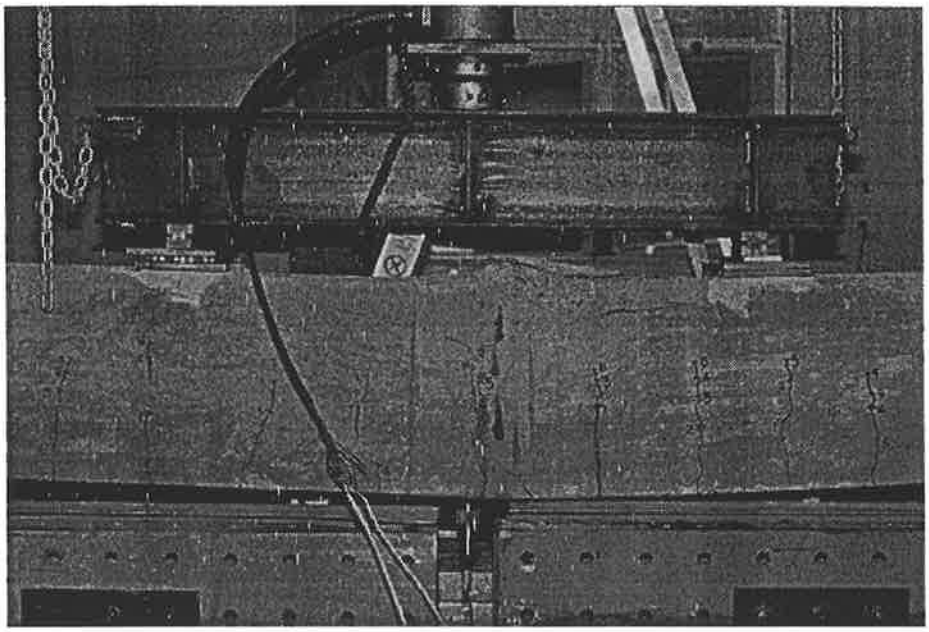


Fig. 5.9. Failure of CB1

5.4.4 Beam PB1

This beam was constructed from individual units as shown in Fig. 5.10a, with the completed beam shown in (b). The beam was constructed by spot welding the side units together through the webs of the ribs, as shown in (b). The five side units were welded together in this manner to form the two sides of the beam. The two halves of the beam were then joined together by MIG welding the bottom unit into place. Construction of one half of the beam is shown in Fig. 5.11. The stirrups and longitudinal reinforcing was the same as for Beam CB1 and fitted inside the ribs, as shown in Table 5.1.

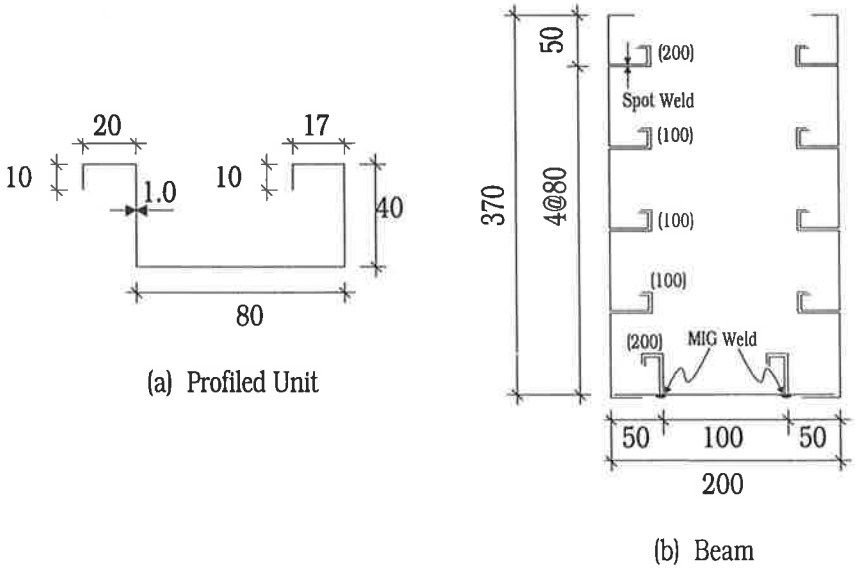


Fig. 5.10. Profiled Sheeting for PB1

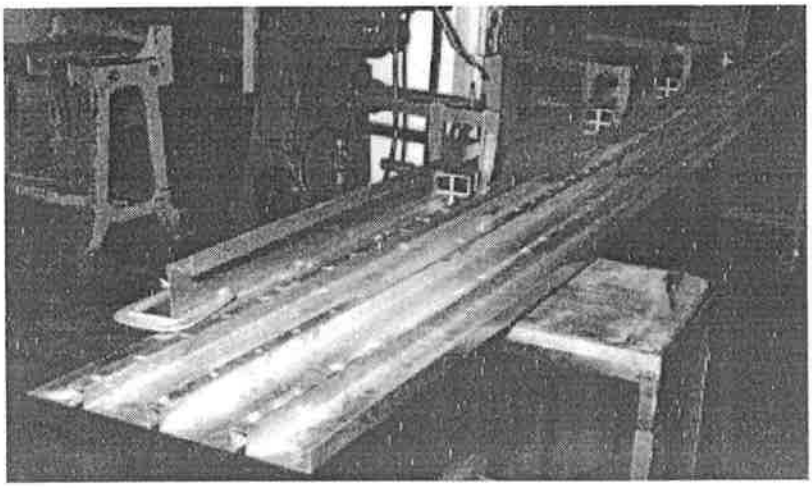


Fig. 5.11. Construction of PB1

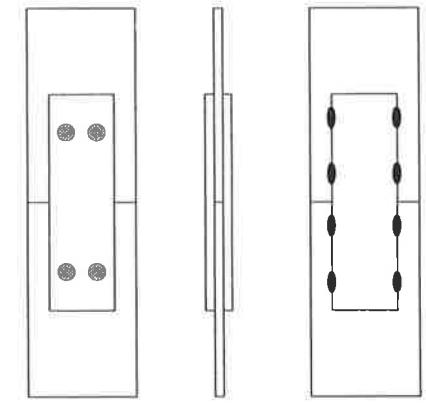


Fig. 5.12. Testing strength of welds

Test were performed to determine the strength of the spot welds and MIG welds on the 1.0 mm sheeting. The test specimens were constructed as shown in Fig. 5.12. Many tests were performed, and the design strength per weld used was taken as the minimum result from the tests. This was taken as 3.0 kN for the spot welds, and 2.5 kN for the MIG welds. The required spacing of the welds varies for each of the different joints throughout the depth of the beam. The calculation for the spacing of the welds is given in Appendix A. The spacing adopted in the beam is given in Fig. 5.10b as the number in brackets, measured in mm.

The load vs midspan deflection curve is shown in Fig. 5.13. The decrease in the stiffness can be seen at the onset of concrete cracking, at a load of approximately 30 kN. The beam was unloaded after a load of 50 kN had been applied, due to a malfunction with the hydraulic equipment. After this was corrected, the beam was then reloaded to 245 kN before

unloading again. It can be seen that the unloading and re-loading lines are almost co-linear with very little offset at Point A where unloading commenced.

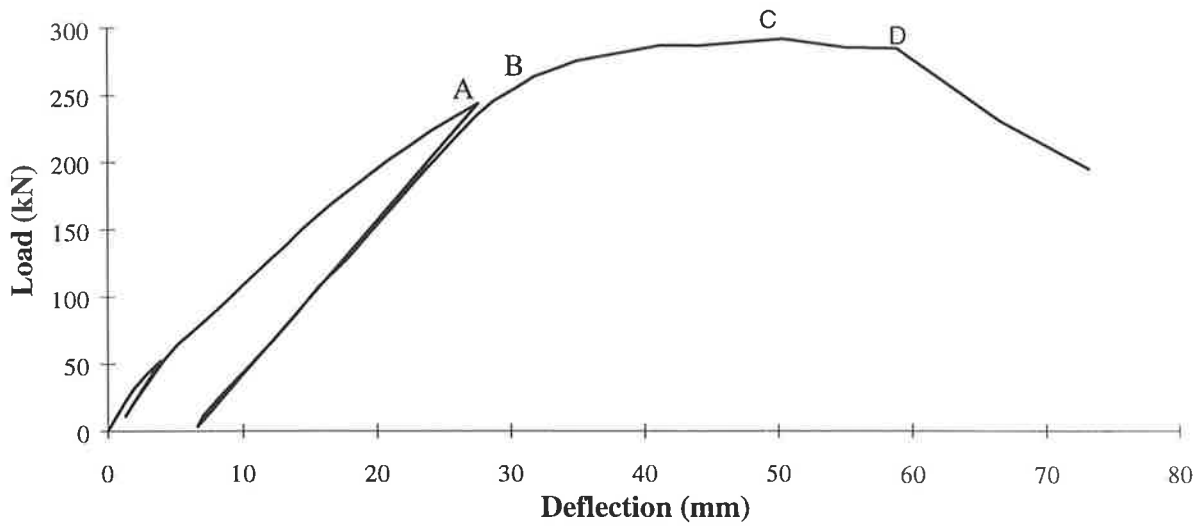


Fig. 5.13. Load Deflection Curve for Beam PB1

It can be seen in Fig. 5.13 that there is a gradual transition from the initial linear portion of the load / deflection curve to the horizontal plateau. The point at which yielding of the main reinforcement occurred was not as easily discernible as for Beam CB1, as shown in Fig. 5.8. This was due to the gradual yielding of the soffit profiled sheeting, which was distributed over a depth of 40 mm, as shown in Fig. 5.10. Thus there was a gradual yielding of the profiled sheeting, and Point B in Fig. 5.13 is taken as the point at which significant yielding occurred in the beam. This occurred at a load of approximately 250 kN, as shown by Point B. Concrete crushing was observed at the maximum load of 292 kN and occurred at a deflection of 50.4 mm. Final failure of the beam was observed when the compression steel buckled at a load of 285 kN and a deflection of 58.9 mm, as indicated by Point D. The buckling of the compression steel occurred when the concrete cover was no longer effective in restraining it.

Buckling of the top flange was noticed as early as 85 kN, and is shown diagrammatically in Fig. 5.14. There were some regions where a small amount of concrete restrained the horizontal element of the top rib. In these regions, the onset of buckling was not observed until the applied load approached 200 kN. When the horizontal element of the top rib buckled, the vertical element of the rib rotated away from the concrete surface, thus causing both elements to become ineffective in compression. This is shown in Fig. 5.14. The

wavelength of the buckle in the horizontal element was very long, and quite hard to determine.

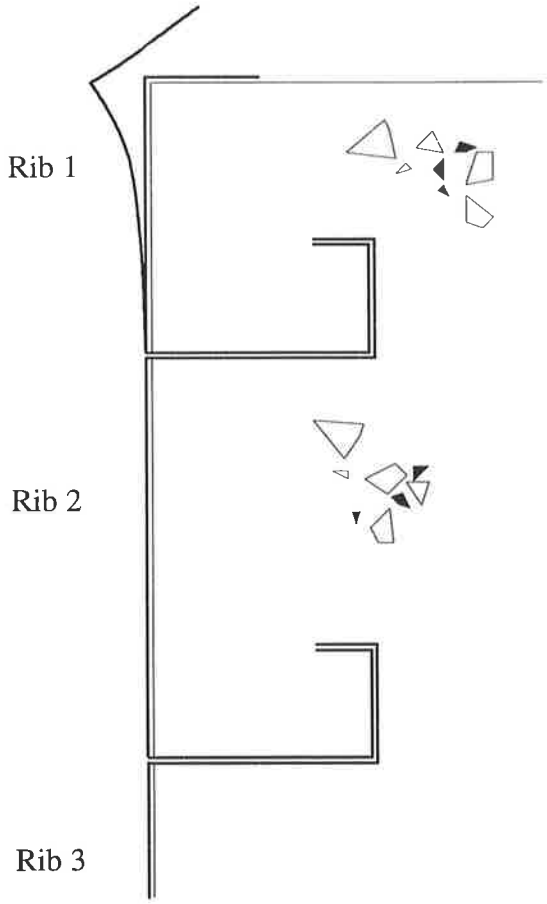


Fig. 5.14. Buckling in PB1

Buckling in Rib 2, as shown in Fig. 5.14, became evident near the peak load. At lower loads the buckling amplitude was greatly limited and difficult to discern. This is due to the concrete restricting axial shorting of the sheeting, and thus limiting its lateral deformation. This made it difficult to determine the exact load to cause the onset of buckling, or the wavelength of the buckles. Most of the buckling appeared to be concentrated at discrete locations, where short wavelength buckles formed. On the descending branch of the loading curve, there were signs of buckling in the top of Rib 3 in Fig. 5.14.

5.4.4.1 Slip Measurements

Transducers were placed along the beam in order to determine the variation in slip along the length of the beam. The location of the transducers is indicated in Fig. 5.15 by the symbol ◂—. In order to measure the relative slip between the concrete and the profiled

sheeting, small cut outs were made in the sheeting, as shown in Fig. 5.16. The cut outs were circular holes 15 mm in diameter, which were formed after the concrete had hardened, using a sheet cutting drill. A 4 mm diameter hole was then drilled into the concrete in the centre of the hole through the sheeting to a depth of 10 mm. A pin was then inserted into the hole in the concrete and epoxied into position. The transducer was attached to the sheeting, and the relative displacement between the sheeting and the pin was then recorded at each load stage. The arrangement of the transducer and the locating pin is shown in Fig. 5.16b.

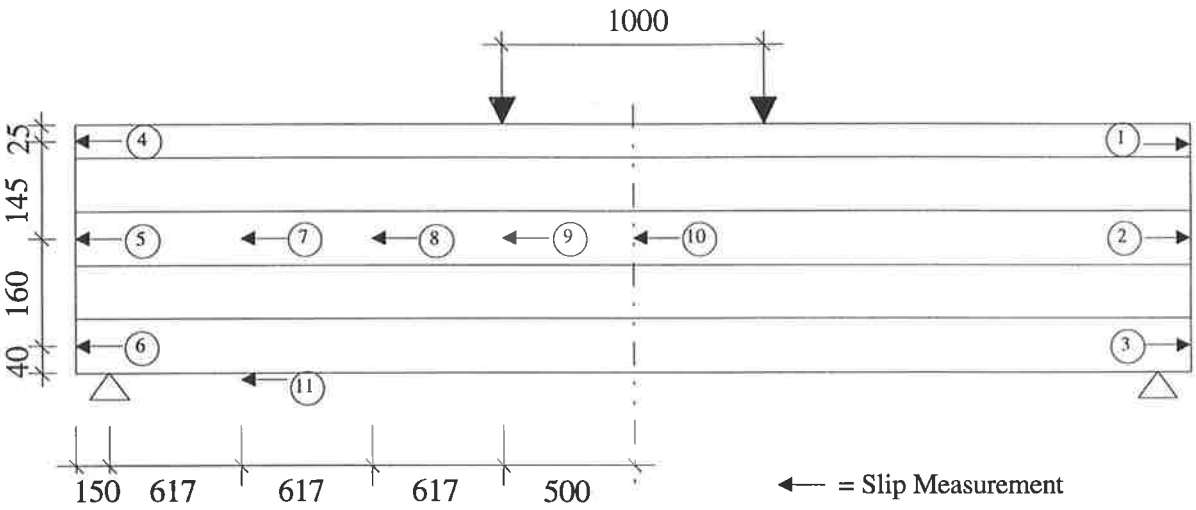
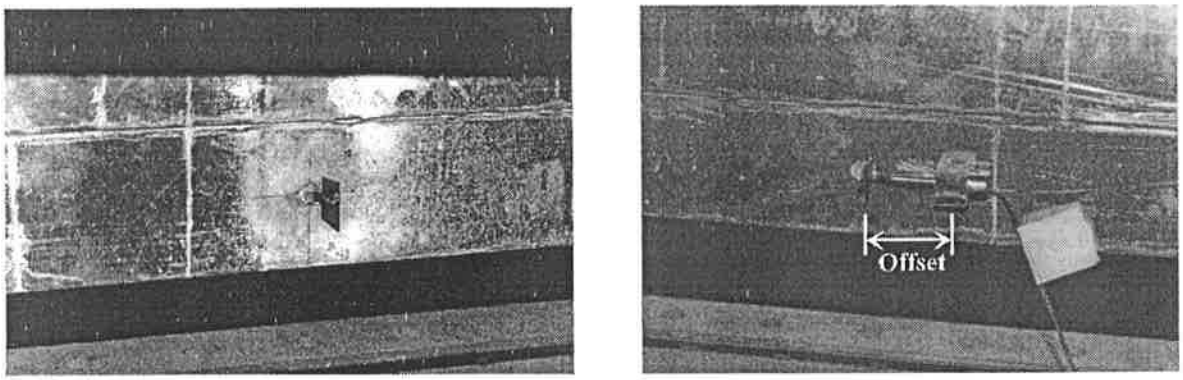


Fig. 5.15. Arrangement of Slip Measurement for PB1



(a) Pin Location (b) Transducer Location

Fig. 5.16. Detail of transducer location

The transducers were arranged as shown in Fig. 5.15 in order to measure the longitudinal variation of the slip along the length of the beam, and also the vertical variation of the longitudinal slip throughout the depth of the beam at the beam ends. The displacement recorded by the transducers along the length of the beam is shown in Fig. 5.17 for different load levels. The load levels have been non-dimensionalised by dividing by the ultimate load

of the beam. The horizontal axis shows the distance along the beam from the support, where the left end of the axis represents the support and the right end represents the centre line of the beam. The applied load levels have been non-dimensionalised by dividing by the ultimate load of 292 kN.

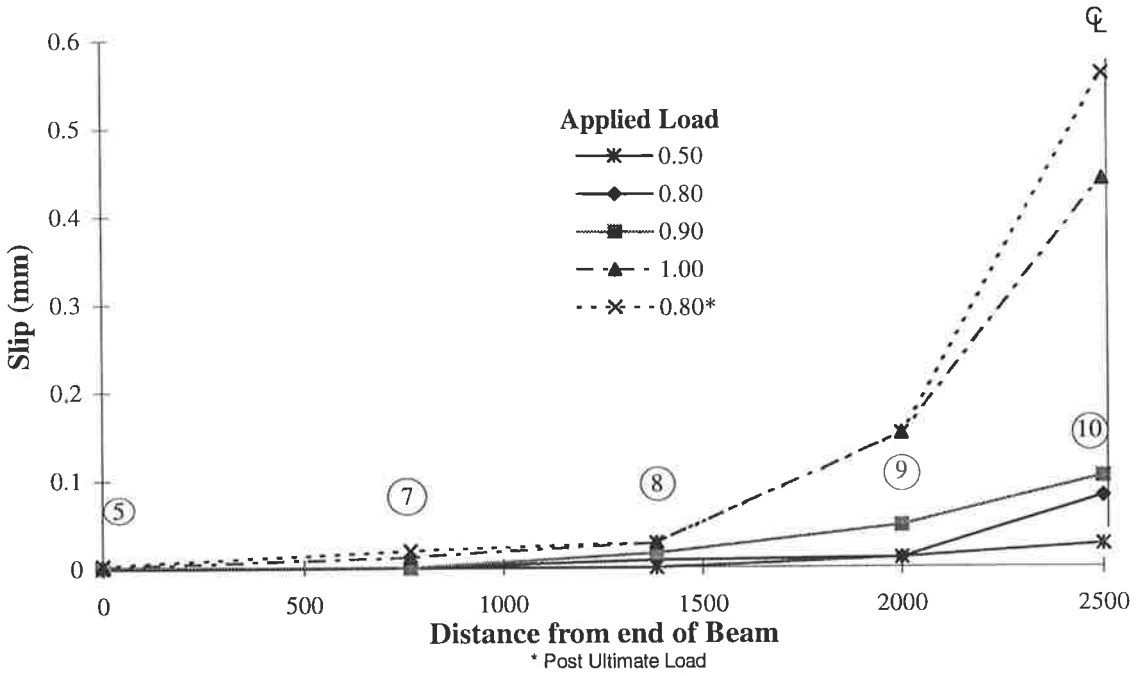


Fig. 5.17. Slip Distribution for Beam PB1

It can be seen in Fig. 5.17 that most of the displacement recorded by the transducers is concentrated in the constant moment region, between the load point and the midspan of the beam. In Fig. 5.17 this is between 2 000 mm and 2 500 mm from the supports. It can also be seen that there is a large increase in the recorded displacement after 90% of the ultimate load had been reached. The final displacement measurements shown in the figure were taken after the ultimate load of the beam had been attained, and the moment resistance was decreasing for increasing imposed deflection. It can be seen that the displacement continues to increase after the maximum load had been reached, and that the largest increase occurs in the constant moment region.

There are several possible explanations for the slip distribution shown in Fig. 5.17. For a symmetrically loaded beam, it would be expected that the slip should be zero at the centre, as discussed in Chapter 2. This is shown by the solid line in Fig. 5.18 for a beam with the strength of the shear connection much greater than that required for full shear connection. This slip distribution was predicted by the non-linear computer program which was

developed at part of this research, and will be discussed further in Chapter 7. However, as the applied moment is constant between the load points in Fig. 5.18, the position of zero slip may vary within the constant moment region, as shown by the dashed line in Fig. 5.18. Thus, it is possible that the maximum slip may occur at the centre of the beam, whilst the point of zero slip still occurs within the constant moment region.

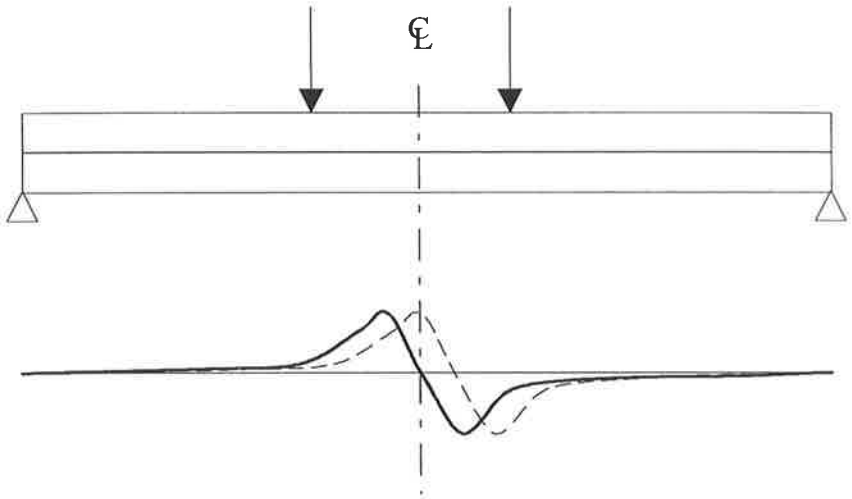


Fig. 5.18. Theoretical Slip Distribution for Beam PB1

Another possible explanation for the slip distribution shown in Fig. 5.17 is due to the elastic deformation of the sheeting. It can be seen from Fig. 5.16b that there is an offset between the attachment of the transducer to the sheeting and the location of the pin in the concrete. Thus, the transducer would record the elastic deformation over this distance, as well as the slip that occurs between the concrete and the sheeting. The typical offsets between the transducers and the locating pins were approximately 100 mm. Thus, assuming that the sheeting was at yield, the additional elastic deformation would be 0.14 mm. The amount of the additional displacement measured would obviously vary, depending on the level of the stress in the sheeting at the location of the transducer. For stresses above the yield point, the increase in the displacement will be larger than 0.14 mm. In the hinge region the strains can increase to many times the yield strain, as was discussed in Section 2.4.3.8 on page 92. Thus, the increase in displacement measured by the transducers may be larger than 0.14 mm in the hinge region. The magnitudes of these values are consistent with the recorded displacements shown in Fig. 5.17, indicating the likelihood that the measured displacements were due to the deformations in the profiled sheeting.

The increase in the transducer readings in Fig. 5.17 after 90% of the ultimate load had been applied corresponds to an applied load of 263 kN. From Fig. 5.13 it can be seen that

this load corresponds to the onset of significant yielding of the sheeting and main reinforcing, as indicated by the decrease in stiffness of the beam. Thus, the strains in the sheeting would exceed the yield strain, and the deformation in the sheeting between the transducer and the locating pin would increase significantly.

The maximum deformation recorded at the centre of the beam was 0.5 mm. This could be attributable entirely to the extension of the sheeting if the strains were 2.7 times the yield strain of the sheeting. Such strains are easily obtainable in the plastic hinge zone at the ultimate rotation of the member. Strain measurements were not taken during the test, and it is not possible to confirm this explanation, however the distribution of the recorded measurements shown in Fig. 5.17 is consistent with the expected variation in strain. Furthermore, the magnitudes of the transducer readings are consistent with this explanation.

The transducers at the ends of the beam were arranged so as to check for any variation in the slip throughout the depth of the beam. The maximum values recorded at both ends of the beam were very small, as indicated by the reading for Transducer 5 in Fig. 5.17. Transducers 4, 5 and 6 , which are shown in Fig. 5.15, each gave readings of 0.003 mm. It should be noted that this magnitude of displacement represents the limit of the accuracy of the transducers used and indicates that negligible slip was recorded, ie. the chemical bond had not been broken.

Transducers 1, 2 and 3 at the opposite end of the beam also recorded very small values of displacement. However, there was a slight variation between the values. Transducers 1 and 3 both recorded maximum displacements of 0.007 mm, whereas Transducer 2 recorded a maximum displacement of 0.015 mm. It is suggested that the 0.008 mm difference between these values is due to experimental variation. All the transducers recorded a residual displacement of at least 0.001 mm when the load was completely removed at the completion of the test.

Individual load vs displacement curves were recorded for all the transducers. These curves were largely similar for all the transducers, and results presented here were typical of the transducers. The load vs displacement curves for Transducers 7, 10 and 11 are shown in Fig. 5.19. It can be seen that Transducers 7 and 11 have different load vs displacement curves, however as Fig. 5.15 shows, they are at the same cross-section along the beam. One

possible reason for this may be due to the presence of flexural cracks near the location of Transducer 11.

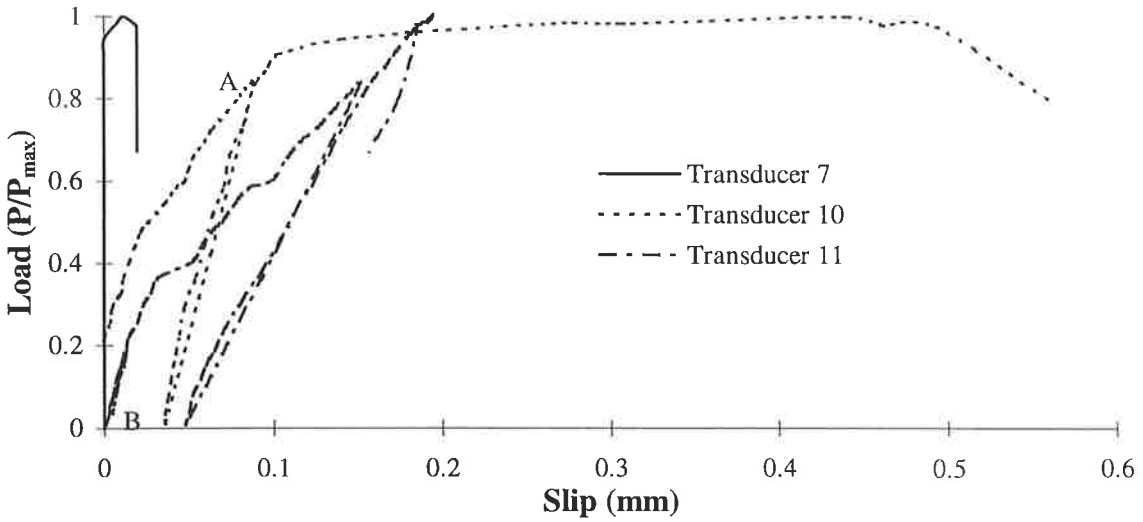


Fig. 5.19. Load vs Displacement for Transducers 7, 10 and 11

Figure 5.19 shows that at unloading of the beam, before the ultimate moment of the beam was reached, there was significant elastic recovery of the displacement measured by Transducers 10 and 11. This elastic recovery was not noted in the push tests of the profiled sheeting, shown in Fig. 5.6, and indicates the influence of the elongation of the sheeting between the transducer and the locating pin. The difference in the slope of the unloading lines of the two transducers indicates the difference in the stress at the two locations, for the same applied load. Transducer 11 is located at the soffit of the beam, as shown in Fig. 5.15, while Transducer 7 is located approximately at the mid-height of the beam. Thus, the stresses in the sheeting at the location of Transducer 11 will be larger than at the location of Transducer 7, and thus give rise to the larger elastic displacements. As the load is reduced, the elastic displacements decrease as shown by the elastic unloading line A-B in Fig. 5.19. An exact calculation of the effect of the extension of the profiled sheeting is not possible, as strain measurements were not taken at the location of each transducer.

Figure 5.19 indicates that after the load has been completely removed there remains some residual displacement between the sheeting and the concrete as shown by Point B for Transducer 10. This residual displacement represents the maximum residual slip that occurred as a result of loading up to a maximum load shown by Point A. This displacement is independent of any elastic deformation of the sheeting as there is no applied load on the beam.

It is possible to remove the elastic portion of the extension, as shown by the elastic line A-B for Transducer 10 in Fig. 5.19. The result of this correction is shown in Fig. 5.20. At loads approaching the ultimate load, the strain in the sheeting at Transducer 10 is likely to approach or exceed the yield strain, and thus the elastic correction shown in Fig. 5.20 will not be sufficient to remove the effect of the sheeting extension from the displacement measurement. However, the strains at Transducer 11 will not exceed yield, and thus the elastic correction will adequately account for the sheeting extension. Figure 5.20 indicates that after removal of the elastic extension component from the measured deflections of Transducers 10 and 11 there is still some measured slip. After initial unloading, the residual slip was 0.04 mm and 0.05 mm for Transducers 10 and 11 respectively.

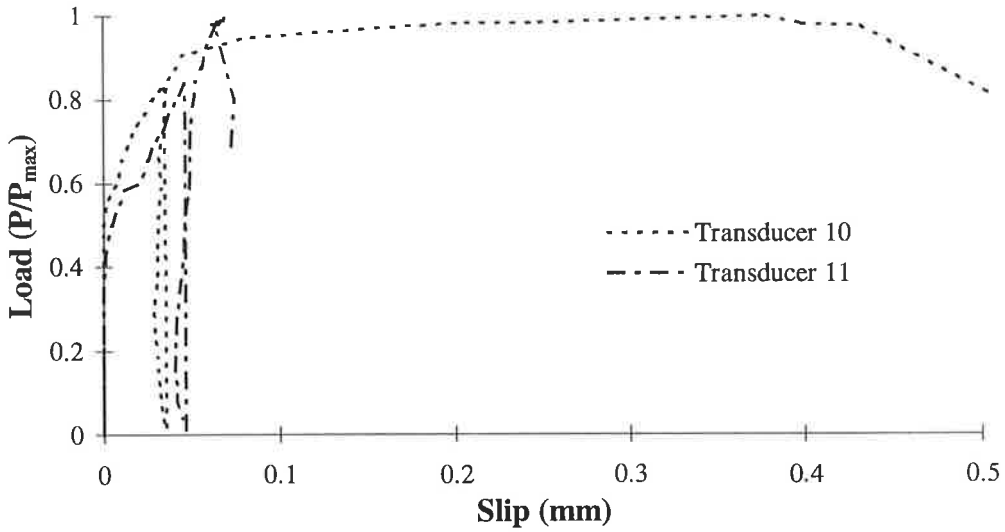


Fig. 5.20. Adjusted Load vs Slip for Transducers 10 and 11

The load vs displacement curves for Transducers 7, 8 and 9 are shown in Fig. 5.21, with the corrected graph for Transducer 10 reproduced as a reference. It can be seen that for all load levels, the displacements increases for transducers closer to the centre line of the beam, which is as expected. However, the magnitudes of the displacements are very small, and from the previous discussion, it is more likely that measurements reflect the strains in the profiled sheeting. The small magnitude of the slips is evidenced when compared to the slips generated in the push tests, as shown by Fig. 5.6, which indicated slip capacities greater than 10 mm. Thus, it appears that Beam PB1 exhibited full shear connection. This will be shown in Section 5.6.1 when the results are compared to the Rigid Plastic theory of Chapter 4.

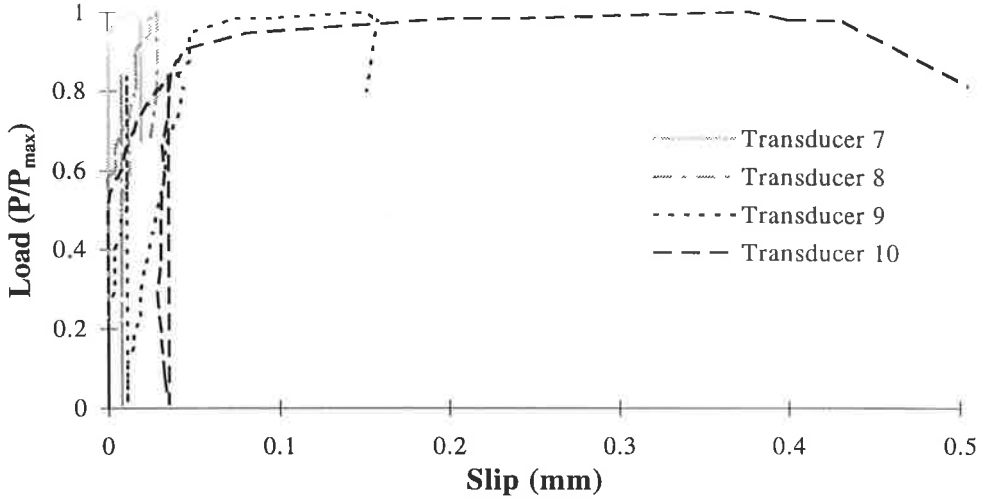


Fig. 5.21. Load vs Slip for Transducers 7, 8, 9 and 10

5.4.5 Beam PB2

This beam was constructed from the same profiled units and had the same overall geometry as for Beam PB1, and is shown in Fig. 5.10. The difference between the two beams was that PB2 was constructed without welding the individual units together. They were assembled together in the formwork by 'clipping' the units together, as shown in Fig. 5.22. The reinforcing was assembled and then placed inside the profiled sheeting as a complete unit, as shown in Table 5.1. The properties of the concrete, reinforcing steel and profiled sheeting were the same as for Beam PB1 and are given in Table 5.2.

The resulting load vs midspan deflection curve is shown in Fig. 5.23. The beam was loaded to a total applied load of 207 kN at Point A, before being unloaded. This occurred before the reinforcing yielded, which is indicated by the leveling of the curve at B. There was a ductile plateau B-D, where the load increased gradually to a maximum of 253 kN at C, followed by a slight reduction in the load carrying capacity to 251 kN at Point D. There was a sudden drop in the load carrying capacity at D when the compression steel buckled. This occurred when the concrete cover had crushed and was no longer able to support the compression steel against buckling.

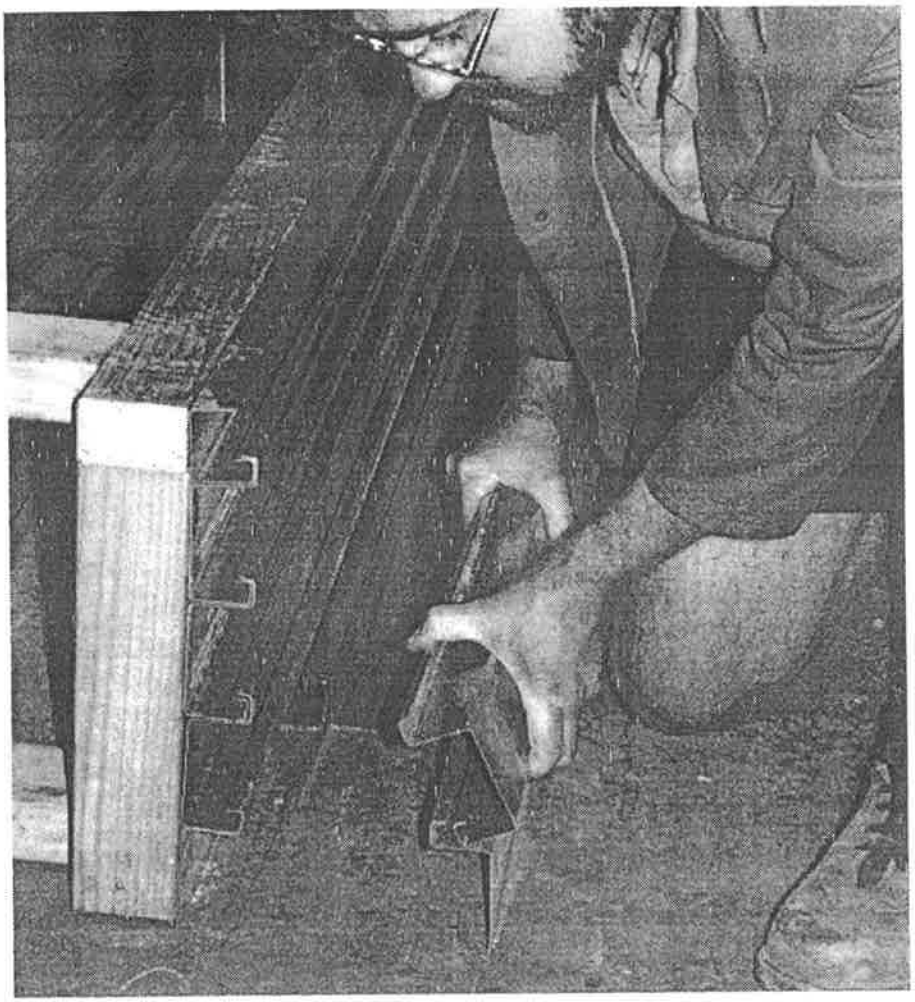


Fig. 5.22. Assembly of PB2

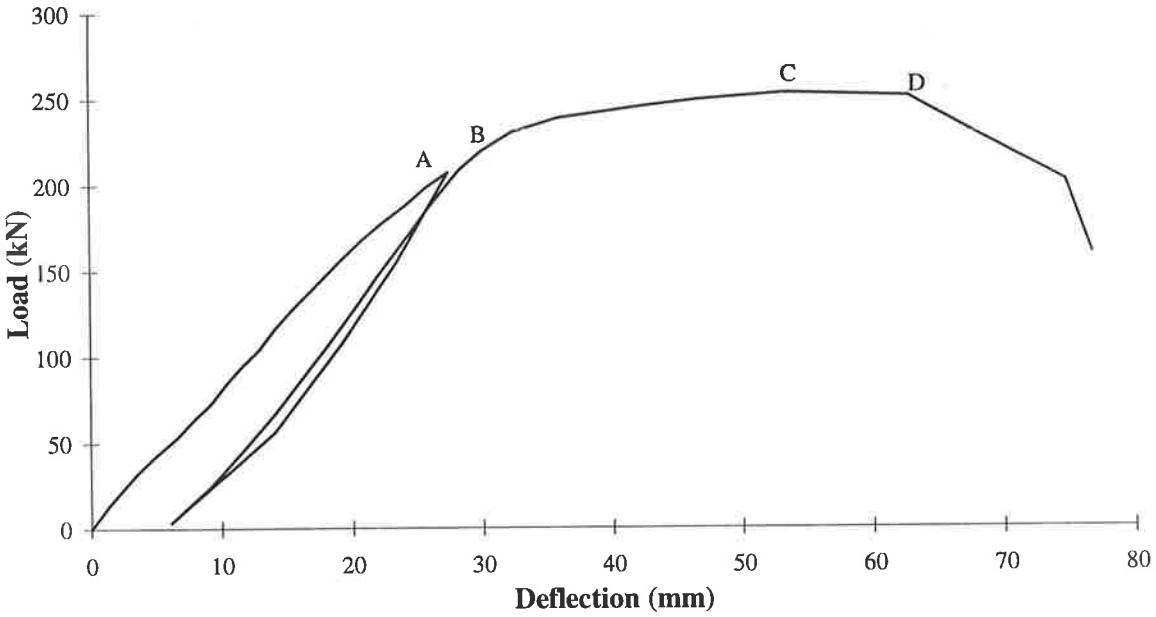


Fig. 5.23. Load vs Midspan Deflection for Beam PB2

Buckling was noticed in the horizontal element of the top rib at an applied load of 50 kN. The buckles were concentrated in a few locations with amplitudes of approximately 3-4 mm. These buckles then forced compatibility deformations in the vertical element of the top rib, which occurred only at the locations of the buckle in the horizontal element. This behaviour was also noted for Beam PB1 and is shown diagrammatically in Fig. 5.14.

Buckling of the other ribs was difficult to detect visually due to the very small amplitude of the buckled shape. The presence of the concrete restrained the sheeting from shortening axially and thus restricted any lateral deformation. After the concrete had crushed, the sheeting was able to shorten significantly and buckling became apparent in the second and third ribs.

5.4.5.1 Slip Measurement

The arrangement of the transducers to measure slip is shown in Fig. 5.24. These transducers were arranged so as to investigate the transverse variation in longitudinal slip throughout the depth of the beam and the longitudinal variation in slip along the length. As was discussed in Chapter 4, under conditions of partial shear connection it is expected that for clipped construction there will be longitudinal slip between the individual units, and thus the slip will not be constant throughout the depth of the beam. The transducers to measure the transverse variation in slip were placed at the cross-section under one of the applied loads, as shown in Fig. 5.24. This arrangement was chosen because the longitudinal variation in slip from PB1 showed the slip to be a maximum within the constant moment region. Thus, it was expected that if the slip was greatest at this location, then the difference in slip between the units would also be greatest. The longitudinal variation in slip was measured at the soffit, as it was anticipated that the magnitude of the slip would be greatest at this location, and thus give the largest overall variation.

The load vs displacement curves for Transducers 9, 11 and 4 are shown in Fig. 5.25. It can be seen that the recorded displacement for Transducer 9 is negative, whereas the recorded displacements for the other transducers are positive. This is due to the fact that Transducer 9 was located in the compression region of the beam, whereas the other transducers were in the tensile region. It can also be seen that upon unloading of the beam, before the ultimate load has been reached, there was significant elastic recovery of the recorded displacements. This was due to the contribution of the extension of the profiled sheeting in the recorded

displacements, as discussed in Section 5.4.4.1. This effect was removed for the following graphs in a similar manner to that for Beam PB1, and the adjusted load vs slip curves for Transducers 9, 11 and 4 are shown in Fig. 5.26.

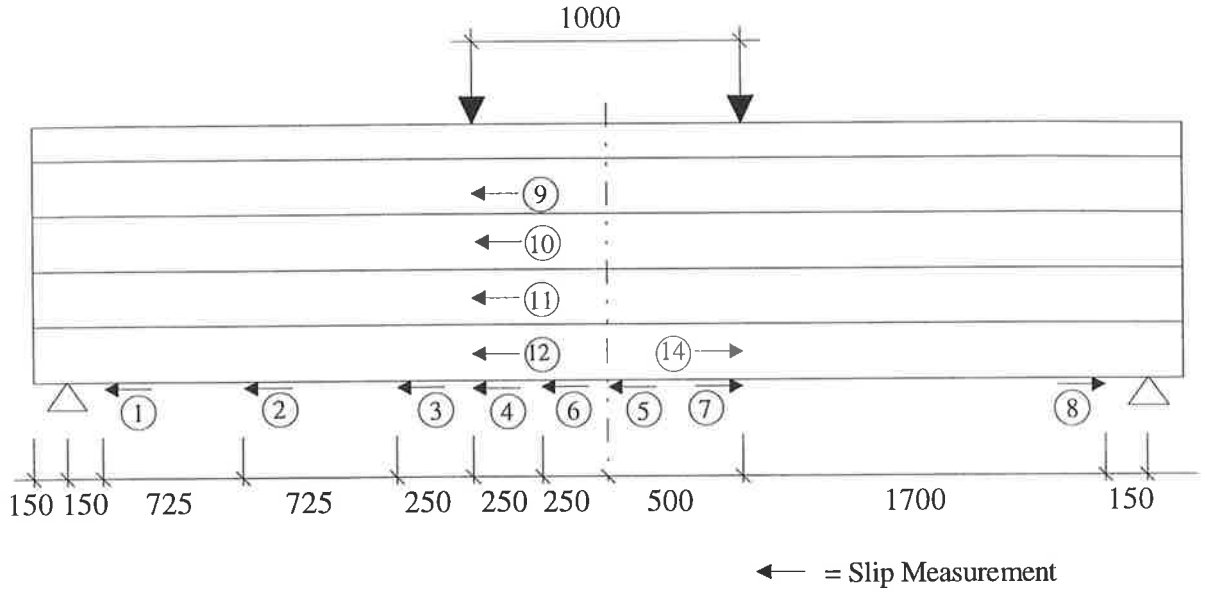


Fig. 5.24. Location of Transducers for Beam PB2

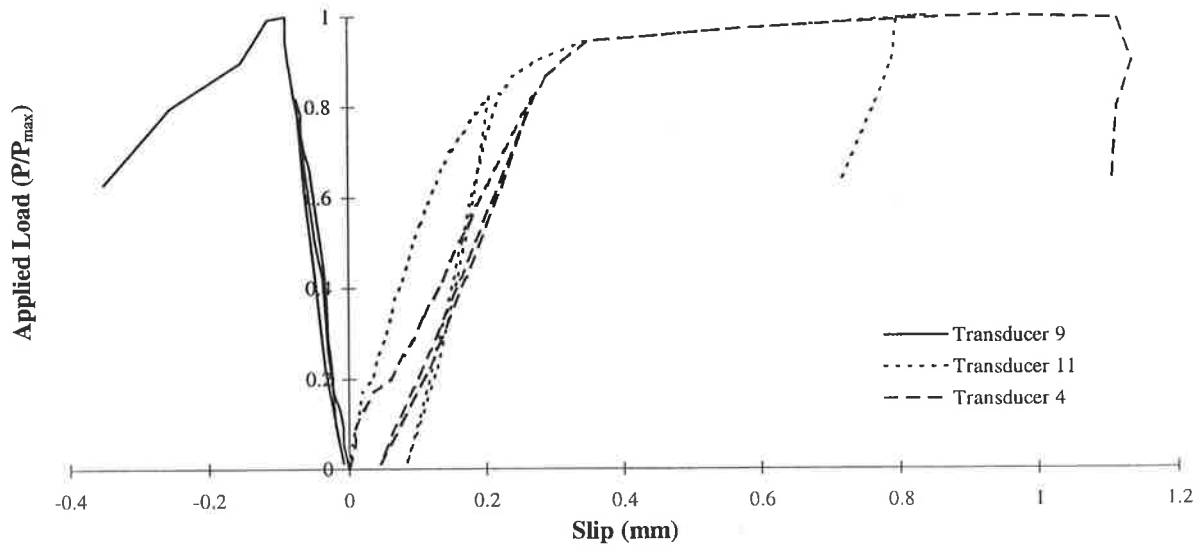


Fig. 5.25. Load vs Slip for Transducers 9, 11 and 4

It can be seen in Fig. 5.26 that after the elastic displacements have been removed from the transducer readings, that Transducer 9 indicated zero displacement until after the ultimate load had been reached, indicating full interaction between the sheeting and the concrete at the location of the transducer. The large increase in displacement after the ultimate load is due to the yielding of the sheeting. Transducers 4 and 11 indicated residual displacements of

0.04 mm and 0.08 mm respectively after initial unloading. These displacements represent the residual slip after unloading, and are not affected by the elastic displacements of the sheeting. These slips are very small in magnitude when compared to the ductility of the sheeting as shown in Fig. 5.6. Figure 5.26 indicates a significant increase in the displacements recorded by Transducers 4 and 11 at the onset of yielding, which is due to the extension of the sheeting.

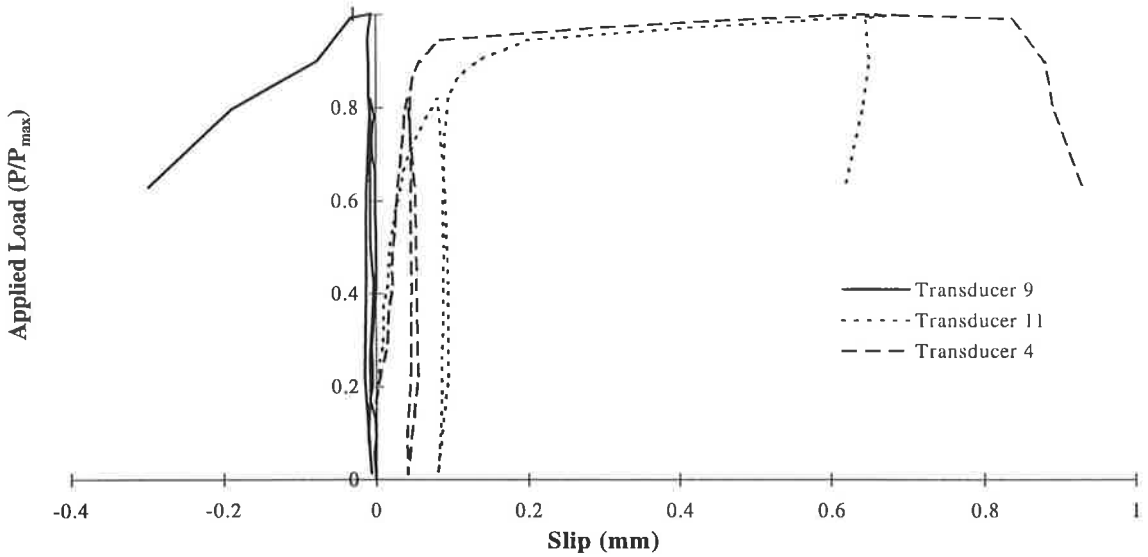


Fig. 5.26. Adjusted Load vs Slip for Transducers 9, 11 and 4

Figure 5.27 shows the variation in recorded displacements with height above the beam soffit, for increasing applied load. The applied load has been non-dimensionalised by dividing by the maximum load of 253 kN. It can be seen that there is a general trend towards increasing displacements at locations closer to the bottom of the beam, and that for most load levels the maximum displacement occurred in the lowest side unit. The reason the bottom side unit has a larger displacement than the soffit is most likely due to the fact that the lowest side unit has only one rib which is embedded in the concrete, whereas the soffit unit has two, as is shown in Fig. 5.10b, and thus develops a smaller bond with the concrete.

It can be seen from Fig. 5.27 that there is negligible recorded displacement until approximately 70% of the ultimate load is reached. From Fig. 5.23 it can be seen that yielding commenced at a load of approximately 210 kN or 80% of the ultimate load, which would have subsequently influenced the results of the displacements. This indicates that the displacements shown in Fig. 5.27 would be strongly influenced by the deformation of the sheeting, and that once again the recorded slips are very small.

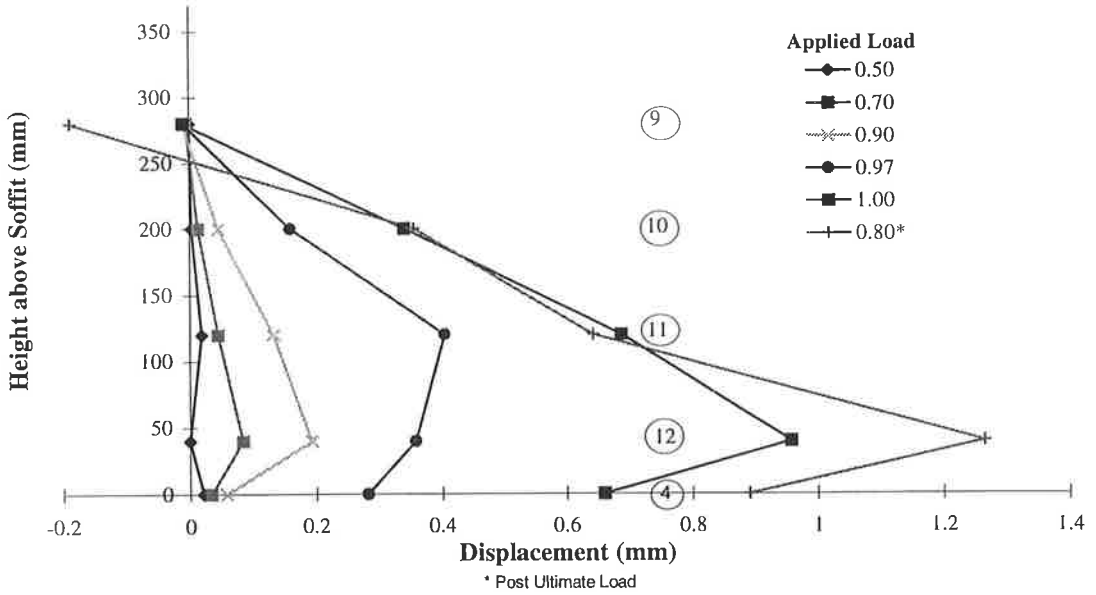


Fig. 5.27. Variation in Slip with Height above Soffit

The longitudinal variation in recorded displacements along the soffit is shown in Fig. 5.28. It can be seen that the displacement is non-zero at the centre of the beam. This is due to local variations in the beam, and the position of zero displacement still lies within the constant moment region. At failure, it was found that the plastic hinge formed toward the right load point. This is consistent with the measurement of displacement, which shows that

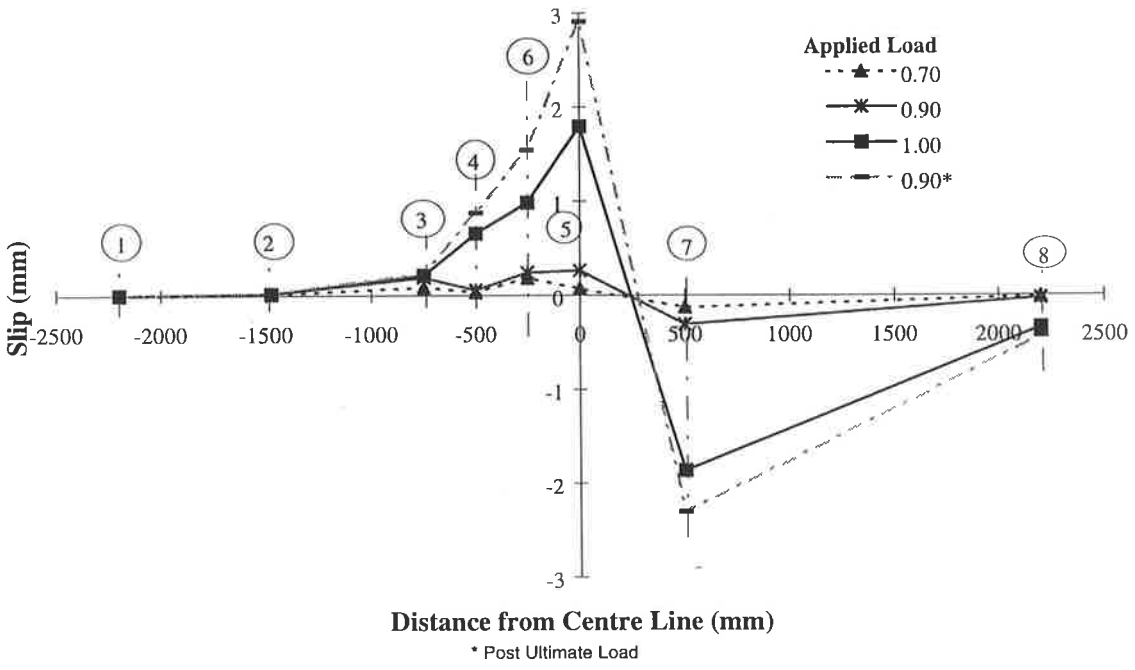
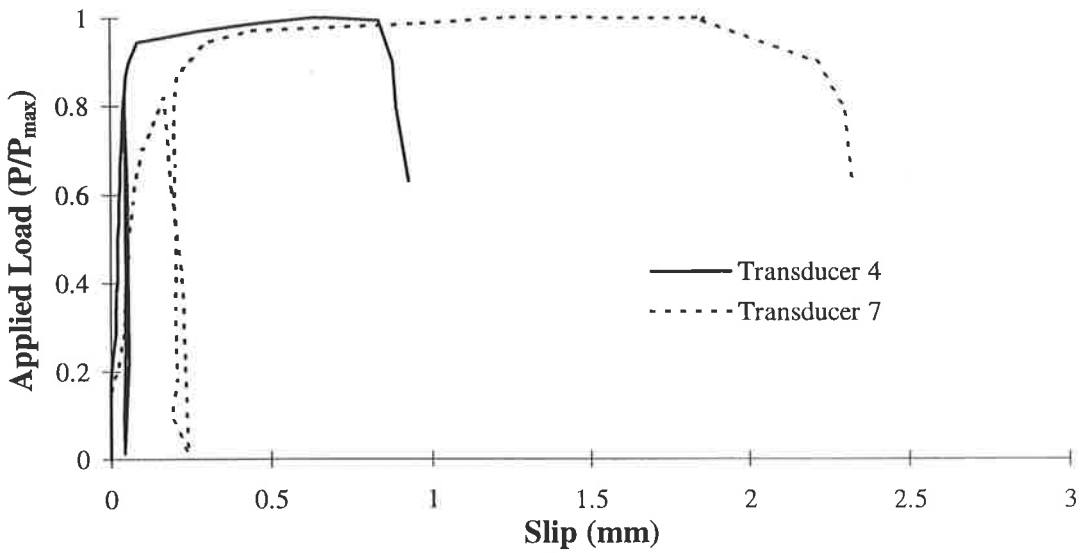


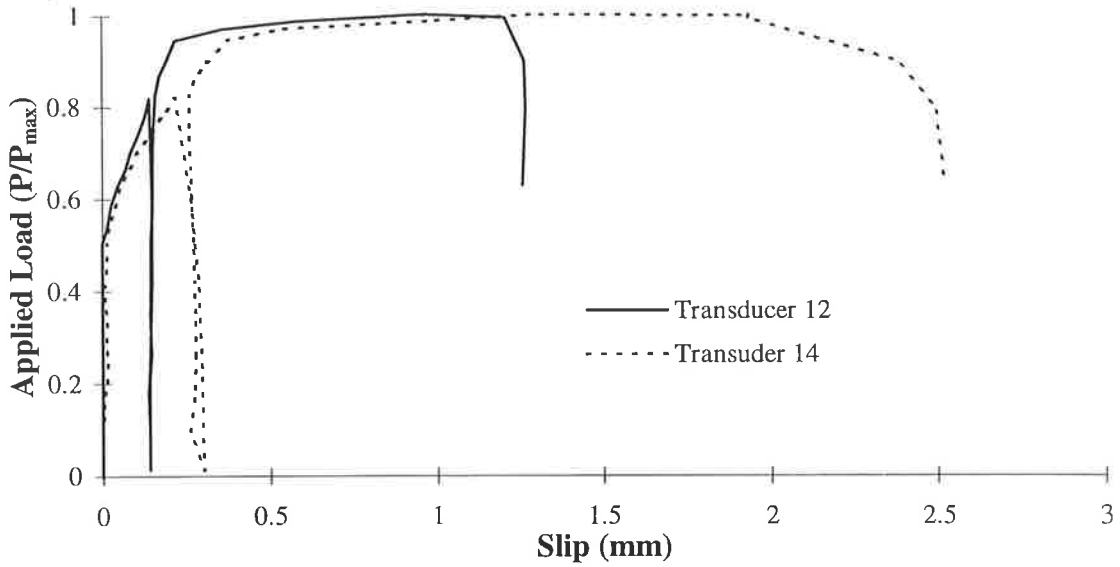
Fig. 5.28. Longitudinal Variation in Slip for Beam PB2

the location of zero displacement is offset toward the right load point. This figure also indicates that the majority of the displacement occurred after 90% of the ultimate load had been reached, and that there was considerable increase in the recorded displacement after the ultimate load.

Figure 5.29 shows the adjusted variation in displacement with increasing load for two sets of transducers which were placed symmetrically about the centre line. The location of the transducers is shown in Fig. 5.24. Both Fig. 5.29a and (b) indicate larger displacements in the right span of the beam at all load levels. This may be simply due to the fact that the location of the plastic hinge was slightly offset toward the right end of the beam. An important point of note is the large increase in displacement that occurs as the ultimate load is approached. The displacements remains relatively small until yielding of the reinforcing occurs, which is indicated by Point B in Fig. 5.23. After this point there is a rapid increase in the displacement in Fig. 5.29, with only very small increase in the applied load. This fact has repercussions for the design of composite beams with non-ductile shear connection between the steel and concrete elements, such as welded stud shear connectors, as was discussed in Chapter 2.



(a) Transducers 4 and 7



(b) Transducers 12 and 14

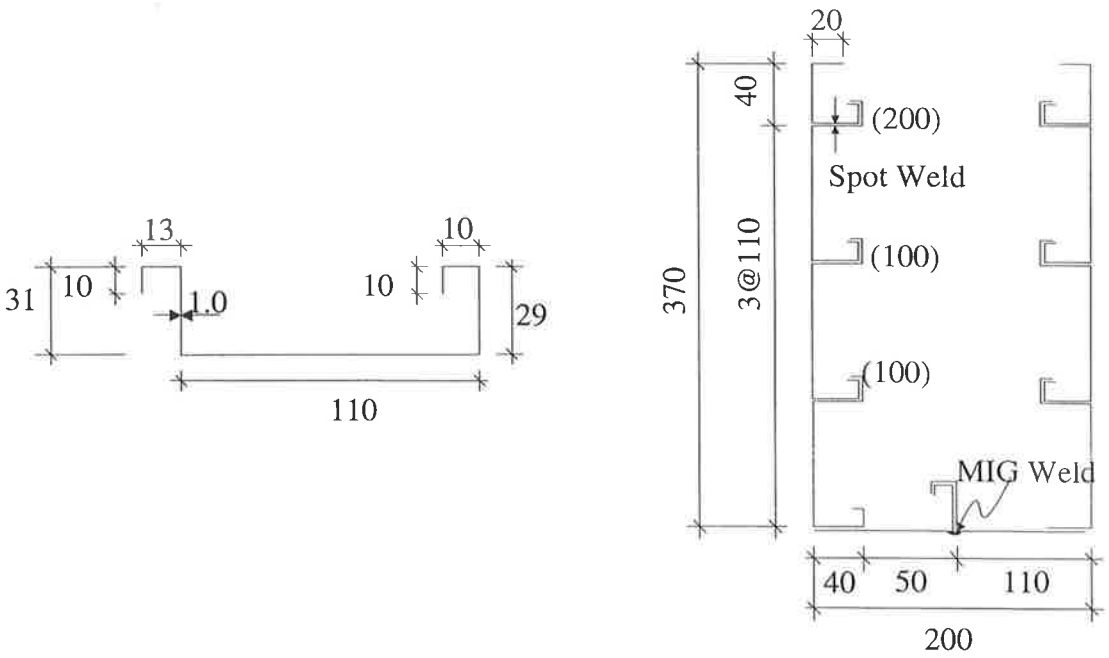
Fig. 5.29. Load vs Slip for Beam PB2

It should be noted that a comparison of the maximum displacement recorded for this beam in Fig. 5.29 is approximately 5 times larger than the maximum displacement recorded for Beam PB1, shown in Fig. 5.21. This increase in displacement can be attributed to the increase in the distance required to develop full shear connection for clipped construction, as discussed in Chapter 4.

5.4.6 Beam PB3

This beam was constructed from individual units as shown in Fig. 5.30a and assembled as shown in (b). The beam was constructed in a similar manner to Beams PB1 and PB2, with the location and spacing of the spot welds and MIG welds as shown in brackets in (b). The geometry of the ribs had been changed from the first series, with the aim of reducing the bond between the concrete and the profiled sheeting. This was achieved by providing fewer ribs which were more widely spaced, and reducing the size of the ribs. The reason for this was to reduce the degree of shear connection, and thus increase the slip at the interface.

The properties of the concrete, reinforcing steel and profiled sheeting are shown in Table 5.2. The concrete was poured, and then the beams were left to cure under wet hessian and plastic for 7 days. The construction sequence was the same as for the beams from the first series.



(a) Profiled Unit (b) Beam

Fig. 5.30. Profiled Beam PB3

5.4.6.1 Push Tests

Two push test specimens were cast with the beams, and tested at the same time as the beams were tested. These were used to determine the bond characteristics of the profiled sheeting, and the resulting stress-slip curve is shown in Fig. 5.31 for the second test. It can be seen from a comparison of this figure with Fig. 5.6 that the bond stress increased for the smaller rib size. This increase in bond stress resulted in premature buckling of the profiled sheeting, as indicated in Fig. 5.32. This buckling occurred on one side of the push specimens, and occurred in both tests. Slip was recorded on the opposite side of the specimen that did not buckle. The slip recorded in Fig. 5.31 is from the side of the specimen that did not buckle. Thus, the result shown represents a lower bound to the actual bond stress, and it is anticipated that the decrease in strength with increasing slip would not be as pronounced, if buckling had not occurred. Despite this, a value of 1.2 MPa was used for the design bond strength, which is 50% higher than the bond stress measured for the beams in Series 1, and shown in Fig. 5.6. Based on the rib contact perimeter S_r for Series 1 of 140 mm and 105 mm for Series 2, the design strength per rib is 112 kN/m for Series 1 and 126 kN/m for Series 2, which represents a 13% difference.

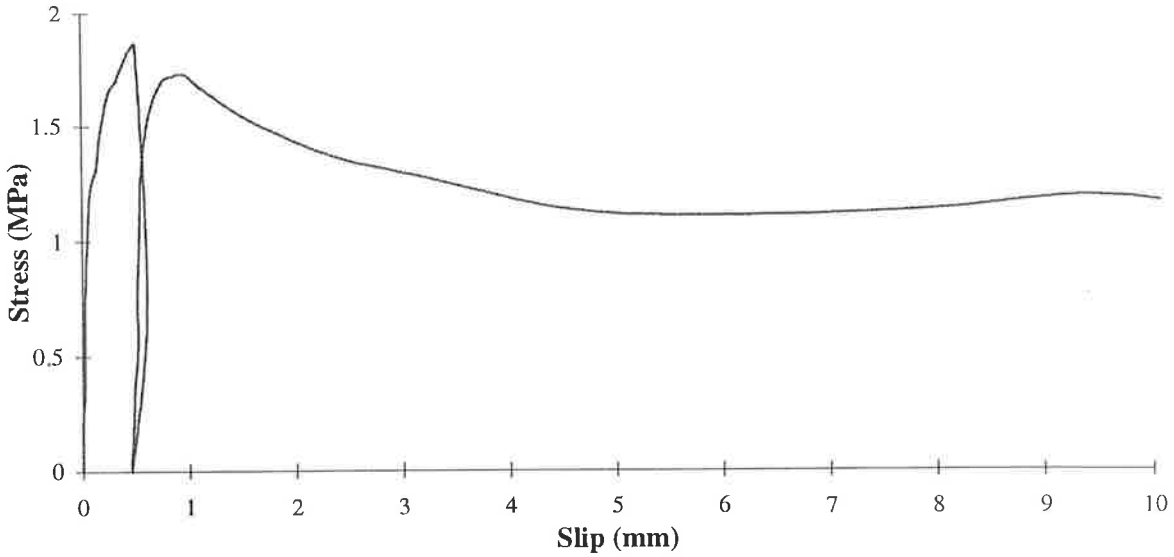


Fig. 5.31. Load vs Slip for Profiled Sheeting for PB3 and PB4

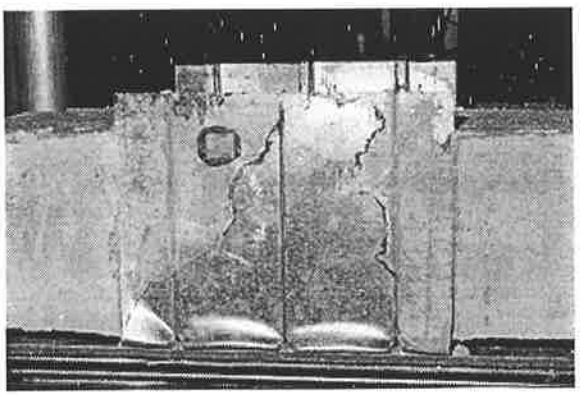


Fig. 5.32. Premature Buckling of Push Test

5.4.6.2 Beam Test

The load vs midspan deflection of the beam is shown in Fig. 5.33. The typical loss in stiffness due to concrete cracking can be seen at a load of approximately 50 kN. The beam was loaded up to a value of 150 kN at Point A before being fully unloaded. There is a defined yield point at a load of 203 kN at B, after which the deflection increases rapidly with only a slight increase in applied load up to a maximum of 215 kN at Point C. Crushing of the concrete became evident at large deflections. The final failure of the beam occurred when the compression steel buckled due to lack of restraint from the crushed concrete cover. This occurred at the maximum load of 215 kN, as shown by Point C. The results of the load vs deflection curve are given in Table 5.4.

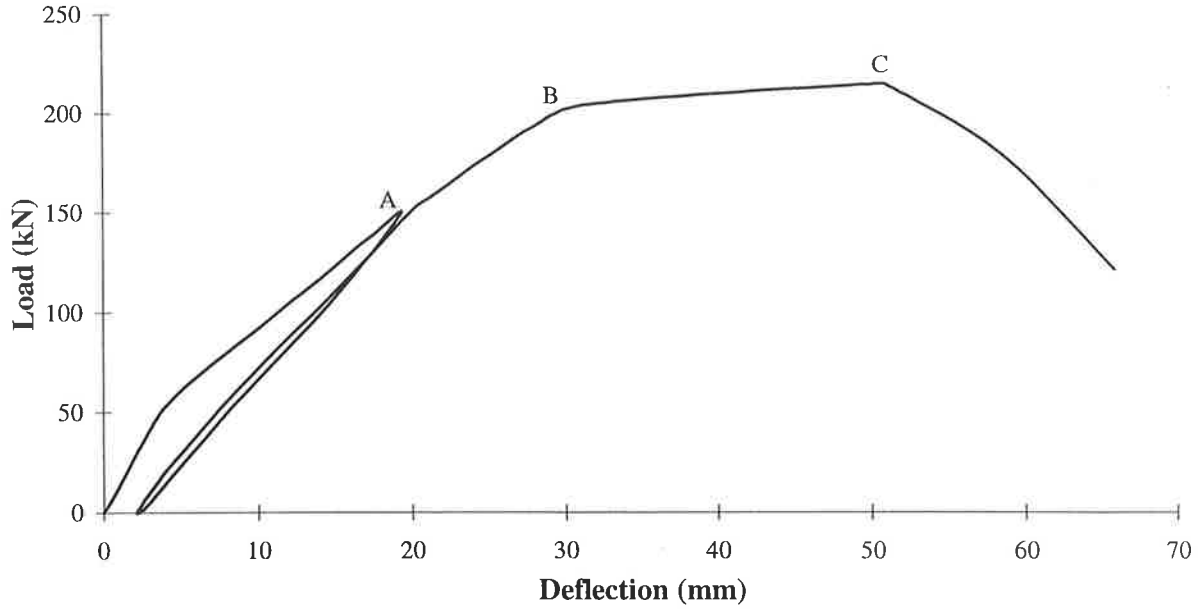


Fig. 5.33. Load vs Midspan Deflection for Beam PB3

The breakdown in the chemical bond was evidenced by a 'cracking' sound that could be heard as the beam was loaded. This cracking was first heard at approximately 60 kN, and then subsided after 80 kN. The cracking sound was more apparent from the tension region of the beam than from the compression region.

At 150 kN there was a sudden buckling of the horizontal element of the top rib. There was no buckling which was visually apparent before this point. The buckling was first noted in the shear span, between the load point and the support. At 160 kN buckling became apparent in the constant moment region between the load points. At 200 kN buckling became visually apparent in the top region of the second rib. However, from the strain gauges that were attached to the middle of the second rib, buckling was detected at a load of 170 kN. This was indicated by a reversal of the strain readings that occurred at this load.

5.4.6.3 Slip Measurement

The placement of the transducers to measure the variation in slip is shown in Fig. 5.34. The arrangement of the transducers in the tension region of the beam is as shown previously in Fig. 5.16. The arrangement of the top transducers is shown in Fig. 5.35. Also shown in Fig. 5.34 is the placement of the strain gauges on the profiled sheeting, and are indicated by SG ▬. The strain gauges were symmetrically placed on both sides of the beam.

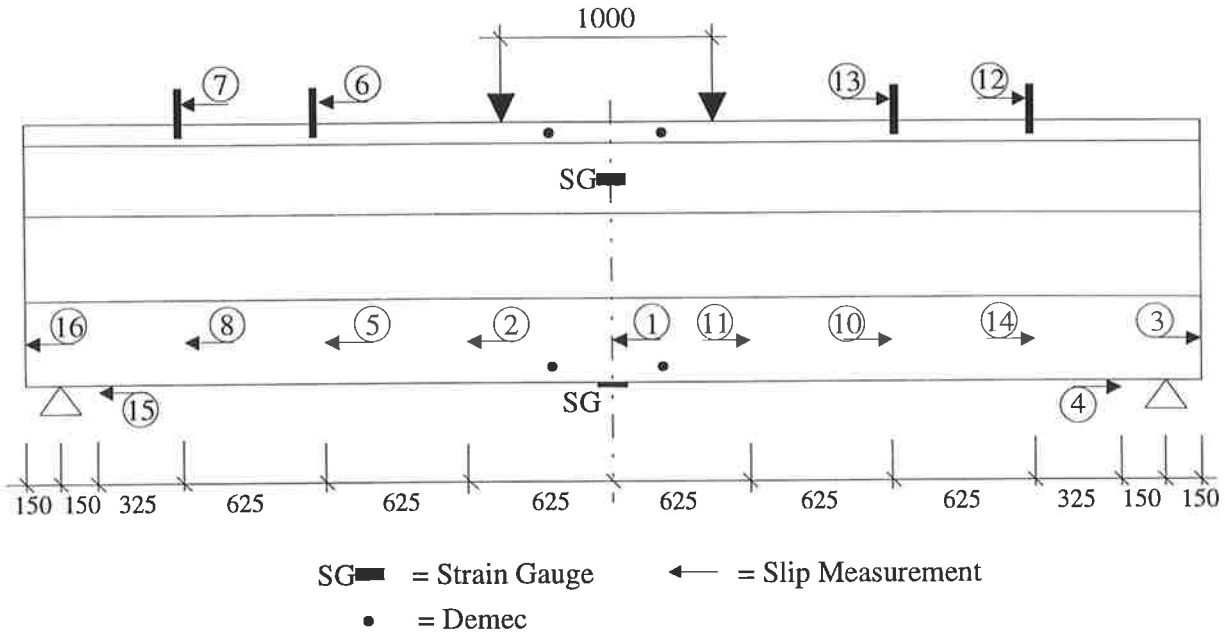


Fig. 5.34. Transducer Location for Beam PB3

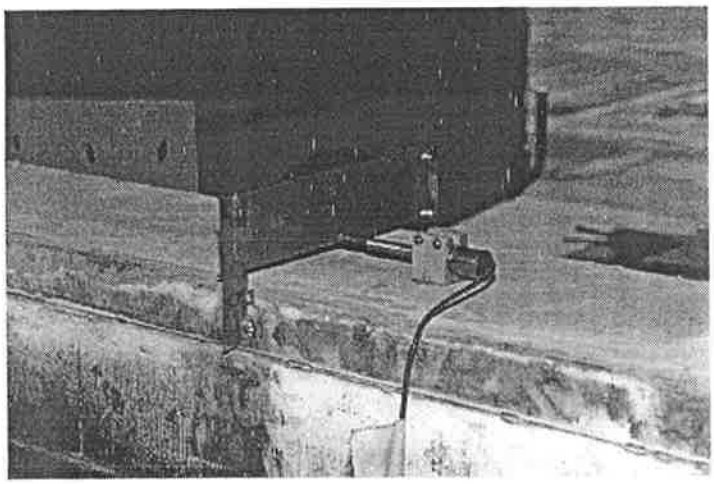


Fig. 5.35. Detail of Top Transducer Attachment

The variation of recorded displacement along the bottom rib is shown in Fig. 5.36. This shows the variation in displacement along the beam for different load increments. The load increments have been non-dimensionalised by dividing by the ultimate load of 215 kN. This figure indicates that zero displacement was measured at the ends of the beam, while the maximum displacements were recorded at the centre of the beam. Local maxima in the slip distribution were also recorded at the transducers which were located 625 mm from the ends of the beam. This behaviour was not noted for any other beam. At 160 kN, or 75% of the failure load, a crack developed at the pin location for Transducer 2, thus making the slip readings unreliable. Figure 5.36 shows the decrease in measured displacement from Transducer 2 as the load increases from 50% to 90% of the ultimate load, which is contrary to

the trend demonstrated by the other transducers, and can be attributed directly to the cracking at the pin location. There was also a slight drop in the measured displacement at Transducer 1 as the maximum load was approached, which may also have been due to the close proximity of a tensile crack. It can be seen that very small displacements were measured at Transducer 11, which was located slightly offset from the load point, and placed symmetrically with Transducer 2 about the centre line of the beam. From visual inspection there were no signs of cracking near the pin location.

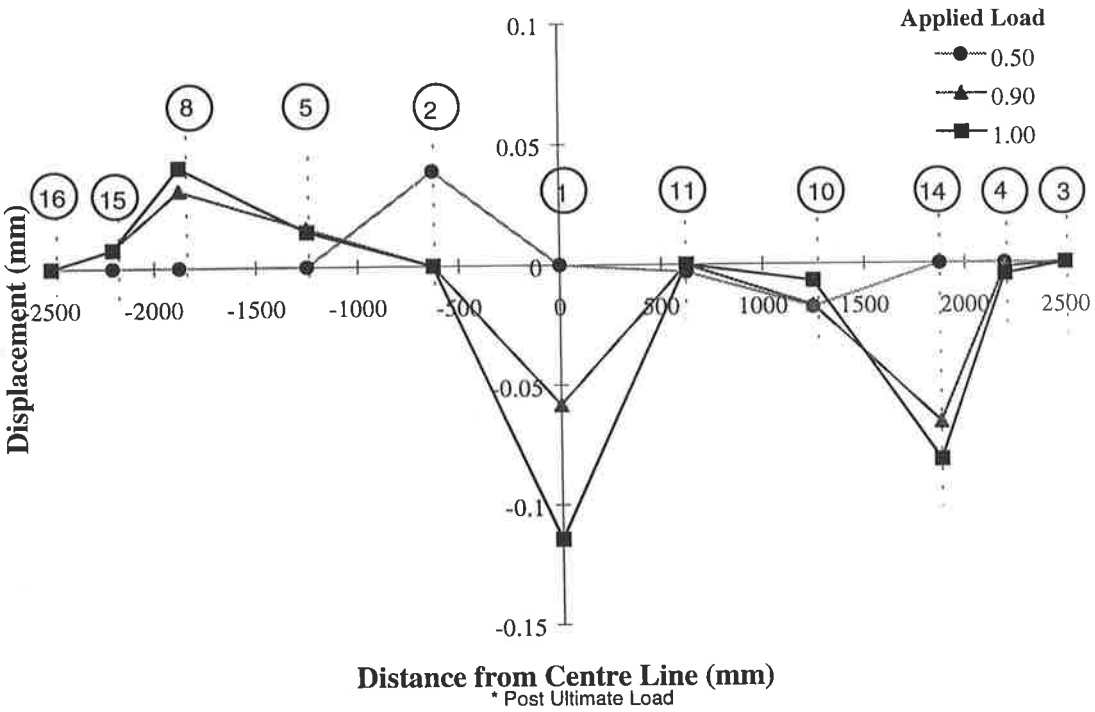


Fig. 5.36. Longitudinal Variation in Slip at Bottom Rib for Beam PB3

Figure 5.37 shows the longitudinal variation in displacement as measured at the top rib, at a number of different load steps, again the load has been non-dimensionalised. This figure indicates that the displacement tends to zero at the right hand end, whilst the same trend is not evident at the left hand end. As transducers were not placed at the centre of the beam, it was not possible to determine the magnitudes of the slips in this region. Figure 5.37 shows a linear interpolation between the slip readings at the ends of the beam, which may not be an accurate estimate for the slips in the centre region. This figure also indicates that the slip increases at all locations as the applied load increases. The displacements after the maximum load was reached are not shown in Fig. 5.37 for clarity.

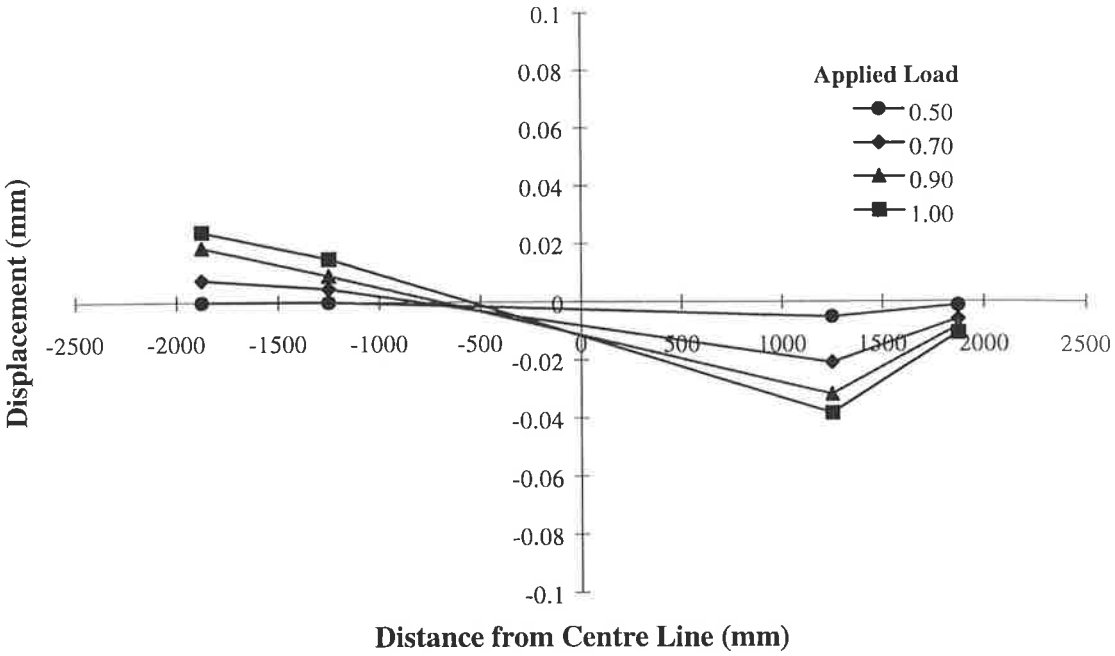
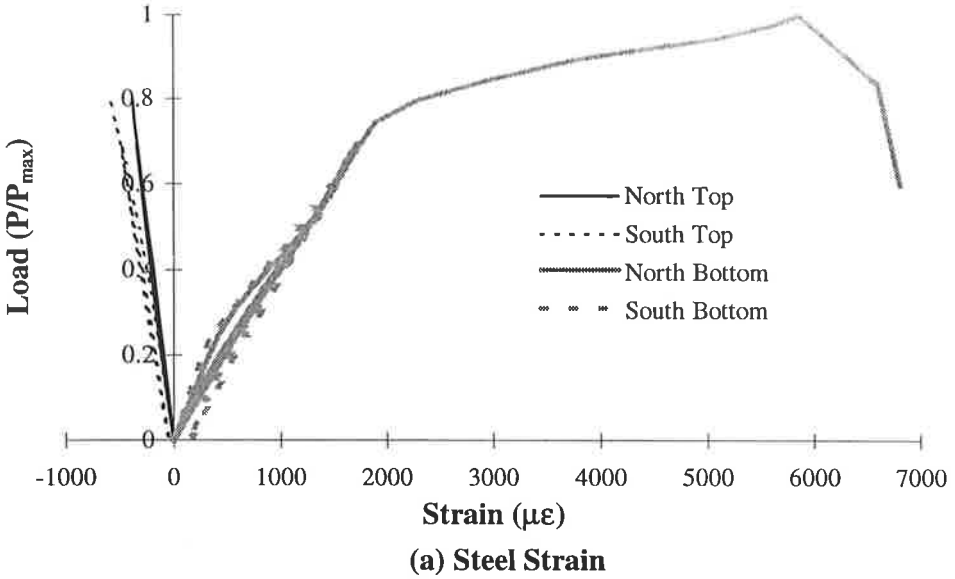


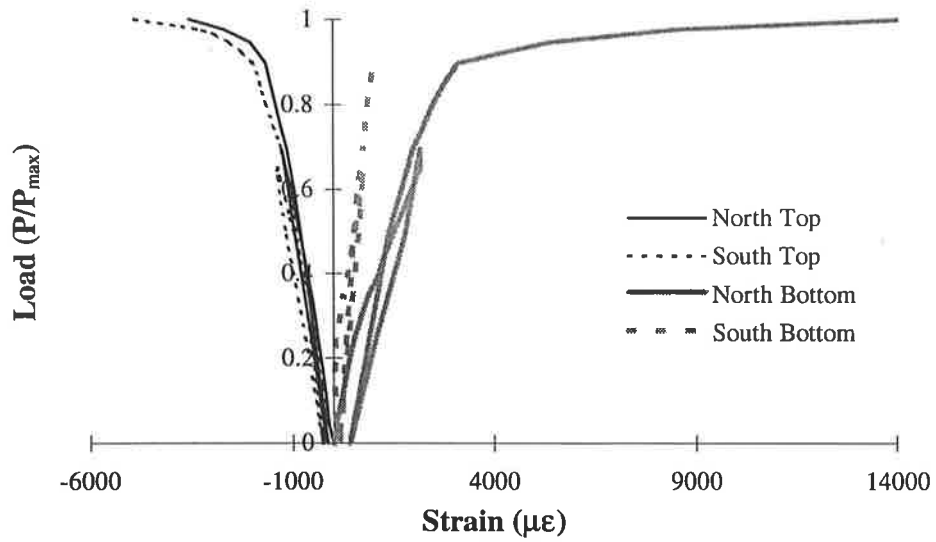
Fig. 5.37. Longitudinal Variation in Slip at Top Rib for Beam PB3

The small magnitude of the displacements recorded at both the top and soffit ribs indicate that the beam exhibited full shear connection. Furthermore, the trend of increasing displacements near the ultimate load indicate the increasing influence of the sheeting strains in the recorded displacements as yielding commenced.

Strain readings were taken from the concrete and profiled sheeting throughout the test, and are shown in Fig. 5.38. The strain readings were taken on both sides of the beam, and are indicated by either North or South. The transducers used to measure slip were placed on the north side of the beam. The strain readings for the profiled sheeting were obtained by attaching strain gauges to the profiled sheeting in the locations shown by SG ▬ in Fig. 5.34. The concrete strain was measured by making small cut-outs in the profiled sheeting, and placing Demec targets on the concrete surface at the locations shown by the symbol ●. A detail showing this arrangement is shown in Fig. 5.39. The demec targets were placed 20 mm from the top and bottom edges of the beam, and were placed symmetrically about the centre line of the beam, separated by 200 mm. The curvature was determined from strain readings taken from the concrete and from the profiled sheeting, and the resulting moment vs curvature response is shown in Fig. 5.40.



(a) Steel Strain



(b) Concrete Strain

Fig. 5.38. Strain Readings for Beam PB3

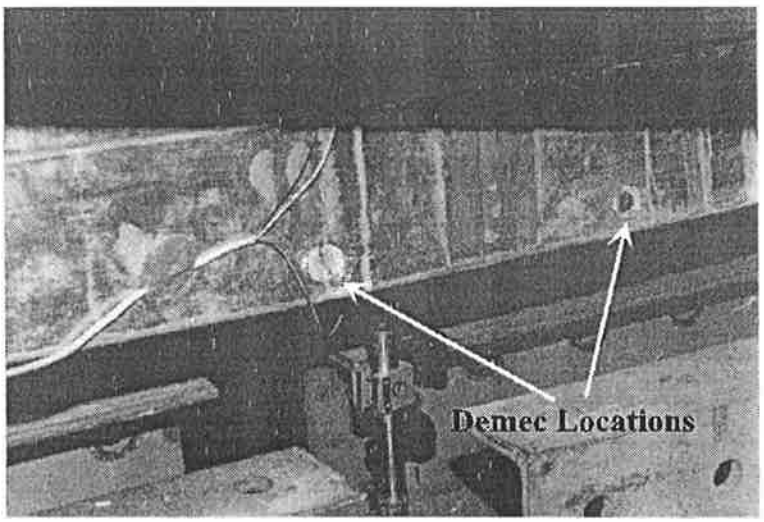


Fig. 5.39. Detail showing Demec Arrangement

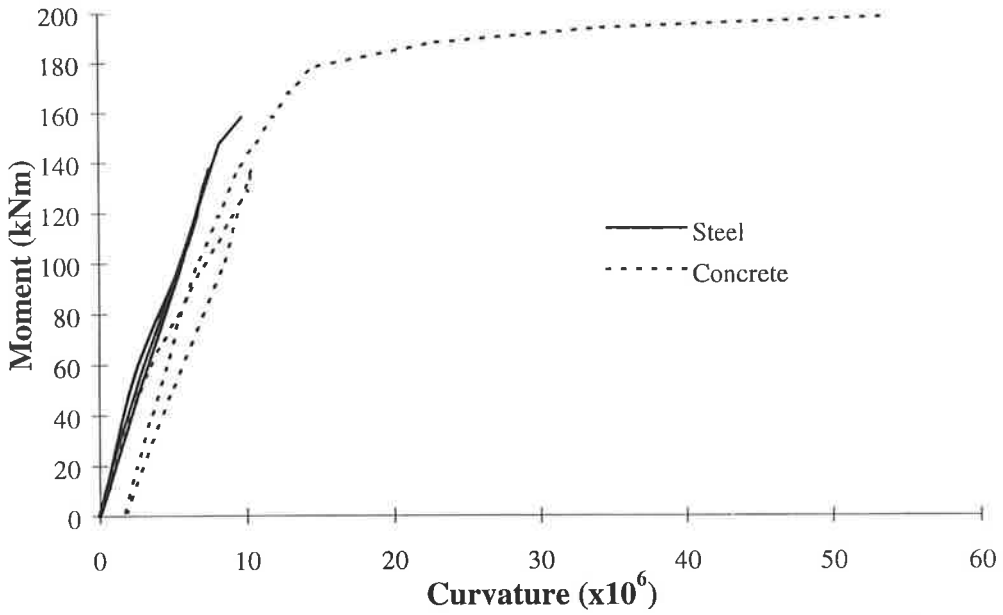


Fig. 5.40. Moment vs Curvature for Beam PB3

It can be seen from Fig. 5.40 that the curvature in the concrete is greater than the curvature in the sheeting for all load levels. The difference between the two curvatures remains minimal until after the concrete has cracked, after which point the difference increases. This difference can be seen in Fig. 5.41 which shows the variation in strain between the concrete and the profiled sheeting at different load levels. The level of the applied load is indicated by the numbers shown, which represent the proportion of the ultimate load being applied.

This result of different curvatures in the steel and concrete elements was not expected, as the sheeting and the concrete must maintain similar vertical deflections at all locations along their lengths, thus requiring that the curvatures should also correspond. A possible reason for the difference may be due to shear strains which may be present in the joints between the ribs. These joints were designed for sufficient strength, but may represent a weakness with regards to shear stiffness. The greater curvature of the concrete element will lead to increased slip strains in the tensile region, which in turn results in greater slip.

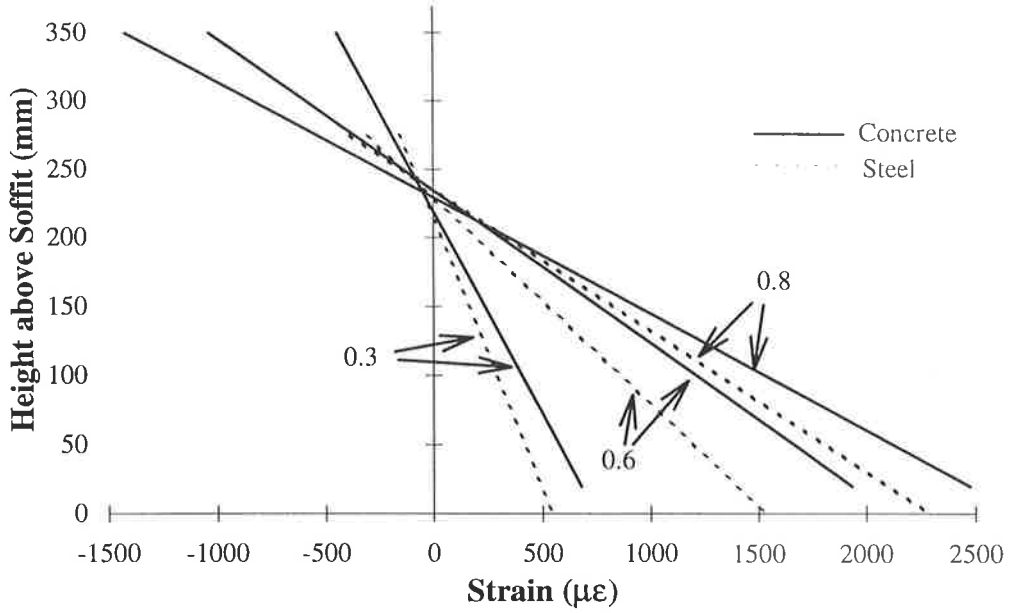


Fig. 5.41. Variation in Strain in Concrete and Steel Sections in PB3

5.4.7 Beam PB4

This beam was similar in all respects to Beam BP3, except that the individual profiled units were not welded together. They were 'clipped' together and assembled into the falsework, which was assembled on the ground. The reinforcing was assembled into a cage and then placed inside the completed profiled sheeting. The properties of the concrete, reinforcing steel and the profiled sheeting are the same as for Beam PB3, and are given in Table 5.2.

The load vs midspan deflection response of the beam is given in Fig. 5.42. The loss in stiffness due to cracking can be seen at a load of approximately 40 kN. The beam was loaded up to an applied load of 223 kN, Point A, before being unloaded. Yielding of the main tension reinforcement is indicated by the change in slope of the load-deflection curve that occurs before unloading at Point B. There is a slight increase in the load carrying capacity to a maximum load of 235 kN at Point C with a large increase in deflection. After the maximum load there is a slight reduction in the load carrying capacity to 229 kN at Point D before unloading of the beam occurs due to buckling of the compression steel. The results of the load vs deflection response are tabulated in Table 5.4. The failed beam is shown in Fig. 5.43.

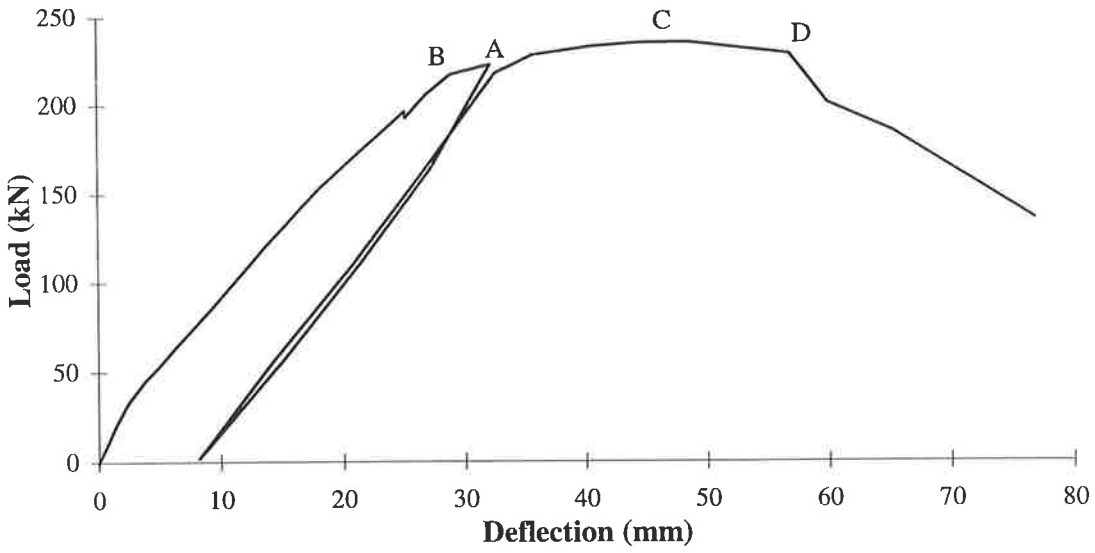


Fig. 5.42. Load vs Midspan Deflection Curve for Beam PB4

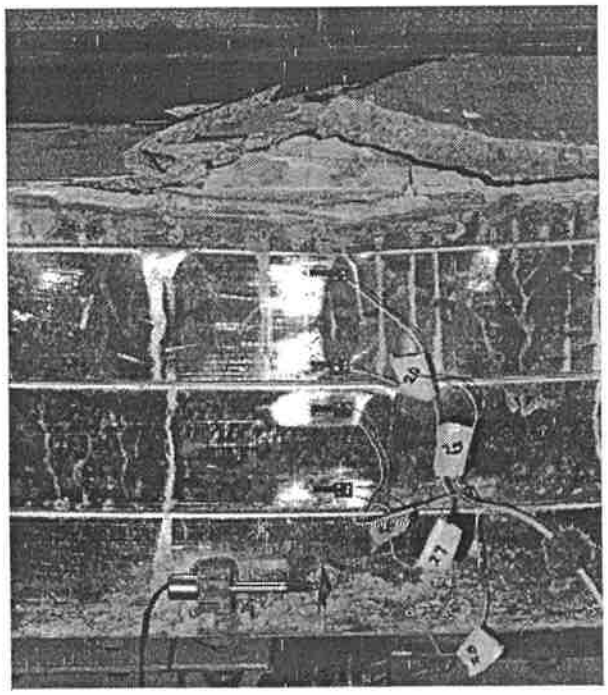


Fig. 5.43. Failure of Beam PB4

The break down in the chemical bond was evidenced by a 'crackling' sound that could be heard at the load was increased. This cracking was first heard at 40 kN, and continued until an applied load of 100 kN. The first signs of buckling were not visually apparent until the applied load reached approximately 100 kN. The buckling was first observed in the horizontal element of the top rib, as for the previous beams.

5.4.7.1 Slip Measurement

The arrangement of the transducers and the strain gauges is shown in Fig. 5.44. The strain gauges were symmetrically placed on both sides of the beam. The transducers were placed at four cross-sections along the beam, with three additional transducers placed in the bottom rib. This arrangement of the transducers was adopted to investigate the transverse variation in the longitudinal slip at a number of cross-sections. Also the longitudinal variation in the slip could be measured for a number of different ribs.

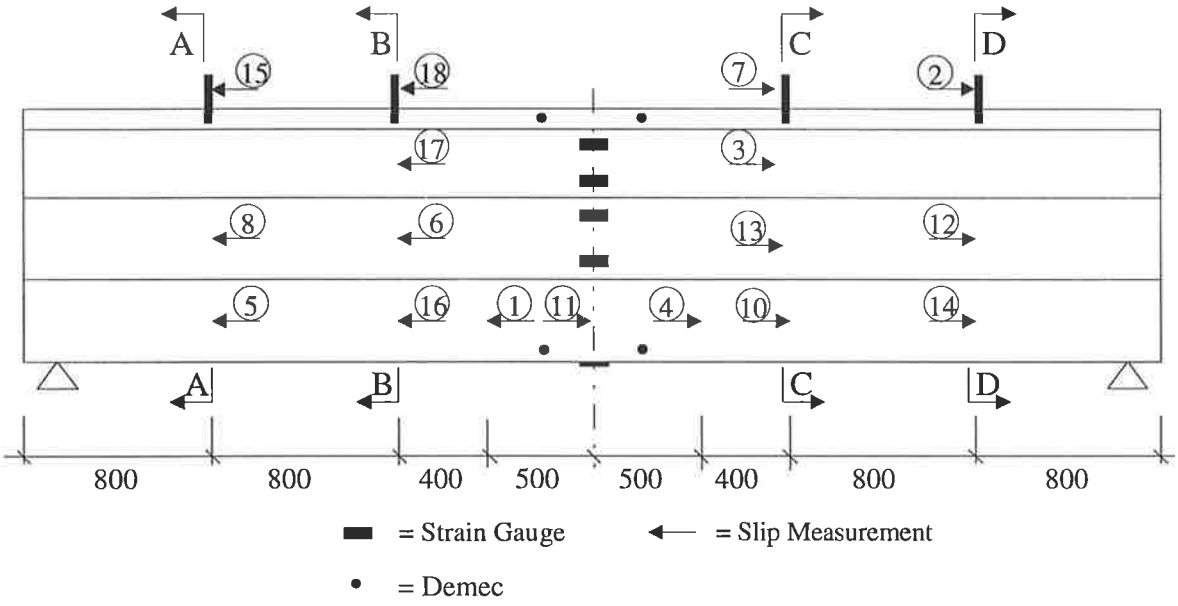
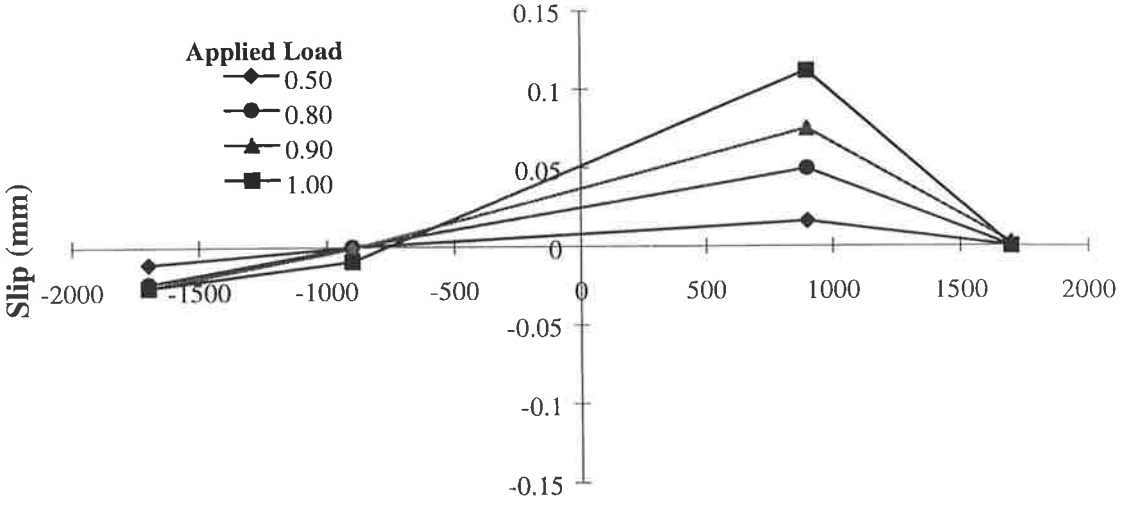


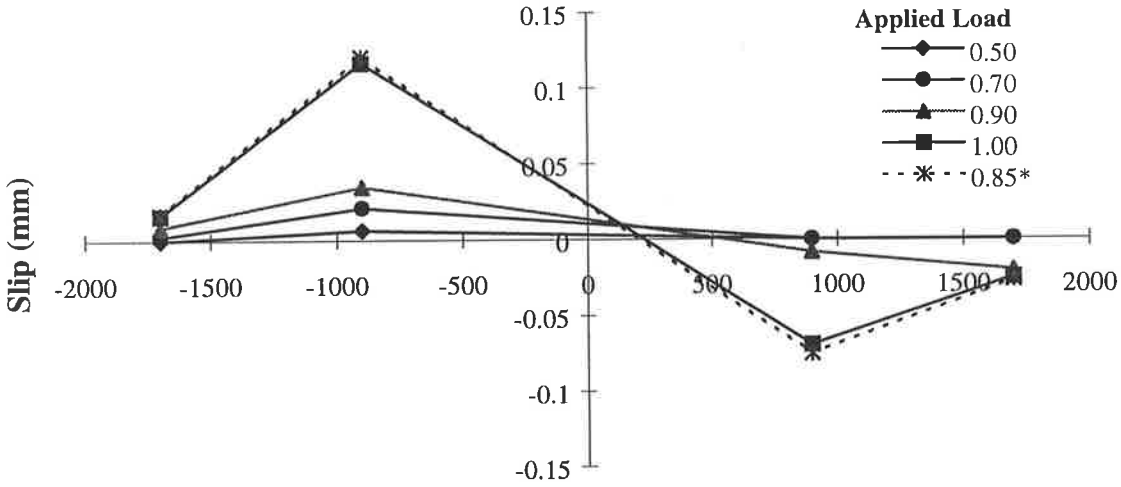
Fig. 5.44. Arrangement of Transducers for PB4

The longitudinal variation in recorded displacement along the length of the beam is shown in Fig. 5.45. Figure 5.45a shows the variation in slip for the top rib, while (b) and (c) show the variation along the third and bottom ribs respectively. It can be seen from a comparison of the three figures that the displacement is reversed for the top rib. This was the same response as was measured for Beam PB2, which was also assembled using clipped construction. Generally there is an increase in displacement toward the locations of the applied loads, and a minimum at the ends and at the centre line of the beam. It should be noted that the maximum displacement recorded in Beam PB4 is nearly a factor of 5 times less than the maximum displacement recorded in Beam PB2, which is of the same construction, but with different rib geometry. This is due to the difference in bond stress, which was demonstrated from the push tests.



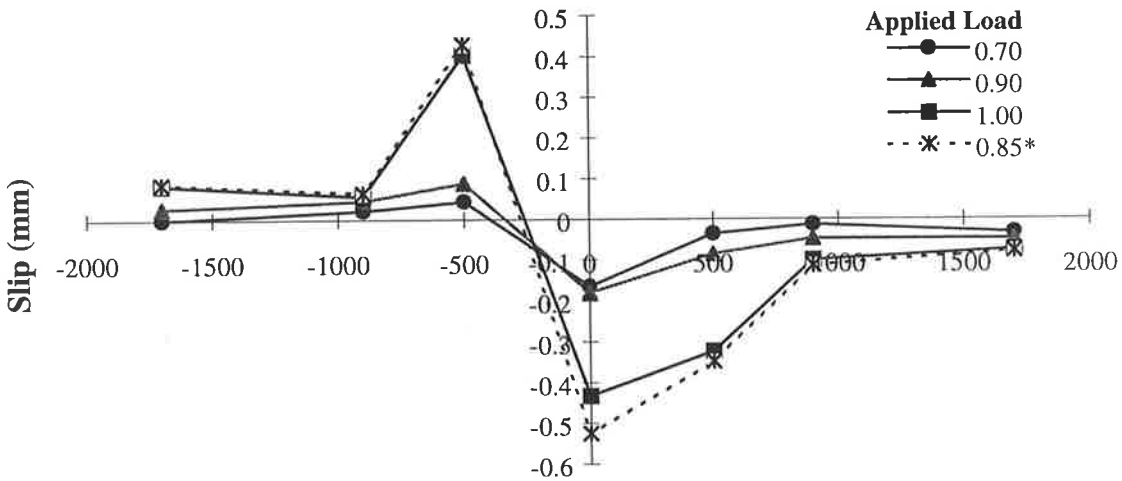
Distance from Centre Line (mm)

(a) Longitudinal Variation along Top Rib



Distance from Centre Line (mm)
* Post Ultimate Load

(b) Longitudinal Variation along Third Rib



Distance from Centre Line (mm)
* Post Ultimate Load

(c) Longitudinal Variation along Bottom Rib

Fig. 5.45. Longitudinal Variation in Slip for Beam PB4

The complete load vs displacement curves for the transducers at Section C in Fig. 5.44 are shown in Fig. 5.46. This figure is representative of the load vs displacement curves for the other cross-sections in the beam. It can be seen in this figure that the greatest proportion of the recorded displacement occurs before yielding of the main reinforcing occurs. From Fig. 5.42 it can be seen that yielding occurs at approximately 90% of the ultimate load, and from Fig. 5.46 a large proportion of the displacement has already occurred before this load is reached.

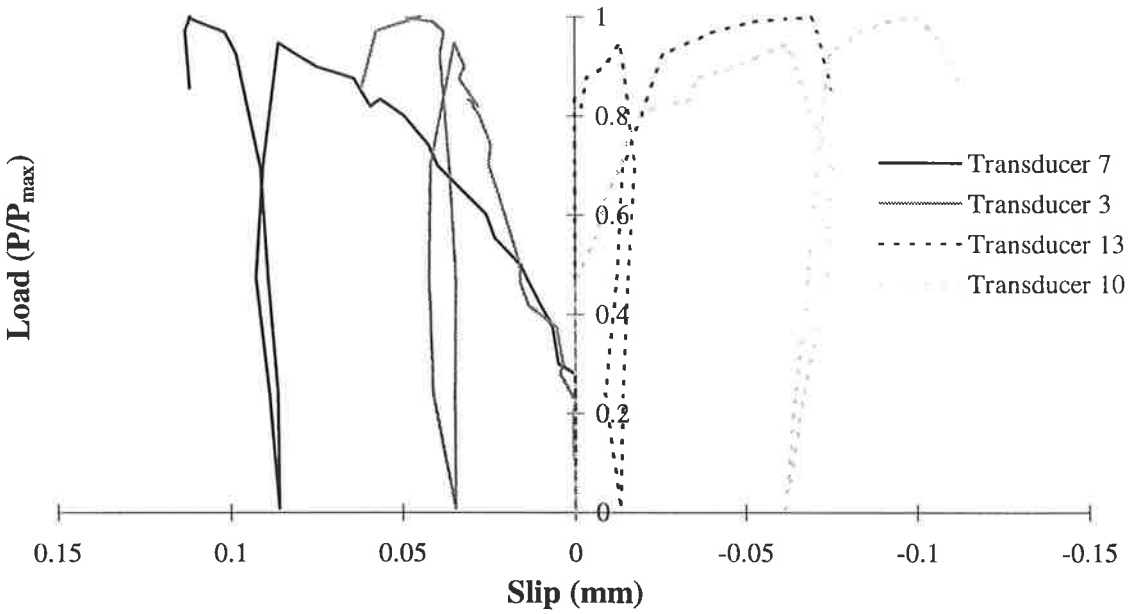


Fig. 5.46. Variation in Slip at Section C

Figure 5.47 shows the recorded strains in the concrete and profiled steel units for different levels of applied load. The applied load is indicated by the values shown, and is presented as a fraction of the ultimate load of the beam. The strain in the concrete was determined from Demec gauges in a similar manner to that used for Beam PB3. Their locations are shown in Fig. 5.44. The sheeting strain was determined from strain gauges which were attached in the locations shown in Fig. 5.44. The curvatures of the concrete and profiled sheeting elements is given by the slopes of the solid and dashed lines respectively. It can be seen from Fig. 5.47 that at low levels of applied load, the curvatures in the concrete and the profiled sheeting are similar, however, as the load increases they begin to differ.

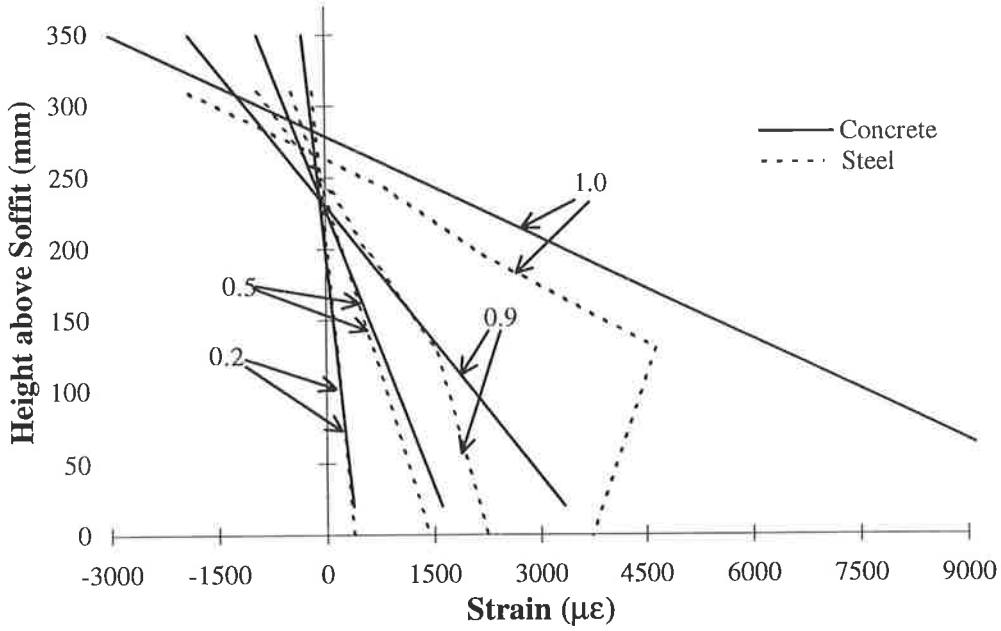


Fig. 5.47. Variation in Concrete and Sheeting Strain for Beam PB4

The similar strain readings in the concrete and sheeting at low levels of applied load indicate full interaction between the two elements. As the applied load approaches the ultimate moment capacity of the beam the strain readings of the two elements are no longer equal, indicating a break down in the bond and thus partial interaction. The difference between the strain readings in the steel and the concrete represents the slip strain at that location. The integration of the slip strain along the length of the member then gives the slip at the interface, as discussed in Chapter 2.

It can also be seen from Fig. 5.47 that the variation in strain throughout the depth of the profiled steel is nearly linear, except for the soffit reading at higher load levels. This indicates that there is negligible slip between the different units, as any slip would necessitate a finite slip strain, and thus a step change in the strain profile. The lower strain readings at the soffit indicates the occurrence of slip at this location, as the slip tends to reduce the stress in the sheeting.

5.4.8 Beam PB5

The cross-section for Beams PB5 and PB6 is shown in Fig. 5.48. Both beams were constructed by spot welding through the tops of the ribs, as shown in the figure. The spacing of the spot welds along each rib joint was 100 mm. The two sides of the beam were

constructed individually, as shown in Fig. 5.49, and then joined together by MIG welding the bottom rib, as shown in Fig. 5.48.

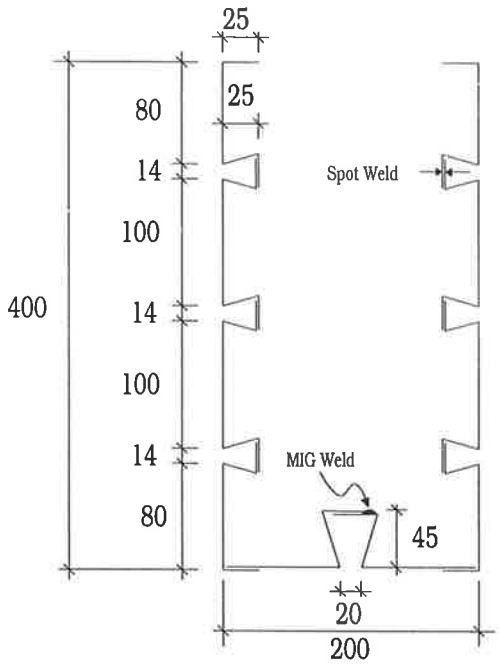


Fig. 5.48. Profiled Beam PB5 and PB6

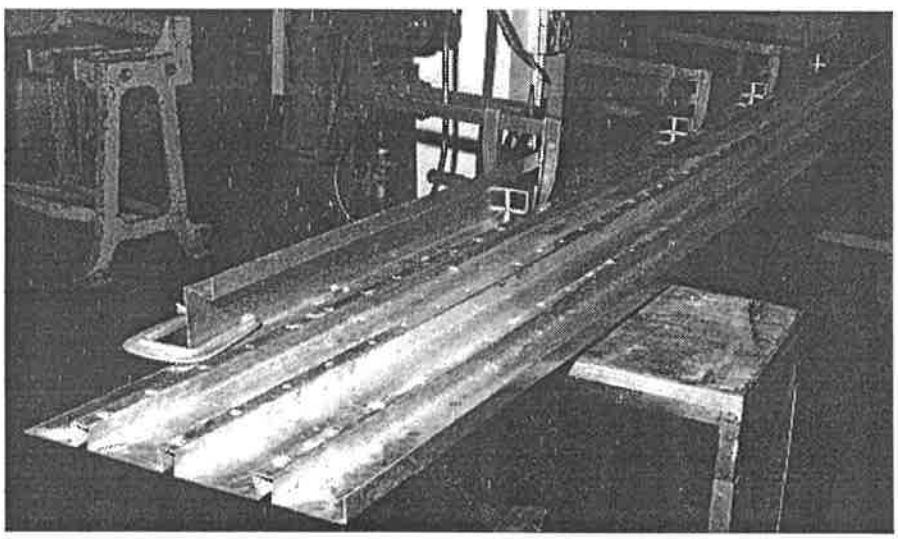


Fig. 5.49. Construction of Beam PB5

5.4.8.1 Push Tests

Push tests were carried out to determine the bond characteristics of the profiled sheeting, and the resulting shear stress / slip curve is shown in Fig. 5.50. It can be seen from a comparison of this figure with the previous push test results shown in Fig. 5.6 and Fig. 5.31

that the bond stress for the dove tail rib is significantly lower than for the L-Rib geometry. This can be attributed to the more open rib geometry, as discussed previously in Chapter 3. There is a rise in the shear stress with no increase in slip until the chemical bond stress breaks down. Figure 5.50 indicates a progressive breakdown of the chemical bond, with a maximum strength of 0.45 MPa. After the chemical bond has been broken the bond stress reduces to 0.20 MPa, after which there is a gradual increase in shear stress with increasing slip.

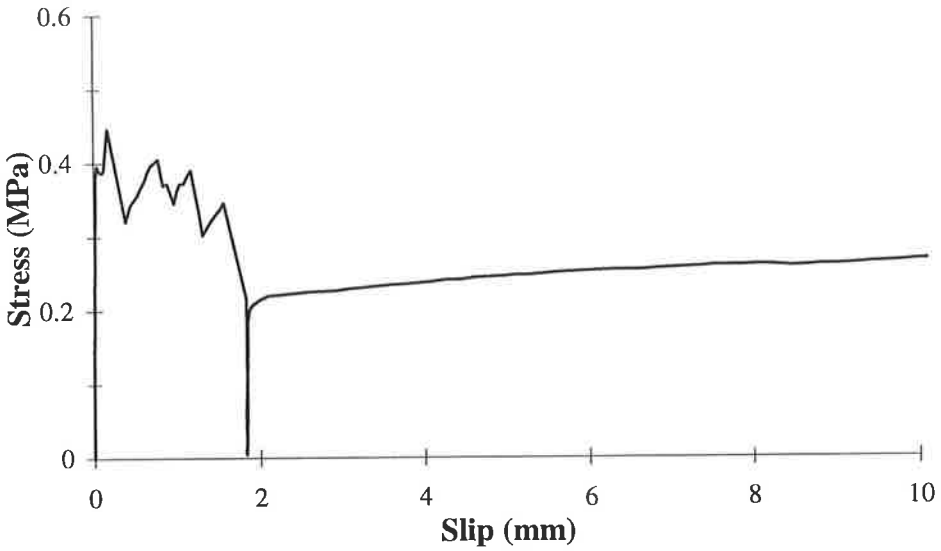


Fig. 5.50. Load vs Slip for Dove Tail Sheeting

As most codes of practice do not allow the chemical bond to be relied upon to resist the longitudinal shear in composite slabs (ASCE, 1992; British, 1982; European, 1990), the strength of the chemical bond will not be used in design of the composite profiled beams. The bond strength that will be used in design is the mechanical shear resistance of the sheeting, which has a minimum value of 0.20 MPa. Thus, a value of 0.20 MPa will be used as this represents a conservative lower bond.

5.4.8.2 Beam Test

The load vs midspan deflection response is shown in Fig. 5.51. This figure shows the characteristic decrease in stiffness at the onset of concrete cracking, at a load of approximately 30 kN. The beam was loaded up to an applied load of 206 kN at Point A before being unloaded. From the curve it can be seen that yielding of the main tension reinforcement had already occurred before the beam was unloaded. This is indicated by the sharp decrease in stiffness of the beam at Point B before unloading. There is a significant

plastic plateau, with a slight increase in the load carrying capacity of the beam, up to a maximum of 217 kN at Point C. After this load, there was a slight reduction in the load carrying capacity to 216 kN at Point D, after which there was significant spalling of the concrete in the compression region between the two point loads and a rapid drop in the load carrying capacity.

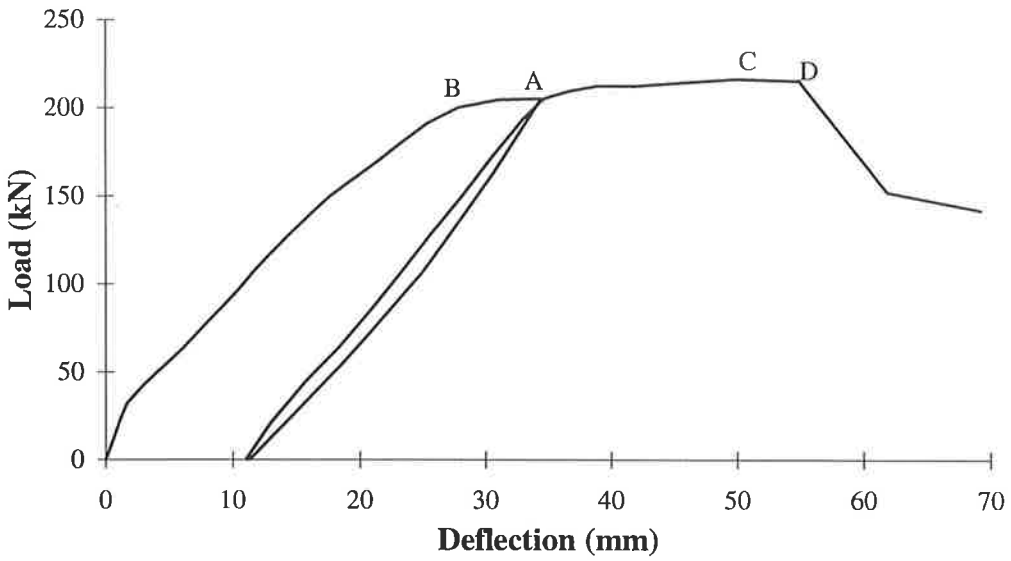


Fig. 5.51. Load Deflection Curve for Beam PB5

5.4.8.3 Slip Measurement

The distribution of the transducers and strain gauges is shown in Fig. 5.52. The strain gauges were symmetrically placed on both sides of the beam. The longitudinal variation in displacement at the top and bottom ribs is shown in Fig. 5.53a and (b) respectively.

Figure 5.53 shows a comparison between the slip at the top of the beam, and the slip at the soffit, at different sections along the beam. It can be seen that there is some variation in the distribution of the displacement measurements at the top and bottom of the beam. The variation in the displacements at the top of the beam indicates that the displacement increases to a maximum near the applied load points, whereas the displacement distribution at the bottom of the profiled sheeting is more uniform throughout the length of the beam, with a slight decrease towards the supports.

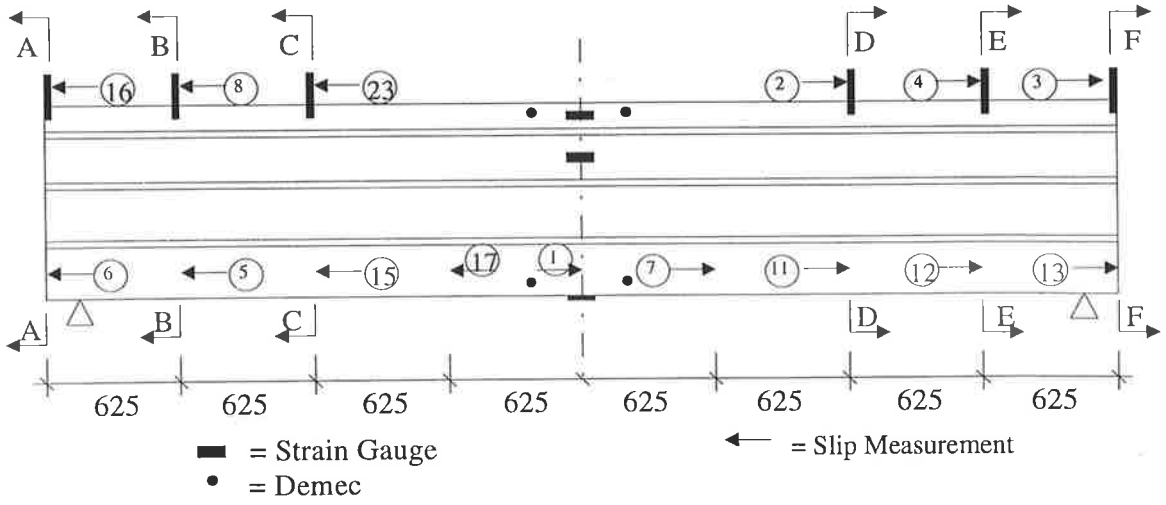
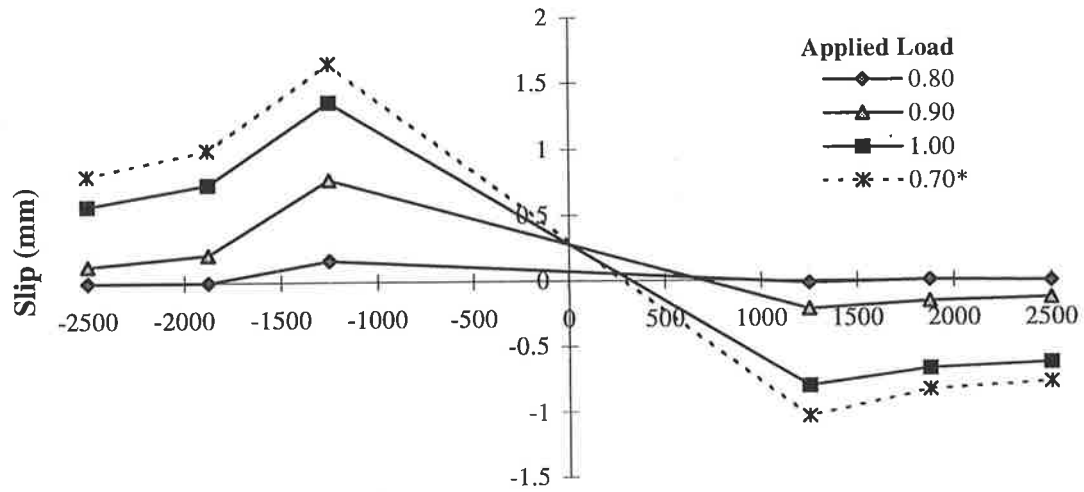
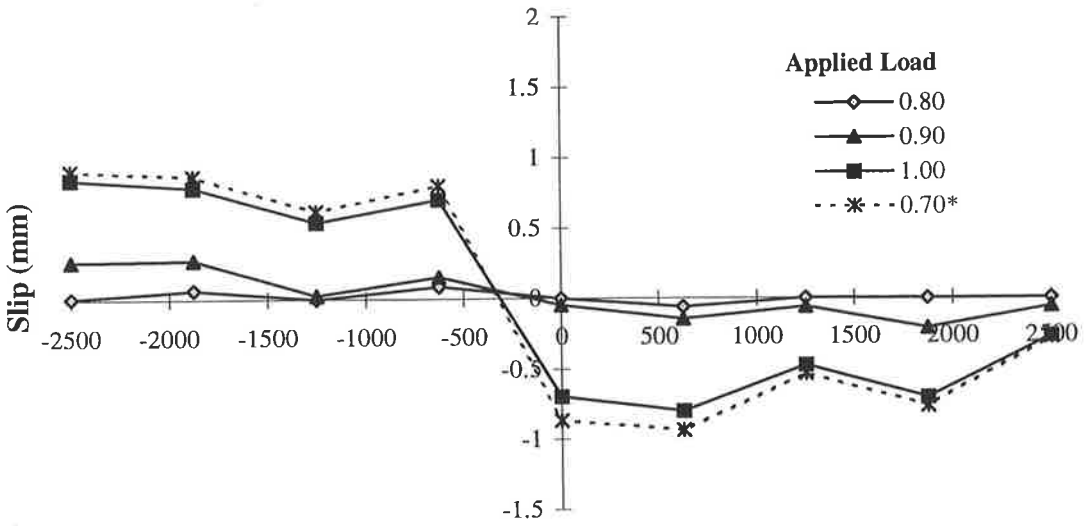


Fig. 5.52. Arrangement of Transducers for Beam PB5



(a) Slip at Top Rib

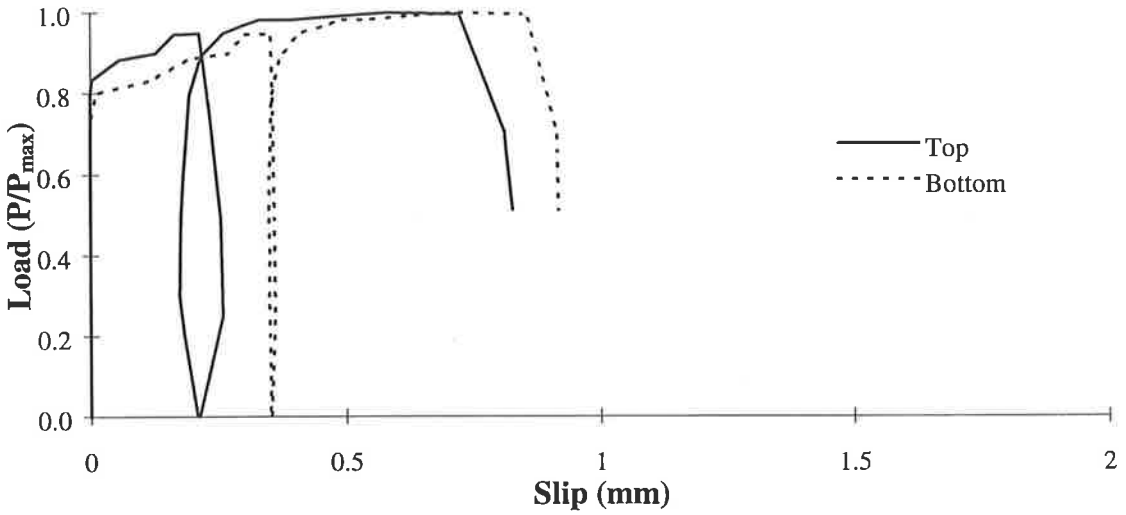


(b) Slip at Bottom Rib

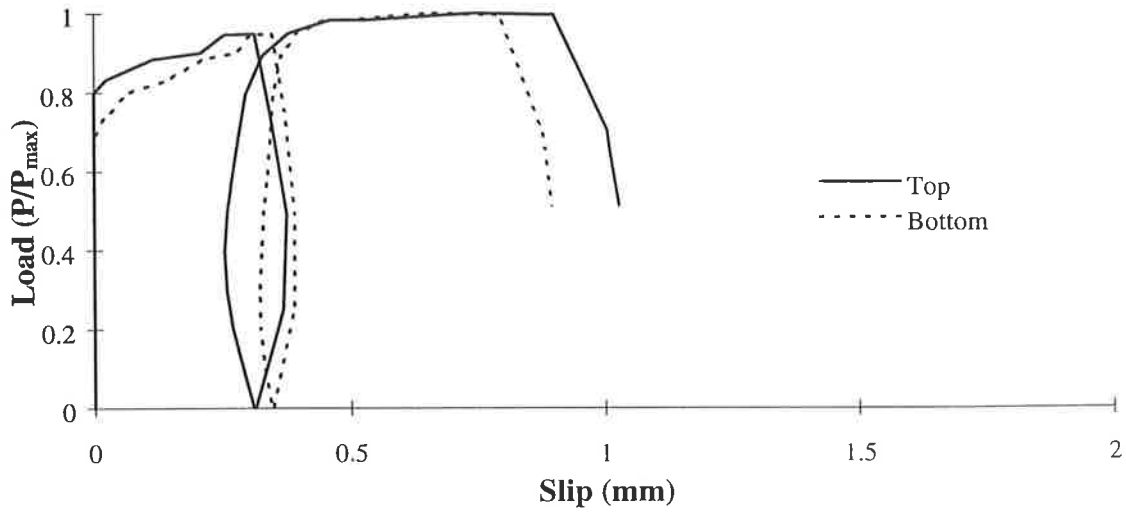
Fig. 5.53. Longitudinal Variation in Slip for Beam PB5

The longitudinal variation of the displacements shown in Fig. 5.53 is significantly different to those recorded for the other profiled beams. The uniform distribution of the displacement readings in the shear spans no longer follow the variation in strain as was the case for the previous displacement measurements. This indicates that the displacements measured by the transducers represents the slip between the profiled sheeting and the concrete. Thus, this beam exhibits partial interaction.

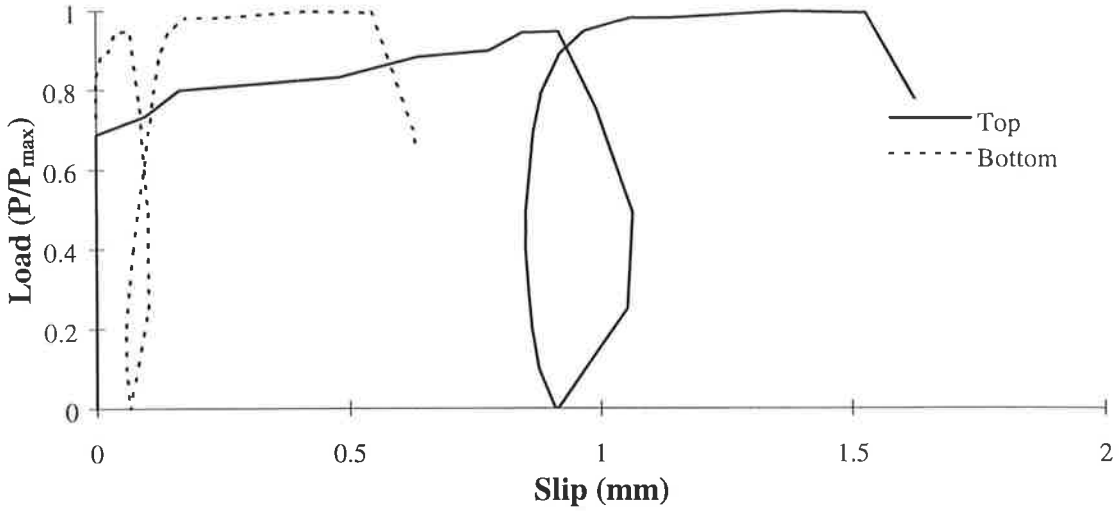
Figure 5.54 shows a comparison between the recorded displacements at the top and soffit of the beam at a number of different cross sections along the beam. The positions of the cross sections is shown in Fig. 5.52. It can be seen that the recorded displacements are similar at cross sections A-A and B-B, while at section C-C the displacement at the top rib is significantly larger than that at the soffit.



(a) Section A-A



(b) Section B-B



(c) Section C-C

Fig. 5.54. Transverse Variation in Slip for PB5

Figure 5.55 indicates the strain readings in the concrete and profiled sheeting at different levels of applied load. The applied load is indicated by the values shown and is expressed as a fraction of the maximum load of the beam. The curvatures of the concrete and profiled elements is given by the slopes of the solid and dashed lines respectively. It can be seen that at low applied loads there is negligible difference between strain readings in the concrete and the profiled sheeting, indicating full interaction. As the applied load increases there is an increasing difference between the strain readings for the concrete and the profiled sheeting, indicating a breakdown in the bond and thus partial interaction.

It can be seen in Fig. 5.55 that at higher loads the slopes of the solid and dashed lines are different, indicating that the curvatures are different between the two elements. The difference in the curvatures indicates that there is vertical movement between the sheeting and the concrete (Ahmed, 1996). The vertical movement arises due to the finite stiffness of the ribs, which rely on their keying action to provide restraint against vertical slip. In order for the curvatures to be similar in the concrete and the sheeting, the ribs must restrict all vertical slip, which would require them to be infinitely stiff. This would only be possible under conditions of full interaction which occurs before the chemical bond has been broken.

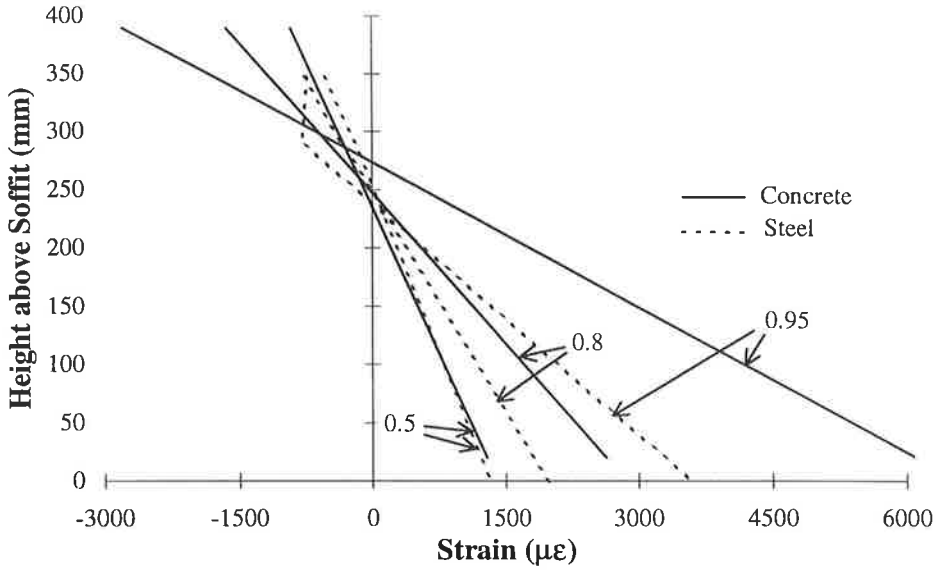


Fig. 5.55. Concrete and Sheeting Strain Readings for Beam PB5

The strains obtained from the demec readings and the strain gauges can be used to determine the curvature in the cross-section at different applied loads. The moment-curvature response of the beam can thus be determined, and is shown in Fig. 5.56. It can be seen that the curvatures of the concrete and steel elements are very similar up to an applied moment of approximately 120 kNm, or 60% of the ultimate moment, after which point it appears that the stiffness of the steel element increases. However, this apparent increase in stiffness may be explained by an examination of the strain readings from the profiled sheeting, shown in Fig. 5.57. It can be seen from Fig. 5.57 that the strain readings from the soffit show a change in slope at an applied load of approximately 60% of the maximum load, which corresponds to the apparent change in stiffness shown in Fig. 5.56.

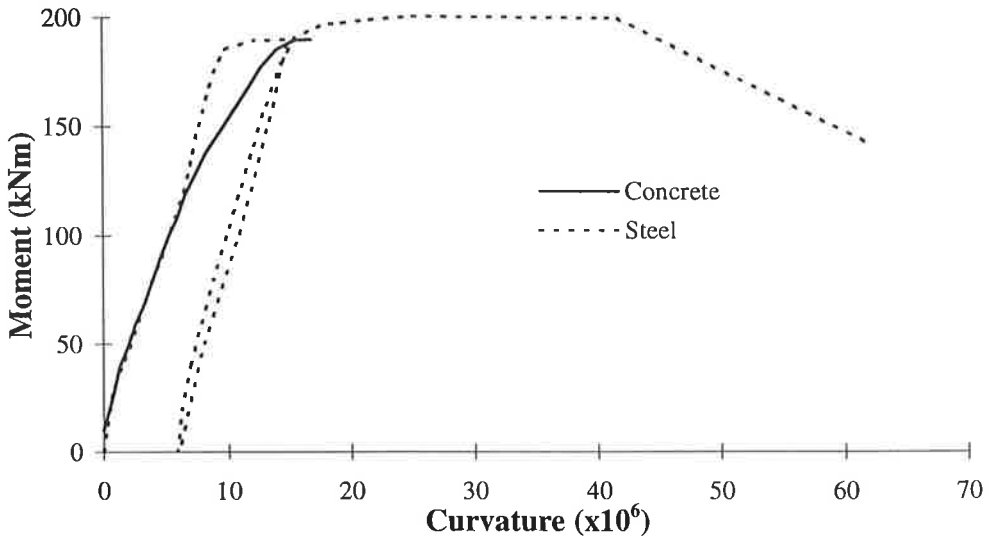


Fig. 5.56. Moment-Curvature Response for Beam PB5

The change in the slope of the strain readings from the soffit at 60% of the maximum load shown in Fig. 5.57 is most likely due to slip between the concrete and the soffit sheeting. Any slip at the interface would reduce the strains in the sheeting, and thus cause an apparent increase in the stiffness of the sheeting as shown in Fig. 5.56. However, there was no measurable slip at the bottom rib at this applied load as indicated by the load-slip curve from Transducer 1, shown in Fig. 5.58. The change in slope shown in Fig. 5.57 may be due to a local variation in the stress in the steel due possibly to a crack in the concrete.

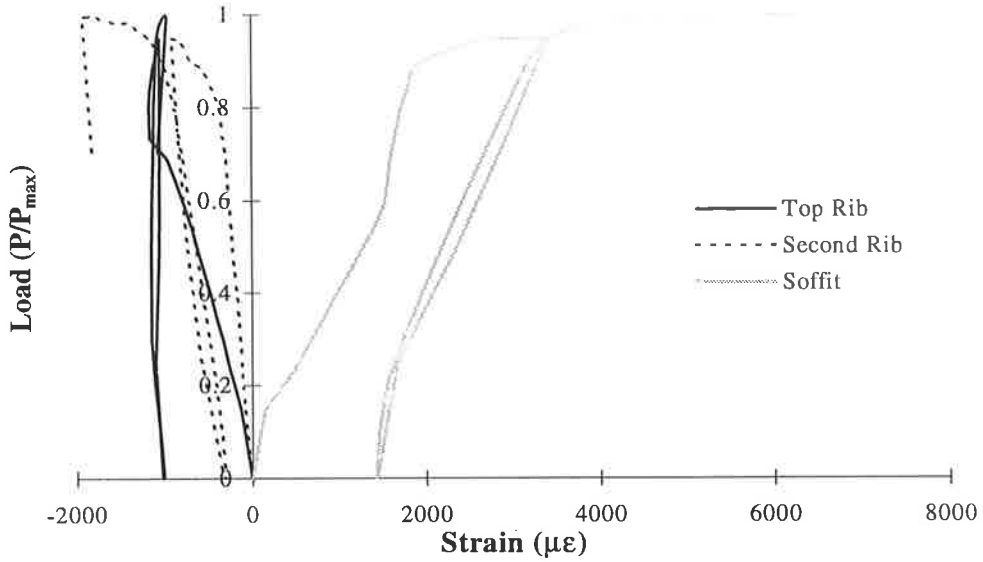


Fig. 5.57. Strain Readings from Profiled Sheeting

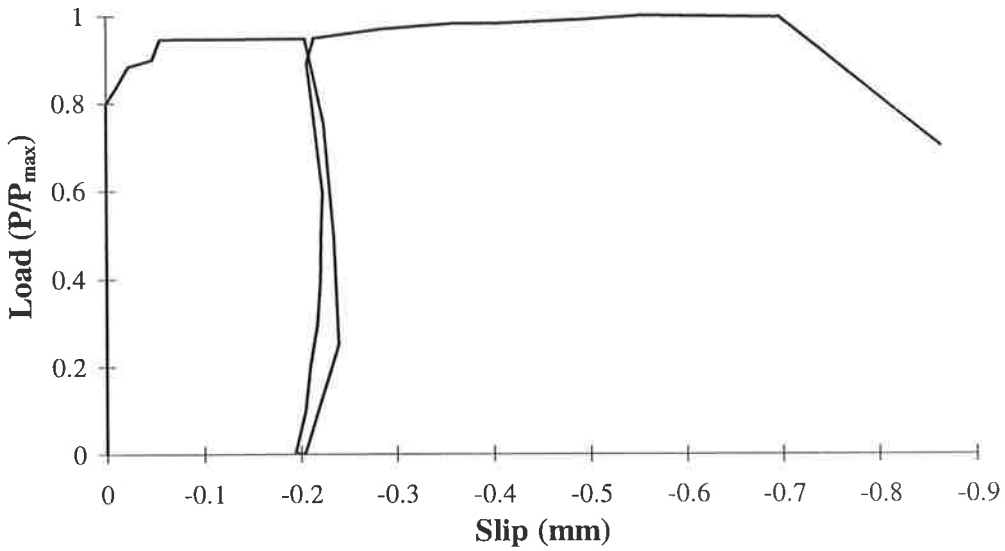


Fig. 5.58. Load vs Slip for Transducer 1

The curvature of the concrete element, which was obtained from the demec gauges, was not able to be determined after yielding of the main reinforcing. This was due to the failure

of the demec targets in the tension region, which resulted after tension cracks passed through the location at which they were fixed.

5.4.9 Beam PB6

This beam was identical to Beam PB5, with the cross-section shown in Fig. 5.48. The material properties are given in Table 5.2. The load vs midspan deflection plot from the test is shown in Fig. 5.59. This curve shows the characteristic decrease in stiffness due to cracking of the concrete at a load of approximately 35 kN. A large drop in stiffness due to yielding of the steel can be seen to occur at Point B just before unloading. After the beam was full reloaded, there was a significant increase in deflection with a slight increase in the applied load from 246 kN at Point A to 262 kN at Point C. After this there was a slight reduction in the load carrying capacity to 261 kN before rapid unloading of the beam occurred due to buckling of the main compression reinforcement.

Buckling was first visually apparent in the profiled sheeting at an applied load of 110 kN, and occurred in the horizontal element of the top rib between the applied loads. It occurred first on the northern side of the beam and was then followed by the southern side of the beam at a load of 150 kN. The buckling in the horizontal element spread towards the supports as the load was increased. At an applied load of approximately 160 kN, buckling became visually apparent in the vertical element of the top rib on both sides of the beam. Buckling became visually apparent in the second rib between the load points at an applied load of 210 kN.

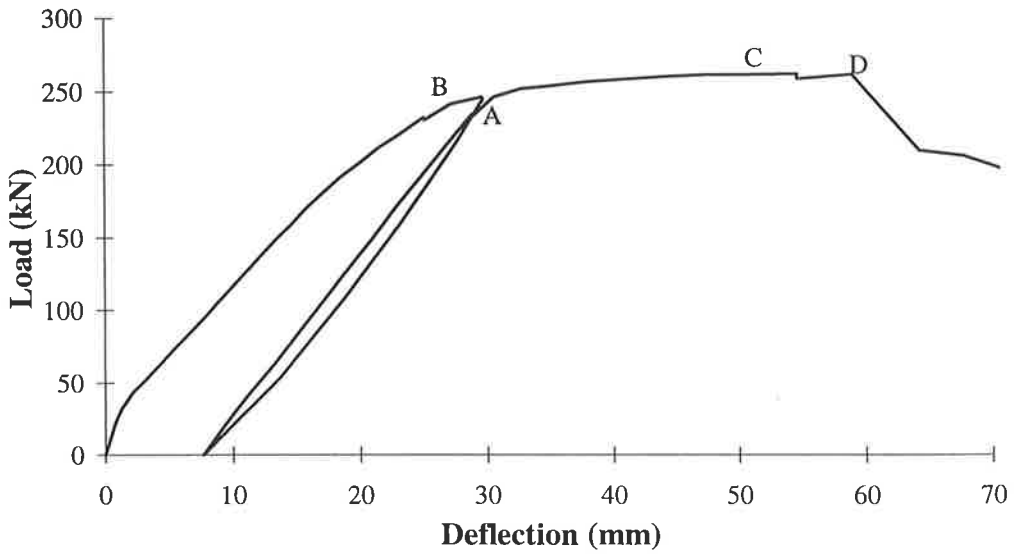
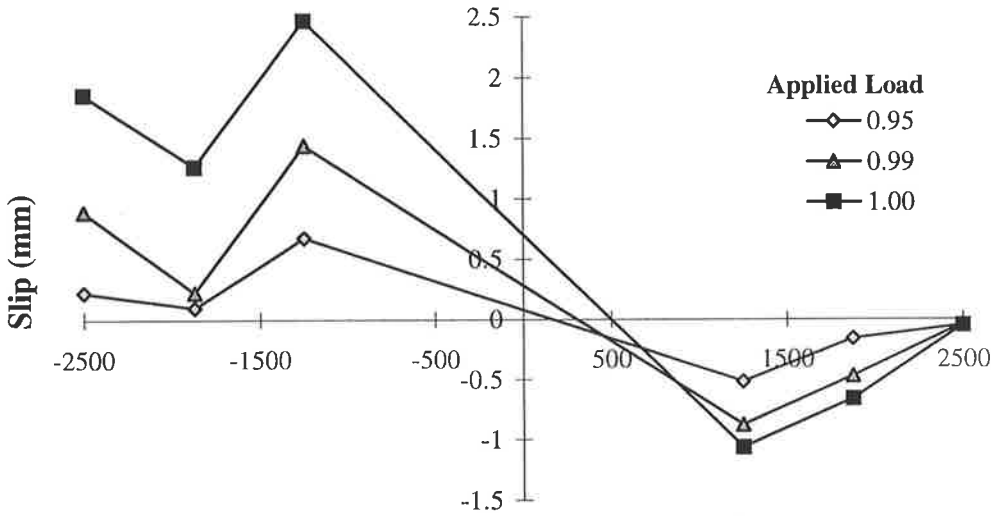


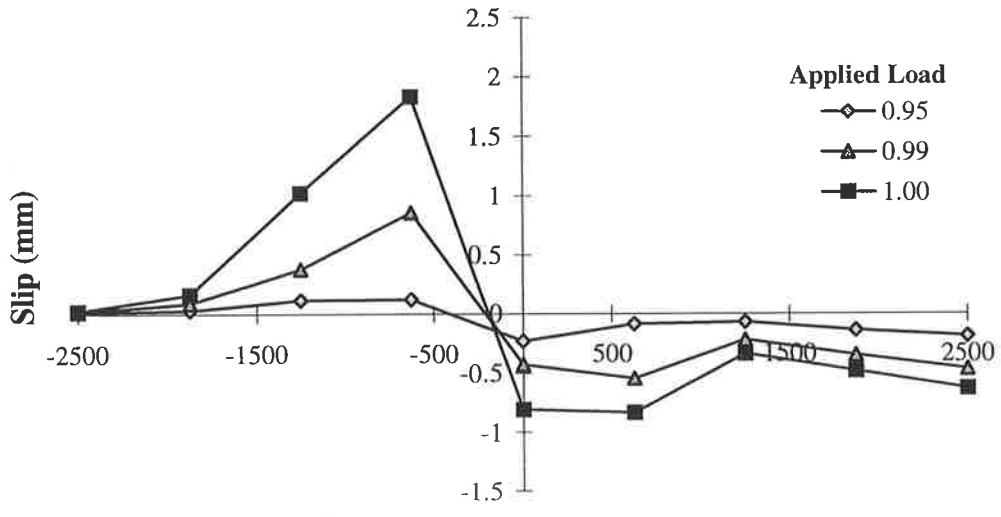
Fig. 5.59. Load vs Midspan Deflection for Beam PB6

5.4.9.1 Slip Measurement

The arrangement of the transducers is the same as for Beam PB5, and is shown in Fig. 5.52 on page 312. The longitudinal variation in slip at the top and bottom rib is shown in Fig. 5.60a and (b) respectively. It can be seen in both figures that the slip is greatest near the load points, and decreases towards the supports. Larger slips were recorded in the left span of the beam at both the top and soffit, and may be explained by the final plastic hinge being located towards the left hand applied load.



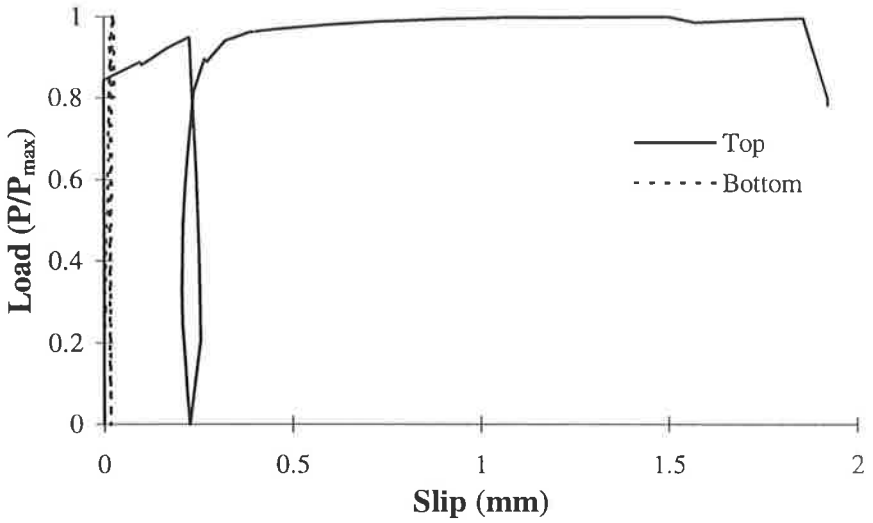
(a) Slip at Top Rib



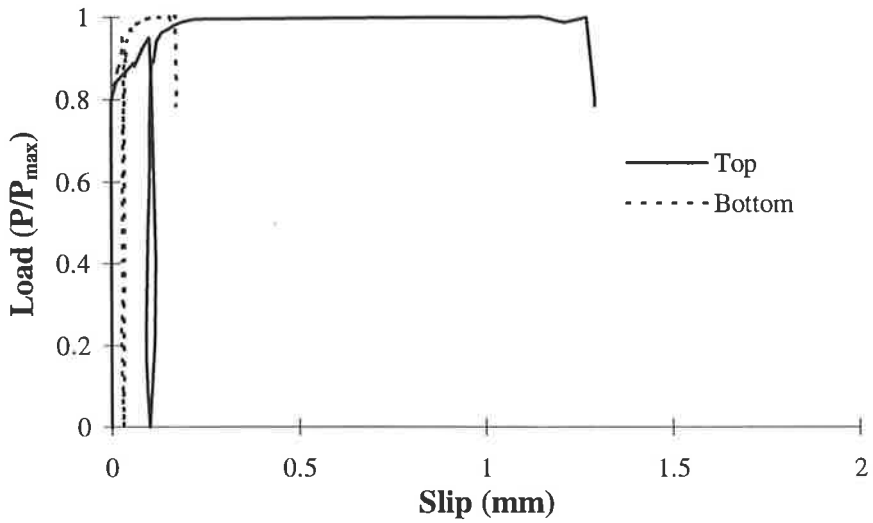
(b) Slip at Bottom Rib

Fig. 5.60. Longitudinal Variation in Slip in Beam PB6

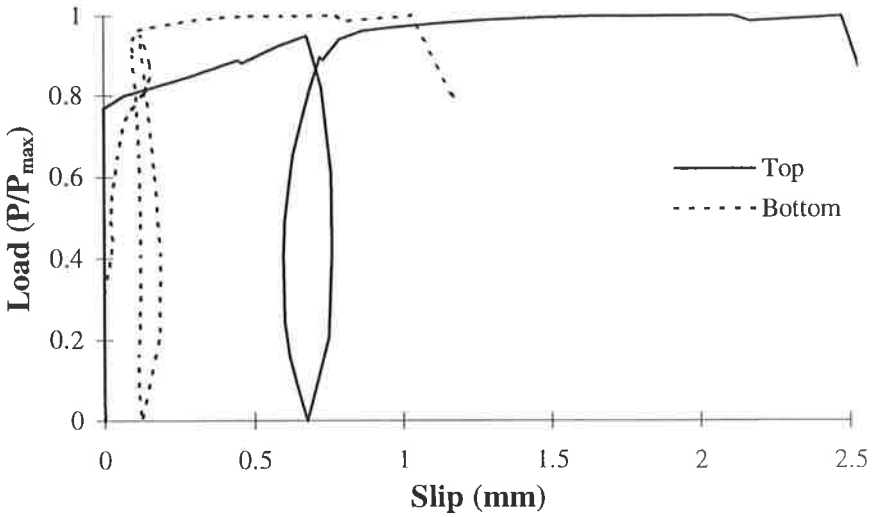
The variation in the slip between the top and bottom of the beam at different cross-sections is shown in Fig. 5.61. The positions of the cross sections is shown in Fig. 5.52. It can be seen in Fig. 5.61 that the slip at the bottom of the beam is considerably smaller than the slip recorded at the top of the beam. This same trend is evident from a comparison between Fig. 5.60a and (b). The large increase in slip which occurs after yielding of the main tension reinforcement is evident at the top of the beam and to a lesser degree at the bottom.



(a) Section A-A



(b) Section B-B



(c) Section C-C

Fig. 5.61. Transverse Variation in Slip in Beam PB6

The strain readings in the concrete and the profiled sheeting are shown in Fig. 5.62 at different levels of applied load. The applied load is indicated by the values shown, and is expressed as a fraction of the maximum load of the beam. The curvatures of the concrete and profiled elements is given by the slopes of the solid and dashed lines respectively. It can be seen that at low applied loads there is negligible difference between strain readings in the concrete and the profiled sheeting, indicating full interaction. At higher loads it can be seen from that the curvature in the concrete is always larger than the curvature in the profiled sheeting, and that the difference increases at higher loads. This what is expected when vertical slip is present.

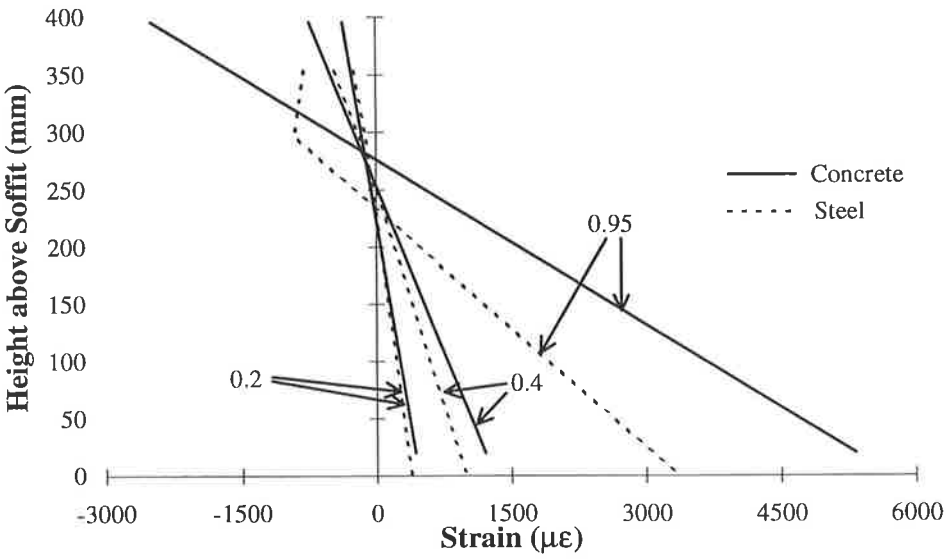


Fig. 5.62. Concrete and Sheeting Strain Readings for Beam PB6

The strain readings can be used to determine the curvature in the cross-section at different applied loads. The resulting moment-curvature curve is shown in Fig. 5.63, and indicates this increase in curvature of the concrete section. This figure shows that at the same applied moment, there is a larger curvature in the concrete section than in the profiled sheeting, and that this difference increases for increasing applied load, which is consistent with the strain readings shown in Fig. 5.62.

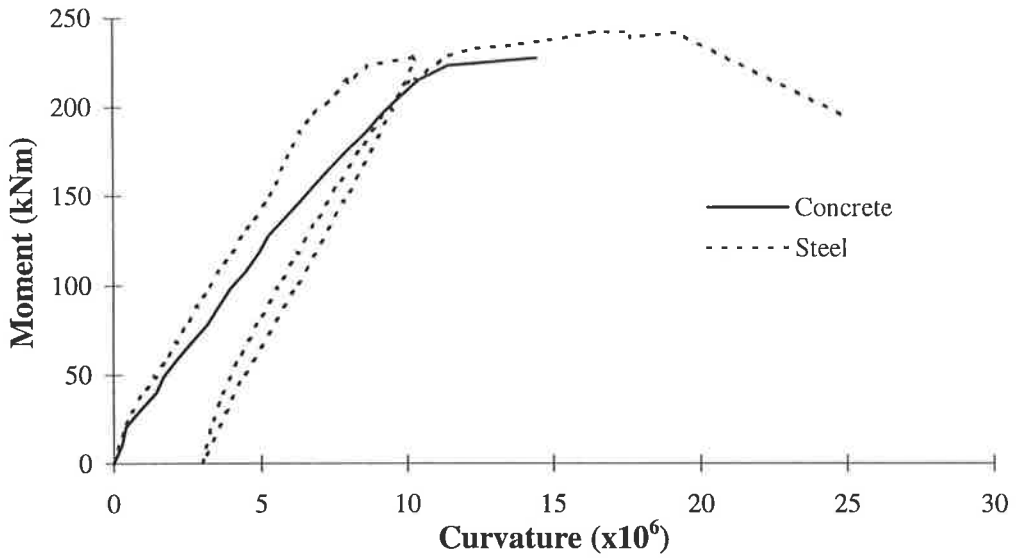


Fig. 5.63. Moment vs Curvature for Beam PB6

5.5 Summary

A summary of the 7 beam tests is presented in the following section. The load vs midspan deflection results of Series 1 are shown in Fig. 5.64 while those of Series 2 are shown in Fig. 5.65. The unloading and reloading curves prior to the ultimate moment have been omitted for clarity. A summary of each of the beams in given in Table 5.4. The load vs deflection curves have been idealised as shown in Fig. 5.66 and tabulated in Table 5.4.

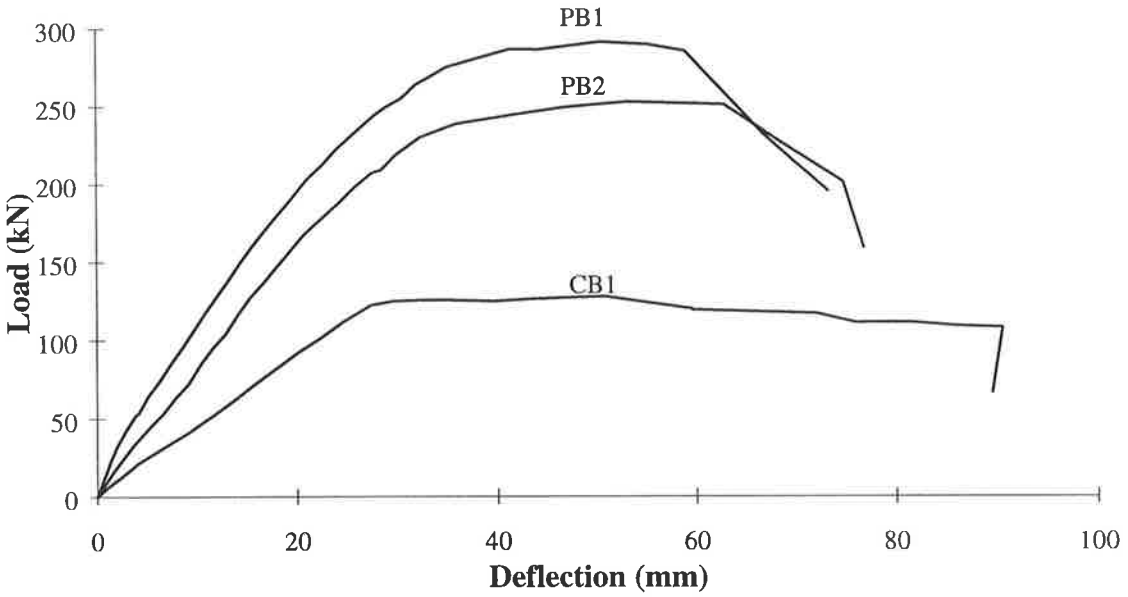


Fig. 5.64. Summary of Series 1

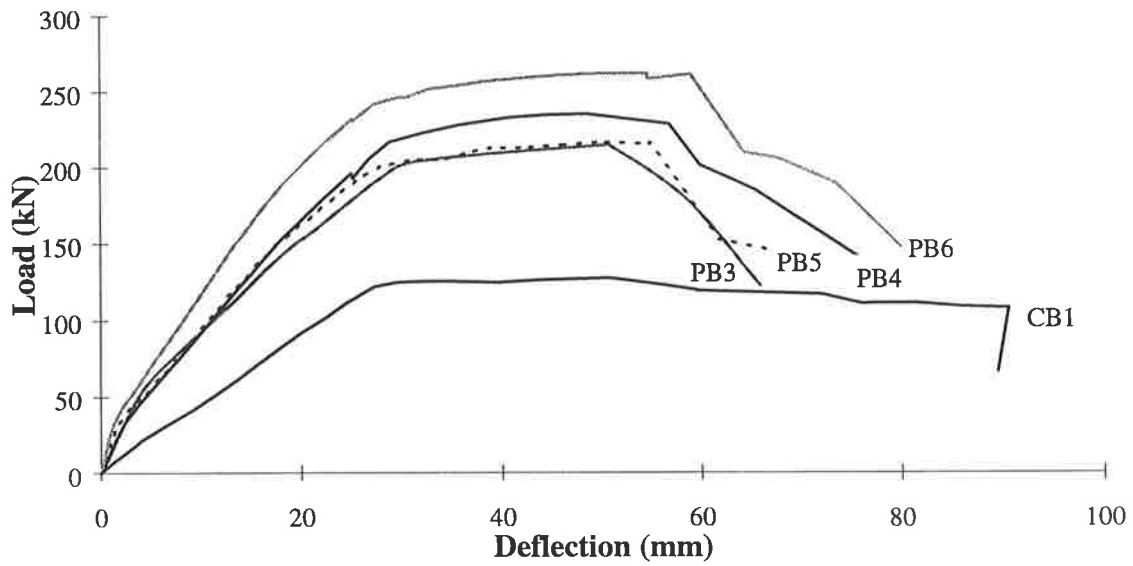


Fig. 5.65. Summary of Series 2

Beam	Rib Type	b_r	h_r	Welded	Point B Start of Yielding		Point C Ultimate Moment		Point D End of Yield Plateau		Theoretical Ultimate Load (kN)	Percent Difference %	Maximum Slip (mm)	Location of Maximum
					Load (kN)	Deflection (mm)	Load (kN)	Deflection (mm)	Load (kN)	Deflection (mm)				
CB1	-	-	-	-	125	30	128	51	108	91	127	1 %	-	-
PB1	L-Rib	80	40	Yes	276	35	292	55	286	59	253	13 %	0.51	Centre (0.5L)
PB2	L-Rib	80	40	No	230	32	253	54	251	63	253	0 %	2.52	Centre (0.5L)
PB3	L-Rib	110	30	Yes	203	31	215	51	-	-	213	1 %	0.12	Centre (0.5L)
PB4	L-Rib	110	30	No	217	29	235	49	229	60	213	9 %	0.53	0.3L
PB5	Dove Tail	115	25	Yes	200	28	217	50	216	55	225	-4 %	1.66	0.23L
PB6	Dove Tail	115	25	Yes	242	27	262	55	261	59	230	12 %	2.56	0.23L (top) 0.36 (Bottom)

Table 5.4 . Summary of Profiled Beam Tests

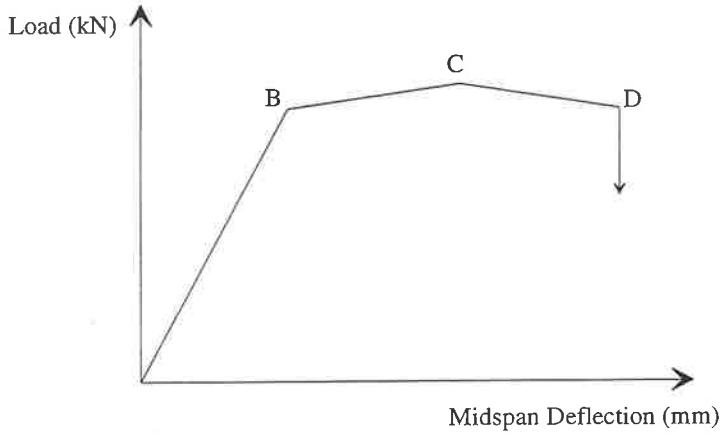


Fig. 5.66. Idealised Load vs Deflection Curve

5.6 Comparison of Results

This section compares the results from the experimental tests with the simplified Rigid Plastic theory presented in Chapter 4, and also with a fully non-linear computer analysis of the beams. A description of the computer analysis is given in Chapter 7. A summary of the comparison between the experimental and the theoretical flexural strengths are given in Table 5.4, where the strengths have been expressed in terms of the applied load in kN. The same comparison is given in Table 5.5 with the strengths expressed in terms of the applied moment in kNm.

Beam	Experimental Strength (kNm)	Theoretical Strength (kNm)	Percent Difference (%)
CB1	118	117	1 %
PB1	270	234	13 %
PB2	234	234	0 %
PB3	199	197	1 %
PB4	217	197	9 %
PB5	201	208	-4 %
PB6	242	213	12 %

Table 5.5 . Summary of Profiled Beam Tests

5.6.1 Rigid Plastic Analysis

5.6.1.1 Beam CB1

Beam CB1 was the control beam, which was constructed without the use of profiled sheeting. The dimensions and properties of the beam were given in Section 5.4.3. The flexural strength of the beam can be determined from simple rigid plastic analysis (Warner et al., 1989). The resulting strength is 117 kNm, which is within 1% of the measured result. This indicates the good fit provided by the rigid plastic theory.

5.6.1.2 Beam PB1

Beam PB1 was constructed from welded profiled sheets with an overall cross-section shown in Fig. 5.10 on page 277. From the push test result shown in Fig. 5.6 the design bond

stress was determined as 0.8 MPa. This bond stress is based on the rib contact area between the sheeting and the concrete. There are 10 encased ribs in the cross-section shown in Fig. 5.10, each with a rib contact perimeter of $S_r = 140$ mm. The bond force required for full shear connection is given by Eq. 4.21 on page 256 as $F_{b,fsc} = 357$ kN when γ is given by Eq. 4.10 on page 254, or 442 kN when $\gamma = 1$. The distance required for full interaction can be calculated from Eq. 4.23 as $L_{fsc} = 320$ mm or 395 mm, depending on the value of γ. Thus, the beam will have full shear connection throughout its length, except for a distance of 395 mm at each end. The moment capacity of the section with full shear connection is given by Eq. 4.25 on page 257 as $M_{fsc} = 234$ kNm, which is 13% less than that measured experimentally. The moment capacity for this beam is unaffected by the choice of γ. The reason for this is that the decrease in the moment from the concrete element is balanced by an equivalent increase in the moment from the profiled steel element.

5.6.1.3 Beam PB2

This beam was nominally the same as Beam PB1 except that the individual units were not welded to each other. The bond force required to be transferred to one of the profiled units to fully yield it is given by Eq. 4.27 on page 260 as $F_{pu} = 61.3$ kN. The distance required to develop this bond is given by Eq. 4.29 as $L = 547$ mm. This distance is 70% longer than that required to develop full shear connection for the welded construction, but is still within the shear span of the beam. Thus, there is full shear connection at the point of maximum moment at a distance of 2.0 m from the end of the beam.

In Section 4.3.3 it was stated that a beam constructed using clipped construction will have the same flexural strength as a beam constructed using welding construction provided there is full shear connection. Thus, the theoretical strength of Beam PB2 is 234 kNm. This is precisely equal to the magnitude of the measured maximum applied load.

5.6.1.4 Beam PB3

Beam PB3 was constructed using welded construction with an overall cross-section as shown in Fig. 5.30 on page 295. From the push test result shown in Fig. 5.31 the design bond stress was taken as 1.2 MPa. This bond stress is based on the rib contact area between the sheeting and the concrete. There are 8 encased ribs in the cross-section shown in Fig. 5.30,

each with a rib contact perimeter of $S_r = 105$ mm. The bond force required for full shear connection is given by Eq. 4.21 on page 256 as $F_{b,fsc} = 284$ kN when γ is given by Eq. 4.10 on page 254, or 334 kN when $\gamma = 1$. The distance required for full interaction can be calculated from Eq. 4.23 as $L_{fsc} = 282$ mm or 331 mm, depending of what value of γ is used. Thus, the beam will have full shear connection throughout its length, except for a distance of 331 mm at each end. The moment capacity of the section with full shear connection is given by Eq. 4.25 as $M_{fsc} = 197$ kNm, which is within 1% of the result measured experimentally. The moment capacity for this beam is unaffected by the choice of γ.

5.6.1.5 Beam PB4

This beam was nominally the same as Beam PB3 except that the individual units were not welded to each other. The bond force required to be transferred to one of the profiled units to fully yield it is given by Eq. 4.27 on page 260 as $F_{pu} = 58.9$ kN. The distance required to develop this bond is given by Eq. 4.29 as $L = 467$ mm. This distance is 65% longer than that required to develop full shear connection for the welded construction, but is still within the shear span of the beam. Thus, there is full shear connection at the point of maximum moment at a distance of 2.0 m from the end of the beam. As a beam constructed using clipped construction has the same flexural strength as a beam constructed using welding construction provided there is full shear connection, the theoretical strength of Beam PB4 is 197 kNm, which is approximately 9% less than the measured maximum applied load.

5.6.1.6 Beam PB5

Beam PB5 was constructed using welded construction with an overall cross-section as shown in Fig. 5.48 on page 309. From the push test result shown in Fig. 5.50 the design bond stress was taken as 0.20 MPa. This bond stress is based on the rib contact area between the sheeting and the concrete. There are 7 encased ribs in the cross-section shown in Fig. 5.48, each with a rib contact perimeter of $S_r = 80$ mm. The bond force required for full shear connection is given by Eq. 4.21 on page 256 as $F_{b,fsc} = 288$ kN when γ is given by Eq. 4.10 on page 254, or 333 kN when $\gamma = 1$. The distance required for full interaction can be calculated from Eq. 4.23 as $L_{fsc} = 2570$ mm or 2973 mm, depending on what value of γ is

used. Thus, the beam will exhibit partial shear connection at the point of maximum moment, which is 2.0 m from the end of the beam.

The bond force which can be developed at the point of maximum moment is given by Eq. 4.7 on page 251 as $F_b = 224$ kN. The moment capacity of the section with partial shear connection is given by Eq. 4.20 on page 256 as $M_{psc} = 208$ kNm, which is within 4% of the result measured experimentally. The moment capacity for this beam is unaffected by the choice of γ. As a comparison, the full shear connection strength is $M_{fsc} = 213$ kNm. Thus, the decrease in load carrying capacity from full shear connection is only 2%.

5.6.1.7 Beam PB6

This beam was nominally the same as Beam PB5. Due to construction differences the overall depth of the section was 416 mm instead of the nominal 410 mm, while the width of the section was 195 mm instead of the nominal 200 mm. All other dimensions were the same as for Beam PB5. Thus, the maximum bond force that can be developed at the critical cross-section is $F_b = 224$ kN, while the moment that can be developed at this cross-section is $M_{psc} = 213$ kNm, which is 12% less than that measured experimentally. The full shear connection strength is $M_{fsc} = 218$ kNm, which is 10% less than that measured experimentally.

5.6.2 Non-Linear Computer Simulations

A non-linear finite difference computer program has been developed which can analyse a composite profiled beam. The program is restricted to the analysis of profiled beams constructed using welded construction. A description of the program is given in Chapter 7. A comparison of the output from the computer program with the experimental results of the profiled beams is given in the following figures.

Figure 5.67 shows the comparison between the experimental results of Beams PB1 and PB2 with the predicted results from the computer program. From this figure a number of observations can be made. Firstly, the predicted curve from the computer initially follows the stiffer curve of Beam PB1. Secondly, the computer curve indicates yielding at an applied load of 235 kN and an ultimate load of 256 kN. This compares more favourably with the

yield load and ultimate load of Beam PB2 of 230 kN and 253 kN respectively than with Beam PB1. Finally, the ultimate load predicted by the computer corresponds closely with that predicted using the theory of Chapter 4 and given in Section 5.6.1.3 as 253 kN.

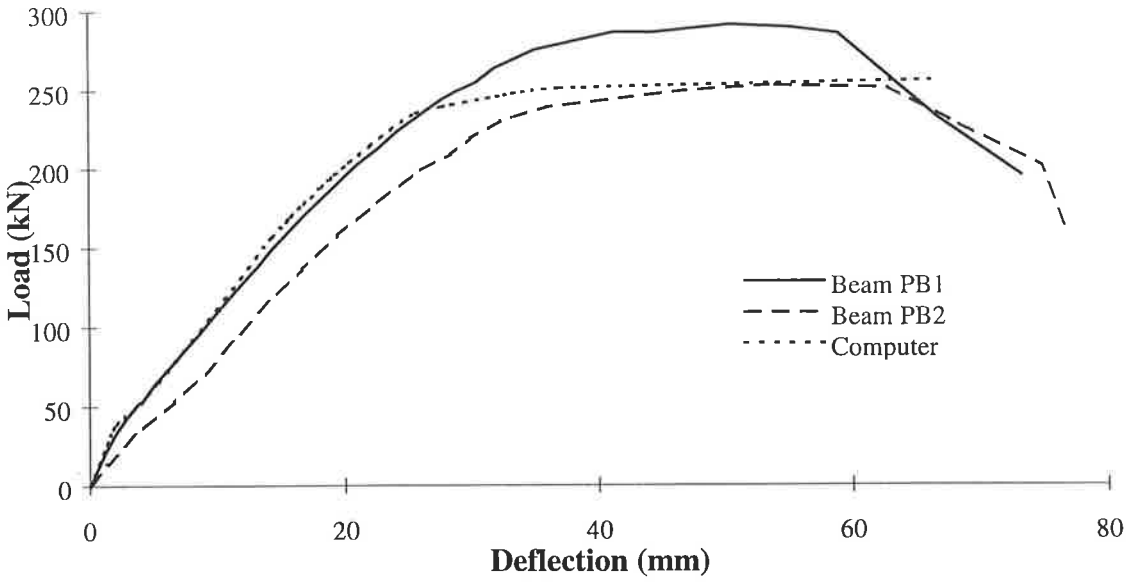


Fig. 5.67. Comparison of PB1 & PB2 with Computer Results

Figure 5.67 shows that Beam PB2 has a lower stiffness and ultimate load than does Beam PB1. This difference may be due to the fact that in Beam PB1 the individual units are welded together, whilst those of Beam PB2 are not. It was shown in Section 5.6.1.3 that Beam PB2 developed full shear connection by the location of the maximum moment, but that the distance required to develop full shear connection was 70% greater than for Beam PB1. Furthermore, it was shown in Section 5.4.5.1 that the maximum displacements measured in Beam PB2 were 5 times larger than those measured in Beam PB1. These effects may have contributed to the lower stiffness and strength of Beam PB2.

A comparison between the predicted and the measured results for Beams PB3 and PB4 is shown in Fig. 5.68. From this figure it can be seen that the predicted curve initially follows the stiffer curve of Beam PB4. The computer curve indicates yielding at an applied load of 200 kN and an ultimate load of 214 kN. This compares more favourably with the yield load and ultimate load of Beam PB4 of 217 kN and 235 kN respectively than with Beam PB3.

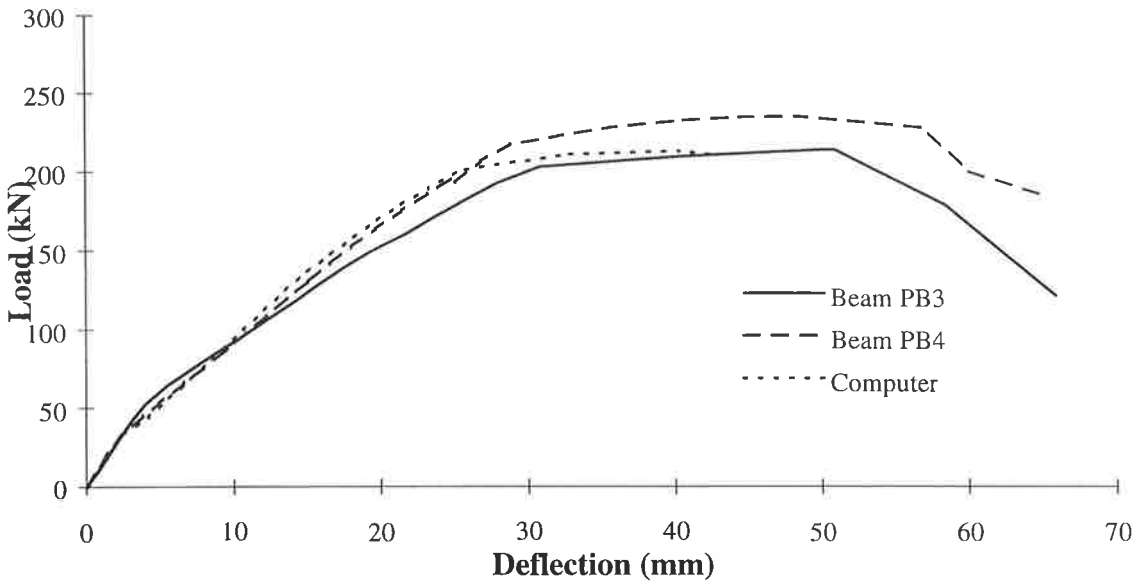


Fig. 5.68. Comparison of PB3 & PB4 with Computer Results

Figure 5.68 indicates that both Beams PB3 and PB4 have much closer stiffnesses up to the yield load than was noted for Beams PB1 and PB2 in Fig. 5.67. This is despite the fact that the individual units in Beam PB4 were not welded together, as was the case for Beam PB2. Thus, it might have been expected that Beam PB4 would have a lower stiffness than Beam PB3. The difference between the two series may be attributed to the higher bond stress in Beams PB3 and PB4, which would have reduced the effect of the non-welded units. As was discussed in Chapter 4, the flexural capacity of welded and non-welded profiled beams is the same for full shear connection. The difference in strength of 9% between Beams PB3 and PB4 can be attributed to variations in material strength and slight geometrical variations.

A comparison between the predicted and the measured results for Beams PB5 and PB6 is shown in Fig. 5.69. It can be seen from this figure that the predicted curve initially follows the stiffer curve of Beam PB6. The computer curve indicates yielding at an applied load of 216 kN and an ultimate load of 228 kN. This compares more favourably with the yield load and ultimate load of Beam PB5 of 200 kN and 217 kN respectively than with Beam PB6.

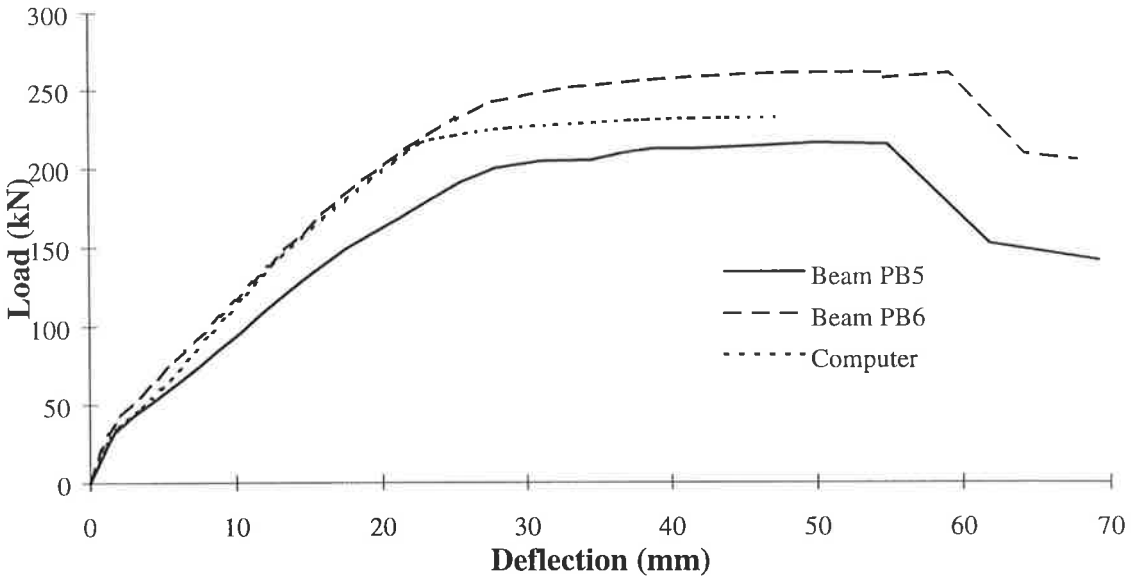


Fig. 5.69. Comparison of PB5 & PB6 with Computer Results

A comparison of the variation in the end slip at the left support with the results of the computer simulation is given in Fig. 5.70. From this figure it can be seen that the computer simulation gives reasonable results when compared to those measured experimentally. It can also be seen that there was no endslip recorded until the applied load had reached 80% and 89% of the ultimate load for Beams PB5 and PB6 respectively. This compares well to the computer result which shows slip commencing at approximately 83% of the ultimate load. The shear-stress / slip curve used for the profiled sheeting in the computer program is shown in Fig. 5.71. This curve indicates that a finite slip is required to develop a shear stress at the interface, and the maximum bond strength was taken as 0.2 MPa.

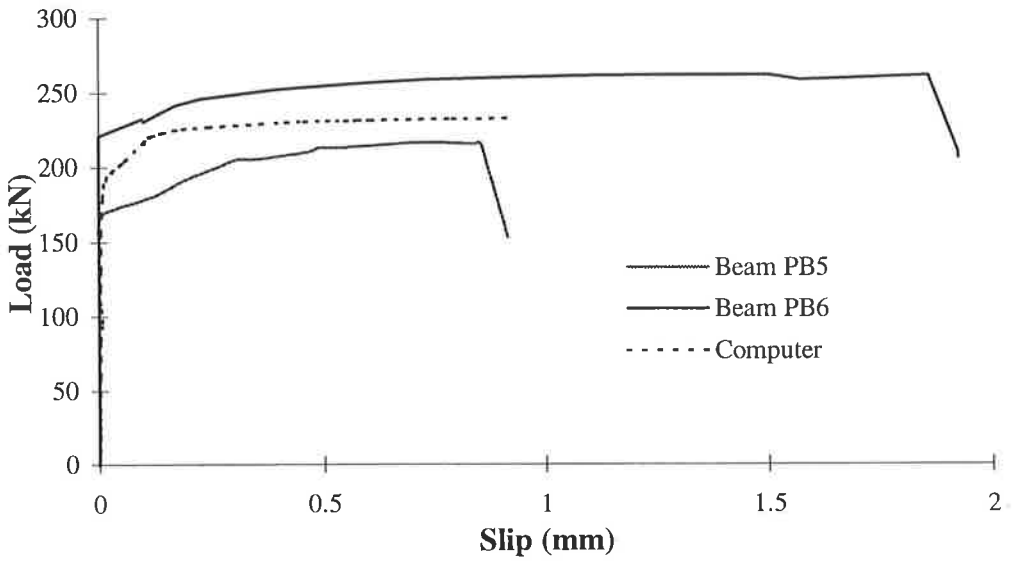


Fig. 5.70. Comparison of End Slip with Computer Results for PB5 and PB6

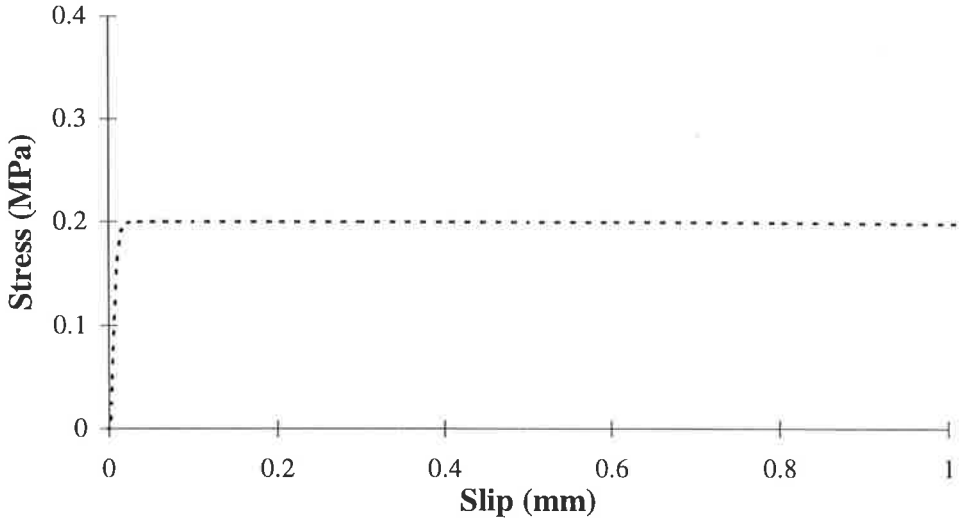


Fig. 5.71. Sheeting Load vs Slip Relationship used in Computer Program

A comparison of the slip distribution that was calculated from the computer simulation with that measured experimentally is shown in Fig. 5.72. It can be seen that the slip distribution of the computer simulation closely describes the measured distribution of slip. This figure indicates that the expected variation in slip is constant throughout the shear span, which is the general trend that was observed in the two tests. The slips are slightly underestimated in the left span, which may be explained by the location of the plastic hinge being offset toward the left load point.

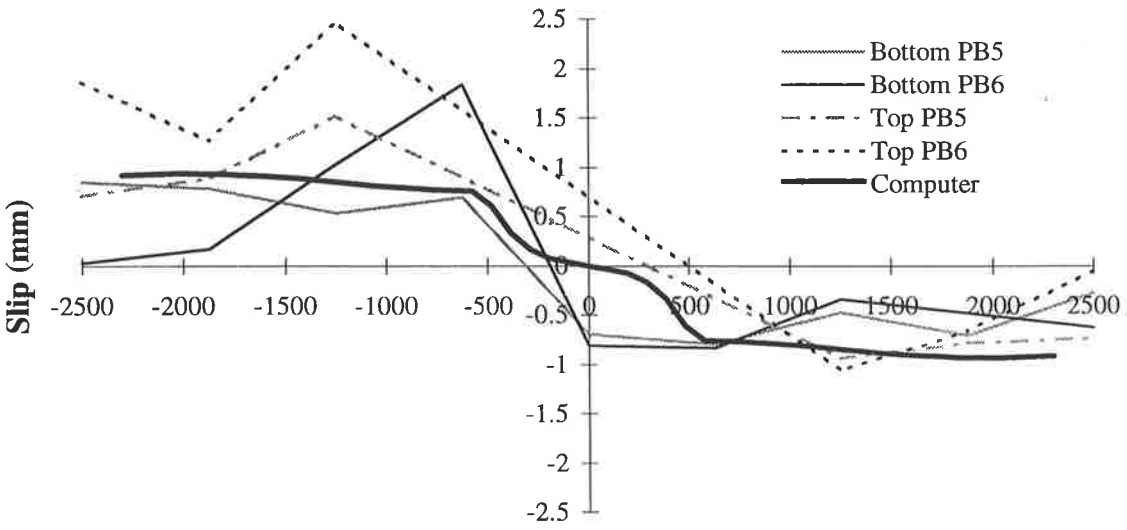


Fig. 5.72. Comparison of Slip Distribution with Computer Results for Beams PB5 & PB6

5.7 Conclusions

The results of tests on six profiled composite beams has been presented. The beams were arranged in three pairs, in which the first two pairs investigated the influence of welded vs non-welded construction with different L-Rib geometries. The third pair of tests was carried out on two nominally identical beams with welded Dove-Tail construction.

The rib geometries of the first two pairs of beams were such that very high bond stresses were developed at the sheeting-concrete interface and as a consequence, slips measured at the interface were of a very small magnitude. The strengths of the beams exceeded the theoretical strength for full shear connection derived using the theory of Chapter 4. The displacements which were measured at the interface were influenced by the strains in the sheeting and tended to exhibit the variation in strain expected throughout the length of the member. This variation in strain is characterised by large increases in the plastic hinge region, tapering away rapidly to zero at the supports.

The unwelded beam of the first pair of tests was less stiff, and had a lower ultimate load than the companion welded beam. This was not true for the second pair of tests, in which the unwelded beam had a slightly higher stiffness and ultimate load than its companion welded beam. The reason for this difference is due to the difference in the bond strengths of the rib geometries. The lower strength and stiffness of the unwelded beam of the first pair of tests indicates that there was some loss of interaction between the sheeting and the concrete. This occurred due to the greater interface stresses that develop in non-welded construction. However, the bond strength in the second pair of tests was 50% higher than that of first pair. This higher bond strength reduced the effect of the higher interface stresses in non-welded construction, and ensured complete interaction.

The third pair of tests were carried out on welded Dove-Tail rib beams. The longitudinal shear strength of the ribs was much less than the previous L-Rib geometries, and as a consequence both beams exhibited partial shear connection. Beam PB6 had a higher stiffness and ultimate load than did Beam PB5. This can be partly attributed to the slightly greater depth of Beam PB6 compared to PB5. The slip distribution was generally constant throughout the shear span, with a slight reduction toward the supports. The loss of full shear connection reduced the load carrying capacity of the beams by only 2%.

Chapter 6

Shear Tests

6.1 Introduction

This chapter describes the results of a series of tests that were carried out in order to determine the increase in transverse shear strength that side profiled sheeting provides in a composite profiled beam. Firstly, a review of the current work in the area of shear strength of reinforced concrete beams and composite profiled beams is presented in Section 6.2. Next, the test arrangement adopted for this experimental program is presented in Section 6.3. The results are presented in Section 6.5 and compared with theoretical values in Section 6.5.4.

It is well accepted that the formulation of a simple model that can accurately describe the shear behaviour of reinforced concrete members has proven to be difficult to derive. The aim of the shear tests presented in this thesis is not to derive an accurate formulation of the mechanism of shear transfer of composite profiled members, as this would require an accurate formulation for the shear transfer in reinforced concrete structures, which itself has proven elusive. The aim is to quantify the increase in the shear capacity of a reinforced concrete member, when it is encased by light gauge profiled steel sheeting.

With this aim in mind, simple test specimens were constructed, which will enable a direct comparison between the strength of a reinforced concrete member and a profiled composite member.

A series of tests were carried out to investigate the resistance of reinforced concrete members with side profiled steel sheeting. A total of 24 specimens were tested, with the main parameters that were varied being the shape of the profiled sheeting, the surface condition of the sheeting and the thickness of the sheeting.

6.2 Literature Review

6.2.1 General Shear Tests

Hofbeck et al. (1969) developed a small scale specimen to investigate the transfer of shear in reinforced concrete members across a shear plane. This same arrangement was also adopted by other researchers (Hanson, 1960; Fenwick and Paulay, 1968; Mattock and Hawkins, 1972; Dulacska, 1972). The test specimen used by Hofbeck et al. is shown in Fig. 6.1. When the specimen is axially loaded as indicated by the arrows V, shear without a moment is produced on the shear plane indicated. When adequate longitudinal and end reinforcement is provided, failure occurs along the shear plane indicated. Reinforcement across the shear plane is in the form of closed stirrups, anchored by wrapping around the longitudinal reinforcement so that it can develop its full yield strength in tension.

The benefit of the arrangement shown in Fig. 6.1 is that it provides simple, small scale specimens which can be easily constructed and tested. Furthermore, shear is applied directly to the specimen without any moment. It has been shown that the initiation of shear cracking in reinforced concrete beams is strongly influence by the presence of flexural cracks which arise due to the moment in the member (Kelfeld and Thurston, 1966; ACI-ASCE Committee 426, 1973; Kim and White, 1991). By arranging the test specimen such that there is no moment in the cross-section, then the shear behaviour can be studied without the unknown influence of flexural cracking.

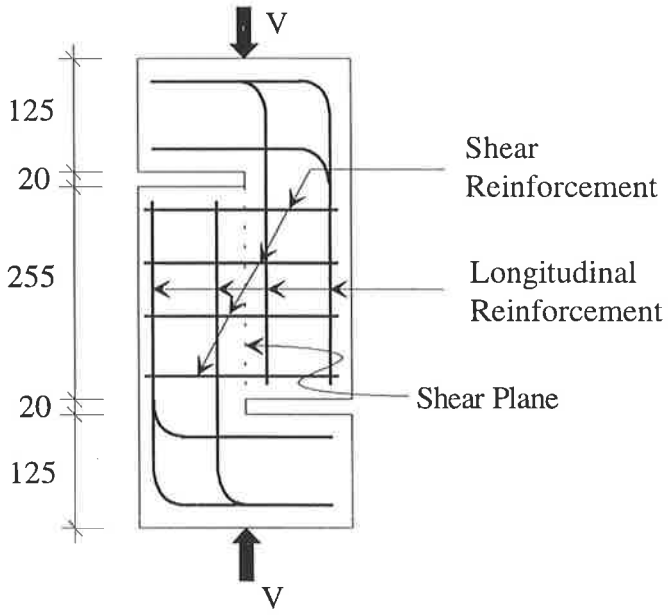


Fig. 6.1. Previous Test Arrangements

Specimens were prepared which were initially cracked before testing, as well as uncracked specimens (Hofbeck et al., 1969; Mattock and Hawkins, 1972). The results were presented in the form of a transverse shear stress v_u against reinforcement index pf_y, where p is the reinforcement ratio = A_{sv}/bd and f_y is the yield strength of the shear reinforcement. A graph of the results is shown in Fig. 6.2. It can be seen that the initially uncracked specimens have a higher shear strength than the initially cracked specimens. The initially cracked

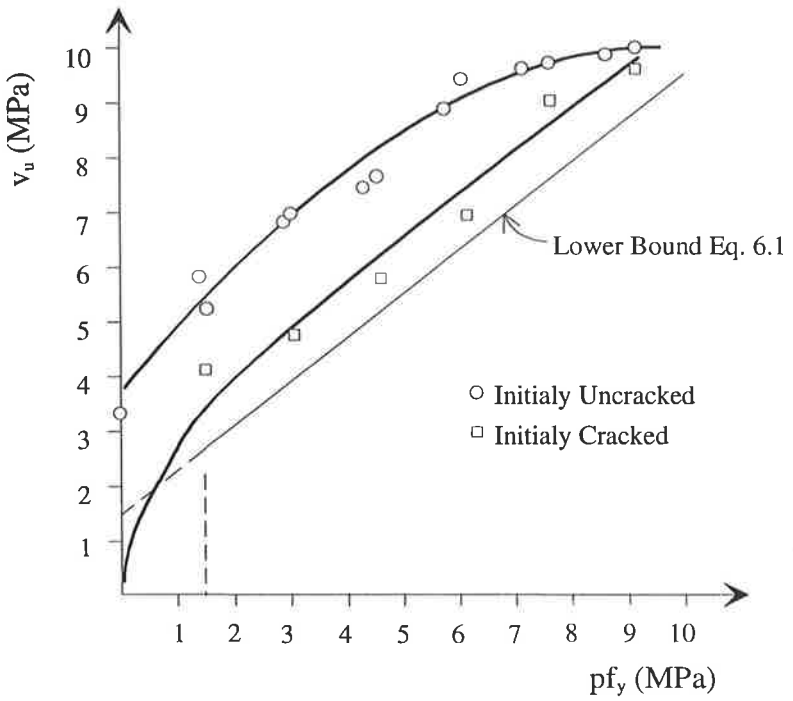


Fig. 6.2. Typical Test Results of Mattock (Mattock and Hawkins, 1972)

specimens were incorporated into the testing program to determine the shear strength of members where a crack exists along the shear plane before shear is applied. Such cracks can occur for a variety of reasons unrelated to shear, such as joints between precast and cast-insitue concrete, cracks due to tension forces caused by restrained shrinkage or temperature deformations, and flexural cracks due to imposed bending moments.

Mattock and Hawkins (1972) proposed an equation to determine the shear strength of a cracked shear plane. This was a lower bound to their results, and is given by Eq. 6.1 and is shown in Fig. 6.2 by the thin solid line.

$$v_u = 1.4 + 0.8pf_y + 0.8\sigma_n \quad \text{.....(6.1)}$$

where

$$pf_y + \sigma_n \geq 0.66f_{ct}$$

$$v_u \leq 0.3f_c$$

σ_n = Externally applied stress acting normal to the shear plane.

Equation 6.1 described the results of tests with no externally applied normal stresses, ie $\sigma_n = 0$, as well as tests with a compressive normal stress (Hofbeck et al., 1969; Mattock and Hawkins, 1972), and also correlated with results of tests with a tensile stress normal to the shear plane (Kriz and Raths, 1965). The first term in Eq. 6.1 can be considered to be the strength attributed to interface interlock (Oehlers and Bradford, 1995), while the second term can be considered to be the dowel resistance due to the reinforcement crossing the shear plane. The third term can be considered to be the active frictional resistance based on the active normal stress acting on the shear plane. A comparison between the experimental results of the shear tests and the theoretical values predicted by Eq. 6.1 is given in Section 6.6.

Statistical analysis of results of shear tests on reinforced concrete beams without stirrups indicate that the most significant variables affecting the shear strength are the tensile strength of the concrete f_{ct}; the reinforcement ratio p; the ratio of moment M to the shear V; and the effective depth of the beam (Kennedy, 1967; Zsutty, 1968; Zsutty, 1971). These were combined together to produce the best fit to the experimental data, and the resulting equation

is given by Eq. 6.2. A similar equation was also derived using a failure theory for concrete (Placas and Regan, 1971).

$$v_u = 0.41\left(\frac{A_{sv}f_c}{b_v d_v}\frac{d_v}{a}\right)^{1/3} \quad \text{.....(6.2)}$$

where

A_{SV} = Area of fully anchored longitudinal steel crossing the shear plane

f_C = Concrete compressive strength

b_V = Width of the beam

d_V = Depth of the beam to centroid of steel reinforcing

a = Shear span from beam reaction to the first concentrated load point.

Equation 6.2 was derived for slender beams with $a/d_V > 2.5$. The above equation was shown to give good correlation with test data from 151 beam tests from 6 different researchers (Zsutty, 1968), with a coefficient of variation of 9.1%. For short beams with $a/d_V < 2.5$, arching action plays a significant role, and the shear strength is increased. Thus, Eq. 6.2 was modified as follows (Zsutty, 1971):

$$v_u = 0.41\left(\frac{2.5}{a/d_v}\right)\left(\frac{A_{sv}f_c}{b_v d_v}\frac{d_v}{a}\right)^{1/3} \quad \text{.....(6.3)}$$

Equations 6.2 and 6.3 were derived using an empirical process, and as such do not help in understanding the fundamental manner in which shear is transferred. They were derived in response to the difficulty faced by researchers in predicting the shear strength of reinforced concrete members. As such, they represent a simple estimate of the shear strength without offering insight into the underlying mechanism of shear transfer.

The specimen arrangement shown in Fig. 6.1 is ideal for the testing program undertaken for this thesis, as it allows a simple method to qualitatively investigate the effects different sheeting geometries. Thus, an adoption of this form of shear tests was used in this research. The results of the tests are compared to the formulations proposed Mattock and Hawkins, and Zsutty. Before the shear test adopted in this research is presented, the results of full scale

shear tests on profiled composite beams will be discussed. This is outlined in the following section.

6.2.2 Shear in Profiled Beams

The profiled composite beam concept, where the profiled sheets were used compositely for the sides of a concrete beam, as well as the soffit, was first developed by Oehlers (1992; 1993). Oehlers proposed that the side profiled sheeting transfers shear forces through active normal forces acting on the embedded ribs, as shown in Fig. 6.3. This action is similar to the dowel action of longitudinal reinforcing bars in resisting shear (Zsutty, 1971; Warner et al, 1989).

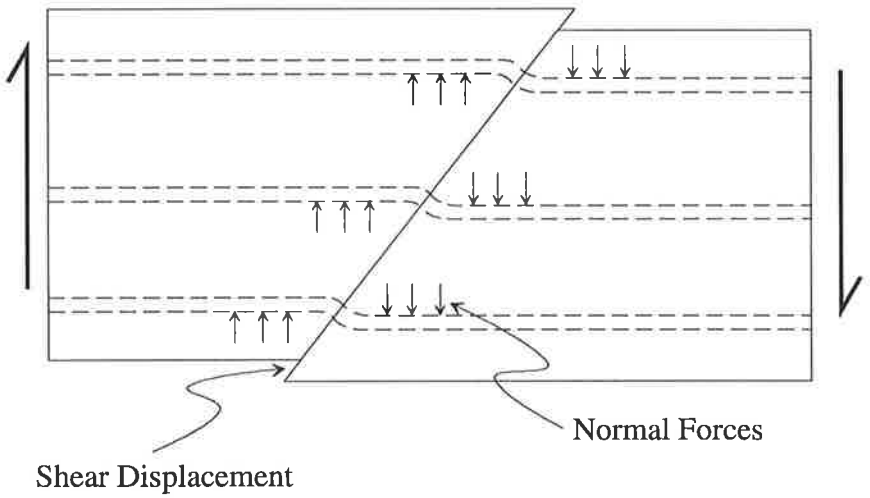


Fig. 6.3. Normal Forces induced by Shear Action (Oehlers, 1993)

A series of beams were tested in flexure and shear, in order to assess the contribution of the profiled sheeting to the strength and ductility. The beam cross sections were shown previously in Fig. 4.5 on page 233 and the resulting load-deflection curves from the shear tests are shown in Fig. 6.4. The load-deflection responses for flexure were discussed earlier in Chapter 4, and are shown in Fig. 4.6. Results from these tests showed that the side profiled sheeting increases the shear strength by approximately 110%.

Oehlers (1992) carried out simplified calculations to determine theoretically the increase in shear strength due to the side profiles. Two different models were proposed which represented upper and lower bounds to the additional shear capacity of the side sheeting. The first was based on the load at which buckling of the side sheeting occurred due

to shear. The shear stress at which buckling occurs in a thin sheet which is simply supported on four sides is given by Eq. 6.4 (Trahair and Bradford, 1988).

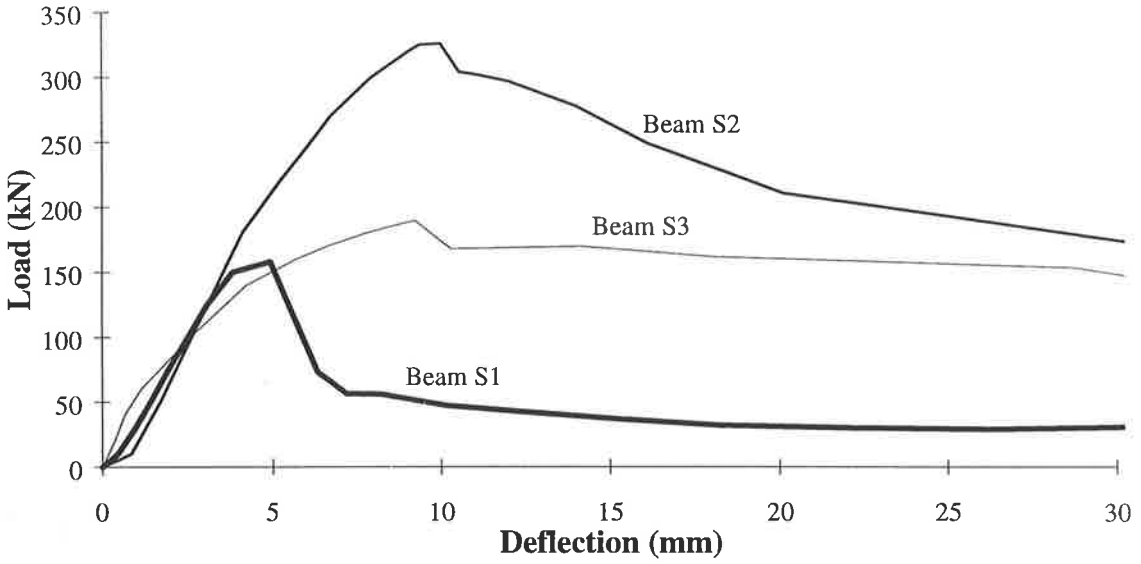


Fig. 6.4. Shear Strength of Profiled Beams (Oehlers, 1993)

$$f_{ov} = \frac{k\pi^2 E}{12\left(1-\upsilon^2\right)\left(d_r/t\right)^2} \quad \text{.....(6.4)}$$

where

k	=	5.35
E	=	Young's Modulus of profiled sheeting
ν	=	Poison's Ratio
d_r	=	Distance between ribs, as shown in Fig. 4.9 on page 235

The shear strength of each web section between the ribs is given by:

$$F_{ov} = f_{ov} d_r t \quad \text{.....(6.5)}$$

This can then be summed for each of the web sections in the side sheeting to determine the total contribution of the side sheeting to the shear resistance.

As an alternative to using the shear buckling stress to determine the shear capacity of the side profiles, Oehlers also used the shear yield stress $\tau_y = f_{py}/\sqrt{3}$ (Trahair and Bradford,

1988) in order to estimate an upper bound to the strength of the side profiles in shear. The resulting theoretical shear strength of the sheeting was then added to the measured shear strength for beam S1, which did not have side profiled sheeting. This approach was taken due to the difficulty in estimating the shear strength contribution of the reinforced concrete beam. A comparison of the two procedures is given in Table 6.1.

Beam No.	Shear Failure Load (kN)		
	Experimental Ulitmate Load	Theoretical Ultimate Load	
		Local Buckling	Yeilding
S1	121.8	-	-
S2	218.5	190	221
S3	127.5	135	167

Table 6.1. Shear Strength of Profiled Beams (Oehlers, 1992)

The soffit sheeting was neglected in the calculation of the shear strength of the profiled beams. This was appropriate as the sheeting was stopped short of the support, and would not have been able to develop sufficient tensile force at the location of the crack. Table 6.1 indicates that the shear strength of Beam S2 lies close to the theoretical strength that is based on the yield strength of the sheeting, whereas the experimental result for Beam S3 lies close to the theoretical strength based on local buckling. Thus, it is not clear from these two tests which of these methods is the best way of predicting the shear strength.

Bradford and Kyakula (1994) carried out preliminary shear tests on profiled composite beams, and proposed a code-oriented approach based on Australian standards of concrete and steel structures (SAA, 1988a; AS 4100, 1990). The transverse shear in a profiled beam was considered to be resisted by three distinct components; the enclosed concrete beam, the embedded ribs, and the sheeting between the ribs. In accordance with AS 3600 (SAA, 1988a), the strength of a reinforced concrete beam without shear reinforcement is given by Eq. 6.6.

$$V_{uc} = \beta_1 \beta_2 b_v d_o \left(\frac{A_{st} f_c}{b_v d_o} \right)^{1/3} \qquad \text{.....(6.6)}$$

where

A_{st} = Area of fully anchored longitudinal steel provided in the tension zone.

β_1 = $1.4-(d_0/2000)\geq 1.1$

β_2 = $(2d_o/a)\leq 2$

d_o = Distance from the extreme compression fibre of the concrete to the centroid of the outermost layer of tensile reinforcement

Equation 6.6 was derived from a modification of the equation proposed by Zsutty (1971) as given by Eq. 6.3. The term β_1 accounts for the increase in shear strength observed in shallow beams (CEB, 1978), while the term β_2 accounts for the beneficial arching effect that occurs when large concentrated loads are applied close to the supports. In the use of Eq. 6.6, the term A_{st} specifically refers to the area of longitudinal steel provided in the tension zone, whereas A_{sv} in Eq. 6.2 refers to all longitudinal steel crossing the shear plane. The reason for this distinction is not clear, as all reinforcing bars crossing the shear plane are effective in resisting shear through dowel action.

Equation 6.6 gives the shear strength of a reinforced concrete beam without shear stirrups. The additional strength due to the shear stirrups is given by Eq. 6.7.

$$V_{us}=\frac{A_{sv}}{s}f_{sy}d_o\cot\theta \quad \text{.....(6.7)}$$

where

A_{sv} = Area of all legs of one stirrup crossing the shear plane

s = Spacing of the stirrups

f_{sy} = Yield stress of the stirrups

θ = Angle of the crack with the horizontal, which can be conservatively assumed as 45°.

The total shear capacity is given as the sum of the contributions of the concrete and the stirrups, and is given by Eq. 6.8.

$$V_{uc,s}=V_{uc}+V_{us} \quad \text{.....(6.8)}$$

The term V_{us} in Eq. 6.8 determines the contribution to the shear strength of stirrups which cross the shear plane at an angle between 0^o and 90^o. When considering the contribution to the shear resistance of the stirrups of Fig. 6.1, Eq. 6.7 gives a value of zero.

This is due to the fact that the angle θ between the shear plane and the stirrups is 90^{o}, giving $\cot\theta = 0$. Thus, the stirrups used in the test arrangement shown in Fig. 6.1 should be considered as tension reinforcement, A_{st} in Eq. 6.6, and the term V_{us} in Eq. 6.8 is taken as zero.

Bradford and Kyakula suggested that A_{st} in Eq. 6.6 can be taken as the sum of the areas of the conventional tension reinforcement and the area of the soffit sheeting, provided the profiled sheeting can develop adequate anchorage at the crack location. However, this condition of ensuring the soffit sheeting is adequately anchored may not always be met. Patrick (1994) showed that most profiled sheeting is not able to develop full shear connection in composite slabs at the face of the support. In order to develop full shear connection the slab must be extended behind the support with the addition of proprietary anchors attached to the sheeting. Thus, a check must be made on the bond developed in the profiled sheeting before it can be included in the calculation of A_{st}. When the bond is not sufficient to cause yield of the sheeting, then the full value of A_{st} should not be used, and a reduced area should be used instead. This will be discussed further in Section 6.6.

The embedded ribs were considered by Bradford and Kyakula (1994) to resist the shear by acting as tension ties across the crack. The additional shear resistance V_r due to the ribs is given by Eq. 6.9.

$$V_r = n_r \frac{b_f t f_{py}}{\cos\theta} \qquad \text{.....(6.9)}$$

where

n_r = Number of ribs crossing the shear crack

b_f = Width of rib flange, as shown in Fig. 3.34 on page 144.

There are a number of points that should be made about the use of Eq. 6.9. Firstly, tension which develops longitudinally in the ribs is not able to resist transverse shear. Thus, the derivation of Eq. 6.9 incorrectly resolves the horizontal forces into the vertical direction. Secondly, the use of Eq. 6.9 assumes that the ribs will be fully yielded at the location of the shear crack. As was stated previously, this will not often be the case unless the beam is continuous, or other means are used to anchor the sheeting. Furthermore, if the sheeting is

fully anchored the equation proposed by Bradford and Kyakula only considers the tension force developed in the flange of the rib, and ignores the contribution from the webs of the ribs. The reason for this is unclear, and it seems more appropriate to use the entire area of the rib in calculation of the tension force.

The resistance of the ribs to vertical shear is better expressed using Eq. 6.10 which was derived by Bradford and Kyakula (1994) to determine the contribution to the vertical shear capacity of the external sheeting between the ribs. Thus, Eq. 6.10 can be used to determine the vertical shear capacity of the sheeting between the ribs, as well as for the capacity of the ribs themselves. The vertical shear capacity can be calculated from the buckling capacity of the sheeting under shear loading. The sheeting was assumed to be simply supported between the ribs, and the shear capacity is given by Eq. 6.10 (Trahair and Bradford, 1988). This expression is the same as Eq. 6.4, where 82 is the elastic critical non-dimensional slenderness ratio (Section 2.4.3). This value of 82 can be derived by realising that the elastic critical stress is equal to the yield stress in shear $\tau_y = f_{py}/\sqrt{3}$ for a steel with E = 200 000 MPa and $\nu = 0.3$ when $d_r/t\sqrt{f_{py}/250} = 82$.

$$V_b = n_s \left(\frac{82}{\frac{d_r}{t}\sqrt{\frac{f_{py}}{250}}} \right)^2 V_w \qquad \text{.....(6.10)}$$

where

n_s = number of side ribs

V_w = $0.6 d_r t f_{py}$

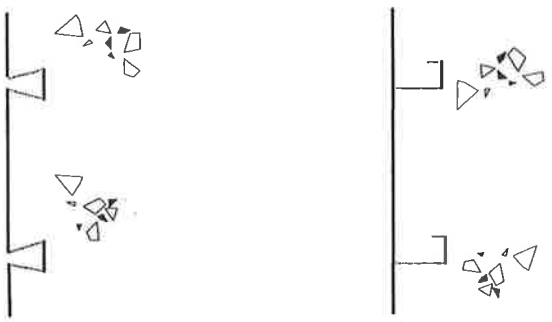
The term V_b must be summed for each element of sheeting between the ribs. If the spacing of the ribs is not constant, then V_b must be calculated for each different rib spacing.

The shear strength of a profiled beam was determined by Bradford and Kyakula (1994) as the sum of the above three components, and is given by:

$$V_u = V_{uc,s} + V_r + V_b \qquad \text{.....(6.11)}$$

Due to the issues raised previously with the determination of V_r, it is recommended in the calculation of V_r in Eq. 6.11 that Eq. 6.10 be used instead of Eq. 6.9, where b_f is substituted for d_r and n_r is substituted for n_s, as given by Eq. 6.12. Thus, the shear resistance of the sheeting is based on the bucking capacity of the vertical elements of the sheeting, as shown in Fig. 6.5 by the solid lines. Where there is sufficient longitudinal bond strength between the sheeting and the concrete, then the dowel action of the ribs may be calculated, by adding the

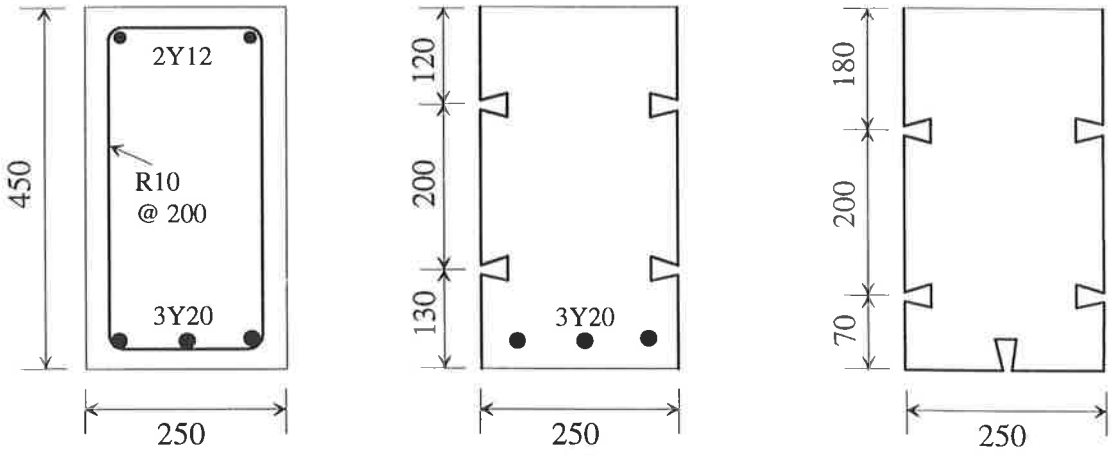
$$V_r = n_r \left(\frac{82}{\frac{b_f}{t}\sqrt{\frac{f_{py}}{250}}} \right)^2 0.6 b_f t f_{py} \quad \text{.....(6.12)}$$



(a) Dove Tail Rib (b) L-Rib

Fig. 6.5. Sheeting that is Effective in Resisting Vertical Shear

Three shear tests were carried out as part of the investigation by Bradford and Kyakula (1994). The three different cross-sections tested are shown in Fig. 6.5. The beams were 3.0 m long with a span of 2.5 m and were tested by applying a single point load at the centre. Beam S1 was a normal reinforced concrete beam whose results were used for a comparison with the other profiled beam sections. Beam S2 had 1.0 mm Bondek II profiled sheeting at the sides only, 3Y20 deformed reinforcing bars at the bottom, and no other reinforcement. Beam S3 had 1.0 mm Bondek II profiled sheeting on the sides and soffit with no other reinforcing.



(a) Beam S1 (b) Beam S2 (c) Beam S3

Fig. 6.5. Test Beams used by Bradford and Kyakula (1994)

The results of their tests are shown in Fig. 6.6. The control beam S1 failed by flexure at a total applied load of 281 kN. Beam S2 failed by shear at a total applied load of 400 kN. A single shear crack propagated from the bottom of the beam at approximately half the shear span, and continuing up to the load point. Beam S3 failed at a total applied load of 310 kN, with a similar cracking pattern to Beam S2, with the addition of a second major crack emanating from the same location as the first.

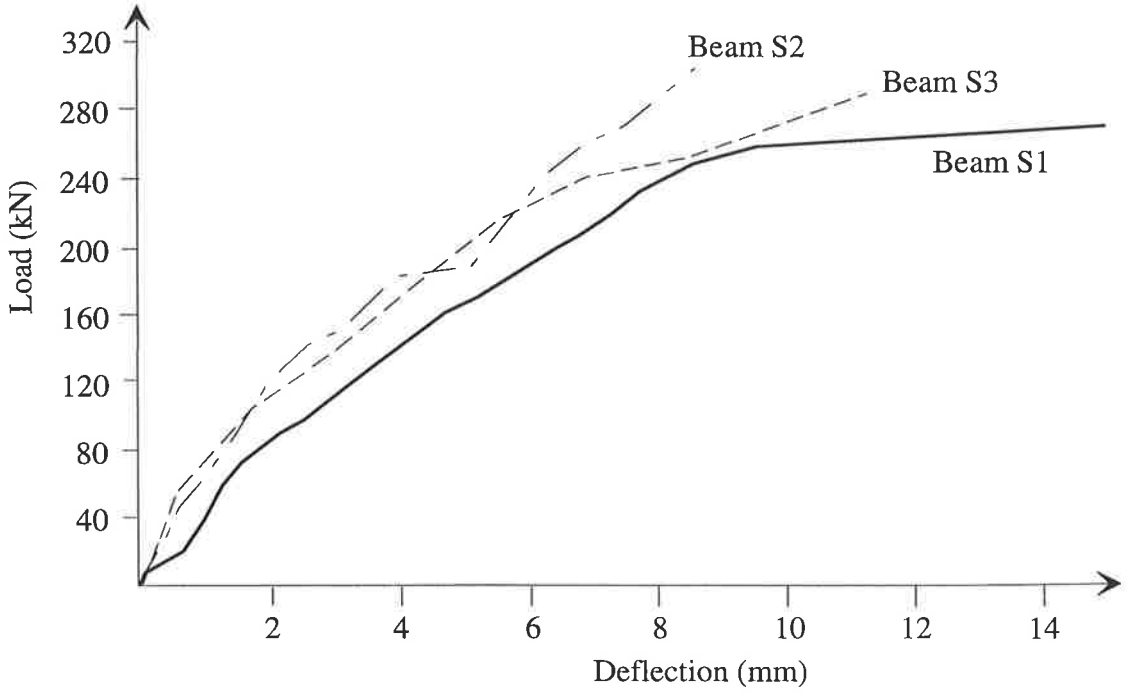


Fig. 6.6. Shear Test Results of Bradford and Kyakula (1994)

A comparison of the shear strengths of the composite profiled beams with Eq. 6.11 is given in Table 6.2. Beam S1 for both Oehlers and Bradford & Kyakula was a plain reinforced concrete beam without profiled sheeting. The values given in the Theory columns were derived from Eq. 6.8 as the shear strength of a reinforced concrete member. It can be seen that the term $V_{uc,s}$ under-estimates the shear strength of the concrete beam without the profiled sheeting of Oehlers by 32%, whilst it overestimates the shear strength of the same beam of Bradford and Kyakula by 49%. These large differences indicate the difficulty in determining the shear strength even of a standard reinforced concrete beam. However, as this research is focused more on determining the increase in shear strength due to the side sheeting and not on predicting the strength of normally reinforced concrete beams, these differences will not be looked at further.

	Oehlers (1991)		**Bradford & Kyakula (1994)**	
Beam No.	Theory (kN)	Experiment (kN)	Theory (kN)	Experiment (kN)
S1	83	122	210	141
S2	193	219	256	200
S3	117	128	176	155

Table 6.2. Comparison with Theory and Experiment

In determining the theoretical increase in shear capacity due to the side profiles for Beam S2 of Oehlers, the increase in shear strength due to the sheeting given by Eq. 6.10 was added to the experimentally derived strength of Beam S1. The contribution of the ribs was not included in the calculation of the shear resistance as no part of the ribs was perpendicular to the direction of the applied shear, as shown in Fig. 4.5 on page 233. This is a conservative approximation which would result in an underestimation of the shear resistance of the side profiled sheeting. This method gives a predicted shear strength which is within 12% of that measured experimentally.

The theoretical strength for Beam S3 of Oehlers was determined using Eq. 6.11 whilst ignoring the contribution V_r. This was done for the same reasons outlined previously. The result was 8% less than that measured experimentally, which is in reasonable agreement.

The increase in the shear strength due to the side profiles of Beams S2 and S3 of Bradford and Kyakula cannot be determined from a comparison with Beam S1, as the shear stirrups of Beam S1 were omitted in Beams S2 and S3, and this would effect their shear strength. Thus, Eq. 6.11 must be used to determine the total shear resistance of the sections.

Given that the error in predicting the strength of Beam S1 with no side sheeting was 49%, the error of 28% in predicting the shear resistance of Beam S2 and 14% for Beam S3 represents a significant improvement. It should be noted that the application of Eq. 6.10 to determine the shear resistance of the ribs assumes that their strength is limited by buckling in shear, with an upper bound as determined by the shear yield stress $f_{py}/\sqrt{3}$. However, the ribs had embossments rolled into the flanges, as shown in Fig 3.100 on page 194, which would have reduced the buckling load below that predicted by Eq. 6.10. This fact may have contributed to the over-estimation of the failure load.

6.2.3 Conclusions

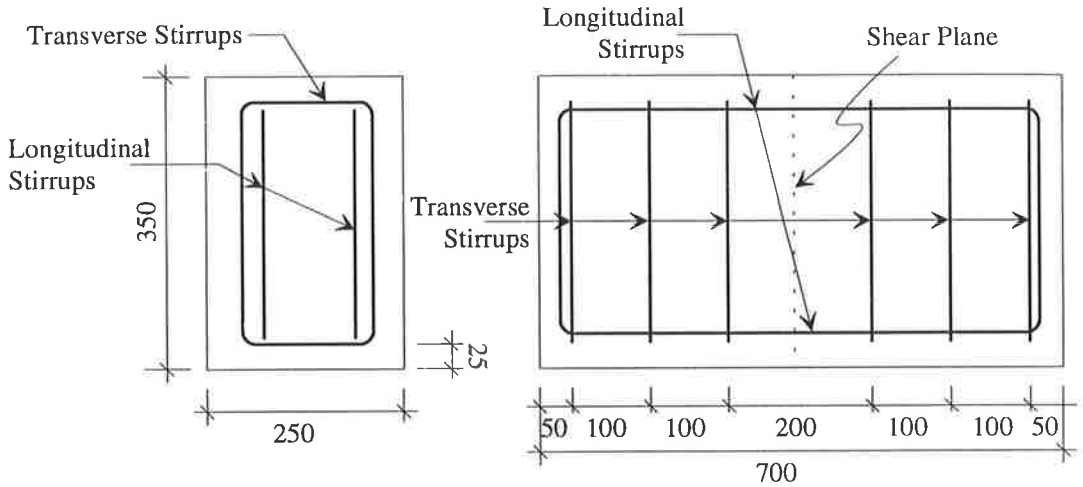
The determination of the shear strength of standard reinforced concrete beams is highly variable. This is further complicated by the addition the external side profiles which resist some of the vertical shear. Factors which must be considered include: the level of longitudinal bond developed between the sheeting and the concrete; buckling of the side profiles; contribution to shear resistance of internal ribs, and distribution of the shear resistance between the sheeting and the reinforced concrete beam.

The small number of tests carried out on profiled composite beams clearly indicate an increase in the transverse shear strength with the addition of the side profiles. However, an adequate model which determines the increase in shear strength is still not available. The following sections discuss a testing procedure which is aimed at determining this model.

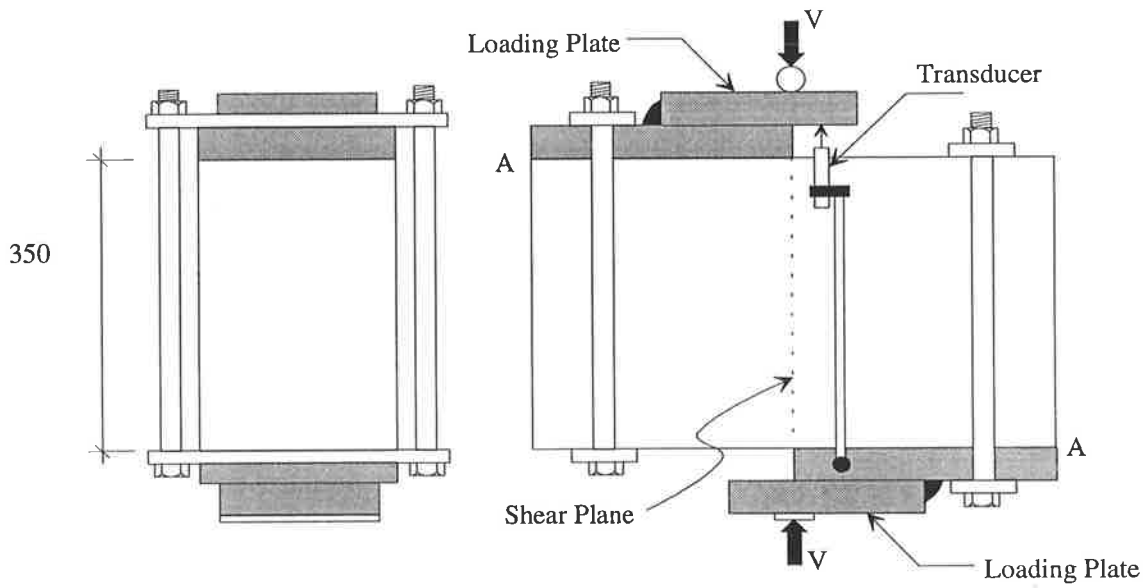
6.3 Current Test Setup

The setup adopted in this testing program is an adaptation of that used by previous researchers (Hofbeck et al., 1969; Mattock and Hawkins, 1972; Dulacska, 1972) as outlined in Section 6.2. The arrangement of the test setup for the current program is shown in Fig. 6.7. Figure 6.7a shows the arrangement of the reinforcement in the specimens, and shows two longitudinal stirrups crossing the shear plane. There are a total of four legs crossing the shear plane. The remaining transverse ties are used to restrain the longitudinal stirrups. All the reinforcement used is undeformed 6 mm round bar.

The significant difference between the arrangements shown in Fig. 6.1 and Fig. 6.7 is that for the tests performed by the previous researchers in Fig. 6.1, the loading rig and the test specimen are monolithic, whereas in the present test procedure in Fig. 6.7, the loading rig is separate from the test specimen. A photograph of the test setup is shown in Fig. 6.8, which shows the arrangement of the loading plates and the clamps. Figure 6.9 shows a detail of the top loading plate.



(a) Reinforcement Arrangement



(b) Loading Arrangement

Fig. 6.7. Shear Test Setup

The specimen is subject to a transverse shear force V, which acts across the shear plane shown in Fig. 6.7b. The top and bottom loading plates are attached to the specimen by external clamps, made with ϕ25 mm bar, as shown in Fig. 6.7b and Fig. 6.8. The bolts on the

clamps are pretensioned before the load is applied to the specimen, in order to prevent the loading plate from lifting up at Position A in Fig. 6.7b. Before the plates are attached to the specimen, a thin layer of silica paste is applied to the upper and lower surface of the specimen, in order to remove any surface irregularities and allow a smooth contact between the plate and the specimen.

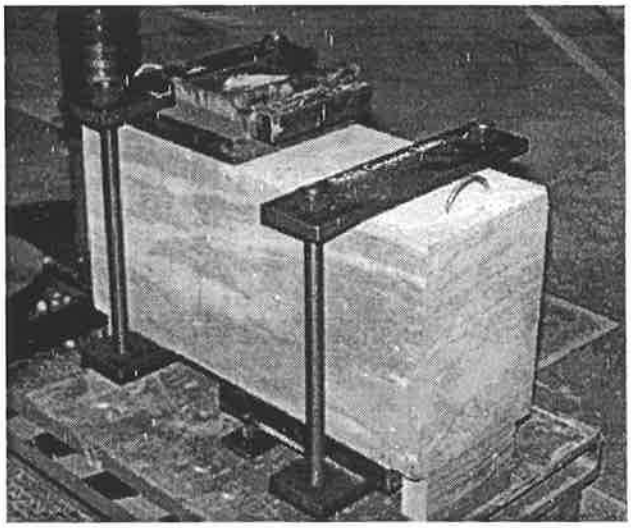


Fig. 6.8. Photo of Shear Test Setup

During the test there is some slight extension of the clamps, and the back of the plate may lift up by approximately 1.0 mm. It was attempted to tighten the bolts further during the test, but this proved too difficult. It was thought that the effect of the lifting up of the back of the plate would be negligible. Figure 6.10 shows a detail of the loading plate for a specimen under full load. It can be seen from the figure that the front half of the loading plate remains in contact with the specimen, which is where the shear is being applied to the shear plane.

The relative displacement of the two halves of the specimen was measured by attaching a transducer to the lower loading plate, and measuring the displacement of the upper plate. This is shown schematically in Fig. 6.7b. Transducers were placed on both sides of the specimen, in order to check for any uneven shear across the specimen. For all the tests performed, the difference between the displacements measured on the two sides of the specimen was not significant, and the displacement results presented here represent the average of the readings from the two transducers.

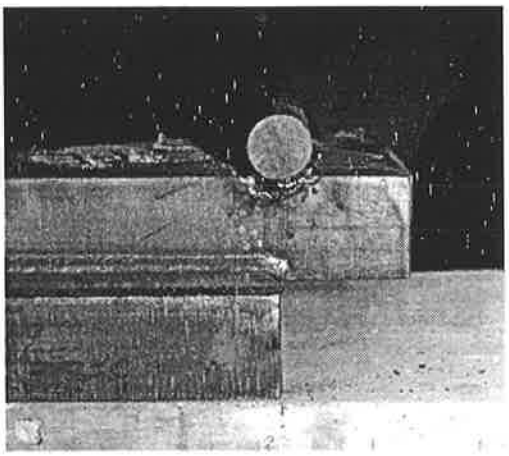


Fig. 6.9. Detail of Loading Plate

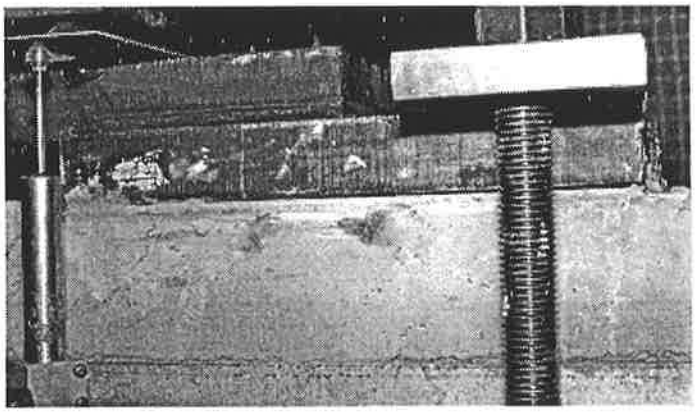


Fig. 6.10. Detail of Shear Test Setup

6.4 Test Program

A total of 24 specimens were tested in three series. Parameters that were varied were the shape of the encased profile rib, the presence of the external sheeting, the surface condition of the sheeting, the thickness of the sheeting, and the bond length of the sheeting. The different rib geometries that were tested were Trapezoidal, Dove Tail and L-Rib. The different rib geometries were tested to gain a qualitative understanding of the difference in shear capacities for each of the rib geometries. Due to the acknowledged practical difficulties of constructing trapezoidal composite profiled beams (Uy, 1995), only two tests with trapezoidal ribs were incorporated into the testing program. The contribution of the external side sheeting to the shear resistance was investigated by testing specimens with and without the sheeting between the ribs. The influence of the chemical bond was investigated by eliminating the chemical bond in some of the tests through the use of a debonding agent, which was applied to the surface of the sheeting prior to casting the specimens. The

thickness of the sheeting was varied from 0.6 mm to 2.0 mm to determine its effect on the shear resistance of the profiled sheeting. The final parameter that was varied was the bond length of the sheeting. This varied from a minimum of 200 mm bond length on each side of the shear plane to a maximum of 350 mm. There were no embossments used for any of the shear tests. A summary of the tests is given in Table 6.3.

Test No.	Profile Shape	Surface Condition	Sheeting Thickness (mm)	Length of Sheeting (mm)
S1.1	-	-	-	-
S1.2	-	-	-	-
S1.3	Trapezoidal	Ungreased	1.0	700
S1.4	Dove Tail	Ungreased	1.0	700
S1.5	Dove Tail	Ungreased	1.0	700
S1.6	L-Rib	Ungreased	1.0	700
S1.7	L-Rib	Ungreased	1.0	700
S1.8	Trapeziodal	Ungreased	1.0	700
S2.1	-	-	-	-
S2.2	L-Rib	Ungreased	1.0	400
S2.3	L-Rib	Ungreased	1.0	400
S2.4	L-Rib	Greased	1.0	400
S2.5	L-Rib (Cut)	Ungreased	1.0	400
S2.6	L-Rib (Cut)	Ungreased	1.0	400
S2.7	Dove Tail	Ungreased	1.0	400
S2.8	Dove Tail	Ungreased	1.0	700
S3.1	L-Rib	Ungreased	1.0	700
S3.2	-	-	-	-
S3.3	L-Rib	Ungreased	0.6	700
S3.4	L-Rib	Ungreased	0.6	700
S3.5	L-Rib	Ungreased	2.0	700
S3.6	L-Rib	Ungreased	2.0	700
S3.7	L-Rib (Cut)	Greased	1.0	700
S3.8	L-Rib (Cut)	Ungreased	1.0	700

Table 6.3. Summary of Shear Tests

Two specimens were constructed without any side profiled sheeting. These were used to quantify the increase in the shear strength due to the presence of the side sheeting. The dimensions of the specimens, and the arrangement of the stirrups were the same for all the shear tests.

For each of the series, the concrete mix was ordinary portland cement, with a maximum aggregate size of 10 mm, a target strength of 32 N/mm^2 and a slump of 80 mm. Companion test cylinders were taken from the mix, and tested at the time of testing the specimens. After pouring the specimens, they were covered with hessian and plastic, and kept moist for two weeks.

At the time of testing the specimens, the properties of the concrete were determined from the test cylinders and the results are given in Table 6.4. The cylinder tests for Series 1 were carried out 57 days after pouring, while the shear tests were carried out between 62 and 68 days after pouring. The cylinder tests for Series 2 and 3 were carried out 93 and 92 days after pouring, while the shear tests were carried out between 106 and 108 days after pouring for Series 2 and between 81 and 86 days after pouring for Series 3.

Cylinder No.	f_c (MPa)	E_c (MPa)	f_{ct} (MPa)
Series 1			
1	31.7	34 700	3.3
2	28.9	33 700	3.2
3	30.8	30 700	3.2
4	29.2	38 800	3.5
Ave	30.2	34 500	3.3
Series 2			
1	34.4	30 000	3.1
2	32.8	29 100	3.2
3	36.8	31 400	3.7
Ave	34.7	30 100	3.4
Series 3			
1	40.1	27 000	3.2
2	37.6	32 300	3.3
3	38.4	32 000	3.3
4	39.6	31 000	3.4
Ave	39.0	30 800	3.3

Table 6.4. Measured Concrete Properties

The compressive strength f_c was determined from tests which were performed on 100 mm diameter cylinders, using the procedure outlined in the Australian Code (AS 1012.9, 1986). The tensile capacity of the concrete f_{ct} was determined using the Brazilian test, which were performed on 150 mm diameter cylinders, using the testing procedure outlined in the

Australian Code (AS 1012.10, 1985). The Young's Modulus of the concrete E_c was determined at the time of testing the beams, using the procedure outlined in the Australian Code (AS 1012.17, 1976).

The results from the tests on the steel reinforcing used for the specimens are shown in Table 6.5, where σ_y is the yield strength and σ_u is the ultimate tensile strength. The stress vs strain curve for the ϕ 6 mm round bar that was used for the stirrups is shown in Fig. 6.11. From this figure it can be seen that the steel did not exhibit significant yielding before fracture occurred, and so only the ultimate tensile strength is reported in Table 6.5.

	Steel Reinforcing		Profiled Sheeting	
	σ_y (MPa)	σ_u (MPa)	σ_y (MPa)	σ_u (MPa)
Series 1	-	625	288	365
Series 2	-	650	280	358
Series 3	-	658	275	360

Table 6.5. Measured Steel Properties

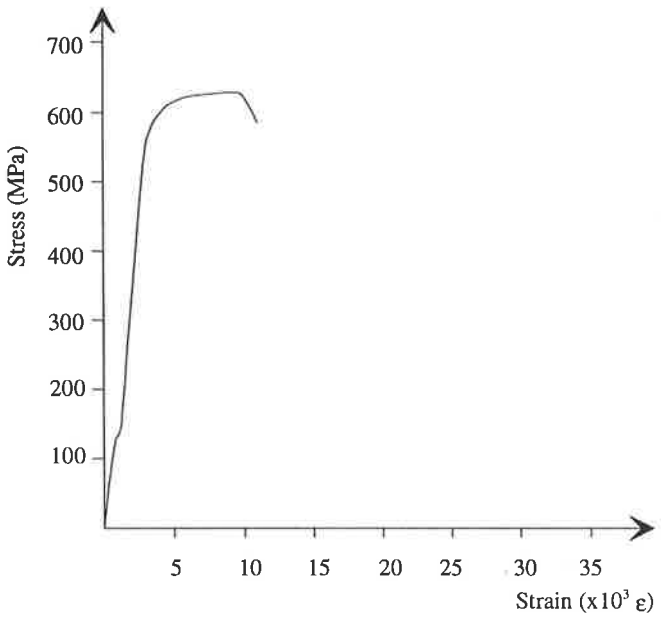


Fig. 6.11. Stress - Strain Curve for Shear Reinforcing

The sheeting used to construct the profiled specimens was grade G2 galvanised sheeting, with a Total Coated Thickness of 1.00 mm, and a Base Metal Thickness of 0.98 mm. This is the same material that was used for the beam tests and the push tests. The stress-strain curve for the material is shown in Fig. 5.2 on page 269. The individual units

were cut to length using a guillotine, and then folded to the required shape using a brake press.

During testing of the push specimens, the load was applied using an hydraulic actuator which was operated in position control. This was to allow the descending branch of the loading curve to be followed. The rate of increase in displacement of the hydraulic actuator was applied in a gradual controlled manner such that the loading rate was approximately 45 kN/min. This was maintained until the first crack was formed. The rate of advance of the hydraulic ram was kept constant, but because the actuator was set in position control, the loading rate decreased due to the decrease in stiffness of the specimen after cracking occurred. After the maximum load was reached, and the specimen began load-softening, the rate of displacement was increased. The typical time taken to reach the ultimate load from the start of the test for most specimens was approximately 20 minutes.

6.5 Test Results

The results of each of the series are presented in this section. The load vs displacement curves are given for each of the tests, along with a description of the test. A summary of the results is presented in Section 6.5.4. The load vs displacement curves for each of the specimens have been tabulated in Table 6.6 on page 386.

6.5.1 Series 1

This series was aimed at investigating the difference in the shear characteristics of different geometry ribs. The rib geometries that were used were Trapezoidal, Dove Tail and L-Rib. There were two specimens of each rib type which were nominally identical. Also, there were two specimens which did not have any sheeting. These were used to determine the increase in shear strength due to the sheeting.

6.5.1.1 Plain Specimens

Specimen S1.1

The load vs displacement responses of the two plain specimens are shown in Fig. 6.12. Specimen S1.1 achieved a load of 395 kN before cracking first occurred. This load at which

cracking first commenced is labelled by Point A in Fig. 6.12, and is tabulated for all the tests in Table 6.6. The crack propagated rapidly and extended through the entire depth of the specimen. After this load was reached, the load dropped to 333 kN, as indicated by Point B. As the displacement increased, the load increased to 382 kN at Point C before decreasing, and thus did not surpass the first maximum achieved before cracking occurred. The drop in load carrying capacity was very rapid, as the displacement of the two halves increased. The load carrying capacity tended to stabilise at approximately 125 kN, as shown by Point D. The location of Point D was chosen to give an approximate value for the residual shear strength of the specimen before fracture of the shear stirrups occurred. It can be seen in Fig. 6.12 that there is a continual decline in the shear resistance with increasing displacement, however Point D was chosen as an approximate average value for the residual strength. The shear strength at Point D can be used for qualitative comparisons between the different tests, rather than quantitative evaluation. When the displacement had increased to approximately 9 mm, two of the shear reinforcement stirrups fractured. This was accompanied by a large decrease in the shear capacity of the specimen.

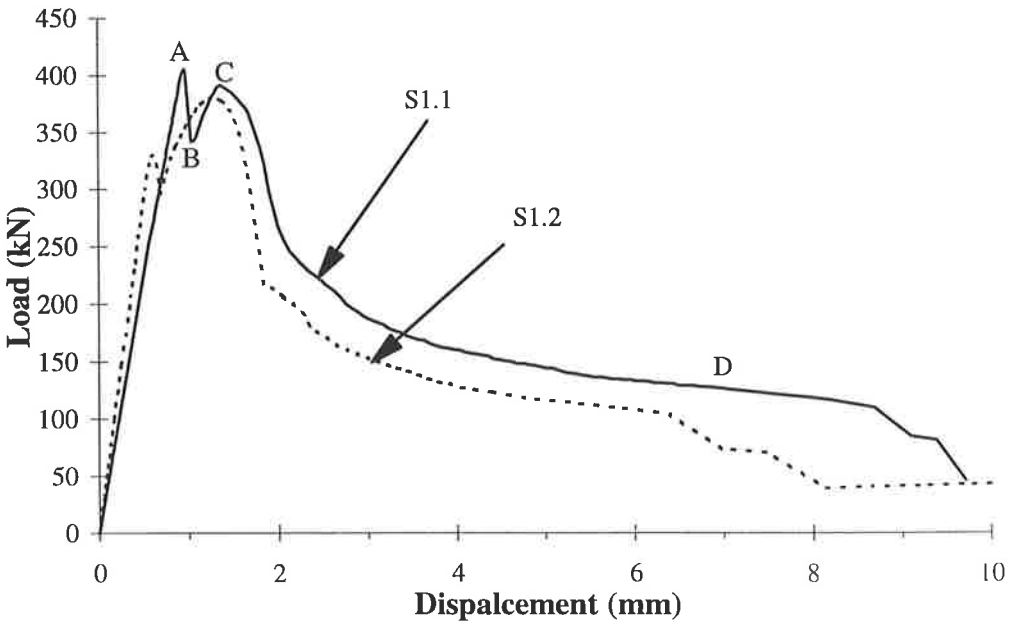


Fig. 6.12. Load vs Displacement for S1.1 and S2.2

Specimen S1.2

Specimen S1.2 behaved in a similar manner to S1.1, except that the maximum load achieved after initial cracking was greater than the load at which cracking commenced. The cracking load was 329 kN, whist the maximum load attained after cracking was 381 kN. There was a similar rapid reduction in the load carrying capacity after the maximum load had

been reached. The load decreased to 104 kN before the first shear stirrup fractured at a relative displacement of approximately 6 mm.

The initial crack that developed at an applied load of 329 kN was at a slight angle to the vertical, as shown by the dashed line in Fig. 6.13. This crack developed through the whole cross-section as the load dropped slightly to 296 kN. As the load increased the cracking developed into the s-shape shown by the solid line. A photo of the failed specimen is shown in Fig. 6.14.

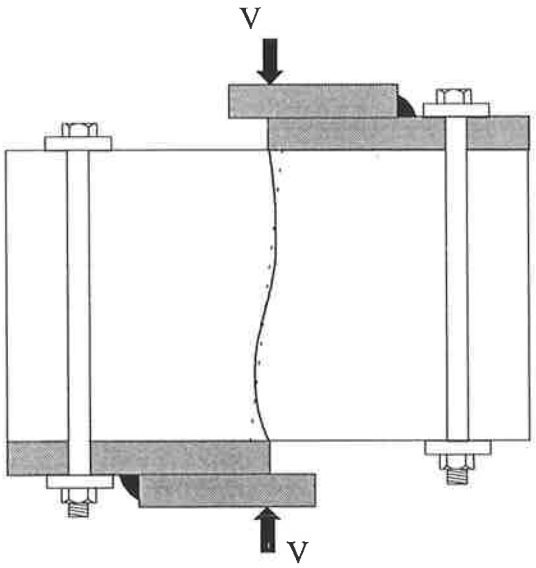


Fig. 6.13. Schematic of Shear Plane for Plain Specimens

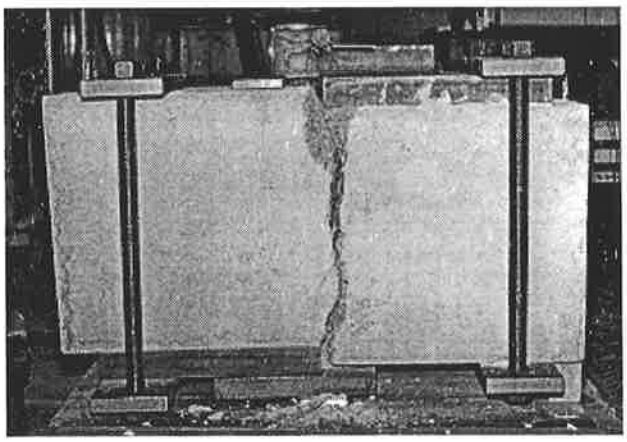
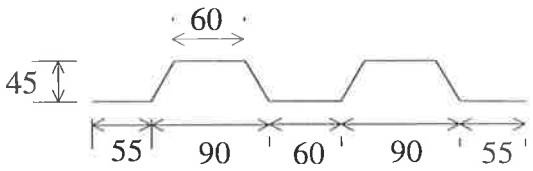


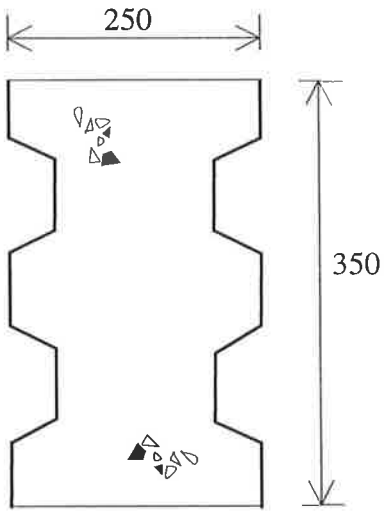
Fig. 6.14. Photo of Shear Plane for Plain Specimens

6.5.1.2 Trapezoidal Ribs

The geometry of the trapezoidal ribs is shown in Fig. 6.15a, and the cross-section of the specimen is shown in Fig. 6.15b. There were no embossments used in the profiled sheets. The sheeting was not coated with a debonding agent.



(a) Profile Dimensions



(b) Specimen Dimensions

Fig. 6.15. Trapezoidal Specimen

The load vs displacement curves of the two trapezoidal specimens are shown in Fig. 6.16. It can be seen that the two specimens behaved quite similarly. For both specimens, the maximum load was reached just before cracking occurred, as indicated by Point A. There was a rapid reduction in the load carrying capacity to Point B after cracking had occurred. Both specimens exhibited an increase in load carrying capacity after the initial drop subsequent to crack initiation. This increase was more pronounced for Specimen S1.3 than S1.4. The shear resistance then decreased with increasing displacement, as shown by Point D. The decrease in shear strength after cracking occurred indicates that there was poor interaction between the profiled sheeting and the concrete. After failure of the concrete, there was not an alternative mechanism to resist the shear and thus there was a rapid reduction in the load carrying capacity.

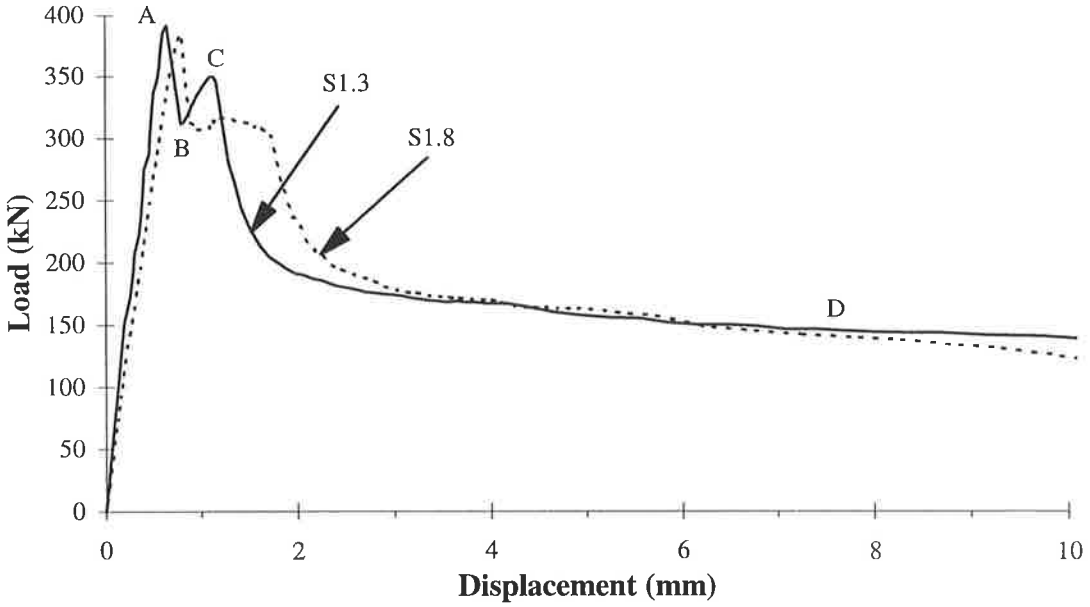


Fig. 6.16. Load vs Displacement for Trapezoidal Specimens

Specimen S1.3

The uppermost element of the sheeting above the top rib distorted slightly away from the concrete surface at an applied load of 135 kN. Excluding this distortion, there was no visible deformation of the sheeting ribs at the time of first cracking. The load at which cracking initiated was also the maximum load of 392 kN. After cracking, the load decreased rapidly to 313 kN, before rising again to a smaller maximum of 350 kN. The load decreased with increasing displacement to a plateau of approximately 145 kN. Distortion of the ribs was not visible until the relative displacements of the two sides of the specimen had exceeded 5 mm, which from Fig. 6.16 corresponds to a residual shear strength of less than 50% of the maximum.

The final shape of the sheeting at the completion of the test is shown in Fig. 6.17. This shows the typical shear deformation that occurs between the ribs. Figure 6.18 shows the outward deformation of the sheeting at the completion of the test. It can be seen that due to the trapezoidal shape of the ribs, the sheeting is free to distort away from the concrete surface. The specimen is shown in Fig. 6.19 after the sheeting has been removed. Portions of the concrete have been broken away from the specimen between the ribs. It was not possible to determine the load at which this occurred, due to the presence of the profiled sheeting. It can also be seen in Fig. 6.19 that the failure surface is not a straight line between the loading plates. This same behaviour was noted to a lesser degree for Specimen S1.2 as shown in Fig. 6.14. This may have lead to the slight rise in the shear resistance of the specimen after initial cracking.

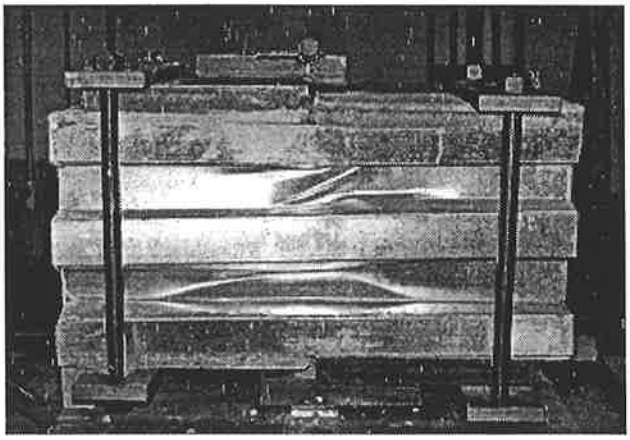


Fig. 6.17. Failure of S1.3

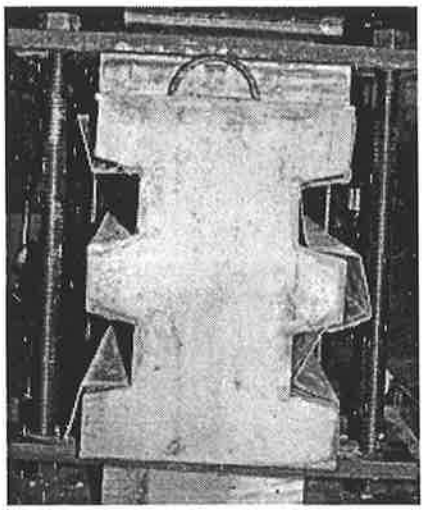


Fig. 6.18. Outward Deformation of Sheeting for S1.3



Fig. 6.19. Failure surface for S1.3 after removal of sheeting

Specimen S1.8

As the load increased a cracking sound could be heard from the uppermost steel element, at an applied load of 290 kN, which indicated that the chemical bond between the sheeting and the concrete was breaking down. There was no visible distortion of the sheeting at this load stage. Cracking occurred at a load of 383 kN, after which the load decreased to 308 kN. Slip between the profiled sheeting and the concrete in a direction transverse to the shear plane was first visible when the applied load had reduced to 310 kN, which occurred when the relative displacement had reached 1.6 mm. There was a slight increase in the load carrying capacity to 317 kN before decreasing to plateau of approximately 145 kN.

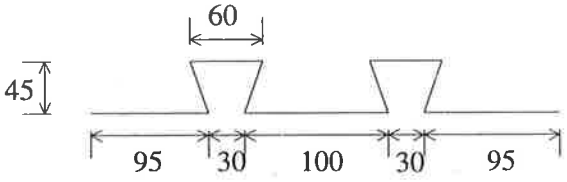
The failure surface is shown in Fig. 6.20 after the removal of the external sheeting. It can be seen that the failure surface is more vertical than for Specimen S1.3. Consequently, the load vs displacement curve shown in Fig. 6.16 does not show the same rise in shear resistance after initial cracking occurred.



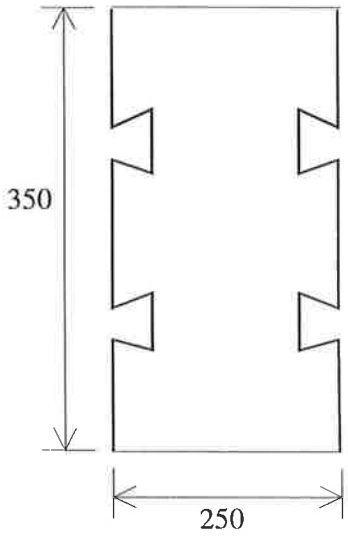
Fig. 6.20. Failure Surface of S1.8

6.5.1.3 Dovetail Ribs

Figure 6.21a shows the arrangement of the profiled sheeting for the dovetail ribs, whilst Fig. 6.21b shows the cross-section of the specimen.



(a) Profile Dimensions



(b) Specimen Dimensions

Fig. 6.21. Dove Tail Specimen

The load vs displacement curves for the dovetail ribs are shown in Fig. 6.22. It can be seen that there is a significant difference in the behaviour of the two specimens. Specimen S1.4 shows a significant increase in strength after initial cracking of the concrete, whereas Specimen S1.5 shows no increase at all.

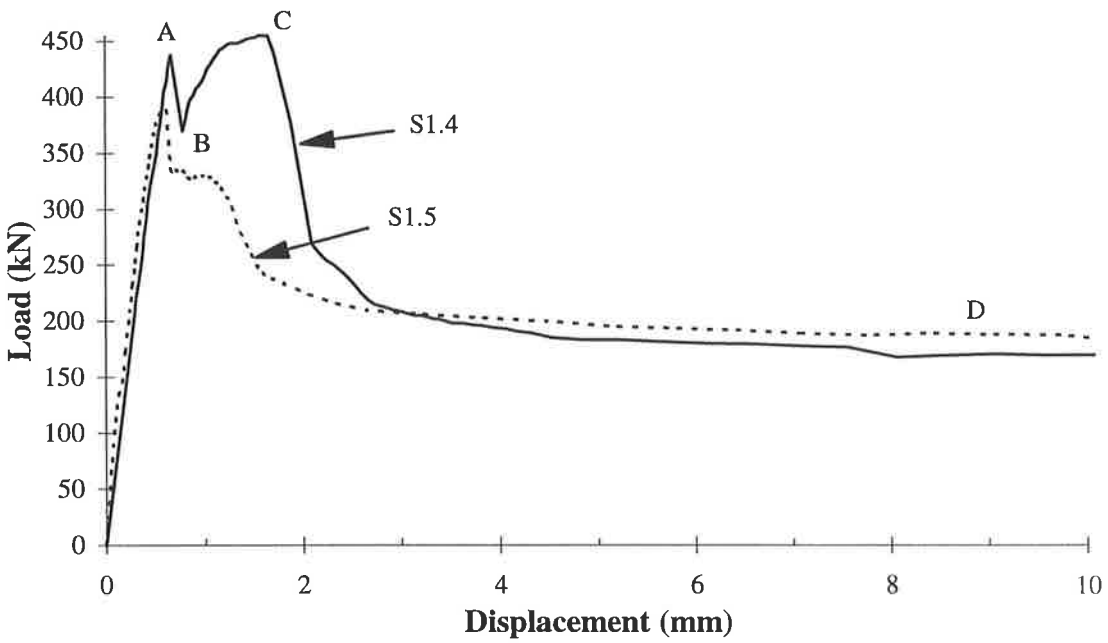


Fig. 6.22. Load vs Displacement for Dovetail Ribs

Specimen S1.4

As the load was increased, cracking noises were heard at approximately 250 kN indicating the breakdown in the chemical bond between the concrete and the profiled

sheeting. The outermost elements of the sheeting pulled away slightly from the concrete before cracking occurred. The specimen reached an applied load of 438 kN before cracking occurred at Point A in Fig. 6.22, after which the load decreased to 370 kN at Point B. Figure 6.23 shows the profiled sheeting after cracking had occurred, which caused an increase in the outward movement of the external profiled elements. There was a subsequent increase in the load carrying capacity to 455 kN at Point C. After the maximum load had been reached, deformation was visible in the inner ribs, however no distortion was perceptible in the sheeting between the two ribs. This is shown in Fig. 6.24. After the maximum load there was a rapid reduction in the load to an approximately stable value of 170 kN, as shown in Fig. 6.22.

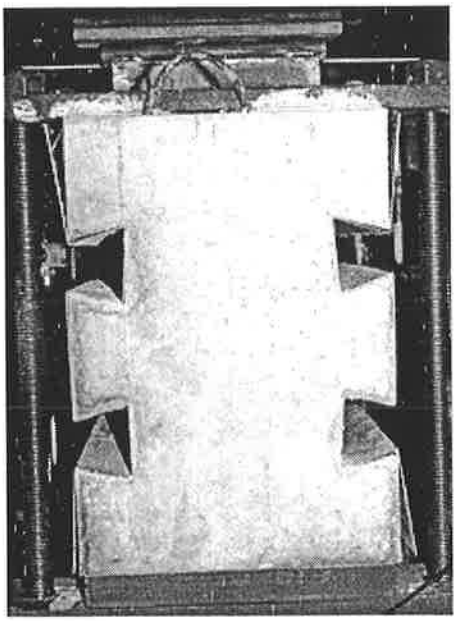


Fig. 6.23. Lateral Deformation of Sheeting for S1.4

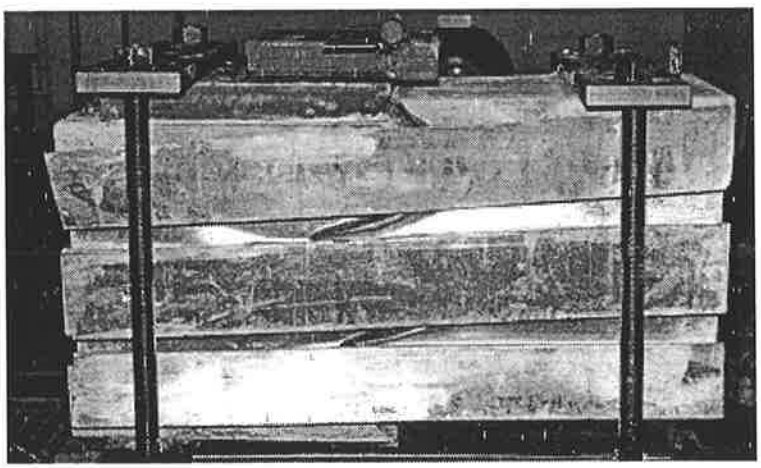


Fig. 6.24. Shear Deformation of Sheeting for S1.4

Specimen S1.5

Break down of the chemical bond between the profiled sheeting and the concrete occurred at an applied load of approximately 330 kN, as indicated by cracking noises coming from the sheeting. Cracking of the specimen occurred at an applied load of 390 kN, which was also the maximum load for the specimen. This maximum load is significantly less than Specimen S1.4. It was found after the test had concluded, that the silica paste which was used to create a smooth contact surface between the loading plates and the concrete, had not been evenly spread over the contact surface. The paste stopped short of the front edge of the loading plates, and lead to a diagonal shear crack, instead of a vertical crack, as shown schematically in Fig. 6.25.

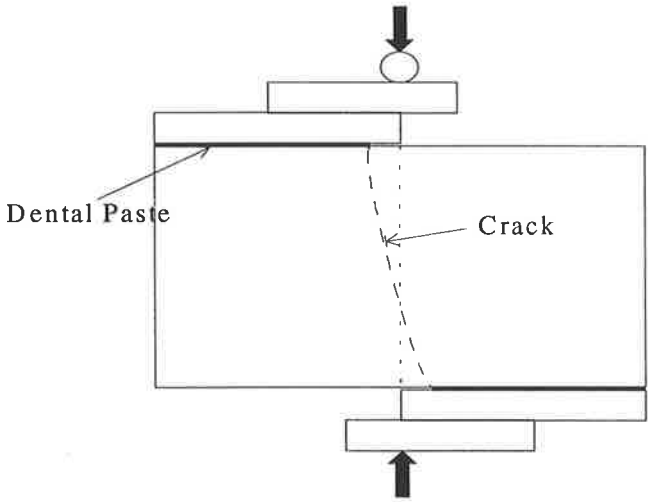
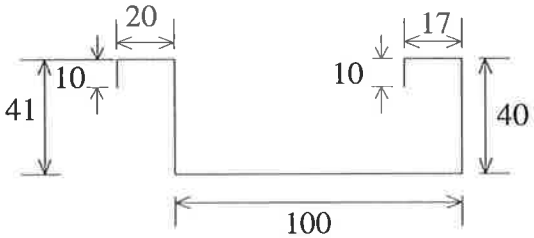


Fig. 6.25. Diagonal Shear Crack for Specimen S1.5

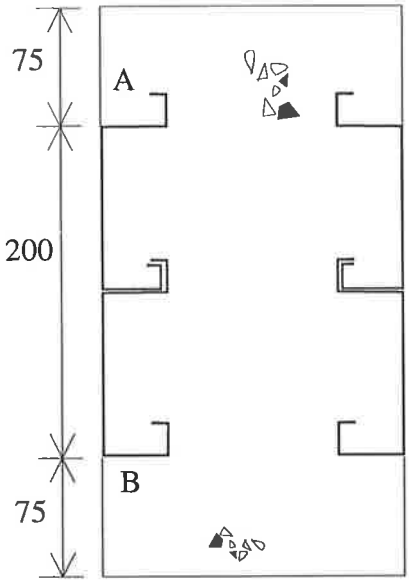
Longitudinal slip between the concrete and the profiled sheeting was perceptible at the ends of the specimen when the transverse relative displacement was 1.5 mm. This occurred when the applied load had reduced to approximately 250 kN, which is only 65% of the maximum load. At this point, the longitudinal slip was of the order of 0.1 mm. Buckles first became visible in the ribs after the applied load had reduced to 230 kN, which was only slightly after the load at which end slip was first noticed. The deformations in the profiled sheeting were the same as for Specimen S1.4, and shown in Fig. 6.23 and Fig. 6.24.

6.5.1.4 L-Ribs

The geometry of the profiled sheeting used for the L-Ribs is shown in Fig. 6.26a and the specimen is shown in Fig. 6.26b. The ribs were constructed individually, and then assembled by 'clipping' them together. The individual units were not welded together.



(a) Profile Geometry



(b) Specimen Geometry

Fig. 6.26. Geometry of L-Rib Specimens

The load vs displacement curves of the specimens are shown in Fig. 6.27. It can be seen that the form of the two curves are quite similar, with specimen S1.7 attaining a slightly

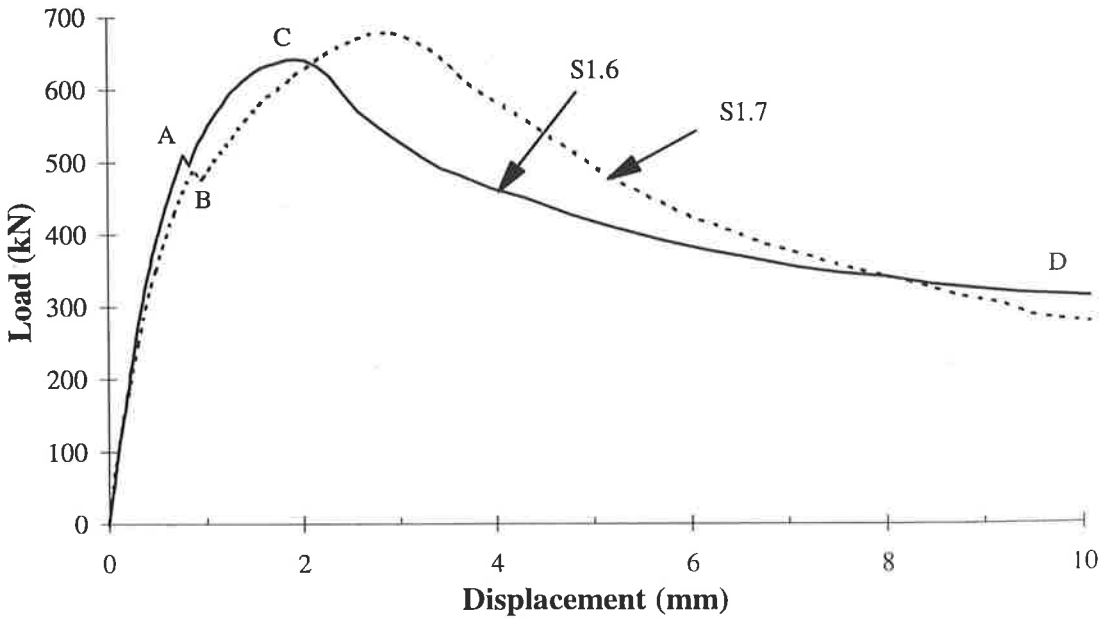


Fig. 6.27. Load vs Displacement for L-Ribs

higher load. It can also be seen, that the influence of cracking of the concrete resulted in only a minor reduction of the load. The failure was notably more ductile than for the previous specimens. Also, the increase in strength after the concrete first cracked was much greater.

Specimen S1.6

As the load was applied, there was a gradual breakdown in the chemical adhesion between the concrete and the profiled sheeting. This occurred in the regions between the encased ribs. The absence of the chemical bond could easily be determined from the hollow or drummy sound that resulted from tapping the profiled sheeting. At an applied load of 350 kN on the loading branch of the curve it appeared that the chemical bond had completely broken down.

Cracking of the specimen occurred at an applied load of 510 kN at Point A in Fig. 6.27. There was a slight reduction in the load to 496 kN at Point B. As the load increased, inclined cracks developed along the top of the specimen. The pattern of cracking at failure is shown in Fig. 6.28 as is the deformed shape of the profiled ribs. The shear deformation is clearly evident, as the ribs are bent in double curvature. The load increased up to a maximum of 642 kN, before slowly reducing to a value of 315 kN at 10 mm displacement. The reduction in load carrying capacity after the maximum load was gradual and imperturbable.

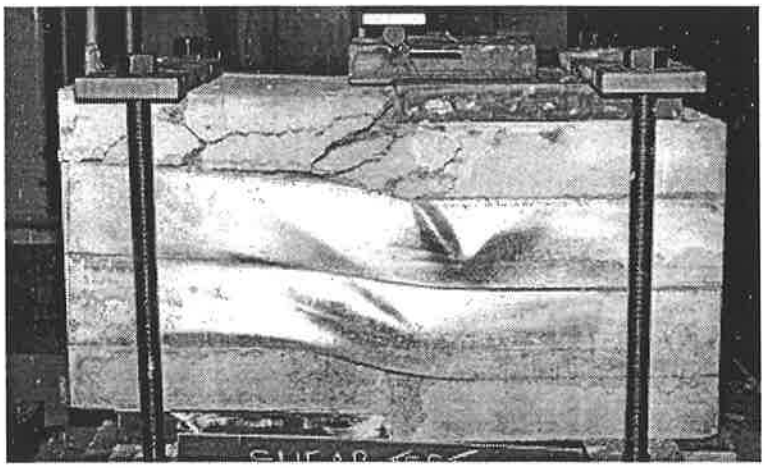


Fig. 6.28. Cracking pattern of S1.6

At the right hand end of the specimen shown in Fig. 6.28, the slip between the concrete and the sheeting can be seen. This view is magnified in Fig. 6.29. It can be seen that the slip at the top of the specimen is greater than at the bottom, and that the slip varies throughout the depth of each individual rib. This also occurred at the opposite end of the specimen, although the magnitude of the slip is not as great. This effect arises as a result of the shear deformation

in the ribs at the shear plane, which tends to distort a parallelogram into a trapezoid, as shown schematically in Fig. 6.30.

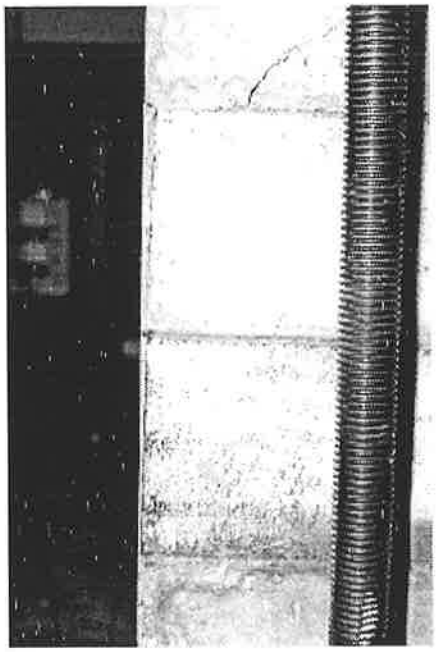


Fig. 6.29. Detailed View of End Slip for S1.6

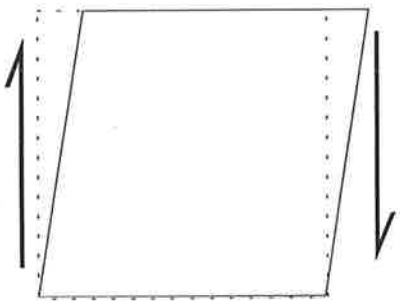


Fig. 6.30. Shear Deformation

Specimen S1.7

Specimen S1.7 showed similar load-displacement response to S1.6, as shown in Fig. 6.27. However, the cracking pattern of the specimen was somewhat different. The first cracks to appear were diagonal cracks, which started from the front face of the loading plates. This occurred at an applied load of 490 kN, and correspond to the slight drop in load shown in Fig. 6.27. This crack opened up as the load increased, and other finer cracks also developed. After the maximum load had been reached, the cracking pattern continued to develop, and cracks were evident from the ends of the specimen. The final crack pattern at the completion of the test, as seen from the side and end view of the specimen, is shown in Fig. 6.31 and Fig. 6.32 respectively.

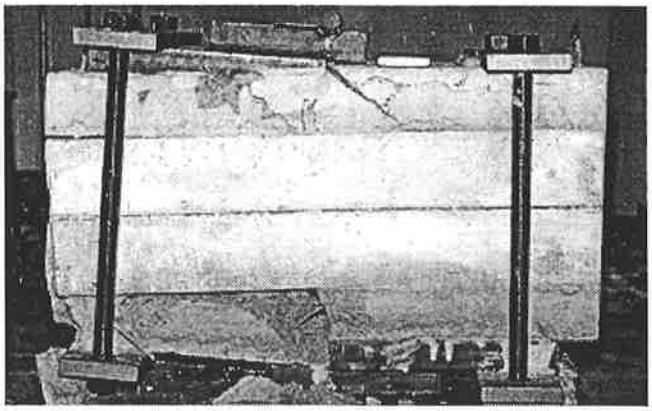


Fig. 6.31. Cracking Pattern for S1.7

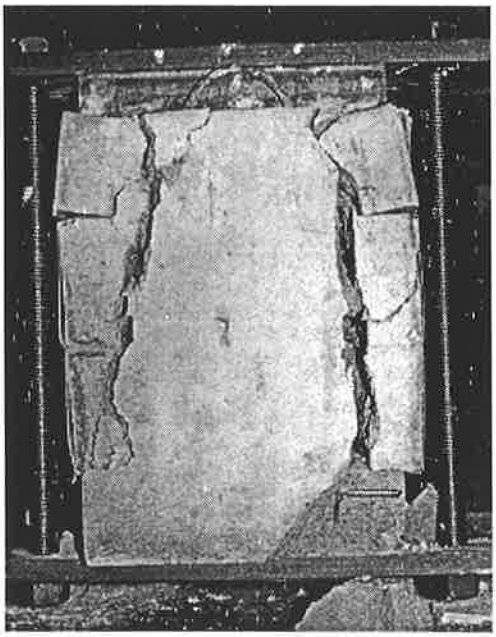


Fig. 6.32. End View of S1.7

It can be seen from Fig. 6.32 that the profiled ribs separated from the main body of the specimen, with the concrete still intact between the ribs. The side view shown in Fig. 6.31 indicates that the ribs were not bent into the same double curvature as occurred in specimen S1.6. Thus, the side sheets did not fail in shear, but rather debonded due to failure of the concrete in the plane between the sheeting and the enclosed concrete. Despite this change in the failure mode, the ultimate strength of 679 kN is 5% higher than that of Specimen S1.6 of 642 kN.

6.5.2 Series 2

6.5.2.1 Introduction

From the previous series it was found that the L-Rib sheeting provided the largest increase in the shear resistance, with the lowest rate of unloading in the post-ultimate load range. As a consequence of this, it was decided to focus the majority of the remaining tests on defining the critical properties of the L-rib sheeting in resisting transverse shear.

This series of tests was performed to investigate the influence on the shear strength of various changes in the L-Rib geometry. Specifically, the influence of the bond between the concrete and the profiled sheeting was looked at, as well as the contribution of the sheeting between the ribs to the overall shear resistance. To this end, specimens were designed with a shorter length of profiled sheeting, thus providing less area over which longitudinal bond could develop. The results could then be used to determine the sensitivity of the strength of the sheeting to the bond length. One specimen was also coated with grease before casting, to further reduce the effect of the bond. The contribution of the sheeting between the ribs was determined by producing specimens with this portion of the sheeting removed.

6.5.2.2 Plain Specimen

Specimen S2.1

A specimen was constructed and tested without any profiled sheeting, while the shear reinforcement was the same as for those specimens with the side profiled sheeting. The result of this test was to be used as a comparison, to determine the increase in the shear strength due to the side profiled sheeting.

The load-displacement curve for this specimen is shown in Fig. 6.33. The cracking load is 366 kN, which is similar to the values obtained from the plain specimens in Series 1. It can be seen from Table 6.4 and Table 6.5 that the compressive and tensile strengths of the two concrete mixes are quite similar, as are the properties of the reinforcing. Thus, the results of the shear tests may be compared with reasonable accuracy. A difference in the behaviour of this specimen from those plain ones in Series 1 shown in Fig. 6.12 is the lack of shear resistance after the maximum load has been reached, as denoted by Point C. The failure surface of the specimen was the same as that shown in Fig. 6.14 on page 356.

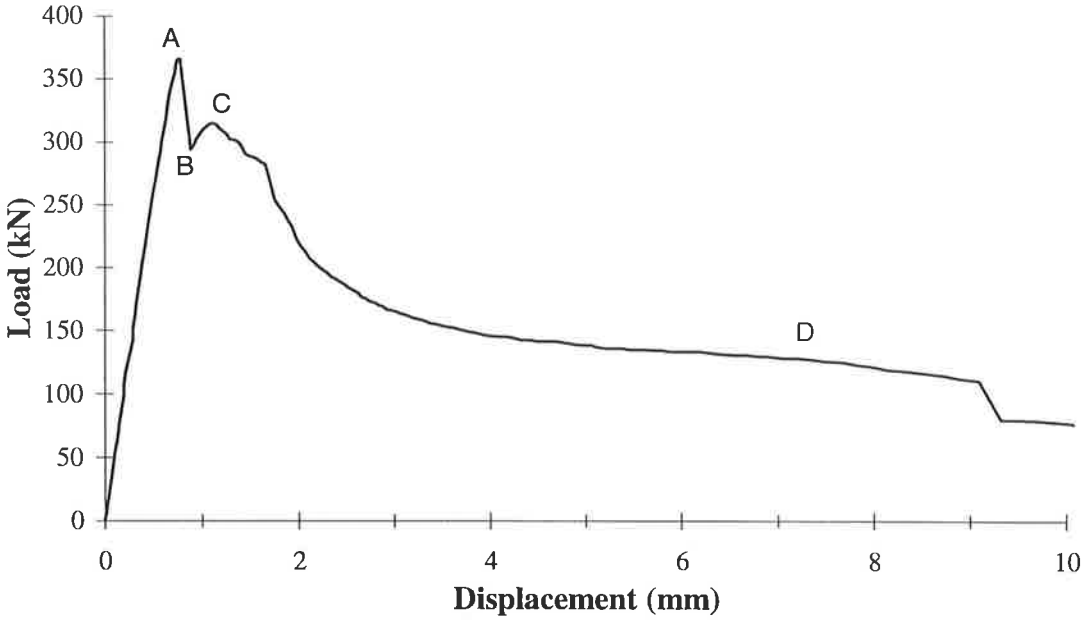


Fig. 6.33. Load vs Displacement for S2.1

6.5.2.3 L-Ribs

Specimens S2.2, S2.3 and S2.4 all had the same geometry. The geometry of the ribs is the same as the L-Ribs used in Series 1 and is shown in Fig. 6.26. The difference between these tests and those of Series 1, is that for this series the total length of the sheeting is 400 mm, which gives 200 mm of bond length on both sides of the shear plane, whereas for the previous series, the total length of the ribs was 700 mm. Specimen S2.4 differed from the other two tests in that grease was applied to the contact surface of the profiled sheeting before casting of the concrete.

Specimen S2.2

The load-displacement curves for specimens S2.2, S2.3 and S2.4 are shown in Fig. 6.34. It can be seen from this figure that the behaviour for each of these specimens were quite similar. There was a slight difference in the behaviour of S2.4, notably after the concrete had cracked. For specimen S2.2, cracking first occurred at an applied load of 495 kN. At this point cracking was not yet visible, and the cracks could only be identified after the shear resistance had dropped to 480 kN. Endslip was first noticed after the shear resistance had dropped to 460 kN, which corresponds to a displacement of the loading plates of 2.2 mm.

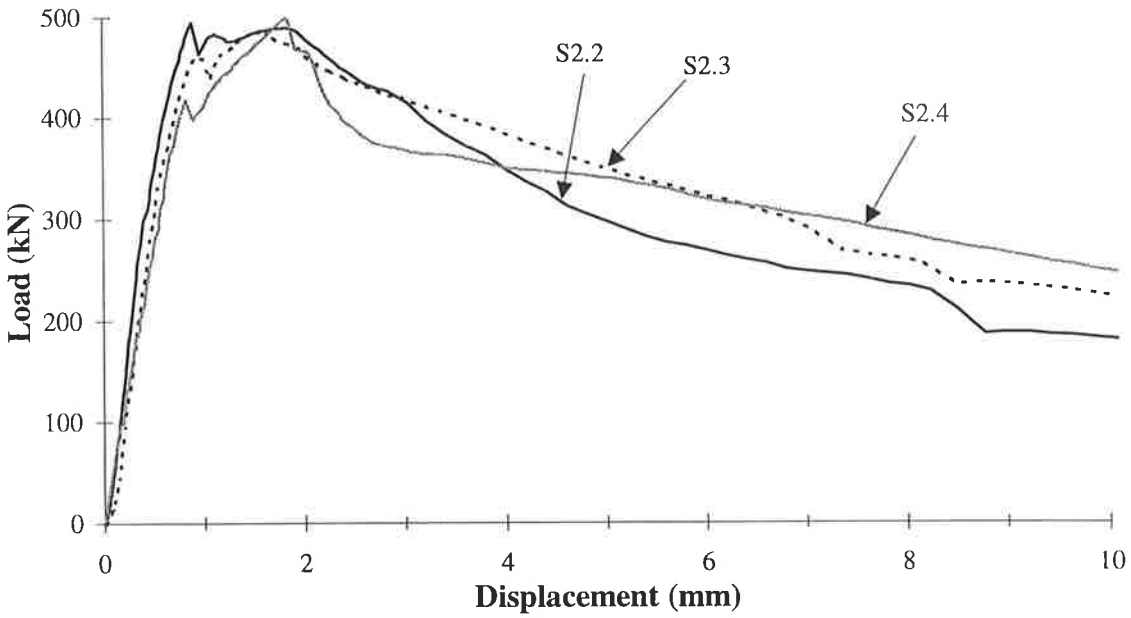


Fig. 6.34. Load vs Displacement for S2.2 and S2.3

The final shape of the specimen at the conclusion of the test is shown in Fig. 6.35. In this figure diagonal cracking can be seen on the outside face of the specimen. These cracks were limited to the concrete cover, and did not continue past the shear reinforcement. Throughout the section of the specimen, the shear plane was vertical, passing between the front edges of the two loading plates. There is some buckling which can be observed in the top rib. This did not occur until after advanced displacements had occurred, and thus the shear resistance had already been considerably reduced.

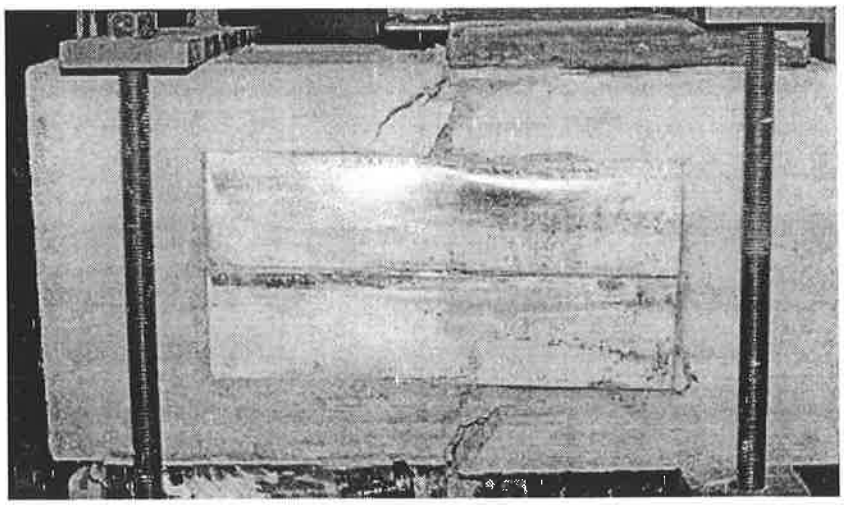


Fig. 6.35. Failed Shape of S2.2

Slip was observed at the ends of the sheeting, as shown in Fig. 6.36. It can be seen that the slip varies throughout the depth of the sheeting, as was observed for the full length L-Ribs in Series 1. The location of maximum slip varies for the different sides of the specimen, depending on the direction of the shear.



Fig. 6.36. Slip for L-Rib Specimens

Specimen S2.3

The cracking load was 465 kN and the subsequent maximum load was 487 kN. Endslip was visible right from the onset of cracking, although the magnitude was of the order of only 0.1 mm. The endslip continued to increase with increasing displacement of the loading plates. The crack pattern and slip distribution was similar to S2.2 as previously shown in Fig. 6.35 and Fig. 6.36 respectively.

Specimen S2.4

This specimen was the same as S2.2 and S2.3, except that grease was applied to the contact surface before pouring of the concrete. The overall behaviour is shown in Fig. 6.34, and is quite similar to the previous two specimens. Cracking first occurred at an applied load of 420 kN. End slip was noticeable as soon has cracking had first commenced, and continued to increase throughout the test. The development of the cracks followed a very similar pattern to the previous two tests and are shown in Fig. 6.37. It can also be seen from this figure that there was slightly more buckling in sheeting in this specimen, than was observed in the previous ones.

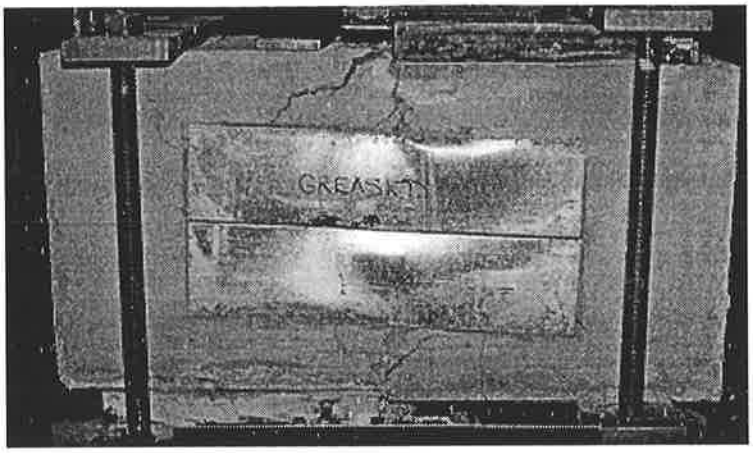
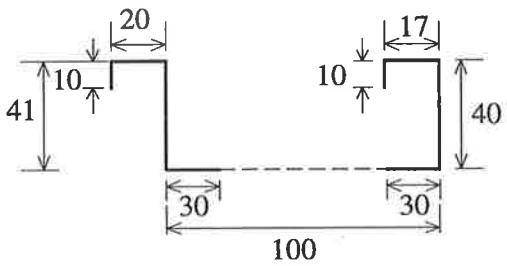


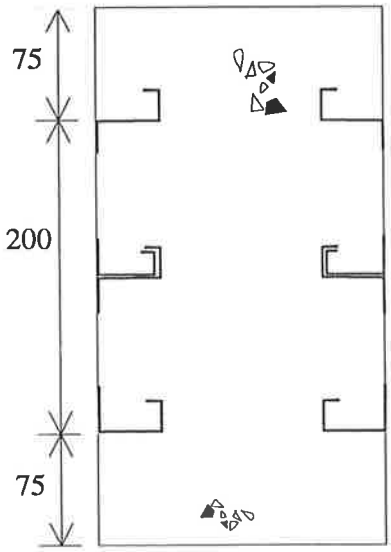
Fig. 6.37. Cracking Pattern of S2.4

6.5.2.4 L-Rib Cut Out

Specimens S2.5 and S2.6 were constructed to investigate the contribution of the sheeting between the ribs. The geometry of the ribs is shown in Fig. 6.38. The load-displacement response of the two specimens is shown in Fig. 6.39. It can be seen from this



(a) Profile Geometry



(b) Specimen Geometry

Fig. 6.38. Geometry of L-Ribs for S2.5 and S2.6

figure that the responses of the two specimens are very similar. Also shown in this figure is the response from specimen S2.3, which consisted of the complete rib. From a comparison of these curves, it appears that the sheeting between the ribs contributes very little to the overall shear resistance of the specimen.

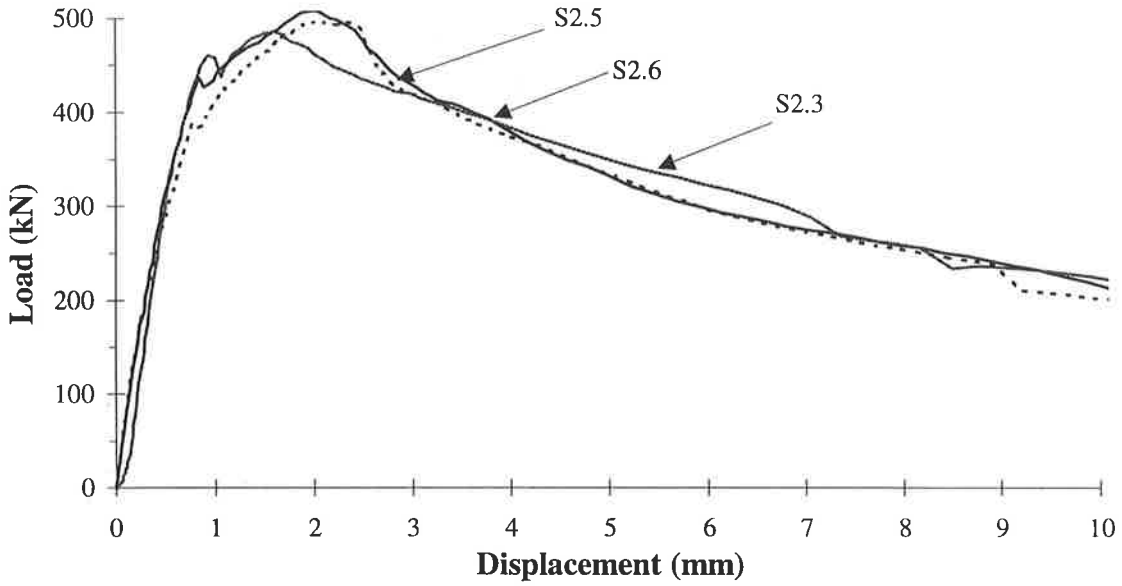


Fig. 6.39. Load vs Displacement Response for S2.3, S2.5 and S2.6

Specimen S2.5

The concrete first cracked at an applied load of 438 kN, after which there was only a slight drop in load. The ultimate load of the specimen was 509 kN. The first crack that could be visually identified was a diagonal crack leading from the front edge of the top loading plate. This is shown in Fig. 6.40. The first signs of endslip became visible at an applied load of 500 kN. This corresponded to the formation of a vertical shear crack which originated from the bottom loading plate. The final deformed shape of the specimen is shown in Fig. 6.41. This shows the distribution of diagonal cracks that formed from the ribs towards the loading plate.

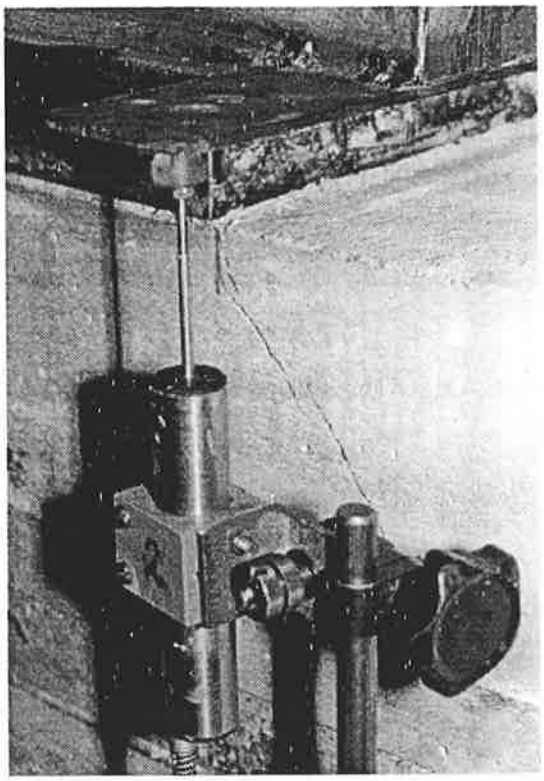


Fig. 6.40. Cracking for S2.5

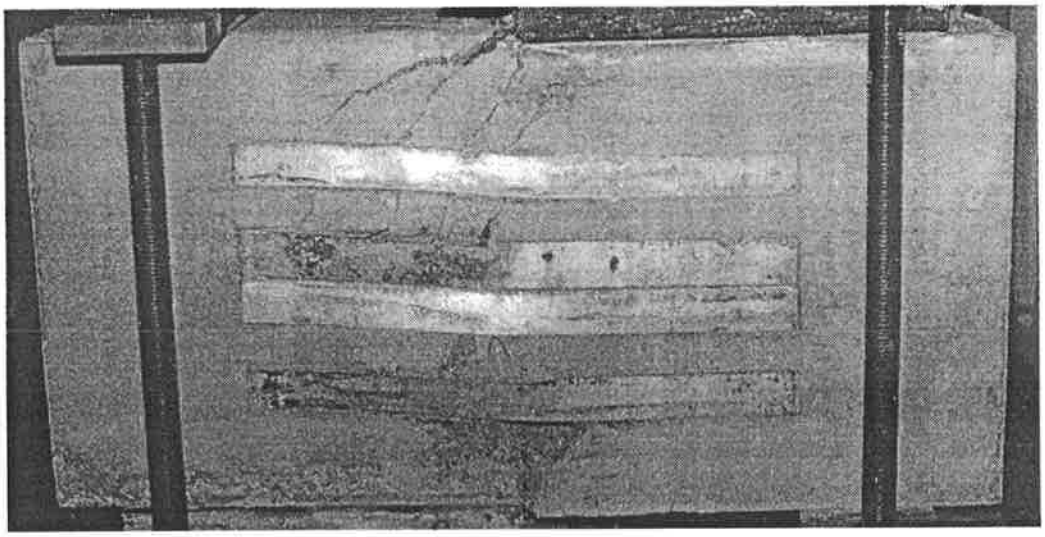


Fig. 6.41. Failure of S2.5

Specimen S2.6

Cracking first commenced at an applied load of 395 kN, and the ultimate load was 497 kN. The formation of cracks and the overall behaviour of this specimen was similar to specimen S2.5. It can be seen from Fig. 6.39 that the two load-displacement curves are almost identical.

6.5.2.5 Dove Tail Specimens

Specimen S2.7

This specimen was the same as Specimens S1.4 and S1.5, except that the length of the profiled sheeting was only 400 mm, which provided 200 mm of sheeting on each side of the shear plane. The resulting load-displacement curve is shown in Fig. 6.42, with the curve from one of the dovetail specimens from Series 1. It can be seen that the reduction of the bond length does not appear to adversely effect the shear capacity of the dovetail ribs. From Fig. 6.42 it appears that there is a slight increase in the post-failure shear capacity for the specimen with the reduced rib length.

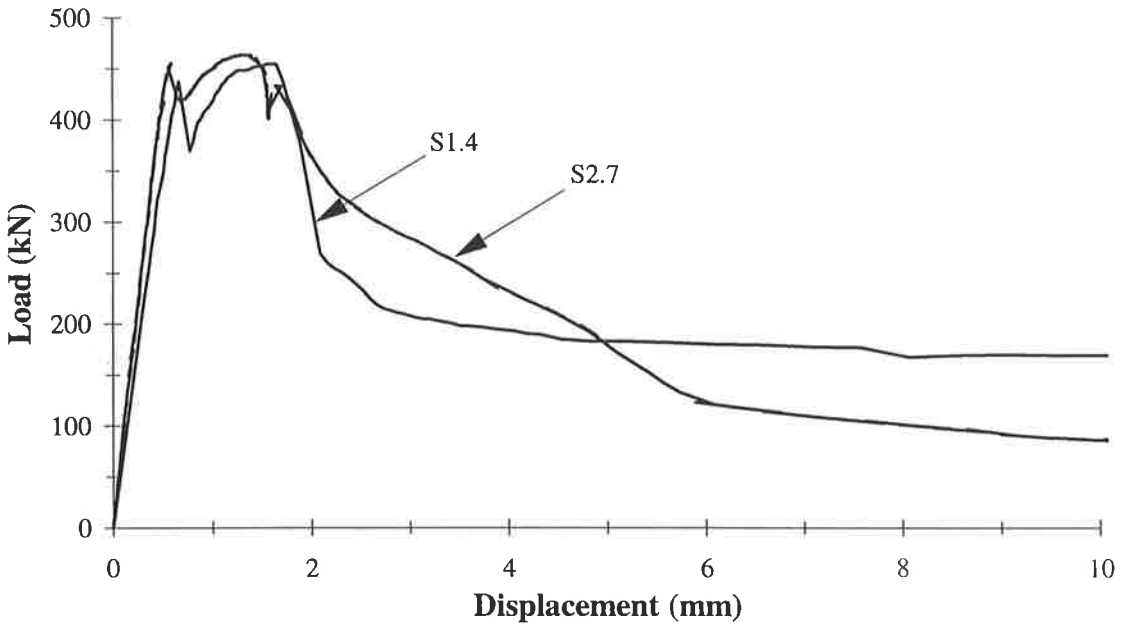
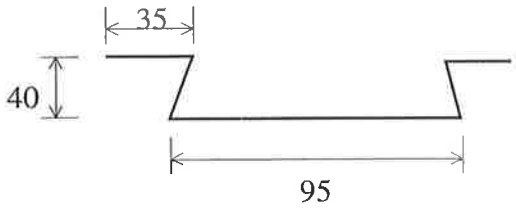


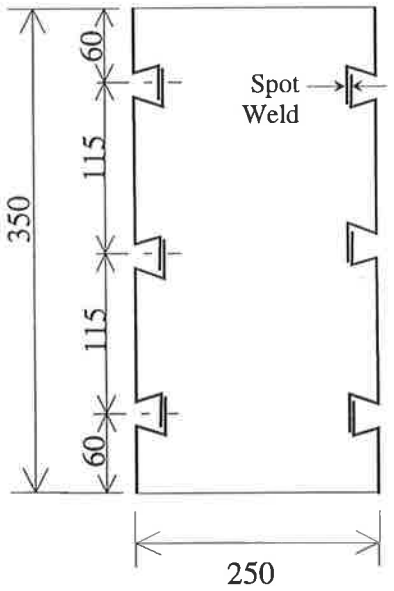
Fig. 6.42. Load vs Displacement for S2.7

Specimen S2.8

The geometry of the profiled sheeting for this specimen is the same as that used to construct a full scale composite profiled beam. The beam was constructed as part of an initial investigation into the feasibility of profiled beam construction. The shear specimen was constructed so as to determine an estimate for the shear capacity of the beam when it is tested. The length of the sheeting was 700 mm, and the geometry of the sheeting is shown in Fig. 6.43. The resulting load-displacement curve from the test is shown in Fig. 6.44, with the result from specimen S2.7 plotted also as a comparison. The geometry of specimen S2.7 is not identical to that of S2.8, as shown from a comparison of Fig. 6.21 and Fig. 6.43.



(a) Profile Dimensions



(b) Specimen Dimensions

Fig. 6.43. Geometry of Sheeting for S2.8

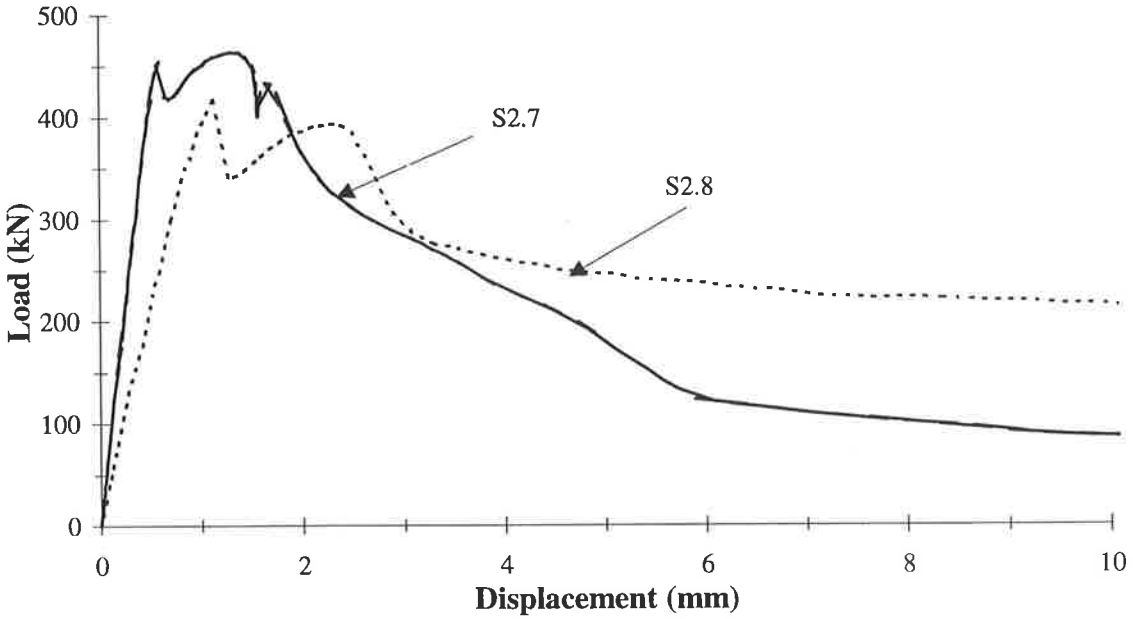


Fig. 6.44. Load vs Displacement for S2.8

It can be seen from Fig. 6.44 that the strength and stiffness of this rib geometry is less than that used for specimen S2.7, but that the residual strength after the ultimate load has

been reached is greater. As the specimen was being loaded, it was not possible to detect any end slip, but after the shear resistance had reduced to approximately 70% of the ultimate, some slip became evident.

6.5.3 Series 3

6.5.3.1 Introduction

This series of tests was performed to investigate the influence on the shear strength of various changes in the L-Rib geometry. Specifically, the effect of the sheeting thickness on the shear strength was investigated, as well as further tests to determine the contribution of the sheeting between the ribs to the overall shear strength. A test was also carried out on a specimen which had the same L-Rib profiled sheeting as used in the previous series, but had no shear reinforcement present. This test was carried out to check the shear performance of the side profiled sheeting in the absence of other shear transfer mechanisms. The remaining tests had the standard arrangement of shear reinforcement, as shown in Fig. 6.7a on page 348. The sheeting thickness was varied from 0.6 mm to 2.0 mm, with the geometry of the L-Rib the same as for the previous series. The contribution of the sheeting between the ribs was determined by producing specimens with this portion of the sheeting removed, as was carried out in the previous series. These tests used 1.0 mm thick sheeting.

Specimen S3.1

This specimen was constructed using the same L-Rib geometry as was adopted for the previous series and shown in Fig. 6.21 on page 361 except that there was no shear reinforcement present. This specimen was constructed so as to determine the strength of the profiled sheeting by itself. The resulting load-displacement curve is shown in Fig. 6.45, with the results from the Series 1 tests plotted also for a comparison. It can be seen from this figure that the presence of the shear reinforcement has only a small effect on the strength of the specimen. There is, however, a marked change in the post-ultimate behaviour of the specimen without the shear reinforcement, with a much more rapid reduction in load carrying capacity after the ultimate load had been reached.

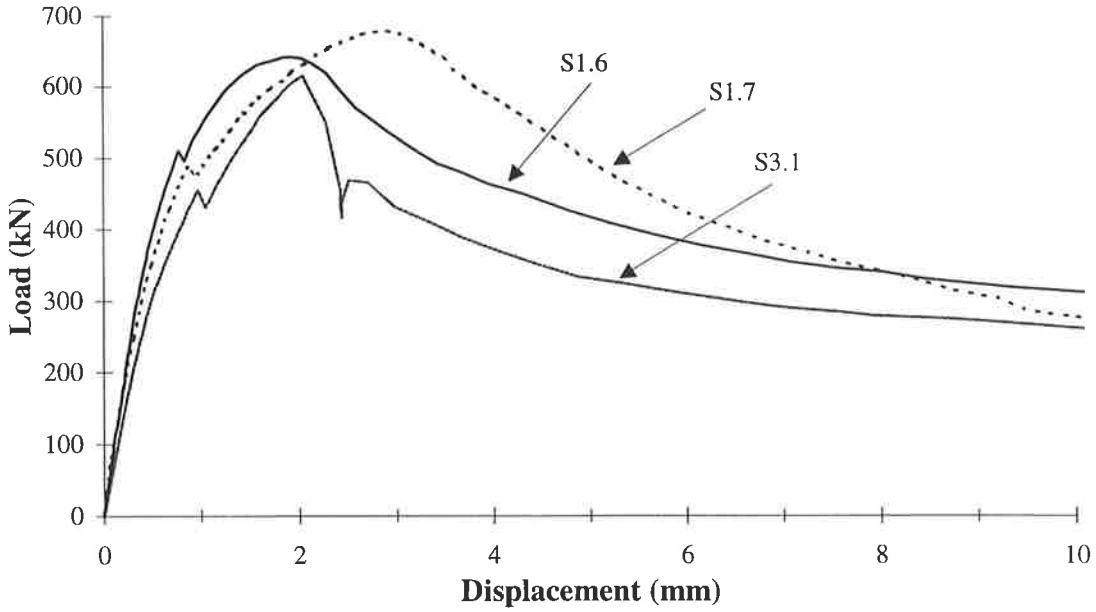


Fig. 6.45. Load vs Displacement for S3.1

Specimen S3.2

This specimen contained no profiled sheeting, and was intended to be used as a calibration test. However, due to a malfunction of the hydraulic equipment the load was applied within a span of 1 second, and no readings of displacement were taken. The ultimate load of this specimen was 620 kN, but due to the rapid application of the load, it is expected that this value represents an upper bound to the shear resistance of the specimen, had the load been applied in a more controlled manner.

6.5.3.2 L-Rib, Thickness 0.6 mm

Specimens S3.3 and S3.4 had the same L-Rib geometry as was used in the previous two series. The ribs extended for the full length of the specimen. The sheeting used for these tests was 0.6 mm Total Coated Thickness, as opposed to the 1.0 mm TCT sheeting used in the previous series. These tests were performed in order to determine the effect of the thickness of the sheeting on the shear resistance. The average ultimate load for the two 0.6 mm specimens is 558 kN, compared to 660 kN for the two 1.0 mm specimens. This represents a decrease of 15%.

Specimen S3.3

The cracking load for this specimen was 415 kN, and the ultimate load was 510 kN. The load-displacement curve is shown in Fig. 6.46, with the results from the tests on the 1.0 mm sheeting shown for comparison. It can be seen from this figure that the overall form

of the load-displacement curve is similar, but that the ultimate load is lower for the thinner gauge sheeting.

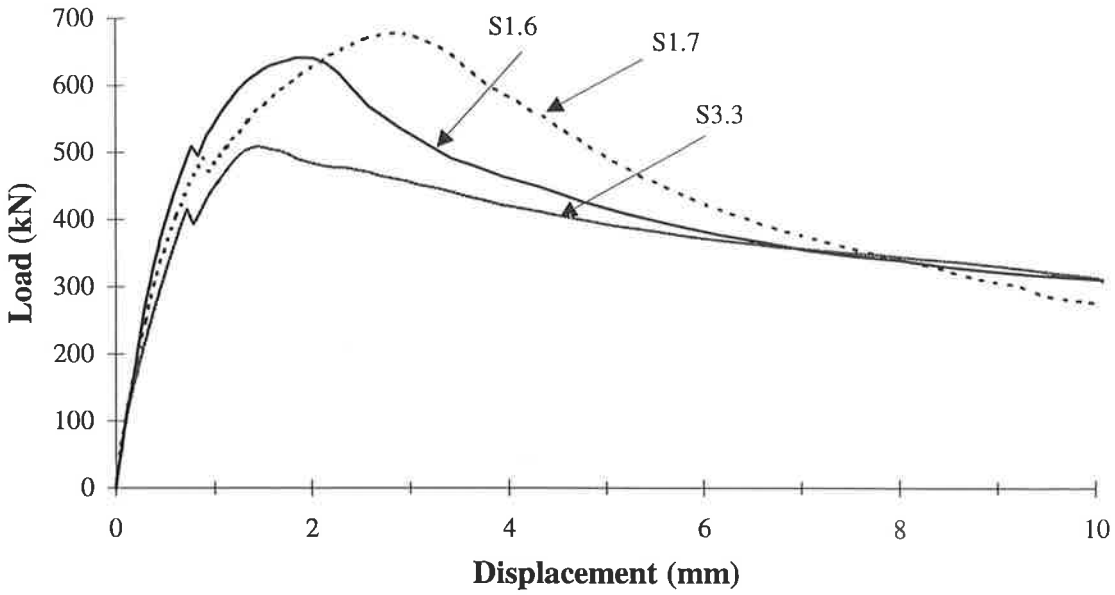


Fig. 6.46. Load vs Displacement for S3.3 and S3.4

A cracking sound was heard at an applied load of 360 kN, which indicated the breaking down of the chemical bond. Buckling was noticed in the profiled sheeting between the ribs at an applied load of 500 kN, which occurred before the maximum load was reached. End slip did not become noticeable until after large displacements had occurred between the loading plates, and thus the shear resistance had dropped significantly. The specimen after failure is shown in Fig. 6.47, which shows the buckling in the sheeting.

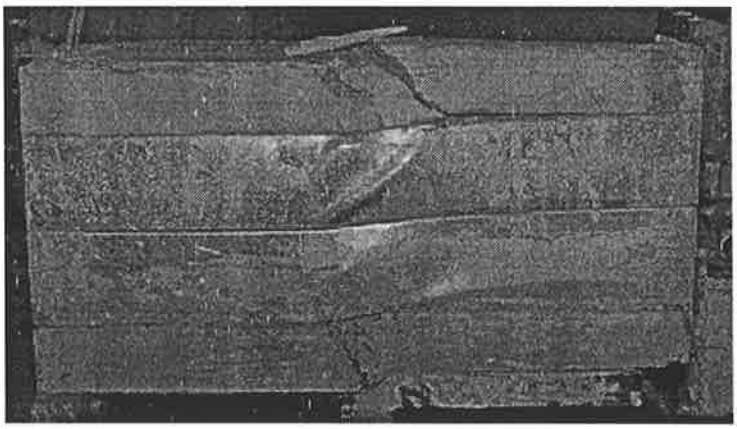


Fig. 6.47. Specimen S3.3 after Testing

Specimen S3.4

This specimen is the same as S3.3. For this test there was an error with the data logging equipment, and the load-displacement curve was not recorded. The ultimate load for this specimen was 607 kN. Cracking was heard at an applied load of 160 kN, indicating the break down of the chemical bond. Buckling was first noticed at an applied load of 260 kN, which was well below the ultimate load of the member, and that at which buckling was noticed for specimen S3.3.

6.5.3.3 L-Rib, Thickness 2.0 mm

Specimens S3.5 and S3.6 had the same L-Rib geometry as was used in the previous two series. The ribs extended for the full length of the specimen. The sheeting used for these tests was 2.0 mm Total Coated Thickness. These tests were performed in order to determine the effect of the thickness of the sheeting on the shear resistance. The load-displacement curves from the tests are shown in Fig. 6.48, along with the results for the 1.0 mm sheeting. It can be seen that the 2.0 mm ribs produce a significant increase in the shear resistance of the specimens. The average ultimate load for the two 2.0 mm specimens is 826 kN, compared to 660 kN for the two 1.0 mm specimens. This represents an increase of 25%.

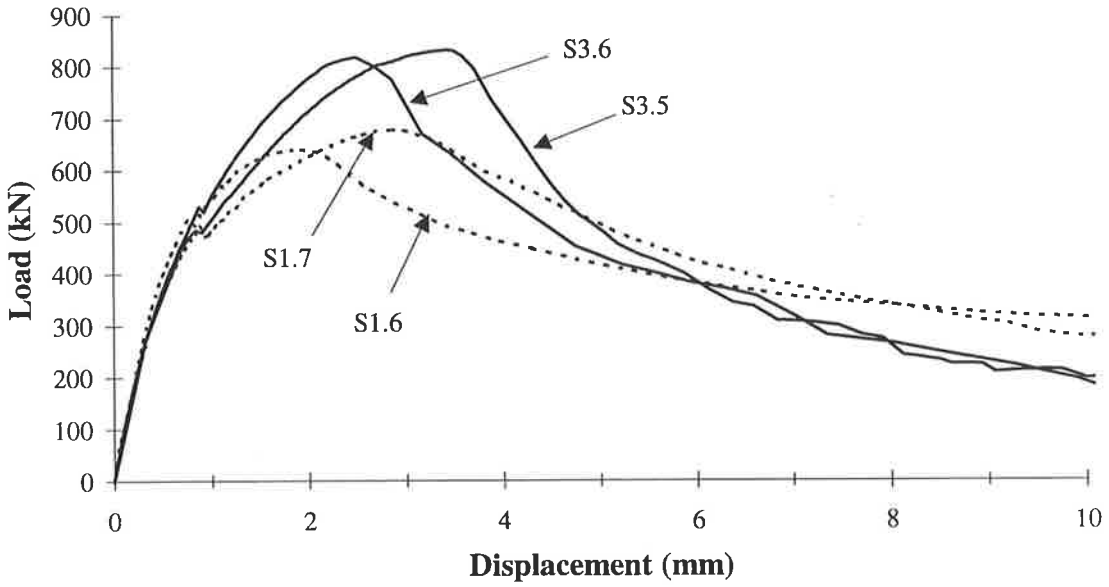


Fig. 6.48. Load vs Displacement for S3.5 and S3.6

Specimen S3.5

Cracking was first evident at an applied load of 630 kN, although there was no drop in the shear resistance that accompanied this. The ultimate load of the specimen was 833 kN. There was no buckling evident in the sheeting at any stage during the testing. The cacking remained minor until the displacement of the loading plates had reached 6 mm, which corresponds to a shear resistance of approximately 350 kN. The ribs deformed only slightly, as shown in Fig. 6.49. The ribs remained almost completely straight and sheared the concrete, as shown in Fig. 6.50.

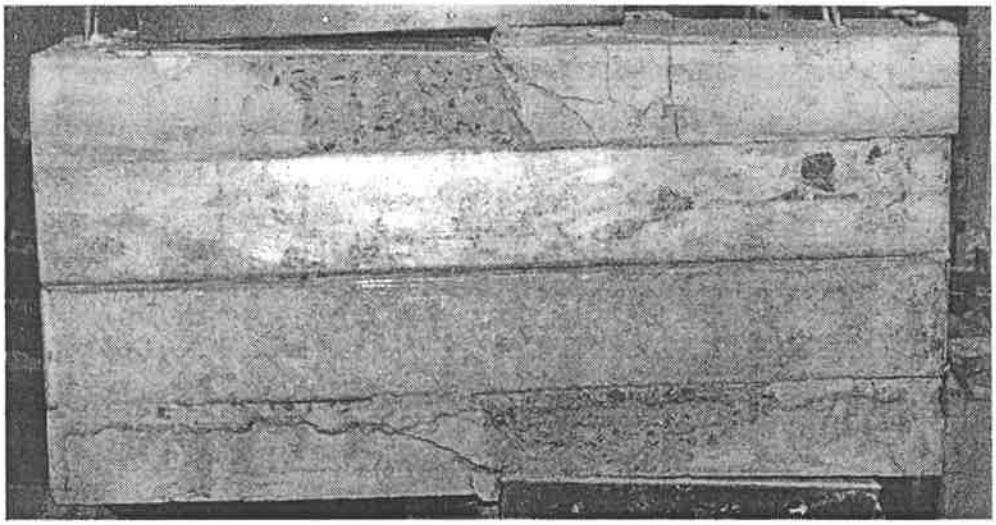


Fig. 6.49. Specimen S3.5 after Testing



Fig. 6.50. End View of Specimen S3.5

Specimen S3.6

Cracking first occurred at an applied load of 530 kN and the ultimate load was 819 kN. At the ultimate load the cracks were only very fine, and did not open up until after significant displacement of the loading plates had occurred. The overall behaviour of the specimen was similar to S3.5 and the final appearance is similar to that shown in Fig. 6.49 and Fig. 6.50.

6.5.3.4 L-Rib Cut

Specimens S3.7 and S3.8 were the same as the cut out tests in Series 2, S2.5 and S2.6, except that the profiled sheeting extended the full length of the specimen. The ribs for Specimen S3.7 were greased before the concrete was poured, so as to eliminate any chemical bond between the concrete and the profiled sheeting, whereas the ribs for Specimen S3.8 were left ungreased.

The load-displacement curve for the two specimens is shown in Fig. 6.51, with the result from S2.5 shown also as a comparison. It can be seen from the figure that there is a slight increase in the shear resistance of these specimens over those with the profiled sheeting that does not extend the full length of the specimen, and that the ungreased specimen has a slightly higher ultimate load than the greased specimen. Due to the variability that had been observed in some of the shear specimens, it is not possible to draw solid conclusions about

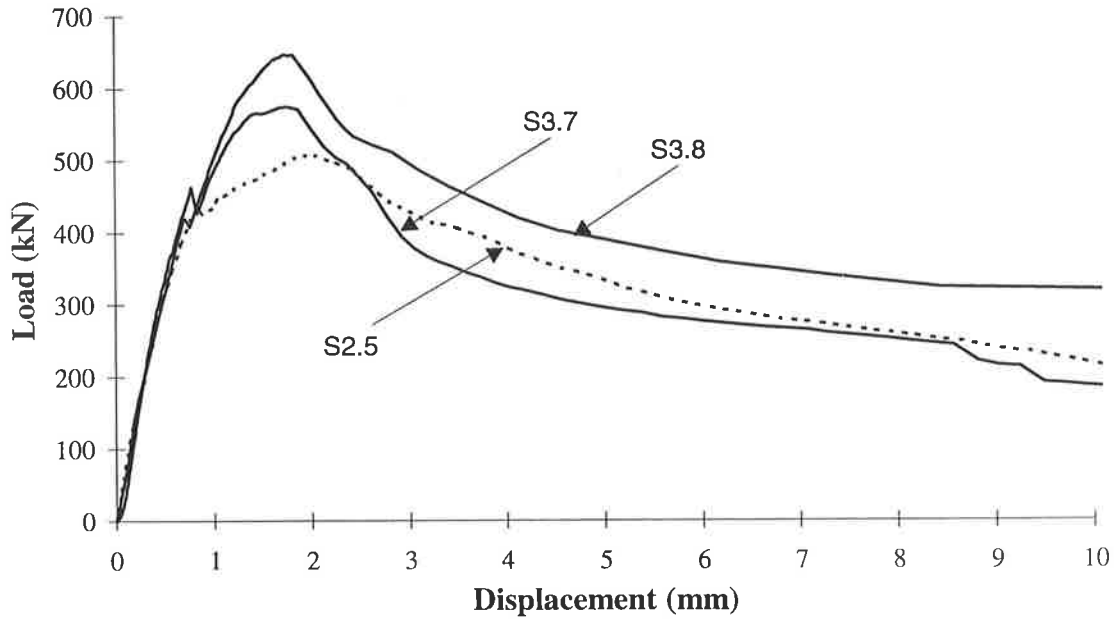


Fig. 6.51. Load vs Displacement for S3.7 and S3.8

the effect that greasing had on the behaviour of Specimen S3.7, when compared to the result from Specimen S3.8. However, it is likely that the grease was responsible for the 12% decrease in ultimate load.

Specimen S3.7

The cracking load was 463 kN, and the ultimate load was 575 kN. Some slight buckling of the sheeting was noticeable at an applied load of 390 kN. The first crack to form was a single vertical crack between the front edges of the two loading plates. Slip became visible after the ultimate load had been reached, and increased rapidly with increasing displacement of the loading plates. The degree of cracking at the completion of the test was less than had been observed for the previous L-Rib Specimens, and the slip was larger. The specimen is shown in Fig. 6.52 at the completion of the test.

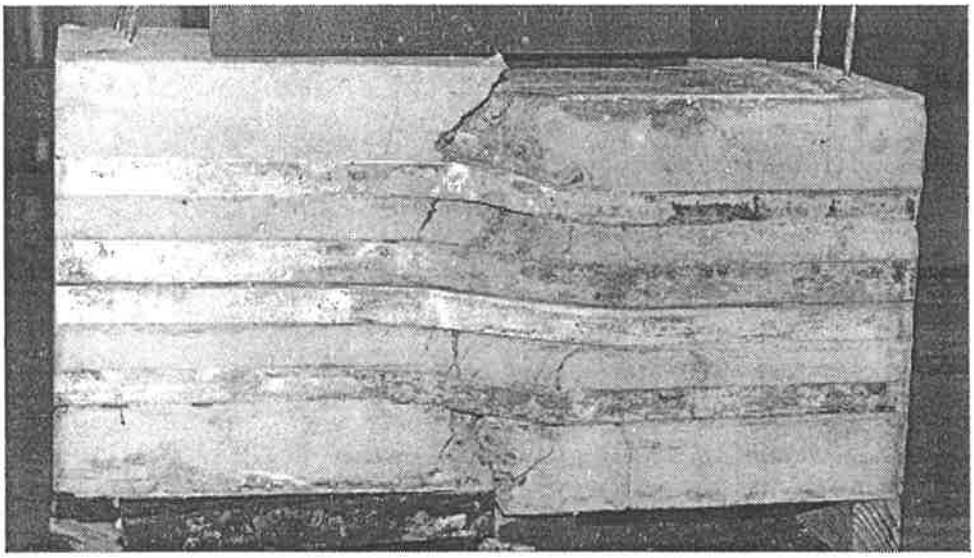


Fig. 6.52. Specimen S3.7 after Testing

Specimen S3.8

Cracking first occurred at an applied load of 420 kN, and the ultimate load was 647 kN. Buckling was noticed in the ribs at an applied load of 640 kN, ie. just before the ultimate load was reached. End slip was noticeable just after the ultimate load had been reached. This continued to increase as the shear resistance decreased. The cracking pattern and the final appearance of the specimen was similar to S3.7, as shown in Fig. 6.52.

6.5.4 Summary

A summary of the results is given in Table 6.6. The results have been tabulated for each test at four distinct points. These points are shown schematically in Fig. 6.53.

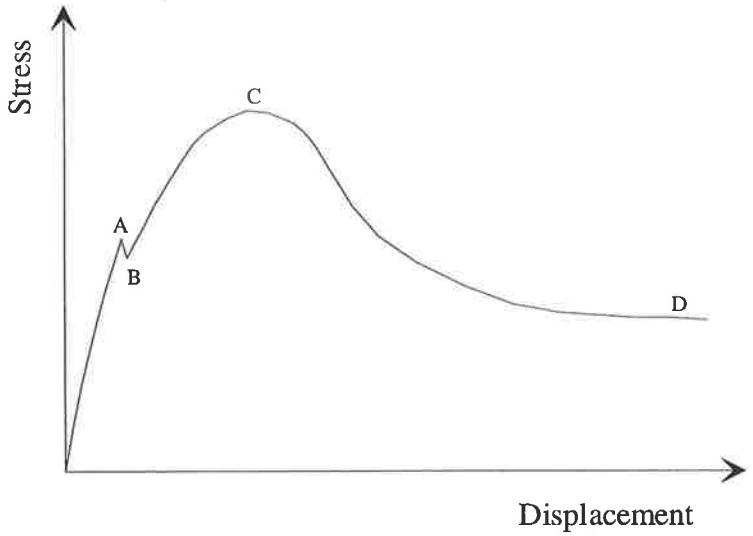


Fig. 6.53. Typical Load vs Displacement Curve

Test No.	Profile Shape	Cracking Load Point A		Post-Cracking Load Point B		Post Cracking Maximum Point C		Residual Load (kN) Point D	
		Load (kN)	Displacement	Load (kN)	Displacement	Load (kN)	Displacement	Load (kN)	Displacement
S1.1	-	406	0.96	342	1.04	391	1.36	125	7.3
S1.2	-	329	0.61	296	0.70	381	1.30	105	6.4
S1.3	Trapazoidal	392	0.65	313	0.79	350	1.12	145	7.7
S1.4	Dove Tail	438	0.67	370	0.78	455	1.65	170	9.0
S1.5	Dove Tail	389	0.62	332	0.67	336	0.76	185	10.0
S1.6	L-Rib	510	0.77	496	0.84	642	1.93	315	10.0
S1.7	L-Rib	491	0.89	472	0.95	679	2.86	280	10.0
S1.8	Trapeziodal	383	0.80	317	0.88	317	1.27	145	6.7
S2.1	-	366	0.78	294	0.89	315	1.11	125	7.7
S2.2	L-Rib	495	0.88	464	0.96	490	1.83	185	10.0
S2.3	L-Rib	460	0.93	438	1.07	486	1.61	230	9.5
S2.4	L-Rib	417	0.83	398	0.90	499	1.83	250	10.0
S2.5	L-Rib (Cut)	436	0.85	427	0.89	508	2.00	215	10.0
S2.6	L-Rib (Cut)	388	0.78	384	0.84	496	2.11	205	9.5
S2.7	Dove Tail	455	0.60	418	0.69	464	1.37	100	8.0
S2.8	Dove Tail*	417	1.13	339	1.28	393	2.32	220	8.5
S3.1	L-Rib	455	0.98	431	1.05	615	2.04	265	9.0
S3.2	-	-		-		620**		-	
S3.3	L-Rib	415	0.73	393	0.79	510	1.45	320	9.5

Test No.	Profile Shape	Cracking Load Point A		Post-Cracking Load Point B		Post Cracking Maximum Point C		Residual Load (kN) Point D	
		Load (kN)	Displacement	Load (kN)	Displacement	Load (kN)	Displacement	Load (kN)	Displacement
S3.4	L-Rib	-		-		607		-	
S3.5	L-Rib	485	0.85	481	0.91	833	3.41	210	9.0
S3.6	L-Rib	530	0.88	520	0.93	819	2.50	150	10.0
S3.7	L-Rib (Cut)	463	0.78	427	0.84	575	1.76	185	10.0
S3.8	L-Rib (Cut)	420	0.72	409	0.77	647	1.82	320	8.0

* The sheeting geometry for this specimen was different to the other Dove Tail specimens.
** This specimen was tested very rapidly, and this value represents an upper bound to the strength

Table 6.6. Summary of Shear Tests

6.5.4.1 Sheeting Rib Geometry

The effect of changes in the rib geometry on the shear behaviour is shown in Fig. 6.54. Only one of each type of rib geometry is shown in this figure, so as to indicate the trend of results. The variation in behaviour can be seen for the different profiled geometries. There is an increase in the load at which cracking occurs as the rib opening decreases. That is, the trapezoidal rib specimens offer the least average increase in the cracking load over the average of the plain specimens of 5%, followed by the dove-tail rib with an average increase of 13%, while the L-rib offers the greatest average increase of 36%.

The strength of all specimens except the trapezoidal rib specimen had a larger ultimate load carrying capacity than the load at which cracking occurred. The reason for the lower post-cracking maximum in the trapezoidal specimen may be due to the fracture of the concrete between the profiled ribs, which then lead to a decreased area of the shear plane, and thus a reduced shear resistance after initial cracking.

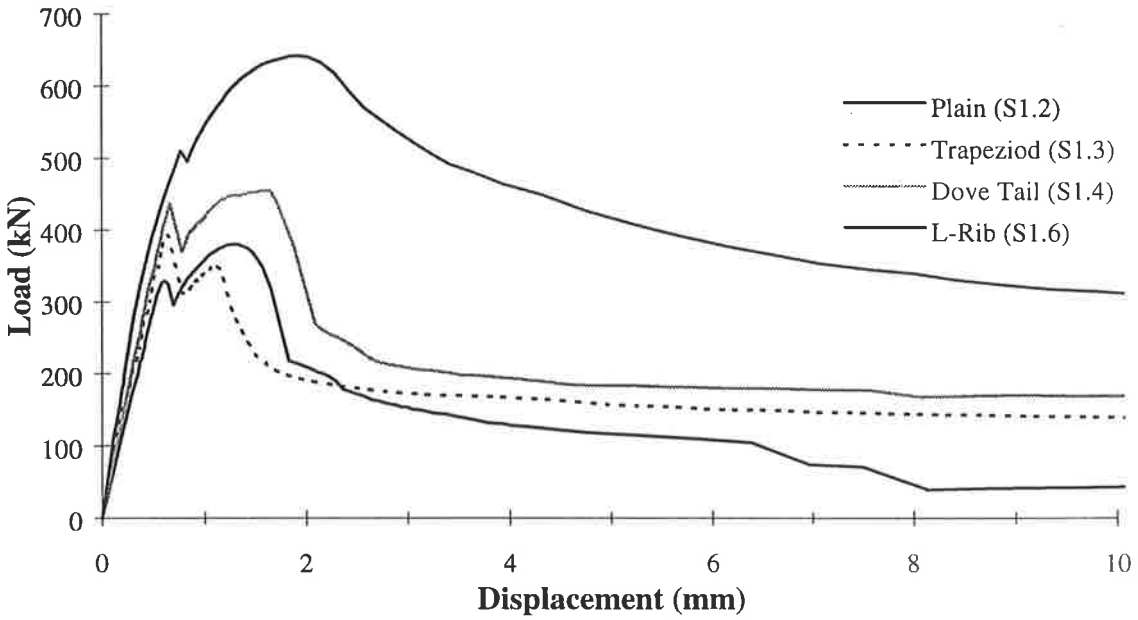


Fig. 6.54. Influence of Sheeting Rib Geometry on Shear Strength

The average post-cracking maximum load of the trapezoidal rib specimens was 13% less than the average of the plain specimens. The average ultimate shear resistance of the two dovetail rib specimens show an increase of 2% over the plain specimens. There was, however, significant variation between the two results of the dovetail tests, with one test recording an ultimate shear resistance 18% larger than the average of the plain specimens,

while the other test recorded an ultimate shear resistance 13% less than the average. The L-Ribs can be seen to have performed the best of any of the profiled rib geometries. The drop in strength at first cracking is minimal, the average increase in strength over the plain specimens is 73%, the decrease in shear resistance after the maximum has been achieved is much less, and the displacement at the maximum load is larger which indicates good ductility.

6.5.4.2 Sheeting Thickness

The effect of variation in sheeting thickness on the shear behaviour is shown in Fig. 6.55. The load vs displacement curves are compared with the results of the plain specimens, to give an indication of the increase in shear resistance due to the side sheeting. As stated in Section 6.5.3.2, there were two specimens tested with a sheeting thickness of 0.6 mm, however due to problems with the electronic recording equipment, only one load-displacement curve was recorded. The ultimate load of the second 0.6 mm specimen was 607 kN. There is a clear increase in the ultimate shear resistance with increasing thickness of the sheeting. This varies from 559 kN for the 0.6 mm sheeting, to 661 kN for the 1.0 mm sheeting, to 826 kN for the 2.0 mm sheeting. The specimens with the 2.0 mm sheeting show a greater reduction in the shear capacity after the ultimate load than the other specimens.

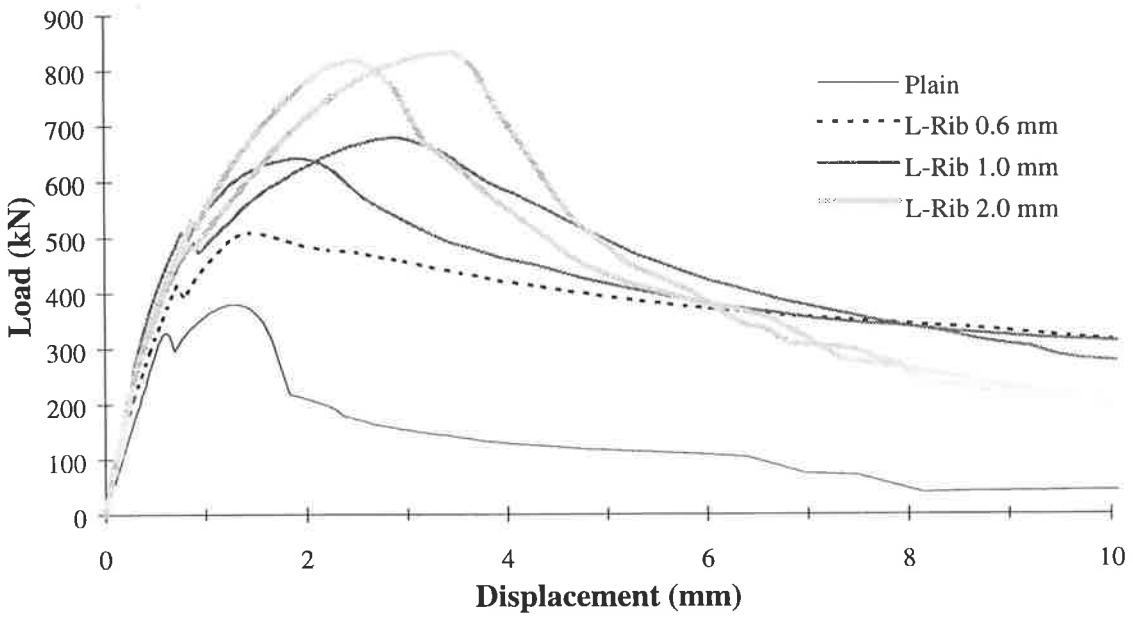


Fig. 6.55. Influence of Sheeting Thickness on Shear Strength

6.5.4.3 External Sheeting Contribution

The effect of the external sheeting between the ribs on the shear resistance of the specimen can be seen in Fig. 6.56. The load vs displacement curves are compared with the results of the plain specimens, to give an indication of the increase in shear resistance due to the side sheeting. Its contribution to the shear resistance was determined by testing specimens with and without the sheeting between the ribs. The arrangement of the profiled sheeting for the specimens with the sheeting between the ribs is shown in Fig. 6.26 on page 364 while those without the sheeting is shown in Fig. 6.38 on page 372. It can be seen in Fig. 6.56 that there is little difference in the shear response of the different specimens. For specimens with a 700 mm length of sheeting the average ultimate shear resistance for the specimens with the complete L-Ribs was 661 kN while the result without the external sheeting was 647 kN This represents a decrease of 14 kN or 2% for the specimen without the external sheeting. For specimens with a 400 mm length of sheeting the average ultimate shear resistance for the specimens with the complete L-Ribs was 488 kN, while the result for the L-Ribs with the external sheeting removed was 502 kN. This represents a slight increase of 14 kN or 3% for the specimens without the external sheeting. These small variations indicate that the contribution of the external side sheeting between the ribs to the transverse shear resistance is minimal for the 1.0 mm thick sheeting.

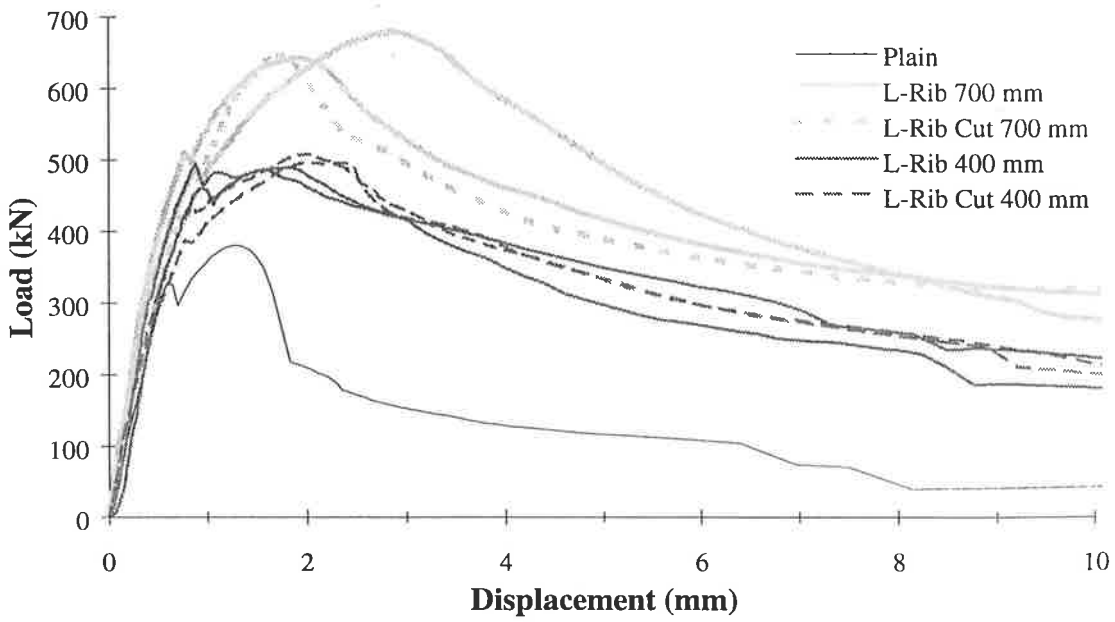


Fig. 6.56. Influence of Sheeting between Ribs on Shear Strength

6.5.4.4 Longitudinal Bond

The influence of the longitudinal bond between the sheeting and the concrete is shown in Fig. 6.57 for those specimens with the complete L-Ribs, while the results for the specimens with the cut L-Ribs are shown in Fig. 6.58. The amount of longitudinal bond that developed between the concrete and the sheeting was varied by adjusting the bond length of the sheeting on either side of the shear plane. For those specimens with the 700 mm length of sheeting there was a bond length of 350 mm on either side of the shear plane, while for those with a 400 mm length of sheeting the bond length was 200 mm. The bond between the sheeting and the concrete was further reduced by the application of a debonding agent, which was applied to the surface of the sheeting prior to pouring the specimens. The debonding agent was the same as was used for the push tests of Chapter 3.

It can be seen in Fig. 6.58 that the specimens with the longest bond length had the highest ultimate transverse shear resistance, with an average value of 661 kN. The results of the specimens with the 400 mm length of sheeting were similar for the greased and non-greased specimens. The average of the ultimate transverse shear resistance for the ungreased specimens was 488 kN, while the ultimate shear resistance of the greased specimen was 499 kN. The difference between the results of the greased and non-greased specimens is 2%, which can be accounted for by natural variations in the specimens.

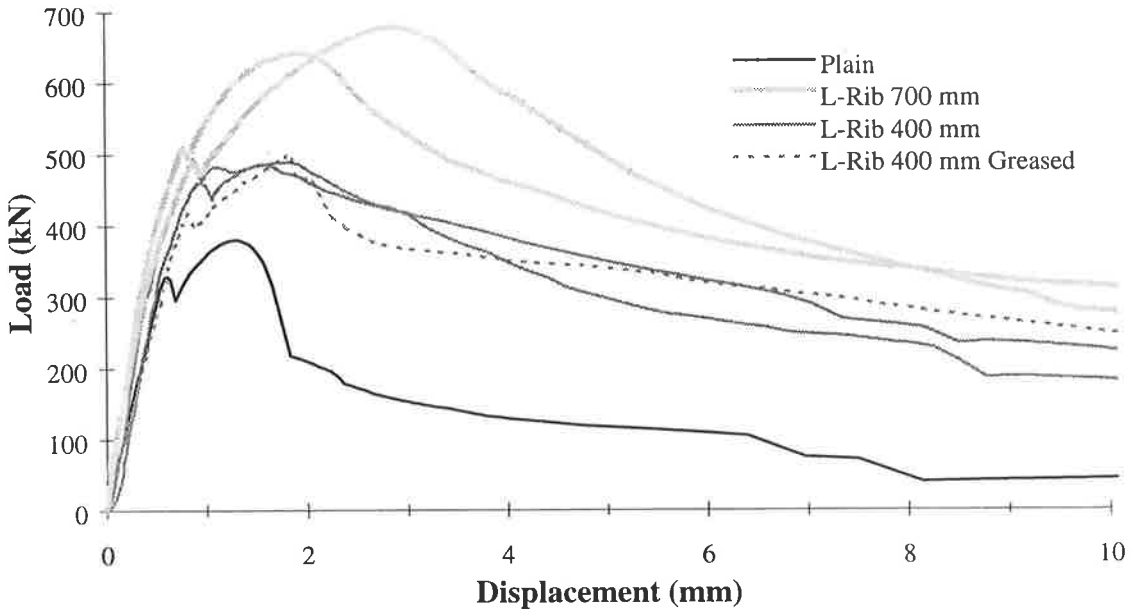


Fig. 6.57. Influence of Longitudinal Bond on Transverse Shear Strength for Uncut L-Ribs

The results of the tests on the specimens with the cut L-Rib sheeting are shown in Fig. 6.58. It can be seen that there is a general trend towards a decrease in the ultimate transverse shear resistance for those specimens which develop a lower longitudinal bond. The specimen with the ungreased 700 mm length of sheeting has the highest strength of 647 kN, followed by the greased specimen with a strength of 575 kN, while the specimens with the 400 mm length of sheeting had the lowest ultimate transverse shear strength with an average value of 502 kN.

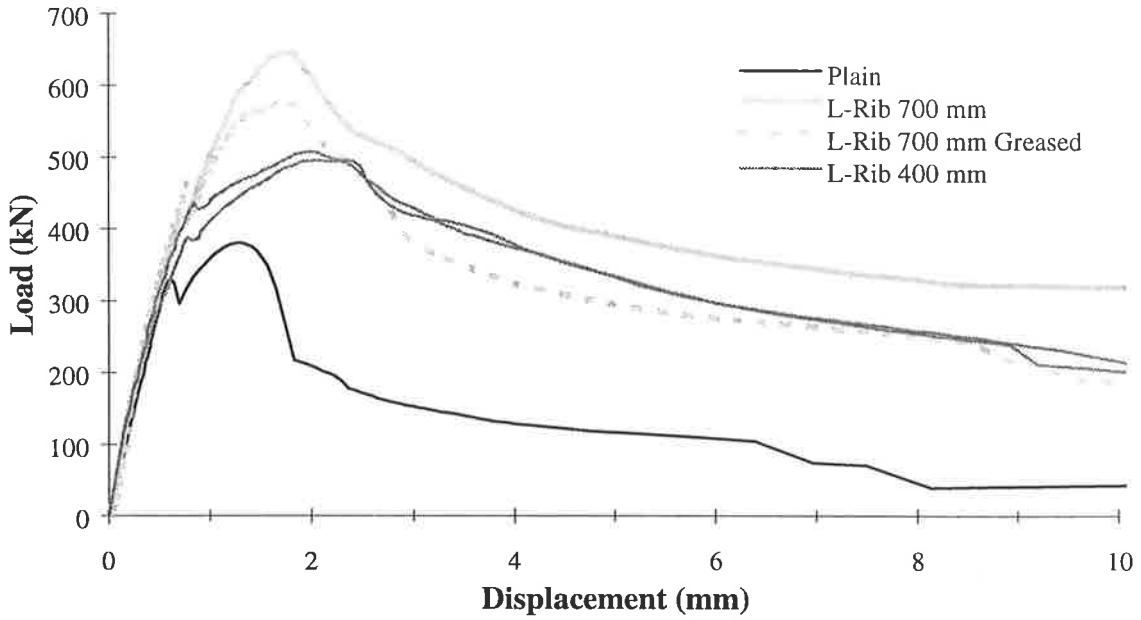


Fig. 6.58. Influence of Longitudinal Bond on Transverse Shear Strength for Cut L-Ribs

6.5.4.5 Internal Stirrups

The influence of the presence of the internal stirrups is shown in Fig. 6.59. All specimens were constructed with the arrangement of internal stirrups as shown in Fig. 6.7, except one specimen with 1.0 mm thick L-Rib sheeting which had no stirrups present. The result of this test is shown compared to two other identical specimens which contain stirrups. It can be seen that there is a slight reduction in the cracking load and the ultimate shear resistance for the specimen without the stirrups. The cracking load reduced 7% from 501 kN to 455 kN, while the ultimate load reduced by 7% from 661 kN to 615 kN. Another important difference in the behaviour is the more rapid reduction in the load after the ultimate load has been reached for the specimen without the stirrups.

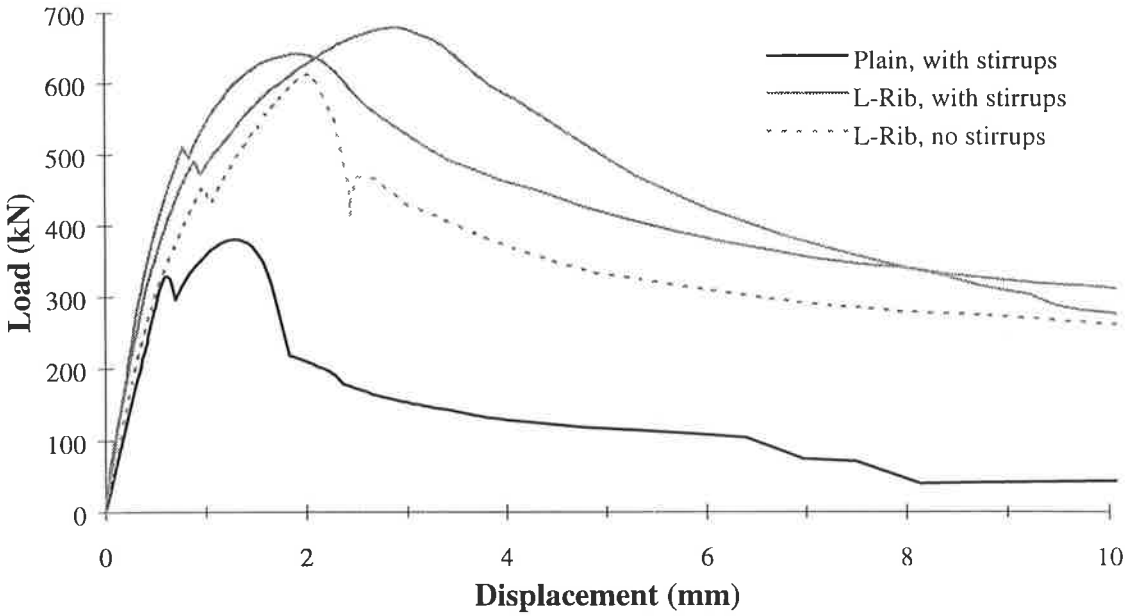


Fig. 6.59. Influence of Internal Stirrups

6.6 Analysis of Results

It is most common to display the results of the tests in the form of a shear stress v_u against a reinforcement parameter pf_y, where $v_u = V_u/b_v d_v$, p is the reinforcement ratio = $A_{sv}/b_v d_v$, and f_y is the yield strength of the shear reinforcement. The reinforcement ratio depends on the area of fully anchored reinforcing which crosses the shear plane. The stirrups were fully anchored by looping them around the longitudinal bars, as shown in Fig. 6.7a, however, the profiled sheeting was not fully anchored at the location of the shear plane, and thus its contribution must be considered further. Furthermore, the yield stress of the sheeting was different to that of the shear stirrups, and their individual contributions to the shear resistance must be assessed. Thus, an alternative to using the term pf_y to define the strength of the transverse reinforcement crossing the shear plane is required. The term f_v in Eq. 6.13 is defined so as to describe the strength of the shear reinforcement when a combination of profiled sheeting and stirrups are used.

$$f_v = \frac{A_{sv} f_{sy} + F_b}{A_{cv}} \quad \text{.....(6.13)}$$

where

A_{cv} = Area of concrete forming the shear plane = $b_v d_v$ for a rectangular section.

The term F_b in Eq. 6.13 represents the transverse strength of the profiled sheeting at the shear plane. If the sheeting is fully anchored at the shear plane, then F_b is given by Eq. 6.15, otherwise F_b is given by the bond strength of Eq. 4.7 on page 247.

$$F_b = A_{pv} f_{py} \quad \text{.....(6.15)}$$

where

A_{pv} = Area of profiled sheeting crossing the shear plane

The development of longitudinal bond between the profiled sheeting and the concrete was assessed using the push test described in Chapter 3. The results of the bond strength were taken from the push tests with the same profiled geometries as those used in the shear tests. The dove tail and trapezoidal results are from Series 1 of the push tests, as described in Table 3.4 on page 145, while the result of the L-Rib is from the push tests carried out for the profiled beams in Chapter 5. The results of the tests have been summarised in the second column of Table 6.7. Column 3 in the table gives the ratio of the bond force developed at the shear plane F_b to the force required to yield the sheeting in tension F_{py}. This ratio is based on the contact area of the ribs, the number of ribs in the cross-section and the bond development length. The values in Table 6.7 are based on a development length of 350 mm, except for the last row, which is based on a development length of 200 mm.

Profiled Sheeting	**Bond Strength (MPa)**	**Bond Force / Yield Force F_b/F_{py}**	**f_v (MPa)**
Plain	0.0	0.0	0.84
Trapezoidal (350 mm)	0.11	0.08	1.15
Dove Tail (350 mm)	0.36	0.23	1.42
L-Rib (350 mm)	0.80	0.86	2.18
L-Rib (200 mm)	0.80	0.49	1.61

Table 6.7. Bond Strength Results for Profiled Sheeting

It can be seen from Table 6.7 that the trapezoidal rib specimens develop only a small proportion of their yield strength at the shear plane. The proportion increases for the dove tail specimens and is the greatest for the L-Rib specimens. When the bond length is reduced to 200 mm the ratio of the bond force to the yield force is 0.49.

The value of f_v for the different specimens are tabulated in Table 6.7. In the determination of these values the actual cross-sections were taken into account. That is, the area of the shear plane A_{cv} for trapezoidal specimen was based on the cross-section shown in Fig. 6.15 on page 357 while that for the Dove Tail specimen was based on Fig. 6.21 on page 361. The area of the shear plane for the L-Rib specimen was based on the rectangular cross-section $b_v d_v$.

A comparison between the experimental ultimate shear stress v_u and that predicted by theory is given in Table 6.8. The ultimate load of the specimens was converted to a shear stress by dividing by the area of the shear plane A_{sc}. The shear reinforcement parameter f_v in Eq. 6.13 is given in column 3, while the experimental shear stress is given in column 4. The shear strength based on Mattock and Hawkins' (1972) theory as given by Eq. 6.1 on page 336 is given in column 5. The term pf_y in Eq. 6.1 was replaced by f_v in column 3, and σ_n in Eq. 6.1was set to zero as there was no externally applied normal force. The shear strength based on Bradford and Kyakula's (1994) theory as given by Eq. 6.11 on page 343 is given in column 6. Column 7 gives the results predicted by Bradford and Kyakula, except the term $V_{uc,s}$ which predicts the strength of the reinforced concrete beam is replaced by the average of the measured results for the plain specimens. A comparison between the experimental and the theoretical shear stress is given in Fig. 6.60 for each of the different analyses.

In the determination of the term $V_{uc,s}$ in Eq. 6.11 the term A_{st} was calculated by adding the area of the fully anchored shear reinforcement A_{sv} and a portion of the area of the profiled sheeting based on the bond developed at the shear crack, as given by Eq. 6.16.

$$A_{st} = A_{sv} + \frac{F_b}{F_{py}} A_{pv} \qquad (6.16)$$

for $F_b < F_{py}$

Test No. (1)	Profile Shape (2)	f_v (MPa) (3)	Ultimate Shear Stress (MPa)			
			Experiment (4)	Mattock (5)	Bradford (6)	Bradford* (7)
S1.1	-	0.84	4.37	2.07	0.42	4.14
S1.2	-	0.84	4.35	2.07	0.42	4.14
S2.1	-	0.84	3.60	2.07	0.44	4.14
S3.2	-	0.84	7.09	2.07	0.46	4.14
S1.3	Trapazoidal	1.15	4.73	2.32	1.89	5.50
S1.8	Trapeziodal	1.15	4.28	2.32	1.89	5.50
S1.4	Dove Tail	1.42	5.73	2.53	1.75	5.24
S1.5	Dove Tail	1.42	4.23	2.53	1.41	5.24
S2.7	Dove Tail	1.42	5.84	2.53	1.78	5.24
S2.8	Dove Tail	1.42	4.95	2.53	1.78	5.24
S1.6	L-Rib	2.18	7.34	3.15	5.92	9.21
S1.7	L-Rib	2.18	7.76	3.15	5.92	9.21
S2.2	L-Rib	1.61	5.60	2.69	5.83	9.21
S2.3	L-Rib	1.61	5.55	2.69	5.83	9.21
S2.4	L-Rib	1.61	5.70	2.69	5.83	9.21
S3.1	L-Rib	2.18	7.03	3.15	5.99	9.21
S3.3	L-Rib	2.18	5.83	3.15	3.50	6.74
S3.4	L-Rib	2.18	6.94	3.15	3.50	6.74
S3.5	L-Rib	2.18	9.52	3.15	41.50**	44.72**
S3.6	L-Rib	2.18	9.36	3.15	41.50**	44.72**
S2.5	L-Rib (Cut)	1.61	5.81	2.69	5.37	8.75
S2.6	L-Rib (Cut)	1.61	5.67	2.69	5.37	8.75
S3.7	L-Rib (Cut)	2.18	6.57	3.15	5.53	8.75
S3.8	L-Rib (Cut)	2.18	7.39	3.15	5.53	8.75

** The 2.0 mm thick specimens did not fail by buckling, hence these values overestimate the shear strength

Table 6.8. Comparison between Theory and Experiment

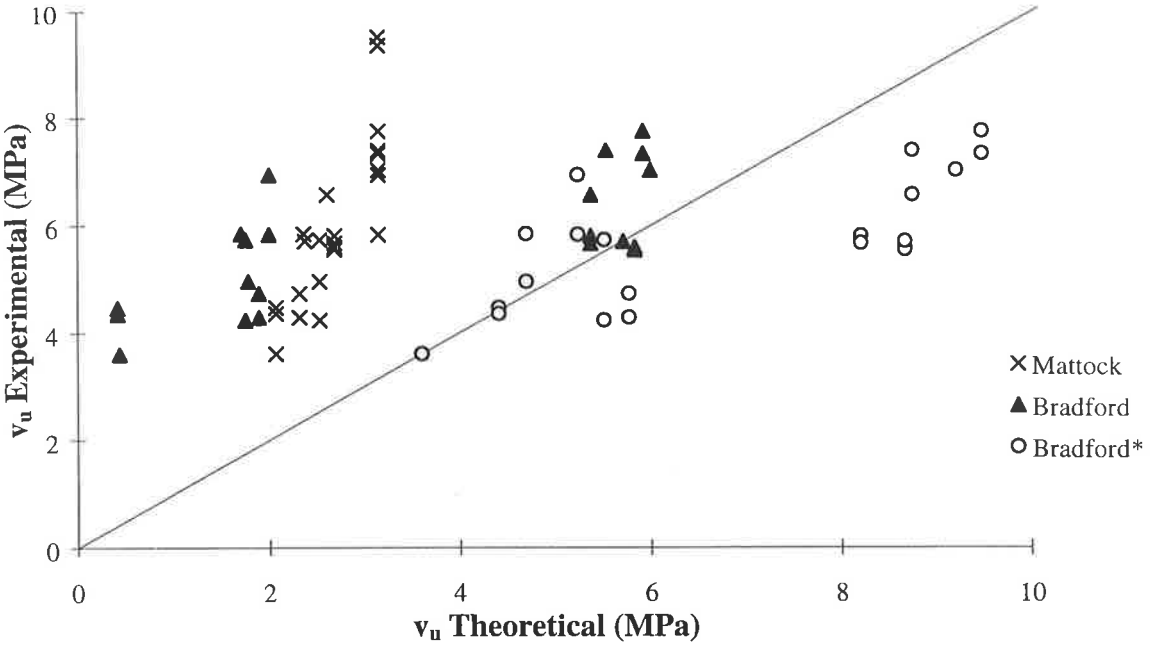


Fig. 6.60. Comparison of Theoretical and Experimental Ultimate Shear Stress

It can be seen in Fig. 6.60 that both Mattock and Bradford give conservative estimates for the shear strength of the specimens, whilst the results of column 7, labelled Bradford* in Fig. 6.60, tend to overestimate the shear strength of some of the specimens and underestimate the strength for others. As was previously discussed in Section 6.2, the term $V_{uc,s}$ in Eq. 6.11, as given by Eq. 6.8, does not account for the shear contribution of reinforcing that is at 90° to the shear plane. Thus, Eq. 6.11 (labelled Bradford in Fig. 6.60) underestimates the strength of the plain reinforced concrete specimens, as shown in Fig. 6.60 for the three specimens with the lowest theoretical v_u values. Once the strength of the enclosed concrete is incorrectly estimated, the ultimate shear strength for the specimens with profiled sheeting will also be underestimated.

This can be corrected by obtaining a better estimate for the strength of the plain concrete specimen. However, as was stated at the outset of this discussion, the aim of this section is to determine the increase in shear strength due to the side profiles, not investigate the shear strength of concrete members. In order to determine the accuracy of Eq. 6.11 in predicting the increase in the shear strength due to the side profiles, the measured strength of the plain specimens can be substituted for $V_{uc,s}$ and then the terms V_b and V_r calculated from Eqs. 6.10 and 6.12 can be added. This is shown in Fig. 6.60 by the series labelled Bradford*. It can be seen that this offers a much better prediction of the shear strength of the specimens.

The results of the tests are also presented in Fig. 6.61 by plotting the shear strength against the term f_V, along with the curves determined by Mattock and Hawkins (1972), which were shown previously in Fig. 6.2 on page 335. It can be seen in Fig. 6.61 that the test results match the uncracked curve derived by Mattock more closely than the cracked curve. This is due to the fact that the tests carried out for this theses were performed on specimens which were not pre-cracked.

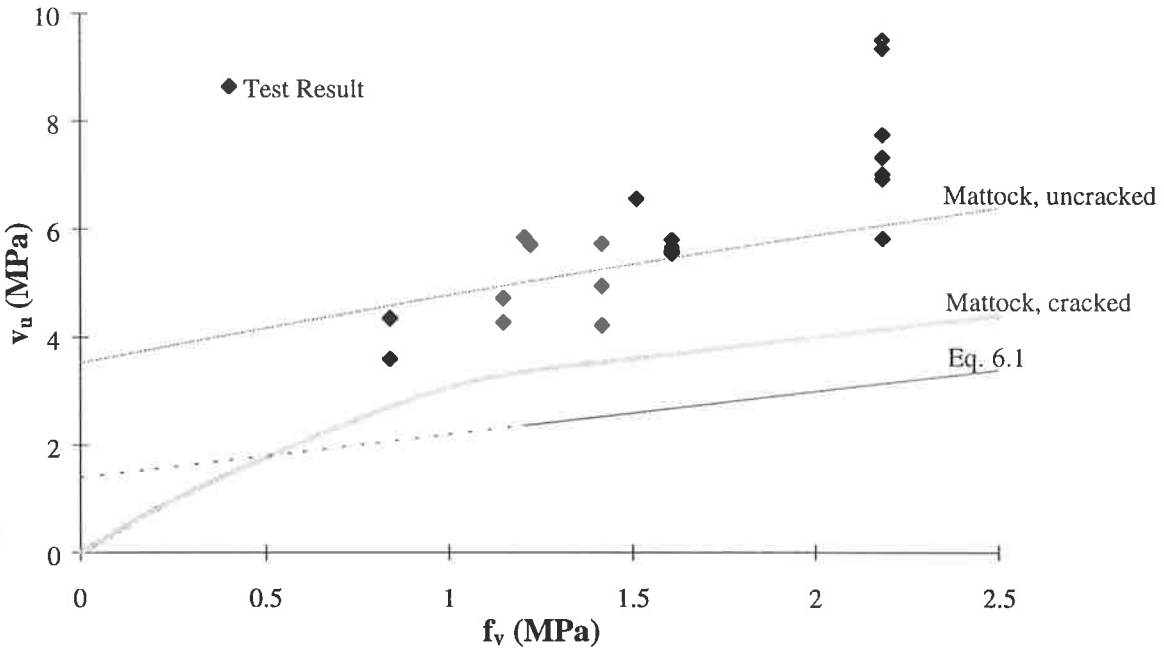


Fig. 6.61. Comparison of Shear Test Results with Previous Researchers

The linear regression is shown in Fig. 6.62, along with the 5% confidence limits. The coefficient of correlation was $R^2 = 0.74$ for the linear regression line shown. The slope and intercept of the regression line were 2.1 and 2.4 respectively. This slope is much higher than the value of 0.8 determined by Mattock and Hawkins. For a regression line through the data with a slope of 0.8 the resulting coefficient of determination is only $R^2 = 0.46$, which indicates a poor fit through the data. The two data points with the high value of v_u outside the confidence limits were the results from the tests on the 2.0 mm thick sheeting. These specimens did not fail by shear through the sheeting, and were not included in the regression analysis due to the different failure mechanism.

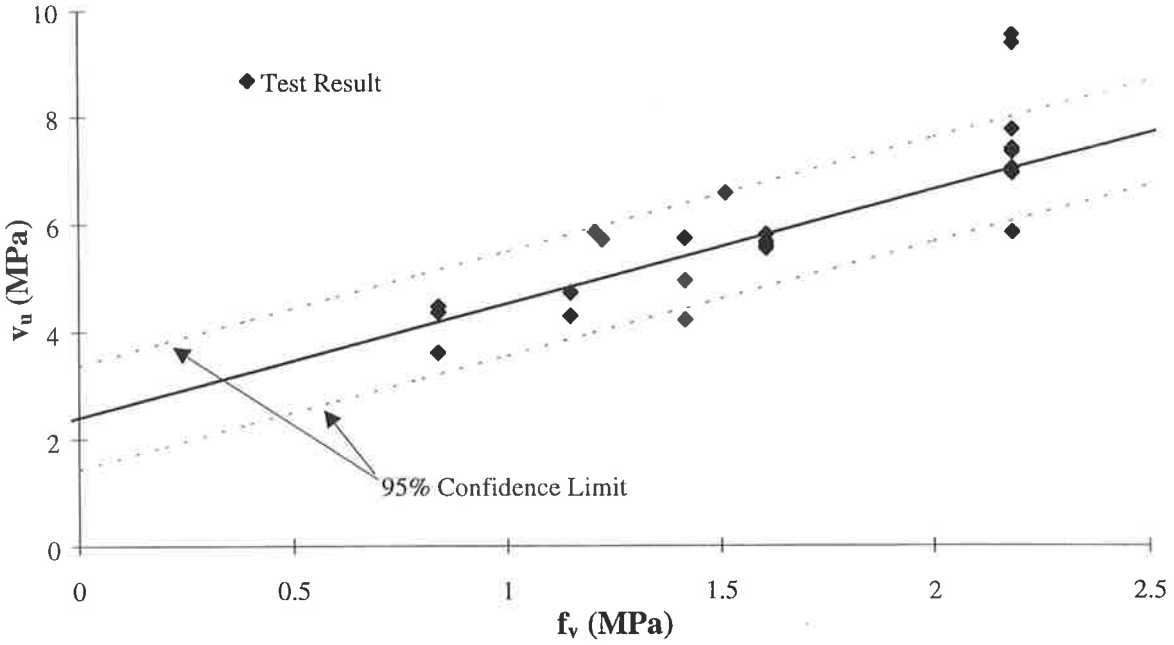


Fig. 6.62. Regression Analysis of Shear Test Results

When designing reinforced concrete members with side profiled sheeting, an estimate for the shear strength is given by the lower bound confidence limit, as shown in Fig. 6.62. The equation of this line is given by:

$$v_u = 1.4 + 2.1 f_v \quad \text{.....(6.17)}$$

This has the same intercept as Eq. 6.1, but a larger slope. It is expected that the intercept of the two models would be similar, as this gives the shear strength of the members without reinforcing. The larger slope for the profiled specimens indicates the increased effectiveness of the side profiled sheets in resisting shear, as opposed to the dowel action of the internal stirrups.

Equation 6.17 represents a simplified equation to predict the shear strength of reinforced concrete members with side profiled sheeting. It is empirically based, and represents an alternative to Eq. 6.11. However, as Eq. 6.11 is rationally based and provides a conservative estimate for the shear strength with reasonable accuracy, it is recommended that it be used to determine the shear of profiled beams.

6.7 Conclusions

From the results of the shear tests as given in Table 6.8 and shown in Figures 6.60, 6.61 and 6.62, a few comparisons and conclusions can be made regarding the shear strength of reinforced concrete members with side profiled sheeting.

- The use of Eq. 6.1 to predict the shear strength of the profiled specimens was always conservative, with a mean error of 54%
- Equation 6.11 predicted the shear strength of the specimens with profiled sheeting with a mean error of 32%, while for those specimens without profiled sheeting the error was 91%. This indicates that the strength contribution of the shear stirrups are not well predicted by this equation for the test arrangement used in this study.
- When the measured strength of the concrete specimens without side profiled sheets was substituted for $V_{uc,s}$ in Eq. 6.11 the predicted values had a mean error of 20% compared to the measured values. This represented a significant reduction from 32% error when the strength of the enclosed reinforced concrete member was also estimated.
- The predicted shear strength of the specimens with the 2.0 mm sheeting is over 4 times that measured. This discrepancy is due to fact that the predicted shear strength was based on shear buckling of the profiled sheeting. However, the mode of failure was not by buckling of the sheeting, but by shear failure in the concrete along a plane parallel to the sheeting.
- An equation describing the shear strength of reinforced concrete members with side profiled members was derived based on the results of the experimental program. The form of the equation was the same as the empirical equation derived by Mattock and Hawkins (1972), but reflected in increase in effectiveness of the side profiled sheeting, compared to internal stirrups, in resisting transverse shear. However, it is recommended that Eq. 6.11 be used in the determination of the shear resistance of profiled beams, as it represents a rational analysis of the shear behaviour of the members.
- The external sheeting between the ribs causes only a minor increase in the shear strength for L-Rib profiled sheeting. For the 1.0 mm sheeting thickness used in the study, the contribution of the external sheeting can be neglected with little error.

- The amount of longitudinal bond developed between the sheeting and the concrete at the location of the shear plane strongly effects the shear performance of the profiled sheeting.

- The resistance of the sheeting to transverse shear is strongly dependant on the overall geometry of the sheeting. Of the three basic geometries tested, the L-Rib had the highest transverse shear strength, followed by the dove tail rib and then the trapezoidal rib.

Chapter 7

Computer Analysis of Composite Members with Partial Interaction

7.1 Introduction

In the analysis of composite beams, it is found that the overall strength and ductility of the member is influenced by the strength and stiffness of the connection between the concrete and the steel elements. Due to the fact that the strength of most shear connections is related to the slip at the connectors, there is a relationship between the overall behaviour of the member and the slip that occurs at the connection. Thus, the problem of defining the behaviour of a composite member becomes one of determining the variation in slip at the connection between the two elements. This situation is unique to composite construction.

A computer program has been developed as part of this research project to aid in the understanding of the behaviour of composite members. This chapter describes the working of the computer program. The chapter starts with a review of other work in the area, and then goes on to describe the program used in this research. The program is divided into two main

sections which are dealt with separately: cross-section analysis; and member analysis. Finally, a validation of the computer program is presented in Section 7.7 by comparing the output of the program with experimentally measured results.

7.2 Literature Review

The analysis of composite steel-concrete beams incorporating slip has been carried out using computer modelling for many years. The earliest studies on this subject (Newmark et. al., 1951) used elastic theory and linear load-slip (P-s) relationships for the shear connection. Due to the non-linear behaviour of composite members, especially at or near the ultimate load condition, this study has many draw backs over more advanced non-linear computational analyses. However, it represents a useful starting point in the analysis of composite members by hand, and can be extended to allow for non-linear effects such as concrete cracking, and plasticity in the connectors (Oehlers and Sved, 1994)

More recently, uplift as well as slip has been included in non-linear partial interaction analyses (Aribert and Aziz, 1986; Roberts, 1981; Robinson and Naraine, 1988; Aribert and Labib, 1982). However, it was found in these studies that uplift had negligible effect on the distribution of slip along the beam, and thus its incorporation in the present analysis is not warranted.

Aribert and Aziz (1986) used transfer matrix methods and non-linear analyses in their solution method, whereas other researchers have used finite element methods. Both of these methods work well in the analysis of composite beams, however these implementations require either an extensive investment in programming, or the purchase of a commercial finite element package. It was considered that other solution procedures would be well suited to analysing composite beams and require less time to program. These will be discussed later.

Johnson and Molenstra (1991) analysed a composite beam with partial interaction using a method of forward integration. Their approach was to divide the member into a series of segments, and then solve a series of differential equations using an iterative approach, checking the boundary conditions at the supports.

It is only more recently that other composite members have been looked at, such as composite slabs. Poh and Attard analysed a composite slab with partial interaction using a

segmental approach (Poh and Attard, 1993). They approximated the interface behaviour as being rigid-plastic, thus the bond stress was considered independent of the slip, and had unlimited slip capacity. The bond force was considered to consist of three components: adhesion bond, mechanical interlock, and frictional resistance. The frictional component was developed at the supports and resulted in a bond strength that varied with applied load, but was independent of the level of slip. Daniels and Crisinel modelled a composite slab with interface slip using a finite element approach (Daniels and Crisinel, 1989; 1993). Their procedure allowed any form of connection behaviour to be used.

The authors will report on a procedure that is able to analyse any composite member with partial interaction, including composite beams and composite slabs, as well as a new form of construction known as profiled beam construction. The method adopted for the present study is similar to that adopted by Johnson and Molenstra which used a form of forward integration along the member. The most significant difference in the analysis is that the connection behaviour can follow any load-slip curve, and may incorporate a softening stage in the connection which occurs after maximum load in the connectors has been reached and after ultimate slip.

7.3 Analysis Procedure

7.3.1 Introduction

The analysis procedure adopted in this study uses a finite difference analysis that uses forward integration to determine the variation in curvature, slip and bond force along the member. An iterative approach is used to ensure compatibility of the solution with the imposed boundary conditions. There are essentially two stages to the analysis which are shown diagrammatically in Fig. 7.1. The first of these is a cross-sectional analysis, in which the slip strain and curvature are determined at a given cross-section, for a known applied moment, and a given bond force. This procedure is described fully in Section 7.4.

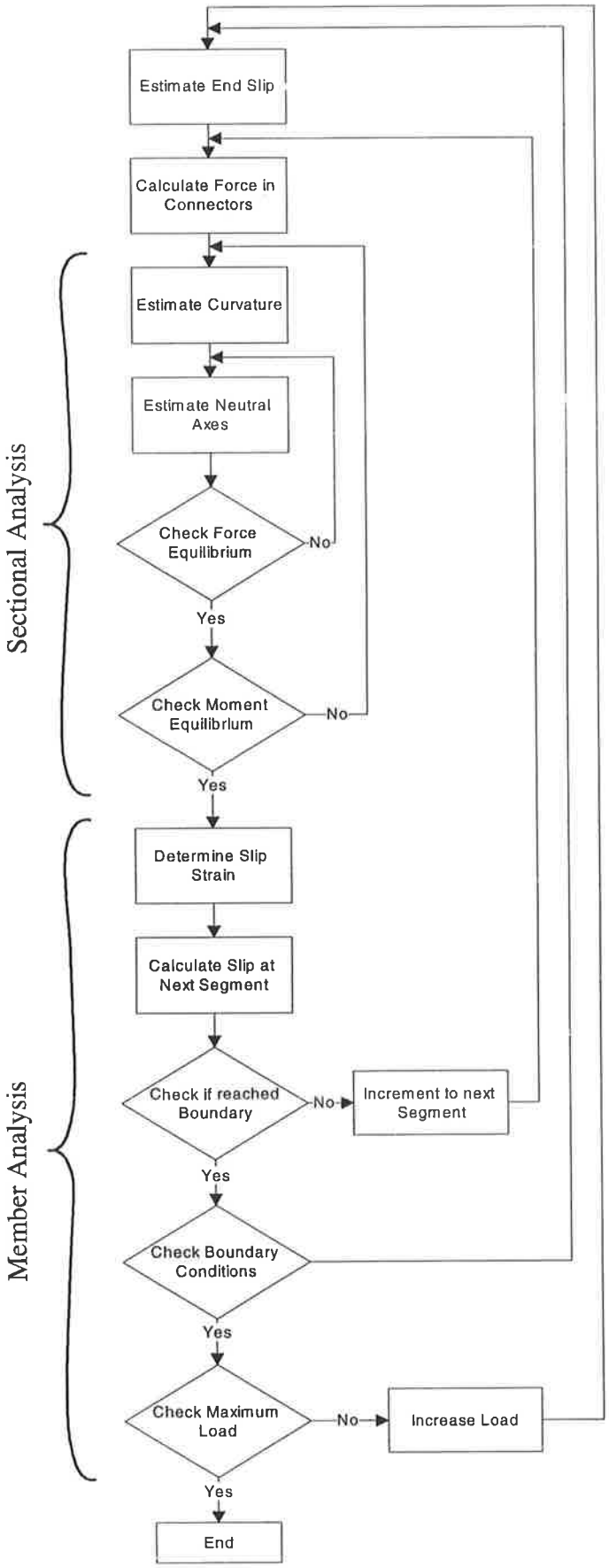
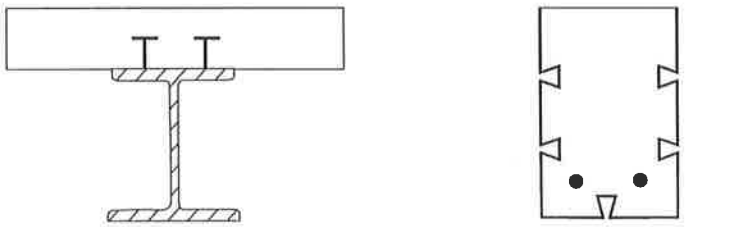


Fig. 7.1. Program Flow Diagram

The second stage of the analysis consists of integrating the results of the cross-sectional analysis along the length of the member. Once the slip strain and the bond force are known at one segment, the procedure can be repeated at the next segment. In order to apply the cross-sectional analysis to the analysis of the full member, the load-slip characteristics for the connection must be known. With this information, the variation in bond force, slip, and curvature can be determined for the complete member. This procedure is described in Section 7.6.

The analysis is carried out for a given applied load and thus a known moment distribution. Once the boundary conditions have been satisfied, the load is increased and the procedure is repeated. This is continued until the member can no longer sustain an increase in the applied load. At each load step, the variation in bond force, slip, and curvature are recorded, allowing them to be plotted against the applied load, as the member is loaded monotonically from zero to ultimate load in discrete load steps. At this stage, the analysis does not continue into the post-ultimate range, but this may be added in the future.

Typical cross-sections are shown in Fig. 7.2 for a composite beam and a profiled beam. In both of these cases shown, there is a concrete element, a steel element and a connection between the two elements. For the composite beam, the connection is most commonly in the form of welded stud shear connectors, while for the profiled beam the connection is most commonly in the form of ribs in the profiled sheeting, which typically have embossments rolled into them to increase the strength of the connection.



(a) Composite Beam (b) Profiled Beam

Fig. 7.2. Composite Cross Sections

7.4 General Considerations

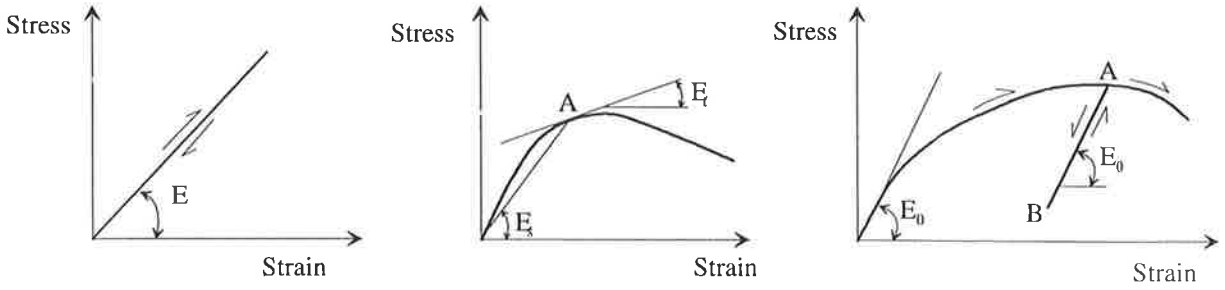
7.4.1 Bounds of Tolerance

When using numerical methods to solve analytical problems, the term 'sufficiently close to' is used instead of 'equal to', as an equality is rarely met and instead tolerances of acceptance are required. These tolerances can be adjusted and are set so as to provide a balance between accuracy and computational time. The choice of appropriate bounds of acceptance can be found by successively decreasing the tolerance, and checking to see that the computed solution converges to a single value. When the tolerance is set to a very small value, say a 0.0001% error of the correct value, then the value obtained is considered as the most accurate. As the tolerance is decreased, then the resulting change in the output is noted until an acceptable error is reached. What is classified as an 'acceptable error', and the tolerances used in different sections of the computation will be discussed later.

7.4.2 Material Properties

7.4.2.1 General

Material properties are shown in Fig. 7.3 for a linear elastic material, a non-linear elastic material and a non-linear anelastic material. A linear elastic material is characterised by a constant slope of the stress-strain diagram, with the same loading and unloading line as shown in Fig. 7.3a. A non-linear elastic material maintains the same loading and unloading line, but can now no longer be characterised by a constant slope. For such a material, the modulus of elasticity can be defined in terms of the tangent stiffness E_t, or the secant stiffness E_S, as shown in Fig. 7.3b for a point A on the curve. For a non-linear anelastic material the loading and unloading paths do not coincide, so that the state of stress depends not only on the current strain but also on the previous strain history, as shown in Fig. 7.3c. In this figure, the unloading curve follows the same slope as the initial slope E_O of the loading curve. It follows that an incremental or 'historical' form of analysis is needed to handle anelastic behaviour whenever unloading of the structure as a whole or unloading of local regions may take place.



(a) Linear Elastic (b) Non-Linear Elastic (c) Non-Linear Anelastic

Fig. 7.3. Generalised Material Properties

The behaviour of concrete is best represented as a non-linear anelastic material. In most computational analyses of concrete members for monotonically increasing loads, the anelastic behaviour of concrete is often ignored. This is due to the fact that as the structure is loaded, there is no strain reversal in the material, and thus no unloading. However, the anelastic behaviour has been included in this analysis due to the fact that as the bond between the concrete and the steel element breaks down, the location of the neutral axis changes and portions of the concrete will undergo unloading.

For the present program, an incremental approach has been adopted to allow for anelastic concrete behaviour. This can be represented in a generalised form by Eq. 7.1, which shows that the current state of stress is dependant on the current level of strain and also on the strain at the previous load step. This will be further explained in the following section with the particular stress strain curves adopted in the present study for concrete and steel.

$$\sigma = f(\varepsilon, \varepsilon_{old}) \quad \text{.....(7.1)}$$

where

ε = Strain at the current load step under consideration

ε_{old} = Strain at the previous load step

7.4.2.2 Concrete Compression Properties

The stress strain curve for concrete in compression that is used in this study is that proposed by Warner (1969). The curve is non-dimensionalised by dividing the stress by the maximum stress, and dividing the strain by the strain at the maximum stress. This is shown

in Fig. 7.4 which indicates the maximum non-dimensional stress of S = 1.0 occurs at a non-dimensional strain of $\varepsilon_c = 1.0$. The equation describing the curve is divided into three sections, and can be represented by the following equations which are also shown schematically in Fig. 7.4.

$$0 \le \varepsilon_c < 1; \qquad S = \gamma_1 \varepsilon_c + (3 - 2\gamma_1)\varepsilon_c^2 + (\gamma_1 - 2)\varepsilon_c^3 \qquad \text{.....(7.2a)}$$

$$1 < \varepsilon_c \le \gamma_2; \qquad S = 1 - \frac{1 - 2\varepsilon_c + \varepsilon_c^2}{1 - 2\gamma_2 + \gamma_2^2} \qquad \text{.....(7.2b)}$$

$$\varepsilon_c > \gamma_2; \qquad S = 0 \qquad \text{.....(7.2c)}$$

where

$$S = \frac{\sigma}{\sigma_u} \qquad \text{.....(7.3)}$$

$$\varepsilon_c = \frac{\varepsilon}{\varepsilon'_c} \qquad \text{.....(7.4)}$$

$$\gamma_1 = \frac{E_o \varepsilon'_c}{\sigma_u} \qquad \text{.....(7.5)}$$

S = Non-dimensionalised stress, as given by Eq. 7.3

ε_c = Normalised strain, as given by Eq. 7.4

γ_1 = Initial slope of stress-strain curve, as given by Eq. 7.5

γ_2 = Ultimate strain of the concrete, as a ratio of the strain at the maximum stress

E_o = Initial stiffness of the concrete

σ_u = Compressive strength of concrete

ε'_c = Strain at which σ_u occurs

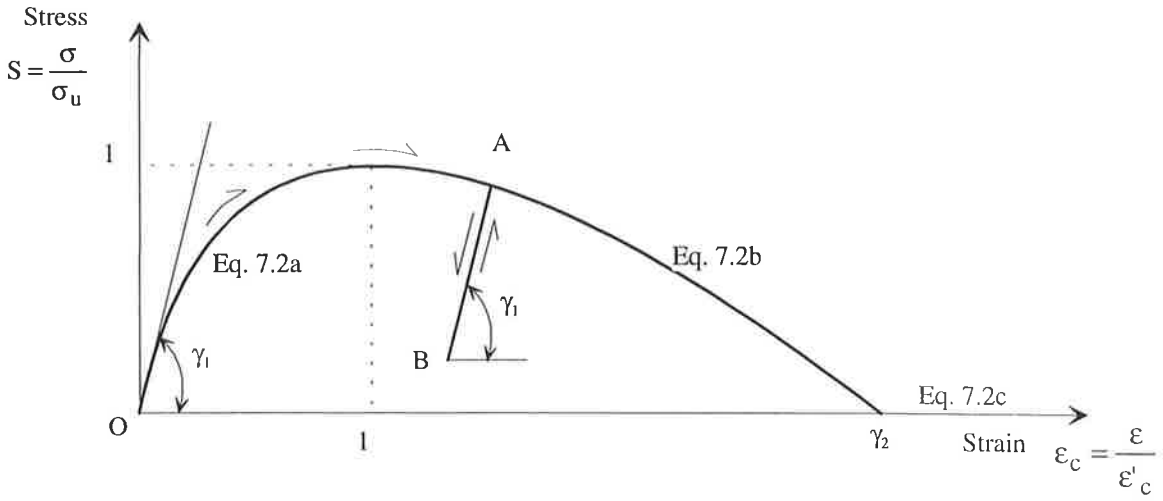


Fig. 7.4. Concrete Compression Properties

The terms E_o, ε'_c and σ_u are derived from compression tests on companion cylinders. The value of ε'_c is usually taken as 0.002 (Warner et al., 1989). The parameter γ_2 allows for the extended unloading behaviour that can occur when the concrete is laterally restrained (Barnard, 1964). For unrestrained concrete in a reinforced concrete beam, γ_2 can be taken as 3 (Warner, 1969), whereas for highly restrained concrete such as in a circular hollow filled steel tube γ_2 can be taken as 10 (Trezona, 1995).

In order to account for possible unloading of the concrete, a check must be made on strain in the concrete at each load step. If the strain is less than the strain at the previous load step, then the stress follows the path A-B, instead of A-O as shown in Fig. 7.4. The unloading line and the subsequent reloading line follow the same path, which has the same slope as the initial stiffness of the concrete. For the curve shown in Fig. 7.4 this slope is defined by γ_1. Computationally, anelastic behaviour is allowed for by introducing the terms ε_{max} and S_{max} to denote the maximum strain and stress which has occurred in the particular concrete element during all previous loading stages. If the current value of strain is larger than ε_{max}, then Eqs. 7.2 apply, otherwise the stress is determined from A-B in Fig. 7.4 which is given by:

$$0 < \varepsilon_c \le \varepsilon_{max}\ ; \qquad S = S_{max} - \gamma_1(\varepsilon_{max} - \varepsilon_c) \qquad \text{.....(7.6)}$$

where

S_{max}= Maximum recorded stress and is related to ε_{max} by Eqs. 7.2.

7.4.2.3 Concrete Tensile Properties

The influence of the tensile strength of the concrete on the behaviour of composite members has often been poorly addressed. This is due in part to its inherent variability, and also because an adequate, simple model is yet to be established to describe concrete cracking. A brief review of different models will be presented, followed by a description of the model used in this analysis.

The tensile properties of concrete in reinforced concrete members are such that even after the formation of cracks, it is possible for the concrete to continue to carry some tensile forces between the cracks. The contribution to the flexural stiffness by the concrete in the tension zone can be significant at loads slightly above the cracking moment, but diminishes as the load increases towards the ultimate moment. This increase in the flexural stiffness of the member is known as the tension stiffening effect. There are various ways of modelling the tensile behaviour of concrete which include:

1. To assume an average tensile stress to act over an effective area of concrete in the tension zone (also known as crack smearing);
2. To modify the steel stresses to include the effect of tension stiffening in the surrounding concrete;
3. To adopt a discrete crack model to describe the formation of cracks along the member.

The use of crack smearing has been adopted by many researchers (Bazant and Oh, 1984; Massicotte et al., 1990; Gupta and Maestrini, 1990; Gilbert and Warner, 1978; Kenyon, 1993). Essentially it entails adopting a modified stress-strain curve for the concrete in tension which accounts for the effects of tension stiffening. The general form of the stress-strain diagram for concrete in tension is shown in Fig. 7.5. This indicates a linearly increasing stress for an increase in strain up to a maximum of σ_t. After this, there is a decrease in stress for an increase in strain. The slope of the initial portion of the curve A-B is taken as equal to the initial slope for the concrete in compression. The form of the descending portion of the curve B-C varies for different models. It is shown as a linear variation in Fig. 7.5, which is the form adopted by Bazant and Oh (1984). Other models describe the descending portion using a non-linear function (Gilbert and Warner, 1978) while other models use a bi-linear descending branch (Massicotte et al., 1990; Gupta and Maestrini, 1990; Kenyon, 1993).

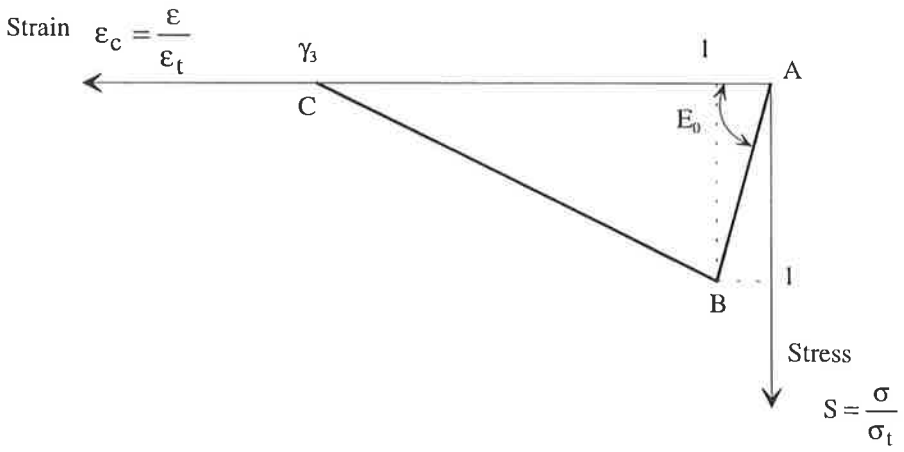


Fig. 7.5. Concrete Tensile Properties

Due to the variable nature of the tension stiffening effect, the theoretical models were always calibrated against test data. This helped determine values for parameters such as γ_3 shown in Fig. 7.5. After calibration, each of the models showed good correlation with experimental results and described the cracking behaviour with reasonable accuracy. Thus, for the purposes of this analysis, the model for the tensile behaviour of the concrete proposed by Bazant and Oh (1984) and shown in Fig. 7.5 will be adopted, as it had already been shown to give reasonable results.

For the present study, the method of crack smearing has been used to allow for the concrete tensile behaviour. The stress strain curve for concrete in tension is shown in Fig. 7.5. This figure shows the concrete behaves linearly up to the concrete tensile strength, with a slope equal to that in compression. Most often the tensile strength of concrete is expressed mathematically as a function of the compressive strength. For this study the strength of the concrete in tension is given by Eq. 7.7, where both σ_u and σ_t are in units of N/mm^2. This follows the recommendation of American Concrete Institute (1989) and Standards Association of Australia (1988). The strain ε_t at which the tensile strength is reached is given by Eq. 7.8.

$$\sigma_t = 0.6\sqrt{\sigma_u} \quad \text{.....(7.7)}$$

$$\varepsilon_t = \sigma_t / E_o \quad \text{.....(7.8)}$$

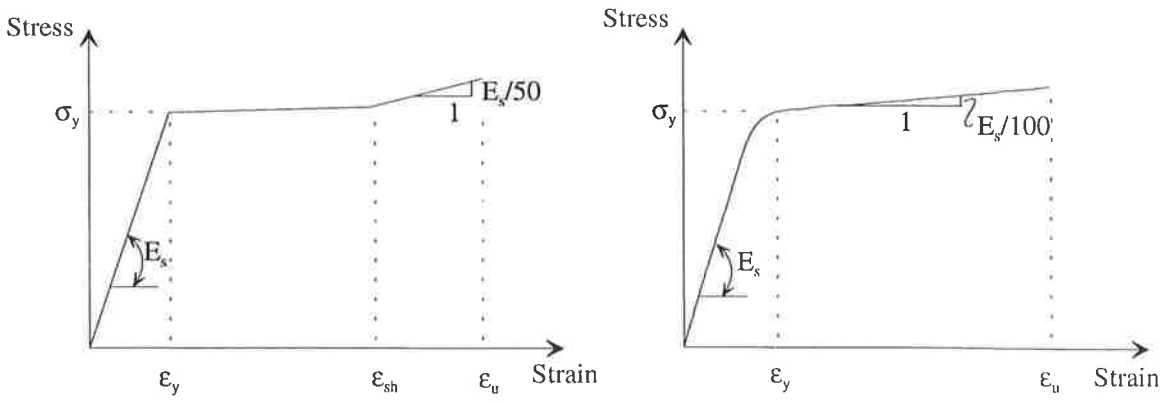
Once the concrete tensile strength has been exceeded, the stress in the concrete diminishes with increasing strain up to a strain of γ_3 times the cracking strain. Massicotte et

al. (1990) adopted a value of $\gamma_3 = 16$, whereas other researchers have adopted a limiting strain equal to yield strain of the reinforcing (Gupta and Maestrini, 1990; Link et al., 1989). Gilbert and Warner (1978) determined that tension stiffening disappears at a strain of 10 times the cracking strain, and this model compared well with experimental tests (Kenyon, 1993). For this study a value of γ_3 of 10 was adopted. This allows for the decreasing effect of tension stiffening at higher loads as the crack pattern becomes more developed and bond diminishes.

7.4.2.4 Steel Material Properties

The stress stain curve used for structural steel sections is shown in Fig. 7.6a. This represents the typical curve for structural steel and for reinforcing steel. The curve is considered to be composed of three sections. The material behaves linearly up to the yield stress, σ_y, with a slope given by the Young's modulus of the steel, E_s. After this, the material deforms plastically to a strain of ε_{sh}. This value is typically of the order of 10 times the yield strain. For the analysis of the composite beams in this study, actual values were obtained from tension tests on the reinforcing steel, and typical values obtained were of the order of 12 times the yield strain. For the analyses in this study, the tensile and compressive curves are considered to be identical, thus excluding the possibility of the steel section buckling prematurely.

A slight increase in stress during yielding was incorporated into the computer analysis to help remove problems with convergence. This problem can occur when a value of stress in the steel can correspond to an infinite number of values of strain, such as when the stress-strain curve is horizontal. The slope of the curve in the yielding region was taken as $E_s/10{,}000$. After the strain exceeds the limit of the yield plateau, strain hardening commences. The strain hardening modulus given as 2% of the initial modulus. This slope is considered constant up to the ultimate strain of the material, ε_u. The value of ε_u varies, depending on the grade of the steel used. For most structural steels, a value of 0.25 may be used.



(a) Mild Steel (b) Cold Formed Steel

Fig. 7.6. Steel Stress-Strain Properties

For cold formed steel sheeting, the typical stress strain curve is shown in Fig. 7.6b. This material is used for composite slab construction and profiled beam construction. Due to the cold working of the material during manufacture, its ultimate strain is lower than for structural steel, with typical values limited to less than 0.20. Another influence of cold working is that there is a less defined yield point. The compressive behaviour of the steel sheeting is influenced by local buckling due to the thin sections used. However, the buckling strength of the sheeting is enhanced by the restraint offered by the concrete, which is cast against one side (Uy and Bradford, 1994b; 1994c). This effect has been discussed in Chapter 4. For this study, the effect of local buckling is modelled by reducing the maximum compressive stress, while maintaining the same form of the stress strain curve as for tension.

7.5 Cross Sectional Analysis

7.5.1 Introduction

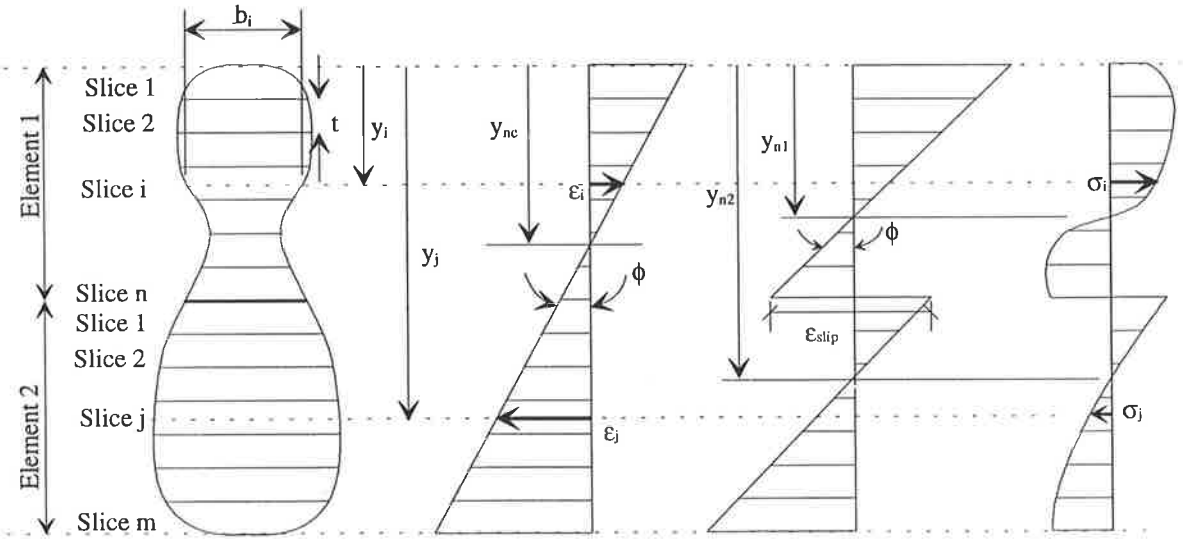
The aim of this section is to develop a general procedure for the analysis of any composite cross-section with known generalised material properties. A cross-sectional analysis procedure based on partial interaction analysis will be presented first of all. This generalised procedure will then be adapted for the specific case of a composite beam. This cross-sectional analysis will then be the basis for the full member analysis given in Section 7.6.

Several assumptions are made in this analysis, which will be discussed later. These assumptions are:

- Plane sections remain plane (known as Bernoulli's principle)
- Effects of transverse shear are neglected
- There is no vertical movement between the two elements
- Curvatures remain small

7.5.2 Partial Interaction Analysis

Consider the generalised cross-section shown in Fig. 7.7a. This cross-section is composed of a top element, a bottom element and a connection between the two (not shown). When the cross-section shown in Fig. 7.7a is subjected to an externally applied bending moment, strains will develop in the cross-section as shown in Fig. 7.7b for the case of complete interaction. Based on the assumption of plane sections remaining plane, the strain profile is uni-linear, with zero strain at the neutral axis. For the case of partial interaction, there will be a step change between the strain profile in the top element and that in the bottom element, ie. there is a bi-linear strain profile. The step change is denoted in Fig. 7.7c by ε_{slip}, and is known as the slip strain. For generalised non-linear materials, stresses will develop in the cross section as shown in Fig. 7.7d.



(a) Cross-Section (b) Full Interaction Strain Profile (c) Partial Interaction Strain Profile (d) Partial Interaction Stress Profile

Fig. 7.7. Generalised Cross-Section

Knowing the total externally applied moment, the curvature and the neutral axes locations must be known in order to determine the strains throughout the cross-section. When the stress-strain relationships for the materials are known, the stress variation throughout the cross-section can be determined, and thus the forces and moments in the cross-section can be determined. These internal forces and moments can then be compared with the external actions to achieve overall equilibrium. Thus, in order to solve for equilibrium, there are three unknowns to solve for at each cross-section: the curvature, and the locations of each of the neutral axes in the two elements.

Based on the assumption of no vertical movement between the elements, the curvatures must be the same in the two elements, thus only one curvature needs to be considered. If vertical movement between the elements were able to occur, then two separate curvatures would need to be determined, thus bringing the number of unknowns to four. Such a situation occurs for reinforced concrete beams with side plates attached by gluing or bolting (Ahmed, 1996). For composite members considered in this analysis, vertical separation is not an important consideration (Aribert and Aziz, 1986; Robinson and Naraine, 1988; Aribert, 1993), and so one curvature will be considered for both elements.

The solution procedure involves a two step iterative process. Each of these steps will be discussed, followed by the mathematical derivation of the procedure.

The first step involves making an estimate of the curvature in the cross-section. At a given curvature, the location of the neutral axes must be found such that internal equilibrium is maintained, ie. the sum of compressive forces in the cross-section equals the sum of the tensile forces in the cross-section. However, considering overall equilibrium of the axial forces results in only one equation, whereas there are two unknowns, ie. two neutral axes, to be determined. Thus there needs to be two equations of axial equilibrium.

The two equations of equilibrium come from an understanding of the behaviour of the connection between the elements. As the external moment is applied, a force will be transferred between the two elements if a connection is present. This force must act in equal and opposite directions in each of the two elements, in order to maintain axial equilibrium. By considering one element at a time, and ensuring that the axial force in each element is equal to the force transferred by the connection, then two equations of equilibrium can be derived.

The derivation of the force transferred by the connectors is found from the load-slip characteristics of the connectors. This requires an understanding of the variation in the slip along the length of the member, and will be the focus of the member analysis in Section 7.6. In order to be able to carry out the cross-section analysis, a value for the bond force must be set. Once this is set from the member analysis, two equations can be established for axial equilibrium of each segment, and these can be solved to determine the locations of the neutral axes.

Once the neutral axes locations have been found, the internal moment in the cross-section is checked against the externally applied moment. If the two are not equal, then the curvature is adjusted until moment equilibrium is achieved. For each adjustment in the curvature, new locations of the neutral axes must be found.

Considering the stress profile shown in Fig. 7.7d, the general equations of statics give:

$$\int \sigma \, dA = 0 \qquad (7.9)$$

$$\int \sigma y \, dA = M \qquad (7.10)$$

where

y = Distance from the neutral axis

In the general case where the materials are not linear elastic, the integrals of Eqs. 7.9 and 7.10 become computationally difficult to solve as a closed form solution. Some researchers have solved these equations by direct integration (Smith and Young, 1956; Brooms and Viest, 1958; Breem, 1964; Sved, 1988) for non-linear material properties. The major disadvantage of this method is that the material stress-strain relationships have to be in a form that can be integrated easily.

Another method of solution is to replace the integrals by finite summations. This is carried out by dividing the cross-section into a series of slices as shown in Fig. 7.7a. This approach has commonly been used by many researchers (Warner, 1969; Wong, 1990; Aas-Jakobsen and Grenacher, 1974) and is the method adopted for the present study. The top element is divided into a total of n slices, while the bottom element is divided into a total of

m slices. The coordinate axes are set at the top of the cross-section, and the strain is evaluated at the mid-height of each slice. The equation for the strain in each fibre for the top element is given by Eq. 7.11. A similar equation can be developed for the bottom element.

$$\varepsilon_{i,1} = (y_{n1} - y_i)\phi \quad \text{.....(7.11)}$$

where

$\varepsilon_{i,1}$ = strain at the mid-height of the i-th slice of the top element

y_i = location of the mid-height of the i-th slice, measured from the top fibre

y_{n1} = neutral axis location of the top element, measured from the top fibre

ϕ = curvature in the cross-section

Using this procedure, the material stress-strain behaviour can easily be input in any form, such as an equation or as a series of discrete points taken from actual material tests. The stress at the mid-height of each slice can then be evaluated from the strain in the slice and the material stress-strain characteristics. At each load step a check is made on the previously stored value of strain for each slice to determine weather there is any unloading. If the strain in any slice is less than the strain from the previous load step, then Eq. 7.6 is used to determine the stress in that slice. The value of stress at the mid-height of each slice is assumed to act over the whole slice, giving the force in each slice as

$$F_i = \sigma_i b_i t \quad \text{.....(7.12)}$$

where

σ_i = stress in the i-th slice

b_i = width of the i-th slice

t = thickness of the slices

Now the integrals of Eq. 7.9 and 7.10 can be replaced by the summations

$$\sum_{i=1}^{n} F_i = F_b \quad \text{.....(7.13)}$$

$$\sum_{j=1}^{m} F_j = -F_b \quad \text{.....(7.14)}$$

$$\sum_{i=1}^{n} y_i F_i + \sum_{j=1}^{m} y_j F_j = M \quad \text{.....(7.15)}$$

where

F_i = force in the i-th slice of the top element

F_j = force in the j-th slice of the bottom element

n = total number of slices in the top element

m = total number of slices in the bottom element

In order to solve Eqs. 7.13 and 7.14 for a given curvature, an iterative process must be used. First, an estimate is made of the neutral axis location. Then Eq. 7.11 is used to determine the strain distribution throughout the member. Knowing the particular stress-strain properties of the materials, the stress in each slice is found from the strain. This is substituted into Eq. 7.12 to determine the force in each slice, which is in turn substituted into Eqs. 7.13 and 7.14. The location of the neutral axis can be adjusted until Eqs. 7.13 and 7.14 are satisfied. Once the correct location of the neutral axis is found, the moment in the cross-section can be found by summing the moment contributions for each slice about any point, as given by the left hand side of Eq. 7.15. If the internal moment is not in equilibrium with the externally applied moment, then the curvature can be adjusted, and the above procedure repeated for the same value of bond force. The sectional analysis routine is shown schematically in Fig. 7.1

Once Eq. 7.15 has been satisfied, then the resulting strain profile can be used to determine the slip strain in Fig. 7.7c at the position of the cross-section being analysed. This is given by Eq. 7.16, and is shown in Fig. 7.7c.

$$\varepsilon_{slip} = \phi(y_{n2} - y_{n1}) \quad \text{.....(7.16)}$$

where

y_{n1} = Neutral axis location in the top element

y_{n2} = Neutral axis location in the bottom element

7.6 Member Analysis

7.6.1 Introduction

In order to analyse a complete member, the member is divided up into K segments as shown in Fig. 7.8. The solution procedure consists of estimating a value of slip and hence connector force for the first segment, and then using this value in the cross-sectional analysis for that segment. A value of slip strain is calculated which can then be integrated to determine the slip at the next segment. This procedure is continued until a segment is reached with a known boundary condition. The boundary condition is checked, and if it is not met, then the initial value of slip for the first segment is changed and the procedure repeated. For symmetrically loaded members, the mid point of the beam can be used to check the boundary condition of zero slip. For non-symmetrically loaded members, the end support can be checked for the boundary condition of zero bond force. This procedure will be detailed in the following section.

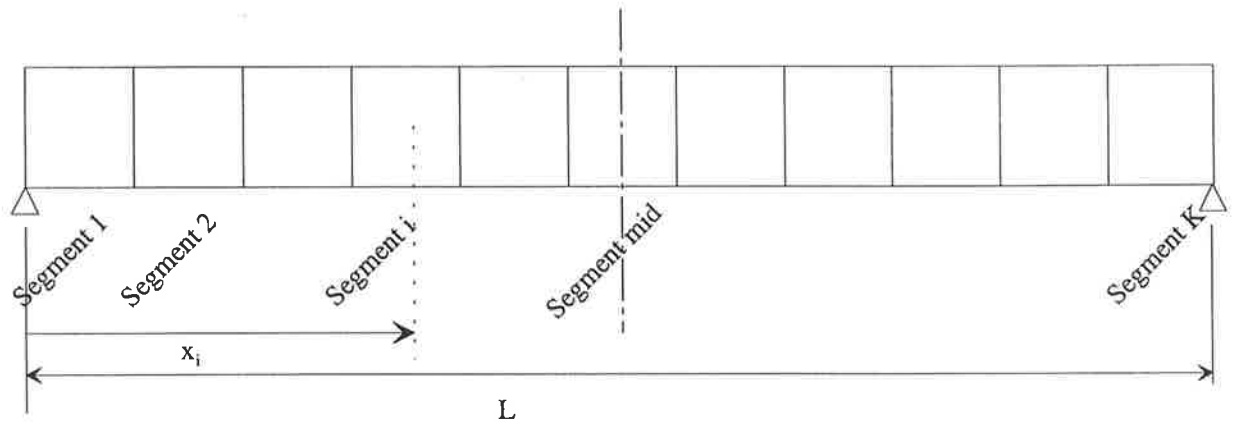


Fig. 7.8. Segmented Member

7.6.2 Simply supported members

In order to solve for the overall behaviour of the member under an applied load, the interface bond characteristics must be known. This is represented in terms of a load-slip curve, or a shear stress-slip curve, as shown in Fig. 7.9. Thus, for a known value of slip, the force in the connectors can be determined from the known characteristics. This can be represented in the general case by some function such as that given by Eq. 7.17.

$$P_i = \frac{f(slip_i)}{c} \qquad (7.17)$$

where

P_i = shear flow for the i-th segment

$slip_i$ = slip at the mid-length of the i-th segment

$f(slip_i)$ = relationship between load and slip for one connector

c = spacing of the connectors

In the case of discrete connectors, Fig. 7.9 represents a generalised load-slip relationship for a single connector. For linear elastic connectors the relationship $f(slip_i) = k.slip_i$, where k is the stiffness of the connectors, as shown in Fig. 7.9. For this analysis, the connectors are modelled as uniformly distributed over the segment in which they are situated. Thus, in order to determine the force transferred by the connectors in a segment, the value determined from Fig. 7.9 for a single connector is divided by the spacing of the

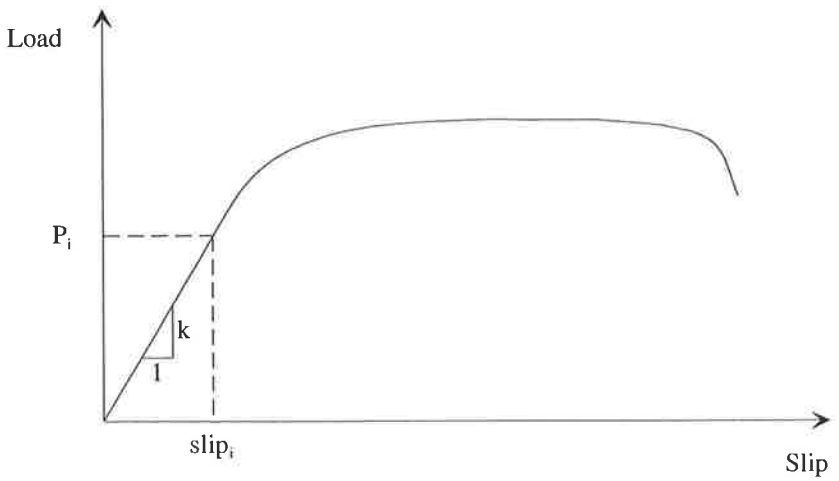


Fig. 7.9. Generalised Load Slip Characteristics for one Connector

connectors in that segment. For uniformly distributed connection, such as a composite slab, Fig. 7.9 represents the shear stress-slip curve for the connection, and is usually constant along the member.

The first step in the analysis is to make an initial estimate for the value of the slip in Segment 1, as shown in Fig. 7.1. With this value of slip, the load in the connectors for the first segment can be determined from the load-slip curve for the connectors. For segments farther from the support, the total force transferred across the interface is the sum of all forces in the connectors between the segment under consideration and the end of the beam. This is shown in Fig. 7.10, which shows the variation in bond force along the length of the member. Thus, the bond force acting at the i-th cross-section is found by summing the load in the connectors for each of the segments from the end of the beam to the location of the i-th cross section. This can be represented by the following equation:

$$F_{b,i} = \sum_{j=1}^{i} P_j \Delta x$$

$$= F_{b,i-1} + P_i \Delta x \qquad \text{.....(7.18)}$$

where

Δx = Length of one segment

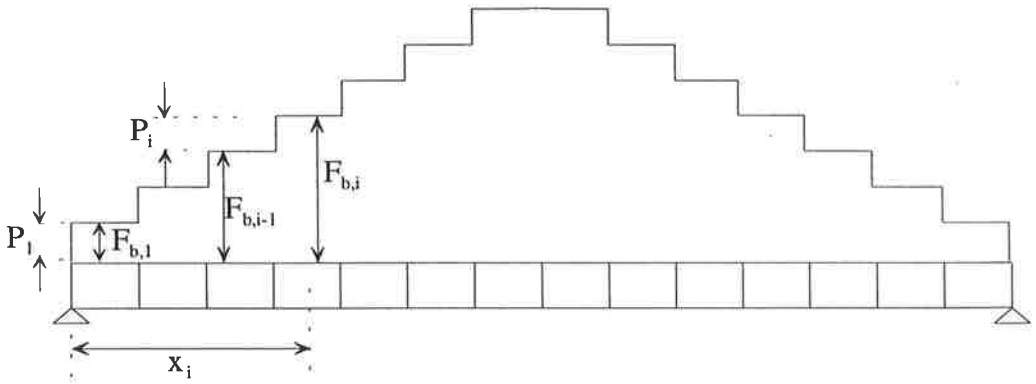


Fig. 7.10. Variation of Bond Force along Member

Thus, for the first segment, where i = 1, the bond force is also equal to the force in the connectors. The bond force is considered to act at the mid-length of the segment. From the distribution of imposed loads, the overall moment variation is known. Thus, the moment acting at the mid-length of the segment can be determined. Thus, for the first segment, the

moment acting on the cross-section is known as well as the bond force. These values can be used in Eqs. 7.13, 7.14 and 7.15, and a two fold iterative procedure is used to solve for equilibrium. When the correct value of curvature is found such that the error between the internal and external moment is sufficiently small, the value of slip strain is calculated from Eq. 7.16.

Strains are related to displacements by the distance over which they are considered to act. Thus the slip strain is related to the change in slip by the segment length. Hence the slip strain just determined from the cross-sectional analysis represents the rate of change of the slip at the cross-section under consideration. That is to say, the slip strain at any location can be considered to be the derivative of the slip at that section, and the problem of defining the variation in slip becomes one of solving an ordinary differential equation. This differential equation can be expressed in the form of Eq. 7.19, where the function f_1 is a non-linear function which represents the combined calculations of the cross-sectional analysis of the previous section. Equation 7.19 indicates that the slip strain, or rate of change of slip, is a function of the applied moment, and the bond force acting at a given cross-section.

$$\frac{ds}{dx} = f_1(M, F_b) \quad \text{.....(7.19)}$$

The bond force varies along the length of the member and is itself a function of the slip. It can be seen from Eq. 7.18 that the equation describing the variation of bond force follows the form of a finite difference equation, and can be expressed as a differential equation for the limiting case as Δx approaches zero. This is given in Eq. 7.20, where the function f_2 represents the load-slip relationship for the connectors per unit length of beam, and is derived from Eq. 7.17.

$$\frac{dF_b}{dx} = \frac{f(s)}{c} = f_2(s) \quad \text{.....(7.20)}$$

Equations 7.19 and 7.20 represent two coupled differential equations, which need to be solved simultaneously. It is not necessary that the functions f_1 and f_2 be expressed as explicit equations, and the iterative approach of solving f_1 is well suited to this procedure. The simplest method of solving two coupled differential equations is Euler's method (Chapra and Canale, 1988). The solution is expressed in the form of Eqs. 7.21 and 7.22, where the moment, bond force and slip are represented as discrete functions of the segment location.

$$s_{i+1} = s_i + f_1\left(M_i, F_{b,i}\right)\cdot h \quad \text{.....(7.21)}$$

$$F_{b,i+1} = F_{b,i} + f_2\left(s_i\right)\cdot h \quad \text{.....(7.22)}$$

where

s_i = Slip at the centre of the i-th segment

s_{i+1} = Slip at the centre of the i+1 segment

$F_{b,i}$ = Bond Force at the centre of the i-th segment

$F_{b,i+1}$ = Bond Force at the centre of the i+1 segment

h = Width of segment, Δx

Equations 7.21 and 7.22 indicate that the slip and the bond force at the next segment are related to the slip and bond force of the previous segment by Eqs. 7.19 and 7.20, which give the rate of change of each with distance. Thus, Eqs. 7.21 and 7.22 can be successively implemented throughout the length of the member, in order to determine the variation in slip.

For symmetrically loaded members, the slip must be zero at the centre of the span. If the centre slip from the analysis is found to be greater then zero, then the initial estimate of end slip is reduced and the procedure is repeated. Similarly if the centre slip is negative, the end slip is increased and the procedure repeated. Successive iterations are performed until the slip at the centre is sufficiently close to zero. In the case of a non-symmetrically loaded member, the iterations are continued to the other end, and then the boundary condition of zero bond force is checked at the end of the member. The estimate of end slip at the first end is altered until the bond force in the final segment is sufficiently close to zero.

The analysis method described above is limited in accuracy by the number of segments. For more segments, the greater the accuracy of the solution. There comes a trade off in the level of accuracy versus the computational time. A more advanced method of analysis allows greater accuracy with little increase in computational time. The Runge-Kutta method (Chapra and Canale, 1988) represents one such procedure. It is the method chosen for this study. However, as it is based on a similar procedure to Euler's method, it was worth while to incorporate the previous discussion. The main equations 7.21 and 7.22 are reformulated as:

$$s_{i+1} = s_i + \frac{1}{6}\left[k_{s1} + 2k_{s2} + 2k_{s3} + k_{s4}\right] \cdot h \quad \text{.....(7.23)}$$

$$F_{b,i+1} = F_{b,i} + \frac{1}{6}\left[k_{f1} + 2k_{f2} + 2k_{f3} + k_{f4}\right] \cdot h \quad \text{.....(7.24)}$$

where

$$k_{s1} = f_1\left(M_i, F_{b,i}\right) \quad \text{.....(7.25a)}$$

$$k_{s2} = f_1\left(M_{i+0.5}, F_{b,i} + 0.5hk_{f1}\right) \quad \text{.....(7.25b)}$$

$$k_{s3} = f_1\left(M_{i+0.5}, F_{b,i} + 0.5hk_{f2}\right) \quad \text{.....(7.25c)}$$

$$k_{s4} = f_1\left(M_{i+1}, F_{b,i} + hk_{f3}\right) \quad \text{.....(7.25d)}$$

$$k_{f1} = f_2\left(s_i\right) \quad \text{.....(7.25e)}$$

$$k_{f2} = f_2\left(s_i + 0.5hk_{s1}\right) \quad \text{.....(7.25f)}$$

$$k_{f3} = f_2\left(s_i + 0.5hk_{s2}\right) \quad \text{.....(7.25g)}$$

$$k_{f4} = f_2\left(s_i + hk_{s3}\right) \quad \text{.....(7.25h)}$$

The k's in the square brackets in Eq. 7.23 represent the slip strains evaluated at different locations in each segment and the k's in Eq. 7.24 represent the shear flow force evaluated at different locations. The terms inside the square brackets represents a weighted average of the slip strains and shear flow forces over the segment. Equations 7.25 are evaluated for each segment, and then substituted into 7.23 and 7.24, to determine the slip and bond force at the next segment. This procedure results in a more accurate estimate for the slip and bond force than the Euler's method, without requiring such fine divisions for the number of segments.

7.6.3 Ultimate Moment

The procedure outlined in Section 7.6.2 is carried out for a given applied load, and thus a known moment distribution for simply supported members. Once equilibrium has been found at every cross-section and the boundary conditions have been satisfied, the load is increased and the procedure is repeated. This is continued until the member is unable to

sustain any increase in load. As the ultimate moment is approached, there is a rapid increase in deflection and also a large increase in slip, for a small increase in load. In order to accurately determine the ultimate moment, the increments in load are reduced near the maximum load.

It must be appreciated that the overall behaviour of the member is highly dependent on the rotation capacity of the most highly stressed segments. Typically there will be one portion of the beam in which the curvature will be larger than all the others and as the load increases, this segment will continue to maintain the largest curvature. This critical segment will finally limit the maximum moment in the member, for simply supported members. After the ultimate moment of the beam has been reached, the behaviour of the member depends on the loading arrangement. If the member is loaded under load control, then the member will collapse after the maximum moment has been reached. If the member is loaded under displacement control, then the softening branch of the member will be recorded. The correct modelling of this softening branch requires an understanding of the behaviour of the composite members in the overload condition.

Previous studies have shown that the modeling of the unloading path of softening structures is affected by the length of the segments used in the analysis (Bazant et al, 1987; Warner and Yeo, 1984b; Wong, 1989). The reason for this is due to the behaviour of the member once the maximum load is reached. After the maximum load, any increase in deformation results in a decrease in the applied load. For a simply supported member, the applied moment must decrease at all cross-sections along the member. However, this reduction in applied moment will not be associated with a reduction in the curvature at all cross-sections. There will exist a portion of the beam in which the curvatures will continue to increase, whereas for all other sections along the beam, the curvatures will decrease. The section of the beam which develops increasing curvature for decreasing moment is called the discontinuity length.

The correct modeling of the softening behaviour is highly dependent on the correct choice of the discontinuity length. For this reason, much work has been done in defining the discontinuity length in reinforced concrete structures (I.C.E., 1962; Cohn and Petcu, 1963; Corley, 1966; Park et al., 1982), and for the negative moment region of composite beams (Lay, 1965; Barnard and Johnson, 1965a; Lukey and Adams, 1969; Kemp and Dekker, 1991). When a segmental method of analysis is employed, the length of the segments can then be set

equal to the discontinuity length (Warner and Yeo, 1984b; Wong, 1989; Kenyon, 1993). The critical segment can then maintain an increasing curvature during load softening, whereas the other segments will undergo decreasing curvatures. If the length of the segments are not the same as the discontinuity length, then the load-displacement and load-slip curves will be either under-estimated, or over-estimated.

Despite the work undertaken in hinge formation in reinforced concrete members, there has been a lack of work in the investigation of discontinuity lengths in other members, such as profiled beams, or composite slabs, or for positive moment regions in composite beams. It is noted, however, that for simply supported composite slabs advanced modelling of any discontinuity is not necessary. This is due to the fact that experimental results have typically shown significant and rapid reduction in load carrying capacity after the ultimate moment has been achieved (Porter, 1968; 1974). This implies that post-ultimate behaviour is non-ductile and the concept of a discontinuity is not necessary. Secondly, for continuous composite slabs, the cross-section in the negative moment region resembles that of a standard reinforced concrete slab which can be modelled in a similar manner to other reinforced concrete members.

Due to the lack of work in the area of discontinuity lengths in profiled beams, this area has not been incorporated into the current computational program. As a result the softening behaviour of composite profiled beams is not included in this analysis. With further work in this area, it would be possible to include the softening behaviour into the analysis.

7.6.4 Deflected Shape

For a given imposed load, once the boundary conditions have been satisfied, the deflected shape can be determined by integrating the segment curvatures. A typical member is shown in Fig. 7.11, where the curvature in a typical segment is denoted by ϕ_i. The rotation θ_i, is given by Eq. 7.26 and is assumed to be concentrated at the centre of the segment, as shown in Fig. 7.11. The deflection at any point along the member is given by Eq. 7.27.

$$\theta_i = \phi_i \Delta x \quad \text{.....(7.26)}$$

$$\Delta_i = \theta_0 x_i - \sum_{j=1}^{i} \theta_j (x_i - x_j) \quad \text{.....(7.27)}$$

$$\theta_{end} = \theta_0 - \theta_1 - \theta_2 - \theta_3 - \ldots - \theta_i \quad \text{.....(7.28)}$$

where

Δx = Length of one segment

Δ_i = deflection of the i-th segment

θ_{end} = slope at the i-th segment

x_i = distance of the i-th cross section from the end of the member

θ_0 = slope at the end of the member

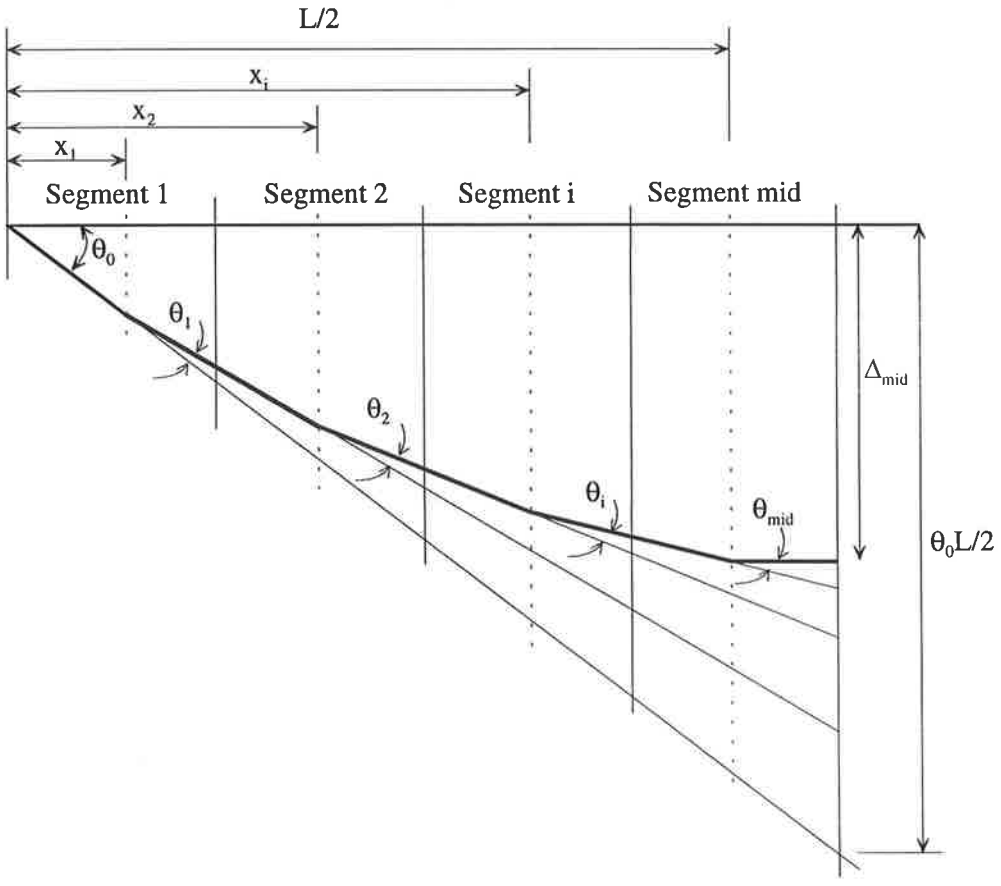


Fig. 7.11. Deflections of a segmented member

In order to solve Eq. 7.27 for the deflected shape, the known boundary conditions must be applied in order to solve for the initial end slope θ_O. For the case of a symmetrically

loaded member, the known boundary condition is that the slope is zero at the centre, hence setting $\theta_{end} = 0$ in Eq. 7.28 gives

$$\theta_0 = \theta_1 + \theta_2 + \ldots + \theta_{mid} \quad \ldots\ldots(7.29)$$

For a non-symmetrically loaded member, the boundary condition used is the deflection at the final segment must be zero. Thus θ_0 can be solved from Eq. 7.27.

$$\theta_0 = \frac{1}{L}\left(\theta_1(L - x_1) + \theta_1(L - x_2) + \ldots + \theta_k(L - x_k)\right) \quad \ldots\ldots(7.30)$$

With θ_0 determined, and θ_i also known for each segment, the deflection at any location can now be found from Eq. 7.27.

7.7 Comparison with Experimental Results

The results from the computer program have been compared with experimental results in order to determine the accuracy of the computer model. A comparison with previous composite beam results of other researchers is given in Section 7.7.1 while a comparison with the profiled beam results of Chapter 5 was given in Section 5.6.2 on page 327.

7.7.1 Composite Beams

A comparison between the experimental moment vs deflection curve of Davies (1969) with that from the computer program is shown in Fig. 7.12. The tests from Davies were carried out on half scale beams with the dimensions and properties given in Fig. 7.13. The beams were simply supported with a central span of 3 048 mm, and loaded with a single central point load. The shear connection was provided by 32 No. 9.5 mm studs at 95 mm centres. Tests were carried out on the studs and the shear strength was determined to be 23 kN, with the load - slip characteristics shown in Fig. 7.14.

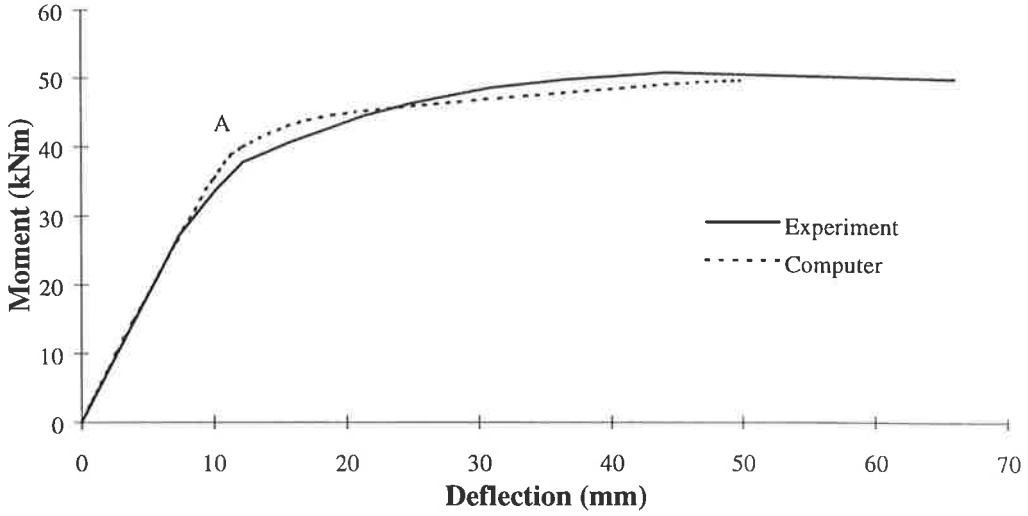


Fig. 7.12. Comparison with Davies (1969)

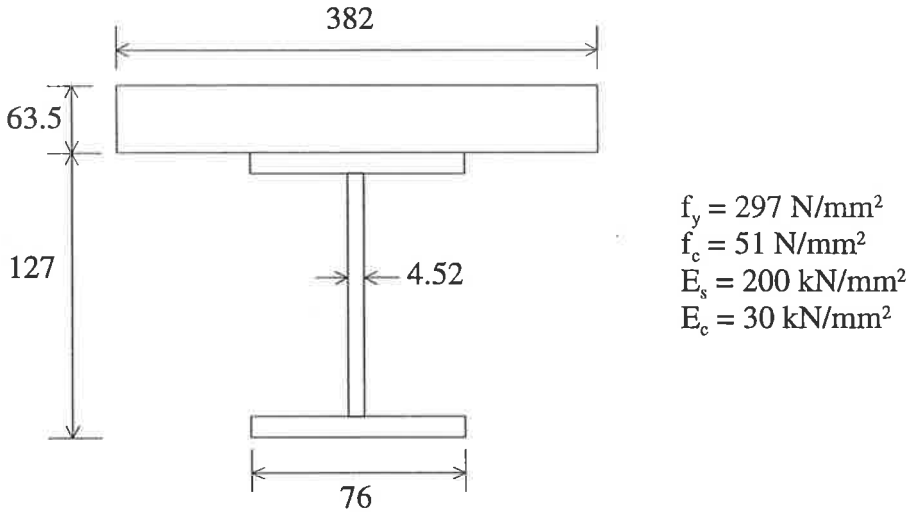


Fig. 7.13. Properties of Beams used by Davies (1969)

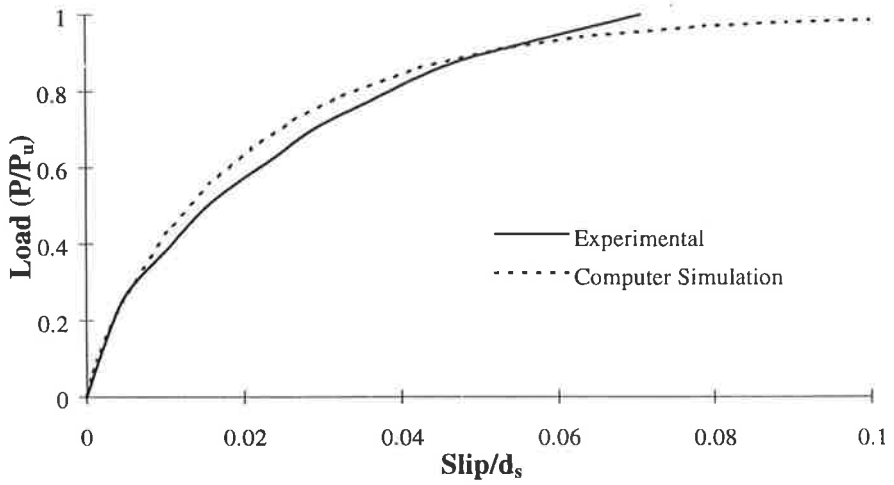


Fig. 7.14. Load - Slip Characteristics for beams by Davies (1969)

There is close agreement between the two curves shown in Fig. 7.12. It can be seen that the experimental curve tends to deviate slightly from the computer curve at A. This can be attributed to the fact that the computer model does not account for residual stresses in the steel beam. These residual stresses cause the gradual transition from linear to yielded behaviour, as shown by the experimental curve (Ansourian and Roderick, 1978; Rotter and Ansourian, 1979). The predicted ultimate moment was 49.7 kNm, compared to the measured ultimate moment of 51 kNm.

The experimental and computer load vs slip curves are shown in Fig. 7.15. It can be seen that there is close agreement between the experimental and computer predicted curves. The experimental curve is slightly stiffer than the computer curve, which may be related to small scale non-linearities. The tests by Davies were on a half scale model, with a stud diameter of $d_{sh} = 9.5$ mm. Load slip characteristics for the studs were quoted with the maximum load occurring at slips of 200×10^{-4} in, which is 0.51 mm, or approximately $0.05 d_{sh}$. The strength of the concrete was determined to be 51 N/mm^2. These results are much stiffer than results from other push tests, as discussed in Section 2.2.3 on page 11, which describe the slip at maximum load in terms of the concrete strength. For the concrete strength of 51 MPa, Eq. 2.6 on page 16 gives the slip at the maximum load of the connectors as $0.28 d_{sh}$, which is a factor of more than 5 times less than those results of Davies. This large discrepancy in the behaviour of the shear connectors may be the reason for the slight underestimation in the slip in Fig. 7.15.

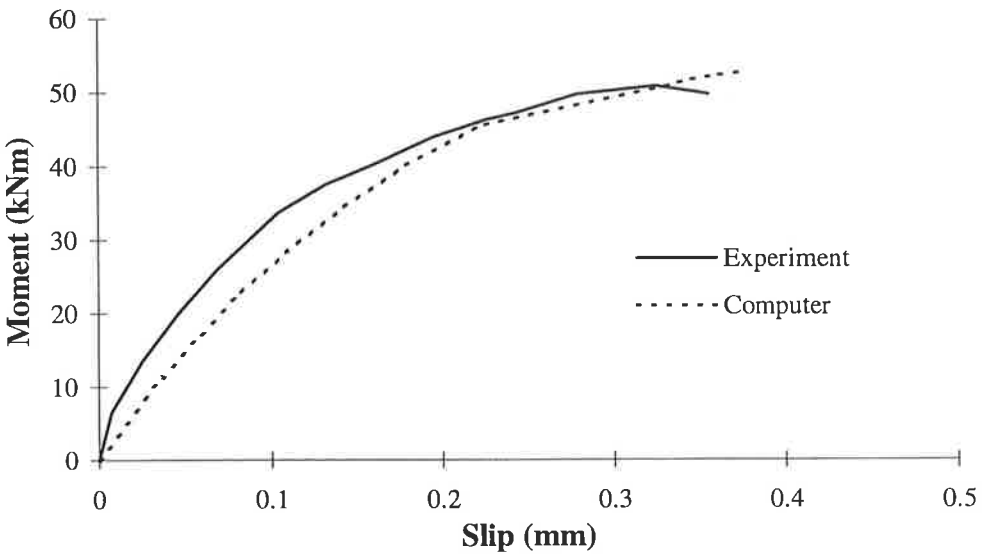


Fig. 7.15. Comparison with Davies (1969)

A comparison between the experimental moment vs deflection curve of Yam and Chapman (1968) with that from the computer program is shown in Fig. 7.16. The tests from Yam and Chapman were carried out on beams with the dimensions and properties given in Fig. 7.17. The beams were simply supported with a central span of 5 486 mm, and loaded with a single central point load. The shear connection was provided by 32 No. 19 mm studs at 121 mm centres. Tests were carried out on the studs and the shear strength was determined to be 64 kN with the load-slip characteristics shown in Fig. 7.18.

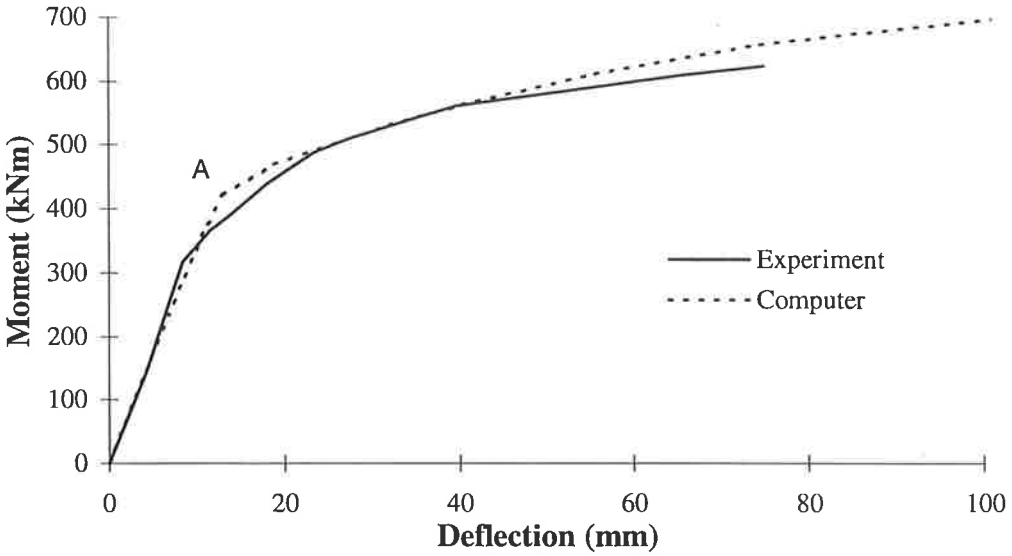


Fig. 7.16. Comparison with Yam and Chapman (1968)

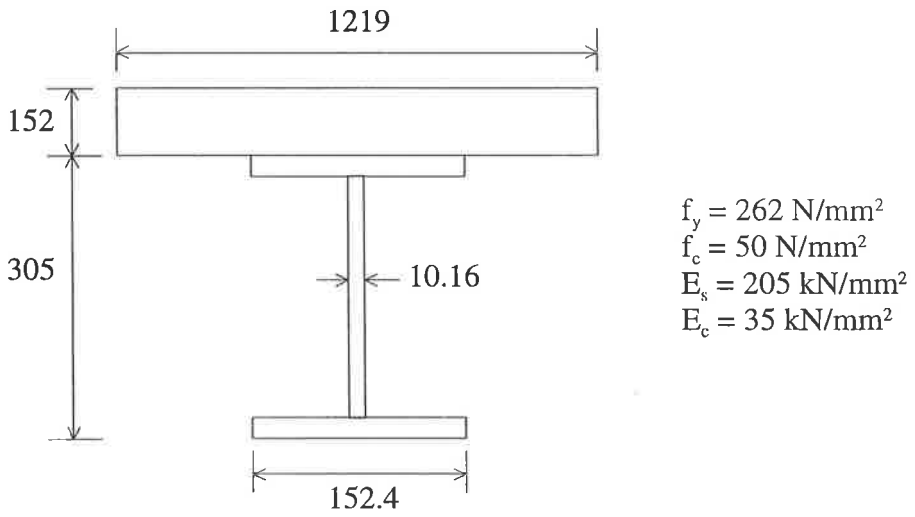


Fig. 7.17. Properties of Beams used by Yam and Chapman (1968)

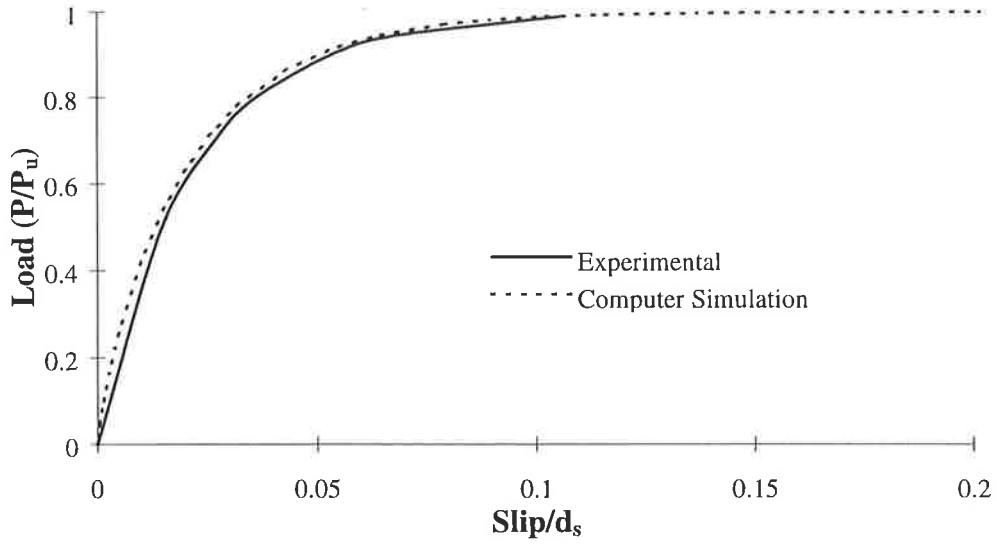


Fig. 7.18. Load -- Slip Characteristics for Connectors used by Yam and Chapman (1968)

There is close agreement between the two curves shown in Fig. 7.16. It can be seen that the experimental curve tends to deviate slightly from the computer curve at A. This can again be attributed to the residual stresses in the steel beam, as was noted previously.

A comparison between the computed and the measured slip distributions is shown in Fig. 7.19. The slip distribution reported by Yam and Chapman was given at 87% of the failure load ($M/M_u = 0.87$). Two computed slip distributions are shown in Fig. 7.19; one at 87% and one at 89% of the failure load. It can be seen that the computer curve for 89% of the

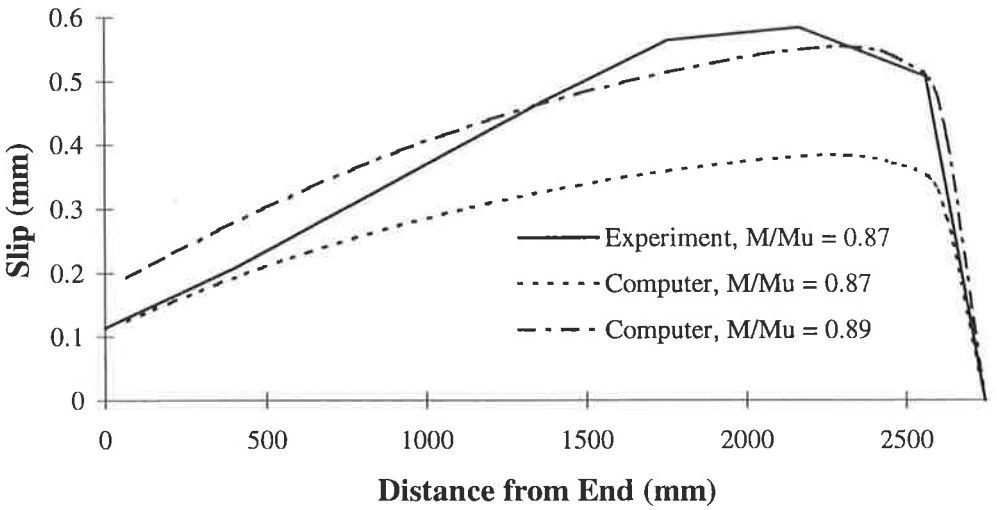


Fig. 7.19. Slip Distribution for Yam and Chapman (1968)

failure load is a better representation of the measured slip distribution in the high moment region, but overestimates the slip in the lower moment regions towards the supports. Overall there is reasonable agreement between the measured and predicted curves. This indicates that the computer program predicts the slip distribution with reasonable accuracy.

7.8 Conclusions

This chapter has presented a numerical approach for determining the effects of partial interaction on composite members. It has been shown that the numerical method of finite differences can be solved using forward integration to provide a simple and effective method of modelling the behaviour of members with partial interaction. The results of the computer simulation are in reasonable agreement with measured values for composite beams (Section 7.7) and for profiled beams (Section 5.6.2).

This computer program can be used on a composite member with partial interaction to determine the slip distribution along its length and the variation in end slip with increasing load. These values can be used in the absence of experimental data to check the accuracy of the mathematical model presented in Chapters 2 and 4 for composite and profiled beams respectively.

The computer model may also be used to investigate the effects of different parameters on the overall behaviour of the composite member where experimental testing would prove costly and time consuming. An example of such an application would be the effect of the stiffness of the shear connectors on the overall behaviour, which as yet is not adequately accounted for in the theory of Chapter 3.

Chapter 8

Conclusions

8.1 Introduction

This chapter details the findings contained within this thesis. The thesis looked at aspects pertaining to the strength and ductility of composite steel and concrete members. There were four fundamental areas that were investigated. The first area of this thesis involved investigation of the effect on the strength and ductility of composite beams due to the limited slip capacity of the shear connection. The second area of this thesis was involved in the development of a small scale testing procedure to evaluate the shear connection performance of profiled sheeting. The third area of the thesis was in the determination of the flexural capacity of composite profiled beams with partial shear connection. Finally, the fourth area of the thesis was in the determination of the transverse shear capacity of composite profiled beams.

8.2 Conclusions

8.2.1 Composite Beams

A theoretical analysis of simply supported composite steel and concrete beams with partial shear connection has been presented. In particular, a method for determining the total end slip that occurs in a composite beam under ultimate moment conditions has been described. This calculated end slip is then compared to the allowable slip capacity of the connection, thus allowing designers to avoid premature fracture of the shear connectors.

A two tier analysis procedure was used to determine the total endslip. The first tier assumes linear concrete and steel material properties, with fully yielded shear connectors. The second tier allows for full non-linear behaviour of the steel and concrete, and the shear connectors.

The first tier may be used as a simple procedure give an approximate understanding of the controlling parameters that contribute to endslip. However, as this procedure always underestimates the endslip, it is unconservative, and thus should be used with caution. It is applicable to long, slender composite beams with a high applied moment gradient, such as when loaded by a single point load. In this situation the yield zone in the steel does not extend over a significant portion of the beam, and thus linear elastic analysis (incorporating yielding of the connectors) can be justified, as the endslip is a function of the properties along the entire length of the beam.

The second tier analysis incorporates separate effects to account for non-linearity in the concrete and the steel, as well as a term which includes the slip increment due to plastic deformation of the member in the hinge region. By separating the slip increment developed in the hinge region, a distinction can be drawn between the slip capacity of the shear connectors that is required to reach the ultimate moment of the member, and that which is required to ensure full plastic deformation of the member. This is due to fact that there is little increase in the moment resistance of the member during the plastic hinge formation, but there is significant increase in member deflections and rotations. Thus, it is possible to distinguish between the two different limit states of sufficient strength, and sufficient ductility. This allows the designer flexibility to separate the two effects if necessary.

There was reasonable agreement between the theoretically predicted maximum slips and those measured from experimental testing. It appears that the theory does not adequately predict end slips for beams with greater than full shear connection. However, as such beams are unlikely to fail by premature fracture of the shear connectors, this results does not effect the validity of the theory presented. Furthermore, when the maximum slip does not occur at the end of the shear span, the theory still shows adequate correlation to the maximum slips within the shear span.

8.2.2 Interface Bond Push Tests

The investigation into the load-slip behaviour of profiled steel sheeting lead to the design of a new test procedure to determine the shear characteristics. A new testing procedure was deemed necessary due to several shortcomings with other techniques which have been proposed by other researchers. The conclusions which arose from this test development are detailed in Section 8.2.2.1.

After the new proposed arrangement of the push test had been finalised, a series of tests were performed on re-entrant and open rib profiles. The series of tests investigated various qualitative effects related to the load-slip characteristics of the profiled sheeting as different parameters were varied. The conclusions arising from this investigation are detailed in Section 8.2.2.2.

8.2.2.1 Design of Push Tests

These conclusions arose out of the results of the preliminary series of push tests, as well as from an analysis of the results and behaviour of the subsequent specimens. They relate specifically to the design and setup of push tests for the determination of the interface bond properties between profiled sheeting and concrete.

- The accurate measurement of interface bond requires careful consideration of a number of factors. The most important of these is the application of an external lateral restraining force on the sheeting. It has been shown that for profiled sheeting incorporating embossments, longitudinal slip between the sheeting and the concrete is accompanied by lateral movement of the sheeting away from the concrete surface.

This lateral movement is also present for profiles with a re-entrant rib geometry, although the magnitude is less than that observed in open rib profiles. Thus, any external lateral force will restrict the free deformation of the sheeting, and thus alter the shear bond characteristics of the profile.

- The decrease in chemical bond strength with increasing rib opening suggests that peeling action tends to reduce the effectives of the chemical bond for more open rib geometries. It is expected that the chemical bond should remain constant for any rib geometry, and that it should be a function of the concrete properties and the surface condition of the sheeting. The apparent variation in the chemical bond strength as measured from these tests indicates that this test procedure should not be used in the determination of the chemical bond strength of profiled sheeting.
- The application of the debonding agent was effective in reducing the chemical bond significantly, but did not completely remove it. However, the debonding agent also tended to lubricate the surface, and hence changed the subsequent behaviour of the shear-stress / slip relationship. The maximum mechanical bond was reduced, and the slip at which it occurred was increased. Thus, it is recommended that the use of a debonding agent should not be used in the preparation of the push test specimens.

8.2.2.2 Behaviour of Re-entrant and Open Rib Profiles

These conclusions are based on the results of the 36 specimens tested as part of this research project. These conclusions represent a qualitative assessment of the results, and identify general trends that occurred.

- The shear strength of profiled sheeting is related to the rib opening: profiles with a larger rib opening have a decreased shear resistance. This decrease in shear resistance with increasing rib opening occurred for all thicknesses of sheeting, for profiles with and without embossments, and also for sheeting with and without any debonding agent applied to the interface.
- There is a maximum rib opening which if exceeded will result in the complete loss shear capacity after failure of the chemical bond. For profiles without embossments this limit is approximately $b_r/b_f = 1$, which corresponds to a square rib. For profiles with the embossments adopted in this study, this limit is approximately $b_r/b_f = 2.7$. It is anticipated that this limit is a function of the embossment geometry, however

this parameter was not varied in the present study. The limit in the rib opening is related to the ability of the sheeting to resist the lateral forces which develop during longitudinal slip and tend to force the sheeting away from the concrete. For non-embossed profiles, this limit is reached when the rib opening is equal to the width of the rib flange, and the sheeting is free to move laterally away from the concrete. For profiles with embossments in the webs of the ribs, the limiting rib opening is increased due to the keying action of the embossments. The limiting rib opening is increased by increasing the height of the embossments.

- Embossments improved the mechanical shear resistance of the sheeting. The increase in shear resistance was more noticeable for the open rib geometries; the non-embossed profiles with large rib openings failed completely after failure of the chemical bond, whereas the embossed profiles exhibited continued shear resistance after failure of the chemical bond.
- The shear strength of the profile is increased by increasing the thickness of the sheeting. The relationship between the shear strength of the profile f_b and the thickness t_p is of the form $f_b = a.t_p^n$, where n is between 1.3 and 1.5.

8.2.3 Flexural Strength of Profiled Beams

The use of light gauge steel sheeting as permanent and integral shuttering to the sides and soffit of reinforced concrete beams is relatively new. The research in this project was directed in a large part to further understanding and quantifying the behaviour of profiled beams. There are many advantages to the use of profiled beams, and it is worth re-iterating them at this point, before the detailed findings of this research are presented. The benefits of profiled beams include:

- The profiled box section becomes a permanent and integral component of the beam, eliminating the need for formwork stripping;
- The side profiled sheeting is equally effective in positive and negative moment regions;
- It increases the shear and flexural strength of the encased beam;

- The profiled sheeting acts integrally with the concrete, and reduces the amount of conventional reinforcement required, with subsequent savings in supply and fixing;
- Encasement of concrete on three sides reduces moisture loss, and hence reduces shrinkage of the concrete. This in turn reduces the long term deflections due to creep and shrinkage, and allows an increase in the span/depth ratios;
- Being manufactured off site and under factory conditions will save in total construction time and delays;
- The light weight of the box section makes transport form the factory easy and cost effective, and
- It provides a clean, attractive streamlined finish that can be left exposed if desired.

A model describing the ultimate moment capacity of profiled beams has been developed. It is based on rigid plastic analysis, and requires an understanding of the load-slip characteristics of the sheeting used. The equations which were derived give the ultimate moment of the profiled beam based on the degree of shear connection at the critical cross-section. The equations were derived for two different forms of construction; welded construction and clipped construction. A series of 6 full scale profiled beam tests were carried out to investigate their behaviour and to validate the proposed theory. The conclusions resulting from this investigation are as follows:

- There are two distinct forms of profiled beam construction; welded construction and clipped construction. Welded construction is when the sheeting is formed into a rigid U-shaped section which encloses the concrete on three sides, such that there is no discontinuity in the sheeting around the perimeter that would permit longitudinal slip. This may be achieved by using a single sheet to form the shape of the beam, or the shape of the beam may be built up from individual units which are subsequently welded together into a braced box section before being erected on site. Clipped construction is when the units are assembled on site by 'clipping' individual units together, and the interlocking is achieved only by the shape of the ribs. Thus the individual units are free to slip longitudinally, relative to one another.
- Under conditions of full shear connection the moment capacity of beams constructed by welded and clipped construction are the same.

- Greater development lengths are required to develop full shear connection when clipped construction is used.
- The results from the experimental tests were in close agreement with the values predicted using the theory developed. This indicated that the rigid plastic analysis procedure provides a simple and accurate model to describe the ultimate moment of a profiled beam.
- The addition of the profiled sheeting increased the flexural strength of the beam by as much as 130% compared to the reinforced concrete beam.
- The L-Rib geometry adopted in 4 of the beam tests provided very high bond strength, and as a consequence slips measured at the interface were of a very small magnitude. The strengths of the beams exceeded the theoretical strength for full shear connection. The displacements which were measured at the interface were influenced by the strains in the sheeting and tended to exhibit the variation in strain expected throughout the length of the member. This variation in strain is characterised by large increases in the plastic hinge region, tapering away rapidly to zero at the supports.
- Two tests were carried out on welded Dove-Tail rib beams. The longitudinal shear strength of the ribs was much less than the L-Rib geometries, and as a consequence the beams exhibited partial shear connection. The slip distribution was generally constant throughout the shear span, with a slight reduction toward the supports. The loss of full shear connection reduced the load carrying capacity of the beams by only 2%.

8.2.4 Shear Strength of Profiled Beams

A series of tests were carried out to investigate the effect of the side profiled sheeting on the transverse shear strength of profiled beams. A small scale test specimen was designed and used to obtain results on the shear performance of different rib geometries, as well as to determine the influence of various parameters such as; sheeting thickness, surface condition and development length. The results of the tests were compared to predicted values using theory developed by other researchers. The conclusions of this section are as follows:

- The transverse shear strength of a reinforced concrete member is highly variable, and is dependent on many different parameters. The addition of the profiled sheeting increases the complexity of the problem of predicting the shear strength.

- There was considerable variation between the predicted shear strengths and those measured. This difference was greatest for the specimens without profiled sheeting, with a mean error of 91%. When the measured strength of the concrete specimens was substituted for $V_{uc,s}$ in Eq. 6.11 the error in the predicted values was considerably reduced from a mean error of 32% for the profiled specimens to a mean error of 20% compared to the measured values.

- The external sheeting between the ribs causes only a minor increase in the shear strength for L-Rib profiled sheeting. This can be attributed to the low shear buckling strength of the sheeting due to a high b/t ratio.

- The amount of longitudinal bond developed between the sheeting and the concrete at the location of the shear plane strongly effects the transverse shear performance of the profiled sheeting.

- The resistance of the sheeting to transverse shear is strongly dependant on the overall geometry of the sheeting. Of the three basic geometries tests, the L-Rib had the highest transverse shear strength, followed by the dove tail rib and then the trapezoidal rib.

8.3 Further Research

There were several areas requiring further research which became apparent during the course of the investigations in this thesis. These areas include:

- Determination of the effect on the endslip estimate in composite beams due to non-yielding of some of the shear connectors. The analysis presented in Chapter 2 assumed that all the shear connectors were fully yielded at the ultimate moment. This will often be the case for members subjected to high moment gradients over their whole length, such as members loaded by point loads at the centre. However, for members with a significant constant moment region, such as a beam loaded at its third points, the slips in the constant moment region may not be sufficient to cause yielding in the shear connectors. In this case the bond force would be

overestimated using the procedures proposed in this thesis, which would result in an unconservative estimate of the endslip.

- Further work into defining the hinge behaviour of composite steel and concrete beams under positive moment is required. In particular, there needs to be a better estimate made of length of the hinge region. This improved estimate can be used to further refine the estimate of the slip increment due to hinge formation.

References

1. Aas-Jakobsen, A. and Grenacher, M., (1974), "Analysis of Slender Reinforced Concrete Frames," Publications, International Association of Bridge and Structural Engineers, Vol. 34-1, Zurich, pp. 1-17

2. ACI 318, (1989), "Building Code Requirements for Reinforced Concrete", American Concrete Institute, Detroit, USA.

3. ACI Committee 408, (1966), "Bond Stress - The State of the Art", Journal of the American Concrete Institute, Vol. 63, No. 11, pp 1161-1188.

4. ACI-ASCE Committee 426, (1973). "Shear Strength of Reinforced Concrete Members," Proceedings, ASCE, Vol. 99, ST6, June 1972, pp. 1091-1188.

5. Ahmed, M., (1996), "Strengthening of reinforced concrete beams by bolting steel plates to their sides", Thesis presented for the degree of Masters on Engineering Science, Department of Civil and Environmental Engineering, The University of Adelaide, Australia.

6. American Concrete Institute, (1989), "ACI 318-89 Building Code Requirements for Reinforced Concrete." ACI, Detroit, Michigan.

7. American Institute of Steel Construction, (1985), "Manual of structural steel for buildings", Washington, AISC, 1985.

8. American Iron and Steel Institute cold-formed steel design manual, (1987), SG-673 1185-5M-RI. American Iron and Steel Institute, Washington, D.C.

9. American Society of Civil Engineers Standard, (1992), "Standard for the Structural Design of Composite Slabs," ASCE, New York.

10. Andekola, O.A., (1968), "Partial Interaction between elastically connected elements of a composite beam", International Journal of Solids and Structures, Vol. 4, pp. 1125-1135.

11. Ansourian, P., (1977), "The Stability of Composite Beams in Negative Bending", Stability of Steel Structures. International Association for Bridge and Structural Engineering, Liège, pp. 145-154.

12. Ansourian, P., (1982), "Plastic rotation of composite beams", Journal of the Structural Division, ASCE, Vol. 108, No. ST3, March, pp. 643-659.

13. Ansourian, P. and Roderick, J.W., (1978), "Analysis of Composite Beams", Journal of the Structural Division, ASCE, Vol. 104, No. ST10, October, pp. 1631-1645.

14. Aribert, J.M., (1987), "Sur un modèle général de fonctionnement mécanique de la connexion acier-béton pour divers types de poutres et planchers mixtes, avec comparison à l'expérience," First International RILEM Congress, September 1987, Paris. Chapman Hall, Vol. 2, pp 871-878.

15. Aribert, J.M., (1990), "Dimensionnement de poutres mixtes en connection parielle", Mixed Structures including New Materials, IABSE Symposium, Brussels. International Association for Bridge and Structural Engineering, Reports, Vol 60, pp 215-220.

16. Aribert, J.M., (1991), "Very partial shear connection of composite beams with profiled steel sheeting", Proceedings of the third international conference on steel-concrete composite structures, Sept, Conference Committee of ICCS-3.

17. Aribert, J.M., (1993), "Application and Recent Development of a Numerical Model for Composite Beams with Partial Shear Connection", Composite Construction in Steel and Concrete II, Eds: Easterling, W.S. and Roddis, W.M., American Society of Civil Engineers.

18. Aribert, J.M. and Al Bitar A., (1989), "Optimisation of the design in partial connection of beams in composite floors with thin profiled steel sheeting", Construction Métallique, No. 4, 1989, pp. 3-33

19. Aribert, J.M. and Aziz, A.K., (1985), "Calculation of composite beams up to ultimate state with the effect of uplift at steel-concrete interface", Construction Métallique, No. 4, 1985, pp. 3-36

20. Aribert, J.M. and Aziz, A.K., (1986), "Modèle général pour le calcul des poutres mixtes hyperstatiques jusqu'a la ruine," Construction Métallique, No. 3, pp. 3-41

21. Aribert, J.M., and Labib, A.G., (1982), "Modèl de calcul élastoplastique de poutres mixtes à connexion partielle" Construction Métallique, Putenuz, Vol 19, No 4, pp. 3-51.

22. Azman, A. and Warner, R.F., (1984), "Ductility Requirements for Continuous Reinforced Concrete Structures", Department of Civil Engineering, Report No. R62, January, The University of Adelaide.

23. Barnard, P.R., (1964), "The Collapse of Reinforced Concrete Beams," Proceedings, ASCE, International Symposium on Flexural Mechanics of Reinforced Concrete, Miami.

24. Barnard, P.R., and Johnson, R.P., (1965a), "Plastic behaviour of continuous composite beams", Proceedings of the Institution of Civil Engineers., Vol. 32, pp. 180-197.

25. Barnard, P.R., and Johnson, R.P., (1965b), "Ultimate Strength of Composite Beams", Proceedings of the Institution of Civil Engineers., Vol. 32, pp. 161-179.

26. Bazant, Z.P. and Oh, B.H., (1984), "Deformation of progressively cracking reinforced concrete," ACI Journal, Vol. 81, No. 3, May-June, pp. 268-278.

27. Beeby, A.W., (1968), "Short-term deformations of reinforced concrete members", Cement and Concrete Association, London. Tech. Rep. TRA 408, March.

28. Bradford M.A. and Kyakula M., (1994), "Shear Strength of Profiled Composite Beams", Australian Civil Engineering Transactions, IEAust., Vol. CE36, No. 2, pp. 173-178.

29. Branson, D.E., (1963), "Instantaneous and time-dependant deflections of simple and continuous reinforced concrete beams", Part 1. Auburn University, 78pp.

30. Bridge, R.Q., (1984), "Composite Steel Deck Floor Systems", Steel Construction Journal, Australian Institute of Steel Construction, Vol. 18, No. 1, May.

31. British Standards Institute, (1982), "Structural use of Steelwork in Buildings; Part 4. Code of Practice for Design of Floors with Profiled Steel Sheeting", BS5950, Part 4.

32. BS 5950. Part 3, (1990), "Structural use of steelwork for buildings - Part 3. Design in composite construction", British Standards Institute, UK.

33. Burnet, M.J., Oehlers, D.J., (1994), "Application of profiled steel sheeting as integral formwork for the sides of reinforced concrete beams." Proceedings of the Australian Structural Engineering Conference, The Institution of Engineers, Australia. pp. 1130-1144.

34. Buttry, K.E., (1965), "Behaviour of Stud Shear Connectors in Lightweight and Normal-Weight Concrete", MSc Thesis, University of Missouri, Colombia.

35. Canadian Standards Association, (1984), "Steel Structures for Buildings (Limit States Design)", CAN3-S16.1-M84, December, Chapter 17.

36. Carriera, D.J. and Chu, K.H., (1986), "Stress-strain relationship for reinforced concrete in tension", ACI Journal, Vol. 83, No. 1, pp. 21-28.

37. CEB, (1978), CEB-FIP Model Code for Concrete Structures, CaCA, London.

38. Chan, W.L., (1955), "The Ultimate Strength and Deformation of Plastic Hinges in Reinforced Concrete Frameworks", Magazine of Concrete Research, Vol. 7, No. 21, November, pp. 121-132.

39. Chapman, J.C. and Balakrishnan, S., (1964), "Experiments of Composite Beams," The Structural Engineer, November 1964, Vol. 42, No. 11, pp. 369-383.

40. Chapra, S.C. and Canale, R.P., (1988). "Numerical Methods for Engineers", McGraw-Hill.

41. Climenhaga, J.J. and Johnson, R.P., (1972a), "Moment-Rotation Curves for Locally Buckling Beams", Journal of the Structural Division, Proceedings of the ASCE, Vol. 98, No. ST6, June, pp. 1239-1253.

42. Climenhaga, J.J and Johnson, R.P., (1972b), "Local Buckling in Continuous Composite Beams", The Structural Engineer, Vol. 50, No. 9, September, pp. 367-374

43. Cohn, M.Z. and Petcu, V.A., (1963), "Moment Redistribution and Rotation Capacity of Plastic Hinges in Redundant Reinforced Concrete Beams," Indian Concrete Journal, Vol. 37, No. 8, August, pp. 282-290

44. Commission of the European Communities, (1990), "Draft Eurocode No. 4: Common Unified Rules for Composite Steel and Concrete Structures", Luxembourg.

45. Commission of the European Communities, (1990), "Draft Eurocode No. 4: Common Unified Rules for Composite Steel and Concrete Structures", Luxembourg.

46. Commité Européen du Béton, (1970), "International Recommendations for the Design and Construction of Concrete Structures", Commité Européen du Béton -Fédération Internationale de la Precontrainte.

47. Corley, W.G., (1966), "Rotational Capacity of Reinforced Concrete Beams", Journal of the Structural Division, Proceedings of the ASCE, Vol. 92, No. ST5, October, pp. 121-146.

48. Cranston, W.B., (1965), "Tests on Reinforced Concrete Frames; Pinned Portal Frames", Technical Report TRA/392, Cement and Concrete Association, London, August.

49. Crisinel, M., (1988), "New System of Connection with non-Welded Shear Connectors," Composite Construction in Steel and Concrete," ASCE, New Hampshire.

50. Crisinel, M., (1990), "Partial-interaction analysis of composite beams with profiled sheeting and non-welded shear connectors," Journal of Constructional Steel Research, Vol. 15, pp 65-98.

51. Crisinel, M, Fidler, M. and Daniels, B., (1986), "Flexure Tests on Composite Floors with Profiled Sheeting", Publication ICOM 158, École Polytechnique Fédérale de Lausanne.

52. Daalov, T., Petrov, K., (1990), "Research on beams with open steel box reinforcement." International Association of Bridge and Structural Engineering Symposium - Mixed Structures, pp. 89-94

53. Daniels, B., (1988), "Shear bond pull-out tests for cold-formed steel composite slabs". Publication ICOM 194. École Polytechnique Fédérale, Lausanne.

54. Daniels, B.J., and Crisinel, M., (1993), "Composite slab behaviour and strength analysis. Part 1: Calculation procedure." Journal of Structural Engineering, Vol. 119, No. 1, pp. 16-35.

55. Daniels, B.J., Nussbaumer, A. and Crisinel, M., (1989), "Non-Linear analysis of composite members in bending and shear". (Publication ICOM 223.) École Polytechnique Fédérale, Laussane.

56. Davies, C., (1969), "Tests on half-scale steel-concrete composite beams with welded stud connectors", The Structural Engineer, Vol. 47, No. 1, pp 29-40.

57. Dulacska, H., (1972), "Dowel action of reinforcement crossing cracks in concrete," Journal of the American Concrete Institute, Vol. 69, No. 12, Dec.

58. Eurocode 4, (1992), "Design of Composite Steel and Concrete Structures - Part 1.1: General Rules and Rules for Buildings" - Commission of the European Communities.

59. Fenwick, R.C. and Paulay, T., (1968), "Mechanisms of Shear Resistance of Concrete Beams, "Journal of the Structural Division, ASCE, Vol. 94, No. ST10, pp. 2325-2350.

60. Foo, S.K., (1990), "Softening Hinges in Prestressed and Partially Prestressed Concrete Structures", PhD Thesis, Department of Civil Engineering, Monash University, Australia.

61. Gere, J.M., and Timoshenko, S.P., (1987), "Mechanics of Materials", Van Nostrand Reinhold.

62. Gilbert, R.I. and Warner, R.F., (1978), "Tension stiffening in reinforced concrete slabs," Journal of the Structural Division, ASCE, Vol. 104, No. ST12, December, pp. 1885-1900.

63. Gupta, A.K. and Maestrini, S.R., (1990), "Tension-stiffness model for reinforced concrete bars," Journal of Structural Engineering, ASCE, Vol. 91, No. 3, March, pp. 769-790

64. Hanson, N.W., (1960), "Precast-Prestressed Concrete Bridges-2. Horizontal Shear Connections", Journal of the Portland Cement Association, Research and Development Laboratories, Vol. 2 No. 2, pp 38-58.

65. Hawkins, N.M. and Mitchell, D., (1984), "Seismic Response of Composite Shear Connectors", *Journal of Structural Engineering*, ASCE, Vol. 110, No.9, September, pp 2120-2136

66. Hawkins, N.M. and Roderick, J.W., (1976), "The Behaviour of Composite Beams", Proceedings, Institution of Civil Engineers, Australia, Vol. CE18, No. 2, pp. 102-108.

67. Hofbeck, J.A., Ibrahim, I.O. and Mattock, A.H., (1969), "Shear transfer in reinforced concrete," Journal of the American Concrete Institute, Vol. 66, No. 2, Feb., pp. 119-128

68. I.C.E. Research Committee, (1962), "Ultimate Load Design of Concrete Structures", Proceedings I.C.E. (London), Vol. 21, No. 2, February, pp. 399-442.

69. Johnson, R.P., (1975), "Composite Structures of Steel and Concrete. Volume 1. Beams, Columns, Frames and Applications in Buildings," Constructional Steel Research and Development Organisation, London.

70. Johnson, R.P. and Molenstra N., (1991), "Partial shear connection in composite beams in buildings," December, Proceedings of the Institution of Civil. Engineers, Part 2, pp. 679-704.

71. Kelfeld, W.J. and Thurston, C.W., (1966), "Studies of the Shear and Diagonal Tension Strength of Simply Supported Reinforced Concrete Beams", ACI Journal, Proceedings Vol. 63, No. 4, April, pp. 451-476.

72. Kemp, A.R., and Dekker, N.W., (1991), "Available rotation capacity in steel and composite beams", The Structural Engineer, Vol. 69, No. 5, March, pp. 88-97.

73. Kennedy, R.P., (1967), "A Statistical Analysis of the Shear Strength of Reinforced Concrete Beams," PhD Thesis, Stanford University, Stanford, California.

74. Kenyon, J.M., (1993), "Non-Linear analysis of reinforced concrete plane frames," PhD Thesis, Department of Civil Engineering, The University of Adelaide, Australia.

75. Kim, W. and White, R., (1991), "Initiation of Shear Cracking in Reinforced Concrete Beams with no Web Reinforcement," ACI Structural Journal, Vol. 88, No. 3, May-June, pp 301-308.

76. Kozak, J., (1990), "Composite steel girder, precast concrete slabs and insitu concrete." International Association of Bridge and Structural Engineering Symposium - Mixed Structures, pp. 261-262

77. Kriz, L.B. and Raths, C.H., (1965), "Connections in Precast Concrete Structures - Strength of Corbels", Journal of the Prestressed Concrete Institute, Vol. 10, No. 1, pp. 16-61.

78. Kyakula, M., (1992), "Composite Profiled Beams." Masters Thesis, Department of Structural Engineering, The University of New South Wales.

79. Lay, M.G., (1965), "Flange local buckling in wide-flange shapes", Journal of the Structural Division, ASCE, Vol. 91, No. ST6, December.

80. Lay M.G. and Galambos, T.V., (1967), "Inelastic Beams under Moment Gradient", Journal of the Structural Division, Proceedings of the ASCE, Vol. 93, No. ST1, February, pp. 381-399.

81. Link, R.A., Elwi, A.E. and Scanlon, A., (1989), "Biaxial tension stiffening due to generally oriented reinforcing layers," Journal of Engineering Mechanics, ASCE, Vol. 115, No. 8, August, pp. 1647-1662.

82. Lowe, P.G., (1991), "Externally Reinforced Concrete - A new structural material and repair medium", Innovation and Economics in Building Conference, Brisbane, Australia, pp. 541-547.

83. Lowe, P.G., (1993), "Externally Reinforced Concrete - II", 13th Australasian Conference on the Mechanics of Structures and Materials, University of Wollongong, pp. 541547.

84. Lowe, P.G. and Choong, K.C., (1990), "Externally Reinforced Concrete", 12th Australasian Conference on the Mechanics of Structures and Materials, Brisbane, Australia, pp. 177-182.

85. Lukey, A.F., and Adams, A.M., (1969), "Rotation capacity of beams under moment gradient", Journal of the Structural Division, ASCE, Vol. 95, No. ST6, June.

86. Massicotte, B., Elwi, A.E. and MacGregor, J.G. (1990), "Tension Stiffening Model for Planar Reinforced Concrete Members," Journal of Structural Engineering, ASCE, Vol. 116, No. 11, November, pp. 3039-3057.

87. Mattock, A.H. and Hawkins, N.M., (1972), "Shear transfer in reinforced concrete - Recent research," PCI Journal, March-April, pp 55-75.

88. McBean, P.C., (1990), "The Myer Centre, Adelaide - A case study" The Institution of Engineers Australia, Structural Engineering Conference, Adelaide, pp. 409-415

89. McGarraugh, J.B. and Baldwin, J.W., (1971), "Lightweight concrete-on-steel composite beams", Engineering Journal, AISC, Vol. 8, No. 3, July, pp. 90-98.

90. Menzies, J.B., (1971), "CP117 and Shear Connectors in Steel-Concrete Composite Beams," The Structural Engineer, Vol. 49, No. 3, March, pp. 137-153.

91. Mottram, J.T. and Johnson, R.P., (1990), "Push tests on studs welded through profiled steel sheeting," The Structural Engineer, Vol. 68, No. 10, May, pp. 187-193.

92. Newmark N.M., Siess C.P. and Viest I.M., (1951), "Tests and analysis of composite beams with incomplete interaction.", Proceedings of the Society for Experimental Stress Analysis, Vol. 9, No. 1, pp. 75-92.

93. Oehlers, D.J., (1990), "Deterioration in Strength of Steel Connectors in Composite Bridge Beams," Journal of Structural Engineering, ASCE, Vol. 116, No. 12, pp. 3417-3431.

94. Oehlers, D.J., (1992), "Profiled Beam Construction", Research Report R89, January, Department of Civil and Environmental Engineering, The University of Adelaide, South Australia.

95. Oehlers, D.J., (1993), "Composite Profiled Beams". Journal of Structural Engineering, ASCE, Vol. 119, No. 4, pp. 1085-1100.

96. Oehlers, D.J. and Bradford, M.A., (1995), "Composite Steel and Concrete Structural Members. Fundamental Behaviour" Elsevier Science Ltd, Oxford, U.K.

97. Oehlers, D.J. and Coughlan C.G., (1986), "The shear stiffness of stud shear connectors in composite beams," Journal of Constructional Steel Research, Vol. 6, October, pp. 273-284.

98. Oehlers, D.J. and Foley, L., (1985), "The fatigue strength of stud shear connections in composite beams," Proceedings of the Institution of Civil Engineers, Part 2, Vol. 79, pp 349-364.

99. Oehlers, D.J., and Johnson, R., (1987), "The strength of stud shear connections in composite beams", The Structural Engineer, Vol 65B, June, pp 44-48.

100. Oehlers, D.J. and Sved, G., (1995), "Flexural strength of composite beams with limited slip capacity shear connectors," Journal of Structural Engineering, ASCE, Vol. 21, No. 6, June, pp. 932-938.

101. Oehlers, D.J., Wright, H.D. and Burnet, M.J., (1994), "Flexural Strength of Profiled Beams," Journal of Structural Engineering, ASCE, Vol. 120, No. 2, pp 378-393.

102. Ollgaad, J.G., Slutter, R.G. and Fisher, J.W., (1971), "Shear Strength of Stud Connectors in Lightweight and Normal Density Concrete," Engineering Journal, American Institute of Steel Construction, Vol. 8, April, pp. 55-64

103. Park, R., Priestly, M.J.N. and Gill, W.D., (1982), "Ductility of Square-Confined Concrete Columns," Journal of the Structural Division, ASCE, Vol. 108, No. ST4, April, pp 929-950.

104. Patrick, M., (1990) "A new partial shear connection strength model for composite slabs." Steel Construction. Journal of Australian Institute of Steel Research, Vol. 24, No. 3, August, pp. 2-17.

105. Patrick, M., (1991), "Slip Block Test Results for Bondek II Profiled Steel Sheeting", BHP Research - Melbourne Labs Rep. No. BHPRML/PS64/91/002, June.

106. Patrick, M., (1994), "Shear Connection Performance of Profiled Steel Sheeting in Composite Slabs", Thesis presented for the degree of Doctor of Philosophy, School of Civil and Mining Engineering, The University of Sydney.

107. Patrick, M. and Bridge, R.Q., (1987), "Ductility of Simply-Supported Composite Beams", *Steel Construction*, Vol. 22, No. 2, pp 3-39.

108. Patrick, M. and Bridge, R.Q., (1988) "Behaviour of Australian composite slabs." Composite Construction in Steel and Concrete, Proceedings of an Engineering Foundation Conference, ASCE, pp. 663-679.

109. Patrick, M. and Poh, K.W., (1990), "Controlled Test for Composite Slab Design Parameters", Proceedings of the IABSE Symposium on Mixed Structures Including New Materials, Brussels, Vol. 60, July, pp. 227-231.

110. Patrick, M., Tse, D. and Poon, S.L., (1989), "Bondek Composite Beams. Stage 1 Design Method", B.H.P. Melbourne Research Laboratories Research Report MRL/PS64/89/011.

111. Petraasek, I., (1990), " Thin walled cold-formed beams with top chord encased in concrete slab" International Association of Bridge and Structural Engineering Symposium - Mixed Structures, pp. 253-254

112. Placas, A. and Regan, P.E., (1971) "Shear Failures of Reinforced Concrete Beams," Proceedings, American Concrete Institute, Vol. 68, Oct., pp 763-773.

113. Poh, KW, Attard, M., (1995), "Calculating the load-deflection behaviour of simply-supported composite slabs with interface slip." Engineering Structures, Vol. 15, No. 5, pp. 359-367.

114. Porter, M.L. (1968), "Investigation of light gauge steel forms as reinforcement for concrete slabs", MS Thesis, Iowa State University, Ames, Iowa.

115. Porter, M.L., (1974), "The Behaviour and Analysis of Two-Way Simply Supported Concrete Composite Floor Slabs Constructed with Cold-Formed Steel Decking", PhD Thesis, Iowa State University, Ames, Iowa.

116. Porter, M.L., and Ekberg, C. (1976), "Design recommendations for steel deck floor slabs", Journal of the Structural Division, Proceedings of the American Society of Civil Engineers, Vol 103, ST3, pp 663-677, 1976.

117. Porter, M.L., and Ekberg, C. (1977), "Behaviour of Steel-Deck-Reinforced Slabs", Journal of the Structural Division, Proceedings of the American Society of Civil Engineers, Vol. 103, No. ST3, pp. 663-677.

118. Porter, M.L., and Ekberg, C., (1978), "Compendium of ISU research conducted on cold-formed steel-deck-reinforced slab systems", Engineering Research Institute, Iowa State University, Ames, Iowa.

119. Prasannan, S. and Luttrell, L.D., (1984), "Flexural Strength Formulations for Steel-Deck Composite Slabs", Internal Report, Department of Civil Engineering, West Virginia University, Morgantown.

120. Roberts, J.M., (1981), "Finite difference analysis of composite beams with incomplete interaction by the finite element method" Computers and Structures., Vol 14, No 5-6, pp. 453-462

121. Robinson, H., (1969), "Composite Beam Incorporating Cellular Steel Decking," Journal of the Structural Division, Proceedings of the American Society of Civil Engineers, March 1969, Vol. 95, No. ST3, pp. 355-380.

122. Robinson, H., and Naraine, K.S., (1988), "Slip and uplift effects in composite beams". Composite Construction in Steel and Concrete. (Buckner C.D. and Viest I.M. eds) ASCE. New York, pp. 487-497

123. Rotter, J.M. and Ansourian, P., (1979), "Cross-section behaviour and ductility in composite beams", Proceedings of the Institution of Civil Engineers, Part 2, Vol. 67, June, pp. 453-474.

124. Rotter, J.M. and Ansourian, P., (1980), "Design of ductile steel-concrete composite beams", Civil Engineering Transactions, Institution of Engineers Australia, Vol. CE22, No. 3, pp. 202-208.

125. Sawyer, H.A., (1964), "Design of concrete for two failure stages", Proceedings of International Symposium on the Flexural Mechanics of Reinforced Concrete, Miami, ACI Special Publications SP-12, pp. 405-437.

126. Somes, N.F., (1966), "Moment-Rotation Characteristics of Prestressed Concrete Members; Rectangular Sections", Technical Report TRA/398, Cement and Concrete Association, London, September.

127. Standards Association of Australia, (1976), "AS 1012.17, 1976. Methods for the determination of the static chord modulus of elasticity and Poisson's ratio of concrete specimens", Standards Association of Australia, Sydney, Australia.

128. Standards Association of Australia, (1980), " AS 2327, Part 1 - 1980. SAA Composite Construction Code, Part 1 - Simply Supported Beams", S.A.A., Sydney, Australia.

129. Standards Association of Australia, (1985), "AS 1012.10, 1985. Method for the determination of indirect tensile strength of concrete cylinders", Standards Association of Australia, Sydney, Australia.

130. Standards Association of Australia, (1986), "AS 1012.9, 1986. Method for the determination of the compressive strength of concrete specimens", Standards Association of Australia, Sydney, Australia.

131. Standards Association of Australia, (1988a) "AS3600-1988 Concrete Structures." S.A.A., Sydney, Australia.

132. Standards Association of Australia, (1988b), "AS 1538-1988. Cold Formed Steel Structures Code". Standards Assoc. of Australia, Sydney.

133. Standards Association of Australia, (1990), "AS4100-1990 Steel Structures." S.A.A., Sydney, Australia.

134. Stark, J., (1978), "Design of composite floors with profiled steel sheeting", Recent research and developments in cold-formed steel design and construction, Vol 2, pp 893-922. Fourth International Speciality Conference on Cold Formed Steel Structures. University of Missouri-Rolla, Ames, Iowa.

135. Timoshenko, S.P. and Gere, J.M., (1982), "Theory of elastic stability'. McGraw-Hill International Book Co.

136. Trahair, N.S and Bradford, M.A., (1988), "The behaviour and design of steel structures", Chapman and Hall, New York, NY.

137. Trezona, J.R., (1995), "Analysis and design of circular reinforced concrete columns and concrete filled steel tube columns", Masters Thesis, Department of Civil and Environmental Engineering, The University of Adelaide, Australia.

138. Uy, B., (1995), "Profiled Composite Beam Construction" PhD. Thesis, Department of Structural Engineering, The University of New South Wales.

139. Uy, B. and Bradford, M.A., (1993a), "Time dependant behaviour of profiled composite and reinforced concrete beams at service loads", UNICIV report No. R-315, May. Department of Structural Engineering, The University of New South Wales.

140. Uy, B. and Bradford, M.A., (1993b), "Local buckling behaviour of trough girders composed of an assemblage of profiled steel sheets", UNICIV report No. R-317, June. Department of Structural Engineering, The University of New South Wales.

141. Uy, B. and Bradford, M.A., (1993c), "Elastic local buckling behaviour of thin steel plates in profiled composite beams", UNICIV report No. R-323. Department of Structural Engineering, The University of New South Wales.

142. Uy, B. and Bradford, M.A., (1994a), "Service load tests on profiled steel and concrete composite and reinforced concrete beams", Magazine of Concrete Research, Vol. 46, No. 166, 29-33.

143. Uy, B. and Bradford, M.A., (1994b), "Slenderness limits for thin steel plates restrained by concrete". Proceeding of the Australian Structural Engineering Conference, Sydney, Australia.

144. Uy, B. and Bradford, M.A., (1994c), "Inelastic buckling behaviour of thin steel plates in profiled composite beams", UNICIV report No. R-328. Department of Structural Engineering, The University of New South Wales.

145. Uy, B. and Bradford, M.A., (1995), "Local buckling of trough girders composed of an assemblage of profiled steel sheets", Thin Walled Structures, Vol. 22, pp. 97-120.

146. Veljkovic, M. (1993), "Development of a New Sheeting Profile for Composite Floors", Research Report 1993:47, Luleå University of Technology.

147. Warner, R.F., (1969), "Biaxial Moment Thrust Curvature Relations," Journal of the Structural Division, ASCE, Vol. , No. 56, pp. 923-940

148. Warner R.F. and Yeo, M.F., (1984a), "Collapse behaviour of Concrete Structures with Limited Ductility', Report No. R61, Department of Civil Engineering, The University of Adelaide, Australia.

149. Warner, R.F. and Yeo, M.F., (1984b), "Critical Softening of Hinges in Indeterminate Beams and Portal Frames," Civil Engineering Transactions, Institution of Engineers Australia, Vol. CE26, No. 2. May, pp. 148-149

150. Warner, R.F., Rangan, B.V. and Hall, A.S., (1989), "Reinforced Concrete", Longman Cheshire.

151. Weisberg, S., (1985), "Applied Linear Regression", John Wiley & Sons.

152. Wong, K., (1989), "Non-linear behaviour of reinforced concrete frames", PhD Thesis, Department of Civil Engineering, The University of Adelaide, Australia.

153. Wright, H.D., (1990), "The buckling of long thin plates in contact with a rigid medium", University of Strathclyde, Department of Civil Engineering, Report HDW B1.

154. Wright, H.D., (1993) "Buckling of plates in contact with a rigid medium", The Structural Engineer, Vol. 71 No. 12, pp. 209-215.

155. Wright, H.D., and Francis, R.W., (1990), "Tests on composite beams with low levels of shear connection", The Structural Engineer, August, Vol. 68, No. 15.

156. Yam, L.P., (1981), "Design of Composite Steel-Concrete Structures", Surrey University Press, London.

157. Yam, L.P., and Chapman, J.C., (1968), "Inelastic behaviour of simply supported composite beams of steel and concrete," Proceedings of the Institution of Civil Engineers, Vol. 41, pp. 651-683.

158. Zhang, S. and Fan. L., (1991), "Hollow web steel encased reinforced concrete frame", Proceedings of the Third International Conference on Steel-Concrete Composite Structures, pp. 365-370

159. Zsutty, T.C., (1968), "Beam Shear Strength Prediction by Analysis of Existing Data", ACI Journal, Proceedings Vol. 65, No. 11, pp. 943 - 951.

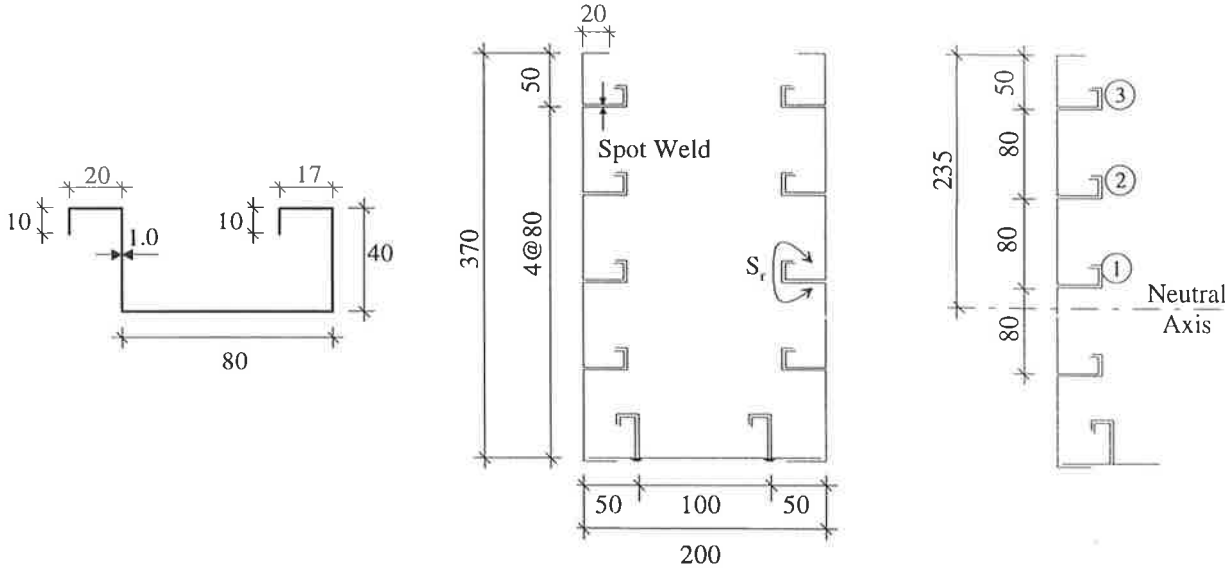
160. Zsutty, T.C., (1971), "Shear Strength Prediction for Separate Categories of Simple Beam Tests", ACI Journal, Proceedings Vol. 68, No. 2, Feb, pp. 138-143.

Appendix A.

Design of Weld Joints

A .1 Profiled Beam PB1

The cross-section of the beam from Fig. 5.10 is shown repeated in Fig. A.1. The total cross-sectional area of profiled sheeting is $A_p = 2452\ mm^2$. The equivalent thickness of the sheeting is given by Eq. 4.6 as $t_e = 2.61$ mm. The plastic neutral axis of the equivalent uniform thickness of sheeting is found by $(2D+b)/4 = 235\,mm$, as shown in Fig. A.1c. At the location of the maximum moment, the sheeting above the neutral axis will be completely in compression, and the sheeting below the neutral axis will be in tension. The tensile and compressive forces must be transferred by longitudinal shear through the joints and by interface bond between the concrete and the sheeting.



(a) Profiled Unit (b) Beam (c) Detail

Fig. A.1. Profiled Sheeting for PB1

The cross-sectional area of an individual profiled unit is $A_u = 220$ mm^2, while the yield stress of the profiled sheeting is $f_{py} = 288$ MPa. The area of sheeting above the neutral axis as shown in Fig. A.1c is 797 mm^2. The total compressive force that is required to yield the sheeting in compression is 230 kN. This force is transferred to the sheeting in the tension zone through interface bond between the concrete and the sheeting and longitudinal shear in the sheeting.

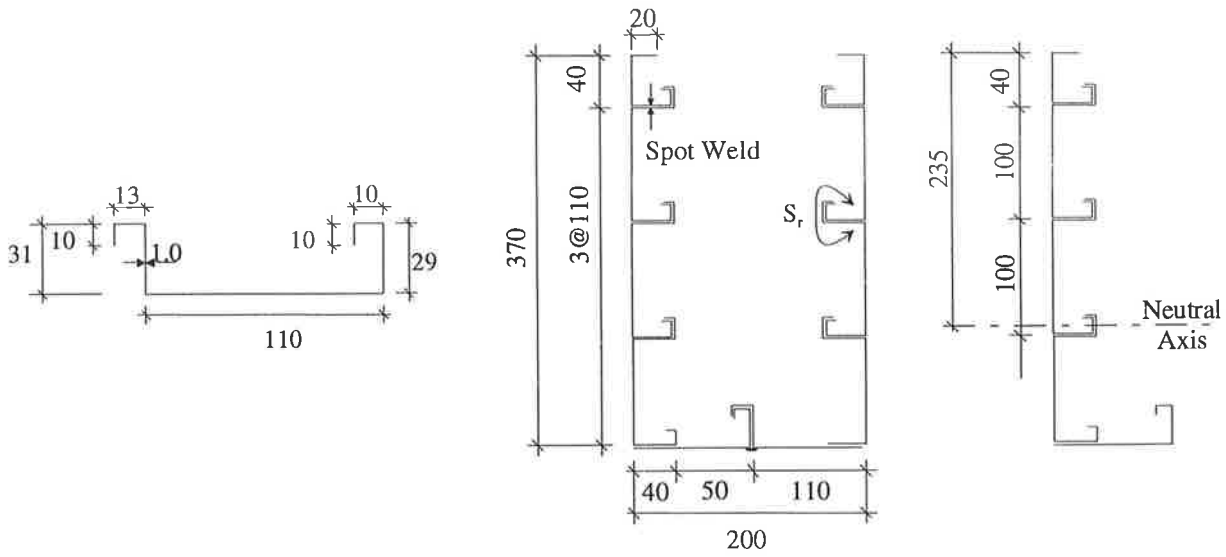
The design bond strength between the sheeting and the concrete is taken as $\tau_b = 0.8$ MPa, based on the results from Section 5.4.2. The rib contact perimeter S_r in Fig. A.1, is 140 mm. Thus, the force that can be transferred between the sheeting and the concrete is $\tau_b S_r = 112$ kN/m per rib. Thus, at the design point which is 1.95 m from the end of the beam, the bond force developed between the sheeting and the concrete in the compression region is 437 kN. This is greater than the force required to yield the sheeting in compression, and thus the welds are not required to carry any longitudinal shear. If a factor of safety of 2.5 is adopted, then the interface bond can resist a force of 175 kN. Thus, 55 kN must be transferred by longitudinal shear through the welds.

The results from a series of tests on the strength of spot welds on the sheeting produced a lower bound design strength of the welds of 3 kN per weld. Thus, a spacing of 100 mm

between welds gives a strength of 30 kN/m. Thus, at the design point at a distance of 1.95 m from the free end, the welds are able to resist a longitudinal shear force of 60 kN.

A .2 Profiled Beam PB3

The cross-section of the beam from Fig 5.30 is shown repeated in Fig. A.2. The total cross-sectional area of profiled sheeting is $A_p = 1800\ mm^2$. The equivalent thickness of the sheeting is given by Eq. 4.6 as $t_e = 1.91$ mm. The plastic neutral axis of the equivalent uniform thickness of sheeting is found by $(2D+b)/4 = 235\,mm$, as shown in Fig. A.2c.



(a) Profiled Unit (b) Beam (c) Detail

Fig. A.2. Profiled Sheeting for PB3

The cross-sectional area of a profiled unit is $A_u = 213\ mm^2$, while the yield stress of the profiled sheeting is $f_{py} = 282$ MPa. The area of sheeting above the neutral axis as shown in Fig. A.2c is $535\ mm^2$. The total compressive force that is required to yield the sheeting in compression is 150 kN. This force is transferred to the sheeting in the tension zone through interface bond between the concrete and the sheeting and longitudinal shear in the sheeting.

The design bond strength between the sheeting and the concrete is taken as $\tau_b = 1.2$ MPa, based on the results from Section 5.4.6.1. The rib contact perimeter S_r in Fig. A.2, is 105 mm. Thus, the force that can be transferred between the sheeting and the

concrete is $\tau_b S_r = 126\,\text{kN/m}$ per rib. Thus, at the design point which is 1.95 m from the end of the beam, the bond force developed between the sheeting and the concrete in the compression region is 490 kN. This is greater than the force required to yield the sheeting in compression, and thus the welds are not required to carry any longitudinal shear. If a factor of safety of 2.5 is adopted, then the interface bond can resist a force of 196 kN. Thus, even with a factor of safety of 2.5, the welds are not required to resist longitudinal shear. Despite this, a weld spacing of 100 mm was adopted for the bottom welds, and 200 mm for the top rib, as shown in Fig 5.30. This conservative measure was taken to ensure that slip between the units did not occur.